

The Optimisation of Luminescent Lanthanide Gold Nanoparticles and Their Detection in Cells with Mass Cytometry

by

JAMIE BRADLEY

A thesis submitted to the University of Birmingham for the degree of

DOCTOR OF PHILOSOPHY

Physical Sciences for Health Centre for Doctoral Training

College of Engineering and Physical Sciences

University of Birmingham

February 2023

UNIVERSITY OF
BIRMINGHAM

University of Birmingham Research Archive

e-theses repository

This unpublished thesis/dissertation is copyright of the author and/or third parties. The intellectual property rights of the author or third parties in respect of this work are as defined by The Copyright Designs and Patents Act 1988 or as modified by any successor legislation.

Any use made of information contained in this thesis/dissertation must be in accordance with that legislation and must be properly acknowledged. Further distribution or reproduction in any format is prohibited without the permission of the copyright holder.

Abstract

Gold nanoparticles (AuNPs) are useful scaffolds for the attachment of luminescent lanthanide complexes and are suited for medical applications due to their modifiable surfaces, biocompatibility and suitable size. These properties have led to the extensive study of AuNPs for diagnostic and therapeutic purposes but their translation to the clinic has proved difficult. The work in this thesis focusses on the synthesis and further characterisation of lanthanide coated AuNPs, the quantification of their uptake at the single cell level with mass cytometry (CyTOF), and their potential as multimodal cellular labels for the identification and detection of mononuclear phagocyte differentiation. The synthesis and characterisation of $LnQuin_2S$-AuNPs and LnS-AuNPs and how different chain lengths affect their photophysical properties and cellular uptake is shown. Using electron energy loss spectroscopy, the localisation of europium atoms around AuNPs is demonstrated, showing that the distance from the europium centre to the gold surface is dictated by the organic structure of its ligands. The effects of coating AuNPs with fluorinated surfactants and a PEG polymer on the photophysical properties of $EuQuin_2S$-AuNPs was studied and it was found that fluorinated surfactants enhance their cellular uptake. The use of CyTOF was then further explored as a highly sensitive, single cell quantitative technique to study the interactions of $EuQuin_2S$-AuNPs with HeLa cells, monocytes, macrophages and dendritic cells. Through novel methods of instrument calibration, the quantification of nanoparticle uptake with CyTOF was validated, showing values in agreement with conventional methods. The distribution of $EuQuin_2S$-AuNPs within a cell population was studied and it was found that their depletion from within cells over time is dependent on cell type. The ratiometric detection of gold and europium/terbium from $EuQuin_2S$-AuNPs and TbS-AuNPs from within cells was also demonstrated. With CyTOF, $EuQuin_2S$-AuNPs can be detected within >99% of macrophages and dendritic cells 7 days after differentiation from NP treated monocytes. Alongside their detection in macrophages by two-photon excitation confocal microscopy, this demonstrated $EuQuin_2S$-AuNPs as potential candidates as multimodal cellular labels.

Acknowledgements

First of all, I'd like to thank my supervisors Zoe, Mike and Ye for their continued support throughout this PhD. I'm sure it lasted far longer than any of us anticipated or hoped when I started back in 2018! Thank you to my fellow Pikramenou group members Elena, Sajni, Irene, Menisha, Patricia, Asier, Andrew, Sarah, Luke, Zhilin, Sunil, Maria, Joe and Grace, it was a pleasure to share an office and lab with you. I'd also like to thank the Hannon and Fossey research groups as well as all the other friendly faces around the chemistry department.

I'd like to thank the Oo group for their friendliness and support, particularly Naomi, Scott and Grace who were so helpful in offering me advice and training in the biomedical research labs. I am particularly grateful for your extended patience with training a chemist in the alien world of cell culture.

My PhD simply would not have been possible without the wonderful assistance from technicians and application specialists at the University of Birmingham. I'd particularly like to thank Shahram for your expertise and advice with mass cytometry, but also Adriana from the flow cytometry facility, Chris, Cécile and Trevor from the chemistry department. Thank you to collaborators Quentin Ramasse and Demie Kepaptsoglou for their time and expertise with our work at the SuperSTEM laboratory. I also extend my gratitude to Dr Song at the University of Warwick for his time and expertise with ICP-MS experiments.

Last but certainly not least I'd like to thank those who have supported me in my personal life during this time. Thanks to Matt for our scientific conversations that kept me inspired throughout. Thank you to Joe and Jess for being such wonderful flatmates for much of my time in Birmingham. Thank you to my mum and dad for their incredible support and love throughout the process. Thank you to Catriona for your extreme patience and goodwill, particularly during the most difficult parts of writing in 2022. And lastly, thank you to my dog Tilly, who literally sat by my side for most of the past few months whilst I wrote this thesis.

LIST OF ABBREVIATIONS ..... F

1 CHAPTER 1: GENERAL INTRODUCTION 8

1.1 Introduction to Lanthanide Chemistry 8

1.2 Introduction to Gold Nanoparticles and their Suitability for Biomedical Applications 13

1.3 Luminescent Metal Complex Functionalised Gold Nanoparticles 15

1.4 Shortfalls in AuNP Biomedical Research: Failure in Translation to the Clinic 18

1.5 Quantifying the Cellular Uptake of Gold Nanoparticles 19

1.6 Thesis Outline 33

1.7 References 34

2 CHAPTER 2: SYNTHESIS, OPTIMISATION AND PHOTOPHYSICAL PROPERTIES OF LUMINESCENT LANTHANIDE GOLD NANOPARTICLES 40

2.1 Introduction 40

2.2 Chapter Outline 47

2.3 Synthesis of Lanthanide Complexes 49

2.4 Photophysical Properties of Lanthanide Complexes in Solution 51

2.5 Synthesis and Characterisation of Lanthanide Coated Gold Nanoparticles 58

2.6 Further Characterisation of Lanthanide Complex Binding to 13 nm Gold Nanoparticle Surfaces 69

2.7 Photophysical Properties of Lanthanide Coated Gold Nanoparticles 86

2.8 Effect of Surfactant and Polymer Coatings on $EuQuin_2S$-AuNP Photophysical Properties and Cellular Uptake 92

2.9 Concluding Remarks 98

2.10 Experimental 100

2.11 References 112

2.12 Appendix 116

3 CHAPTER 3: INVESTIGATIVE STUDIES INTO THE CELLULAR UPTAKE OF LANTHANIDE GOLD NANOPARTICLES WITH CYTOF 128

3.1 Introduction 128
3.2 Chapter Outline 140
3.3 Optimising Sample and Data Preparation for Reliable Single Cell Data Output 142
3.4 Studying EuQuin$_2$S-AuNP Uptake by TEM 153
3.5 Quantification of Nanoparticle Uptake by CyTOF 158
3.6 Ratiometric Detection of Lanthanide Gold Nanoparticles 170
3.7 Studying the Heterogeneity of EuQuin$_2$S-AuNP Uptake in HeLa Cells 177
3.8 Assessing the Nanoparticle Content of HeLa Cells Over Multiple Proliferation Cycles 180
3.9 Conclusion and Future Work 195
3.10 Experimental 198
3.11 References 205
3.12 Appendix 209

4 CHAPTER 4: INVESTIGATIVE STUDIES INTO THE USE OF EUQUIN$_2$S-AUNPS AS MULTIMODAL CELLULAR LABELS 213

4.1 Introduction 213
4.2 Chapter Outline 223
4.3 Results and Discussion 224
4.4 Concluding Remarks 271
4.5 Experimental 273
4.6 References 279
4.7 Appendix 283

5 CHAPTER 5: GENERAL CONCLUSIONS 288

5.1 General Conclusion and Future Work 288

6 CHAPTER 6: GENERAL EXPERIMENTAL 291

6.1 Materials 291
6.2 Techniques and Instrumentation 291

List of abbreviations

AgNP	Silver Nanoparticle
APC	Antigen Presenting Cell
AuNP	Gold Nanoparticle
BODIPY	4,4-difluoro-4-bora-3a,4a-diaza-*s*-indacene
CD	Cluster of Differentiation
CFDA-SE	Carboxyfluorescein diacetate succinimidyl ester
CFSE	Carboxyfluorescein succinimidyl ester
CT	Computed Tomography
CTEM	Conventional Transmission Electron Microscopy
CV	Coefficient of Variation
CyTOF	Cytometry by Time-of-Flight (Mass Cytometry)
DLS	Dynamic Light Scattering
DMEM	Dulbecco's Modified Eagle Medium
DNA	Deoxyribonucleic Acid
DP	Differential Power
DTPA	Diethylenetriaminepentaacetic Acid
EDTA	Ethylenediaminetetraacetic acid
EELS	Electron Energy Loss Spectroscopy
ET	Energy Transfer
FACS	Fluorescence-Activated Cell Sorting
FBS	Fetal Bovine Serum
FCS	Flow Cytometry Standard
FITC	Fluorescein isothiocyanate
FSA	Fluorosurfactant
FSC	Forward Scatter
GFP	Green Fluorescent Protein
GMP	Good Manufacturing Practice
HAADF	High-Angle Annular Dark-Field
HUVEC	Human Umbilical Vein Endothelial Cells
ICP	Inductively Coupled Plasma
ICP-AES	Inductively Coupled Plasma Atomic Emission Spectroscopy
ICP-MS	Inductively Coupled Plasma Mass Spectrometry

IMD	Integrated Mass Data
IL-4	Interleukin-4
iDC	Immature Dendritic Cell
ITC	Isotherm Titration Calorimetry
IQR	Interquartile Range
LPS	Lipopolysaccharide
MRI	Magnetic Resonance Imaging
M0	Resting Stage Macrophages
M1	Classically Activated Macrophages
mDC	Mature Dendritic Cell
MHC	Major Histocompatibility Complex
NIR	Near infrared
NLV	Nanoparticle Loaded Vesicle
NMR	Nuclear Magnetic Resonance
NP	Nanoparticle
PBMC	Peripheral Blood Mononuclear Cells
PBS	Phosphate Buffer Saline
PDI	Polydispersity Index
PEG	Polyethylene Glycol
PET	Positron Emission Tomography
PMA	Phorbol-12-myristate-13-acetate
RPMI-1640	Roswell Park Memorial Institute
SD	Standard Deviation
SPECT	Single Photon Emission Computed Tomography
SPIONS	Superparamagnetic Iron Oxide Nanoparticles
SPR	Surface Plasmon Resonance
SSC	Side Scatter
STEM	Scanning Transmission Electron Microscopy
TE	Transmission Efficiency
TEM	Transmission Electron Microscopy
TFD	*N*-(2-(ethylthio)ethyl)-2,2,3,3,4,4,5,5,6,6,7,7,8,8,9,9,10,10,11,11,12,12,12-tricosafluorododecanamide
TOF	Time-of-Flight
UV	Ultraviolet

Chapter 1: General Introduction

1.1 Introduction to Lanthanide Chemistry

1.1.1 Introduction to Lanthanides and their Properties

The lanthanide (Ln) elements are the group of 15 elements from lanthanum to lutetium, situated in the f-block of the periodic table. For a group of elements once referred to as the 'rare-earth' metals, they are relatively abundant – cerium, the most plentiful of the lanthanides, is only slightly less abundant than copper[1] and even the least abundant, thulium, is more so than mercury.[2] It is in fact the difficulty of obtaining lanthanides in their pure elemental form that is a rarity, a task that took well over a century because of their similar properties and tendency to congregate in the same substances.[3] The 15 elements from Ln to Lu feature electronic configurations ranging from [Xe]$4f^0 5d^1 6s^2$ to [Xe]$4f^{1}45d^1 6s^2$, and the 4*f* electrons are added sequentially across the group when lanthanides adopt a +3 oxidation state. This oxidation state is displayed almost exclusively as it strikes the best balance between ionisation energy cost and lattice-energy or solvation-energy stabilisation of the ion, but in some rare cases Sm, Eu and Yb display a +2 oxidation state, and Ce, Pr, Nd, Tb and Dy display a +4 oxidation state.[4] Due to the lack of shielding afforded by electrons held in the 4*f* orbital, a slight decrease in atomic radii from La(III) (1.17 Å) to Lu(III) (1.00 Å) is observed across the group with increasing atomic number, known as the lanthanide contraction.[5]

Ln(III) cations behave as hard Lewis acids due to their high surface charge density, and therefore strongly coordinate hard Lewis bases such as anionic oxygen and nitrogen atoms.[6] They most commonly adopt a coordination number of 8 or 9, but a range of 3-12 can be observed depending on steric factors governed by the surrounding ligands.[7, 8] As the 4*f* electrons are shielded by the $5s^2$ and $5p^6$ orbitals, they are unavailable for covalent interaction with ligands and coordination of ligands to Ln(III) is purely electrostatic. Consequently, all Ln(III) complexes of the same ligand are isostructural.[9]

Ln(III) luminescence originates from transitions within the 4*f* orbitals but they cannot efficiently absorb light (the molar absorptivity is typically 1-10 $M^{-1}cm^{-1}$)[10] due to *f* – *f* transitions being forbidden by the Laporte and orbital angular momentum selection rules. Organic chromophores with high molar absorptivity are therefore commonly incorporated into coordinating ligands to sensitise their luminescence, known as the antenna effect.[11] After absorption of a photon leading to excitation of the first singlet excited state (S_1) of the chromophore and subsequent intersystem crossing to the longer lived, lower energy triplet state (T_1), the energy can be transferred to the Ln(III) centre (Figure 1.1). Relaxation from the Ln(III) excited to ground state results in the emission of light with wavelengths characteristic of the particular transition of each lanthanide.[12]

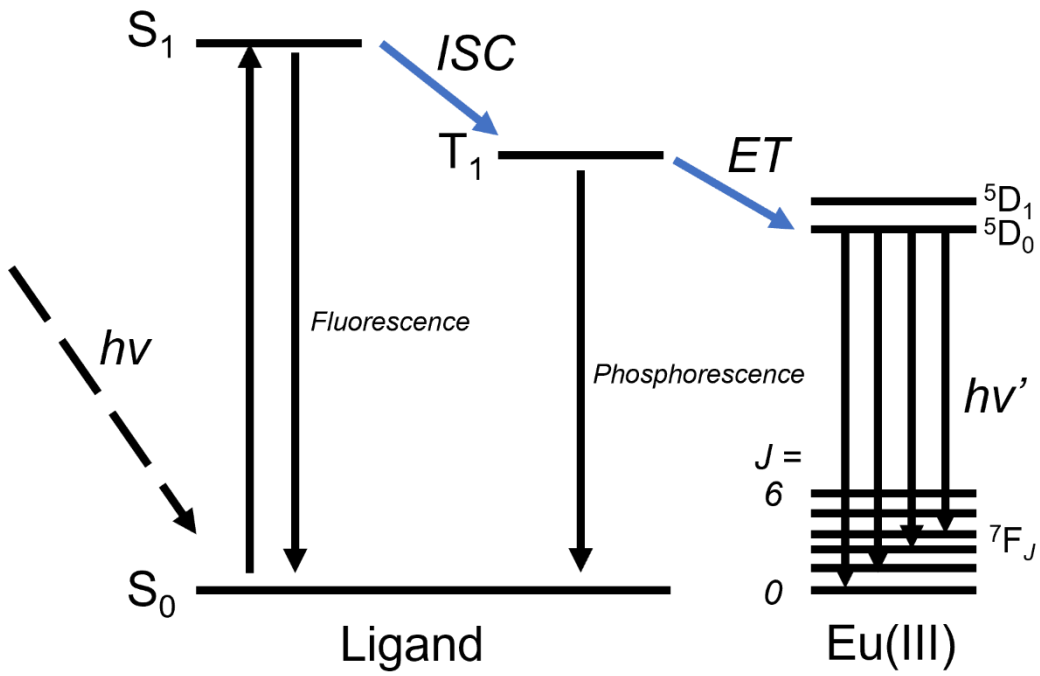


Figure 1.1 - Schematic representation of the antenna effect resulting in emission from Eu(III). Light is absorbed by the first singlet excited state (S_1) of an organic chromophore is excited, and after intersystem crossing (ISC) to the triplet state (T_1) of the ligand and subsequent energy transfer (ET) to the Eu(III) centre, radiative decay to the ground state leads to emission characteristic of Eu(III).

The overall efficiency of emission observed from Ln(III) depends on the efficiency of intersystem crossing, energy transfer and the intrinsic metal centred luminescence quantum yield of the Ln(III) ion. Furthermore, lanthanides usually exhibit very long

luminescence lifetimes and as a consequence they can undergo energy transfer to high frequency vibrational oscillators such as OH and NH and quench luminescence.[13] Ln(III) ions with lower excited state energies are worse affected as the deactivation by vibronic coupling of OH is more efficient.[14] Ln(III) emission in the near-infrared (NIR) region of the electromagnetic spectrum is therefore strongly reduced and often difficult to observe. This makes ligand design particularly important when utilising lanthanides in solvents such as water, where high coordination numbers can reduce the opportunity for hydroxyl oscillators to bind to the Ln(III) centre.

The luminescent properties of lanthanides have been intensively studied for numerous optical imaging applications.[15-19] Despite the quenching effects discussed, they often exhibit long luminescence lifetimes in the μs to ms range,[20] much longer than organic chromophores and transition metal complexes with lifetimes typically in the ns to μs range.[21] This allows for the separation of signal from short-lived fluorescence with time-gated techniques; particularly useful for biomedical applications where autofluorescence from biological material is present.[11, 22] The large stokes shifts allows for clear separation of excitation and emission signals, and characteristic sharp emission peaks are easily distinguishable, advantageous in high-parameter multi-colour experiments with techniques such as flow cytometry.[4] Unlike with organic chromophores, the Ln(III) ion offers protection from photobleaching which makes lanthanides more suitable for long-term imaging or cell-tracking studies.[23] The deeper penetration of tissue afforded by luminescence in the NIR region due to reduced light absorption, photon scattering and autofluorescence, has led to many recent studies on NIR emitting lanthanides such as Yb and Nd for *in vivo* imaging applications .[24-26]

1.1.2 Ligand Design for Lanthanide Complexation in Aqueous Media

The coordination sphere surrounding a Ln(III) cation has a large effect on the properties of a lanthanide complex and ligand design is therefore imperative for achieving the lanthanides intended properties. The dehydration of Ln(III) in aqueous solution is endothermic, meaning complexation of lanthanides is entropy driven.[27] Polydentate ligands can help overcome this difficulty due to the chelate effect to form highly stable complexes in aqueous medium. Ln(III) cations prefer hard binding sites, so anionic ligands such as carboxylates, phosphinates and β-diketonates are well suited due to their large electrostatic components.[28] High coordination numbers are essential in aqueous media to limit solvent coordination to prevent the binding of hydroxyl oscillators quenching emission through non-radiative pathways. The ligand(s) should also possess one or several chromophores to act as a light harvesting antenna, allowing excitation of the Ln(III) centre. This sensitising unit should be in close proximity to the metal centre as the energy transfer processes are distance dependent,[29] have a high molar absorption coefficient, and have a triplet state higher than the lanthanide acceptor state.[30] In this work, attachment of lanthanide complexes to gold nanoparticles must also be considered in the ligand design. This requires terminal groups capable of binding strongly to the gold surface, anchoring the complex to the surface of the nanoparticle. Thiol terminated ligands are a popular choice as they can create Au-S bonds that have a strength close to that of Au–Au bonds.[31, 32] The distance that the ligand holds the Ln(III) metal from the surface of the nanoparticle is also important, as quenching of fluorescence signal is observed at short distances from plasmonic nanoparticles, owed to a ‘near-field’ effect involving energy or electron transfer non-radiative pathways.[33, 34] A previous study by our group showed that adding an alkyl chain ‘spacer’ group that distances a Ru(II) metal centre further away from 13, 50 and 100 nm gold nanoparticles increases the luminescence lifetime.

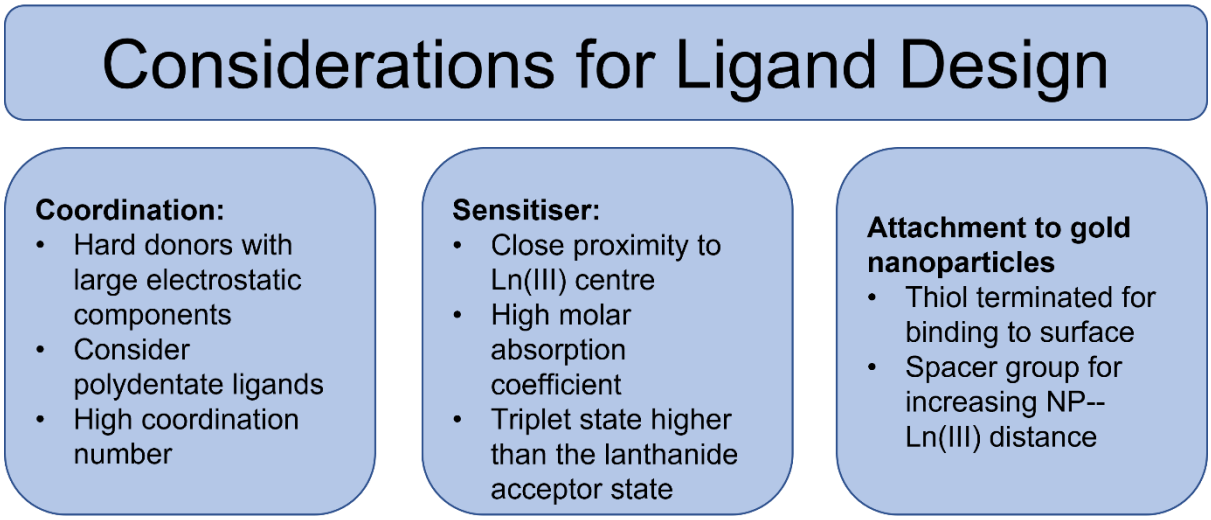


Figure 1.2 - Considerations for the design of suitable ligands for complexing Ln(III) metals for their use in aqueous media, attached to gold nanoparticles.

An important class of acyclic ligands is based on a polyaminopolycarboxylate system, where four or more acetic groups are attached to a polyamino skeleton such as diethylenetriaminepentaacetic acid (DTPA), forming 8-coordinate lanthanide complexes that are highly stable in aqueous medium. Gd(III)-DTPA complexes have been studied extensively as contrast agents for magnetic resonance imaging (MRI), of which there are many examples that are approved for use.[35-38] The stability of these complexes has been shown to be very high, and for many years it was thought that there is practically no acute toxic effects from dissociation of Gd(III) from the ligand,[39] but in 2006 they were associated with a fatal condition called nephrogenic systemic fibrosis.[40] Although these findings have led to renewed interest in finding alternative contrast agents, Gd(III)-DTPA based MRI agents are still widely used and adverse events remain low. Antenna ligands such as phenols,[41] quinolines,[42] napthalenes[43] and bipyridines[44] can also be added to the DTPA backbone to sensitise lanthanide metals to achieve strong luminescence, which will be shown in this work.

1.2 Introduction to Gold Nanoparticles and their Suitability for Biomedical Applications

The nanoscale has been referred to as the 'natural length scale of biology'.[45] Nanotechnology advancements in recent decades have therefore greatly impacted the field of medicine, leading to significant improvements in areas such as drug[46] and vaccine delivery,[47] imaging[48] and diagnostics,[49] tissue engineering[50] and the development of antimicrobial materials.[51] Nanomaterials often possess unique properties compared to bulk materials attributed to larger surface area, self-assembly and quantum effects.[52]

The tuneable size and shape of gold nanoparticles (AuNPs) alongside their resulting unique properties has led to extensive research for their use in medicine.[53] AuNPs have a strong characteristic absorption of radiation in the visible and near-IR region of the electromagnetic spectrum which arises due to a phenomenon known as surface plasmon resonance (SPR). The electrons at the gold surface collectively oscillate in response to incident light, creating a resonant condition that results in a strong absorption of light at a specific wavelength, known as the SPR wavelength.[54] The wavelength of the radiation absorbed is characteristic of the specific size and shape of the AuNP, as well as its immediate surroundings such as attached ligands.[55] Spherical AuNPs larger than 2 nm in diameter exhibit SPR in the visible range, making them easily characterised by visible spectroscopy techniques.[56]

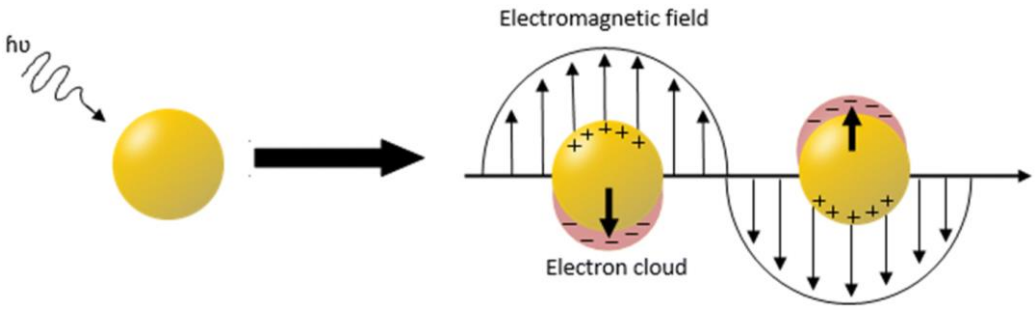


Figure 1.3 - Schematic representation of surface plasmon resonance of spherical gold nanoparticles. Image reproduced from Fuller *et al.*

Alongside their unique optical properties, AuNPs have other qualities that make them attractive for biomedical applications. AuNPs are generally considered biocompatible due

to their water-solubility, suitable size, chemical stability and low toxicity (the toxicity of nanomaterials, however, is complex and often poorly understood and is discussed later in this introduction).[57-59] The modifiable nature of AuNP surfaces allows for their functionality and tailoring of surface chemistry, determined by their stabilising ligands or molecules. Spherical AuNPs are often synthesised with citrate-stabilising ligands that form a capping layer to prevent aggregation and clumping together.[60] The electrostatic forces between carboxylate anions of citrate and the AuNP surface are relatively weak compared to strong chemical bonds formed between gold and elements such as sulphur; an Au—S bond has a strength close to that of the Au—Au bond.[26] This allows simple exchange citrate-stabilised AuNPs with thiol-terminated ligands for almost endless customisation of surface chemistry providing the AuNPs remain thermodynamically stable. Functionalisation of AuNP surfaces with ligands as diverse as DNA,[61] metal complexes,[41, 42, 62] intercalators,[63] antibodies[64] and peptides[65] has been shown, demonstrating the versatility of an AuNP scaffold.

The optical properties, large surface area and the capability to multi-functionalise AuNP surfaces makes them ideal for *in vitro* diagnostic assays, perhaps most notably in lateral flow tests during the COVID-19 pandemic.[66] AuNPs are functionalised with capturing molecules such as nucleic acid fragments or antibodies that specifically bind to the analyte of interest, with detection using properties such as SPR for readout.[49] The large surface area allows the detection of very low concentrations of analytes. AuNPs have also been studied intensively for *in vivo* applications. This includes photothermal therapy for treating diseases such as cancer.[67] When AuNPs are exposed to light of specific wavelength, they absorb the energy and convert it to heat by a process known as plasmonic heating. This can raise the temperature of the surrounding tissue and kill cancer cells.[68] The large surface area of AuNPs has also been exploited for drug delivery, as high quantities of therapeutic agents can be loaded on the surface.[59, 63]

AuNPs have also been utilised as scaffolds for dense localisation of fluorescent and luminescent molecules, enabling their use in biomedical imaging applications. Conventionally used fluorophores such as Cy-5 and BODIPY have been coated on AuNP surfaces via electrostatic forces of attraction.[69, 70] However, limitations of fluorophore attachment include photobleaching and dissociation from the AuNP surface.[71, 72] Alternatively, thiol-terminated metal complexes can be covalently attached, which our group has pioneered over the last two decades for imaging AuNPs in cells.

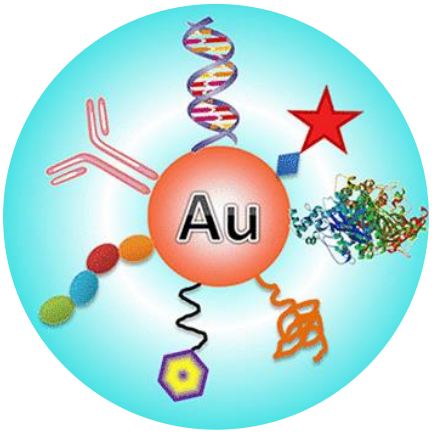


Figure 1.4 - The unique optical properties of AuNPs and the ability to functionalise their surface with fluorescent agents, DNA, antibodies, peptides, intercalators and other agents makes them useful nanomaterials for a range of biomedical applications. Image adapted from Zhou *et al.*

1.3 Luminescent Metal Complex Functionalised Gold Nanoparticles

Lanthanide and transition metal complexes are attractive luminescent agents due to their high photostability, large Stoke shifts and long luminescence lifetimes that allow for the separation of signal from background autofluorescence in biomedical imaging.[73] Suitable design of ligands with terminating groups such as thiols allows for the attachment of hundreds to thousands of complexes onto the surface of single AuNPs, massing a high concentration of complexes in a small area to provide strong luminescence.[74] The water-soluble nature of AuNPs alongside their chemical stability and biocompatibility makes them attractive scaffolds for attaching luminescent complexes for use in biological studies.

We have previously shown the attachment of two luminescent europium complexes to 13 nm AuNPs.[41, 42] The design and photophysical properties of these lanthanide gold nanoparticles will be discussed more in the introduction of chapter 2. Davies *et al.* multifunctionalised with a DTPA-quinoline europium complex and a pH sensitive peptide, delivering europium AuNPs into platelets at pH 6.5. Luminescence microscopy images showed luminescence from the Eu centre, confirming their localisation within platelets (Figure 1.5).

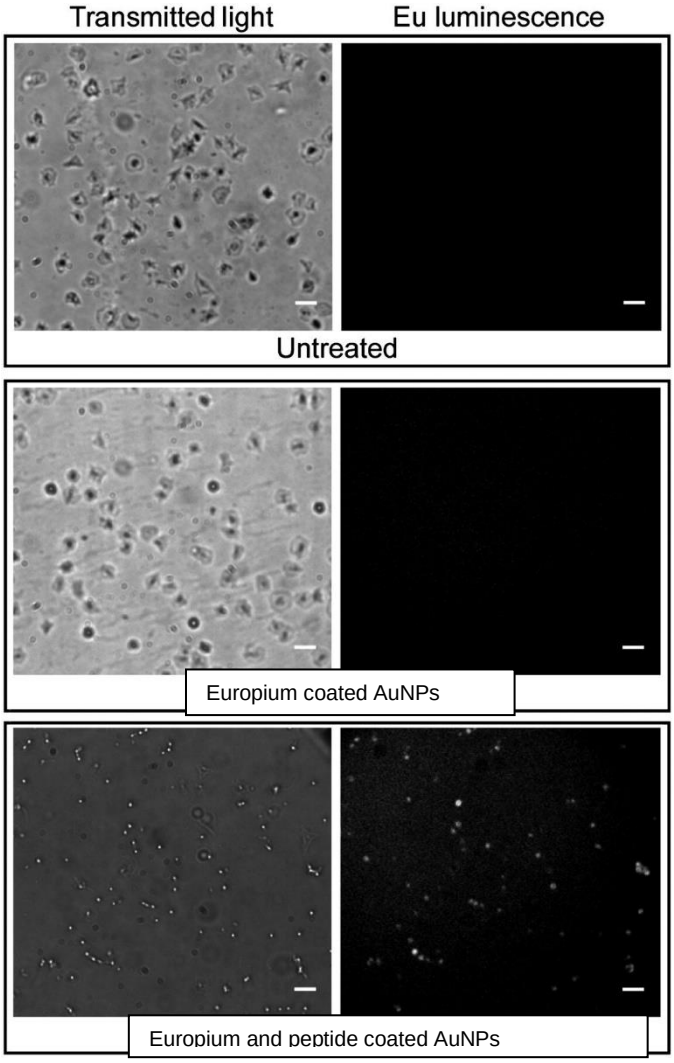


Figure 1.5 - Confocal microscopy of human platelets: untreated (top), treated with europium coated AuNPs (middle), treated with AuNPs coated with a europium complex and a pH sensitive peptide (bottom), which allowed entry to the platelets and emission from europium was subsequently observed. (λ_{exc} = 340 nm, λ_{em} < 510 nm). Scale bar = 10 µm. Image reproduced from Davies *et al.*

Recently, imaging of ruthenium and iridium metal complex coated AuNPs has been shown in several studies by our group. A study by Rogers *et al.* functionalised 13 and 100 nm AuNPs with a polypyridyl Ru (II) complex, attached to the NP surface by a thiol-terminated hexyl chain on one bipyridine ligand.[75] Due to their positive charges, transition metals can cause aggregation upon addition to AuNPs, so the AuNPs were coated with a Zonyl FSA fluorosurfactant prior to complex addition is required to provide further stabilisation. The ruthenium AuNPs were taken up by A549 cancer cells and were detectable within cells by luminescence imaging. TEM images of the NPs within cells revealed nuclear localisation and the interaction of 100 nm NPs with chromatin.

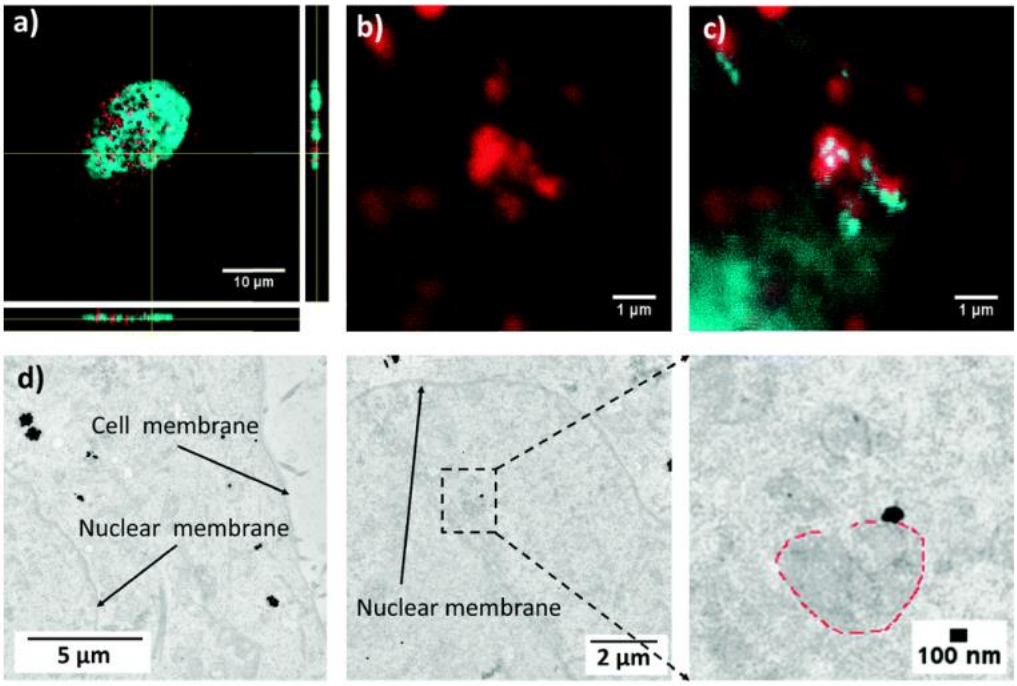


Figure 1.6 -(a) Co-localisation of luminescence from a Hoechst nuclear stain (green) with ruthenium coated AuNPs in a z-stack confocal microscopy image (red); (b) ruthenium luminescence from ruthenium coated AuNPs in a confocal microscopy image; (c) Overlay of (b) with Hoechst nuclear stain luminescence channel; (d) TEM images of A549 cells treated with 100 nm ruthenium coated AuNP, showing a NP in the nucleus of a cell next to condensed chromatin (red dashed line). Image adapted from Rogers *et al.*

A recent study by King *et al.* attached luminescent iridium complexes to 13, 25 and 100 nm AuNPs after stabilisation with Zonyl FSA.[62] Luminescence was observed from the NPs in HeLa cells by lifetime confocal microscopy imaging, with two-photon excitation. A short-lived lifetime directly from the AuNPs was also observed. In a separate study, a similar

luminescent iridium complex was used to coat 100 nm AuNPs and track the flow of blood in narrow vessels.[76] The long-lived lifetime allowed for enhanced resolution in comparison to conventional alternatives. After injecting the iridium coated AuNPs into mice, they entered blood circulation and were clearly detected in small blood vessels in lungs, mesentery and skeletal muscles.

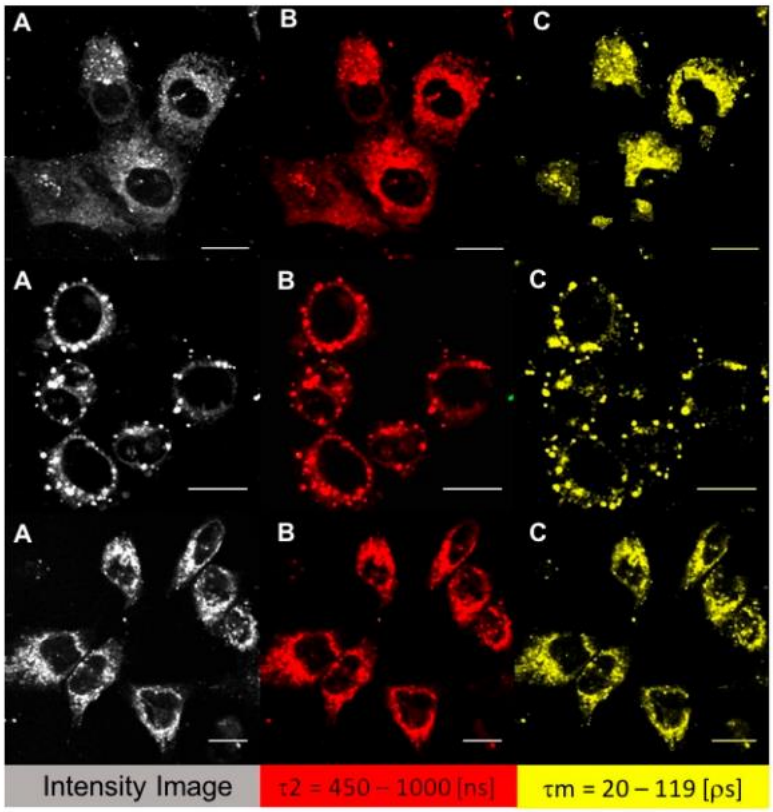


Figure 1.7 - Two-photon luminescence lifetime imaging of 13 (bottom), 25 (top) and 100 (middle) nm iridium coated AuNPs in HeLa cells, (A) is the intensity image, (B) is the iridium luminescence lifetime (450-1000 ns) and (C) is the short-lived lifetime signal (20-119 ps) from gold. Figure adapted from King *et al.*

1.4 Shortfalls in AuNP Biomedical Research: Failure in Translation to the Clinic

Nanomedicines seek to improve on conventional diagnostics and therapies. Although there are over 100 nanomedicines in clinical trials and 30 already approved,[77] these are predominantly organic and lipid based NPs and despite significant research over recent decades, there has been extremely limited success with bringing metal nanomedicines to

the clinic. Exceptions include clinically approved iron oxide NPs for magnetic resonance imaging,[78] hafnium oxide NPs that are in phase II/III clinical trials for the treatment of soft tissue sarcoma[79] and polyethylene glycol coated silica-gold nanoshells for thermal ablation of solid lung tumours that are in ongoing clinical trials.[80]

The disconnect between research investment and academic publication and clinical translation is likely due to many reasons. First of all, the toxicities and nano-bio interactions are unclear, due to the complex nature of nanomaterials and the number of parameters that may contribute, such as size, shape, surface functionalisation and charge.[81] Additionally, the synthetic methods of metal NP synthesis restricts scalability and the ability to screen large numbers of potential candidates in pre-clinical studies.[82] The complexity and cost of manufacturing also makes meeting good manufacturing practice (GMP) requirements more difficult than conventional therapies. The lack of understanding in differences in physiology and pathology between animal studies and humans,[46] as well as patient heterogeneity and the potential caution of use of types of medicines that are different to those conventionally used may also contribute to the lack of translation. What would certainly improve the success rate of nanomaterials reaching the clinic is new technologies that better our understanding of their interactions with biological material. One key interaction is their uptake and internalisation by cells. The cellular uptake of gold nanoparticles is discussed in this introduction alongside current and new techniques for quantification.

1.5 Quantifying the Cellular Uptake of Gold Nanoparticles

1.5.1 Brief Introduction to the Cellular Uptake of Gold Nanoparticles

Utilising AuNPs in cellular studies usually requires their internalisation or ‘cellular uptake’. Understanding AuNP cellular uptake and its extent is therefore of paramount importance to the field. In order for uptake to occur, AuNPs must first reach the cellular membrane and then interact with the cell membrane. This is a complex process dependent on many

factors, including the physicochemical properties of the AuNP species, the biological environment and also the experimental conditions and parameters. This section is primarily focussed on AuNP cellular uptake; however literature of other NP types is also discussed where relevant and appropriate.

When considering the journey of AuNPs to the cell membrane of cells, their interaction within the biological fluid environment is important. In cell culture models, the most common and simplistic use of examining AuNP-cell interactions, AuNPs are mixed with a cell culture media and supplemented with fetal bovine serum (FBS) that maintains and supports the growth of a cell population. This media, albeit more simplistic, mimics the interactions that AuNPs may experience *in vivo*. When AuNPs are introduced to this fluid, they immediately interact with proteins and biomolecules that often adsorb onto the AuNP surface to form a 'protein corona'.[83] This protein corona is often the 'biological identity' of AuNPs and is hugely important for their cellular uptake.[84] Protein corona formation is dependent on AuNP physicochemical properties such as size, shape, polydispersity, charge, surface chemistry, and hydrophobicity, as well as biological factors such as protein source and experimental factors such as mixing,[85] incubation temperature and ionic strength.[86] The formation (or lack of formation) of NP protein coronas and its implications has been studied intensively and is well documented in many literature reviews.[87-90]

Once AuNPs have interacted with the biological environment, properties such as their size and density will determine whether they remain evenly dispersed within the media or sediment to the bottom of the vessel. For AuNPs less than 100 nm in diameter that remain stable in biological media, the Brownian motion experienced is far greater than the gravitational pull, so they remain dispersed, but larger AuNPs or agglomerates may reach the cell surface membrane by sedimentation.[91] A study by Wills *et al.* showed that when large agglomerates of silica nanoparticles form, the largest 2% of agglomerates are responsible for 90% of the cellular uptake.[92] Cho *et al.* have also studied the effects of

sedimentation/diffusion on cellular uptake of AuNPs by using upright and inverted cell culture configurations, finding that cells generally take up more AuNPs when in the upright position, suggesting that sedimentation is an important consideration for AuNP uptake, particularly for large nanospheres and nanocages.[93]

When AuNPs reach the exterior of the cell membrane, they can interact with the plasma membrane or extracellular matrix and enter the cell. Most NPs are predominantly taken up by endocytosis mechanisms.[86] This process involves the association of NPs to the cell membrane and the engulfment of NPs in membrane invaginations. Once scission proteins such as clathrin cut the membrane, NPs are contained within endosomes inside the cell. There are five types of endocytosis: clathrin mediated endocytosis, caveolae dependent endocytosis, clathrin/caveolae independent endocytosis, macropinocytosis, and phagocytosis, all of which have slightly different mechanisms, but lead to the eventual containment of NPs within endosomes inside cells.[94, 95] Endocytosis may be dependent on recognition of specific receptors for initiation, which could be caused by the NP or its biological identity.[96-98] It may also occur non-specifically like in the case of macropinocytosis where large ‘gulps’ of extracellular fluid are internalised during cytoskeleton rearrangement.[99] Furthermore, NPs may be taken up by chance if they are associated with the membrane at the time of invagination of non-NP related endocytosis. A recent thorough perspective article by Dawson and co-workers discusses our current understanding of nanoparticle interactions with the cellular membrane and also details the importance of the duration of the NP-membrane event in cellular uptake.[45] The entry of AuNPs into cells via non-endocytic routes has also been reported. Stellacci and co-workers observed that a ribbon-like, alternating arrangement of two ligands (one hydrophilic and one hydrophobic) on AuNPs led to passive entry through the cell membrane and directly into the cytosol.[100]

Passive penetration of other nanomaterials such as quantum dots and cationic AuNPs and SiNPs has also been shown.[101-103]

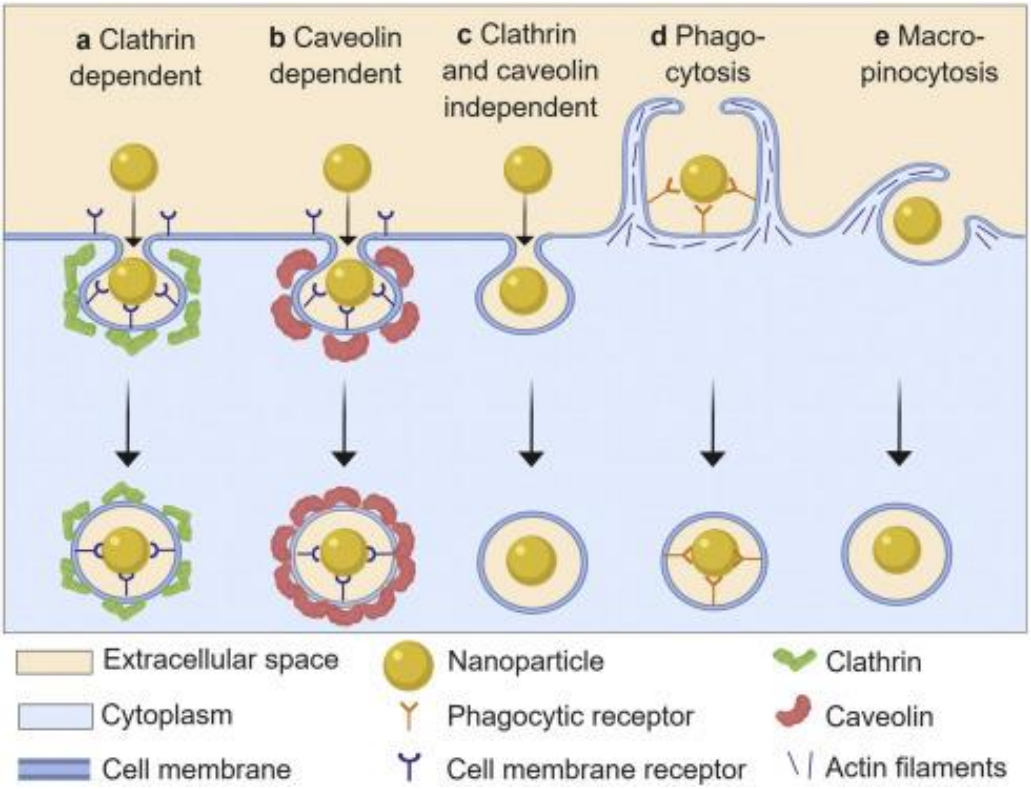


Figure 1.8 - Nanoparticles can be taken up by cells through various endocytic mechanisms, including clathrin-mediated endocytosis, caveolin-mediated endocytosis, clathrin and caveolin-independent endocytosis, phagocytosis, and macropinocytosis. NPs can enter cells by binding to specific cell surface receptors that recognise clathrin or caveolin – two proteins that play a major role in the formation of vesicles, but they can also enter cells through endocytic pathways that do not rely on clathrin or caveolin. These pathways are less understood but may involve lipid rafts or other membrane components. Additionally, NPs can be engulfed by cells through phagocytosis, a process primarily carried out by immune cells like macrophages and neutrophils, and also by macropinocytosis, a non-specific, actin-driven process where cells engulf extracellular fluid along with particles present in the surrounding environment. Image reproduced from Donahue *et al.*

The physicochemical properties of AuNPs influence their cellular uptake.[104] Size effects the 'wrapping' interaction with the cell membrane that occurs during endocytosis, and an AuNP size of around 50 nm has been shown as optimal for highest uptake.[105, 106] Shape is another important factor;[107] for example spherical AuNPs have been shown to be taken up in higher quantities than gold nanorods.[108, 109] Surface charge is very significant and studies have shown a more favourable interaction between cationic NPs than neutral or negatively charged NPs[110] which can lead to higher uptake.[111, 112] Hydrophobicity is also important, as

well as surface functionality. PEGylation of NPs is well known to increase circulation times of NPs by evading phagocytosis from innate immune cells,[113] and has been shown to reduce uptake.[114] Coating AuNPs with biomolecules such as folic acid can also enhance the cellular uptake.[115] Experimental factors also affect the cellular uptake of AuNPs. Chithrani *et al.* have shown how the cellular uptake increases with concentration and also

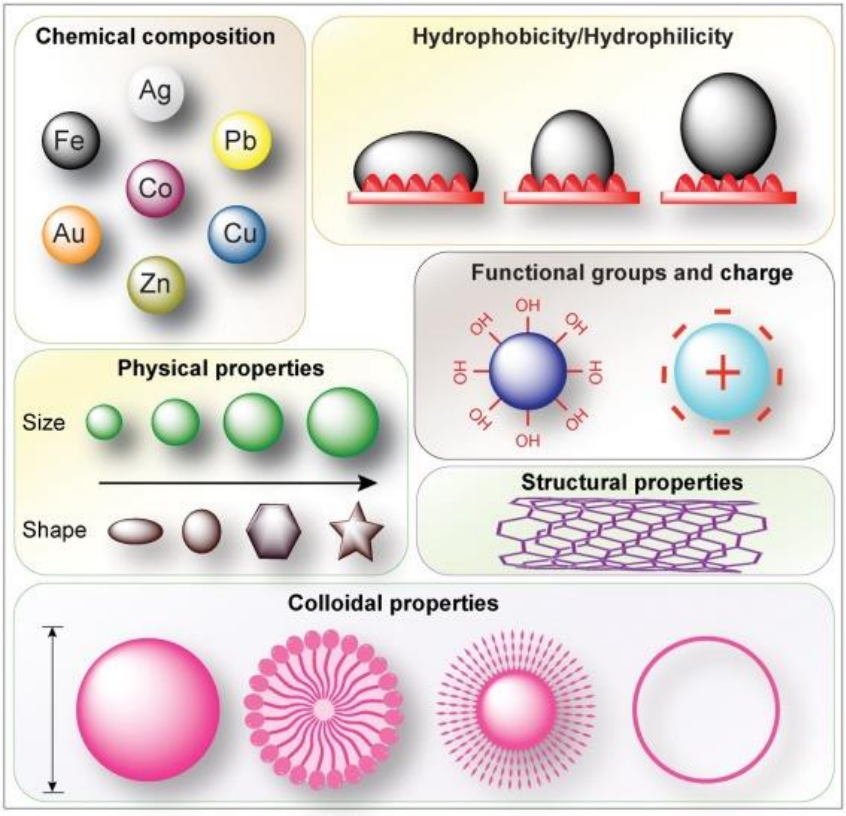


Figure 1.9 - Properties of NPs that influence their cellular uptake. Image reproduced from Augustine *et al.*

that the rate of cellular uptake is fastest within the first few hours of incubation time with AuNPs.[105] A recent study demonstrated that even chirality can affect uptake; Xu *et al.* observed much higher uptake for left-handed chiral AuNPs than their right-handed counterparts.[116] This chirality also led to different *in vitro* and *in vivo* immune responses.

1.5.2 Methods to Quantify Gold Nanoparticle Uptake

The ability to quantify cellular uptake allows the study of the effect of changing parameters such as nanoparticle surface coating, size, concentration and incubation for optimising the design for the intended application. Furthermore, quantifying a number of gold

nanoparticles per cell is highly useful for comparing results of studies on toxicity and cell viability. Insight into safe intracellular gold concentrations and understanding uptake will be essential in regard to the clinical use of AuNPs in medicine.

Many techniques can be used to quantify the uptake of gold nanoparticles, each with their own advantages and disadvantages. Fluorescence based techniques such as confocal microscopy and flow cytometry are very commonly used to quantify the uptake of fluorescent nanoparticles. Although as AuNPs are not generally intrinsically fluorescent, they are often not suitable for analysis by these techniques, or they may require subsequent labelling, which in turn will alter their surface properties. With confocal microscopy, single cells can be studied and provide information on the NP location within the cells. Several previous studies by our group have used confocal microscopy to show intracellular localisation of AuNPs coated with luminescent metal complexes,[42, 62] including a study showing ruthenium coated gold nanoparticle uptake with quantification comparable to parallel ICP-MS experiments (explained later in this section).[117] Other disadvantages of confocal microscopy include that it is low throughput, photobleaching[118] or detachment of fluorophore from NPs may occur,[71] and clusters rather than single NPs can usually only be detected. Flow cytometry allows detection by fluorescence at high throughput and the

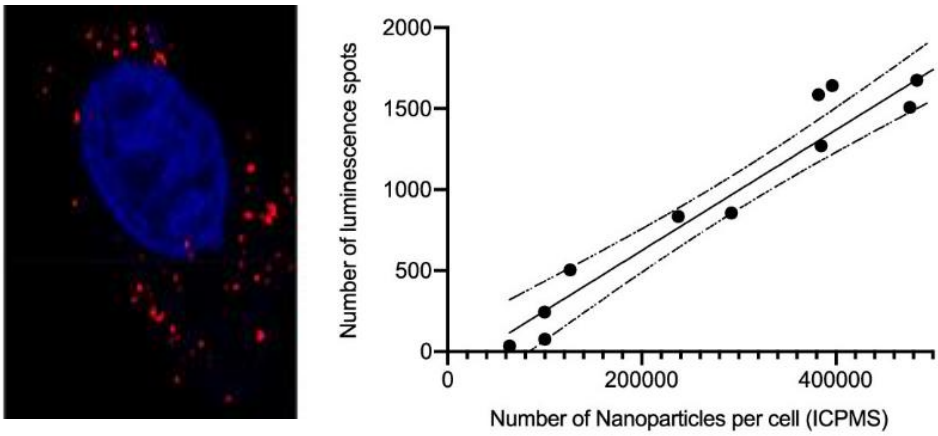


Figure 1.10 - Quantification of the cellular uptake of AuNPs coated with luminescent metal complexes has previously been shown in a study by our group with confocal microscopy by counting the number of luminescent spots in an image (left). Quantification was in broad agreement with ICP-MS. Image modified and reproduce from Dosumu *et al.*

potential to simultaneously measure other cellular parameters by fluorescent antibody labelling, at the expense of intracellular location.[119] However, without normalisation data, Dawson *et al.* showed that due to size-dependence of the fluorescence intensity, results on cellular uptake can be easily misinterpreted.[120]

Transmission electron microscopy (TEM) has been widely used in determining AuNP uptake and can provide extremely high-resolution images of AuNPs within sub-cellular structures. TEM can not only provides information on the intracellular fate of AuNPs,[114] but also on the mechanism of uptake[100, 117] and interactions with cellular organelles.[121] As TEM provides images of thin specimens (ca. 70-90 nm[122]), it is difficult to quantify overall AuNP uptake and it is extremely low throughput. Preparing TEM samples is also difficult and time consuming.[123]

Inductively coupled plasma (ICP) spectroscopy is perhaps the most commonly used technique to quantify the cellular uptake of AuNPs.[124] All atoms in a sample are ionised by an ICP torch of up to 10000 K and detected by either mass (ICP-MS) or atomic emission spectroscopy (known as ICP-AES or ICP-OES).[125] This allows the quantification of gold atoms within a sample and a number of AuNPs per cell can be calculated from prior knowledge of AuNP size and the total number of cells. These techniques provide a simple and accurate quantification of all types of metal NPs and require no modification from their original form. Furthermore, most instrumentation can detect elemental concentrations ranging from ppt to ppm, allowing for a large range in NP uptake to be studied, but large populations of cells are needed. It is also important to consider that this technique does not decipher between NPs intracellularly and extracellularly associated with cells and thorough washing of samples to remove all NPs in solution is vital for accurate results.[126] It also only provides an average number of NPs per cell, rather than any information on the distribution of NPs within a population. Moreover, consistently accurate cell counts are required as well

as the digestion of samples with strong reagents such as aqua regia[127] or hydrogen peroxide.[128]

In recent years, spectroscopic ICP methods have been advanced to output data in a time resolved manner.[129] By detecting discrete pulses of positively charged ions using microsecond data acquisition rates, single NPs and cells can be analysed.[130] Merrifield *et al.* have shown the cellular uptake of 1, 2 or 3 AuNPs per algal cell with single particle ICP-MS (SP-ICP-MS), showing the instruments incredible sensitivity.[131] Malysheva *et al.* used the NP size-determining capabilities of single cell ICP-MS (SC-ICP-MS) to show that AgNPs can undergo different size transformations within cells.[132] However, using SP-ICP-MS to quantifying NP uptake remains largely unexplored and it has not been demonstrated as a technique capable of detecting greater than a few NPs per cell, limiting its application to ultra-trace detection. Another ICP-MS technique capable of detecting NPs within single cells is mass cytometry (see next section).

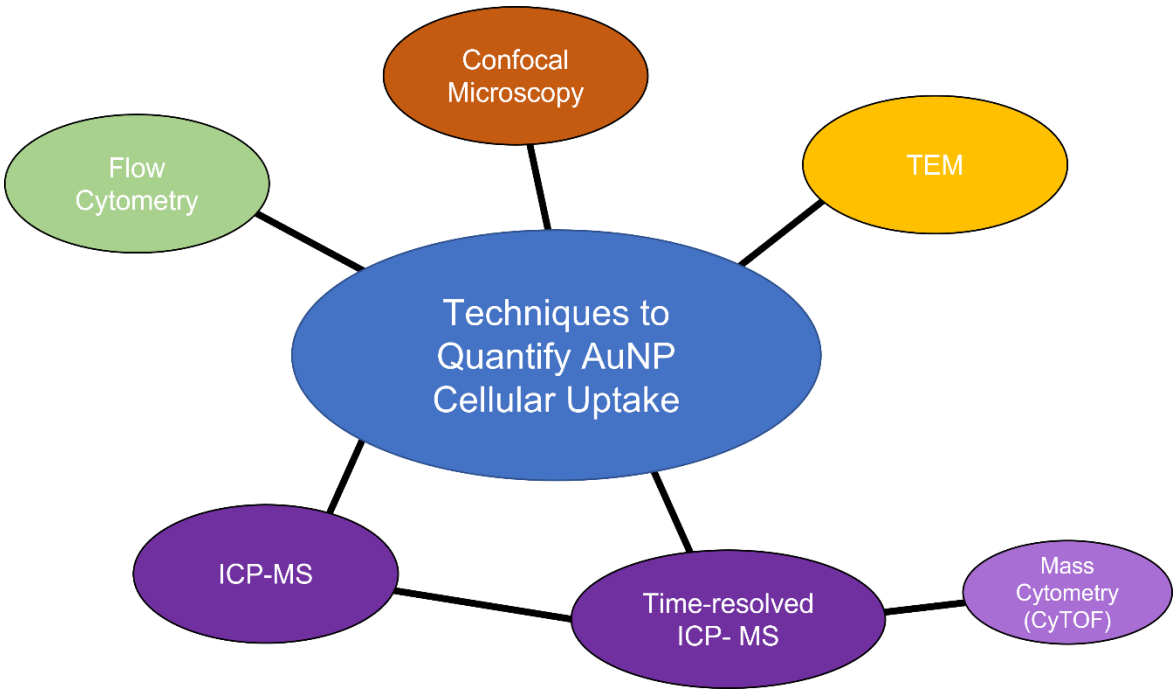


Figure 1.11 - Techniques to quantify the cellular uptake of AuNPs.

1.5.3 Mass Cytometry (CyTOF)

By combining time-of-flight mass spectrometry with single cell microfluidics, mass cytometry (CyTOF) is a recently developed technique that allows for the quantification of metals associated with single cells.[133] CyTOF was primarily designed as a high-parameter cellular phenotyping technology, where antibodies are tagged with unique metal isotopes which are distinguished between in a time-of-flight MS (TOF-MS) with 135 detection channels, eliminating the concern of spectral overlap with fluorophore conjugated antibodies in flow cytometry and allowing for up to 45 parameters to be simultaneously analysed.[134] But since any element between 75 and 209 Da can be detected, it offers label-free uptake quantification of metal NPs such as gold at the single cell level. This single cell analysis capability is its major strength; it reveals the distribution of NPs within a cell population, a key lacking feature of conventional ICP-MS analysis of metal NPs. It also allows for the distinction of cell-associated NPs from non-cell associated NPs in solution, as well as the ability to detect cells that contain no NPs at all. Labelling with other metal isotopes (and antibodies conjugated with metals) also allows for discriminating between live and dead cells, identifying cell types and even the effect of NPs on cell phenotype and function.[135]

In 2015, the latest CyTOF instrument, Helios, was launched, increasing the maximum limit of detection to 4.5 orders of magnitude and allowing quantification of single to thousands of metal NPs per cell.[40] Earlier NP research with CyTOF focussed on conjugation to antibodies and their use as high mass labels to detect rare cell surface markers on cells,[136-138] but this increase in magnitude allowed researchers to use the technology to further study NP uptake and other NP-cell interactions, first demonstrated by Yang *et al.* in 2017.[69] Several further studies have followed, but the use of CyTOF as a technique to study NP-cell interactions still remains in its infancy. A full literature review of previous studies using CyTOF to detect NPs is given in 3.1.1. In this section, a brief introduction how CyTOF

technology works is given, followed by a description of the experimental workflow of CyTOF experiments to quantify NP uptake.

1.5.3.1 Principles of CyTOF

Single cell analysis by CyTOF requires the metals associated with each cell to be detected within separate, discrete time windows, known as events.[139] The Helios instrument has five major components to achieve this: sample introduction and ionisation, ion transport through vacuum interface, high-pass ion optics, ion-separation by TOF mass analyser, and data acquisition and processing (Figure 1.12).[140] First cells are introduced to the nebuliser, where the liquid suspension is aerosolised into single cell droplets. The aerosol is then partially vaporised in the heated spray chamber and directed towards the ICP source. Here, the single cell aerosol droplets are fully vaporised, atomised and ionized in the plasma, resulting in ion clouds corresponding to each cell. Ions are then transported through the vacuum interface, where through a series of cones the pressure is reduced and ions are focussed to the downstream ion optics. An electrostatic field accelerates and deflects the ions perpendicularly towards the TOF region, separating any remaining photons or neutral material that could reduce sensitivity.[140] At this point, the ion cloud still contains all ionised material associated with each cell; predominantly low-mass ions naturally abundant in biology. These are removed by a high-pass ion optic that only allows ions >75 Da through to the TOF detector.[140] In the TOF mass analyser, ions are separated based on their mass-to-charge (m/z) ratio. A pulse of several hundred volts is applied at 13 µs intervals (known as a push), accelerating each beam of ions towards the detector into tight time-resolved bands, respective of their m/z ratio. The detector uses a dynode electron multiplier to detect the separate ions. When an ion strikes the first dynode of the detector, several secondary electrons are released, which in turn generate more electrons at the next dynode.[140] The process is repeated at each dynode, given the required multiplication needed for an electrical pulse that can be captured by the anode of the detector. This output analog signal

is converted to digital values collected by the instrument as a raw integrated mass data (IMD) file, which represents a matrix of ion counts for each selected mass channel for every push.[141]

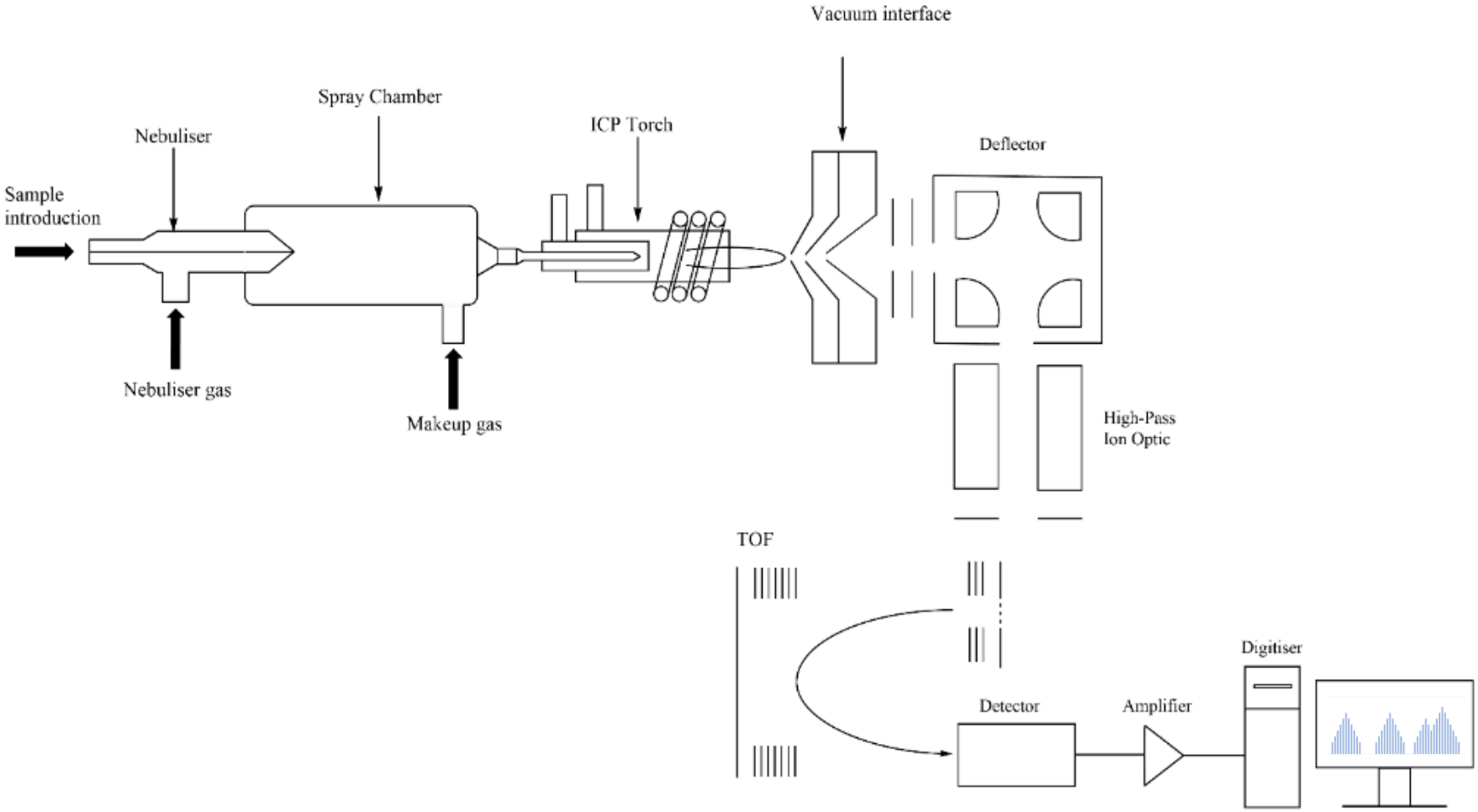


Figure 1.12 - Schematic representation of the main components of mass cytometry instrumentation

This time resolved data can be further processed by excluding continuous ion counts across multiple pushes that are not within the minimum and maximum event length limits (Figure 1.13), leaving discrete events that can be analysed as single cell entities. Further manual data processing known as gating is required to filter out debris and cell-cell doublets/aggregates. It is highly important that few non-cell associated metal contaminants (including NPs) are present in the solution during acquisition, as this can cause continuous ion count detection that exceed the maximum event length threshold, meaning discrete events are not analysed. After manual gating, the signal corresponding to the metal of interest, for example ^{197}Au for AuNPs, can be used to quantify NP uptake, if the transmission efficiency of the metal is known (this is explained in our work in chapter 3).

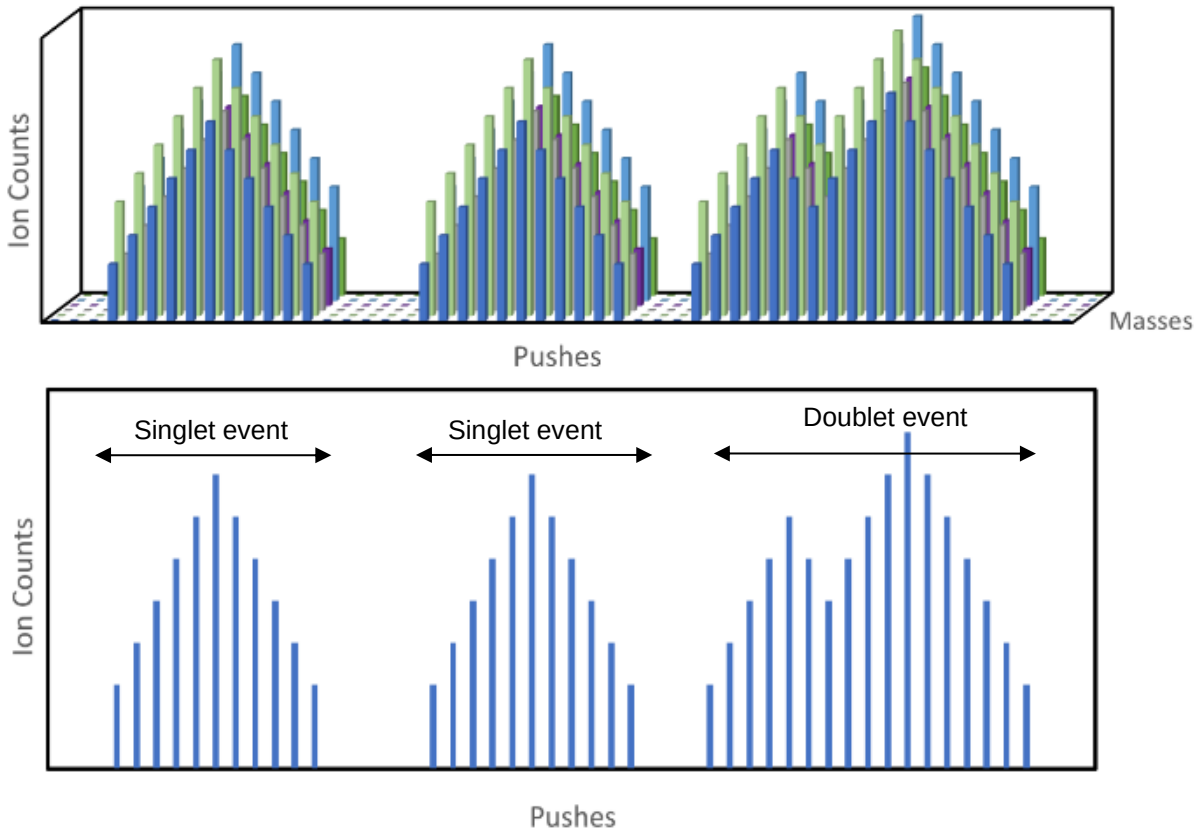


Figure 1.13 – Graphical representation (not real data) of the conversion of signal from a mass channel in CyTOF to quantifiable, time-resolved single cell events. (a) Individual push data from each mass channel of interest is integrated into ion counts. (b) Signals that are within the defined event length threshold are selected for analysis as single events. Doublet events can be removed by manual gating by identifying doublet events using the quantity of iridium detection from the Cell-ID Intercalator-Ir.

1.5.3.2 Workflow of CyTOF experiments to quantify the cellular uptake of NPs

The cell population of interest is incubated with NPs under the conditions of interest, allowing the cellular uptake of NPs. Residual NPs remaining in solution are then removed by washing and each cell sample is transferred to a tube suitable for centrifugation (e.g., a FACS tube) for subsequent labelling steps that reveal important information on each cell. The first labelling step is a cisplatin viability assay that distinguishes live and dead cells, due to the preferential interaction of cisplatin with dead cells that can be detected in the platinum channels of the mass cytometer. If heterogeneous cell samples are used rather than cell lines, cells are then labelled with any extracellular metal conjugated antibodies that reveal phenotypical features and allow the distinction of specific cell types. Cells are then fixed to preserve their current biological state[142] and stained with Cell-ID Intercalator-Ir, an iridium based cationic DNA intercalator that can be used to discriminate single and doubly nucleated cells.[143] This also ensures that no events containing more than one cell are mistakenly analysed as a single cell event if they coincidentally pass through the instrumentation within the same ion cloud. Cells are then further washed to remove any non-cell associated, residual metal contaminants in solution, mixed well to ensure cells are well dispersed, and introduced to the mass cytometer via a micro-fluidic system one cell at a time.

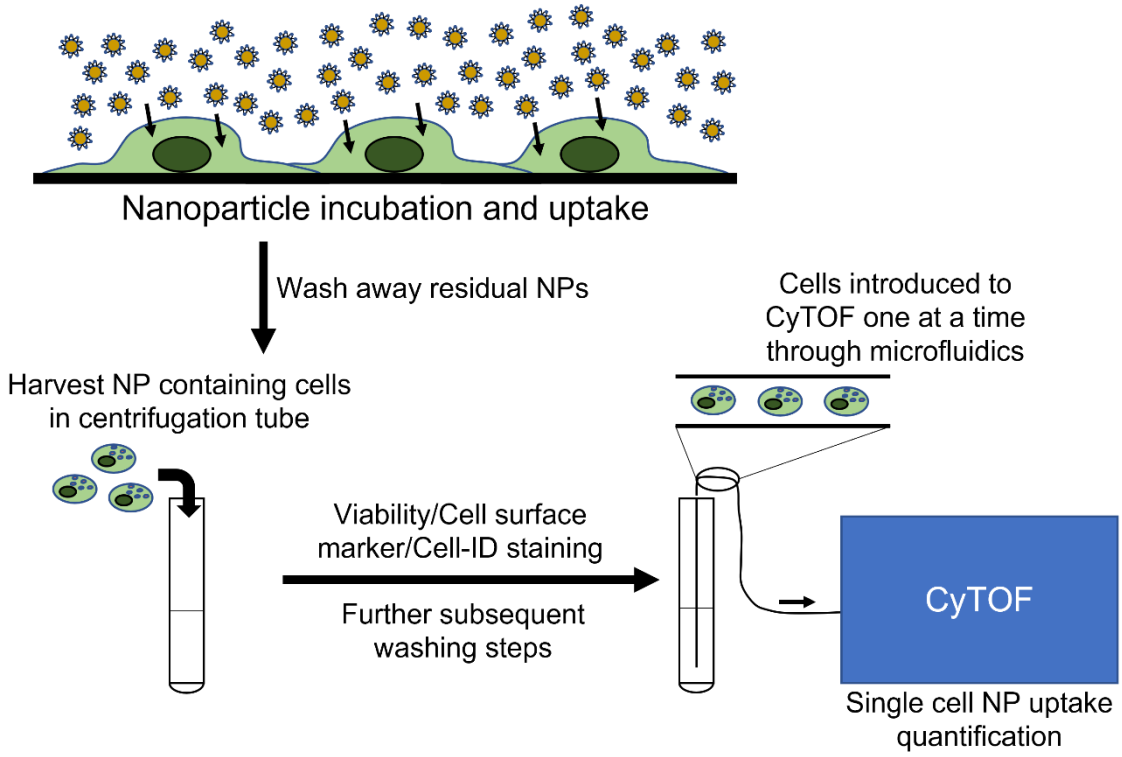


Figure 1.14 - Workflow of CyTOF experiments to quantify the cellular uptake of NPs.

1.6 Thesis Outline

The aim of the work in this thesis is to synthesise and characterise lanthanide coated gold nanoparticles and study their photophysics, cellular uptake and assess their suitability as multimodal cellular labels for monitoring monocyte differentiation into macrophages and dendritic cells. Each research chapter contains a short literature review as an introduction and an outline of the hypotheses and scope. This is followed by the results and discussion, concluding remarks and an experimental section. A general conclusion and future work chapter follows the 3 research chapters, and the general experimental is the final chapter.

Chapter 2 investigates the synthesis, characterisation and photophysical properties of lanthanide gold nanoparticles, as well as the effect of surfactants and polymers on the properties of lanthanide gold nanoparticles.

Chapter 3 further investigates the use of CyTOF as a technique to quantify NP uptake at the single cell level alongside novel applications of CyTOF technology to our research.

Chapter 4 investigates the cellular uptake of lanthanide gold nanoparticles in mononuclear phagocytes and assesses their potential use as cellular labels for detecting monocyte differentiation into macrophages and dendritic cells by CyTOF, as well as their detection in macrophages by luminescence imaging.

1.7 References

1. J. A. Peters, J. Huskens and D. J. Raber, *Progress in Nuclear Magnetic Resonance Spectroscopy*, 1996, **28**, 283-350.
2. D. Parker, R. S. Dickins, H. Puschmann, C. Crossland and J. A. K. Howard, *Chemical Reviews*, 2002, **102**, 1977-2010.
3. W. J. Evans, D. S. Lee, D. B. Rego, J. M. Perotti, S. A. Kozimor, E. K. Moore and J. W. Ziller, *Journal of the American Chemical Society*, 2004, **126**, 14574-14582.
4. L. Armelao, S. Quici, F. Barigelletti, G. Accorsi, G. Bottaro, M. Cavazzini and E. Tondello, *Coordination Chemistry Reviews*, 2010, **254**, 487-505.
5. N. Sabbatini, M. Guardigli and J.-M. Lehn, *Coordination Chemistry Reviews*, 1993, **123**, 201-228.
6. A. K. R. Junker, L. R. Hill, A. L. Thompson, S. Faulkner and T. J. Sørensen, *Dalton Transactions*, 2018, **47**, 4794-4803.
7. W. R. Dawson, J. L. Kropp and M. W. Windsor, *The Journal of Chemical Physics*, 1966, **45**, 2410-2418.
8. D. Parker, J. D. Fradgley and K.-L. Wong, *Chemical Society Reviews*, 2021, **50**, 8193-8213.
9. J. V. Caspar and T. J. Meyer, *Journal of the American Chemical Society*, 1983, **105**, 5583-5590.
10. K. E. Martin, A. G. Cosby and E. Boros, *Journal of the American Chemical Society*, 2021, **143**, 9206-9214.
11. R. Xiong, D. Mara, J. Liu, R. Van Deun and K. E. Borbas, *Journal of the American Chemical Society*, 2018, **140**, 10975-10979.
12. N. Hamon, A. Roux, M. Beyler, J.-C. Mulatier, C. Andraud, C. Nguyen, M. Maynadier, N. Bettache, A. Duperray, A. Grichine, S. Brasselet, M. Gary-Bobo, O. Maury and R. Tripier, *Journal of the American Chemical Society*, 2020, **142**, 10184-10197.
13. J.-C. G. Bünzli and C. Piguet, *Chemical Society Reviews*, 2005, **34**, 1048-1077.
14. J.-C. G. Bünzli, *Accounts of Chemical Research*, 2006, **39**, 53-61.
15. S. Faulkner, S. J. A. Pope and B. P. Burton-Pye, *Applied Spectroscopy Reviews*, 2005, **40**, 1-31.
16. U. Cho and J. K. Chen, *Cell Chemical Biology*, 2020, **27**, 921-936.
17. K. Hanaoka, K. Kikuchi, H. Kojima, Y. Urano and T. Nagano, *Journal of the American Chemical Society*, 2004, **126**, 12470-12476.
18. J.-C. G. Bünzli, *Chemical Reviews*, 2010, **110**, 2729-2755.
19. D. Jin, R. Connally and J. Piper, *Cytometry Part A*, 2007, **71A**, 783-796.
20. Y. Xing and J. Rao, *Cancer Biomarkers*, 2008, **4**, 307-319.
21. X. Ge, R. Wei and L. Sun, *Journal of Materials Chemistry B*, 2020, **8**, 10257-10270.

22. J. Xu, A. Gulzar, P. Yang, H. Bi, D. Yang, S. Gai, F. He, J. Lin, B. Xing and D. Jin, *Coordination Chemistry Reviews*, 2019, **381**, 104-134.
23. A. P. Bassett, S. W. Magennis, P. B. Glover, D. J. Lewis, N. Spencer, S. Parsons, R. M. Williams, L. De Cola and Z. Pikramenou, *Journal of the American Chemical Society*, 2004, **126**, 9413-9424.
24. T. Lazarides, D. Sykes, S. Faulkner, A. Barbieri and M. D. Ward, *Chemistry – A European Journal*, 2008, **14**, 9389-9399.
25. M. Hasegawa, H. Ohmagari, H. Tanaka and K. Machida, *Journal of Photochemistry and Photobiology C: Photochemistry Reviews*, 2022, **50**, 100484.
26. H. Häkkinen, *Nature Chemistry*, 2012, **4**, 443-455.
27. M.-C. Daniel and D. Astruc, *Chemical Reviews*, 2004, **104**, 293-346.
28. F. Liu and J.-M. Nunzi, *Applied Physics Letters*, 2011, **99**, 123302.
29. J. Kümmerlen, A. Leitner, H. Brunner, F. R. Aussenegg and A. Wokaun, *Molecular Physics*, 1993, **80**, 1031-1046.
30. J. Wahsner, E. M. Gale, A. Rodríguez-Rodríguez and P. Caravan, *Chemical Reviews*, 2019, **119**, 957-1057.
31. A. Z. Khawaja, D. B. Cassidy, J. Al Shakarchi, D. G. McGrogan, N. G. Inston and R. G. Jones, *Insights Imaging*, 2015, **6**, 553-558.
32. J. Malone, D. Tiberi, C. Frankish, T. Nguyen, J. Sinclair and S. Malone, *Radiology Case Reports*, 2020, **15**, 850-853.
33. K. Affram, T. Smith, S. Helsper, J. T. Rosenberg, B. Han, J. Trevino and E. Agyare, *Cancer Nanotechnology*, 2020, **11**.
34. P. Caravan, J. J. Ellison, T. J. McMurry and R. B. Lauffer, *Chemical Reviews*, 1999, **99**, 2293-2352.
35. P. Marckmann, L. Skov, K. Rossen, A. Dupont, M. B. Damholt, J. G. Heaf and H. S. Thomsen, *Journal of the American Society of Nephrology*, 2006, **17**, 2359.
36. D. Parker, *Chemical Society Reviews*, 2004, **33**, 156-165.
37. D. E. Reichert, J. S. Lewis and C. J. Anderson, *Coordination Chemistry Reviews*, 1999, **184**, 3-66.
38. E. M. Gale, P. Caravan, A. G. Rao, R. J. McDonald, M. Winfeld, R. J. Fleck and M. S. Gee, *Pediatric Radiology*, 2017, **47**, 507-521.
39. D. R. Bandura, V. I. Baranov, O. I. Ornatsky, A. Antonov, R. Kinach, X. Lou, S. Pavlov, S. Vorobiev, J. E. Dick and S. D. Tanner, *Analytical Chemistry*, 2009, **81**, 6813-6822.
40. Helios, a CyTOF system User Guide, https://www.fluidigm.com/binaries/content/documents/fluidigm/resources/helios-user-guide0400250/helios-user-guide0400250/fluidigm%3Afile, (accessed May, 2021).
41. D. J. Lewis, T. M. Day, J. V. MacPherson and Z. Pikramenou, *Chemical Communications*, 2006, DOI: 10.1039/b518091k, 1433-1435.
42. A. Davies, D. J. Lewis, S. P. Watson, S. G. Thomas and Z. Pikramenou, *Proceedings of the National Academy of Sciences*, 2012, **109**, 1862-1867.
43. M. Vera, H. Santacruz Ortega, M. Inoue and L. Machi, *Supramolecular Chemistry*, 2019, **31**, 336-348.
44. J. M. Couchet, J. Azéma, C. Galaup and C. Picard, *Journal of Luminescence*, 2011, **131**, 2735-2745.
45. K. A. Dawson and Y. Yan, *Nature Nanotechnology*, 2021, **16**, 229-242.
46. M. J. Mitchell, M. M. Billingsley, R. M. Haley, M. E. Wechsler, N. A. Peppas and R. Langer, *Nature Reviews Drug Discovery*, 2021, **20**, 101-124.
47. X. Hou, T. Zaks, R. Langer and Y. Dong, *Nature Reviews Materials*, 2021, **6**, 1078-1094.
48. X. Han, K. Xu, O. Taratula and K. Farsad, *Nanoscale*, 2019, **11**, 799-819.
49. W. Zhou, X. Gao, D. Liu and X. Chen, *Chemical Reviews*, 2015, **115**, 10575-10636.

50. A. Hasan, M. Morshed, A. Memic, S. Hassan, T. J. Webster and H. E. Marei, *International Journal of Nanomedicine*, 2018, **13**, 5637-5655.
51. K. S. Siddiqi, A. Husen and R. A. K. Rao, *Journal of Nanobiotechnology*, 2018, **16**, 14.
52. N. Baig, I. Kammakakam and W. Falath, *Materials Advances*, 2021, **2**, 1821-1871.
53. X. Yang, M. Yang, B. Pang, M. Vara and Y. Xia, *Chemical Reviews*, 2015, **115**, 10410-10488.
54. M. A. Fuller and I. Köper, *Nano Convergence*, 2019, **6**, 11.
55. S. K. Ghosh, S. Nath, S. Kundu, K. Esumi and T. Pal, *The Journal of Physical Chemistry B*, 2004, **108**, 13963-13971.
56. H. M. E. Azzazy, M. M. H. Mansour, T. M. Samir and R. Franco, *Clinical Chemistry and Laboratory Medicine*, 2012, **50**, 193-209.
57. H. J. Johnston, G. Hutchison, F. M. Christensen, S. Peters, S. Hankin and V. Stone, *Critical Reviews of Toxicology*, 2010, **40**, 328-346.
58. G. Zhang, Z. Yang, W. Lu, R. Zhang, Q. Huang, M. Tian, L. Li, D. Liang and C. Li, *Biomaterials*, 2009, **30**, 1928-1936.
59. R. Arvizo, R. Bhattacharya and P. Mukherjee, *Expert Onions For Drug Delivery*, 2010, **7**, 753-763.
60. J. Turkevich, P. C. Stevenson and J. Hillier, *Discussions of the Faraday Society*, 1951, **11**, 55-75.
61. X. Shen, C. Song, J. Wang, D. Shi, Z. Wang, N. Liu and B. Ding, *Journal of the American Chemical Society*, 2012, **134**, 146-149.
62. S. M. King, S. Claire, R. I. Teixeira, A. N. Dosumu, A. J. Carrod, H. Dehghani, M. J. Hannon, A. D. Ward, R. Bicknell, S. W. Botchway, N. J. Hodges and Z. Pikramenou, *Journal of the American Chemical Society*, 2018, **140**, 10242-10249.
63. A. B. Caballero, L. Cardo, S. Claire, J. S. Craig, N. J. Hodges, A. Vladyka, T. Albrecht, L. A. Rochford, Z. Pikramenou and M. J. Hannon, *Chemical Science*, 2019, **10**, 9244-9256.
64. E. S. Day, L. R. Bickford, J. H. Slater, N. S. Riggall, R. A. Drezek and J. L. West, *International Journal of Nanomedicine*, 2010, **5**, 445-454.
65. X. Liu, Y. Wang, P. Chen, A. McCadden, A. Palaniappan, J. Zhang and B. Liedberg, *ACS Sensors*, 2016, **1**, 1416-1422.
66. J. Budd, B. S. Miller, N. E. Weckman, D. Cherkaoui, D. Huang, A. T. Decruz, N. Fongwen, G.-R. Han, M. Broto, C. S. Estcourt, J. Gibbs, D. Pillay, P. Sonnenberg, R. Meurant, M. R. Thomas, N. Keegan, M. M. Stevens, E. Nastouli, E. J. Topol, A. M. Johnson, M. Shahmanesh, A. Ozcan, J. J. Collins, M. Fernandez Suarez, B. Rodriguez, R. W. Peeling and R. A. McKendry, *Nature Reviews Bioengineering*, 2023, **1**, 13-31.
67. X. Huang, P. K. Jain, I. H. El-Sayed and M. A. El-Sayed, *Photochemistry and Photobiology*, 2006, **82**, 412-417.
68. X. Li, J. F. Lovell, J. Yoon and X. Chen, *Nature Reviews Clinical Oncology*, 2020, **17**, 657-674.
69. Y. S. Yang, P. U. Atukorale, K. D. Moynihan, A. Bekdemir, K. Rakhra, L. Tang, F. Stellacci and D. J. Irvine, *Nature Communications*, 2017, **8**, 14069.
70. S. Song, Z. Liang, J. Zhang, L. Wang, G. Li and C. Fan, *Angewandte Chemie International Edition*, 2009, **48**, 8670-8674.
71. K. Yin Win and S.-S. Feng, *Biomaterials*, 2005, **26**, 2713-2722.
72. A. P. Demchenko, *Methods and Applications in Fluorescence*, 2020, **8**, 022001.
73. R. I. Dmitriev, X. Intes and M. M. Barroso, *Journal of Cell Science*, 2021, **134**, 1-17.
74. S. A. Osborne and Z. Pikramenou, *Faraday Discuss*, 2015, **185**, 219-231.
75. N. J. Rogers, S. Claire, R. M. Harris, S. Farabi, G. Zikeli, I. B. Styles, N. J. Hodges and Z. Pikramenou, *Chemical Communications*, 2014, **50**, 617-619.

76. N. J. Rogers, H. C. Jeffery, S. Claire, D. J. Lewis, G. Zikeli, N. J. Hodges, S. Egginton, G. B. Nash and Z. Pikramenou, *Nanomedicine*, 2017, **12**, 2725-2740.
77. A. C. Anselmo and S. Mitragotri, *Bioengineering Translational Medicine*, 2021, **6**, e10246.
78. E. Alphandéry, *RSC Advances*, 2019, **9**, 40577-40587.
79. S. Bonvalot, P. L. Rutkowski, J. Thariat, S. Carrere, A. Ducassou, M. P. Sunyach, P. Agoston, A. Hong, A. Mervoyer, M. Rastrelli, V. Moreno, R. K. Li, B. Tiangco, A. C. Herraez, A. Gronchi, L. Mangel, T. Sy-Ortin, P. Hohenberger, T. de Baere, A. Le Cesne, S. Helfre, E. Saada-Bouzid, A. Borkowska, R. Anghel, A. Co, M. Gebhart, G. Kantor, A. Montero, H. H. Loong, R. Verges, L. Lapeire, S. Dema, G. Kacso, L. Austen, L. Moureau-Zabotto, V. Servois, E. Wardelmann, P. Terrier, A. J. Lazar, J. Bovee, C. Le Pechoux and Z. Papai, *Lancet Oncology*, 2019, **20**, 1148-1159.
80. A. R. Rastinehad, H. Anastos, E. Wajswol, J. S. Winoker, J. P. Sfakianos, S. K. Doppalapudi, M. R. Carrick, C. J. Knauer, B. Taouli, S. C. Lewis, A. K. Tewari, J. A. Schwartz, S. E. Canfield, A. K. George, J. L. West and N. J. Halas, *Proceedings of the National Academy of Sciences*, 2019, **116**, 18590-18596.
81. F. Kiessling, M. E. Mertens, J. Grimm and T. Lammers, *Radiology*, 2014, **273**, 10-28.
82. S. N. Bhatia, X. Chen, M. A. Dobrovolskaia and T. Lammers, *Nature Reviews Cancer*, 2022, **22**, 550-556.
83. C. D. Walkey and W. C. Chan, *Chemical Society Reviews*, 2012, **41**, 2780-2799.
84. D. Walczyk, F. B. Bombelli, M. P. Monopoli, I. Lynch and K. A. Dawson, *Journal of the American Chemical Society*, 2010, **132**, 5761-5768.
85. T. L. Moore, D. A. Urban, L. Rodriguez-Lorenzo, A. Milosevic, F. Crippa, M. Spuch-Calvar, S. Balog, B. Rothen-Rutishauser, M. Lattuada and A. Petri-Fink, *Scientific Reports*, 2019, **9**, 900.
86. S. Behzadi, V. Serpooshan, W. Tao, M. A. Hamaly, M. Y. Alkawareek, E. C. Dreaden, D. Brown, A. M. Alkilany, O. C. Farokhzad and M. Mahmoudi, *Chemical Society Reviews*, 2017, **46**, 4218-4244.
87. M. P. Monopoli, D. Walczyk, A. Campbell, G. Elia, I. Lynch, F. Baldelli Bombelli and K. A. Dawson, *Journal of the American Chemical Society*, 2011, **133**, 2525-2534.
88. M. P. Monopoli, C. Åberg, A. Salvati and K. A. Dawson, *Nature Nanotechnology*, 2012, **7**, 779-786.
89. T. Cedervall, I. Lynch, S. Lindman, T. Berggård, E. Thulin, H. Nilsson, K. A. Dawson and S. Linse, *Proceedings of the National Academy of Sciences*, 2007, **104**, 2050-2055.
90. D. Baimanov, R. Cai and C. Chen, *Bioconjugate Chemistry*, 2019, **30**, 1923-1937.
91. N. Feliu, X. Sun, R. A. Alvarez Puebla and W. J. Parak, *Langmuir*, 2017, **33**, 6639-6646.
92. J. W. Wills, H. D. Summers, N. Hondow, A. Sooresh, K. E. Meissner, P. A. White, P. Rees, A. Brown and S. H. Doak, *ACS Nano*, 2017, **11**, 11986-12000.
93. E. C. Cho, Q. Zhang and Y. Xia, *Nature Nanotechnology*, 2011, **6**, 385-391.
94. N. Oh and J. H. Park, *International Journal of Nanomedicine*, 2014, **9 Suppl 1**, 51-63.
95. N. D. Donahue, H. Acar and S. Wilhelm, *Advanced Drug Delivery Reviews*, 2019, **143**, 68-96.
96. S. D. Conner and S. L. Schmid, *Nature*, 2003, **422**, 37-44.
97. G. J. Doherty and H. T. McMahon, *Annual Review of Biochemistry*, 2009, **78**, 857-902.
98. O. Harush-Frenkel, N. Debotton, S. Benita and Y. Altschuler, *Biochemical and Biophysics Research Communications*, 2007, **353**, 26-32.
99. J. P. Lim and P. A. Gleeson, *Immunology & Cell Biology*, 2011, **89**, 836-843.

100. A. Verma, O. Uzun, Y. Hu, Y. Hu, H. S. Han, N. Watson, S. Chen, D. J. Irvine and F. Stellacci, *Nature Materials*, 2008, **7**, 588-595.
101. J. Chen, J. A. Hessler, K. Putchakayala, B. K. Panama, D. P. Khan, S. Hong, D. G. Mullen, S. C. Dimaggio, A. Som, G. N. Tew, A. N. Lopatin, J. R. Baker, M. M. Holl and B. G. Orr, *Journal of Physical Chemistry B*, 2009, **113**, 11179-11185.
102. P. R. Leroueil, S. A. Berry, K. Duthie, G. Han, V. M. Rotello, D. Q. McNerny, J. R. Baker, Jr., B. G. Orr and M. M. Holl, *Nano Letters*, 2008, **8**, 420-424.
103. T. Wang, J. Bai, X. Jiang and G. U. Nienhaus, *ACS Nano*, 2012, **6**, 1251-1259.
104. R. Augustine, A. Hasan, R. Primavera, R. J. Wilson, A. S. Thakor and B. D. Kevadiya, *Materials Today Communications*, 2020, **25**, 101692.
105. B. D. Chithrani, A. A. Ghazani and W. C. W. Chan, *Nano Letters*, 2006, **6**, 662-668.
106. W. Jiang, B. Y. Kim, J. T. Rutka and W. C. Chan, *Nature Nanotechnology*, 2008, **3**, 145-150.
107. X. Xie, J. Liao, X. Shao, Q. Li and Y. Lin, *Scientific Reports*, 2017, **7**, 3827.
108. B. D. Chithrani and W. C. W. Chan, *Nano Letters*, 2007, **7**, 1542-1550.
109. J. A. Champion and S. Mitragotri, *Pharmaceutical Research*, 2009, **26**, 244-249.
110. Y. Li and N. Gu, *Journal of Physical Chemistry B*, 2010, **114**, 2749-2754.
111. R. R. Arvizo, O. R. Miranda, M. A. Thompson, C. M. Pabelick, R. Bhattacharya, J. D. Robertson, V. M. Rotello, Y. S. Prakash and P. Mukherjee, *Nano Letters*, 2010, **10**, 2543-2548.
112. T. S. Hauck, A. A. Ghazani and W. C. Chan, *Small*, 2008, **4**, 153-159.
113. E. Blanco, H. Shen and M. Ferrari, *Nature Biotechnology*, 2015, **33**, 941-951.
114. P. Nativo, I. A. Prior and M. Brust, *ACS Nano*, 2008, **2**, 1639-1644.
115. W. Tao, J. Zhang, X. Zeng, D. Liu, G. Liu, X. Zhu, Y. Liu, Q. Yu, L. Huang and L. Mei, *Advanced Healthcare Materials*, 2015, **4**, 1203-1214.
116. L. Xu, X. Wang, W. Wang, M. Sun, W. J. Choi, J.-Y. Kim, C. Hao, S. Li, A. Qu, M. Lu, X. Wu, F. M. Colombari, W. R. Gomes, A. L. Blanco, A. F. de Moura, X. Guo, H. Kuang, N. A. Kotov and C. Xu, *Nature*, 2022, **601**, 366-373.
117. A. N. Dosumu, S. Claire, L. S. Watson, P. M. Girio, S. A. M. Osborne, Z. Pikramenou and N. J. Hodges, *JACS Au*, 2021, **1**, 174-186.
118. A. J. North, *Journal of Cell Biology*, 2006, **172**, 9-18.
119. H. Shin, M. Kwak, T. G. Lee and J. Y. Lee, *Nanoscale*, 2020, **12**, 15743-15751.
120. K. Shapero, F. Fenaroli, I. Lynch, D. C. Cottell, A. Salvati and K. A. Dawson, *Molecular Biosystems*, 2011, **7**, 371-378.
121. Y. Wang, Y.-F. Wang, X. Li, Y. Wang, Q. Huang, X. Ma and X.-J. Liang, *ACS Nano*, 2022, **16**, 12553-12568.
122. M. Malatesta, *International Journal of Molecular Science*, 2021, **22**.
123. L. Graham and J. M. Orenstein, *Nature Protocols*, 2007, **2**, 2439-2450.
124. P. Krystek, A. Ulrich, C. C. Garcia, S. Manohar and R. Ritsema, *Journal of Analytical Atomic Spectrometry*, 2011, **26**, 1701-1721.
125. S. C. Wilschefski and M. R. Baxter, *Clinical Biochemistry Reviews*, 2019, **40**, 115-133.
126. C. Gottstein, G. Wu, B. J. Wong and J. A. Zasadzinski, *ACS Nano*, 2013, **7**, 4933-4945.
127. F. de Moura Souza, F. Pollo Paniz, T. Pedron, M. Coelho Dos Santos and B. Lemos Batista, *Heliyon*, 2019, **5**, e01308.
128. N. Laur, R. Kinscherf, K. Pomytkin, L. Kaiser, O. Knes and H.-P. Deigner, *PLoS One*, 2020, **15**, e0233357.
129. M. D. Montaño, J. W. Olesik, A. G. Barber, K. Challis and J. F. Ranville, *Analytical and Bioanalytical Chemistry*, 2016, **408**, 5053-5074.
130. F. Laborda, E. Bolea and J. Jiménez-Lamana, *Analytical Chemistry*, 2014, **86**, 2270-2278.

131. R. C. Merrifield, C. Stephan and J. R. Lead, *Environmental Science & Technology*, 2018, **52**, 2271-2277.
132. A. Malysheva, A. Ivask, C. L. Doolette, N. H. Voelcker and E. Lombi, *Nature Nanotechnology*, 2021, **16**, 926-932.
133. O. Ornatsky, D. Bandura, V. Baranov, M. Nitz, M. A. Winnik and S. Tanner, *Journal of Immunological Methods*, 2010, **361**, 1-20.
134. Z. B. Bjornson, G. P. Nolan and W. J. Fantl, *Current Opinions in Immunology*, 2013, **25**, 484-494.
135. J. Bae, M. Ha, H. Perumalsamy, Y. Lee, J. Song and T.-H. Yoon, *Journal*, 2022, **14**.
136. L. Tong, E. Lu, J. Pichaandi, G. Zhao and M. A. Winnik, *The Journal of Physical Chemistry C*, 2016, **120**, 6269-6280.
137. J. Pichaandi, L. Tong, A. Bouzekri, Q. Yu, O. Ornatsky, V. Baranov and M. A. Winnik, *Chemistry of Materials*, 2017, **29**, 4980-4990.
138. A. R. Schulz, S. Stanislawiak, S. Baumgart, A. Grützkau and H. E. Mei, *Cytometry A*, 2017, **91**, 25-33.
139. L. R. Olsen, M. D. Leipold, C. B. Pedersen and H. T. Maecker, *Cytometry A*, 2019, **95**, 156-172.
140. F. Hofer, F. P. Schmidt, W. Grogger and G. Kothleitner, *IOP Conference Series: Materials Science and Engineering*, 2016, **109**, 012007.
141. R. Bavand, A. Korinek, G. A. Botton, A. Yelon and E. Sacher, *The Journal of Physical Chemistry C*, 2017, **121**, 23104-23119.
142. J. Alles, N. Karaiskos, S. D. Praktiknjo, S. Grosswendt, P. Wahle, P.-L. Ruffault, S. Ayoub, L. Schreyer, A. Boltengagen, C. Birchmeier, R. Zinzen, C. Kocks and N. Rajewsky, *BMC Biology*, 2017, **15**, 44.
143. S. D. Tanner, O. Ornatsky, D. R. Bandura and V. I. Baranov, *Spectrochimica Acta Part B: Atomic Spectroscopy*, 2007, **62**, 188-195.

Chapter 2: Synthesis, Optimisation and Photophysical Properties of Luminescent Lanthanide Gold Nanoparticles

2.1 Introduction

2.1.1 The Design of Europium Coated Gold Nanoparticles and Overcoming Quenching of Luminescence

A limitation of using AuNPs as a scaffold for attaching fluorophores or luminescent agents is the quenching that has been reported from the SPR of gold.[1, 2] When fluorophores are within 5 nm from an AuNP surface, quenching has been attributed to a 'near-field' effect involving energy or electron transfer through non-radiative pathways from the fluorophores' excited electron to the gold.[3, 4] Increasing the distance of the fluorophore from the AuNP surface has been shown to prevent quenching and even enhance the lifetime, but lifetimes still remain short in the region of a few ps to 50 ns.[5, 6]

As previously mentioned, lanthanides such as europium have attractive luminescent properties such as their long lifetimes, which our group has utilised by attaching luminescent europium complex onto AuNPs. This was first shown in 2006, where AuNPs with a diameter of 13 nm were used as a scaffold for attaching europium DTPA complexes with an aminothiophenol sensitiser (Figure 2.1).[7] The terminal thiol groups allow for attachment to the AuNP surface; characterisation by UV-Vis spectroscopy showed a clear red-shift in the SPR wavelength of the NPs and after purification with size-exclusion chromatography, characteristic emission from europium was observed. The lifetime of europium luminescence was 0.8 µs, much lower than the complex in solution, suggesting that there is some quenching from the NP surface.

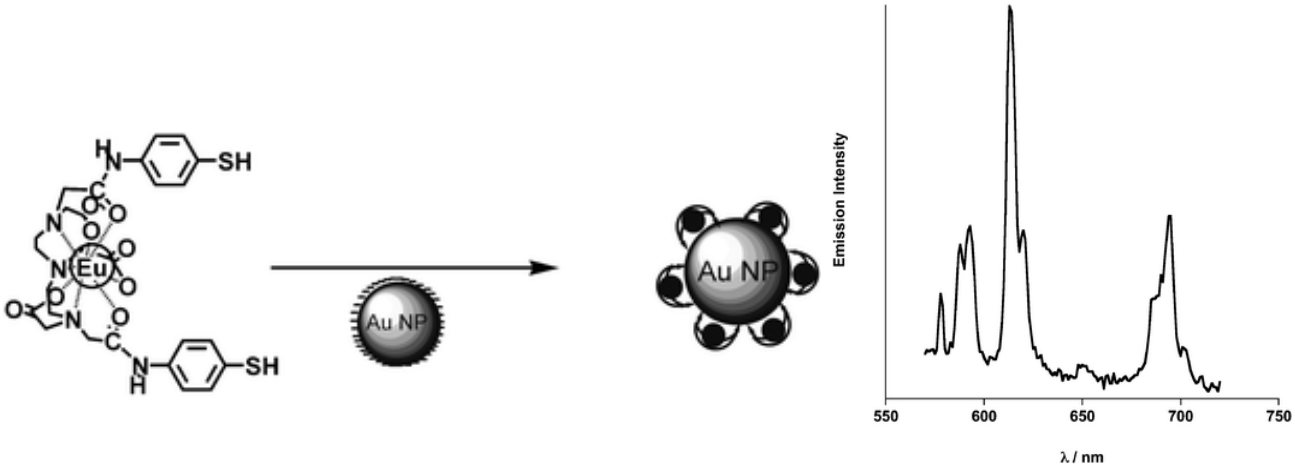


Figure 2.1 - The europium complex referred to as EuSH in this work and its attachment to 13 nm AuNPs to make EuS-AuNPs (left), alongside an emission spectrum of EuS-AuNPs (right).

To overcome quenching, spacer organic groups were incorporated into a different ligand to act as 'legs' that increase the distance of the metal centre from the NP surface. A study by Davies *et al*. reported a europium complex, EuQuinSAc, that had a quinoline sensitiser functionalised with a hexyl chain with a terminal thioacetate group (Figure 2.2).[8] Once attached to AuNPs, a much longer luminescence lifetime of 287 μs was exhibited by the europium centre, indicating success in overcoming quenching. The quinoline sensitiser also has an absorption maximum around 323 nm, corresponding to the $S_1 \leftarrow S_0$ and π-π^* electronic transition. This allows red-shift allows excitation with light from wavelengths up until at least 375 nm which is more applicable to biomedical imaging than the EuSH ligand.

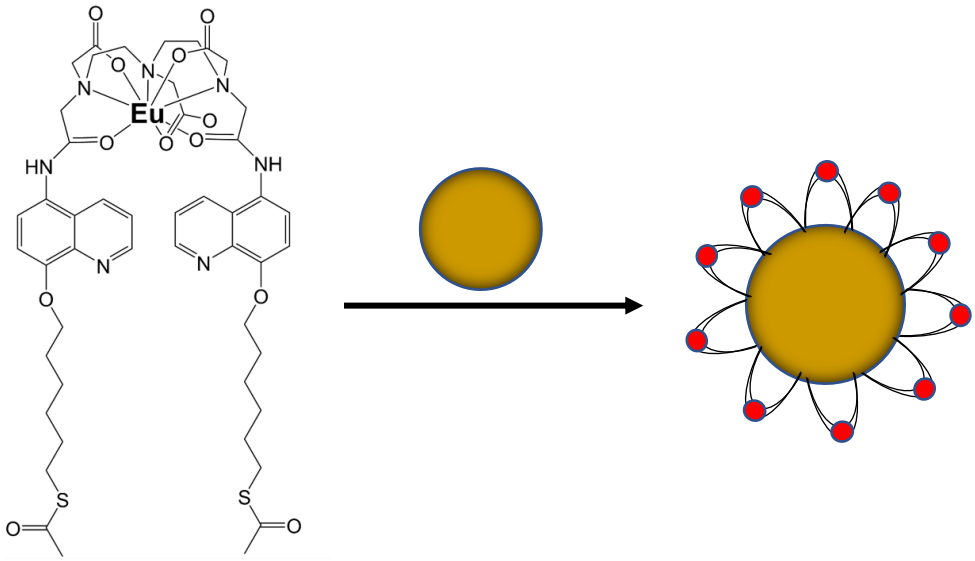


Figure 2.2 – The structure of EuQuinSAc, designed with a hexyl spacer group to increase the distance between the europium centre when it is added to the surface of AuNPs (top); transmitted light image (left hand side image) and luminescence image (right hand side image) of platelet treated EuQuinSAc/Peptide coated AuNPs, with europium emission observed (λ_{exc} = 340 nm). Microscopy images adapted from Davies *et al.*

Our group has also studied the effect of the distance of ruthenium metal centres from AuNPs on luminescence lifetimes. A library of tris(bypyridine) ruthenium complexes were synthesised with a terminal thiol group with either no spacer chain or a spacer chain of 6 or 12 atoms to extend the distance the metal centre is held away from the AuNP surface. These complexes were attached to 13, 25 and 100 nm AuNPs and although the size of the AuNPs had no effect, a 12 carbon atom spacer unit enhanced the lifetime of a ruthenium complex by 70% compared to the free probe in water, whereas shorter spacer units of 6 and 1 carbon atoms only enhanced the lifetime by 40% and 20% respectively.[9]

As previously stated, a fluorosurfactant – Zonyl FSA – is used to stabilise AuNPs upon addition of positively charged iridium and ruthenium complexes. Fluorination of ligands complexed to lanthanides is known to increase their luminescence lifetimes,[10-12] but little is known about what effects fluorinated surfactants may have on the the photophysics of lanthanide complexes attached to AuNPs.

2.1.2 Scanning Transmission Electron Microscopy (STEM) and Electron Energy Loss Spectroscopy (EELS)

Transmission electron microscopy is a microscopy technique used to reveal sub-micrometre structures in solids, in which a beam of electrons is transmitted through the specimen to form an image. There are two different types of TEM – Conventional (CTEM) and Scanning (STEM). CTEM is a wide-beam technique in which an electron beam is projected onto the whole area of interest and an image is collected in parallel.[13] In STEM, a probe forming lens finely focusses a beam of electrons at the specimen, to address each pixel in series as the probe scans across the specimen.[14] Analytical information is usually collected using a focussed beam and the smallest region that can be analysed is defined by the beam diameter.[15] Over the past few decades, electron microscopy performance has been greatly improved by multipole-based aberration correction technology,[16-18] allowing sub-Angstrom resolution in STEM imaging and dynamic imaging of single atoms, through annular dark-field imaging and spectroscopic mapping by electron energy loss spectroscopy (EELS).[19, 20]

Annular dark-field imaging is a method of mapping samples in STEM. Dark-field imaging describes microscopy methods which exclude the unscattered beam from the image, resulting in a dark field around the specimen. In STEM dark-field imaging, an annular detector collects scattered electrons that pass through the sample.[21] High-angle annular dark-field (HAADF) imaging in STEM has become a common analysis technique in materials science because it provides intuitively interpretable, atomic resolution images that are sensitive to atomic number (z).[22] For elements with a higher z, greater electrostatic interactions between the nucleus and electron beam lead to more electrons scattered at higher angles, so they appear brighter in images.[23] No aperture is used in HAADF, which allows the main beam to pass through an EELS detector, so both types of measurement can be performed simultaneously.

EELS is an absorption spectroscopy in which the energy losses of incident electrons are directly measured following transmission through a sample (Figure 2.3).[24, 25] As a material is exposed to a beam of electrons, some electrons undergo inelastic scattering and this can be measured to give energy loss spectral information.[26] This can provide information on elemental composition, valence/conduction electron density (plasmon peaks), band structure, bonding and oxidation states.

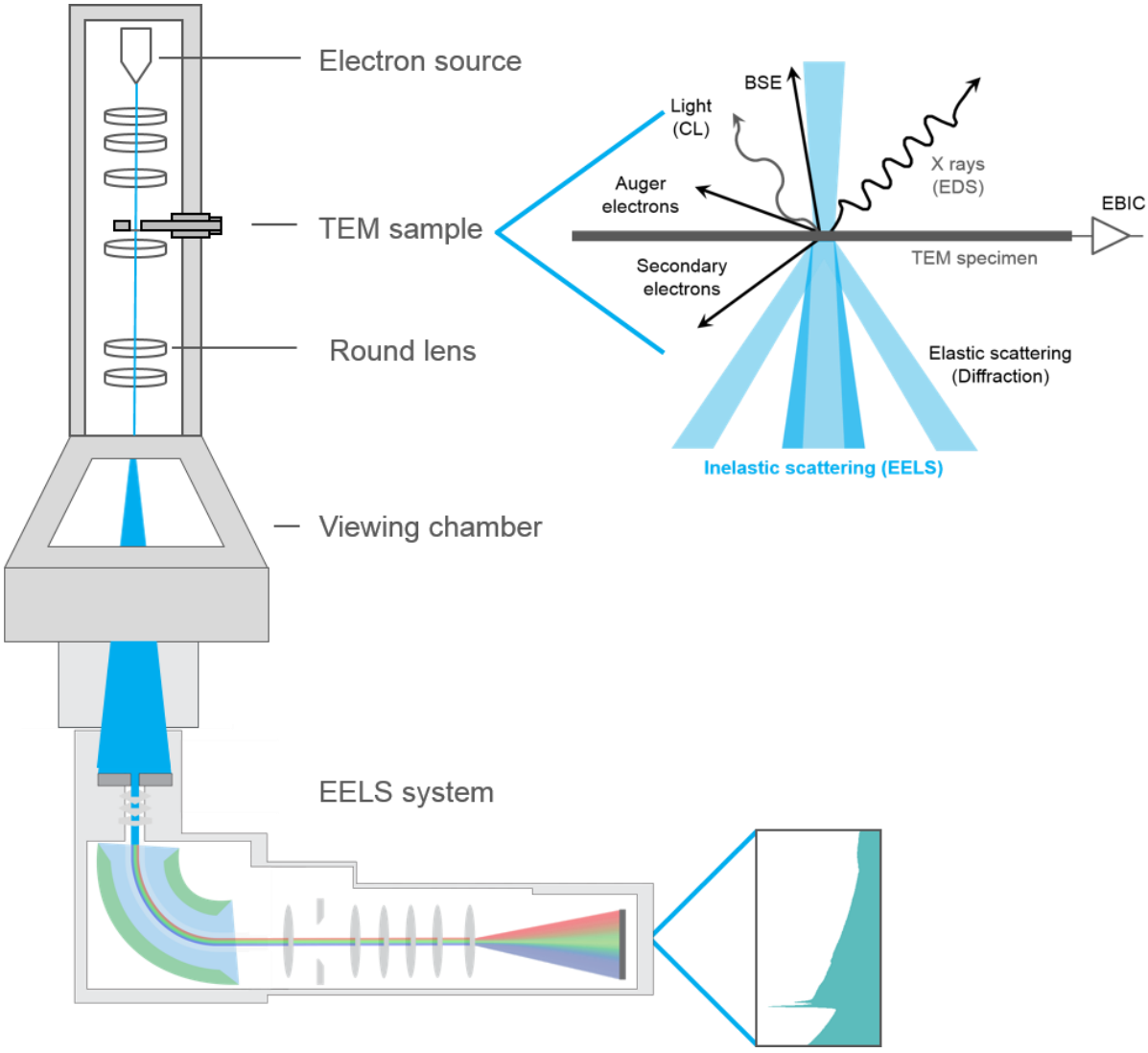


Figure 2.3 - Schematic explanation of the basis of EELS in STEM. Reproduced from Liu *et al*.

An EELS spectrum has many prominent features and is typically separated into three regions. Figure 2.4 shows an EELS spectrum of a 20 nm thin titanium carbide specimen

recorded up to 600 electron volts. The first region contains an intense peak at 0 eV, known as the zero-loss peak, represents electrons that have not lost any energy. The low-loss or valence region (< 50 eV) contains information about electrons that have interacted with the weakly bound electrons in the sample and provides insight into the dielectric properties such as surface plasmons and band gap.[26] At higher energy losses (> 50 eV), in the region known as 'ionisation edges' or 'core-loss region', the spectrum shows characteristic features of electrons that have interacted with the tightly bound core electrons of the atoms. The number of inelastically scattered electrons in this region is much lower and therefore the intensity of these peaks are lower than in the low-loss region.[26] The ionisation edges often have a characteristic shape, such as the carbon K-edge and $L_{2,3}$-edge of titanium in Figure 2.4, and can be attributed to elements based on their absolute position.[27]

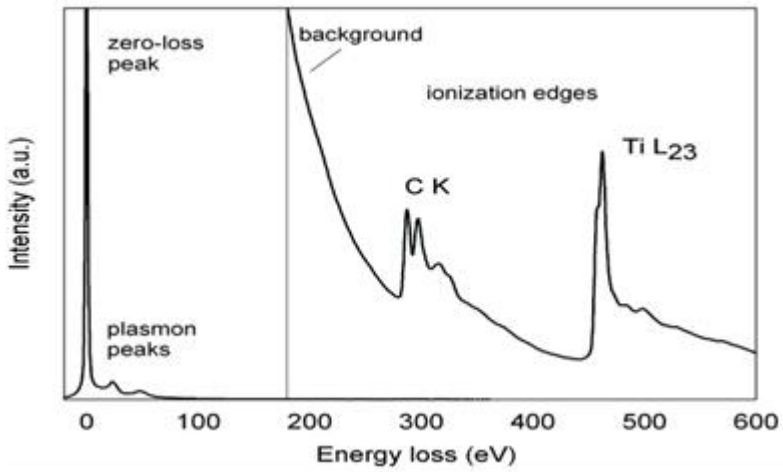


Figure 2.4 - EELS spectrum of a 20 nm thin titanium carbide specimen. Reproduced from Hofer *et al.*

EELS has previously been used as a characterisation technique for studying the elemental composition of bimetallic nanomaterials, such as catalysts. Browning and co-workers studied $Sn(Sb)O_2$ nanophase catalysts with atomic resolution,[28] revealing that Sb exists in the trivalent state at the surface (Sb (III)), but pentavalent (Sb(V)) at the core. They also studied reduction behaviour of metal nanoparticles in alumina-supported Pd catalysts[29] and alloying behaviour of Pd-Cu bimetallic catalysts, where they found that changes in the

reduction temperature of the precursor materials led to compositions varying from pure metallic Pd to Pd-Cu bimetallic alloys.[30] Bavand *et al.* studied the morphology of PtRu nanoparticles and were able to use HAADF and EELS to elementally map different PtRu alloy structures at during various different deposition and annealing processes (Figure 2.5).[31]

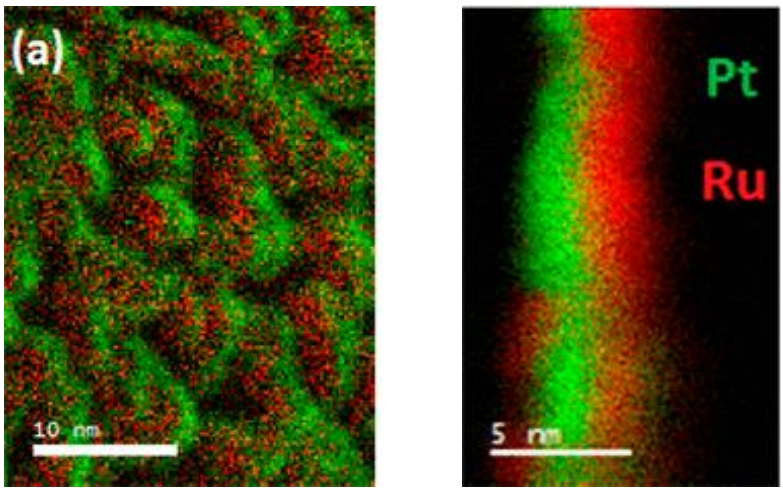


Figure 2.5 - EELS elemental mapping of Ru (red) and Pt (green) of PtRu NPs on highly oriented pyrolytic graphite (HOPG) at room temperature when Pt was deposited onto Ru (left), EELS elemental mapping of PtRu NPs on HOPG at room temperature when Ru was deposited on to Pt (right). Images reproduced from figures 14 and 17 from a study by Bavand *et al.*

There are many techniques that provide evidence of surface functionalisation of gold nanoparticles, such as oxidation of the gold surface through Au-S bond formation shown by x-ray photoelectron spectroscopy,[32, 33] changes in the surface plasmon resonance observed with UV-vis spectroscopy,[7, 34] increases in hydrodynamic diameter measured by dynamic light scattering (DLS)[35] or differential centrifugal sedimentation (DCS)[36], changes in surface charge measured by ζ-potential[34, 37] and co-localisation of luminescence signal with reflectance images of gold nanoparticles images with confocal microscopy,[34, 38] However, high-resolution imaging of organically bound ligands to nanoparticle surfaces has proved difficult. Recently, Wang *et al.* used negative staining to show a compact shell (approximately 1.5 nm) of oligo-ethylene glycol branches on the surface of 10 nm gold nanoparticles.[39] In 2021, Sheibani *et al.* were able to study morphological features of the

biomolecular corona of polystyrene nanoparticles after exposure to biological media by cryo-electron microscopy, but this proved too difficult with 15 nm gold nanoparticles due to the high atomic mass of gold.[40]

2.2 Chapter Outline

In this chapter, the synthesis of visible and near-infrared emitting lanthanide complexes $LnQuin_2SH$ (Ln = Eu, Yb, Nd) and LnSH (Ln = Eu, Tb) and their photophysical properties in solution is shown. These thiol-terminated lanthanide complexes have been designed for their attachment to 13-nm gold nanoparticle surfaces to produce lanthanide coated gold nanoparticle species $LnQuin_2S$-AuNPs and LnS-AuNPs; their suitability as cellular labels, detectable by both luminescence imaging and CyTOF, will be explored in later chapters. Each lanthanide complex has two thiol terminated groups; this has been shown to enhance the stability of AuNP-ligand cojugates.[41] The main interest lies with $LnQuin_2S$-AuNPs, due to their more desirable properties for luminescence imaging, but LnS-AuNPs will also be studied for more insight into how the increase in chain length and apparent distance from the gold nanoparticle surface affects their photophysical properties and their cellular uptake (see chapter 3). The synthesis and characterisation of $LnQuin_2S$-AuNPs and surfactant and polymer coated $EuQuin_2S$-AuNPs, as well as LnS-AuNPs is shown, followed by further characterisation of $EuQuin_2S$-AuNPs and TbS-AuNPs, first by determining an association constant for the binding of the lanthanide complexes through UV-vis spectroscopy, then by providing further evidence of a binding event with isotherm titration calorimetry, before comparing the association constant determined by each method. Novel utilisation of STEM imaging and EELS for elemental mapping for detecting europium atoms at the surface of $EuQuin_2S$-AuNPs and EuS-AuNPs is then demonstrated. Lastly, the effect of coating the nanoparticle surface with fluorinated surfactants Zonyl FSA and TFD, and a PEG polymer prior to the addition of $EuQuin_2SH$ on the loading, photophysical properties and cellular

uptake of EuQuin$_2$S-AuNPs is investigated, with a focus on identifying a lanthanide gold nanoparticle species with optimal photophysical properties and enhanced cellular uptake.

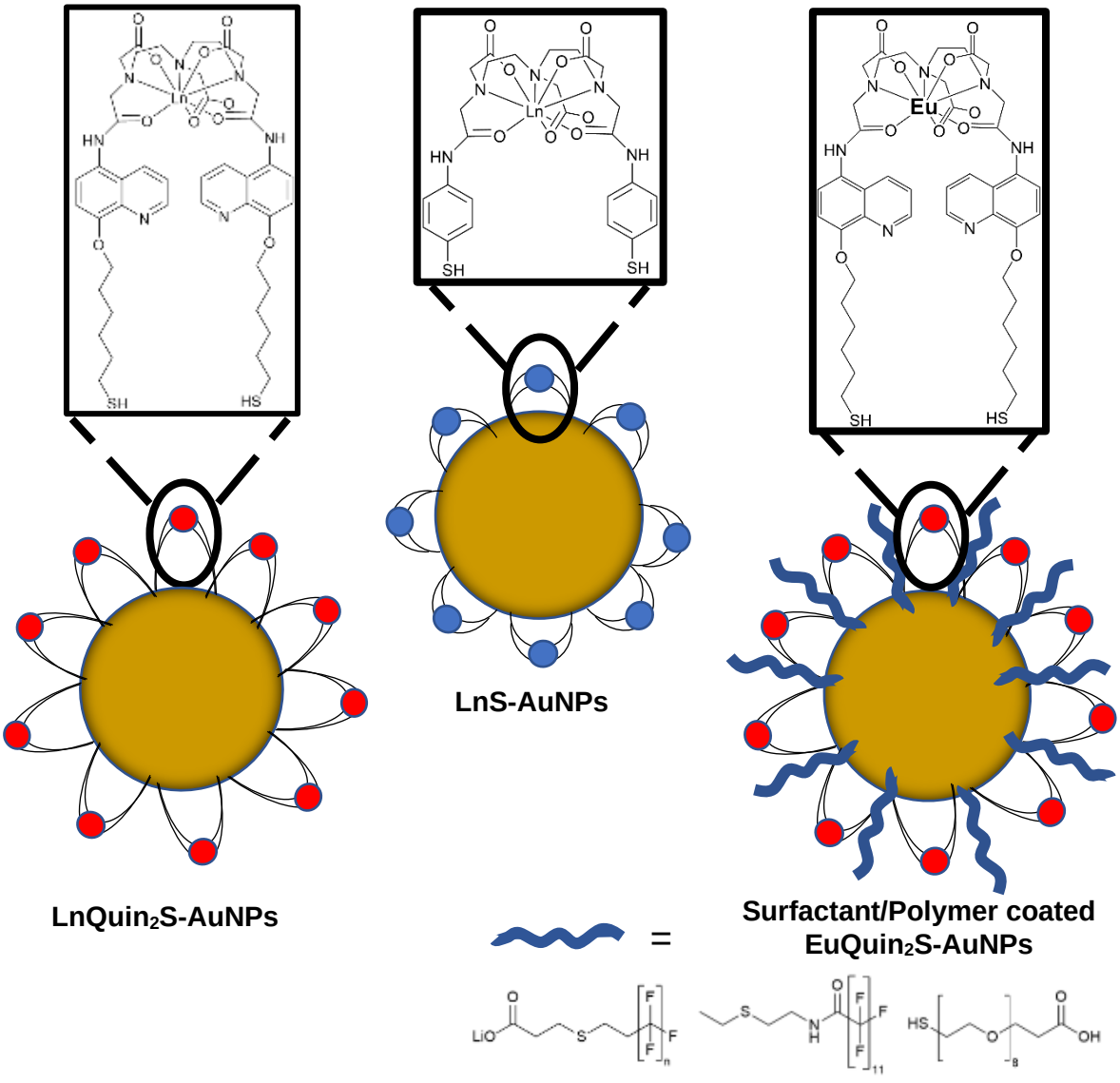


Figure 2.6 – Schematic representation of the LnQuin$_2$S-AuNPs, LnS-AuNPs and surfactant/polymer coated EuQuin$_2$S-AuNPs. In this chapter, the synthesis and characterisation of these NP species is shown, as well as the effect of surfactants and polymers on the loading, photophysics and cellular uptake of EuQuin$_2$S-AuNPs.

2.3 Synthesis of Lanthanide Complexes

2.3.1 Synthesis of $LnQuin_2SH$

H_3Quin_2SH was synthesised via a 6-step synthesis shown in Figure 2.7. Following the synthesis of $H_3QuinSAc$ optimised by previous group members,[42] the terminal thioacetate groups were reduced by NaOH, yielding H_3Quin_2SH (22%). Reduction of the terminal thioacetate groups was confirmed by disappearance of a single at 2.31 ppm in the ^{1}H-NMR spectrum and disappearance of a thioacetate carboxyl peak in the IR spectrum (see experimental 2.10.1.6 for data). All characterisation of H_3Quin_2SH and intermediate products is shown in the experimental section.

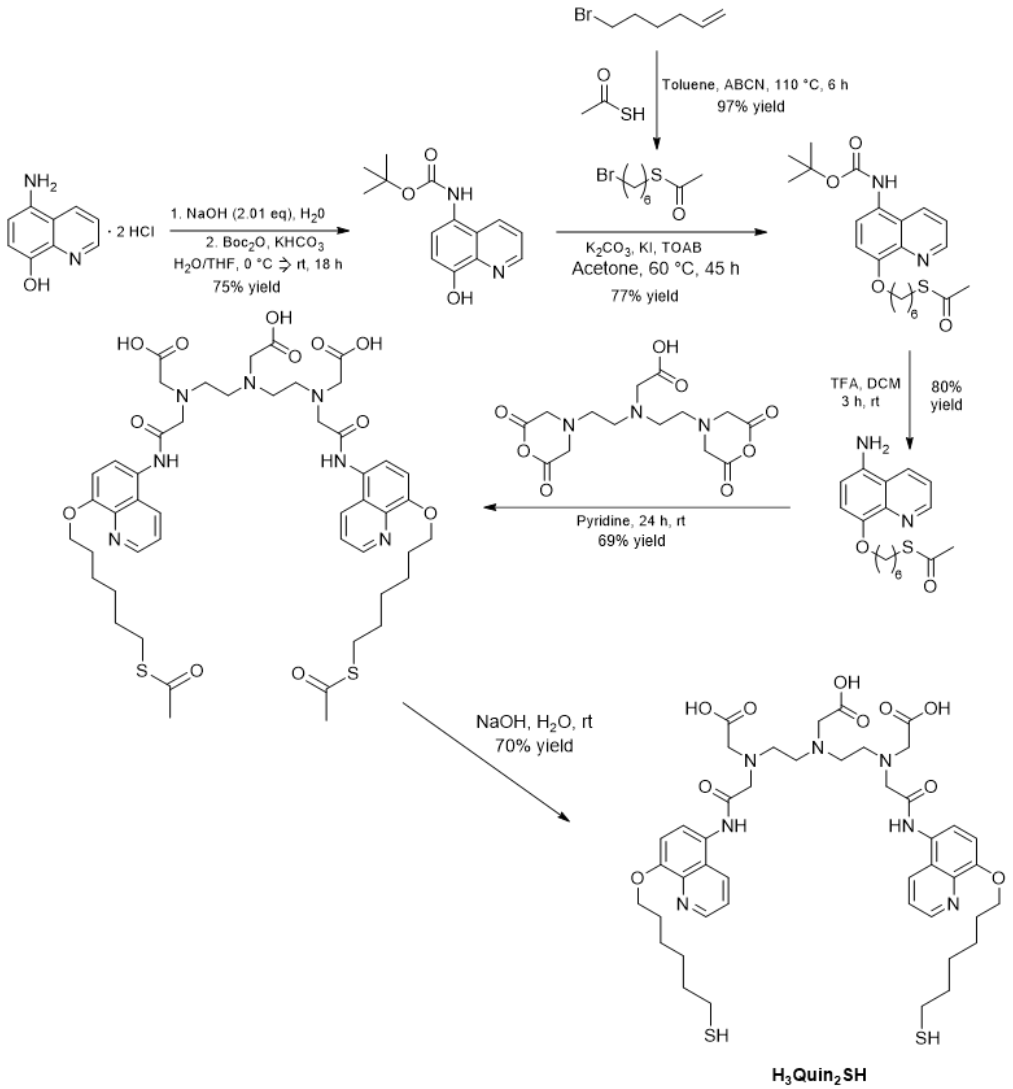


Figure 2.7 - Synthetic scheme for the synthesis of H_3Quin_2SH.

Following ligand synthesis, the lanthanide complexes $LnQuin_2SH$ were formed by the addition of an aqueous solution of $LnCl_3.6H_2O$ to H_3Quin_2SH in a solvent mixture of water and THF (Figure 2.8). Characterisation of $LnQuin_2SH$ complexes is shown in the experimental section.

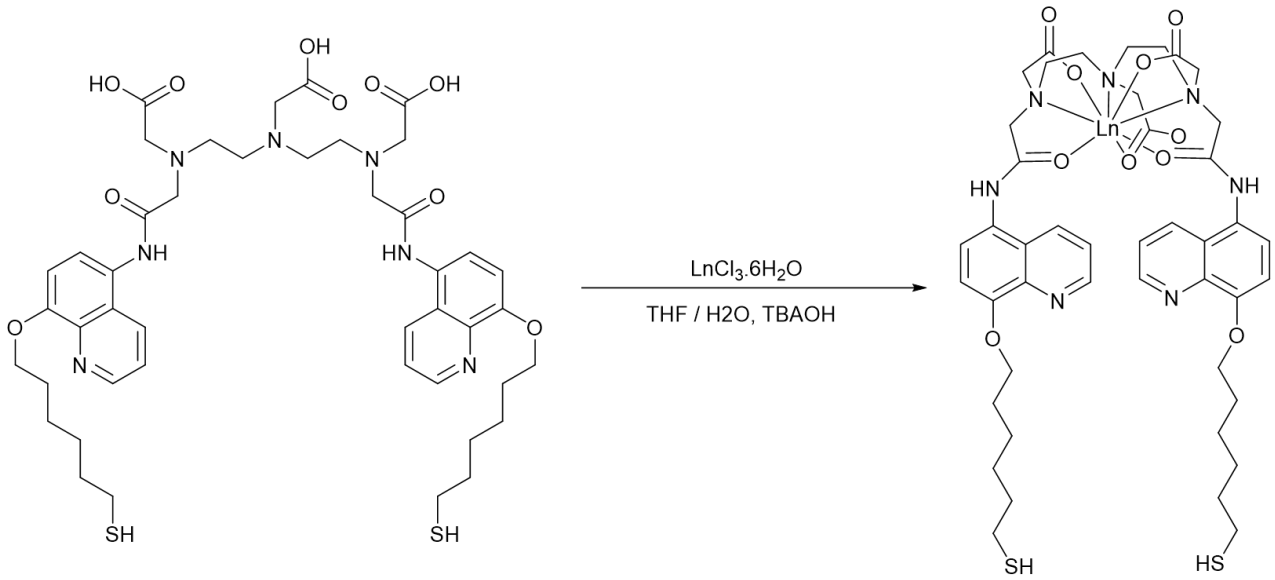
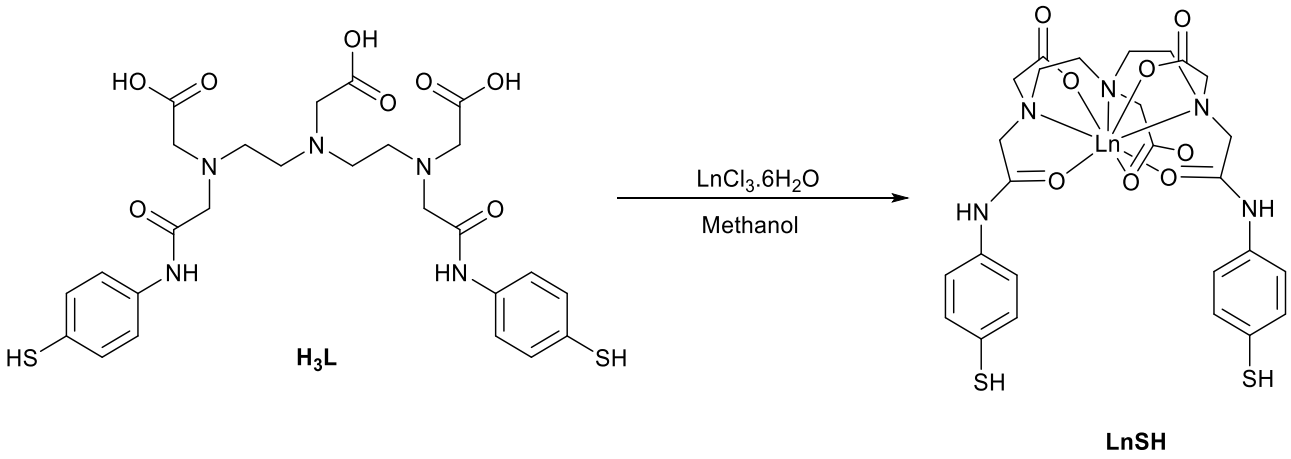


Figure 2.8 - Synthesis of $LnQuin_2SH$

2.3.2 Synthesis of LnSH

The ligand H_3L was synthesised from the reaction of 4-aminothiophenol with DTPA-bis(anhydride) (Figure 2.9). All characterisation of the ligand agreed with previous studies by the group.[7] H_3L was then added to a methanolic solution of $LnCl_3.6H_2O$ (Ln = Eu, Tb) to yield LnSH. Characterisation of EuSH agreed with previous studies by the group.

Figure 2.9 - Synthesis of LnSH



2.4 Photophysical Properties of Lanthanide Complexes in Solution

2.4.1 $EuQuin_2SH$

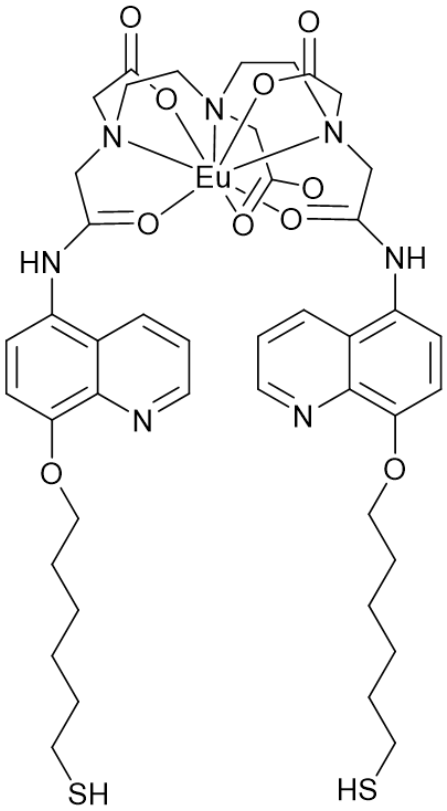


Figure 2.10 - Structure of $EuQuin_2SH$

The excitation spectrum of $EuQuin_2SH$ in MeOH has a band maximum at 330 nm, in close agreement to the corresponding absorption spectrum, where the band maximum was at 323 nm, corresponding to the $S_1 \leftarrow S_0$ and π-π^* electronic transition (Figure 2.11). This confirms the occurrence of ligand to europium energy transfer responsible for the luminescence of Eu(III). Following light excitation into the ligand $^1\pi\pi^*$ state at 325 nm of $EuQuin_2SH$ in methanol, strong red luminescence was observed, characteristic of the $^5D_0 \rightarrow {}^7F_J$ (J = 0-4) emission bands of Eu(III) (Figure 2.12). After subtraction of the baseline, each emission peak was integrated to compare their relative intensities in methanol and CD_3OD (see appendix 2.12.2 for methodology). The emission band at 695 nm ($^5D_0 \rightarrow {}^7F_4$) was particularly strong with a relative intensity of 1.19 with respect to the characteristically

strong band at 616 nm ($^5D_0 \rightarrow {}^7F_2$) (Table 2.1). Although the majority of emission is observed from Eu(III), there is some emission from the quinoline sensitiser (λ_{max} = 440 nm). There was no change in relative intensities of each Eu(III) $^5D_0 \rightarrow {}^7F_J$ transition band, but the total Eu:Quinoline ratio increased from 3.1 to 5.6 when CD_3OD was used as a solvent (Table 2.1). This is likely due to quenching of Eu(III) emission from hydroxyl oscillation of methanol molecules bound to Eu(III), meaning that the quantity of emission observed from the sensitiser is at least partially due to solvent coordination to the Eu(III) centre. This is further supported by an increase in Eu(III) lifetime from 500 µs to 890 µs and quantum yield of 2% to 4.7% when CD_3OD was used as the solvent (Table 2.1).

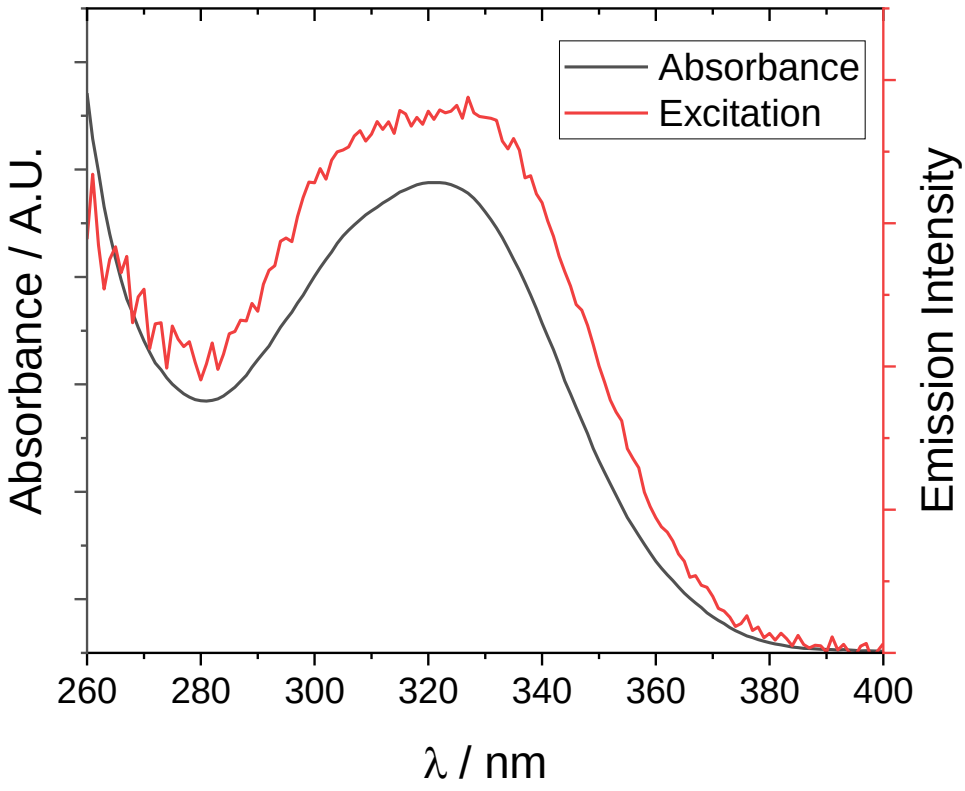


Figure 2.11 - Overlayed absorbance and excitation spectrum of $EuQuin_2SH$ [0.04 mM] in MeOH (λ_{em} = 616 nm).

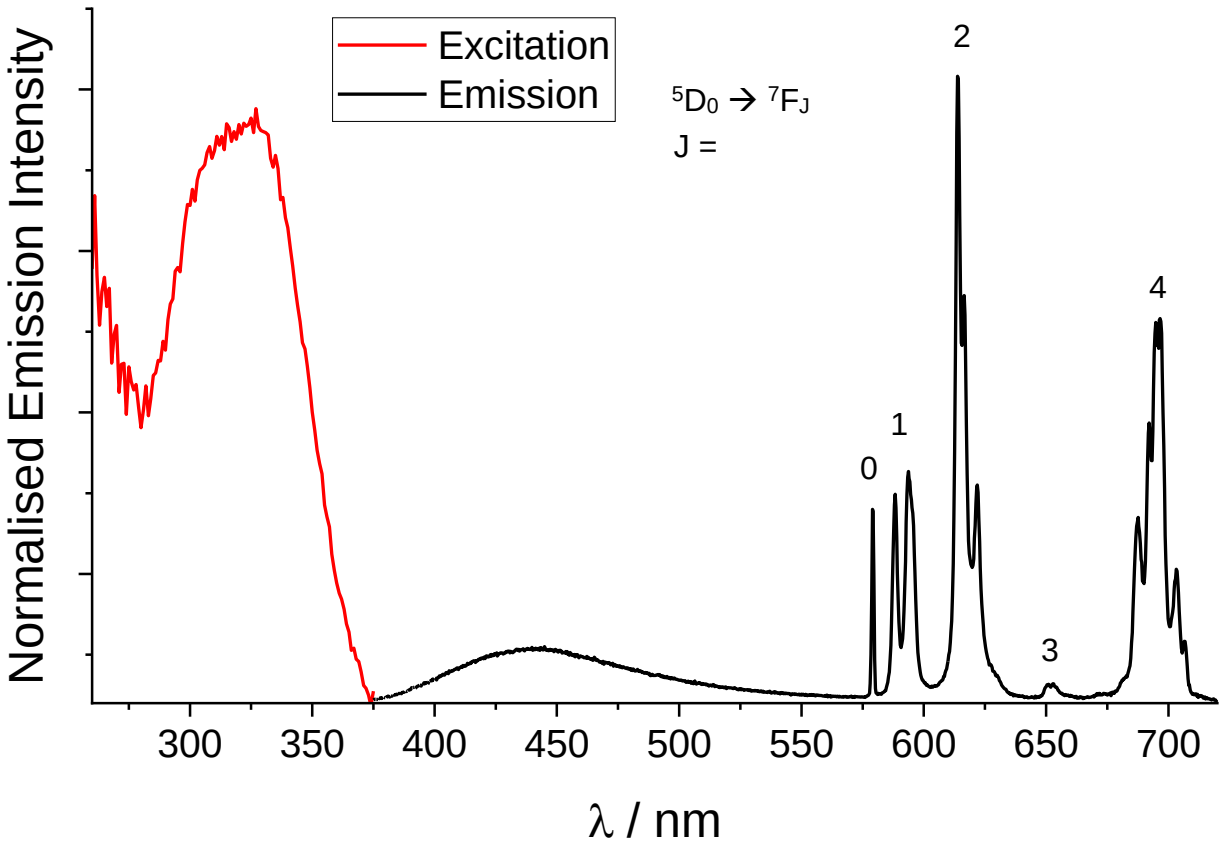


Figure 2.12 - Emission spectrum of $EuQuin_2SH$ in MeOH (λ_{exc} = 325 nm) overlayed with excitation spectrum ((λ_{em} = 616 nm).

Table 2.1 – Peak area integration from each emission band relative to the $^5D_0 \rightarrow {}^7F_2$ band of $EuQuin_2SH$ in methanol and CD_3OD.

Solvent	Quinoline	$^5D_0 \rightarrow {}^7F_0$	$^5D_0 \rightarrow {}^7F_1$	$^5D_0 \rightarrow {}^7F_2$	$^5D_0 \rightarrow {}^7F_3$	$^5D_0 \rightarrow {}^7F_4$	Total / $^5D_0 \rightarrow {}^7F_2$	Total Eu:Quinoline ratio	τ / μs	QY
MeOH	0.86	0.06	0.43	1	0.04	1.19	2.72	3.1	500	2
MeOD	0.48	0.06	0.43	1	0.02	1.17	2.68	5.6	890	4.7

The number of coordinated solvent molecules can be calculated from the difference in lifetimes in deuterated and non-deuterated solvent using the Parker-Beeby equation.[43]:

$$q = A'(\tau_{MeOH}^{-1} - \tau_{MeOD}^{-1} - B)$$

Where *A'* is a revised proportionality constant for europium (A_{Eu} = 2.4 ms^{-1}), τ is the lifetime of Eu(III) in each respective solvent, and *B* is an outer sphere quenching constant. For $EuQuin_2SH$, substituting the respective lifetimes in methanol and CD_3OD of 0.5 ms and 0.89 ms suggests there is an average of 2.1 ± 0.5 solvent molecules bound to Eu(III).

These photophysical properties of $EuQuin_2SH$ are in agreement to the photophysical properties of EuQuinSAc in previous studies by the group.[8] This is expected as the only differences between the complexes are the terminal sulphur containing groups that should have no effect on their emission when dissolved in organic solvent.

2.4.2 Near-infrared Emitting Lanthanides

The excitation spectrum of $YbQuin_2SH$ **(**Figure 2.14**)** and $NdQuin_2SH$ displayed a band maximum at 327 nm, in close agreement to the absorption spectrum, again indicating sensitisation of lanthanide emission by the ligand. Excitation of $YbQuin_2SH$ at 325 nm resulted in near-infrared emission at 980 nm, characteristic of the $^2F_{5/2}$ to $^2F_{7/2}$ transition of Yb(III) (Figure 2.14). Emission was clearly visible in methanol without degassing and the lifetime of Yb(III) was measured as 4 µs, compared to a lifetime of 10 µs in CD_3OD (Table 2.2).

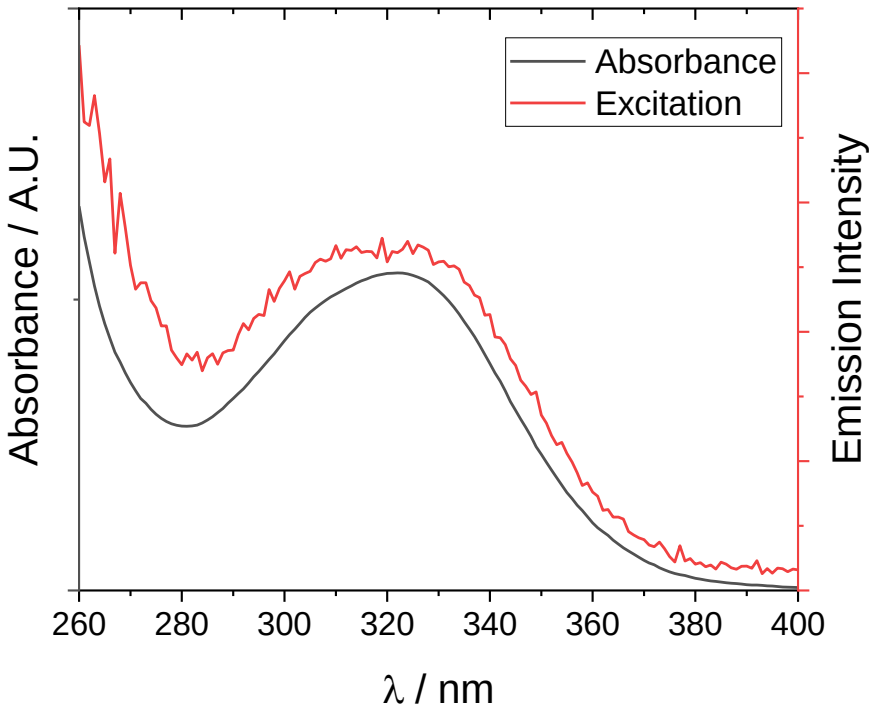


Figure 2.14 - Overlayed absorbance and excitation spectrum of $YbQuin_2SH$ [0.04 mM] in MeOH (λ_{em} = 980 nm).

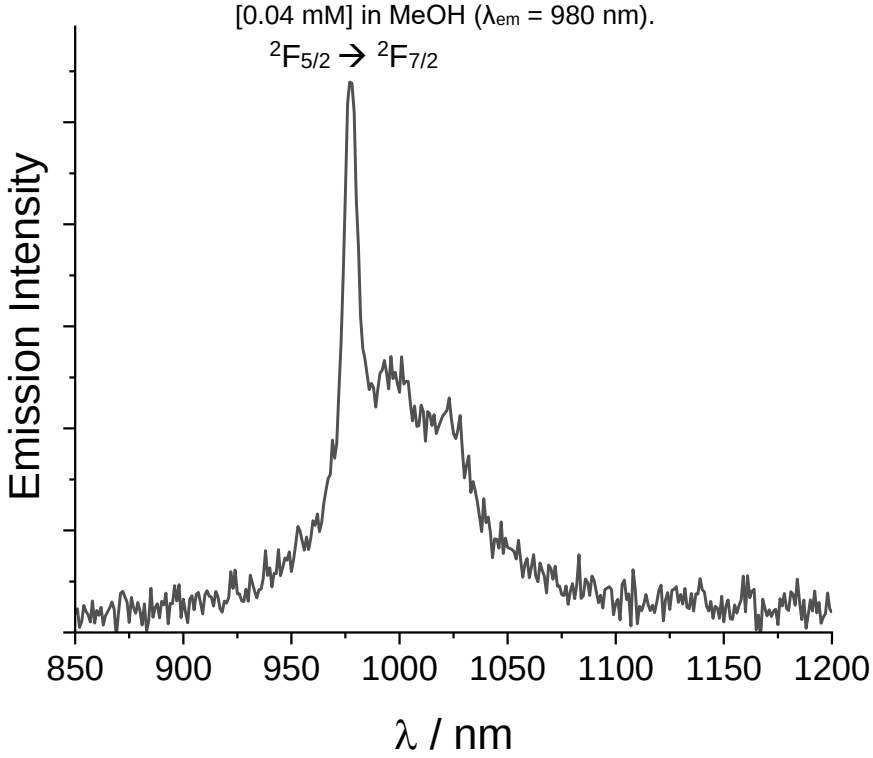


Figure 2.13 - Emission spectrum of $YbQuin_2SH$ [0.04 mM] in MeOH (λ_{exc} = 325 nm).

Table 2.2 - Lifetime measurements of $YbQuin_2SH$ in methanol and CD_3OD.

τ (MeOH) / µs	τ (CD_3OD) / µs
4	10

Excitation of a methanolic solution of $NdQuin_2SH$ at 325 nm led to near-infrared emission assigned to the $^4F_{3/2}$ to ^4I_J (J = 9/2, 11/2, 13/2) transition of Nd(III) (Figure 2.15). Like $YbQuin_2SH$, no degassing was required and emission was observed in MeOH, with a Nd(III) lifetime of 3 µs. In CD_3OD, the lifetime was 5 µs (Table 2.3). These lifetimes are in close agreement with a previous study with similar Yb and Nd complexes without the thiolated methoxy hexyl chain for attachment to gold nanoparticles, where Lewis *et al.* found the lifetimes of Yb(III) and Nd(III) were 16 µs and 6 µs in MeOH and 5 µs and 2 µs in CD_3OD respectively.[44]

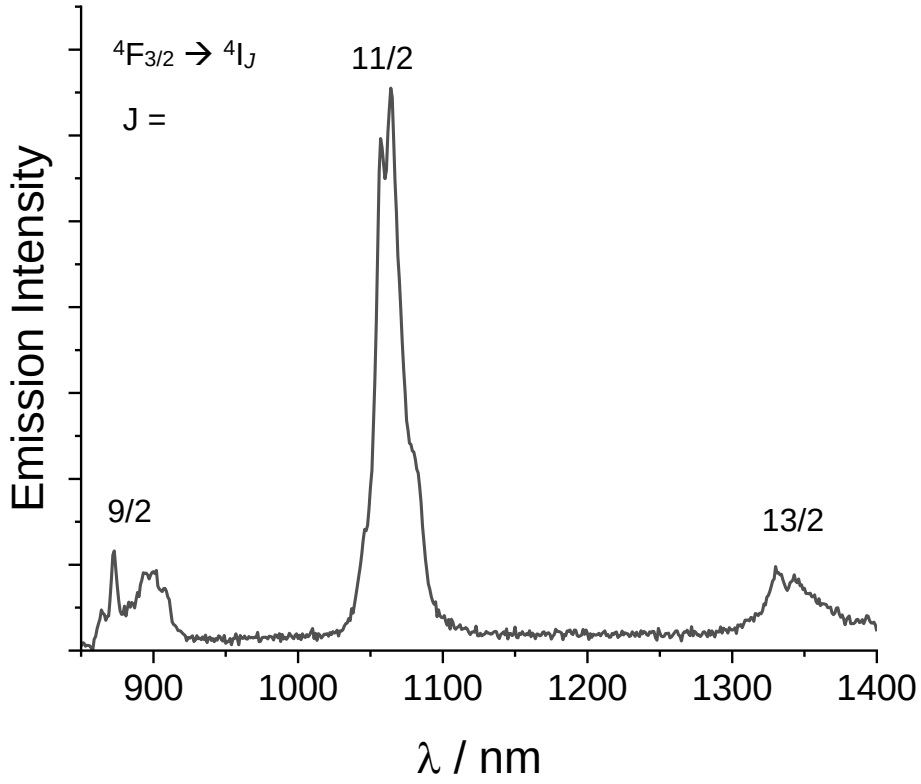


Figure 2.15 - Emission spectrum of $NdQuin_2SH$ [0.04 mM] in MeOH (λ_{exc} = 325 nm).

Table 2.3 - Lifetime measurements of $NdQuin_2SH$ in methanol and CD_3OD.

τ (MeOH) / µs	τ (CD_3OD) / µs
4	10

2.4.3 TbSH

The excitation spectrum of TbSH displayed a band maximum at 264 nm, matching the absorption spectrum and confirming excitation of Tb(III) by ligand sensitisation (Figure 2.16). This is in agreement with studies on EuSH by previous group members.[7, 45] Excitation of a methanolic solution of TbSH at 270 nm led to emission characteristic of the $^5D_4 \rightarrow {}^7F_J$ (J = 0-6) emission bands of Tb(III) (Figure 2.17). The lifetime of Tb(III) in methanolic solution was 1600 µs and 2600 µs in CD_3OD. It was found that an average number of 1.8 ± 0.5 water molecules were bound to each Tb(III) ion, with quenching from hydroxyl oscillation in MeOH explaining the decrease in lifetime.

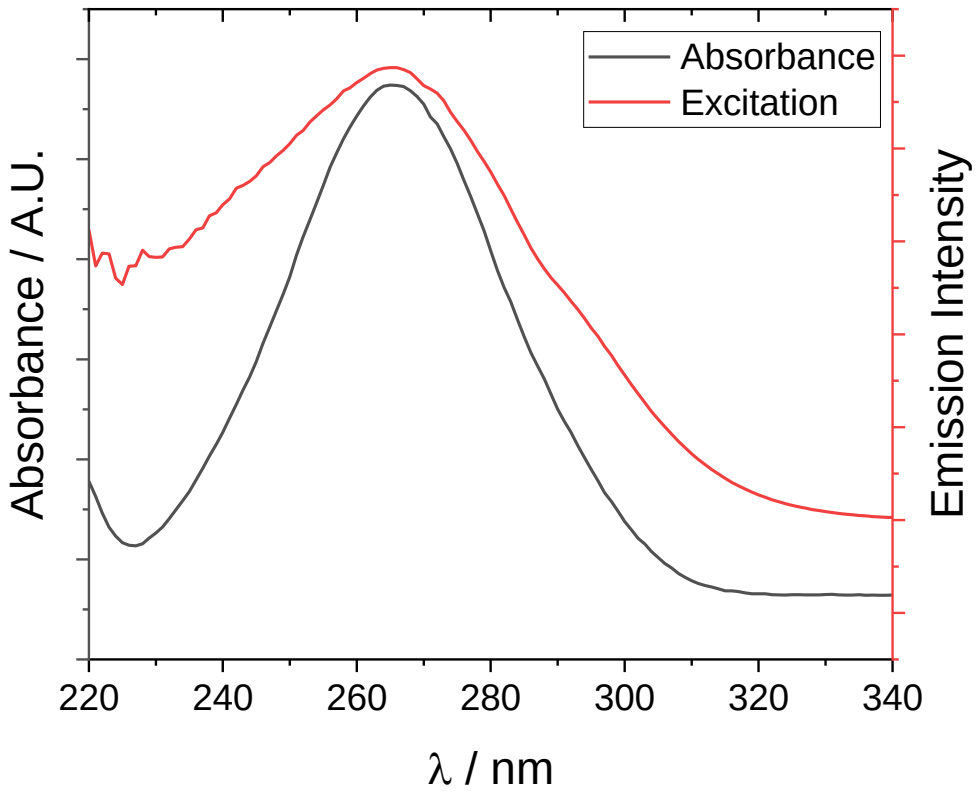


Figure 2.16 - Overlayed excitation (λ_{em} = 545 nm) and absorption spectra of TbSH [16 µM] in MeOH.

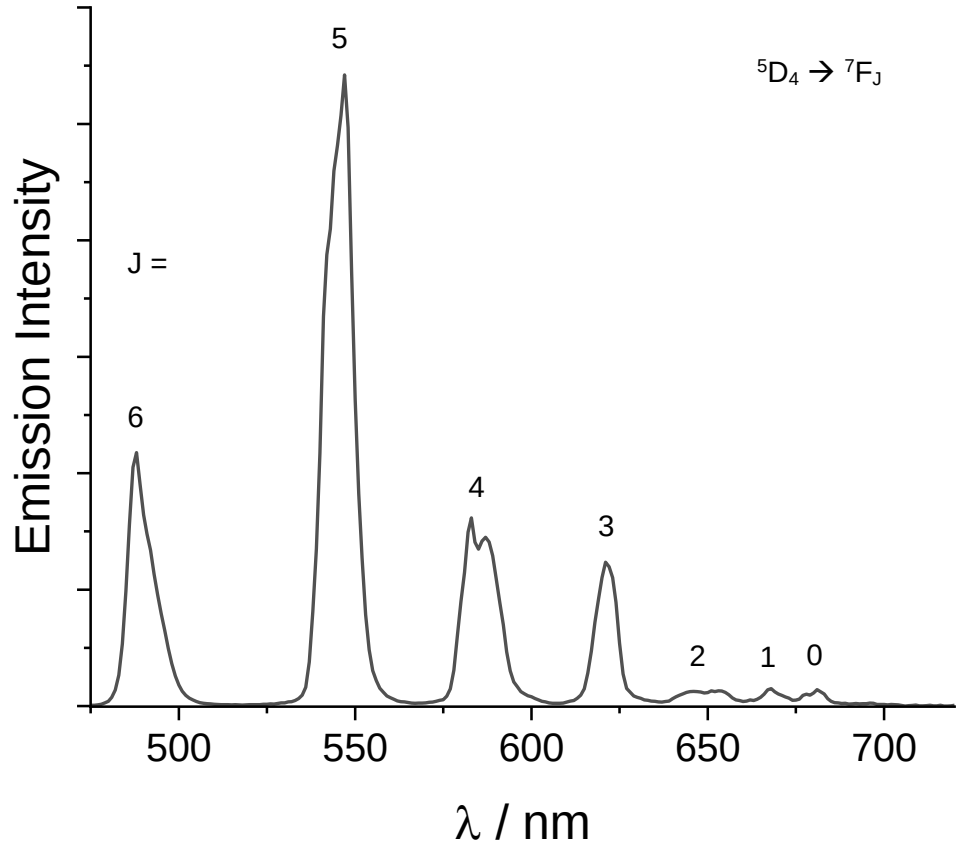


Figure 2.17 - Emission spectrum of TbSH [16 μM], numbers denote $^5D_4 \rightarrow {}^7F_J$ transitions (λ_{exc} = 270 nm).

2.5 Synthesis and Characterisation of Lanthanide Coated Gold Nanoparticles

2.5.1 Synthesis of 13 nm Citrate Gold Nanoparticles

Gold nanoparticles were synthesised using a method described by Schulz *et al.*[46] based on the Turkevich method.[47] This produces water soluble, monodisperse gold nanoparticles stabilised citrate anions on their surface. After synthesis, the nanoparticles were characterised by dynamic light scattering (DLS), zeta-potential (ζ), UV-vis spectroscopy and transmission electron microscopy (TEM). DLS revealed number and intensity values of 13 ± 3 nm and 18 ± 4 nm respectively for the hydrodynamic diameter of the gold

nanoparticles and confirmed their monodisperse nature with a polydispersity index of 0.10 (Table 2.4). ζ-potential measurements revealed an average surface charge of -38 ± 3 mV due to the presence of the citrate anions (Table 2.4). Analysis by UV-vis spectroscopy in MQ water showed a surface plasmon resonance (SPR) peak at 516 nm (Figure 2.18). The average diameter of the gold core was measured as 13.2 ± 0.8 nm by analysis of 30 individual particles from TEM images (Figure 2.18). These images further confirmed the particles monodisperse nature. The results from these characterisation methods are representative of each batch of gold nanoparticles synthesised during this work and agree with previously published data.[34, 38, 48]

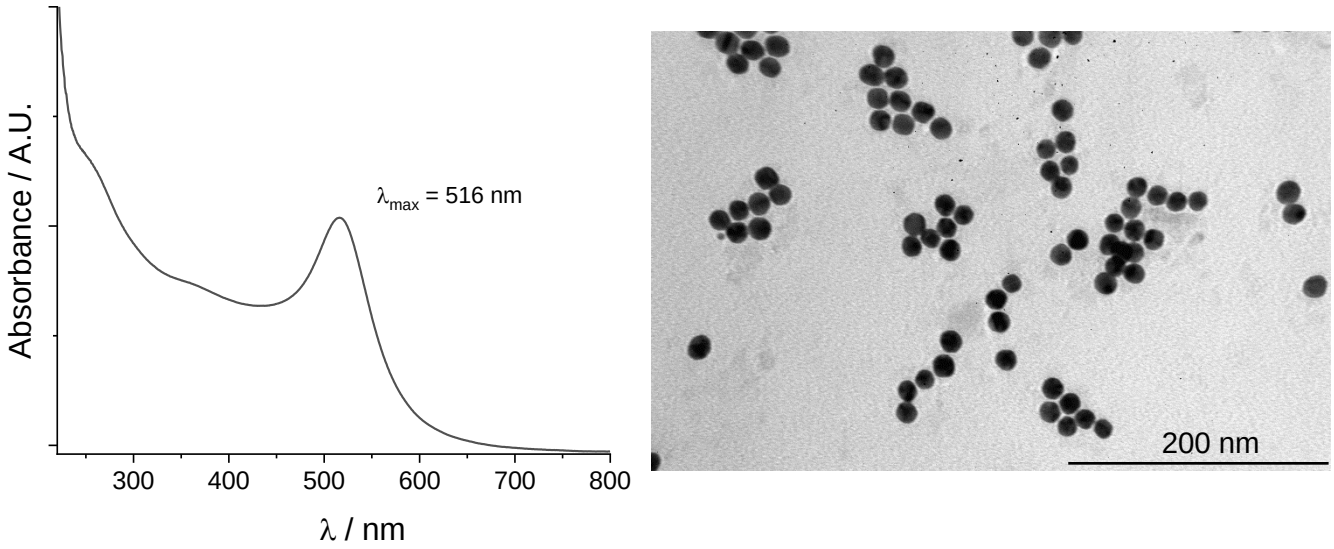


Figure 2.18 - 13 nm citrate gold nanoparticle characterisation. UV-vis spectrum of 13 nm gold nanoparticles in water (left); TEM image of 13 nm citrate gold nanoparticles after synthesis (right) (scale bar = 200 nm).

Table 2.4 - 13 nm citrate gold nanoparticle hydrodynamic diameter measurements by DLS and ζ-potential measurements.

Number / nm	Intensity / nm	PDI	ζ-potential / mV
13 ± 3	18 ± 4	0.10	-38 ± 5

2.5.2 Evaluating the Molar Concentration of AuNP13

The molar concentration (*c*) of the gold nanoparticles after synthesis was calculated as 2.3 nM using the Beer-Lambert law, measuring the absorbance of the nanoparticles at

450 nm by UV-vis spectroscopy and using a molar absorption coefficient for 13 nm gold nanoparticles described by Haiss *et al.*,[49] shown in equation 1:

$$c = \frac{A_{450}}{l\ x\ \varepsilon_{450}} \qquad (1)$$

where c = concentration (nM), A_{450} = absorbance (A.U.) at 450 nm, l = path length (= 1 cm^{-1}) and ε_{450} = molar absorption coefficient (1.39 x 10^8 $M^{-1}cm^{-1}$) at 450 nm. 450 nm is chosen because the absorbance at the λ_{SPR} is more heavily influenced by surface effects. This agrees with a concentration of 2.38 nM calculated theoretically from the number of gold atoms in a 13.4 nm AuNP and the mass of reagents used during synthesis (see appendix 2.12.4). Nanoparticle concentration was also analysed by ICP-MS the discrepancy between the concentrations was 6%, 10% and 14%, giving an average discrepancy of 10%. Due to the good agreement of values for concentration calculated from each method and the ease and low cost of using UV-vis spectroscopy, it was decided that this is a suitably accurate method to use to calculate concentration in this work.

2.5.3 LnQuin$_2$S-AuNPs

Here the synthesis of EuQuin$_2$S-AuNPs is shown, but YbQuin$_2$S-AuNPs and NdQuin$_2$S-AuNPs were prepared following an identical protocol and characterisation of these NPs can be found in the appendix (2.12.5 and 2.12.6). EuQuin$_2$SH [0.4 mM] was added to 13 nm citrate gold nanoparticles [5 nM] in 2.5 µL aliquots and stirred for 2 min, then the change in λ_{SPR} was monitored by UV-vis spectroscopy. A red shift in λ_{SPR} was observed upon EuQuin$_2$SH addition, suggesting the displacement of citrate anions and EuQuin$_2$SH attachment to the surface (Figure 2.19). After the addition of EuQuin$_2$SH to a concentration of 8.8 µM, there was a shift in the λ_{SPR} of 5.8 nm from 515 to 520.8 nm (Figure 2.19) , and further additions did not alter the λ_{SPR}, suggesting no further attachment of EuQuin$_2$SH was possible, most likely due to steric hindrance on the nanoparticle surface. Changes to the shape of the SPR band of AuNPs in UV-Vis spectra can indicate

aggregation,[50, 51] but here no change in shape was observed during addition of $EuQuin_2SH$, suggesting no aggregation took place.

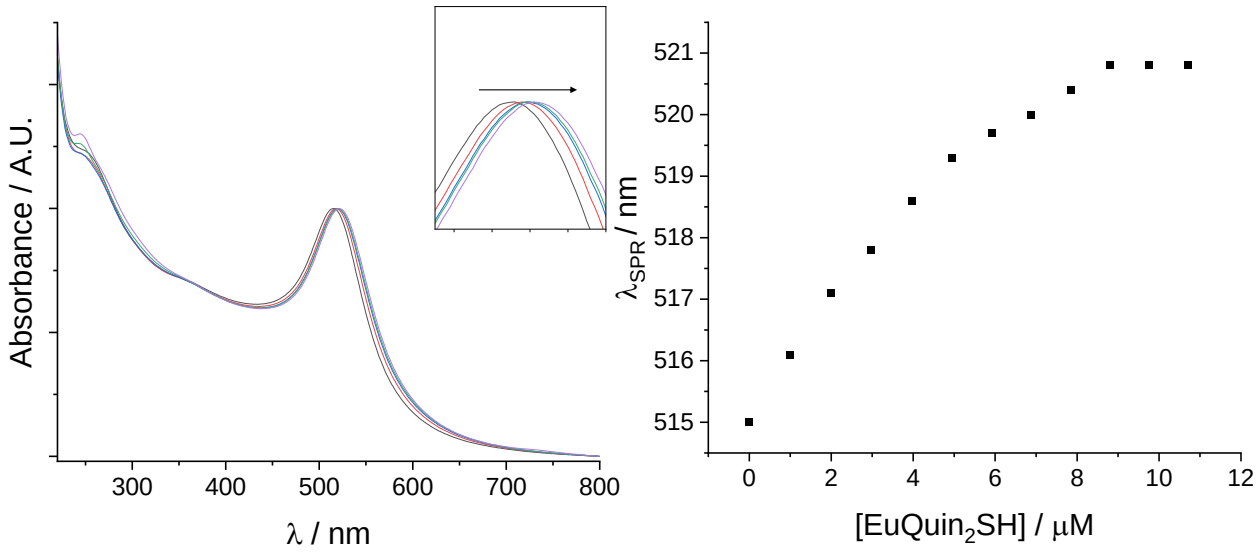


Figure 2.19 - Addition of $EuQuin_2SH$ to 13 nm gold nanoparticles causes a red shift in λ_{SPR}. Normalised UV-vis spectra of a 13 nm gold nanoparticle solution [5 nM] upon 2.5 μL additions of $EuQuin_2SH$ [0.4 mM] (left); The change in the λ_{SPR} of 13 nm gold nanoparticles upon $EuQuin_2SH$ addition measured by UV-vis spectroscopy (right).

The solution was then purified by size exclusion chromatography to remove any unbound metal complexes. The UV-vis spectrum of the $EuQuin_2S$-AuNPs was not altered during the purification step, suggesting that $EuQuin_2SH$ remains attached to the nanoparticle surface (Figure 2.20). DLS analysis revealed the nanoparticles remained monodisperse and the increase hydrodynamic diameter increased as expected (Table 2.5), due to the larger size of $EuQuin_2SH$ on the surface compared to citrate anions. ζ-potential measurements revealed that the nanoparticles became less electronegative, with an average surface charge of -11 ± 6 mV, likely due to the displacement of negative citrate anions with the neutral $EuQuin_2SH$ complex. TEM images revealed that the diameter of the gold core remained unchanged after functionalisation with $EuQuin_2SH$, with an average diameter of 13.3 ± 0.9 (SD) nm measured from 30 individual particles (Figure 2.20). To determine the average number of $EuQuin_2SH$ complexes per nanoparticle, an ionic solution of $EuQuin_2S$-

AuNPs was analysed by ICP-MS. A ratio of 43 Au:Eu atoms was found, meaning there was an average of 1600 EuQuin$_2$SH complexes per NP (Table 2.5).

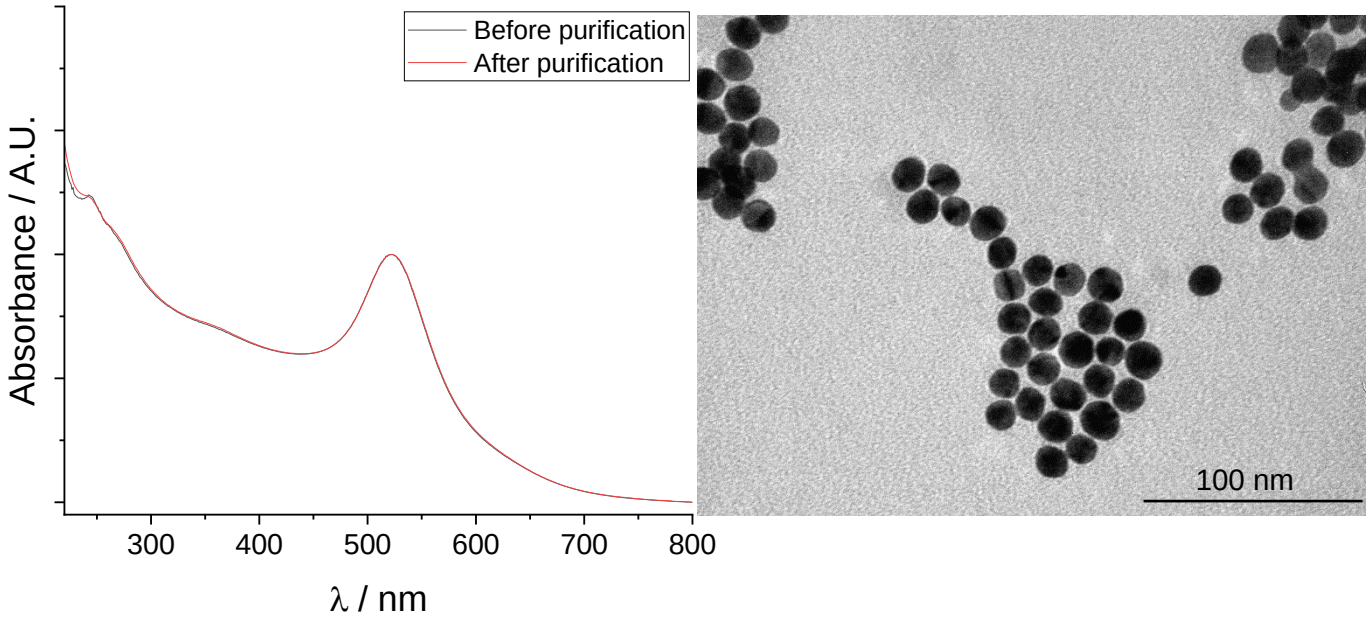


Figure 2.20 - Full characterisation of EuQuin$_2$S-AuNPs after purification. Normalised UV-vis spectra of EuQuin$_2$S-AuNPs before and after purification (left); TEM image of purified EuQuin$_2$S-AuNPs (scale bar = 100 nm) (right).

Table 2.5 - Average hydrodynamic diameter of EuQuin$_2$S-AuNPs measured by DLS and ζ-potential measurements, and the average number of EuQuin2SH complexes determined by ICP-MS.

Number / nm	Intensity / nm	PDI	ζ-potential / mV	EuQuin$_2$SH complexes per NP
14 ± 4	21 ± 7	0.13	-11 ± 6	1600 ± 60

2.5.4 Synthesis of Surfactant and Polymer Coated EuQuin$_2$S-AuNPs: EuQuin$_2$S-Zonyl-AuNPs, EuQuin$_2$S-TFD-AuNPs and EuQuin$_2$S-PEG-AuNPs

Prior to the addition of EuQuin$_2$SH, fluorinated surfactants Lithium 3-[2-(perfluoroalkyl)ethylthio]propionate (Zonyl FSA) and *N*-(2-(ethylthio)ethyl)-2,2,3,3,4,4,5,5,6,6,7,7,8,8,9,9,10,10,11,11,12,12,12-tricosafluorododecanamide (TFD), as well as 1-mercapto-3,5,7,9,11,13,15,17-octaoxaicosan-20-oic acid (PEG), a thiol-terminated PEG polymer were used to coat the nanoparticle surface of 13 nm citrate gold

nanoparticles at pH 7 (Figure 2.21). The length of Zonyl FSA, TFD and PEG were measured on Chem3D as 1.6 nm, 2.0 nm and 3.2 nm respectively, compared to a length of approximately 1.8 nm for $EuQuin_2SH$.

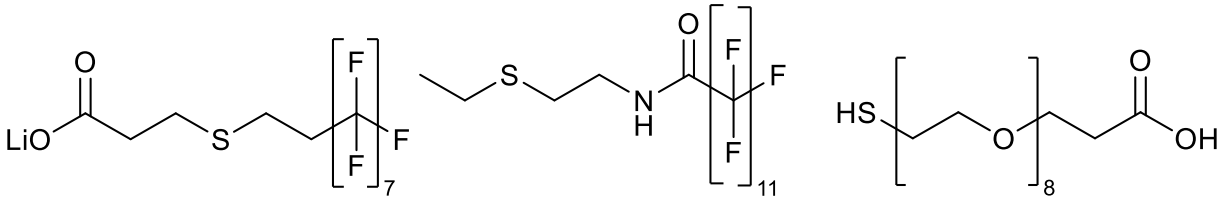


Figure 2.21 - The structures of Lithium 3-[2-(perfluoroalkyl)ethylthio]propionate (Zonyl FSA) (left), *N*-(2-(ethylthio)ethyl)-2,2,3,3,4,4,5,5,6,6,7,7,8,8,9,9,10,10,11,11,12,12,12-tricosafluorododecanamide (TFD) (middle), and 1-mercapto-3,5,7,9,11,13,15,17-octaoxaicosan-20-oic acid (PEG) (right).

Titrations were carried out to determine the amount of surfactant/polymer required to shift λ_{SPR} by 1/3 of its maximum, assuming this led to coating approximately 1/3 of the nanoparticle surface to allow space for $EuQuin_2SH$ attachment. 12 μM zonyl, 10 μM TFD and 2 μM PEG was required to shift the λ_{SPR} of 5 nM citrate-stabilised gold nanoparticles by 1/3 of its maximum (Figure 2.22). The higher amount of Zonyl and TFD required to saturate the surface could be due to the highly polar perfluoroalkyl chain adopting a more rigid conformation than PEG, which is well known to adopt 'mushroom' (PEG chain close takes up large area close to NP surface) or 'brush' (PEG chain extending straight out) like conformations at the surface of nanoparticles depending on the density of the coverage.[52-54]

After partial coating, $EuQuin_2SH$ was added in excess to each NP species. UV-vis spectroscopy revealed that a 6 nm shift in λ_{SPR} for $EuQuin_2S$-Zonyl-AuNPs, $EuQuin_2SH$-TFD AuNPs and $EuQuin_2S$-AuNPs and a 5 nm shift for $EuQuin_2S$-PEG-AuNPs after surfactant/polymer and subsequent $EuQuin_2SH$ addition (Figure 2.22).

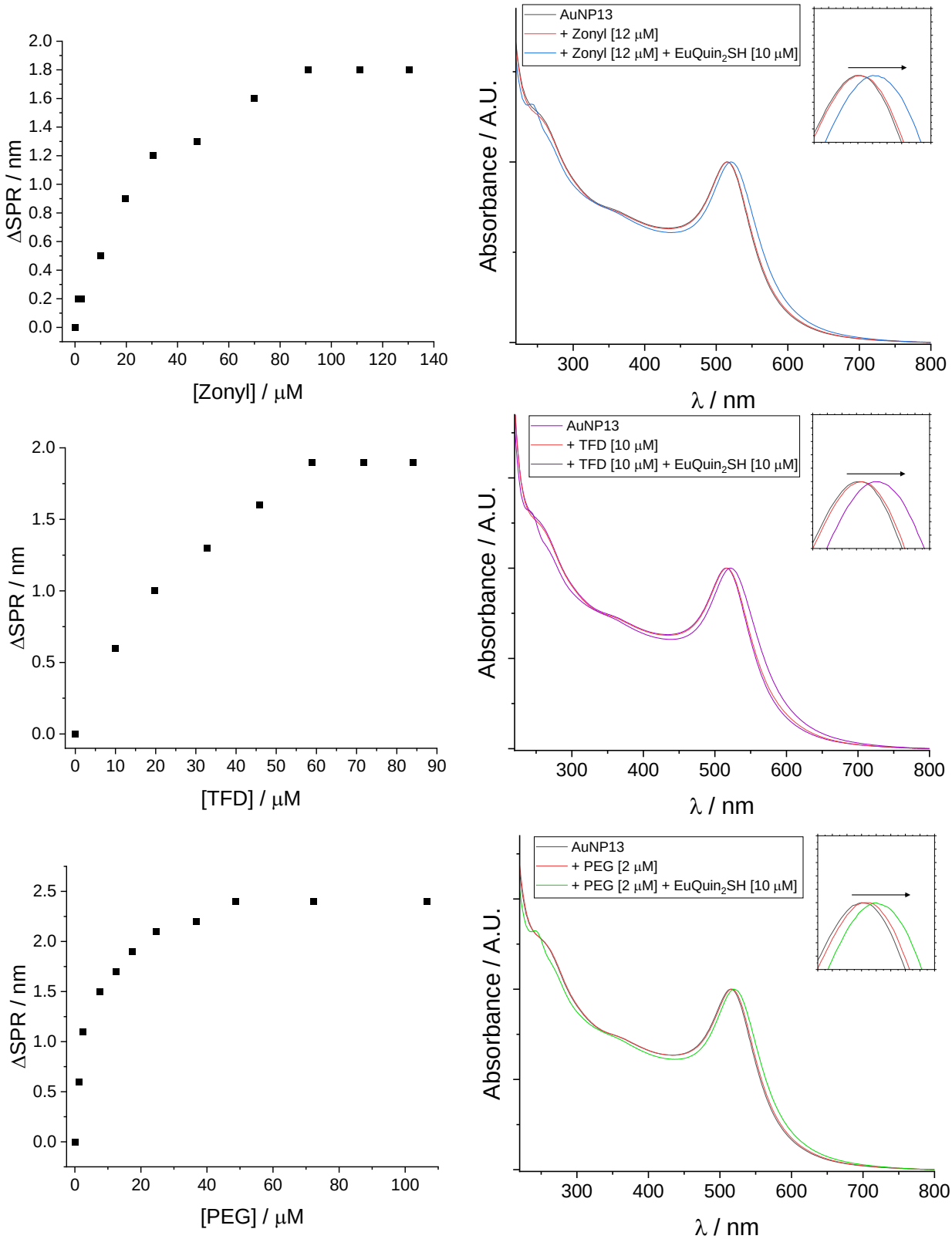


Figure 2.22 - The change in the λ_{SPR} of 13 nm citrate gold nanoparticles upon addition of Zonyl FSA, TFD and PEG, measured by UV-vis spectroscopy (left column); UV-Vis spectra of 13 nm gold nanoparticles [5 nM] upon addition of Zonyl FSA, TFD and PEG to coat approximately 1/3 of the nanoparticle surface, with subsequent addition of $EuQuin_2SH$ in excess (right column).

The nanoparticles were then purified by size exclusion chromatography. There were no observable changes to the UV-vis spectrum before and after purification. There was no statistical difference in the hydrodynamic size between each NP species (Table 2.6). All species remained monodisperse with one peak observed in DLS measurements, but the PDI was higher in the presence of PEG (0.19), Zonyl (0.25) and TFD (0.22). There was no statistical difference between the ζ-potential of each species (Table 2.6). The UV-vis spectra and TEM images of each species show no evidence of aggregation of the gold nanoparticles (Figure 2.23 and Figure 2.24). After digestion of the nanoparticles with aqua regia, ionic solutions were analysed by ICP-MS to determine the average number of $EuQuin_2SH$ complexes per NP (Table 2.6). The average number of $EuQuin_2SH$ complexes per nanoparticle was found to be 1600 ± 60 for $EuQuin_2S$-AuNPs, 1600 ± 80 for $EuQuin_2S$-Zonyl-AuNPs, 1500 ± 70 for $EuQuin_2S$-TFD-AuNPs, and 1400 ± 80 $EuQuin_2S$-PEG-AuNPs, thus it can only be concluded that PEG had any statistically significant effect on the loading of $EuQuin_2SH$.

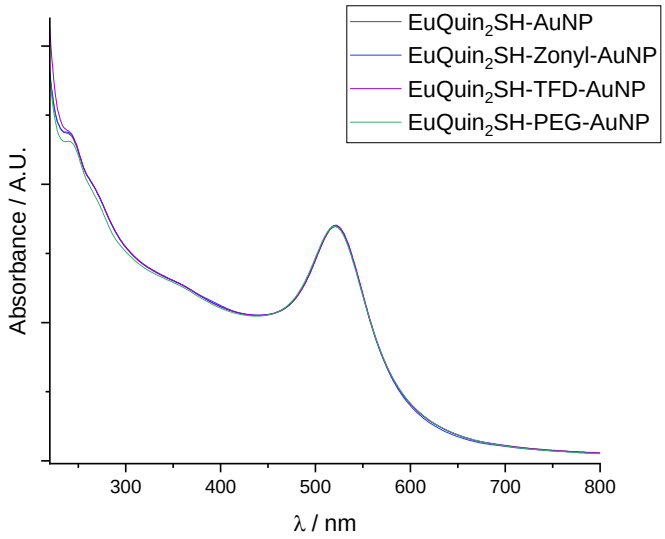


Figure 2.23 - UV-Vis spectrum of $EuQuin_2S$-AuNPs, $EuQuin_2S$-Zonyl-AuNPs, $EuQuin_2S$-TFD-AuNPs and $EuQuin_2S$-PEG-AuNPs at a concentration of 3.8 nM.

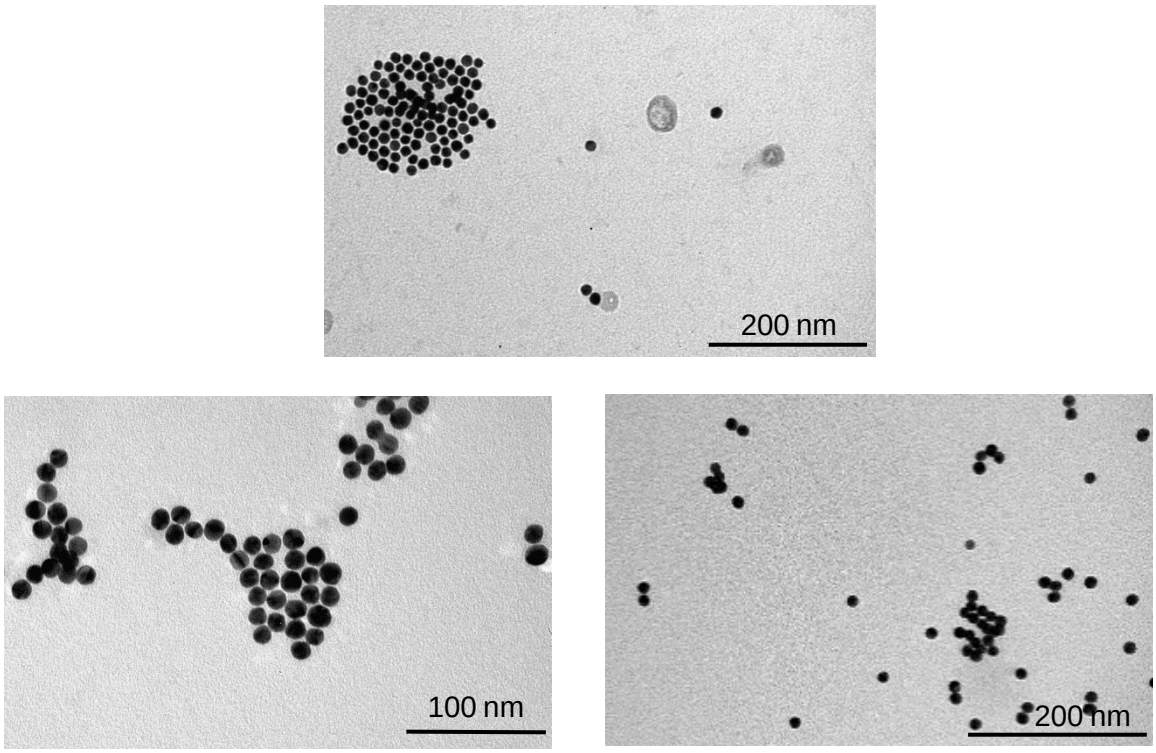


Figure 2.24 - TEM images of purified $EuQuin_2S$-Zonyl-AuNPs, $EuQuin_2S$-TFD-AuNPs and $EuQuin_2S$-PEG-AuNPs.

Table 2.6 - λ_{SPR}, hydrodynamic diameter (± SD), ζ-potential (± SD) and the average number of $EuQuin_2SH$ complexes per NP characterisation of $EuQuin_2S$-AuNPs, $EuQuin_2S$-Zonyl-AuNPs, $EuQuin_2S$-TFD-AuNPs and $EuQuin_2S$-PEG-AuNPs by UV-Vis spectroscopy, DLS, ζ-potential and ICP-MS. For ICP-MS measurements, a mean average of duplicate measurements from 2 independently synthesised nanoparticle species is given (± SD).

NP Species	λ_{SPR}	Number / nm	Intensity / nm	PDI	ζ-potential / mV	$EuQuin_2SH$ complexes per NP
$EuQuin_2S$-AuNP	521	14 ± 4	21 ± 6	0.13	-19 ± 10	1600 ± 60
$EuQuin_2S$-Zonyl-AuNP	521	15 ± 4	29 ± 12	0.25	-24 ± 13	1600 ± 80
$EuQuin_2S$-TFD-AuNP	521	15 ± 4	30 ± 14	0.22	-27 ± 14	1500 ± 70
$EuQuin_2S$-PEG-AuNP	520	16 ± 4	31 ± 10	0.19	-25 ± 14	1400 ± 80

It was expected that a more considerable decrease in $EuQuin_2SH$ loading would be observed in the presence of the surfactants and polymers. However, the binding strengths and conformational changes at the surfaces could explain the result. Ligands with multiple thiol-terminated groups have a higher binding affinity to AuNPs and form more stable AuNP-ligand conjugates.[41] The binding mode of Zonyl FSA and TFD to the surface of gold

nanoparticles are not known, though a previous study by the group show the presence of Zonyl FSA at gold surfaces after the addition of ruthenium and iridium complexes.[55] Dialkyl sulphides have been shown to form weaker interactions with gold surfaces than alkane-thiols,[56, 57] and as both Zonyl FSA and TFD are dialkyl sulphides, it is possible that they could be displaced by $EuQuin_2SH$ at the nanoparticle surface, which is likely to have a strong covalent interaction due to its 2 terminal thiol groups. This could explain why Zonyl FSA and TFD do not reduce the loading, but the thiol-terminated PEG polymer does reduce the loading of $EuQuin_2SH$ by 15%. In the case of PEG, as previously mentioned, the conformation of PEG changes from 'mushroom' to 'brush' like depending on the density of the coverage.[52-54] Upon addition of $EuQuin_2SH$, the PEG polymers may extend further out and become more brush like in conformation due to more steric crowding, allowing more space for $EuQuin_2SH$ to bind to the surface, meaning that it does not reduce the loading by as much as expected.

2.5.5 LnS-AuNPs

Here the synthesis of TbS-AuNPs is shown, but the synthesis of EuS-AuNPs AuNPs were prepared following identical protocol and characterisation of these NPs can be found in the appendix (2.12.7). TbSH (0.4 mM) was added to 5.1 nM 13 nm citrate gold nanoparticles in small aliquots until no change in λ_{SPR} was observed in the UV-Vis spectrum (Figure 2.25). A red shift of 6.3 nm was observed after the addition of 8.2 µM of TbSH (Figure 2.25). There was no observable change in the shape of the SPR band upon TbSH addition, suggesting that no aggegative effects occurred.

After purification by size exclusion chromatography, the UV-vis spectrum was not altered (Figure 2.26), suggesting that the TbSH complexes remained attached to the NP surface. Analysis by DLS revealed that the particles remained monodisperse and slightly larger than 13 nm citrate gold nanoparticles, owing to the larger size of TbSH with respect to the citrate anions they displaced (Table 2.7). Zeta-potential measurements showed an average

negative surface charge of -25 ± 12 mV compared to an average surface charge of -38 ± 5 mV for 13 nm citrate gold nanoparticles, likely owing to the neutral TbSH displacing negative citrate anions (Table 2.7). TEM revealed no observable changes to the gold core size upon complex attachment (Figure 2.26), and ICP-MS revealed a Au:Tb ratio of 45, meaning there was an average of 1500 TbSH complexes per NP.

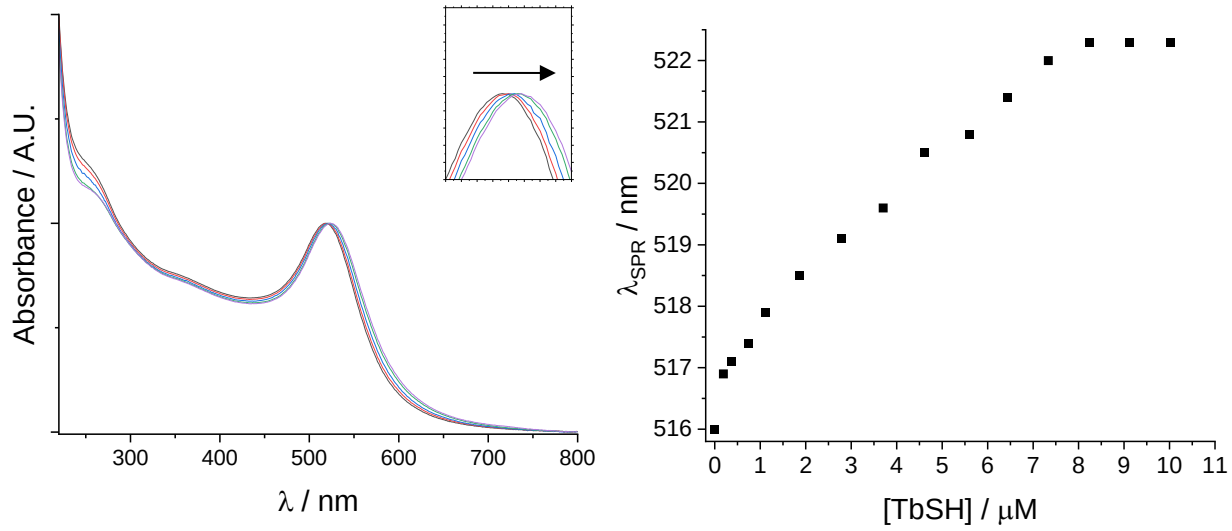


Figure 2.25 - Addition of TbSH to 13 nm gold nanoparticles causes a red shift in λ_{SPR}. Normalised UV-vis spectra of a 13 nm gold nanoparticle solution [5 nM] upon small additions of TbSH [0.4 mM] (left); The change in the λ_{SPR} of 13 nm gold nanoparticles upon TbSH addition measured by UV-vis spectroscopy (right).

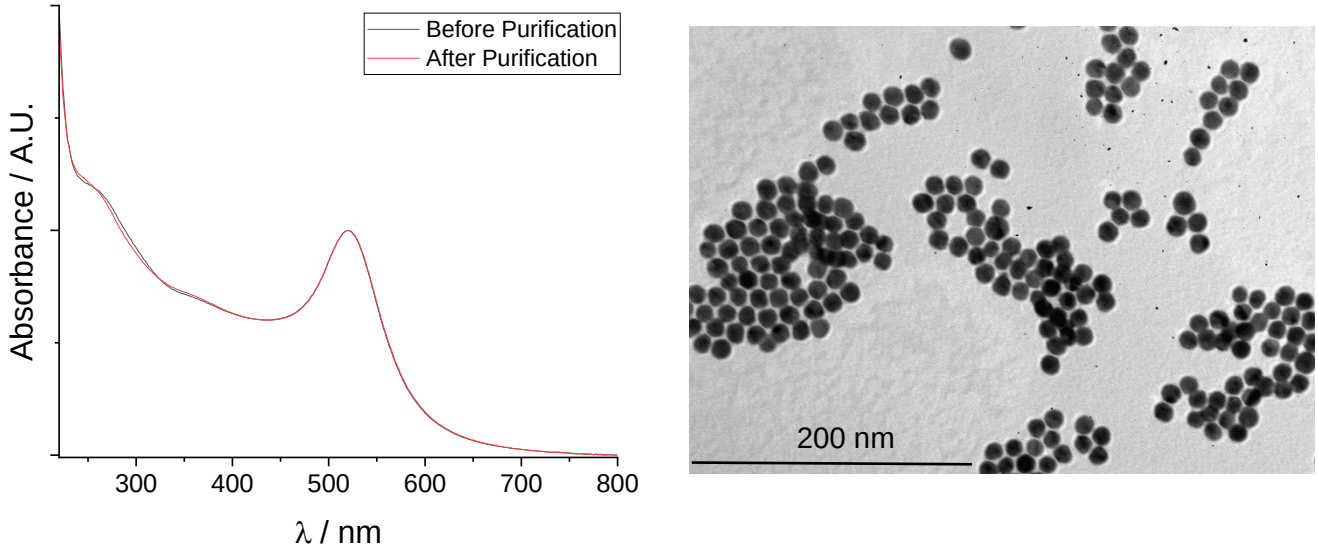


Figure 2.26 - Full characterisation of TbS-AuNPs after purification. Normalised UV-vis spectra of TbS-AuNPs before and after purification (left); TEM image of purified TbS-AuNPs (scale bar = 200 nm) (right).

Table 2.7 - Average hydrodynamic diameter of TbS-AuNPs measured by DLS and ζ-potential measurements.

Number / nm	Intensity / nm	PDI	ζ-potential / mV	TbSH complexes per NP
14 ± 4	19 ± 6	0.11	-25 ± 12	1500 ± 100

2.6 Further Characterisation of Lanthanide Complex Binding to 13 nm Gold Nanoparticle Surfaces

2.6.1 Determination of Association Constants for EuQuin$_2$SH and TbSH Binding to 13 nm Gold Nanoparticles from UV-Vis Spectroscopy

Using the data collected from UV-vis titrations of EuQuin$_2$SH and TbSH onto 5 nM 13 nm citrate gold nanoparticles, binding curves have been fitted to calculate an association constant, K_a, for metal complex attachment to gold nanoparticles. Murphy and co-workers have previously calculated association constants of proteins to gold nanoparticles by monitoring changes to λ_{SPR} with UV-vis spectroscopy and increases in hydrodynamic diameter by DLS, by fitting a Langmuir adsorption isotherm model:[58, 59]

$$\frac{\Delta\lambda}{\Delta\lambda_{max}} = \frac{K_a[A]}{1 + K_a[A]}$$

Where $\Delta\lambda$ is the change in SPR band, $\Delta\lambda_{max}$ is the maximum change in SPR band, K_a is the association constant (M^{-1}), and $[A]$ is the concentration of complex (M). A derivation of the Langmuir adsorption isotherm and how UV-vis spectroscopy is used to calculate K_a can be found in the appendix of this thesis (2.12.8). As this model is based on the Langmuir adsorption isotherm, there are several assumptions made. Firstly, it is based on completely flat surfaces, whereas each binding site on a spherical nanoparticle will have a very small curvature angle. It also assumes that a single monolayer is formed, all surface sites are identical, and the change in λ_{SPR} is attributed to ligand binding only.

After fitting binding curves to the UV-vis titration data, association constants of $(4.5 \pm 1.1) \times 10^5\ M^{-1}$ and $(3.7 \pm 0.6) \times 10^5\ M^{-1}$ for $EuQuin_2SH$ and TbSH respectively. The fact that these values fall within the confidence intervals of each other is perhaps not surprising given that they both have two terminal thiol groups to bind to the AuNP and the complexes are similar in size. These values are in the range of 10 to 100-fold lower than

Murphy and co-workers found for proteins binding to 20 and 90 nm gold nanoparticles, most likely owing to the much smaller size of the metal complexes compared to proteins.

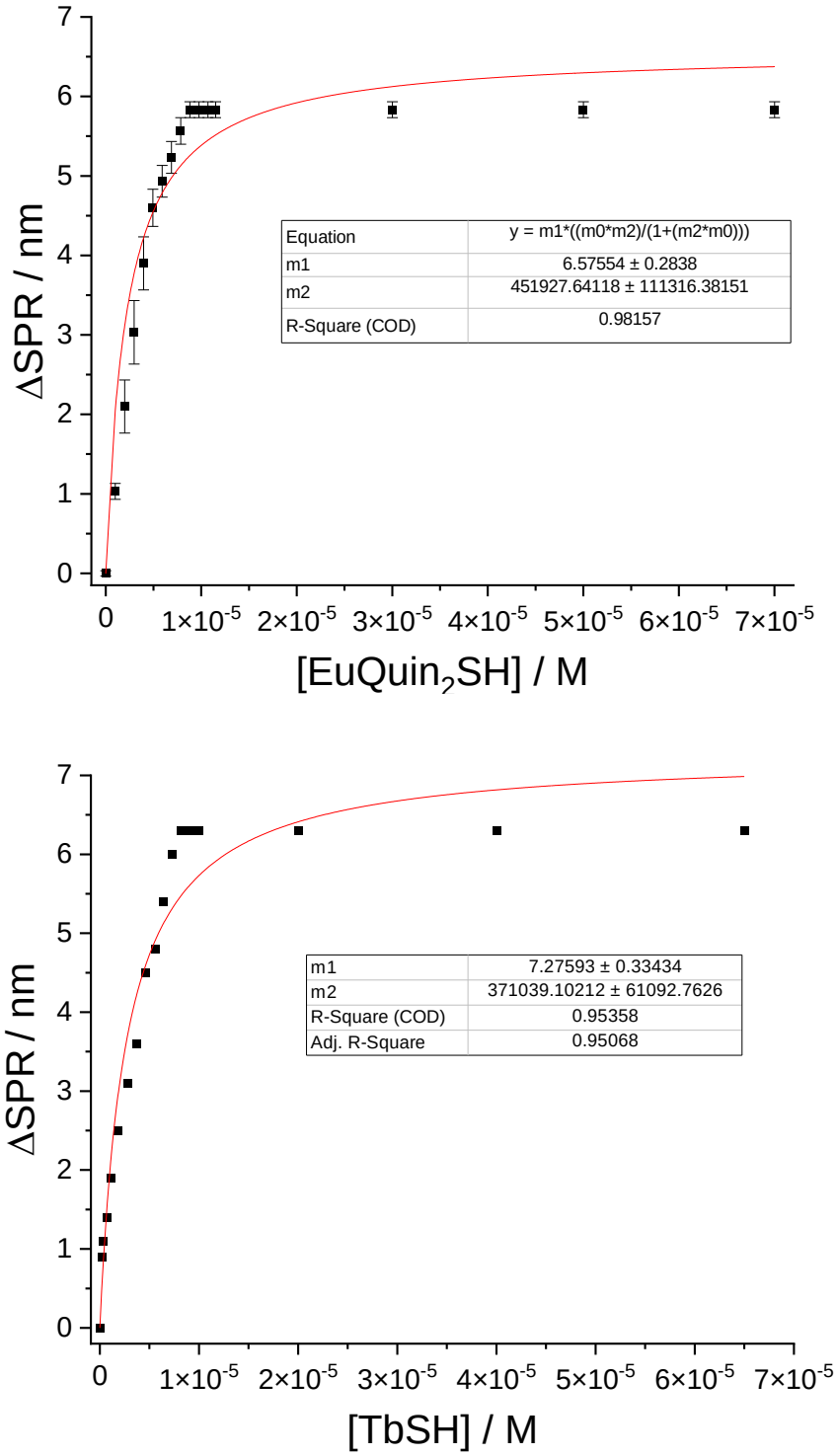


Figure 2.27 - Binding curves fitted to a titration of metal complex ($EuQuin_2SH$ and TbSH) addition to 13 nm citrate gold nanoparticles [5 nM], monitoring changes to λ_{SPR} with UV-vis spectroscopy. In the case of $EuQuin_2SH$, error bars are the range from 3 independent repeat experiments.

2.6.2 Isotherm Titration Calorimetry (ITC)

ITC was used to study the binding of $EuQuin_2SH$ and TbSH to 13 nm citrate gold nanoparticles. An ITC instrument is composed of two identical cells made with chemically inert, thermally conducting material. The sample is contained in one cell, in this case containing 13 nm citrate gold nanoparticles [7.5 nM], and the reference cell contains the buffer solution that the sample is contained within (Figure 2.28). As the binding ligand, in this case $EuQuin_2SH$ or TbSH metal complexes, is titrated into the sample cell in small aliquots, the temperature change between the sample and reference cell is measured in a unit known as the power differential (DP).[60]

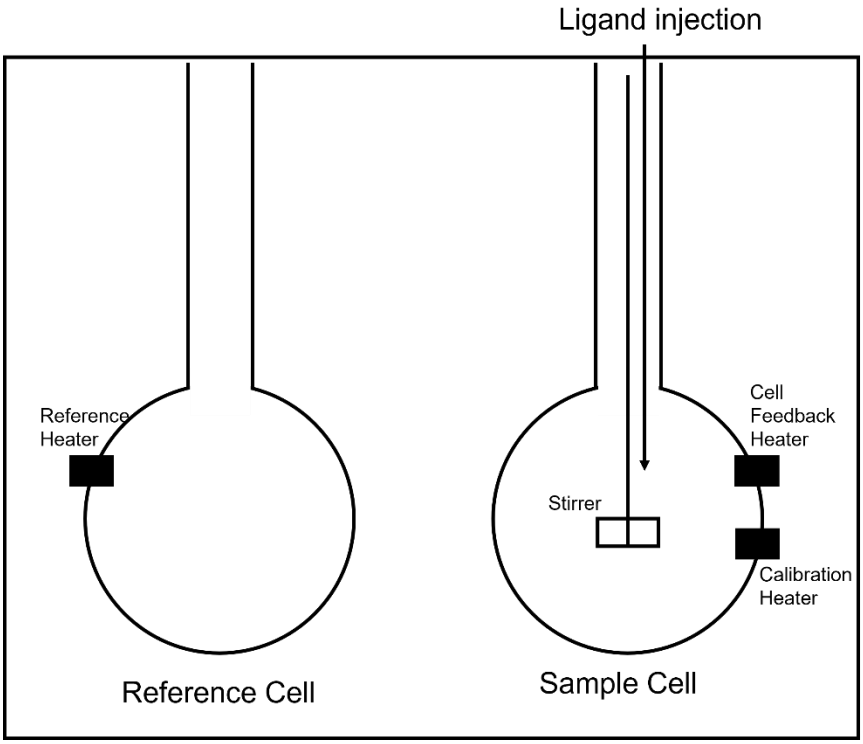


Figure 2.28 - Schematic representation of the instrument setup of ITC.

Control titrations were performed to confirm that no detectable enthalpy change occurred upon the addition of buffer to the nanoparticles without the addition of metal complex. Upon addition of 2 µL aliquots of $EuQuin_2SH$ and TbSH to 13 nm citrate gold nanoparticles, an enthalpic change was observed (Figure 2.29) before a plateau was reached after about 13 aliquots, which corresponds to a metal complex: nanoparticle molar ratio of about 1500-

2000 (Figure 2.30). As shown by ICP-MS, an average of 1600 $EuQuin_2SH$ and 1500 TbSH complexes can attach to each 13 nm gold nanoparticle. This suggests that the enthalpy change is caused by metal complex attachment to the nanoparticle surface, and the plateau is reached when the nanoparticle surface is saturated. This provides further evidence of a binding event occurring between the lanthanide metal complexes and the nanoparticle surface. The larger ΔDP upon TbSH addition after a plateau has been achieved may be due to more buffer mismatch between the sample and reference cell.

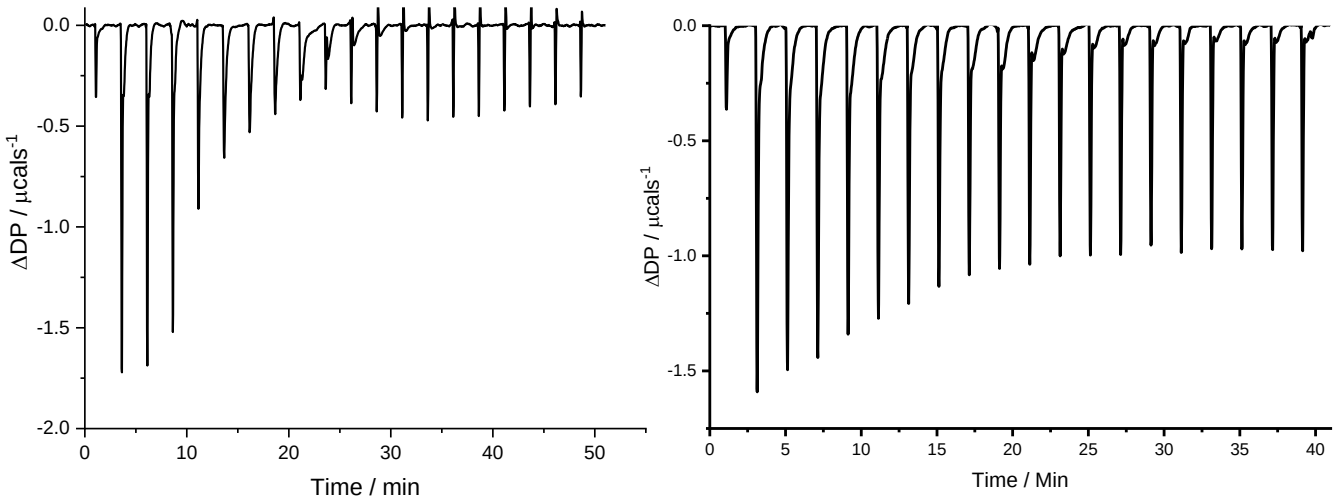


Figure 2.29 - ITC thermograms of the addition of $EuQuin_2SH$ (left) and TbSH (right) in 2 µL aliquots to 7.5 nM 13-nm citrate gold nanoparticles showing the change in differential power (ΔDP) measured.

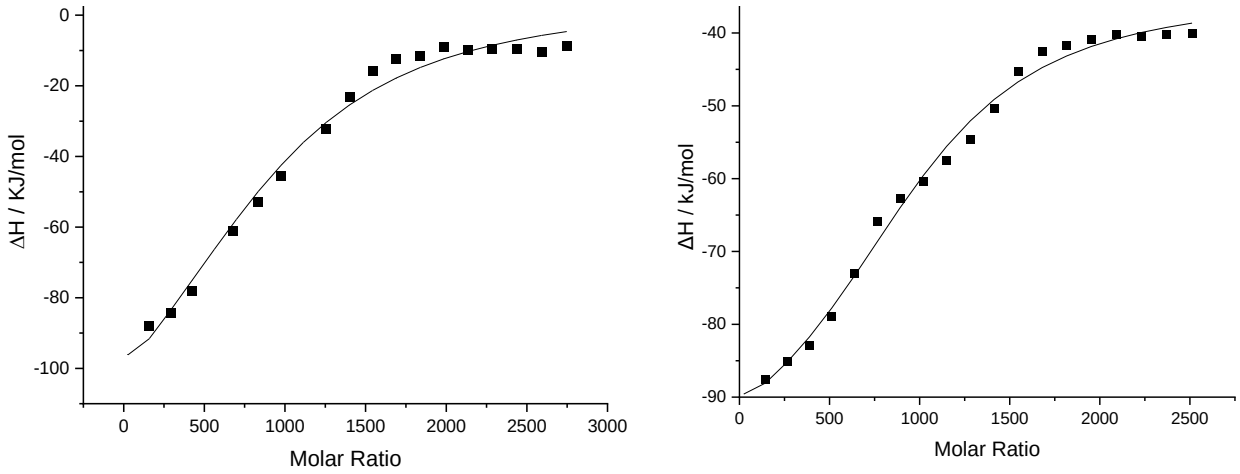


Figure 2.30 - The enthalpy change on addition of $EuQuin_2SH$ (left) and TbSH (right) in 2 µL aliquots to 7.5 nM 13-nm citrate gold nanoparticles measured by ITC with sigmoidal fit. For $EuQuin_2SH$, two data points were discarded as anomalous results.

ITC is a quantitative technique that can also determine the binding affinity, or association constant K_a. The profile of the curve is determined by the c-value (c) using the equation:

$$c = nK_aM$$

Where n is the stoichiometry and M is the molar concentration of the sample cell. Iterative fitting of the data using MicroCal PEAQ-ITC analysis software found K_a values of (3.2 ± 1.0) x 10^5 M^{-1} and (1.7 ± 0.9) x 10^5 M^{-1} for $EuQuin_2SH$ and TbSH binding to 13 nm citrate gold nanoparticles respectively. These values are in agreement with the K_a values of (4.5 ± 1.1) x 10^5 M^{-1} and (3.7 ± 0.6) x 10^5 M^{-1} determined for $EuQuin_2SH$ and TbSH respectively from UV-Vis experiments.

2.6.3 STEM/EELS Imaging of $EuQuin_2S$-AuNPs and EuS-AuNPs

In this work, the use of STEM and EELS to elementally map europium signal from $EuQuin_2S$-AuNPs and EuS-AuNPs around single gold nanoparticles is explored to determine whether a difference in distance from the gold surface can be resolved, owing to their different chain lengths. Gold and europium both have high atomic mass of 197 and 153 respectively, which should give good contrast in HAADF images. By approximately measuring the bond lengths in $EuQuin_2SH$ and EuSH and anticipating that the metal complexes will extend outwards from each nanoparticle after the formation of Au-S bonds from the terminal thiols in each leg of the complex, it was expected that the europium atoms of $EuQuin_2SH$ and EuSH are held around 1.5 nm and 0.6 nm away from the gold core respectively (Figure 2.31). The difference in distance of approximately 0.9 nm owed to the hexyl carbon chain in $EuQuin_2SH$ should therefore be within the resolution limits of STEM and EELS.

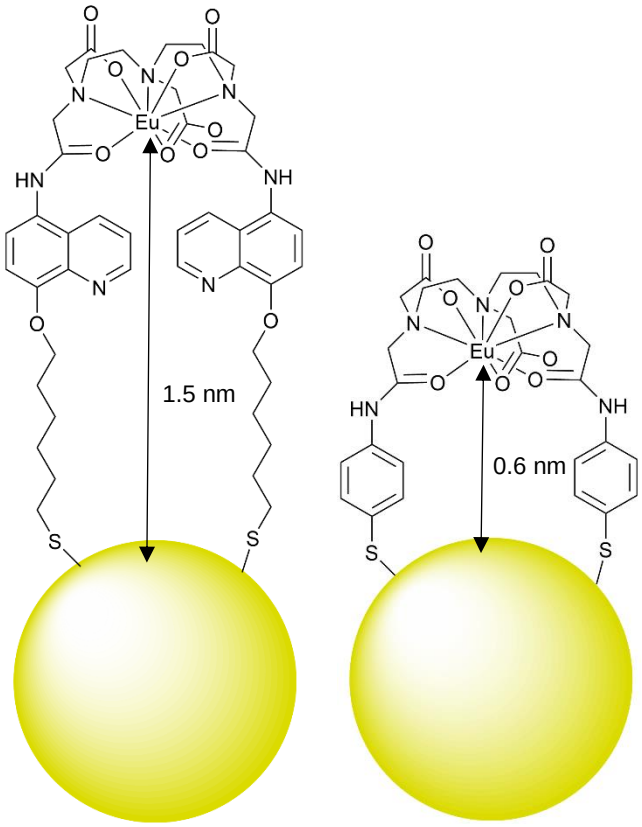


Figure 2.31 - Schematic representation of the estimated distances of europium atoms from $EuQuin_2SH$ and EuSH complexes attached to gold nanoparticle surfaces.

$EuQuin_2S$-AuNPs and EuS-AuNPs were synthesised and purified as previously described and adjusted to a concentration of 2.5 nM, then drop casted onto graphene and ultra-thin carbon grids and allowed to dry at room temperature. Samples were then sent for STEM imaging at the SuperSTEM facility in Daresbury, UK. Image acquisition and analysis was carried out by members of staff at the facility. In these initial studies, the samples were not subjected to conventional heat treatment before imaging. This is usually carried out because carbon contamination can affect the sharpness of EELS spectra, lowering resolution.[61, 62] Figure 2.32 shows a HAADF image of a single $EuQuin_2S$-AuNP revealing a clear halo of bright atoms was observed 1.5-2 nm away from a bright gold core, likely attributed to europium from $EuQuin_2SH$ complexes. This is the distance that we would expect the europium atoms to be held away from the gold core from the $H3Quin_2SH$ ligand

from approximately measuring the bond distances. Numerous images showed this contrast and more are shown in the appendix (2.12.9)

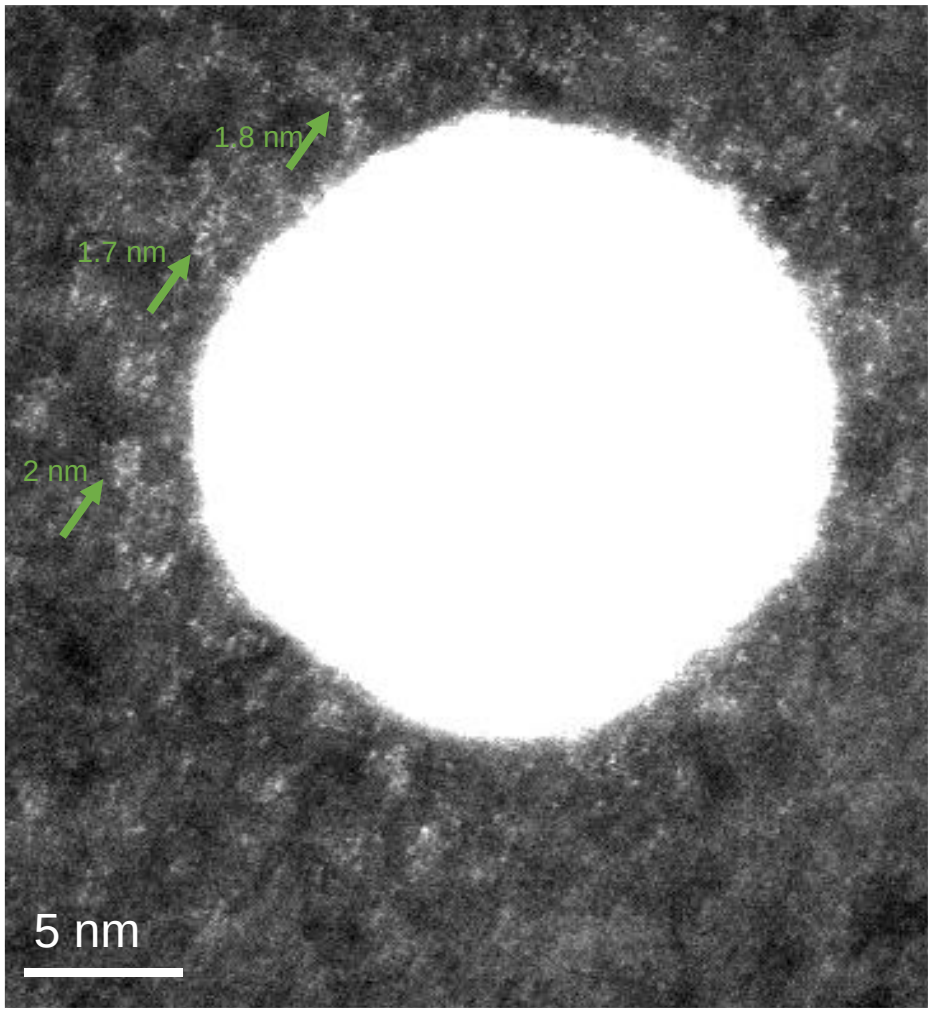


Figure 2.32 - HAADF image of a single $EuQuin_2S$-AuNP on graphene support. Arrows indicate bright spots attributed to europium atoms from $EuQuin_2SH$ surrounding the gold core, with approximate measured distance.

Figure 2.33 shows an EELS spectra of an $EuQuin_2S$-AuNP in the position of a bright spot in the halo. Features are present beginning at 1131 and 1161 eV with delayed maxima, matching exactly the position you would expect a signal attributed to the Eu $M_{4,5}$-edges in Eu(III) atoms.[63, 64] Although the signal is quite weak due to organic contamination issues, this feature was present in several EELS spectra taken in different positions.

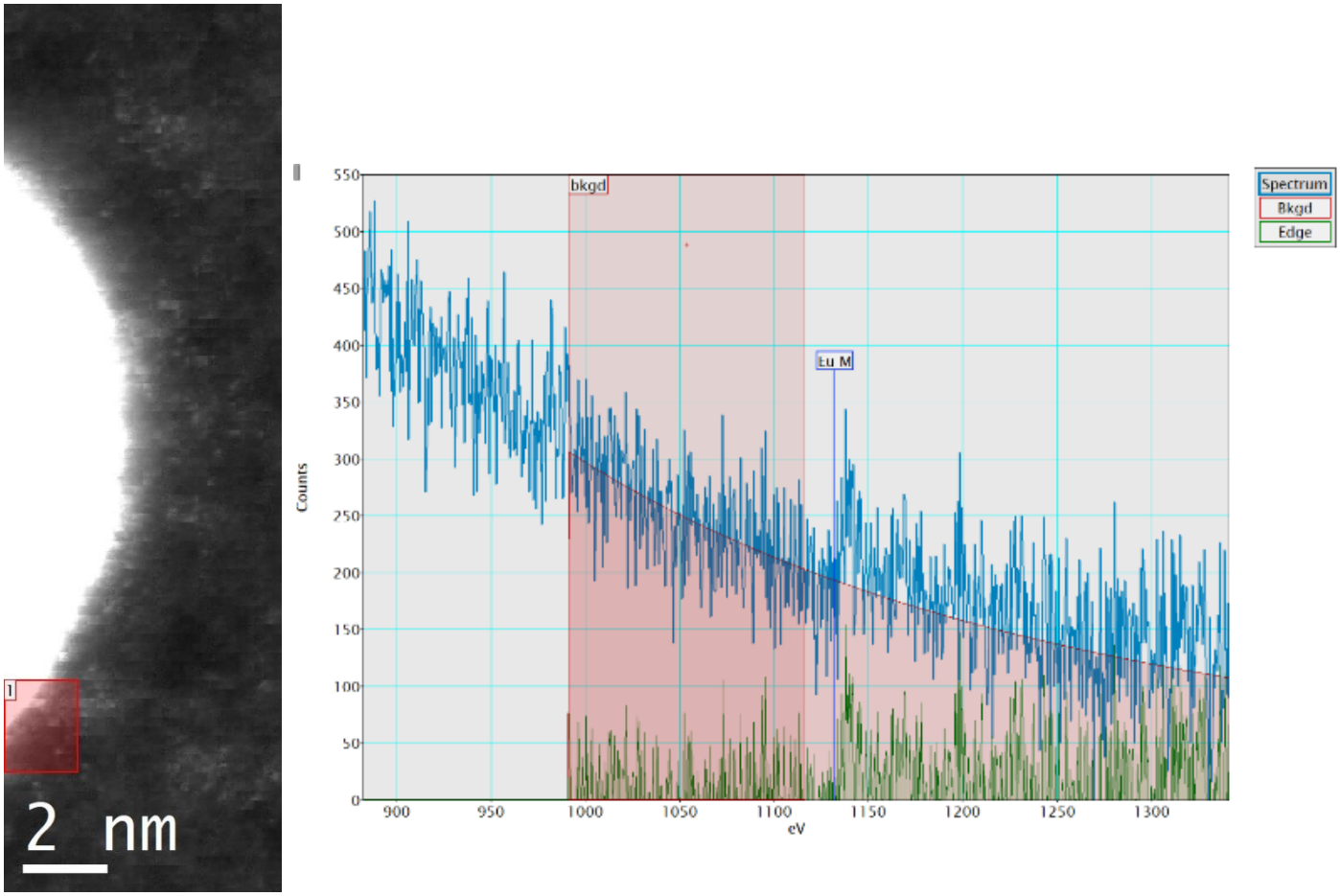


Figure 2.33 - EELS spectrum of a single EuQuin$_2$S-AuNP on a graphene support at the position of a bright spot in the halo around the gold core, highlighted by the red box on the HDAAF image.

Figure 2.34 shows a HAADF image of a single EuS-AuNP imaged on ultra-thin carbon supports. Similarly, a clear halo of bright atoms is observed around the gold core, but this time closer to the surface, approximately 1 nm from the gold nanoparticle, likely attributed to europium held this distance by its chelating H_3L ligand. The closer distance observed is expected due to the absence of a spacer chain in EuSH, compared to EuQuin$_2$SH. It was not possible to image EuS-AuNPs on graphene due to the severity of organic contamination.

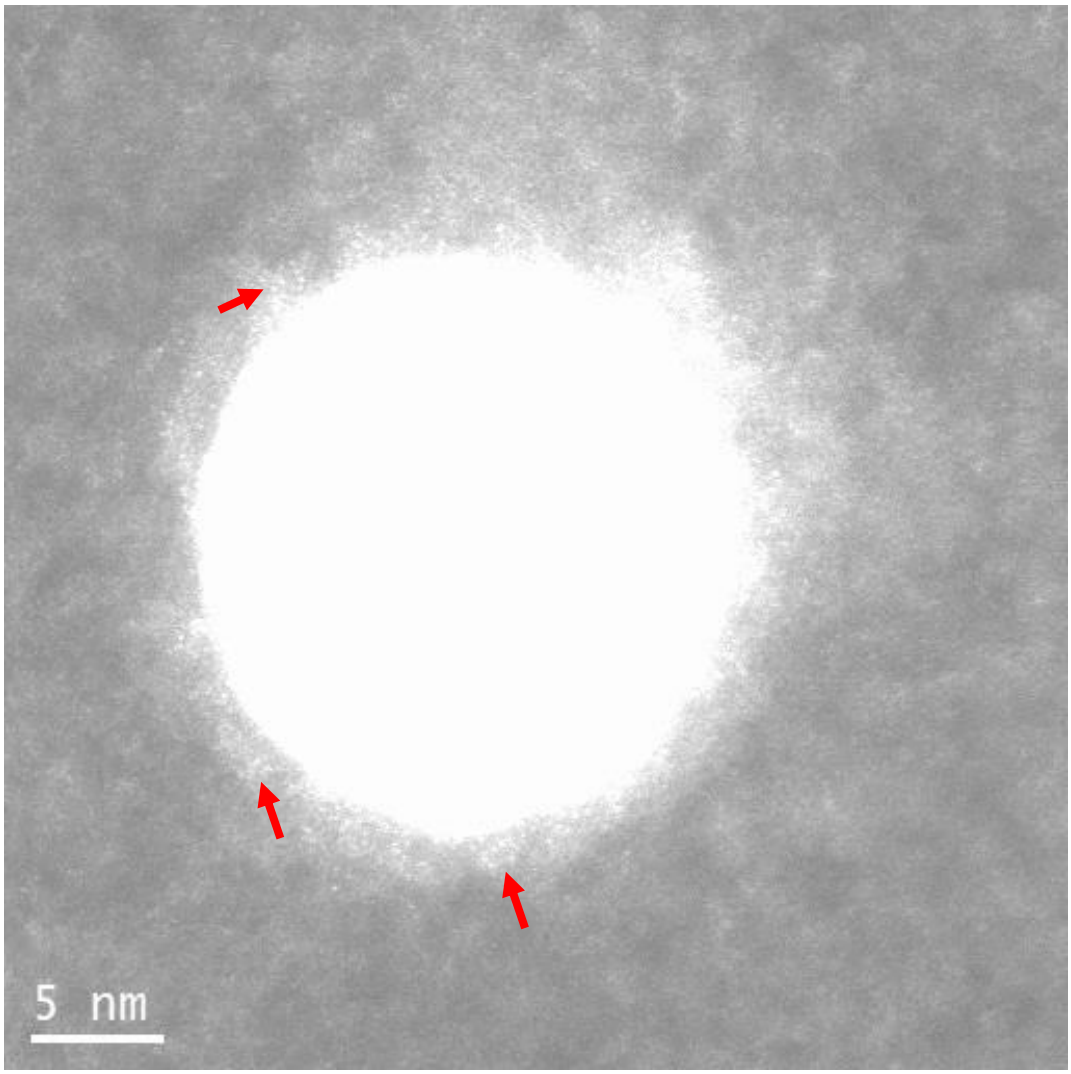


Figure 2.34 - HAADF image of a single EuS-AuNP on an ultra-thin carbon support. Arrows indicate bright spots attributed to europium atoms from EuSH surrounding the gold core.

Weak signals were observed again in the core-loss region of the EELS spectrum in the exact positions expected for Eu $M_{4,5}$-edges in Eu(III) at 1131 and 1161 eV, this time in the neck between two nanoparticles (Figure 2.35). Europium mapping reveals co-localisation of europium and gold all over the nanoparticle, and the arrows in Figure 2.35 show bright spots in the HAADF and europium map in the exact same positions approximately 0.5-1 nm from the gold surface.

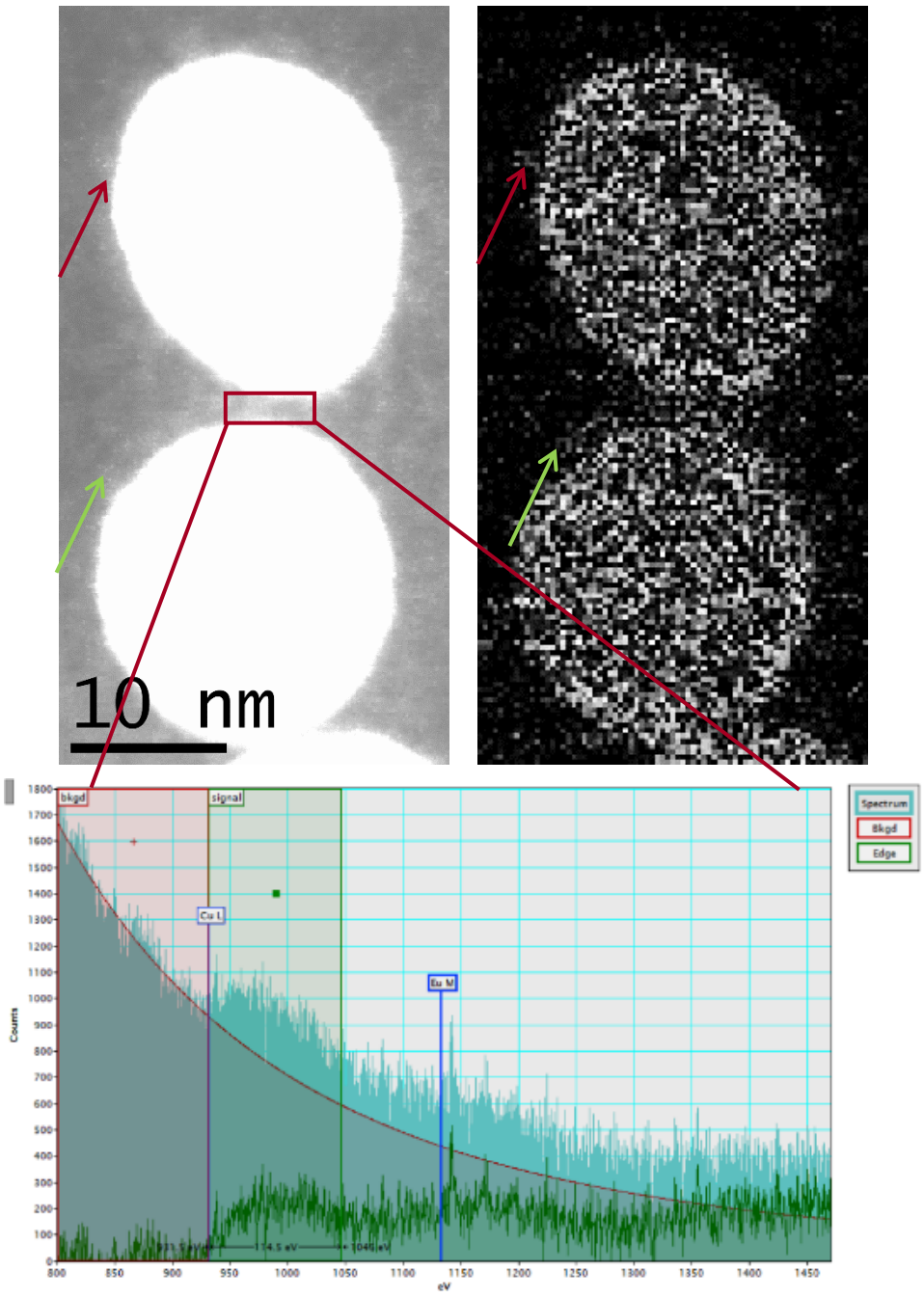
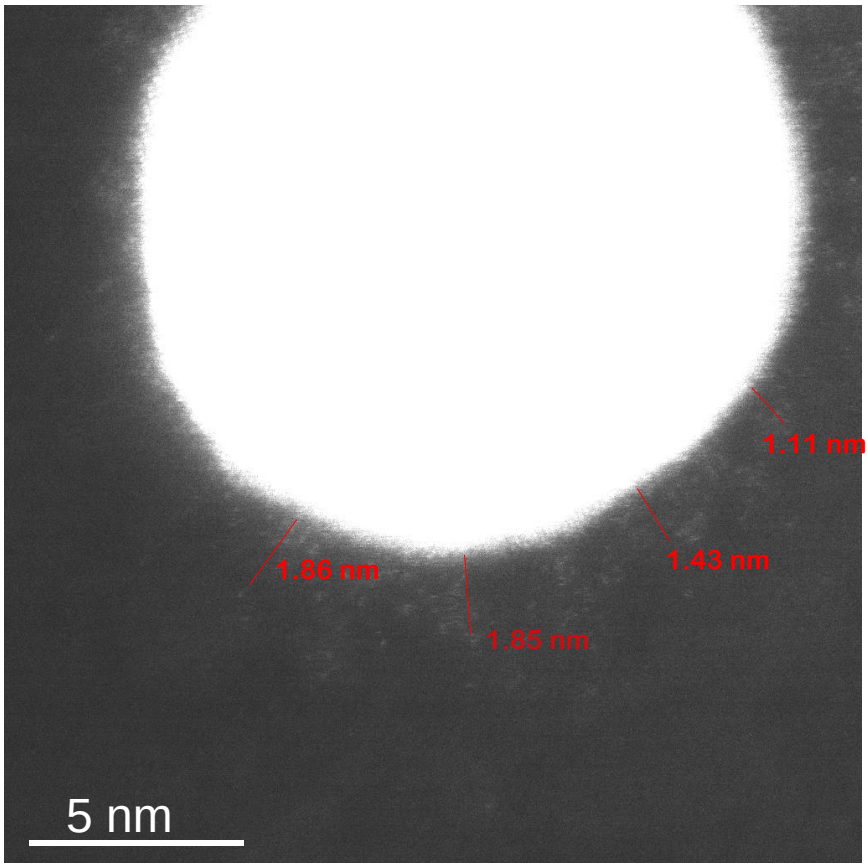


Figure 2.35 - EELS spectrum (bottom) of a two EuS-AuNPs on a graphene support at a position in the neck between the two nanoparticles, highlighted by the red box in the HDAAF image (top left). Europium signal mapping by EELS of two EuS-AuNPs (top right). Arrows indicate co-localisation of bright spots present in HDAAF image and EELS europium map approximately 1 nm from the gold core.

After these promising initial results, fresh $EuQuin_2S$-AuNPs and EuS-AuNPs were synthesised (from different AuNP batches) and sent for further analysis at the SuperSTEM facility. Image acquisition and analysis was carried out by members of staff at the facility, as well as heat treatment of the samples. This time, the samples were heat treated at 135 °C under vacuum at 10^{-5} Torr for 6 hours prior to imaging, in the hope of reducing carbon contamination to increase the signal intensity of europium in the EELS spectra.[62] Ultrathin carbon supports were used for all imaging. Single europium atoms appeared as bright spots approximately 1-2 nm from the AuNP surface (Figure 2.36) This was visible on multiple HDAAF images of $EuQuin_2S$-AuNPs and more images are shown in the appendix (2.12.9)



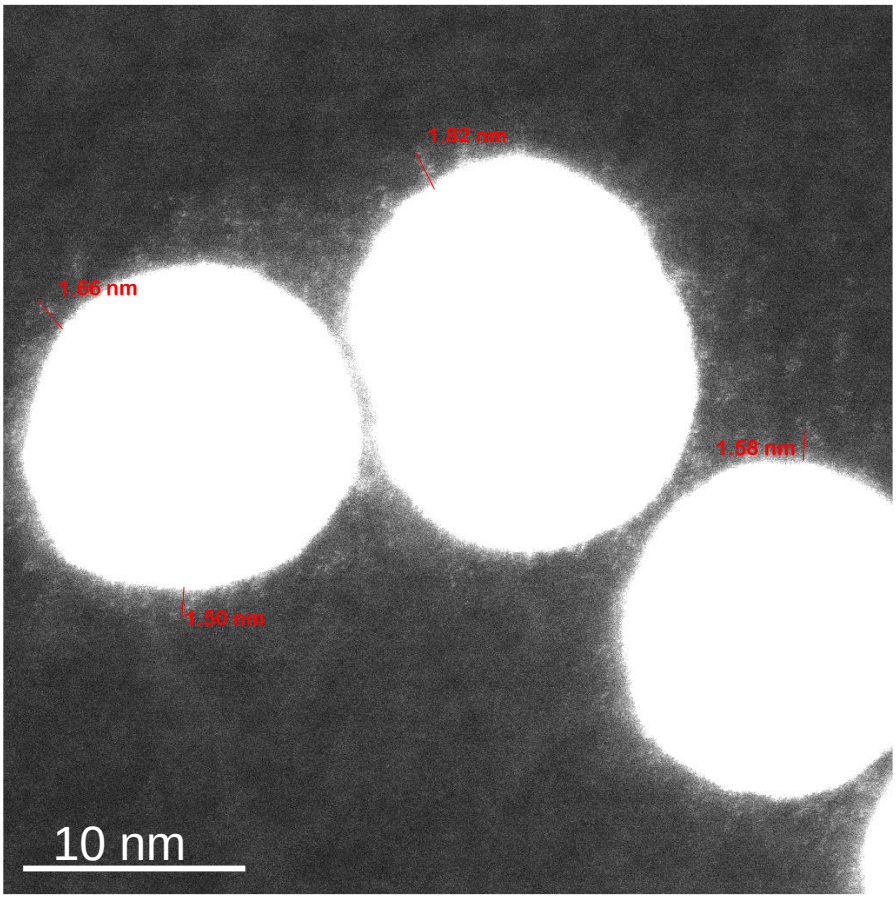


Figure 2.36 - HAADF images of $EuQuin_2S$-AuNPs on an ultrathin carbon supports after heat treatment at 135 °C. Red lines indicate measured distance of europium atoms from $EuQuin_2SH$, which were observed as bright spots surrounding the AuNPs.

EELS spectra were then acquired and a much stronger signal was observed din the core-loss region of in the exact positions expected for Eu $M_{4,5}$-edges in Eu(III) at 1131 and 1161 eV, confirming the presence of europium atoms surround the AuNPs (Figure 2.37). The signal resolved from europium and gold in EELS spectra was artificially coloured red and gold respectively, with the overlay showing Eu present around the AuNP (Figure 2.37). A close up image of a single europium atom confirmed by EELS is also shown (Figure 2.38) and another example is shown in the appendix (2.12.9).

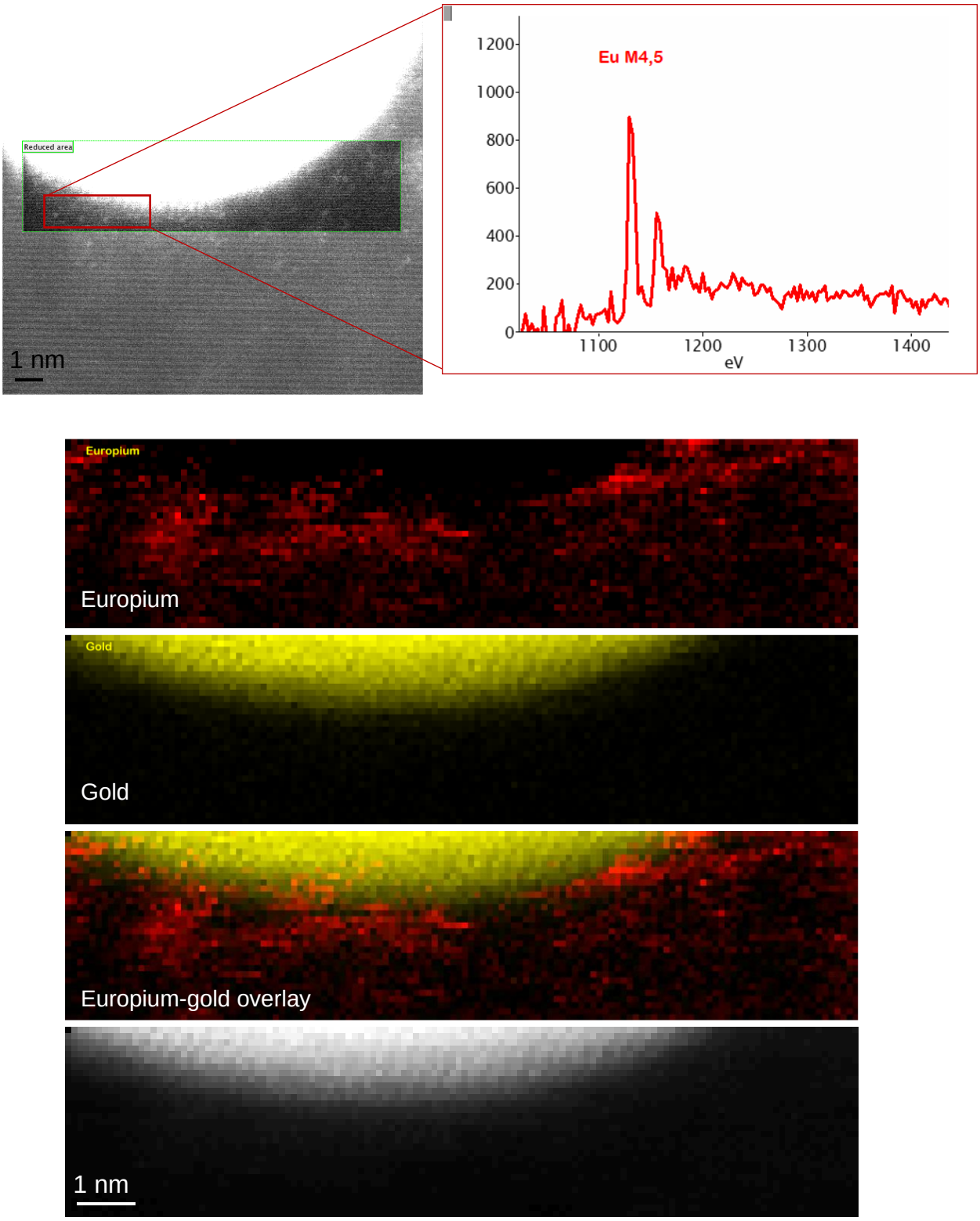


Figure 2.37 - EELS spectrum (top right) confirms the presence of europium surrounding an AuNP of $EuQuin_2S$-AuNPs on an ultrathin carbon supports after heat treatment at 135 °C, at the position of a bright spot in the halo around the gold core, highlighted by the red box on the HDAAF image (top left). Artificially coloured signal of europium (red), gold (gold) and an overlay of europium and gold are shown, determined by separating the signal of each element using EELS mapping.

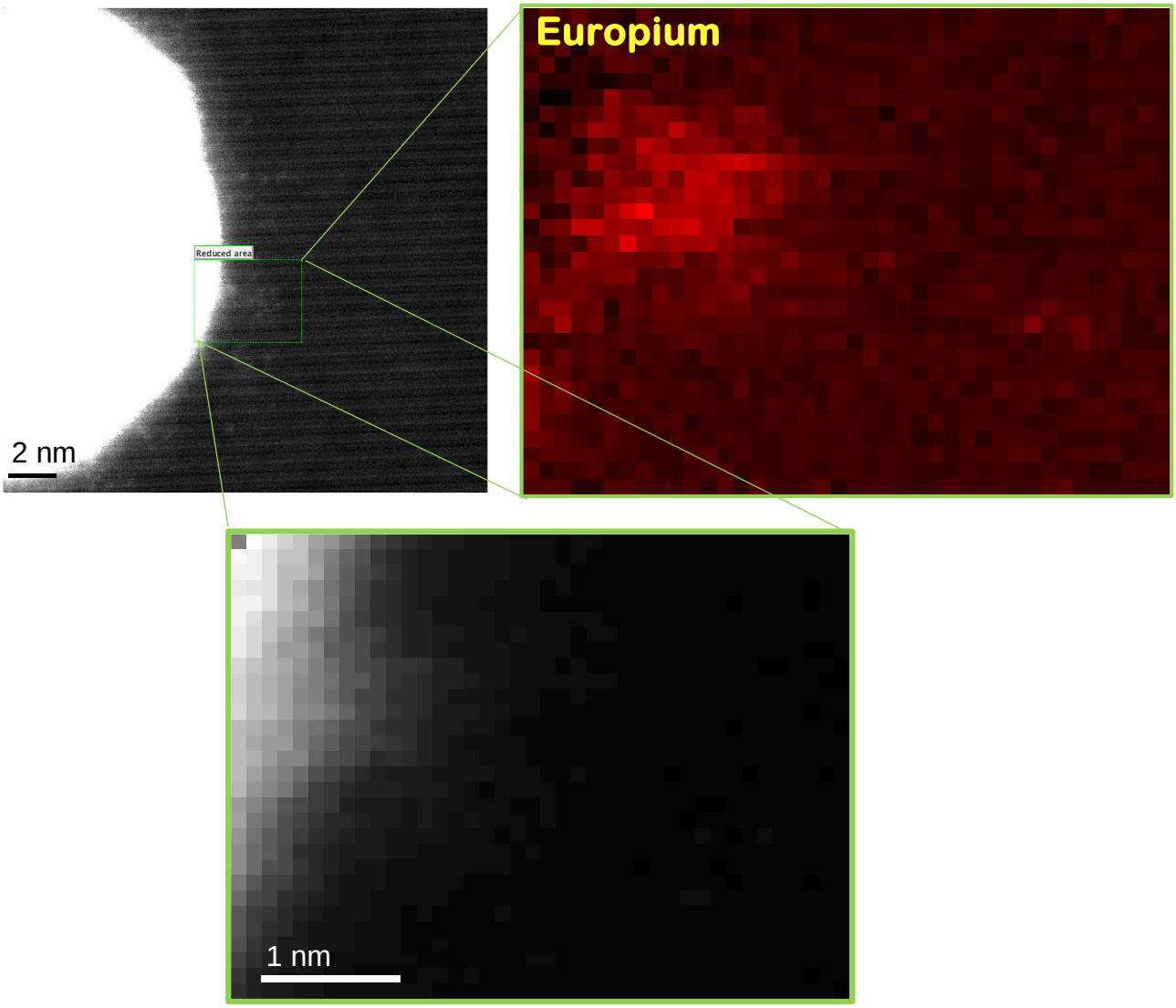


Figure 2.38 - HDAAF image of $EuQuin_2S$-AuNPs after heat treatment at 135 °C with EELS mapping of europium signal in green inset revealing single europium atom (red) surrounding AuNP core.

HDAAF images acquired of EuS-AuNPs also revealed single europium atoms around the gold core, much closer to the surface than with $EuQuin_2S$-AuNPs, 0.4-0.8 nm away from the surface (Figure 2.39). This 'halo' effect was again observed on multiple HDAAF images and more are shown in the appendix (2.12.9).

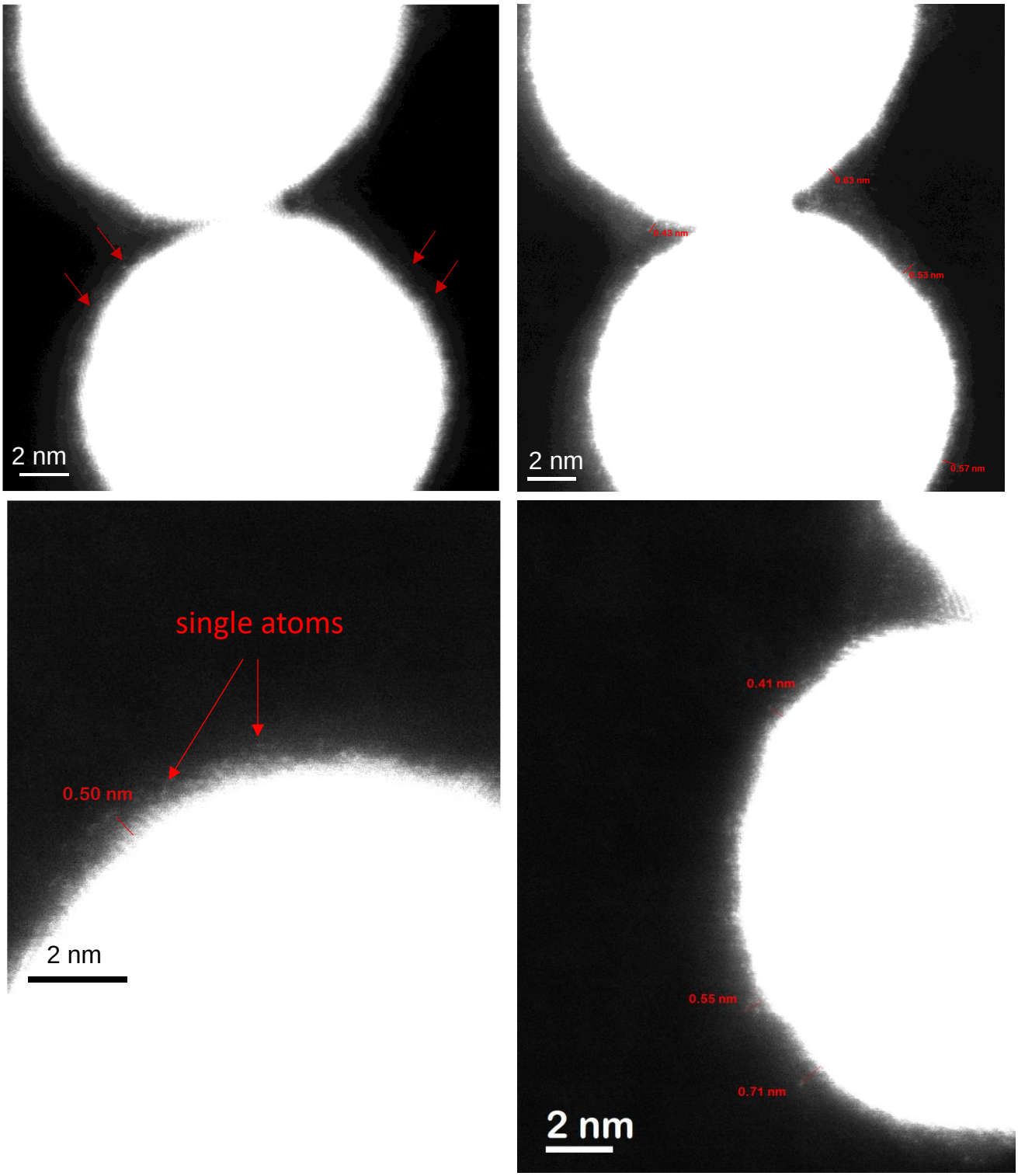


Figure 2.39 - HAADF images of EuS-AuNPs on an ultrathin carbon support after heat treatment at 135 °C. Red lines indicate measured distance of single europium atoms from $EuQuin_2SH$, which were observed as bright spots surrounding the AuNPs.

Much stronger signal corresponding to Eu $M_{4,5}$-edges in Eu(III) at 1131 and 1161 eV were again observed for EuS-AuNPs, confirming the presence of europium attributed to the metal centres of EuSH around the AuNPs (Figure 2.40).

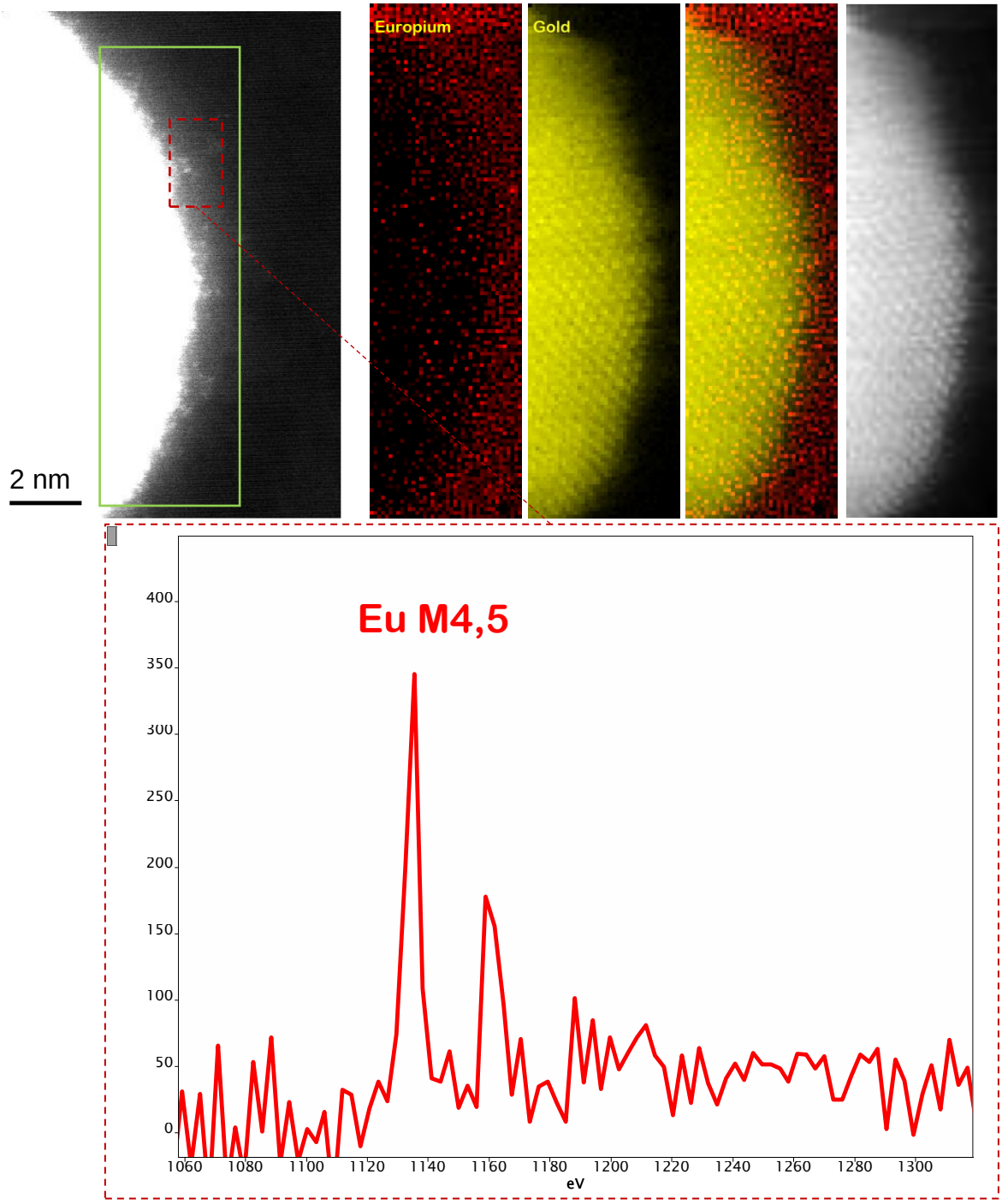


Figure 2.40 - EELS spectrum (bottom) confirms the presence of europium surrounding an AuNP of EuS-AuNPs on an ultrathin carbon supports after heat treatment at 135 °C, at the position of a bright spot in the halo around the gold core, highlighted by the red box on the HDAAF image (top left). Artificially coloured signal of europium (red), gold (gold) and an overlay of europium and gold are shown, determined by separating the signal of each element using EELS mapping.

These results provide compelling evidence that EuQuin$_2$SH and EuSH covalently bind to the surface of gold nanoparticles through Au-S interactions and remain intact to the surface in their expected conformation during purification and storage. To the best of our knowledge, this is the first direct, 'fingerprint' evidence of spatial localisation of metal atoms bound to a metal nanoparticle surface through organic ligands. We hope to further analyse EuQuin$_2$S-AuNPs and EuS-AuNPs by SuperSTEM/EELS and will attempt to achieve a level of quantification of the number of europium atoms present on single AuNPs.

2.7 Photophysical Properties of Lanthanide Coated Gold Nanoparticles

2.7.1 Enhanced Photophysical Properties of EuQuin$_2$S-AuNPs

EuQuinSAc-AuNPs have previously been synthesised by the group from EuQuinSAc (Figure 2.41). This ligand is similar to EuQuin$_2$SH, but the hexyl chains are terminated by a thioacetate group, compared to the thiol in EuQuin$_2$SH.

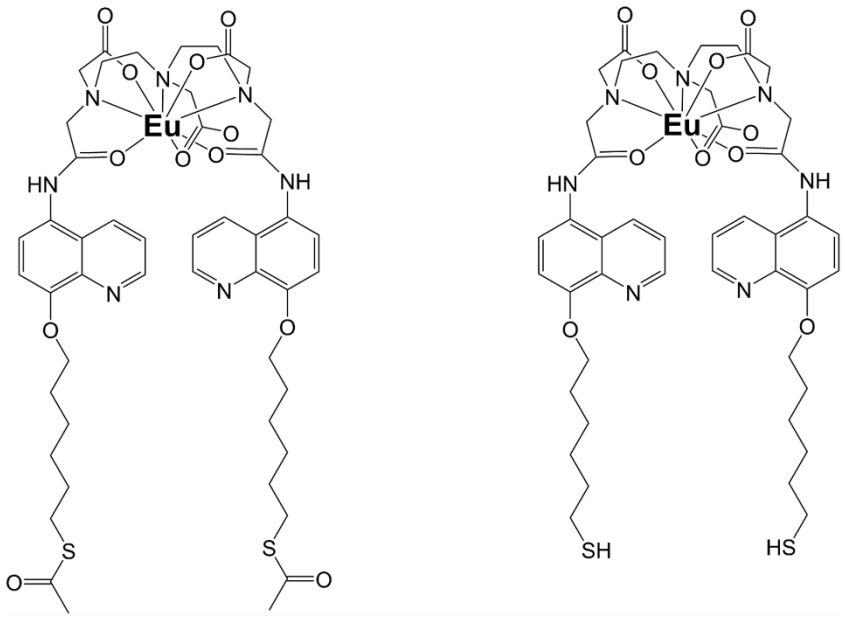


Figure 2.41 - The structures of EuQuinSAc (left) and EuQuin$_2$SH (right).

Davies *et al.* showed the shift in λ_{SPR} of 13 nm citrate gold nanoparticles upon addition of EuQuinSAc was 8 nm, the lifetime was found to be 287 μs and an average of 1335 EuQuinSAc complexes were found to be on each gold nanoparticle.[8] However, attachment of EuQuinSAc to gold nanoparticles in this work yielded different results. Only a 3 nm shift in λ_{SPR} was observed upon addition of EuQuinSAc to 13 nm gold nanoparticles and a plateau was reached after the addition of approximately 5 μM (Figure 2.42). As shown in section 2.5.3, the addition of $EuQuin_2SH$ to 13 nm gold nanoparticles led to a 6 nm shift in λ_{SPR} and approximately 9 μM of $EuQuin_2SH$ was added before a plateau was reached. Furthermore, it has been shown by ICP-MS analysis that there is an average of 1600 ± 60 $EuQuin_2SH$ complexes per gold nanoparticle.

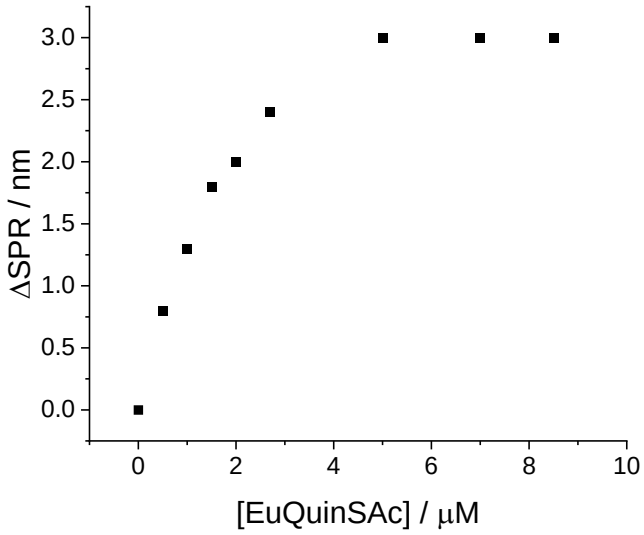


Figure 2.42 - Addition of EuQuinSAc to 13-nm citrate gold nanoparticles only leads to 3-nm shift. The change in the λ_{SPR} of 13 nm gold nanoparticles upon EuQuinSAc addition measured by UV-vis spectroscopy.

Although it is known that thioacetates form Au-S bonds with AuNPs in the same way as thiols,[32] a study by Lee and co-workers showed that their interaction with gold substrates is inferior to thiols, as they adsorb more slowly, are less densely packed and less ordered.[65] This could explain why a higher shift in λ_{SPR} was observed with $EuQuin_2SH$. It was also hypothesised that further oxidation of the thioacetate could have occurred during storage, but this was not confirmed by mass spectrometry or ^{1}H-NMR studies.

After the synthesis and purification of EuQuin$_2$S-AuNPs and EuQuinSAc-AuNPs, they were adjusted to a concentration of 2.5 nM and their photophysical properties were compared. Integration of the area of each emission band revealed there was a 3-fold higher emission intensity from EuQuin$_2$S-AuNPs compared to EuQuinSAc-AuNPs and a longer Eu(III) lifetime of 340 µs, compared to a lifetime of 260 µs for EuQuinSAc-AuNPs (Figure 2.43, Table 2.8).

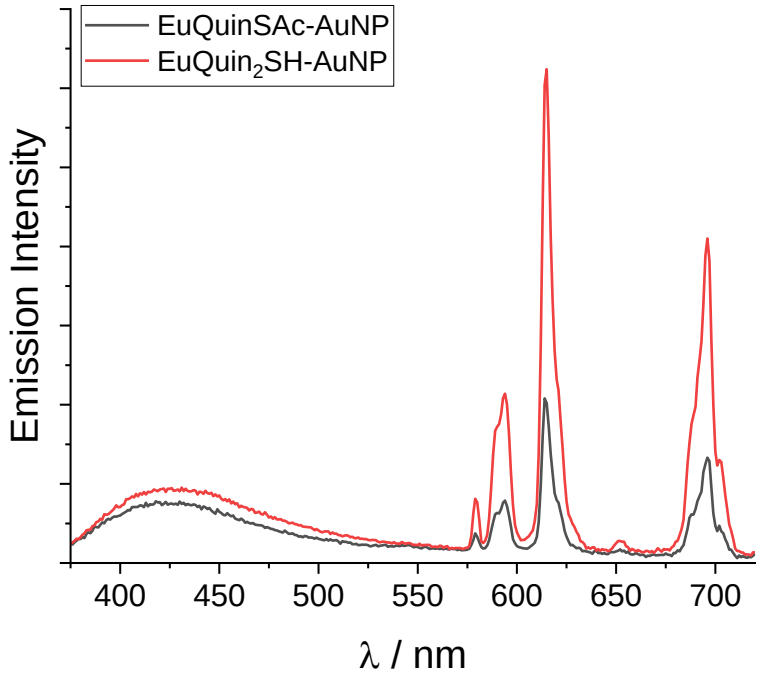


Figure 2.43 - A 3-fold higher emission intensity was observed from EuQuin$_2$S-AuNPs compared to EuQuinSAc-AuNPs. Emission spectra of EuQuin$_2$S-AuNPs (red) and EuQuinSAc-AuNPs (black) at a concentration of 2.5 nM (λ_{exc} = 325 nm).

Table 2.8 - Peak area integration from each emission band relative to the $^5D_0 \rightarrow {}^7F_2$ band from EuQuin$_2$S-AuNPs and EuQuinSAc-AuNPs, the ratio of emission observed from europium emission bands compared to the quinoline sensitiser, and lifetime measurements.

Species	Quinoline	$^5D_0 \rightarrow {}^7F_0$	$^5D_0 \rightarrow {}^7F_1$	$^5D_0 \rightarrow {}^7F_2$	$^5D_0 \rightarrow {}^7F_3$	$^5D_0 \rightarrow {}^7F_4$	Total / $^5D_0 \rightarrow {}^7F_2$	Eu:Quinoline	τ / µs
EuQuin$_2$S-AuNP	1.22	0.05	0.37	1	0.02	0.98	2.42	2.0	340
EuQuinSAc-AuNP	2.01	0.07	0.41	1	0.05	0.97	2.50	1.0	260

The ratio of emission observed directly from the quinoline sensitiser was much higher for EuQuinSAc-AuNPs, suggesting that there was more quenching of energy transfer from the sensitiser to the Eu(III) metal centre. Kamat and coworkers[66, 67] and a study by Stellacci *et al.*[68] found that quenching of the singlet excited state of fluorophores at the surface of gold nanoparticles and surfaces is reduced when they are densely packed at the surface. This could suggest that the stronger luminescence and longer lifetime of $EuQuin_2S$-AuNPs is due to an increase in $EuQuin_2SH$ loading.

2.7.2 Near-infrared Emitting Lanthanide Gold Nanoparticles

$YbQuin_2S$-AuNPs and $NdQuin_2S$-AuNPs were prepared as described in 2.5.3. After adjusting to a concentration of 2.5 nM and a pH of 7, emission, excitation, and lifetime scans were taken. At room temperature, using an excitation wavelength of 325 nm, no emission was observed from either $YbQuin_2S$-AuNPs or $NdQuin_2S$-AuNPs in the near-infrared region from 850-1150 nm and 850-1400 nm respectively, where Yb(III) and Nd(III) emission is characteristically observed. No signal from excitation scans was observed when monitoring emission at 980 nm and 1060 nm for $YbQuin_2S$-AuNPs and $NdQuin_2S$-AuNPs respectively. However, emission was observed at 450 nm for $YbQuin_2S$-AuNPs, likely due to emission directly from the quinoline sensitiser (Figure 2.44). This suggests that excitation of the quinoline sensitiser is occurring, but emission from Yb(III) is Nd(III) is too weak to be detected, due to quenching by hydroxyl oscillation in aqueous solution, and waters high level of absorption in the near-infrared region of the electromagnetic spectrum.[69, 70] Higher concentrations were tested, but still no emission was observed.

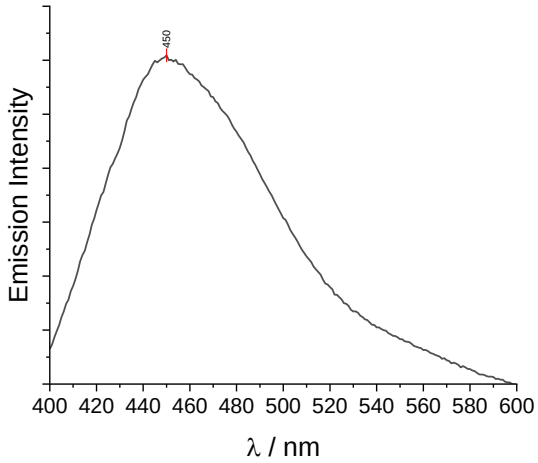


Figure 2.44 - Emission spectrum of $YbQuin_2S$-AuNPs [2.5 nM] in water, in the visible range of the electromagnetic spectrum originating from emission directly from the quinoline sensitiser. (λ_{exc} = 325 nm.)

In an attempt to reduce quenching from hydroxyl oscillation and water absorption, $YbQuin_2S$-AuNPs and $NdQuin_2S$-AuNPs were centrifuged twice and resuspended in D_2O and also in ethanol, but no emission was observed. Both nanoparticle species were also dried onto filter paper and emission scans in the solid state were also attempted, but no emission was observed. It was decided that $YbQuin_2SH$ and $NdQuin_2SH$ are not strongly emissive enough to be suitable as NIR-emitting probes in aqueous solution and no further studies were undertaken with these species.

2.7.3 TbS-AuNPs

Upon excitation of an aqueous solution (pH = 7) of TbS-AuNPs at 270 nm, emission peaks characteristic of the $^5D_4 \rightarrow {}^7F_J$ (J = 0-6) emission bands of Tb(III) were observed (Figure 2.45). At a pH of 7, the lifetime of Tb(III) was 260 µs (Table 2.9) and a 6-fold decrease in lifetime from the 1600 µs measured for TbSH when dissolved in methanolic solution. To achieve a good fitting, the lifetime was fitted with 3 components. The majority component (76%) was only 3 µs, similar to the lifetime of 1 µs previously found for EuS-AuNPs,[7] which is likely explained by quenching of the lanthanide excited state via energy transfer from the complex to the gold surface,[66, 71] given their respective close proximities due to the lack of any spacer groups in the H_3L ligand of TbSH.

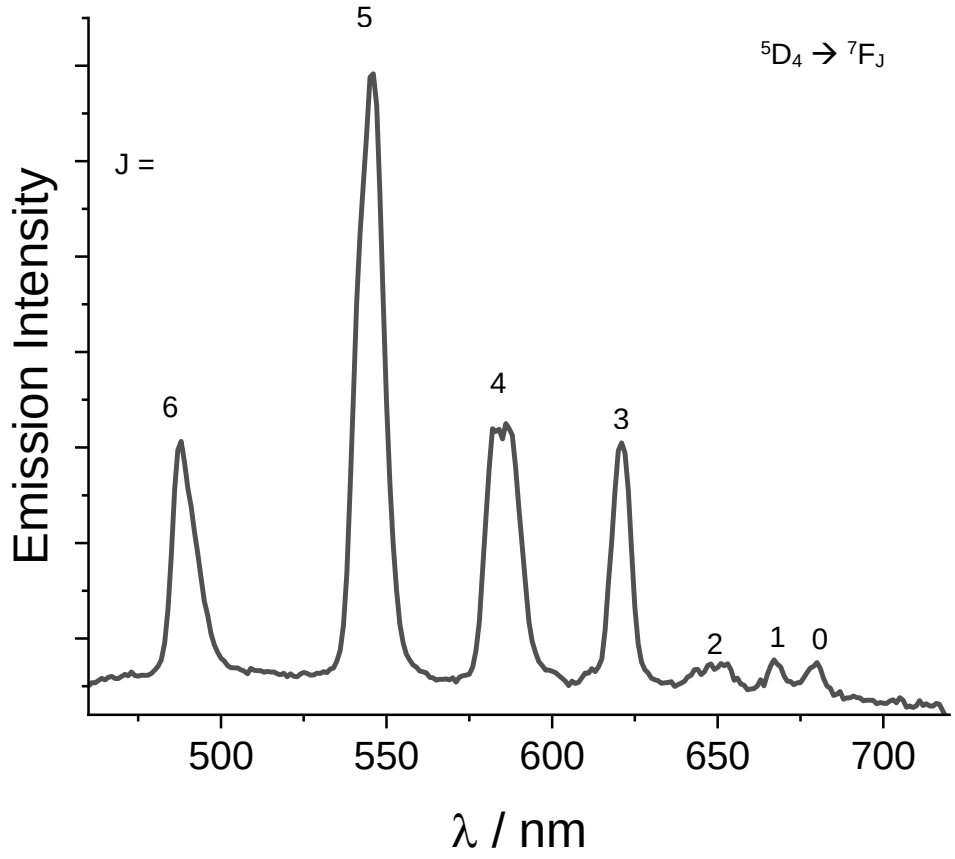


Figure 2.45 - Emission spectra of TbS-AuNPs (2.5 nM) recorded at pH 7 (λ_{exc} = 270 nm).

Table 2.9 - Lifetime data of Tb(III) from TbSH in a methanolic solution and TbS-AuNPs at pH 7 suspended in water.

	τ_1 / µs	τ_2 / µs	τ_3 / µs	τ (combined) / µs
TbSH (MeOH)	610 (10%)	1700 (90%)	N/A	1600
TbS-AuNPs	3 (76%)	43 (4%)	1300 (20%)	260

2.8 Effect of Surfactant and Polymer Coatings on $EuQuin_2S$-AuNP Photophysical Properties and Cellular Uptake

2.8.1 Photophysical properties

After purification of each NP species, the concentration was adjusted to 3.8 nM using UV-Vis spectroscopy by monitoring the absorbance at 450 nm (Figure 2.23). Emission and lifetime spectra of each NP species was then acquired at pH 7. Only small differences were found between the emission intensity observed from each NP species. It was found that $EuQuin_2S$-Zonyl-AuNPs were the most emissive, with an increase in emission by 1.18-fold with respect to $EuQuin_2S$-AuNPs. An increase in emission of 1.12-fold was observed for $EuQuin_2S$-PEG-AuNPs, but a reduction in emission was observed for $EuQuin_2S$-TFD-AuNPs by 0.88-fold. However, as there is error associated with calculating NP concentration and determining the intensity of emission by peak area integration, the difference in emission is not likely to be significant. As there is an estimated 10% error in lifetime measurements, there was only a significant difference between the lifetime of $EuQuin_2S$-TFD-AuNPs and the other NP species, where a reduction of 20% was seen compared to $EuQuin_2S$-AuNPs (Figure 2.47 and Table 2.10). The presence of PEG increased the ratio of Eu(III) emission to quinoline emission to 2.1, compared to 1.8 for $EuQuin_2S$-AuNPs. Zonyl FSA had no effect on the Eu:quinoline ratio, and TFD decreased the ratio to 1.5.

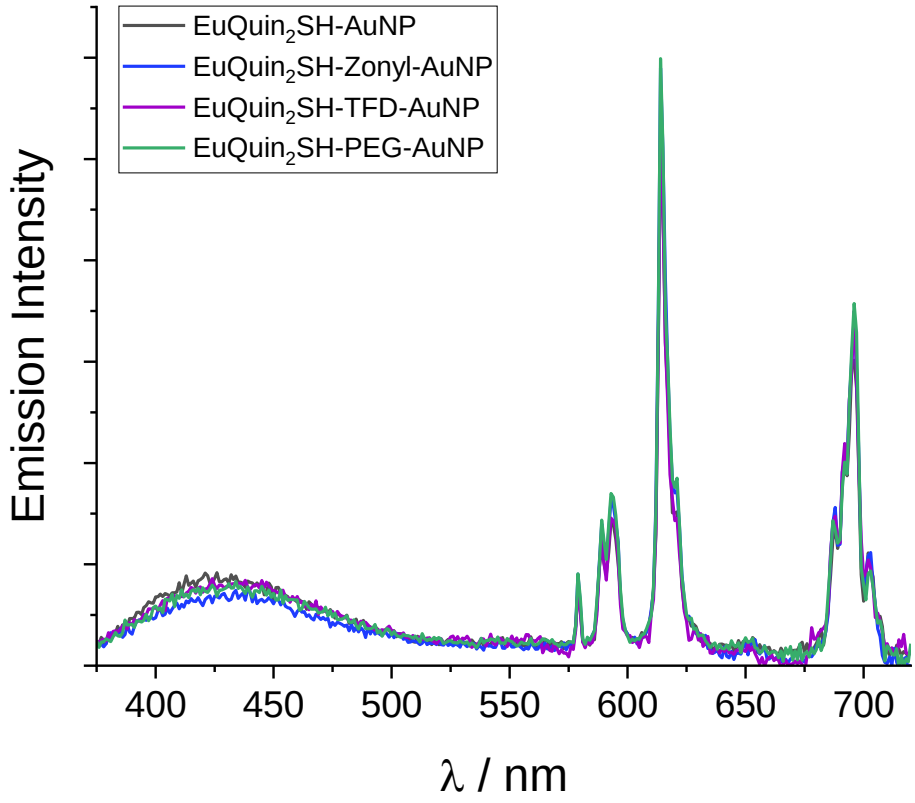


Figure 2.47 - Emission spectra of $EuQuin_2S$-AuNPs, $EuQuin_2S$-Zonyl-AuNPs, $EuQuin_2S$-TFD-AuNPs and $EuQuin_2S$-PEG-AuNPs at a concentration of 3.8 nM (λ_{exc} = 325 nm).

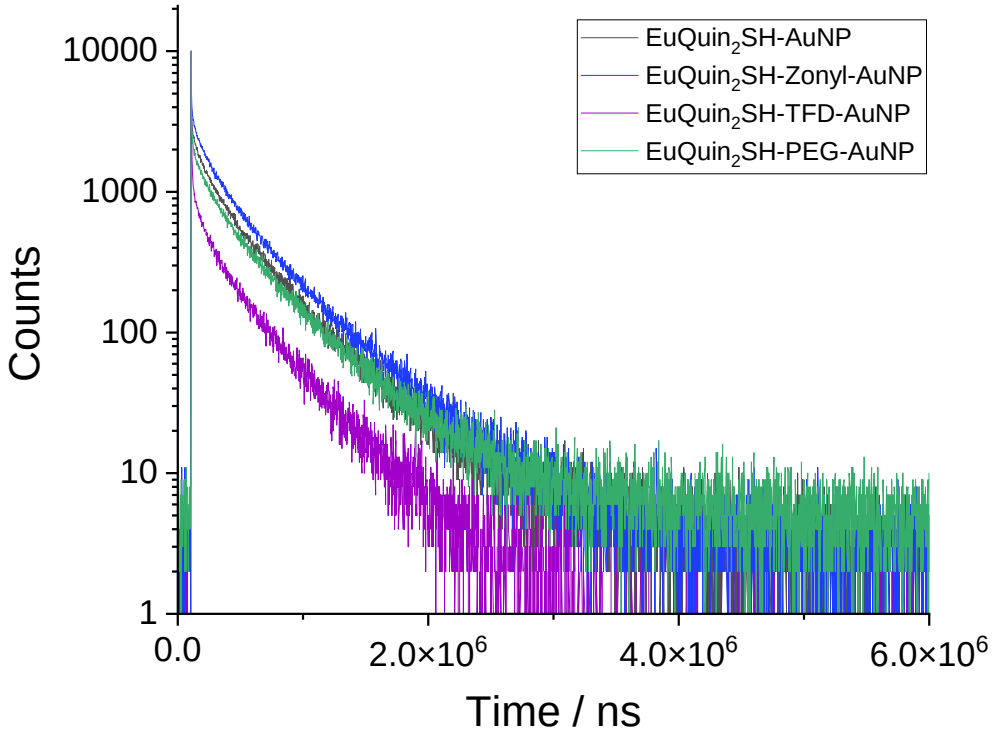


Figure 2.46 - Lifetime spectra of $EuQuin_2S$-AuNPs, $EuQuin_2S$-Zonyl-AuNPs, $EuQuin_2S$-TFD-AuNPs and $EuQuin_2S$-PEG-AuNPs at a concentration of 3.8 nM (λ_{exc} = 325 nm).

Table 2.10 - Lifetimes, normalised emission intensities (from combining peak integration of each emission band) and ratio of Eu(III) emission to quinoline emission of $EuQuin_2S$-AuNPs, $EuQuin_2S$-Zonyl-AuNPs, $EuQuin_2S$-TFD-AuNPs and $EuQuin_2S$-PEG-AuNPs. There is an estimated 10% error associated with lifetime measurements. Emission intensity was calculated by calculating the area under the curve of each Eu(III) emission peak after subtracting the baseline.

NP Species	τ / μs	Normalised Eu (III) Emission Intensity	Eu:Quinoline Ratio
$EuQuin_2S$-AuNP	350	1.00	1.8
$EuQuin_2S$-Zonyl-AuNP	370	1.18	1.8
$EuQuin_2S$-TFD-AuNP	280	0.88	1.5
$EuQuin_2S$-PEG-AuNP	350	1.12	2.1

There are many examples in the literature that show fluorination of sensitising ligands can increase lanthanide lifetimes in the NIR,[10-12] but this is not always the case for visible-light emitting lanthanides.[72] Furthermore, previous studies by the group have shown that Zonyl FSA increases the lifetime of ruthenium coated AuNPs, but decreases the lifetime of iridium coated AuNPs, with respect to the lifetime of each metal complex in solution.[9, 34] However, due to the charged nature of these complexes, it is essential that a surfactant is present on the nanoparticle surface to prevent aggregation of the NPs upon complex addition, so the effect of Zonyl on lifetime or emission has never been studied directly.

As the number of $EuQuin_2SH$ complexes on each NP species is not significantly different for $EuQuin_2S$-AuNPs, $EuQuin_2S$-Zonyl-AuNPs and $EuQuin_2S$-TFD-AuNPs, and only 15% less in the case of $EuQuin_2S$-PEG-AuNPs, it can be concluded that the surfactants and polymers are playing a minimal effect in the photophysical properties of $EuQuin_2S$-AuNPs. As Zonyl FSA slightly increases emission and TFD slightly decreases lifetime and emission, the effect of perfluoronated surfactants on Eu(III) emission on NPs is not clear from this study.

2.8.2 The Effect of Coating EuQuin$_2$S-AuNPs with Fluorinated Surfactants and a PEG Polymer on their Cellular Uptake in Cancer Cells

After purification, EuQuin$_2$S-AuNPs, EuQuin$_2$S-Zonyl-AuNPs, EuQuin$_2$S-TFD-AuNPs and EuQuin$_2$S-PEG-AuNPs were adjusted to a concentration of 1.6 nM. HeLa cells were then treated with each NP species (10x dilution in DMEM) for 4, 8 and 16 hours. The cells were then washed and prepared for CyTOF experiments as described in 3.10.4, and the mean number of NPs taken up by each cell was determined. The methodology of using CyTOF as a quantitative technique to determine NP cellular uptake is discussed in detail in chapter 3.

It was found that fluorinated surfactants significantly enhance the uptake of EuQuin$_2$S-AuNPs in HeLa cells (Figure 2.48). The number of EuQuin$_2$S-AuNPs per cell was 192 ± 60, 291 ± 98 and 321 ± 104 (± SD) at 4, 8 and 16-hour incubation times. EuQuin$_2$S-Zonyl-AuNP uptake was on average 5.1-fold higher than EuQuin$_2$S-AuNP uptake at each incubation time, and EuQuin$_2$S-TFD-AuNP uptake was 2.8-fold higher. In contrast, EuQuin$_2$S-PEG-AuNP uptake was on average 0.8-fold lower than EuQuin$_2$S-AuNP uptake at each incubation time. The mean number of NPs per cell increased for each NP species as incubation time increased from 4 h to 8 h by 1.5-fold for EuQuin$_2$S-AuNPs and EuQuin$_2$S-Zonyl-AuNPs, 1.6-fold for EuQuin$_2$S-TFD-AuNPs and 2-fold for EuQuin$_2$S-PEG-AuNPs. At a 16 h incubation time, there was a 0.8-fold decrease in the number of EuQuin$_2$S-Zonyl-AuNPs, EuQuin$_2$S-TFD-AuNPs and EuQuin$_2$S-PEG-AuNPs per cell compared to 8 h, and a 1.1-fold increase for EuQuin$_2$S-AuNPs.

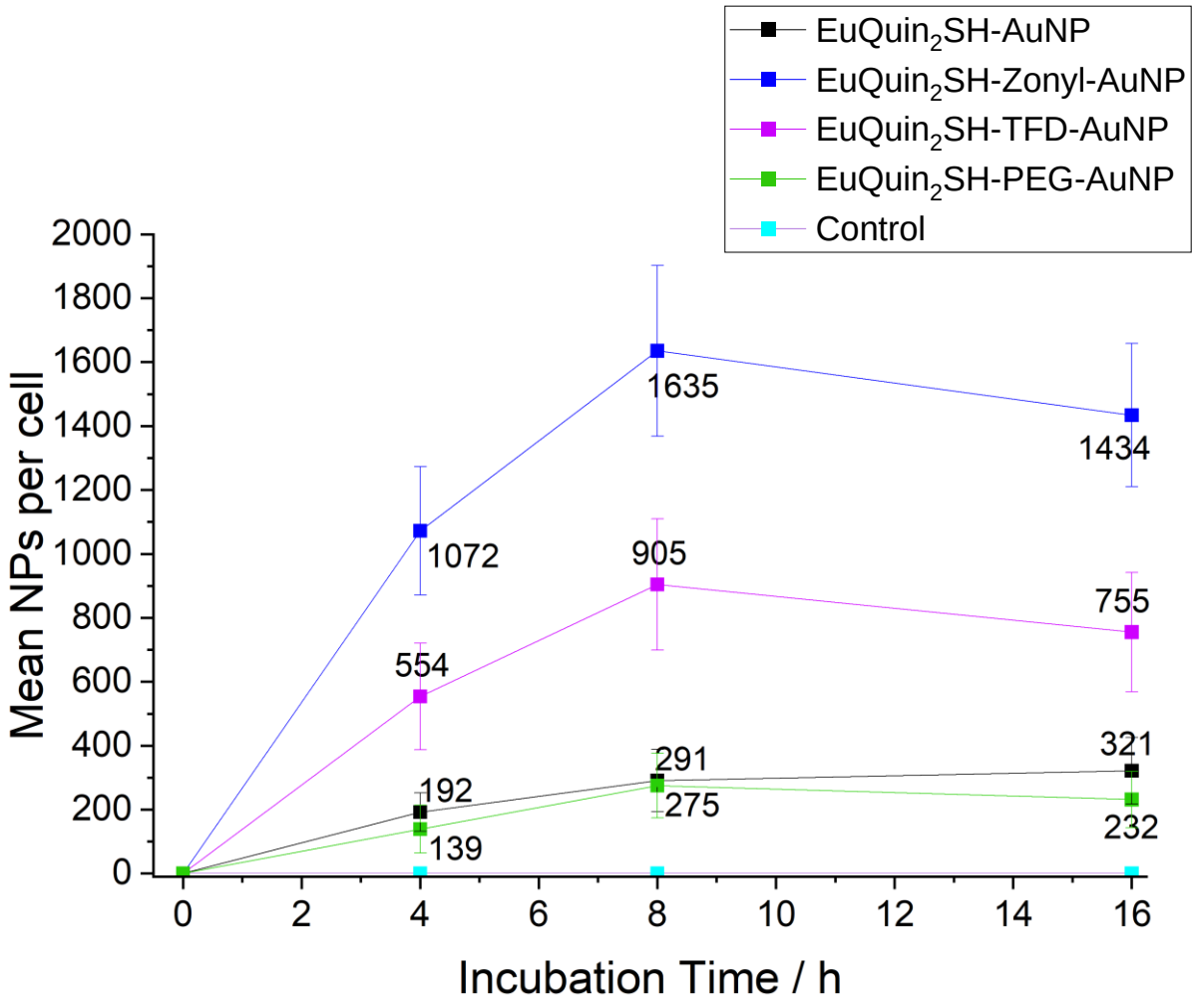


Figure 2.48 - The cellular uptake of EuQuin$_2$S-AuNPs is increased by the presence of fluorinated surfactants at the nanoparticle surface. The mean number of EuQuin$_2$S-AuNPs, EuQuin$_2$S-Zonyl-AuNPs, EuQuin$_2$S-TFD-AuNPs and EuQuin$_2$S-PEG-AuNPs per HeLa cell after 4-, 8- and 16-hour incubations at a concentration of 0.16 nM, measured by CyTOF. Error bars represent the standard deviation in NP content from >100,000 single cells studied in each sample.

A recent study by Argudo *et al.* found that fluorination of the terminal group of a PEG polymer coating increased the cellular uptake of ZnCdS/ZnS quantum dots in HeLa cells by 5.7-fold, likely due to an increased interaction with the phospholipid membrane.[73] Dafik *et al.* have also shown that fluorinated lipids are 3-5-fold more efficient at entering cells than their hydrocarbon counterparts.[74] This supports our findings of higher uptake of EuQuin$_2$S-Zonyl-AuNPs and EuQuin$_2$S-TFD-AuNPs, and indicates that the fluorinated surfactants remain present at the nanoparticle surface after EuQuin$_2$SH addition and purification.

Despite the assumption that the majority of the nanoparticle surface is covered by $EuQuin_2SH$, given the high loading confirmed by ICP-MS, it appears that it is the fluorinated surfactant that mediates the cellular uptake of the nanoparticles.

There was a reduction in uptake of $EuQuin_2S$-PEG-AuNPs by an average of 0.8-fold at each incubation time, with respect to $EuQuin_2S$-AuNPs. It is generally considered that PEG molecules reduce the cellular uptake of nanoparticles,[75-77] but many factors play an important role, and high molecular weight PEG molecules (>2 kDa) have a much greater effect on reducing the uptake of nanoparticles than lower molecular weight PEG molecules,[78-81] as does a higher density of PEG.[82, 83] The low molecular weight (460 Da) of the PEG polymer used in this study, as well as its low density on the nanoparticle surface may explain the modest reduction in uptake.

The findings on the dependency of incubation time on the cellular uptake of $EuQuin_2S$-AuNPs are in broad agreement with similar studies in the literature. Desai et al. previously showed the cellular uptake of polymeric nanoparticles was highest in the first 4 hours of incubation using a caco-2 carcinoma cell line,[84] and Chithrani *et al.* found the cellular uptake of 14, 50 and 74 nm citrate-stabilised AuNPs in HeLa cells reached a plateau at around 6-8 hours, with incubation times ranging from 2 to 10 hours.[85] The reduction in the mean number of NPs per cell after an incubation time of 16 h could be due to the rate of NP uptake slowing, as well as the total number of cells increasing due to proliferation of the HeLa cell population. In a separate HeLa proliferation experiment (see 3.8.2.4), we found the doubling time of HeLa cells to be 16.6 hours. This would suggest that the lower mean NPs per cell is a result of the effects of both proliferation and lower uptake rate. This theory is further supported by a study from Gunduz *et al.*, where it was found that after continuous exposure of low doses of AuNPs to Human Umbilical Vein Endothelial Cells (HUVEC), endocytosis pathways were inhibited and the number of AuNPs per cell decreased over time with proliferation, and exocytosis of NPs did not play a major role.[86]

2.9 Concluding Remarks

In summary, lanthanide complexes $LnQuin_2SH$ (Ln = Eu, Yb, Nd) and LnSH (Ln = Eu, Tb) have been synthesised and their photophysical properties were studied. In the case of $EuQuin_2SH$, some emission was directly observed from the quinoline sensitiser, indicating that energy transfer from the sensitiser to the lanthanide centre was not ideally efficient, and it was found that solvent coordination to the Eu(III) centre had some effect on this energy transfer. NIR emission was observed from $YbQuin_2SH$ and $NdQuin_2SH$ in methanol with lifetimes of 4 and 3 μs respectively. Strong emission was observed from TbSH with a long luminescence lifetime of 1600 μs in methanol.

$LnQuin_2SH$ and LnSH complexes were attached to 13-nm citrate gold nanoparticles to form stable, monodisperse $LnQuin_2S$-AuNPs (Ln = Eu, Yb, Nd) and LnS-AuNPs (Ln = Eu, Tb). These lanthanide gold nanoparticles were characterised by UV-Vis, DLS, TEM and ICP-MS, revealing their hydrodynamic and gold core size, monodispersity and the average number of lanthanide complexes on each particle. The synthesis and characterisation of surfactant and polymer coated $EuQuin_2S$-AuNPs was also demonstrated. $EuQuin_2SH$ and EuSH were further characterised by STEM and EELS, where we were able to elementally map europium atoms colocalised with single AuNPs, showing spatial localisation of metal atoms bound to metal NP surfaces through organic ligands for the first time. These studies also showed that the alkyl chain in $EuQuin_2SH$ held the metal atom further away from the NP surface. The binding of $EuQuin_2SH$ and TbSH to 13-nm citrate gold nanoparticles was also shown by ITC, providing new evidence of a binding event occurring at the NP surface upon metal complex addition. Association constants of the binding of $EuQuin_2SH$ and TbSH to AuNPs was also determined by UV-Vis spectroscopy and ITC. The values from both techniques were in agreement and were not significantly different for each metal complex, likely due to their identical binding modes and similar sizes.

The photophysical properties of each lanthanide gold nanoparticle species was studied. An improvement in the properties of $EuQuin_2S$-AuNPs was observed with respect to the previously studied EuQuinSAc functionalised AuNPs; a longer luminescent lifetime and subsequent stronger emission from the NPs was attributed to an increase in $EuQuin_2SH$ loading shown by ICP-MS. It was also found that the ratio of Eu:Quinoline emission from $EuQuin_2SH$ reduced on nanoparticles compared to in methanolic solution. The lifetime of Tb(III) from TbSH reduced significantly more on nanoparticles with respect to its lifetime in solution compared with $EuQuin_2SH$, likely owing to an increase in quenching due to the closer proximity of the Tb(III) centre to the AuNP surface. No emission in the NIR was observed from $YbQuin_2SH$ or $NdQuin_2SH$, likely due to quenching by hydroxyl oscillators and the lower excited state energies of Yb(III) and Nd(III).

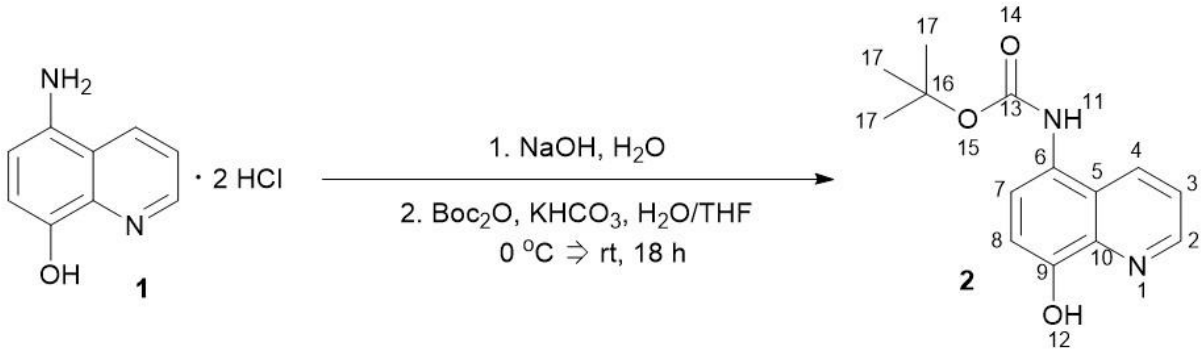
Lastly, the surface of nanoparticles was partially coated with fluorinated surfactants Zonyl FSA and TFD, and a PEG polymer prior to the addition of $EuQuin_2SH$ and their effects on the loading, photophysics and cellular uptake of $EuQuin_2S$-AuNPs was studied. Fluorinated surfactants had no significant effect on the loading of $EuQuin_2SH$ and it was suggested that this could in part be due to the displacement of Zonyl FSA and TFD by the thiol terminated $EuQuin_2SH$ complexes that likely bind more strongly to the nanoparticle surface. PEG reduced the average loading of $EuQuin_2SH$ per NP from 1600 ± 60 to 1400 ± 80, less than the anticipated 33% likely due to conformational changes of the polymer upon addition of $EuQuin_2SH$. The fluorinated surfactants/polymer did not have a large impact on the photophysical properties of $EuQuin_2S$-AuNPs; Zonyl FSA and PEG slightly increased the emission, but the lifetime did not significantly change, and TFD decreased emission and lifetime. The largest observed effect was with the cellular uptake of the NPs in HeLa cells; Zonyl increased the uptake by 5.1-fold and TFD by 2.8-fold, and PEG decreased the uptake by 0.8-fold. This shows that despite the majority of the surface is covered by $EuQuin_2SH$, the presence of surfactants and polymers can still mediate their cellular uptake.

Further studies are needed to fully understand the effect of pH on the lifetime and emission of EuQuin$_2$S-AuNPs and TbS-AuNPs, which could lead to a potential application as pH sensors in cellular environments. We hope to continue STEM and EELS studies to elementally map other lanthanide metals around the gold core, as well as improving the resolution of the images by removing organic contamination in the hope that we can add a degree of quantification of the number of lanthanide ions around each nanoparticle. For potential biomedical applications regarding the cellular uptake of the NPs, EuQuin$_2$S-Zonyl-AuNPs are the ideal candidate due to their enhanced uptake. Further studies into how these EuQuin$_2$S-Zonyl-AuNPs affect the viability of cells and their potential as multi-modal probes for detection through both confocal imaging and CyTOF should be undertaken.

2.10 Experimental

2.10.1 Synthesis of ligands and lanthanide complexes

2.10.1.1 Synthesis of tert-butyl (8-hydroxyquinolin-5-yl)carbamate (2)

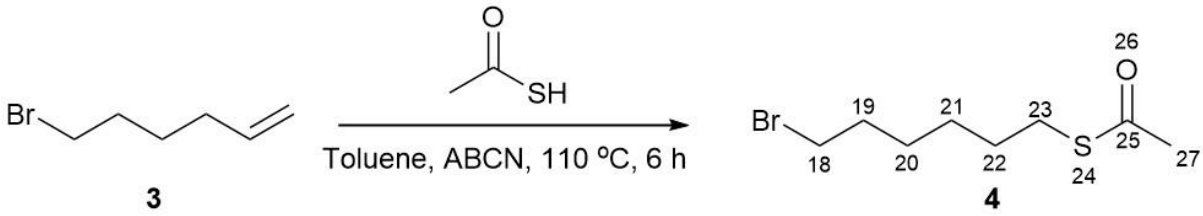


1 (2.00 g, 8.58 mmol, 1.00 eq.) was dissolved in water (20 mL) and NaOH (17.2 mL, 17.2 mmol, 1 M, 2.00 eq.) was added. The solvent was removed *in vacuo* and the crude product was dissolved in water (80 mL) and THF (50 mL). $KHCO_3$ (4.9 g, 44.5 mmol, 5.20 eq.) was added and the solution was stirred at 0 ℃. A solution of di-tertiary butyl carbonate in THF (4.40 mL, 8.80 mmol, 1.03 eq.) was added over 5 min and the solution stirred for 1 h at 0 ℃ then allowed to warm to room temperature and stirred for an additional 17 h. THF was

removed *in vacuo* and the organic material was extracted with DCM (1 × 200 mL, 3 × 100 mL). The organic layer was dried over anhydrous Na_2SO_4 and filtered. The solvent was removed *in vacuo,* yielding a dark red powder (1.69 g, 76%).

^{1}H NMR (400 MHz, $CDCl_3$) δ_H ppm: 8.79 (1H, dd, *J* = 4.2, 1.5 Hz, H2), 8.25 (1H, dd, *J* = 8.6, 1.5 Hz, H4), 7.59 – 7.44 (2H, m, H7, H3), 7.13 (1H, d, *J* = 8.2 Hz, H8), 6.43 (1H, s, H11), 1.52 (9H, s, H17). MS (ESI-TOF)$^+$ m/z: 261.12 $[M + H]^+$.

2.10.1.2 Synthesis of S-(6-bromohexyl) ethanethioate (4)

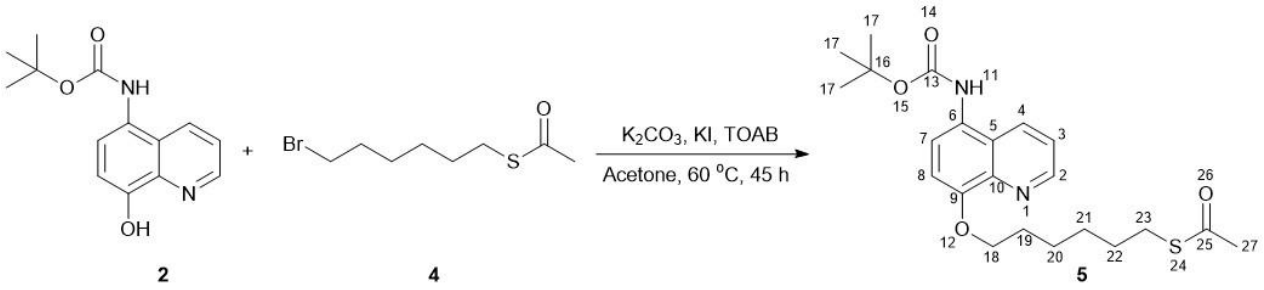


3 **4**

3 (2.0 mL, 15.0 mmol, 1.00 eq.) and a catalytic amount of ABCN (mass?) were dissolved in toluene (25 mL) and stirred at reflux. Thioacetic acid (2.20 mL, 30.8 mmol, 2.05 eq.) was added and the solution was stirred for a further 6 h. The solvent was removed *in vacuo* and ethyl acetate (100 mL) and $NaHCO_3$ (50 mL, 1 M) were added. The organic layer was collected and the aqueous layer was washed twice more with ethyl acetate (2 × 50 mL). The combined organic layers were washed with $NaHCO_3$ (50 mL, 1 M), dried over anhydrous Na_2SO_4 and filtered. The solvent was removed *in vacuo*, yielding a yellow oil (3.5 g, 97%).

^{1}H NMR (400 MHz, $CDCl_3$) δ_H ppm: 3.39 (2H, t, *J* = 6.8 Hz, H18), 2.86 (2H, t, *J* = 7.3 Hz, H23), 2.32 (3H, s, H27), 1.85 (2H, p, *J* = 6.8 Hz, H19), 1.59 (2H, m, H20), 1.52 – 1.32 (4H, m, H21, H22). ^{13}C NMR (400 MHz, $CDCl_3$) δ_C ppm: 196.1, 33.9, 32.7, 30.8, 29.5, 29.1, 28.0, 27.8. MS (ESI-TOF)$^+$ m/z: 241.14 $[M + H]^+$.

2.10.1.3 Synthesis of S-(6-((5-((tert-butoxycarbonyl)amino)quinolin-8-yl)oxy)hexyl) ethanethioate (5)

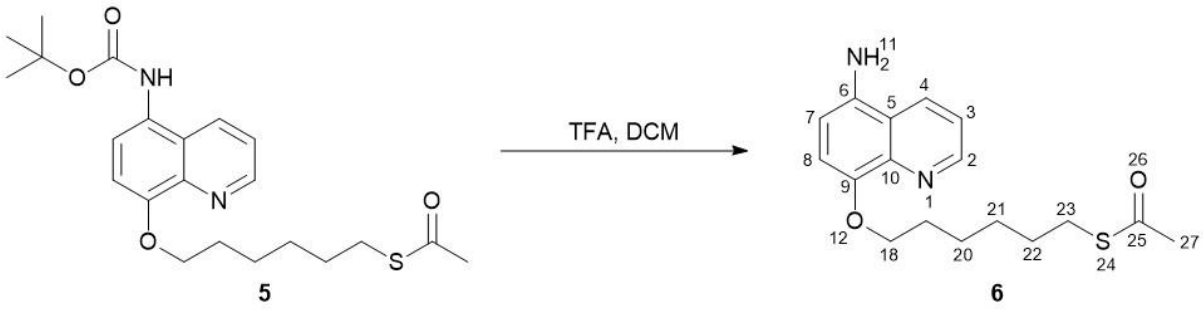


2 4 5

2 (1.69 g, 6.49 mmol, 1.00 eq), K_2CO_3 (7.2 g, 52.2 mmol, 8.03 eq.), KI (1.5 g, 9.04 mmol, 1.39 eq) and tetraoctylammonium bromide (cat. amount) were dissolved in acetone (50 mL) and stirred at reflux (T = 56 ℃) for 15 min. **4** (2.11 g, 8.83 mmol, 1.36 eq.) was dissolved in acetone (5 mL) was added slowly and the reaction was stirred for an additional 45 h at reflux. The solvent was removed *in vacuo* and the crude material was cast between CH_2Cl_2 (150 mL) and deionised water (100 mL). The organic layer was collected and the aqueous layer was washed twice more with CH_2Cl_2 (2 × 100 mL). The combined organic layers were washed with brine, dried over anhydrous Na_2SO_4, filtered, and the solvent was removed *in vacuo.* Purification by flash column chromatography (hexane/ethyl acetate: 50/50) yielded the product as a dark orange residue (2.08 g, 77%).

^{1}H NMR (400 MHz, $CDCl_3$) δ_H ppm: 8.96 (1H, dd, *J* = 4.2, 1.7 Hz, H2), 8.23 (1H, dd, *J* = 8.5, 1.7 Hz, H4), 7.58 (1H, m, H7), 7.46 (1H, dd, *J* = 8.5, 4.2 Hz, H3), 7.01 (1H, d, *J* = 8.5 Hz, H8), 6.47 (1H, s, H11), 4.22 (2H, t, *J* = 7.0 Hz, H18), 2.88 (2H, t, *J* = 7.3 Hz, H23), 2.32 (3H, s, H27), 2.00 (2H, p, *J* = 7.0 Hz, H19), 1.67 – 1.40 (15H, m, H17, H20, H21, H22). MS (ESI-TOF)$^+$ m/z: 419.20 $[M]^+$.

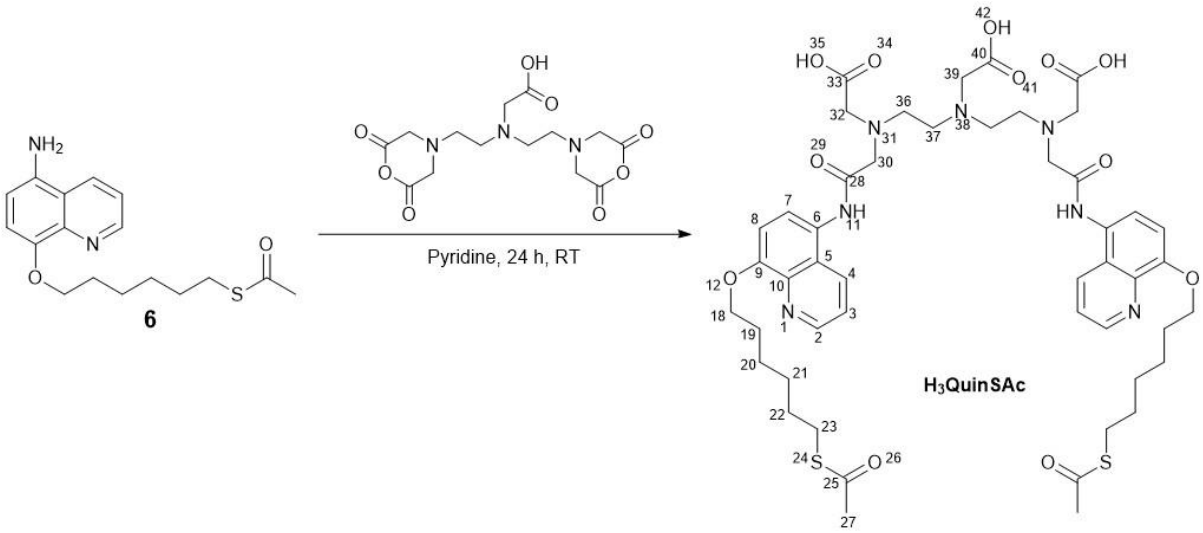
2.10.1.4 Synthesis of S-(6-((5-aminoquinolin-8-yl)oxy)hexyl) ethanethioate (6)



5 (2.08 g, 4.96 mmol, 1.00 eq.) was dissolved in DCM (30 mL) and stirred at room temperature. TFA (14.1 g, 9.5 mL, 123 mmol, 24.7 eq.) was added slowly and the solution was stirred for an additional 3 h. The solvent was removed *in vacuo* and the crude material was cast between CH_2Cl_2 (50 mL) and aqueous $NaHCO_3$ (1 M, 50 mL). The organic layer was collected and the aqueous layer was washed twice more with CH_2Cl_2 (2 × 50 mL). The combined organic layers were dried with anhydrous Na_2SO_4, filtered, and the solvent was removed *in vacuo,* yielding a dark red residue (1.25 g, 3.93 mmol, 80%).

^{1}H NMR (400 MHz, $CDCl_3$) δ_H ppm: 8.94 (1H, dd, *J* = 4.1, 1.7 Hz, H2), 8.18 (1H, dd, *J* = 8.5, 1.7 Hz, H4), 7.39 (1H, dd, *J* = 8.5, 4.2 Hz, H3), 6.91 (1H, d, *J* = 8.2 Hz, H8), 6.75 (1H, d, *J* = 8.2 Hz, H7), 4.16 (2H, t, *J* = 7.0 Hz, H18), 3.80 (2H, br, H11), 2.87 (2H, t, *J* = 7.2 Hz, H23), 2.31 (3H, s, H27), 1.97 (2H, p, *J* = 7.0 Hz, H19), 1.67 – 1.38 (6H, m, H20, H21, H22). MS (ESI-TOF)$^+$ m/z: 319.15 $[M + H]^+$.

2.10.1.5 Synthesis of 2,2'-((((carboxymethyl)azanediyl)bis(ethane-2,1-diyl))bis((2-((8-((6- (acetylthio)hexyl)oxy)quinolin-5-yl)amino)-2-oxoethyl)azanediyl))diacetic acid (H_3QuinSAc)

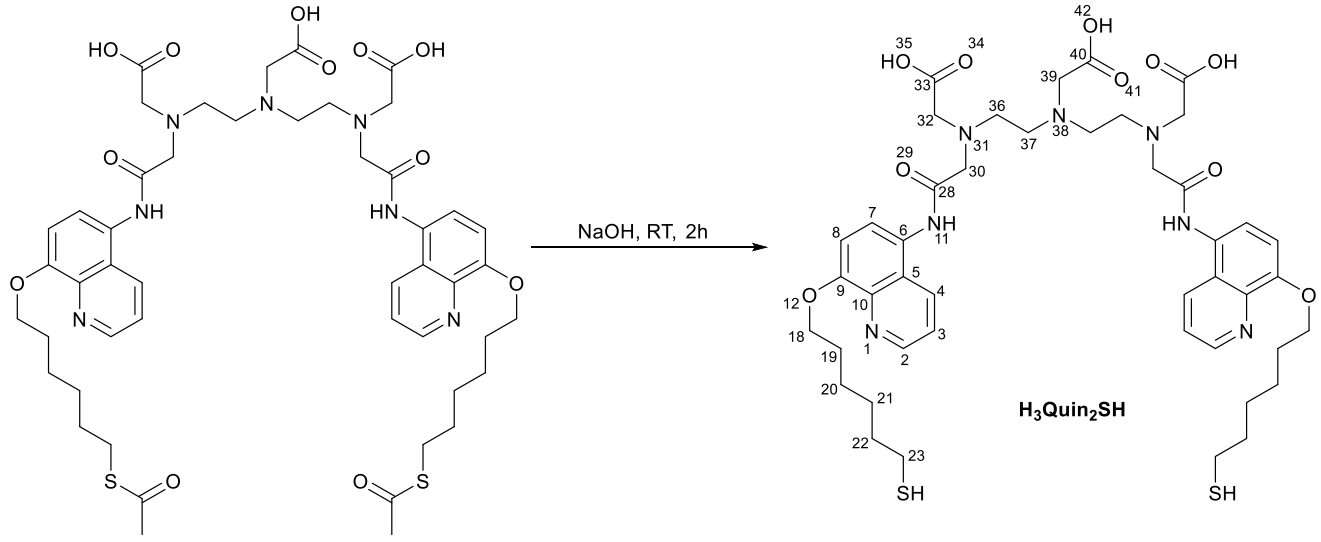


DTPA bisanhydride (0.62 g, 1.74 mmol, 1.00 eq.) was dissolved in pyridine (30 mL) and stirred at room temperature. **6** (1.18 g, 3.70 mmol, 2.13 eq.) dissolved in pyridine (30 mL) was added and the solution was stirred for 24 h. The solvent was removed *in vacuo* and the crude material was dissolved in water (60 mL). The pH was adjusted to 3.5 using an aqueous solution of HCl (1 M) and a red precipitate formed. The solution was filtered and the solid was collected by filtration and washed with MeCN (3 × 50 mL) and hexane (3 × 50 mL). The solid was dried *in vacuo* and H_3QuinSAc was obtained as a light-yellow powder (1.20 g, 69%).

^{1}H NMR (400 MHz, DMSO-d_6) δ_H ppm: 10.10 (2H, s, H11), 8.83 (2H, dd, *J* = 4.0, 1.7 Hz, H2), 8.33 (2H, dd, *J* = 8.6, 1.7 Hz, H4), 7.58 (2H, d, *J* = 8.6 Hz, H7), 7.50 (2H, dd, *J* = 8.6, 4.0 Hz, H3), 7.08 (2H, d, *J* = 8.6 Hz, H8), 4.09 (4H, t, *J* = 6.7 Hz, H18), 3.52 (4H, s, H30/H32), 3.50 (4H, s, H30/H32), 3.43 (2H, s, H39), 3.01 (4H, t, *J* = 6.3 Hz, H37), 2.92 (4H, t, *J* = 6.3 Hz, H36), 2.85 (4H, t, *J* = 7.2 Hz, H23), 2.32 (6H, s, H27), 1.82 (4H, p, *J* = 6.7 Hz, H19), 1.62 – 1.34 (12H, m, H20, H21, H22). ^{13}C NMR (400 MHz, DMSO-d_6) δ_C ppm: 195.4,

173.1, 170.2, 152.3, 148.7, 139.7, 131.3, 125.6, 124.3, 122.2, 121.4, 108.6, 68.3, 58.3, 55.6, 52.3, 51.8, 40.2, 39.9, 39.7, 39.5, 39.3, 39.1, 38.9, 30.6, 29.2, 28.6, 28.4, 28.0, 25.2. HR-MS (ESI-TOF)$^{+}$ m/z: $C_{48}H_{63}N_7O_{12}S_2$ calcd: 994.4055, Found: 994.4058 $[M + H]^{+}$. Anal. Calcd for $C_{48}H_{63}N_7O_{12}S_2$: C, 57.99; H, 6.39; N, 9.86; S, 6.45. Found: C, 58.08; H, 6.45; N, 9.91; S, 6.41. IR (solid), v(cm^{-1}): 2931 (C-H, m), 1682 (S<u>CO</u>CH_3), 1598 (C=O, s). λ_{max} /nm (MeOH) 265 (log ε = 4.6).

2.10.1.6 Synthesis of 2,2'-((((carboxymethyl)azanediyl)bis(ethane-2,1-diyl))bis((2-((8-((6-mercaptohexyl)oxy)quinolin-5-yl)amino)-2-oxoethyl)azanediyl))diacetic acid (H_3Quin_2SH)

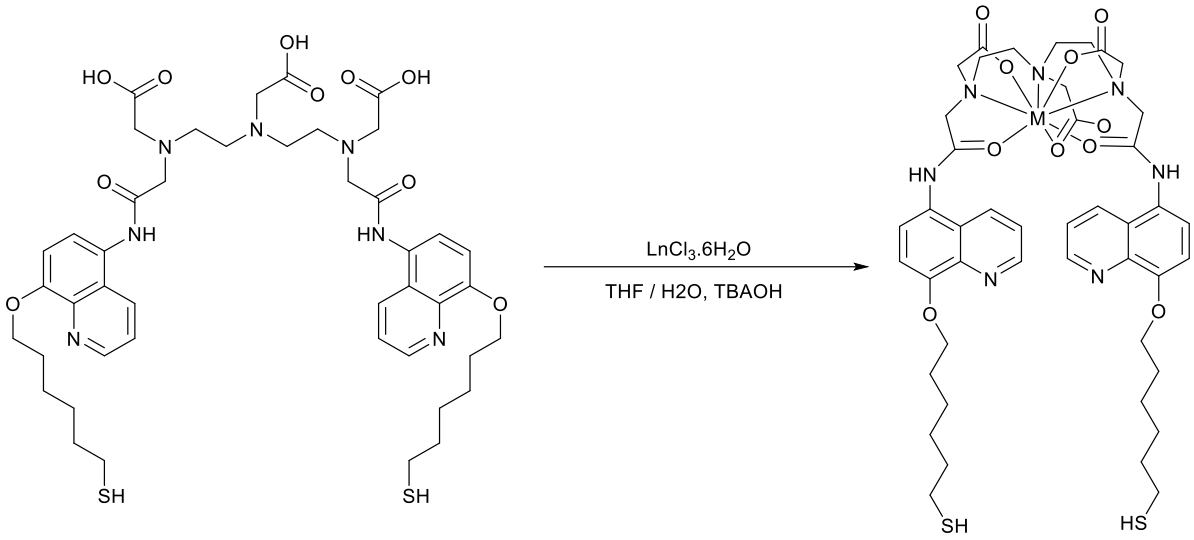


H_3QuinSAc (400 mg, 4.02 x 10^{-4} mol, 1.00 eq.) was dissolved in MeOH (5 mL) and THF (5 mL). NaOH (1M, 4 mL, 4 x 10^{-3} mol, 10 eq.) was added and stirred under N_2 atmosphere. The solvents were removed *in vacuo* and the material was dissolve in the minimum amount of water. A precipitate was formed upon acidification to pH 3.5 by dropwise addition of HCl (1M). The orange solid was filtered, washed with MeCN (3 x 20 mL) and hexane (3 x 20 mL), then dried by cryodesiccation, yielding a light-yellow/brown powder (70%).

^{1}H NMR (400 MHz, DMSO-d_6) δ_H ppm: 10.08 (2H, s, H11), 8.81 (2H, dd, *J* = 4.0, 1.7 Hz, H2), 8.32 (2H, dd, *J* = 8.6, 1.7 Hz, H4), 7.52 (2H, d, *J* = 8.6 Hz, H7), 7.39 (2H, dd, *J* = 8.6,

4.0 Hz, H3), 7.02 (2H, d, *J* = 8.6 Hz, H8), 4.05 (4H, t, *J* = 6.6 Hz, H18), 3.51 (10H, br s, H30, H32, H39), 3.04 (4H, t, *J* = 6.4 Hz, H37), 2.94 (4H, t, *J* = 6.4 Hz, H36), 2.70 (4H, t, *J* = 7.2 Hz, H23), 1.79 (4H, m, H19), 1.64 (4H, m, H22) 1.44 (8H, m, H20, H21). MS (ESI-TOF)$^{+}$ m/z: 911.42 $[M + H]^{+}$. IR (solid), v(cm^{-1}): 2929 (C-H, m), 1594 (C=O, s).

2.10.1.7 Synthesis of $LnQuin_2SH$



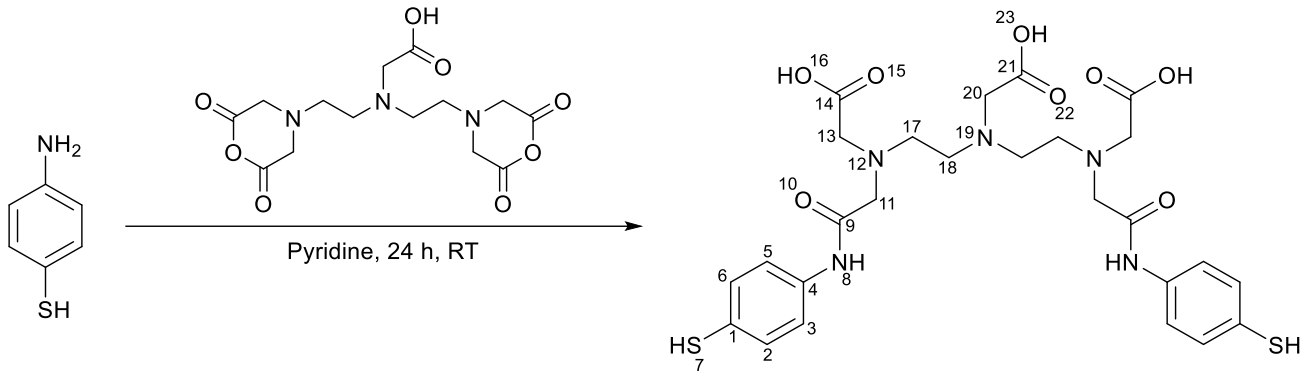
H_3Quin_2SH (50 mg, 0.050 mmol) was dissolved in a 1:1 THF/H_2O mixture (5 mL) and the pH was raised to 5 by the dropwise addition of tetrabutylammoniumhydroxide (TBAOH). $LnCl_3.6H_2O$ (0.050 mmol, 1.0 eq.) was dissolved in water (1 mL) and added to the solution. The THF was removed *in vacuo* and the pH was raised to 5 by the dropwise addition of TBAOH, forming a solid. The solid was filtered, triturated with acetone (10 mL) at 4 ˚C for 1 h, then collected by filtration. The solid was collected by filration, washed with acetone and dried *in vacuo*, yielding $LnQuin_2SH$.

$EuQuin_2SH$ (71%): HR-MS (ESI-TOF)$^{+}$ m/z: $C_{44}H_{56}EuN_7O_{10}S_2$ Calcd: 530.6450, Found: 530.6461 $[M + 2H]^{2+}$. IR (solid), v(cm^{-1}): 2929 (C-H, m), 1594 (C=O, s). λ_{max} /nm (MeOH) 245 (log ε = 4.8), 322 (log ε = 3.9).

$NdQuin_2SH$ (54%):HR-MS (ESI-TOF)$^{+}$ m/z: $C_{44}H_{56}N_7NdO_{10}S_2$ calcd: 526.6406, Found: 526.6409 $[M + 2H]^{2+}$. λ_{max} /nm (MeOH) 245 (log ε = 4.8), 322 (log ε = 3.8).

YbQuin$_2$SH (49%): HR-MS (ESI-TOF)$^+$ m/z: $C_{44}H_{56}N_7O_{10}S_2Yb$ Calcd: 541.1539 Found: 541.1542 $[M + H]^+$. λ_{max} /nm (MeOH) 245 (log ε = 4.8), 322 (log ε = 3.8).

2.10.1.8 Synthesis of 2,2'-((((carboxymethyl)azanediyl)bis(ethane-2,1-diyl))bis((2-((4-mercaptophenyl)amino)-2-oxoethyl)azanediyl))diacetic acid (H_3L)

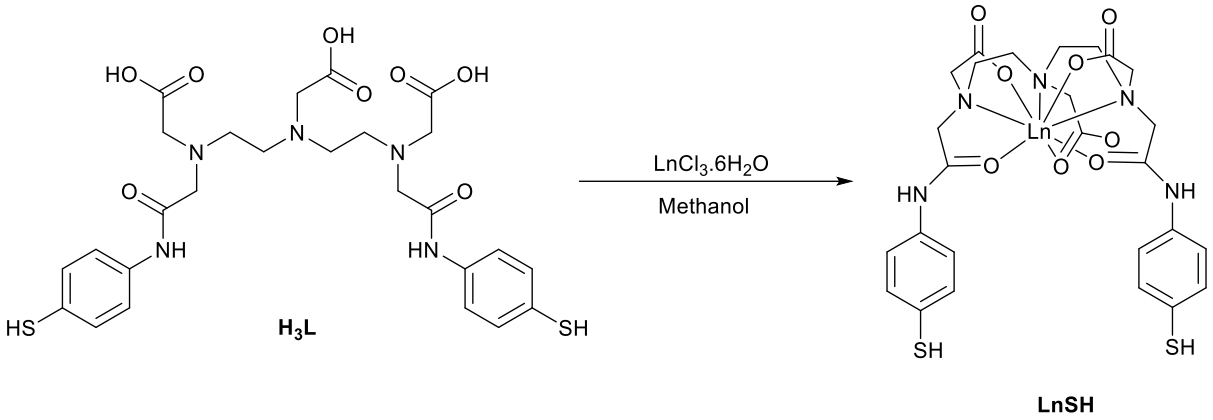


4-aminothiophenol (2.0 g, 16 mmol, 5.7 eq., Fischer Sci.) and DTPA bisanhydride (1.02 g, 2.8 mmol) were dissolved in dry pyridine (10 mL) and stirred under N_2 atmosphere for 24 h at room temperature. The solvent was removed *in vacuo* and the resultant yellow oil was dissolved in deionised water (20 mL). The pH was lowered to 3 by the dropwise addition of conc. HCl (2 M), forming a sticky, off-white solid. The water was decanted and the solid was triturated with acetonitrile (50 mL) and filtered. The crude product was dissolved in pyridine (20 mL) and hydrazine monohydrate (3 mL) was added. The solvent was removed *in vacuo* and the resultant yellow oil was dissolved in deionised water (20 mL). The pH was lowered to 3 by the dropwise addition of conc. HCl (2 M). The solution was filtered, washed with acetonitrile (50 mL) and diethyl ether (50 mL), then dried *in vacuo*, to yield the product as a fine white powder (0.65 g, 1.1 mmol, 38%).

^{1}H NMR (400 MHz, Methanol-d_4) δ_H ppm: 7.44 (4H, d, *J* = 8.9 Hz, H3, H4), 7.14 (4H, d, *J* = 8.9 Hz, H2, H6), 4.02 (2H, s, H20), 3.61 (4H, s, H11/H13), 3.58 (4H, s, H11/H13), 3.48 (4H,

t, *J* = 5.5 Hz, H18), 3.23 (4H, t, *J* = 5.6 Hz, H17). HR-MS (ES-TOF?)$^+$ m/z: $C_{26}H_{33}N_5O_8S_2$ calcd: 608.1849, Found: 608.1846 $[M]^+$. λ_{max} /nm (MeOH) 265 (log ε = 4.6).

2.10.1.9 Synthesis of LnSH



H_3L (0.125 g, 0.20 mmol) was added to a solution of $LnCl_3.6H_2O$ (0.20 mmol, 1.0 eq.) in methanol (3 mL) and sonicated until fully dissolved. Acetonitrile (30 mL) was added, forming a white precipitate, which was collected by filtration, washed with acetonitrile (50 mL) and diethyl ether (50 mL) and dried *in vacuo.*

EuSH (59%): HR-MS (ES-TOF?)$^+$ m/z: $C_{26}H_{30}EuN_5O_8S_2$ calcd: 758.0825, Found: 758.0826 $[M]^+$. λ_{max} /nm (MeOH) 266 (log ε = 4.5).

TbSH (68%): HR-MS (ES-TOF?)$^+$ m/z: $C_{26}H_{30}N_5O_8S_2Tb$ calcd: 764.0867, Found: 764.0854 $[M + H]^+$. λ_{max} /nm (MeOH) 266 (log ε = 4.5).

2.10.2 Synthesis of Nanoparticle Species

2.10.2.1 Synthesis of 13 nm citrate-stabilised gold nanoparticles (AuNP13)

Ethylenediaminetetraaceticacid (EDTA, 162 mg, 0.04 mM), citric acid (13.6 mg, 0.71 mM) and trisodium citrate (60.5 mg, 2.05 mM) were added to a 250 mL round bottom flask with 100 mL of MQ water. The resultant solution was stirred vigorously and brought to reflux (100 °C). When reflux was achieved, a warm solution of gold (III) chloride trihydrate

($HAuCl_4.3H_2O$, 8.6 mg, 0.86 mM) was added. The solution was stirred under reflux conditions for 15 min and then for a further 45 min at room temperature. : λ_{max} (H_2O): 515 nm; DLS: Number: 13 ± 3 nm, Intensity: 18 ± 4 nm, PDI: 0.10; ζ-potential: -38 ± 5 mV; TEM: 13.3 ± 0.6 nm.

2.10.2.2 Synthesis of $LnQuin_2S$-AuNPs and LnS-AuNPs

13 nm citrate-stabilised gold nanoparticles were centrifuged at 10,000 g for 20 min and resuspended in MQ water at a concentration of 5 nM, monitored by UV-vis spectroscopy. $LnQuin_2SH$ (Ln = Eu, Yb, Nd) and LnSH (Ln = Eu, Tb) were dissolved in MeOH at a concentration of 0.4 mM and added to a vial containing 13 nm citrate gold nanoparticles (3 mL, 5 nM) in 2.5 µL aliquots until the final concentration of metal complex was 12 µM, with continuous stirring. Each NP species was stirred for a further 10 min, purified through a G-15 Sephadex size exclusion column to remove any excess $LnQuin_2SH$ or LnSH, and adjusted to the desired concentration by addition of MQ water. $EuQuin_2S$-AuNPs: λ_{max} (H_2O): 521 nm; DLS: Number: 14 ± 4 nm, Intensity: 21 ± 7 nm, PDI: 0.13; ζ-potential: -11 ± 6 mV; TEM: 13.3 ± 0.9 nm. $YbQuin_2S$-AuNPs and $NdQuin_2S$-AuNPs characterisation was not significantly different to $EuQuin_2S$-AuNPs. TbS-AuNPs: λ_{max} (H_2O): 521 nm; DLS: Number: 14 ± 4 nm, Intensity: 19 ± 6 nm, PDI: 0.11; ζ-potential: -25 ± 12 mV; TEM: 13.0 ± 1.1 nm. EuS-AuNP characterisation was not significantly different to TbS-AuNPs.

2.10.2.3 Synthesis of $EuQuin_2S$-Zonyl-AuNPs, $EuQuin_2S$-TFD-AuNPs and $EuQuin_2S$-PEG-AuNPs

13 nm citrate-stabilised gold nanoparticles were centrifuged at 10,000 g for 20 min and resuspended in MQ water at a concentration of 5 nM, monitored by UV-vis spectroscopy. Lithium 3-[2-(perfluoroalkyl)ethylthio]propionate (Zonyl FSA, 12 µM), *N*-(2-(ethylthio)ethyl)-2,2,3,3,4,4,5,5,6,6,7,7,8,8,9,9,10,10,11,11,12,12,12-tricosafluorododecanamide (TFD, 10 µM), or 1-mercapto-3,5,7,9,11,13,15,17-octaoxaicosan-20-oic acid (PEG, 2 µM) were added to the citrate-stabilised gold nanoparticles and stirred continuously for 5 min.

$EuQuin_2SH$ was then added in excess to each NP species and stirred for a further 10 min, before purification using a G-15 Sephadex size exclusion column to remove any excess $EuQuin_2SH$, then the NP species was adjusted to the desired concentration by addition of MQ water.

$EuQuin_2S$-Zonyl-AuNPs: : λ_{max} (H_2O): 521 nm; DLS: Number: 15 ± 4 nm, Intensity: 29 ± 12 nm, PDI: 0.25; ζ-potential: -24 ± 13 mV. $EuQuin_2S$-TFD-AuNPs: λ_{max} (H_2O): 521 nm; DLS: Number: 15 ± 4 nm, Intensity: 30 ± 14 nm, PDI: 0.22; ζ-potential: -27 ± 14 mV. $EuQuin_2S$-PEG-AuNPs: λ_{max} (H_2O): 520 nm; DLS: Number: 16 ± 4 nm, Intensity: 31 ± 10 nm, PDI: 0.19; ζ-potential: -25 ± 14 mV.

2.10.2.4 Synthesis of PEG-AuNPs

13 nm citrate-stabilised gold nanoparticles were centrifuged at 10,000 g for 20 min and resuspended in MQ water at a concentration of 5 nM, monitored by UV-vis spectroscopy. 1-mercapto-3,5,7,9,11,13,15,17-octaoxaicosan-20-oic acid (PEG) (1 mM) was added to a vial containing 13 nm citrate gold nanoparticles (3 mL, 5 nM) in 2.5 µL aliquots to a final concentration of 50 µM, with continuous stirring. To remove any excess PEG, the NPs were washed twice by centrifugation (10,000 g, 20 min) and adjusted to the desired concentration by addition of MQ water. λ_{max} (H_2O): 518 nm; DLS: Number: 16 nm, Intensity: 26 nm, PDI: 0.13; ζ-potential: -50 mV.

2.10.3 Isotherm Titration Calorimetry Experiments

ITC was performed using the automated Malvern Panalytical MicroCal PEAQ-ITC. $EuQuin_2SH$ (0.1 mM) and 13 nm citrate gold nanoparticles (7.5 nM) were suspended in a Tris-HCl buffer (2.5 mM, pH 7) supplemented with 10% methanol to improve metal complex solubility. 300 µL of buffer stabilised gold nanoparticles were added to the instrument sample cell and the temperature was equilibrated to 25 °C. $EuQuin_2SH$ was automatically titrated into the instrument sample cell in 20 injections at a rate of 0.5 μLs^{-1} in 150 s intervals;

the first injection was 0.4 µL and the following 19 injections were 2 µL. A constant stirring speed of 750 rpm was maintained during the experiments to ensure sufficient mixing. The data from experiments was analysed using MicroCal PEAQ-ITC analysis software. ITC experiments with TbSH were ran under identical conditions.

2.10.4 SuperSTEM imaging

$EuQuin_2S$-AuNPs and EuS-AuNPs were prepared as described previously and adjusted to a concentration of 2.5 nM, monitored by UV-vis spectroscopy. 10 µL of each sample was then drop casted onto graphene and ultra-thin carbon supports, allowing evaporation to occur overnight at room temperature. The samples were then posted to the SuperSTEM laboratory, at the EPSRC National Research Facility for Advanced Electron Microscopy, Daresbury, UK, in small plastic casing to avoid as much organic contamination as possible. Image acquisition and analysis was carried out by members of staff at the facility, as well as heat treatment of the samples. At the laboratory, imaging was performed using a Nion UltraSTEM100 dedicated aberration corrected STEM, equipped with a Gatan Enfina EEL spectrometer. The microscope was operated at an acceleration voltage of 100 kV and the beam current was estimated at 40 pA, resulting in an effective electron probe size of less than 0.9 Å. The convergence semi-angle was 27 mrad for HDAAF/BF and 36 mrad for EELS. During data processing, EELS was denoised with principle component analysis.

2.10.5 Analysis of the Number of Lanthanide Complexes per Nanoparticle with ICP-MS

Ultrapure water, HCl (Traceselect Ultra, Aldrich – 68%) and HNO_3 (Traceselect Ultra, Aldrich – 68%) reagents were used for all experiments. Nanoparticle species were digested by the addition of the minimum required volume of aqua regia. Each sample was transferred to a 15 mL polypropylene tube (Agilent) and the total volume for each sample was then made up to 5 mL using with a final HNO_3 concentration of 4%.

2.10.6 Using CyTOF to Study The Effect of Coating EuQuin$_2$S-AuNPs with Fluorinated Surfactants and a PEG Polymer on their Cellular Uptake in Cancer Cells

EuQuin$_2$S-AuNPs, EuQuin$_2$S-Zonyl-AuNPs, EuQuin$_2$S-TFD-AuNPs and EuQuin$_2$S-PEG-AuNPs were prepared and purified as described in 2.10.2.3, then adjusted to a concentration of 1.6 nM. HeLa cells were then treated with each NP species (10x dilution in DMEM) for 4, 8 and 16 hours under the culture conditions described in 3.10.1. Cells were prepared for CyTOF analysis as described in 3.10.4.

2.11 References

1. E. Dulkeith, A. C. Morteani, T. Niedereichholz, T. A. Klar, J. Feldmann, S. A. Levi, F. C. J. M. van Veggel, D. N. Reinhoudt, M. Möller and D. I. Gittins, *Physical Review Letters*, 2002, **89**, 203002.
2. S. Eustis and M. A. El-Sayed, *Chemical Society Reviews*, 2006, **35**, 209-217.
3. W. R. Glomm, S. J. Moses, M. K. Brennaman, J. M. Papanikolas and S. Franzen, *The Journal of Physical Chemistry B*, 2005, **109**, 804-810.
4. F. Liu and J.-M. Nunzi, *Applied Physics Letters*, 2011, **99**, 123302.
5. A. V. Sorokin, A. A. Zabolotskii, N. V. Pereverzev, I. I. Bespalova, S. L. Yefimova, Y. V. Malyukin and A. I. Plekhanov, *The Journal of Physical Chemistry C*, 2015, **119**, 2743-2751.
6. I. O. Osorio-Román, A. R. Guerrero, P. Albella and R. F. Aroca, *Analytical Chemistry*, 2014, **86**, 10246-10251.
7. D. J. Lewis, T. M. Day, J. V. MacPherson and Z. Pikramenou, *Chemical Communications*, 2006, DOI: 10.1039/b518091k, 1433-1435.
8. A. Davies, D. J. Lewis, S. P. Watson, S. G. Thomas and Z. Pikramenou, *Proceedings of the National Academy of Sciences*, 2012, **109**, 1862-1867.
9. S. A. Osborne and Z. Pikramenou, *Faraday Discuss*, 2015, **185**, 219-231.
10. G. Mancino, A. J. Ferguson, A. Beeby, N. J. Long and T. S. Jones, *Journal of the American Chemical Society*, 2005, **127**, 524-525.
11. R. H. C. Tan, M. Motevalli, I. Abrahams, P. B. Wyatt and W. P. Gillin, *The Journal of Physical Chemistry B*, 2006, **110**, 24476-24479.
12. L. Song, J. Hu, J. Wang, X. Liu and Z. Zhen, *Photochemical & Photobiological Sciences*, 2008, **7**, 689-693.
13. M. Winey, J. B. Meehl, E. T. O'Toole and T. H. Giddings, Jr., *Molecular Biology of the Cell*, 2014, **25**, 319-323.
14. A. V. Crewe, J. Wall and J. Langmore, *Science*, 1970, **168**, 1338-1340.
15. J. Liu, *Journal of Electron Microscopy*, 2005, **54**, 251-278.
16. R. Erni, M. D. Rossell, C. Kisielowski and U. Dahmen, *Physical Review Letters*, 2009, **102**, 096101.
17. M. Haider, S. Uhlemann, E. Schwan, H. Rose, B. Kabius and K. Urban, *Nature*, 1998, **392**, 768-769.

18. M. Haider, P. Hartel, H. Müller, S. Uhlemann and J. Zach, *Philosophical Transactions: Mathematical, Physical and Engineering Sciences*, 2009, **367**, 3665-3682.
19. P. E. Batson, N. Dellby and O. L. Krivanek, *Nature*, 2002, **418**, 617-620.
20. P. D. Nellist, M. F. Chisholm, N. Dellby, O. L. Krivanek, M. F. Murfitt, Z. S. Szilagyi, A. R. Lupini, A. Borisevich, W. H. Sides and S. J. Pennycook, *Science*, 2004, **305**, 1741-1741.
21. M. T. Otten, *Journal of Electron Microscopy Technique*, 1991, **17**, 221-230.
22. J. Y. Zhang, J. Hwang, B. J. Isaac and S. Stemmer, *Scientific Reports*, 2015, **5**, 12419.
23. P. D. Nellist and S. J. Pennycook, in *Advances in Imaging and Electron Physics*, ed. P. W. Hawkes, Elsevier, 2000, vol. 113, pp. 147-203.
24. Q. M. Ramasse, C. R. Seabourne, D.-M. Kepaptsoglou, R. Zan, U. Bangert and A. J. Scott, *Nano Letters*, 2013, **13**, 4989-4995.
25. K. Suenaga and M. Koshino, *Nature*, 2010, **468**, 1088-1090.
26. F. Hofer, F. P. Schmidt, W. Grogger and G. Kothleitner, *IOP Conference Series: Materials Science and Engineering*, 2016, **109**, 012007.
27. P. L. Potapov and D. Schryvers, *Ultramicroscopy*, 2004, **99**, 73-85.
28. K. Sun, J. Liu and N. D. Browning, *Journal of Catalysis*, 2002, **205**, 266-277.
29. K. Sun, J. Liu, N. Nag and N. D. Browning, *Catalysis Letters*, 2002, **84**, 193-199.
30. K. Sun, J. Liu, N. K. Nag and N. D. Browning, *The Journal of Physical Chemistry B*, 2002, **106**, 12239-12246.
31. R. Bavand, A. Korinek, G. A. Botton, A. Yelon and E. Sacher, *The Journal of Physical Chemistry C*, 2017, **121**, 23104-23119.
32. S. Zhang, G. Leem and T. R. Lee, *Langmuir*, 2009, **25**, 13855-13860.
33. Y. Xue, X. Li, H. Li and W. Zhang, *Nature Communications*, 2014, **5**, 4348.
34. S. M. King, S. Claire, R. I. Teixeira, A. N. Dosumu, A. J. Carrod, H. Dehghani, M. J. Hannon, A. D. Ward, R. Bicknell, S. W. Botchway, N. J. Hodges and Z. Pikramenou, *Journal of the American Chemical Society*, 2018, **140**, 10242-10249.
35. J. A. Yang, B. J. Johnson, S. Wu, W. S. Woods, J. M. George and C. J. Murphy, *Langmuir*, 2013, **29**, 4603-4615.
36. A. M. Davidson, M. Brust, D. L. Cooper and M. Volk, *Analytical Chemistry*, 2017, **89**, 6807-6814.
37. N. J. Rogers, H. C. Jeffery, S. Claire, D. J. Lewis, G. Zikeli, N. J. Hodges, S. Egginton, G. B. Nash and Z. Pikramenou, *Nanomedicine*, 2017, **12**, 2725-2740.
38. A. N. Dosumu, S. Claire, L. S. Watson, P. M. Girio, S. A. M. Osborne, Z. Pikramenou and N. J. Hodges, *JACS Au*, 2021, **1**, 174-186.
39. S.-T. Wang, H. Zhang, S. Xuan, D. Nykypanchuk, Y. Zhang, G. Freychet, B. M. Ocko, R. N. Zuckermann, N. Todorova and O. Gang, *Journal of the American Chemical Society*, 2022, **144**, 8138-8152.
40. S. Sheibani, K. Basu, A. Farnudi, A. Ashkarran, M. Ichikawa, J. F. Presley, K. H. Bui, M. R. Ejtehadi, H. Vali and M. Mahmoudi, *Nature Communications*, 2021, **12**, 573.
41. S. Zhang, G. Leem, L.-o. Srisombat and R. T. Lee, *Journal of the American Chemical Society*, 2008, **130**, 113-120.
42. J. R. Lilley, PhD Thesis, University of Birmingham, 2017.
43. A. Beeby, I. M. Clarkson, R. S. Dickins, S. Faulkner, D. Parker, L. Royle, A. S. de Sousa, G. J. A. Williams and W. Woods, *Journal of the Chemical Society, Perkin Transactions 2*, 1999, 493-504.
44. D. J. Lewis, F. Moretta, A. T. Holloway and Z. Pikramenou, *Dalton Trans*, 2012, **41**, 13138-13146.
45. S. P. Hammond, PhD Thesis, University of Birmingham, 2009.

46. F. Schulz, T. Homolka, N. G. Bastus, V. Puntes, H. Weller and T. Vossmeyer, *Langmuir*, 2014, **30**, 10779-10784.
47. J. Turkevich, P. C. Stevenson and J. Hillier, *Discussions of the Faraday Society*, 1951, **11**, 55-75.
48. P. Ceroni, Z. Pikramenou, L. Prodi, Q. Pan, D. Adams, J. Weinstein, F. Lewis, C. Bohne, A. Vlcek, D. M. Bassani, A. P. de Silva, C. Moucheron, D. Nocera, A. Diaz-Moscoso, M. Padilla, C. Lemon, S. Campagna, S. Bradberry, E. Galoppini, P. A. Plotz, J. M. Kelly, J. Rohacova, A. Harriman, P. Keane, D. Gust, J. Vos, M. Mauro, L. De Cola, S. K. Sivaraman, G. Lemercier, S. Osborne and F. Monti, *Faraday Discuss*, 2015, **185**, 311-335.
49. W. Haiss, N. T. Thanh, J. Aveyard and D. G. Fernig, *Analytical Chemistry*, 2007, **79**, 4215-4221.
50. S. K. Ghosh and T. Pal, *Chemical Reviews*, 2007, **107**, 4797-4862.
51. R. Li, X. Gu, X. Liang, S. Hou and D. Hu, *Materials*, 2019, **12**.
52. L. Shi, J. Zhang, M. Zhao, S. Tang, X. Cheng, W. Zhang, W. Li, X. Liu, H. Peng and Q. Wang, *Nanoscale*, 2021, **13**, 10748-10764.
53. J. M. Rabanel, P. Hildgen and X. Banquy, *Journal of Controlled Release*, 2014, **185**, 71-87.
54. J. L. Perry, K. G. Reuter, M. P. Kai, K. P. Herlihy, S. W. Jones, J. C. Luft, M. Napier, J. E. Bear and J. M. DeSimone, *Nano Letters*, 2012, **12**, 5304-5310.
55. S. J. Adams, Carrod, A. J., Rochford, L. A., Walker, M., Pikramenou, Z., *ChemistrySelect*, 2018, **3**.
56. E. J. Shelley, D. Ryan, S. R. Johnson, M. Couillard, D. Fitzmaurice, P. D. Nellist, Y. Chen, R. E. Palmer and J. A. Preece, *Langmuir*, 2002, **18**, 1791-1795.
57. D. J. Lavrich, S. M. Wetterer, S. L. Bernasek and G. Scoles, *The Journal of Physical Chemistry B*, 1998, **102**, 3456-3465.
58. J. A. Yang, B. J. Johnson, S. Wu, W. S. Woods, J. M. George and C. J. Murphy, *Langmuir*, 2013, **29**, 4603-4615.
59. J. M. Dennison, J. M. Zupancic, W. Lin, J. H. Dwyer and C. J. Murphy, *Langmuir*, 2017, **33**, 7751-7761.
60. M. M. Pierce, C. S. Raman and B. T. Nall, *Methods*, 1999, **19**, 213-221.
61. S. Diplas, O. M. Løvvik, H. Nordmark, D. M Kepaptsoglou, J. M. Graff, C. Ladam, F. Tyholdt, J. C. Walmsley, A. E. Gunnaes, R. Fagerberg and A. Ulyashin, *Surface and Interface Analysis*, 2010, **42**, 874-877.
62. F. S. Hage, R. J. Nicholls, J. R. Yates, D. G. McCulloch, T. C. Lovejoy, N. Dellby, O. L. Krivanek, K. Refson and Q. M. Ramasse, *Science Advances*, 2018, **4**, eaar7495.
63. J. A. Mundy, D. Hodash, A. Melville, R. Held, T. Mairoser, D. A. Muller, L. F. Kourkoutis, A. Schmehl and D. G. Schlom, *Applied Physics Letters*, 2014, **104**, 091601.
64. L. H. G. Tizei, R. Nakanishi, R. Kitaura, H. Shinohara and K. Suenaga, *Physical Review Letters*, 2015, **114**, 197602.
65. M. I. Béthencourt, L.-o. Srisombat, P. Chinwangso and T. R. Lee, *Langmuir*, 2009, **25**, 1265-1271.
66. B. I. Ipe, K. G. Thomas, S. Barazzouk, S. Hotchandani and P. V. Kamat, *The Journal of Physical Chemistry B*, 2002, **106**, 18-21.
67. P. V. Kamat, S. Barazzouk and S. Hotchandani, *Angewandte Chemie International Edition*, 2002, **41**, 2764-2767.
68. F. Stellacci, C. A. Bauer, T. Meyer-Friedrichsen, W. Wenseleers, S. R. Marder and J. W. Perry, *Journal of the American Chemical Society*, 2003, **125**, 328-329.
69. J. E. Bertie and Z. Lan, *Applied Spectroscopy*, 1996, **50**, 1047-1057.
70. G. A. Carter and D. C. McCain, *Remote Sensing of Environment*, 1993, **46**, 305-310.

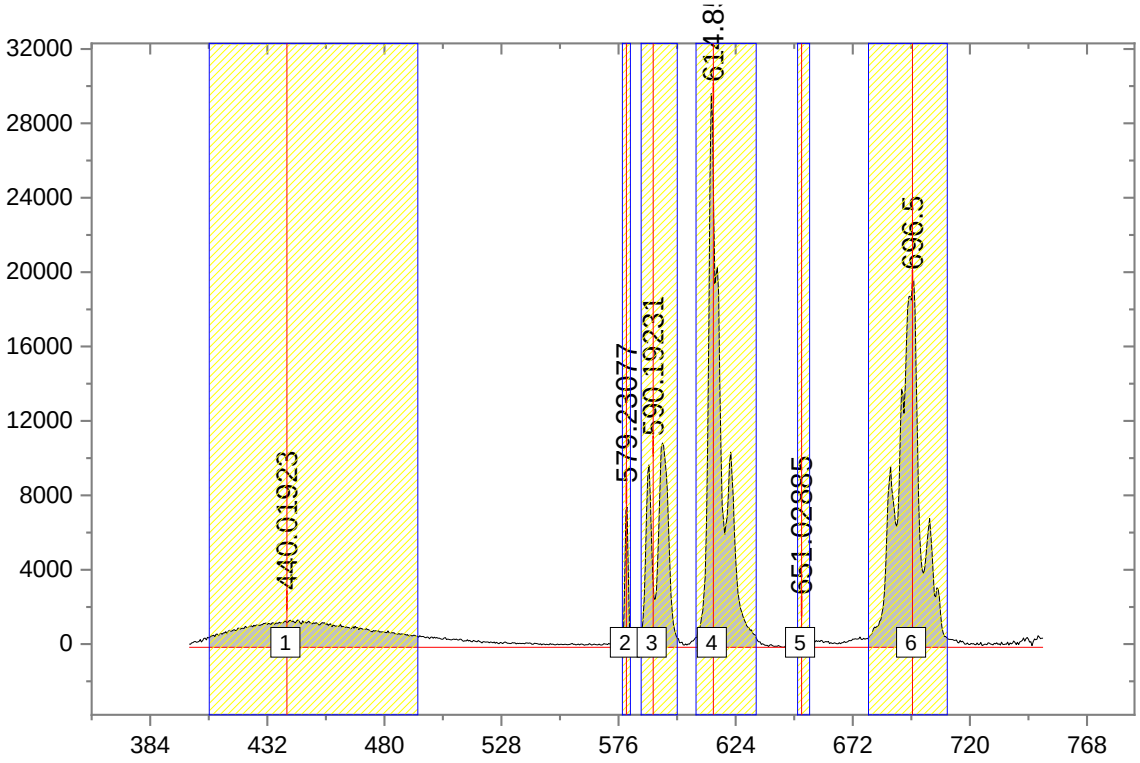
71. K. G. Thomas and P. V. Kamat, *Accounts of Chemical Research*, 2003, **36**, 888-898.
72. P. B. Glover, A. P. Bassett, P. Nockemann, B. M. Kariuki, R. Van Deun and Z. Pikramenou, *Chemistry – A European Journal*, 2007, **13**, 6308-6320.
73. P. G. Argudo, M. Carril, M. T. Martín-Romero, J. J. Giner-Casares and C. Carrillo-Carrión, *Chemistry – A European Journal*, 2019, **25**, 195-199.
74. L. Dafik, V. Kalsani, A. K. L. Leung and K. Kumar, *Journal of the American Chemical Society*, 2009, **131**, 12091-12093.
75. J. S. Suk, Q. Xu, N. Kim, J. Hanes and L. M. Ensign, *Advanced Drug Delivery Reviews*, 2016, **99**, 28-51.
76. G. von Maltzahn, J. H. Park, A. Agrawal, N. K. Bandaru, S. K. Das, M. J. Sailor and S. N. Bhatia, *Cancer Research*, 2009, **69**, 3892-3900.
77. T. W. Shen, C. A. Fromen, M. P. Kai, J. C. Luft, T. B. Rahhal, G. R. Robbins and J. M. DeSimone, *Pharmaceutical Research*, 2015, **32**, 3248-3260.
78. B. Pelaz, P. del Pino, P. Maffre, R. Hartmann, M. Gallego, S. Rivera-Fernandez, J. M. de la Fuente, G. U. Nienhaus and W. J. Parak, *ACS Nano*, 2015, **9**, 6996-7008.
79. P. Nativo, I. A. Prior and M. Brust, *ACS Nano*, 2008, **2**, 1639-1644.
80. R. Gref, M. Lück, P. Quellec, M. Marchand, E. Dellacherie, S. Harnisch, T. Blunk and R. H. Müller, *Colloids and Surfaces B: Biointerfaces*, 2000, **18**, 301-313.
81. H. Liu, T. L. Doane, Y. Cheng, F. Lu, S. Srinivasan, J.-J. Zhu and C. Burda, *Particle & Particle Systems Characterization*, 2015, **32**, 197-204.
82. C. D. Walkey, J. B. Olsen, H. Guo, A. Emili and W. C. Chan, *Journal of the American Chemical Society*, 2012, **134**, 2139-2147.
83. Z. Ait Bachir, Y. Huang, M. He, L. Huang, X. Hou, R. Chen and F. Gao, *International Journal of Nanomedicine*, 2018, **13**, 5657-5671.
84. M. P. Desai, V. Labhasetwar, E. Walter, R. J. Levy and G. L. Amidon, *Pharmaceutical Research*, 1997, **14**, 1568-1573.
85. B. D. Chithrani, A. A. Ghazani and W. C. W. Chan, *Nano Letters*, 2006, **6**, 662-668.
86. N. Gunduz, H. Ceylan, M. O. Guler and A. B. Tekinay, *Scientific Reports*, 2017, **7**, 40493.

2.12 Appendix

2.12.1 H_3Quin_2SH NMR Spectra

2.12.2 Integration of Peaks to Calculate the Intensity of Europium Emission

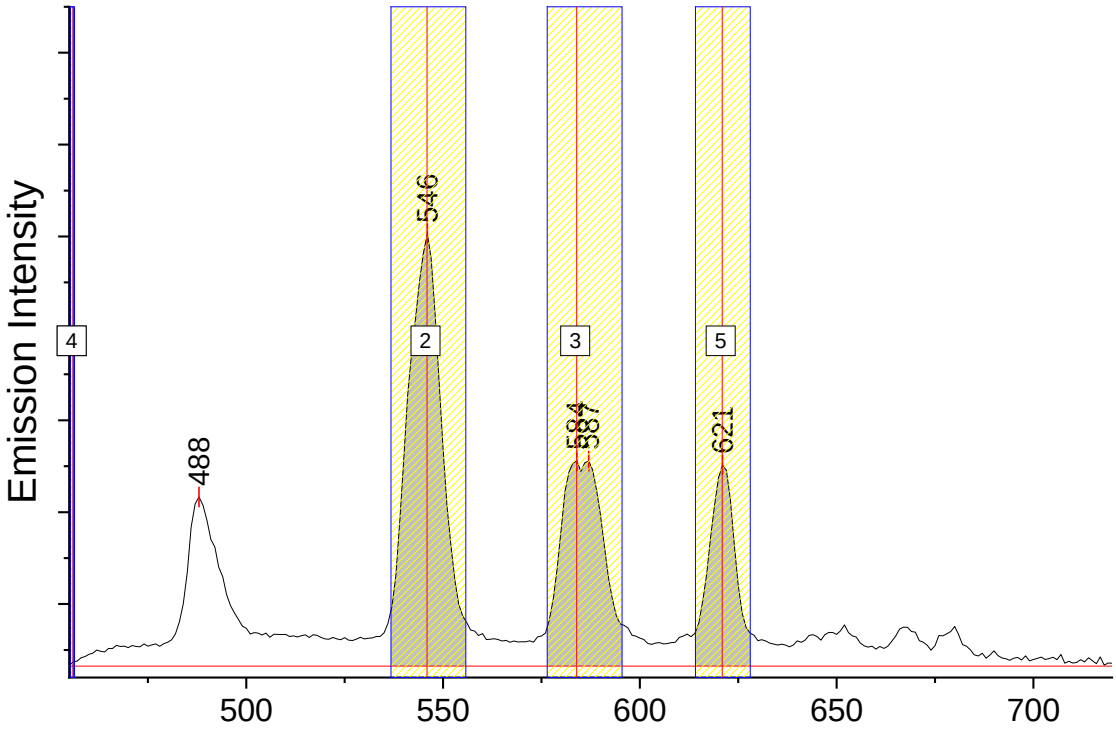
Using Origin Pro, first the baseline was subtracted, then the area under the 5 Eu D → F transitions is calculated. The emission from europium was taken as the sum of the 5 peaks. Quinoline emission estimated by integration of the peak like shown below.



Appendix Figure 2.1 How peaks were integrated to calculate the intensity of europium emission.

2.12.3 Integration of Peaks to Calculate the Intensity of Terbium Emission

Using Origin Pro, first the baseline was subtracted, then the 3 Tb emission peaks at 546, 584 and 621 were integrated to find the emission intensity. The peak at 488 nm was discarded from analysis due to too much scattering in the signal at pH 6.



Appendix Figure 2.2 How peaks were integrated to calculate the intensity of terbium emission.

2.12.4 Calculating Molar Concentration of Gold Nanoparticles

Using Reagent Concentrations

$$C = \frac{m_{Au}}{N_{atoms} \times V \times Mr} = \frac{4.165 \times 10^{-3} g}{71000 \times 0.125\ dm^3 \times 197\ gmol^{-1}} = 2.38\ nM$$

Where m_{Au} = mass of Au used in synthesis

N_{atoms} = estimated number of gold atoms in a spherical 13.2 nm gold nanoparticle

V = volume of water used in synthesis

M_r = molar mass of Au

ICP-MS

$$C_m = \frac{C_{ppb} \times 10^{-6} \times d.f.}{m_{AuNP}} \times \frac{1}{N_A} = \frac{530\ ppb\ \times 55}{2.22 \times 10^{-17} g} \times \frac{1}{6.022 \times 10^{23}\ gmol^{-1}} = 2.18\ nM$$

Where C_m = molar concentration

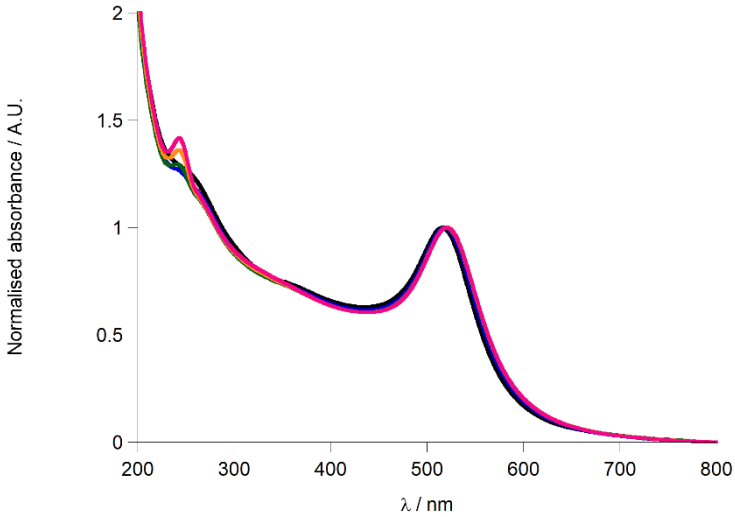
C_{ppb} = average concentration in ppb measured by ICP-MS

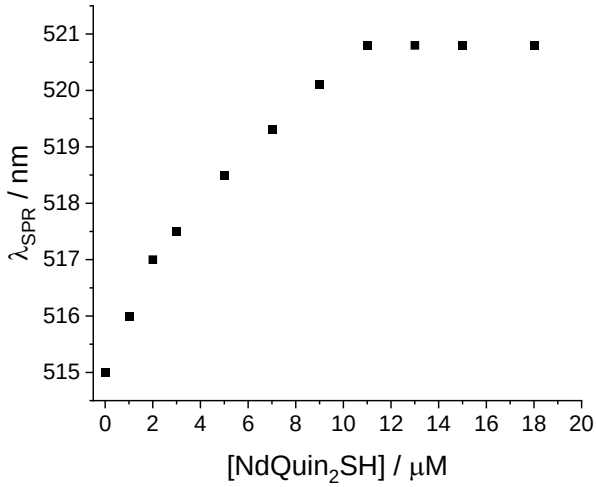
d.f. = dilution factor

m_{AuNP} = mass of 13 nm gold nanoparticle

N_A = avagadro's constant

2.12.5 NdQuin$_2$S-AuNP Characterisation



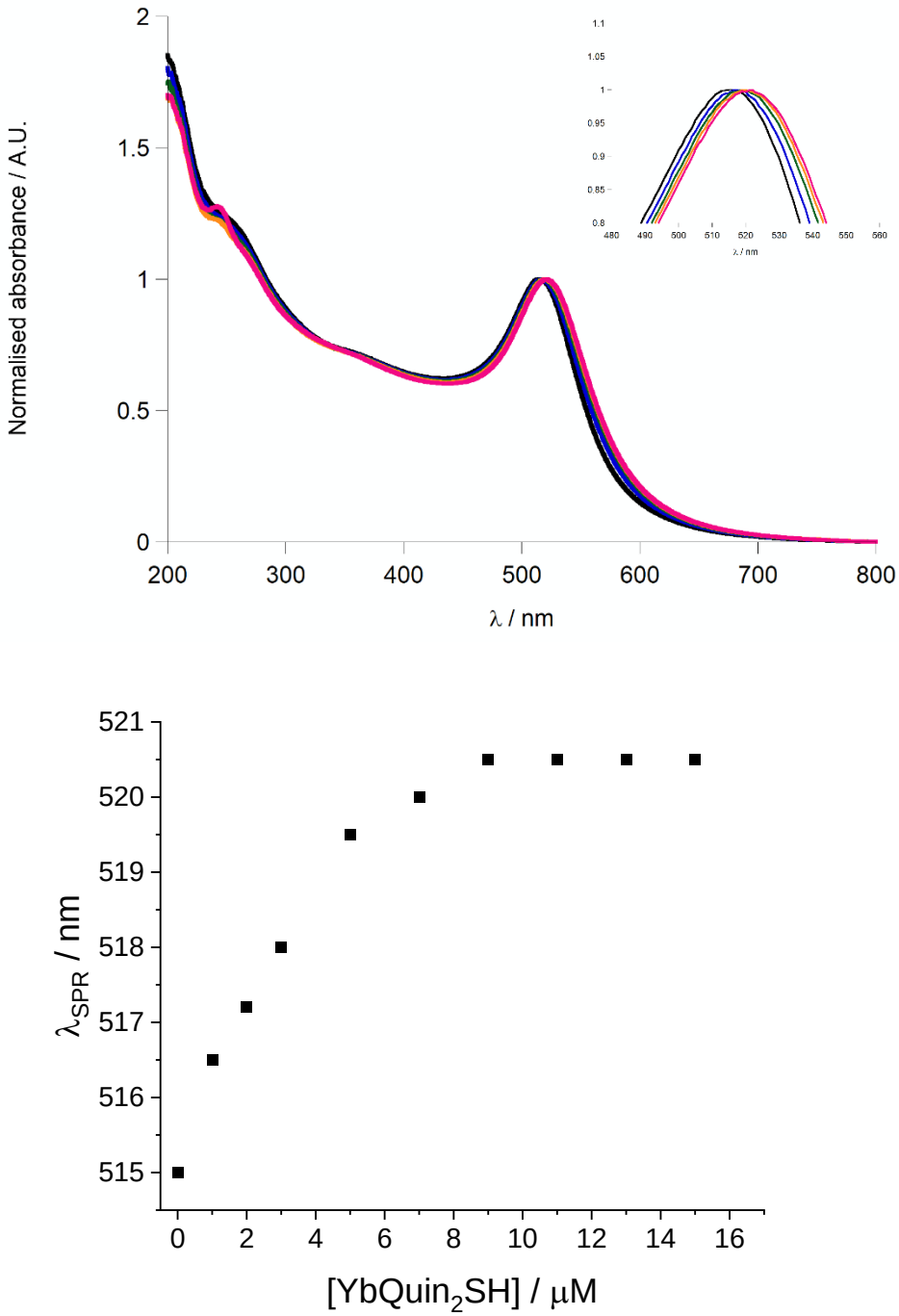


Appendix Figure 2.3 Normalised UV-vis spectra of a 13 nm gold nanoparticle solution [5 nM] upon small additions of NdQuin$_2$SH [0.4 mM] (top); The change in the λ_{SPR} of 13 nm gold nanoparticles upon NdQuin$_2$SH addition measured by UV-vis spectroscopy (bottom).

Appendix table 2.1 Size and polydispersity index of NdQuin$_2$S-AuNPs measured using DLS analysis.

Number / nm	Intensity / nm	PDI
14 ± 4	22 ± 6	0.12

2.12.6 YbQuin$_2$S-AuNP Characterisation

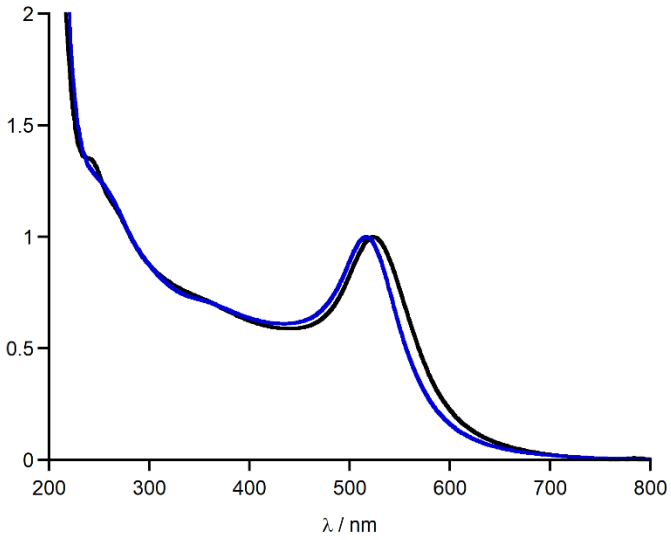


Appendix Figure 2.4 Normalised UV-vis spectra of a 13 nm gold nanoparticle solution [5 nM] upon small additions of YbQuin$_2$SH [0.4 mM] (top); The change in the λ_{SPR} of 13 nm gold nanoparticles upon YbQuin$_2$SH addition measured by UV-vis spectroscopy (bottom).

Appendix table 2. Size and polydispersity index of $YbQuin_2S$-AuNPs measured using DLS analysis.

Number / nm	Intensity / nm	PDI
13 ± 4	20 ± 5	0.09

2.12.7 EuS-AuNP Characterisation



Appendix Figure 2.5 Shift in λ_{max} of 13 nm citrate AuNPs (5 nM) upon addition of EuSH to achieve a final concentration of 10 µM.

Appendix Table 3. Size and polydispersity index of EuS-AuNPs measured using DLS analysis.

Number / nm	Intensity / nm	PDI
13 ± 4	18 ± 6	0.14

2.12.8 Derivation of The Langmuir Adsorption Isotherm (Used for Association Constant Calculations)

At equilibrium

$$r_{ad} = r_d$$

$$\therefore \frac{[A_{ad}]}{[A][S]} = \frac{k_{ad}}{k_d} = K_{eq}^{A}$$

r_{ad}, r_d are the rates of adsorption and desorption

$[A]$ is the concentration of adsorbate A

$[S]$ is the concentration of bare sites (number/m^2)

k_{ad}, k_d are constants of forward and back reactions

The concentration of sites is equal to total no. of sites divided by the area of adsorbate (a)

$$[S_0] = S_0/a$$

And the concentration of all sites is the sum of the free and occupied sites

$$[S_0] = [S] + [A_{ad}]$$

Combining this with the equilibrium equation:

$$S_0 = \frac{[A_{ad}]}{K_{eq}^A[A]} + [A_{ad}] = \frac{1 + K_{eq}^A[A]}{K_{eq}^A[A]}[A_{ad}]$$

Now define the fraction of surface sites covered with A as θ_A,

$$\theta_A = \frac{[A_{ad}]}{[S_0]}$$

This, applied to the previous that combined site balance and equilibrium, yields the Langmuir adsorption isotherm:

$$\theta_A = \frac{K_{eq}^A[A]}{1 + K_{eq}^A[A]}$$

$$\Delta\lambda = \Delta\lambda_{max}\frac{K_a[A]}{1 + K_a[A]}$$

Fit binding curve to data using equation:

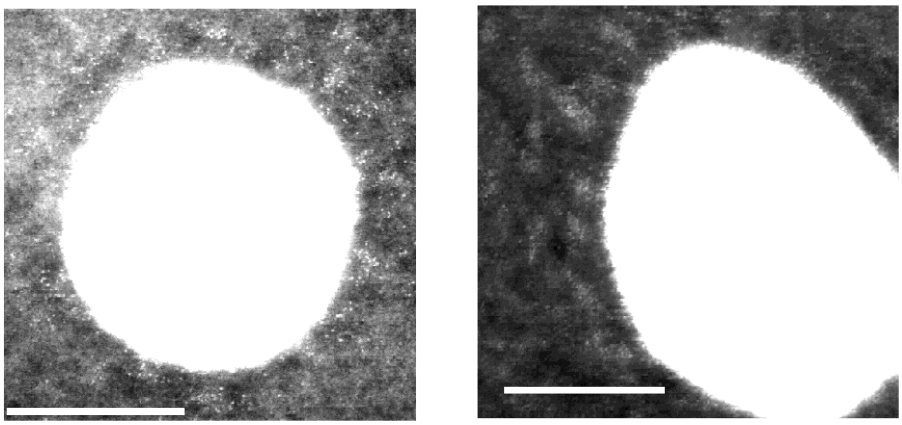
$$\Delta\lambda = m1\frac{m0m2}{1 + m0m2}$$

m0 = [*A*]

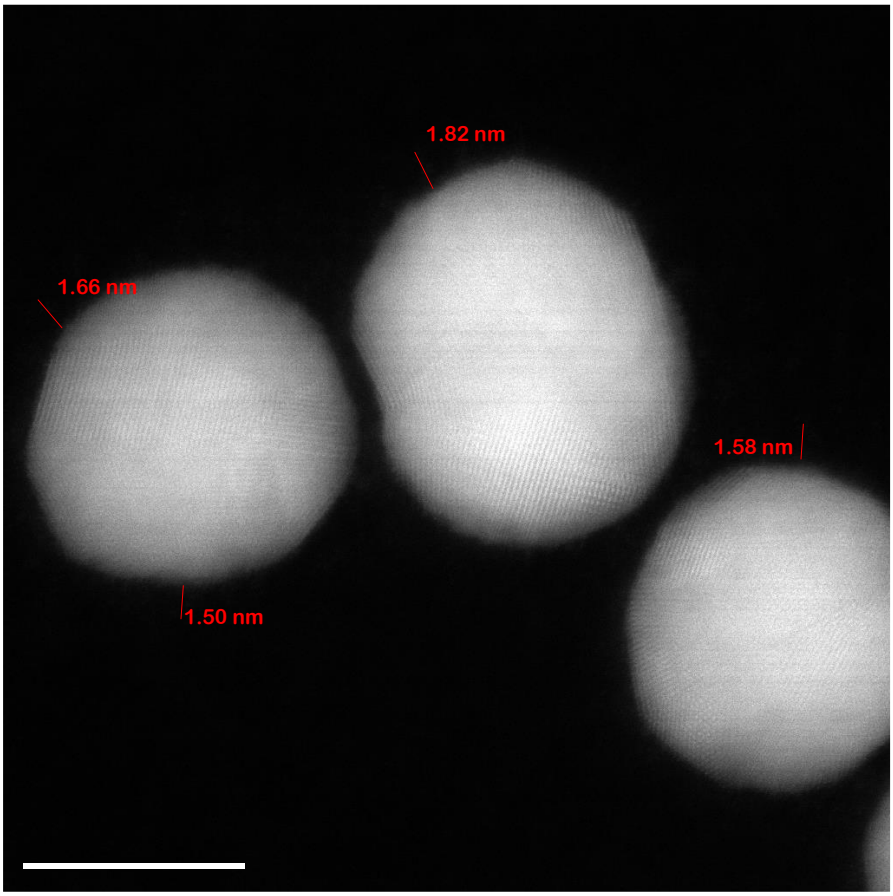
m1 = $\Delta\lambda_{max}$

m2 = Approximation of binding constant, K_a

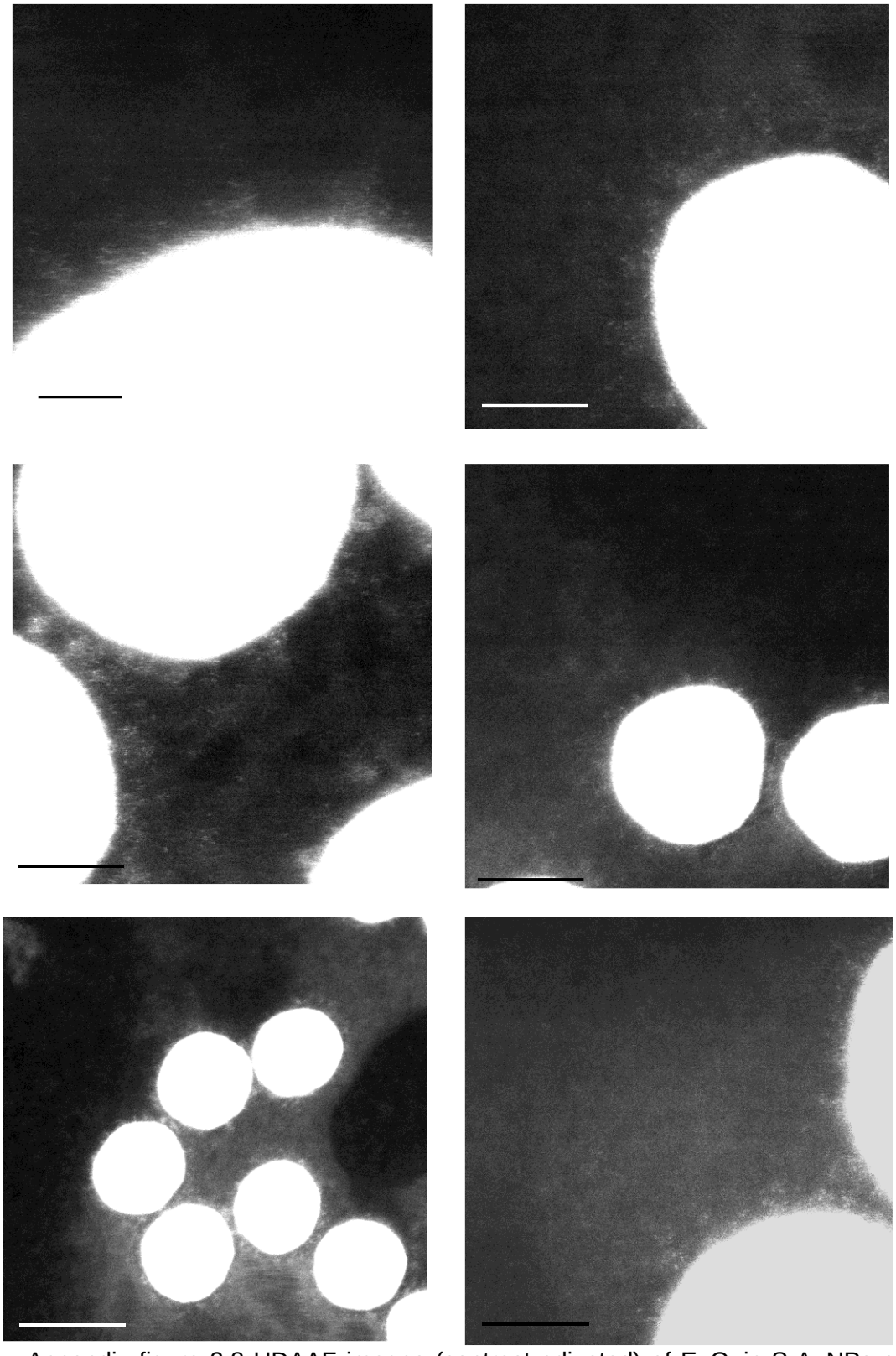
2.12.9 Additional STEM Images of $EuQuin_2S$-AuNPs and EuS-AuNPs



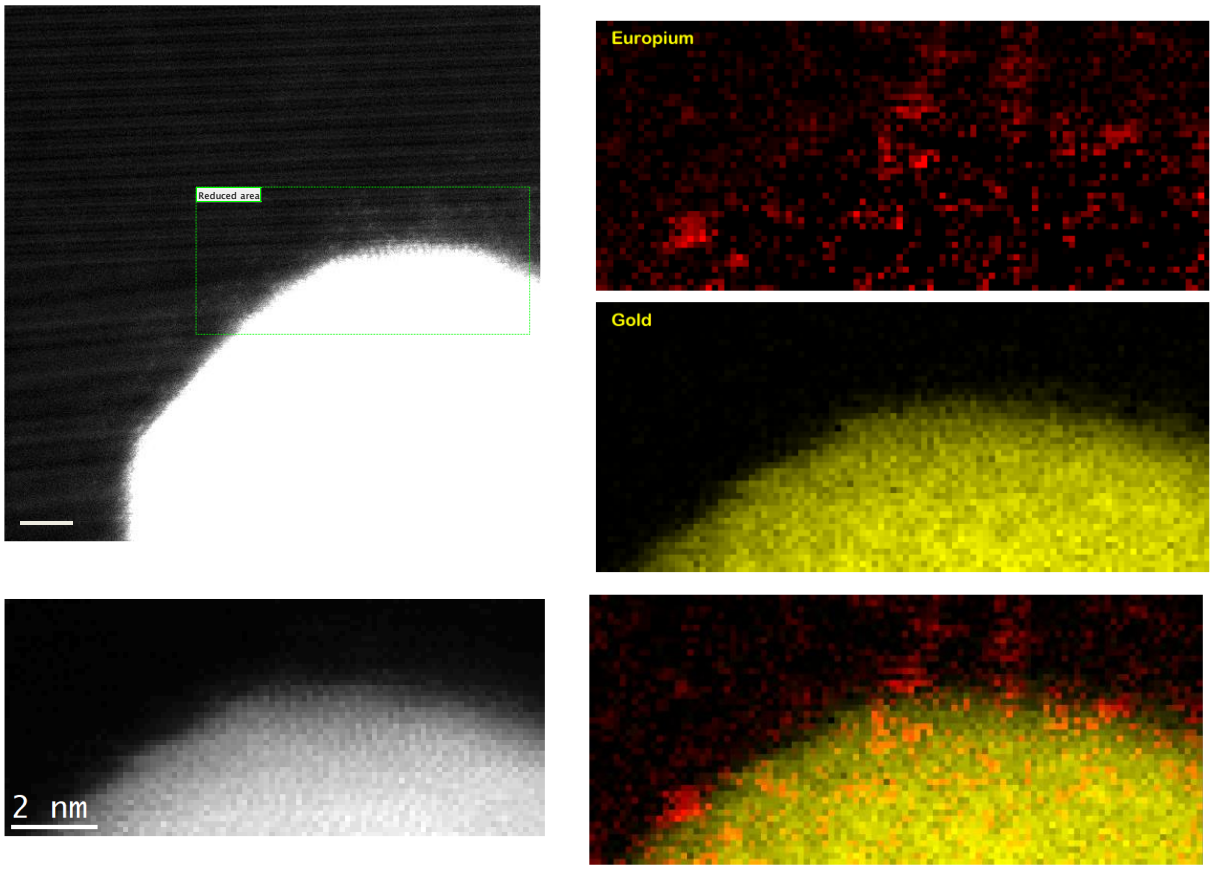
Appendix figure 2.6 HDAAF images of non-heat treated samples of $EuQuin_2S$-AuNPs.



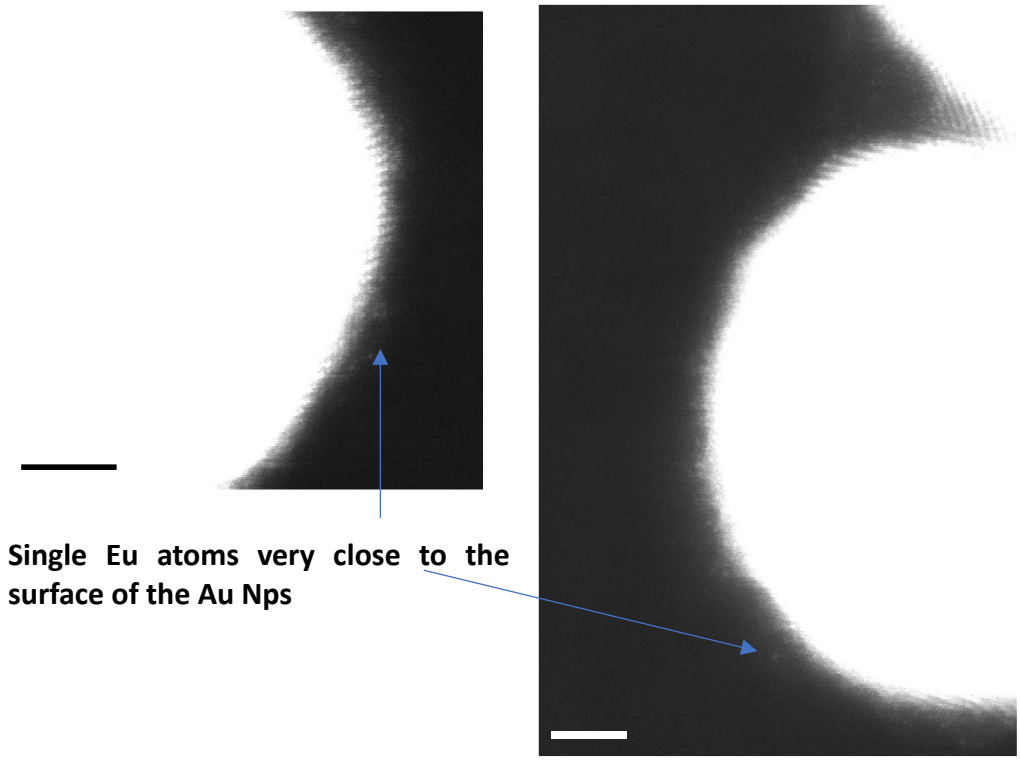
Appendix figure 2.7 HDAAF images (not contrast adjusted) of $EuQuin_2S$-AuNPs on ultrathin carbon supports after heat treatment at 135 °C. Red lines indicate measured distance of single europium atoms from $EuQuin_2SH$, which were observed as bright spots surrounding the AuNPs.



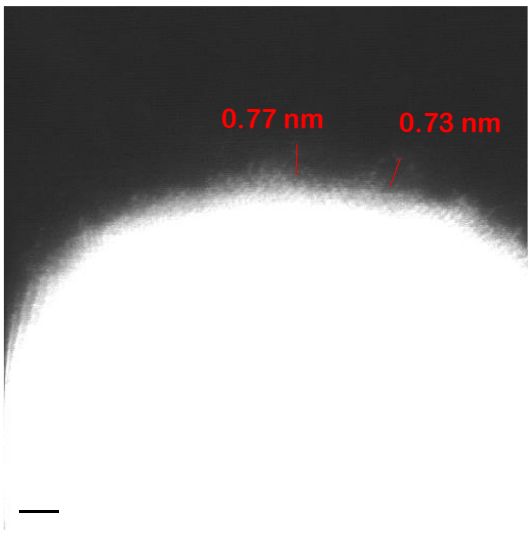
Appendix figure 2.8 HDAAF images (contrast adjusted) of $EuQuin_2S$-AuNPs on ultrathin carbon supports after heat treatment at 135 °C. Red lines indicate measured distance of single europium atoms from $EuQuin_2SH$, which were observed as bright spots surrounding the AuNPs.



Appendix figure 2.9 Additional HDAAF and EELS mapping of $EuQuin_2S$-AuNPs. Artificially coloured signal of europium (red), gold (gold) and an overlay of europium and gold are shown, determined by separating the signal of each element using EELS mapping.



Appendix figure 2.10 HDAAF images (contrast adjusted) of EuS-AuNPs on ultrathin carbon supports after heat treatment at 135 °C.



Appendix Figure 2.11 HDAAF images of EuS-AuNPs, showing single Eu atoms very close to the AUNP surface. Red lines indicate measured distance of single europium atoms from $EuQuin_2SH$, which were observed as bright spots surrounding the AuNPs.

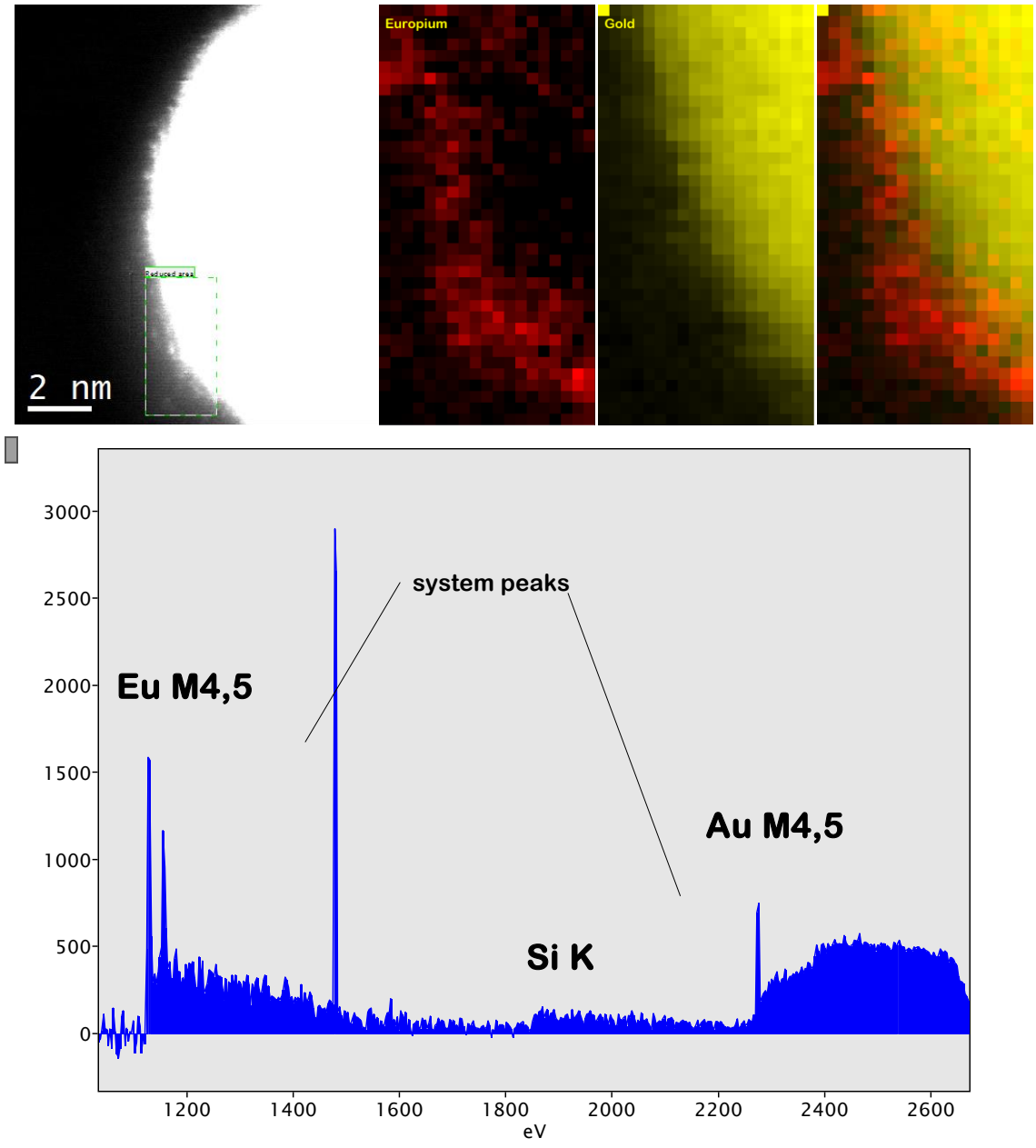


Figure 2.12 Full EELS spectrum (bottom) confirms the presence of europium surrounding an AuNP of EuS-AuNPs on an ultrathin carbon support, at the position of a bright spot in the halo around the gold core, highlighted by the red box on the HDAAF image (top left). Artificially coloured signal of europium (red), gold (gold) and an overlay of europium and gold are shown, determined by separating the signal of each element using EELS mapping.

Chapter 3: Investigative Studies into the Cellular Uptake of Lanthanide Gold Nanoparticles with CyTOF

3.1 Introduction

3.1.1 Previous Studies Using CyTOF to Quantify Nanoparticle Uptake

CyTOF was first used to detect and quantify NP uptake within cells in early 2017 by Irvine and co-workers, where they demonstrated high-throughput quantification of 3 nm AuNPs in RAW macrophages.[1] To quantify NP uptake, they estimated the transmission efficiency (TE) of ^{197}Au atoms from the TE of ^{193}Ir that is determined from the instruments internal calibration, assuming that the ^{197}Au TE would be similar to ^{193}Ir due to their similar ionisation energies of 8.98 (^{193}Ir) and 9.23 (^{197}Au) eV. The instruments counts could then be converted into the number of AuNPs per cell (this calculation is described further in our work in this chapter) and these were compared to the number of AuNPs per cell determined using the more conventional technique, ICP-AES. They found that the average number of AuNPs determined per cell were similar in magnitude with CyTOF and ICP-AES, demonstrating for the first time that CyTOF could be used as a quantitative technique to determine AuNP uptake. Irvine and co-workers also discovered that CyTOF had lower and upper limits of detection of approximately 1×10^4—1.3×10^9 Au atoms per cell, corresponding to ca. 0.15—19000 13 nm AuNPs per cell. This extremely low limit of detection makes CyTOF ca. 2400 times more sensitive than flow cytometry for detecting BODIPY labelled AuNPs. This study then used CyTOF to show the biodistribution of AuNPs within immune cells in mice after injection, simultaneously using the phenotyping capabilities of CyTOF in the same experiment. Furthermore, they showed how this data generation can guide therapeutic development, which was further utilised in another CyTOF study by the same authors in 2018.[2]

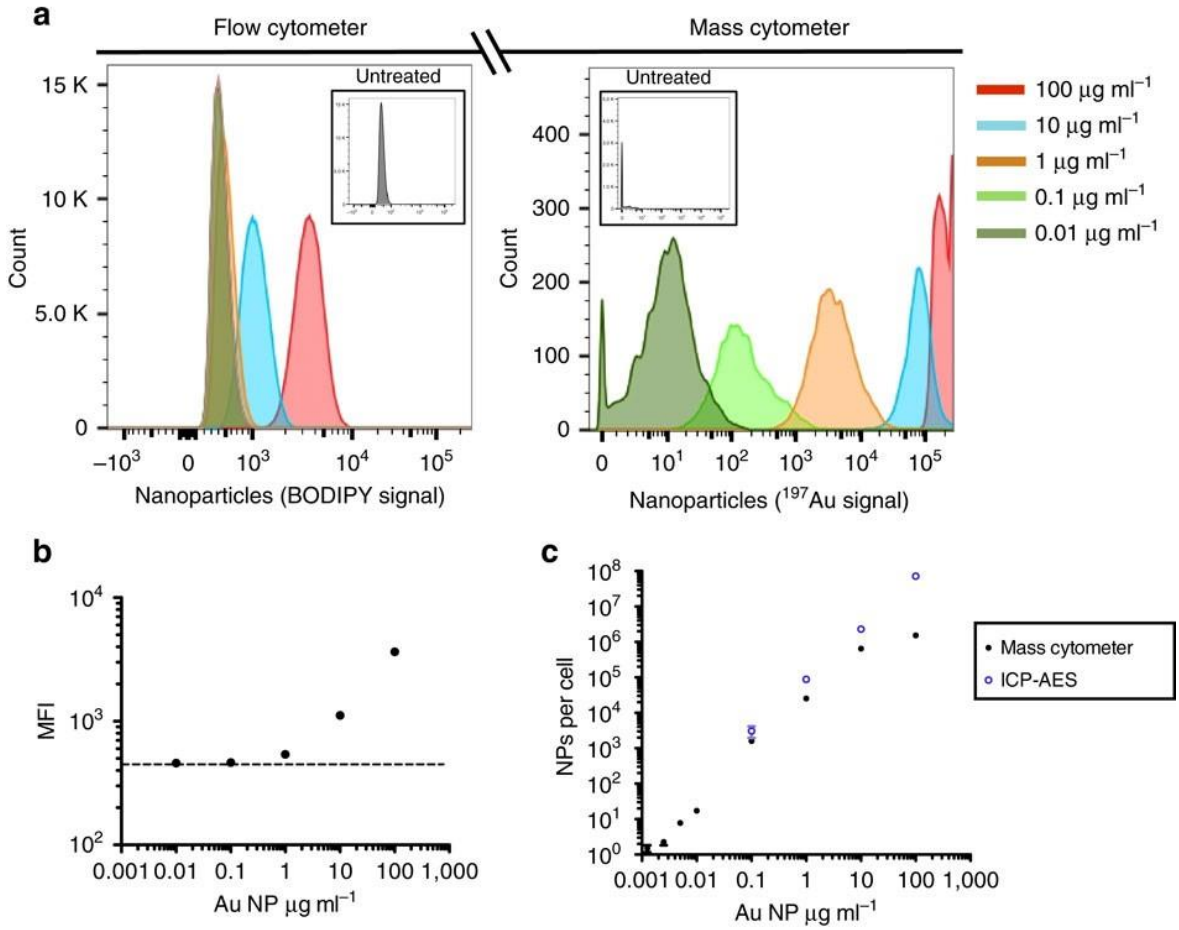


Figure 3.1 - CyTOF provides quantitative, sensitive detection of AuNPs in single cells with a wide dynamic range. (a) Histogram of AuNP signal from RAW macrophages measured by flow cytometry and CyTOF, (b) median fluorescence intensity (MFI) from flow cytometry shows a much higher, lower limit of detection when compared to CyTOF, (c) Quantitative analysis of the number of AuNPs per cell at different treatment concentrations with CyTOF and ICP-AES, showing values similar in magnitude with each technique. Figure reproduced from Yang, Irvine *et al.*

Also in 2017, Ivask and co-workers first demonstrated the use of CyTOF to quantify the number of silver nanoparticles (AgNPs) associated with Jurkat cells.[3] The authors calculated the TE of ^{107}Ag by calibrating the instrument with an ionic solution of $AgNO_3$ and demonstrated that the number of AgNPs per cell determined by CyTOF analysis was in broad agreement with the numbers determined by ICP-MS in comparable experiments. They were also able to quantify the proportion of AgNPs that were internalised and bound to the surface of the cells. In 2019, Oliver *et al*. further studied the TE of ^{107}Ag and found that the calculated TE was approximately 2-fold lower for 50 nm AgNPs compared to $AgNO_3$

solution, indicating that the arrangement of metal atoms as dense NPs reduces the overall number of atoms that eventually reach the TOF detector.[4]

In late 2020 Wu *et al.* determined a TE of ^{197}Au for the first time directly (rather than using ^{193}Ir as an approximate) by linear regression analysis of the counts detected from 10, 20, 50, 80 and 100 nm citrate-coated AuNPs when the CyTOF instrument was in 'event' mode, which, as shown later, yields similar data to that presented in this thesis from work conducted at a similar time.[5] This study then focussed on accumulation of NPs and detecting AuNPs of different sizes at ultra-trace levels in bacteria and showed that even at 1 fg/mL, small subsets of a population may take up hundreds of AuNPs. They also briefly showed that the ultra-trace doses of AuNPs were not detectable in 94% of bacteria after 60 hours.

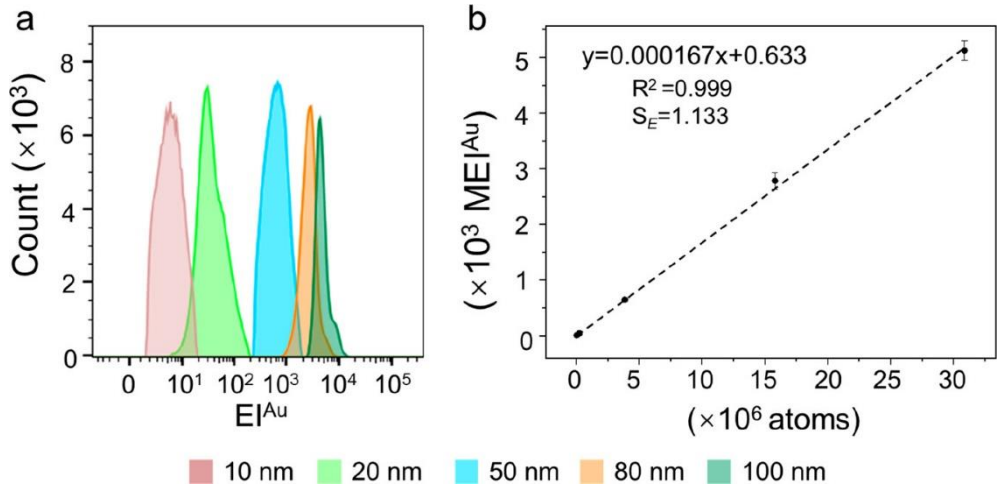


Figure 3.2 – Mass cytometry analysis of different sized AuNPs. (a) Histograms of the relative counts of each NP size in 'event' mode, (b) Calculation of the TE of ^{197}Au by comparing the counts of each AuNP size to their estimated number of atoms.

Studying AgNP cell interactions with CyTOF has advanced further over the last two years, although these studies fall out of the scope of our work, so they are only briefly discussed here. Yoon and co-workers have investigated the biodistribution of AgNPs in human peripheral blood mononuclear cells (PBMCs) and used in-depth phenotyping to discover that AgNP doses can have pro-inflammatory and pro-apoptotic effects on subsets of certain cell types.[6, 7 8] Malysheva *et al.* combined CyTOF with single-particle ICP-MS and synchrotron X-ray absorption spectrometry to study the cellular binding, uptake and the

intracellular transformation of AgNPs.[9] Their study revealed that intracellular AgNPs are the primary driver of toxicity and differences between NP coatings and sizes had minimal effects on the toxicity compared to the total internalised load.

To summarise, over the last 5 years CyTOF has been utilised in 9 studies as a high-throughput, single cell technique to quantify AuNP and AgNP uptake. It has been shown to be ca. 2400 times more sensitive than flow cytometry in detecting AuNPs and comparative studies indicate that absolute average number of NPs per cell values are in broad agreement with conventional ICP-AES techniques. Researchers have also used its phenotyping capabilities to simultaneously study NP uptake alongside biological information such as toxicity. However, the use of CyTOF to quantify NP uptake is not yet conventional with current research largely focussing on technique development and proof-of-concept studies. More research is needed with aspects such as sample preparation, and it is shown in this thesis that the instruments incredible sensitivity can cause issues with data acquisition. No studies have yet investigated the TE of AuNPs of a single size (which will likely affect TE), or in 'solution' mode, where a large amount of data can be acquired over a long time period to increase integration time and correlate this value to the 'event' mode counts. Furthermore, Wu *et al.*'s study did not validate AuNP quantification with another comparable technique such as ICP-MS. The high-throughput, single cell capabilities of CyTOF have not been fully utilised to study the heterogeneity of NP uptake within cell populations, detect more than one metal from a single NP, or to study the reduction of NP content over multiple proliferation cycles. This work will look to further develop and expand on these research themes whilst the interaction of luminescent, dual-metal lanthanide AuNPs is studied with HeLa cells in this chapter, and then monocytes, macrophages and dendritic cells in Chapter 4.

3.1.2 Studying Nanoparticle Uptake Heterogeneity

The cell-to-cell variation or heterogeneity of nanoparticle uptake in cell populations has important implications for their use as therapeutic and diagnostic agents. As with all therapies, a minimum therapeutic dose of nanoparticles is required to treat an individual cell.[10] For example, AuNP photothermal therapies require a minimum light dosimetry to induce cell death which is governed by the intracellular nanoparticle content,[11] so cancer cells with low AuNP uptake may survive in treatments. In contrast, nanoparticle toxicity often increases with dose,[12, 13] so cells that take up a large number of nanoparticles may be at higher risk of toxicity which may need to be considered when nanoparticles are used for diagnostic applications. Furthering our understanding of the heterogeneity of nanoparticle uptake will therefore be important for improving the development pipeline of nanoparticle-based medicines, particularly now computational simulations are playing a larger role in the assessment of nanomaterial toxicity and design.[14-16]

Heterogeneity in nanoparticle uptake is in part caused by cell-to-cell variability. Snijder *et al.* have shown that receptor molecule distributions, cell size and local cell density were all significant factors in the variability of virus particle uptake,[17] which like many nanomaterials, are taken up by endocytosis mechanisms.[18] The cell cycle also affects nanoparticle uptake and although the rate of uptake was found to be similar in each stage of the cell cycle, uptake can be ranked in the order of G2/M > S > G1.[19] However recent studies have demonstrated that it is the increased size of the G2/M cells that leads to their increased uptake rather than the cell cycle itself.[20, 21] In addition, nanoparticles administered to cells in culture media undergo a number of process before they are taken up. They may interact with serum proteins that may subsequently coat the nanoparticle with a 'protein corona'[22, 23] and form nanoparticle clusters of varying sizes[24] before adhering to the cell membrane, affecting the number of nanoparticles which may reside in an internalised endosome after endocytosis, which itself is randomly initiated.[25]

As described previously, many conventional techniques for quantifying nanoparticle uptake such as ICP-MS can only determine an average content per cell and therefore do not provide information on the heterogeneity of uptake, so our understanding has advanced in recent years as quantitative single cell techniques have become more readily available. Rees, Summers and co-workers have studied the uptake heterogeneity of fluorescent 10-15 nm CdTe/ZnS core/shell quantum dots (QDs). In one study, they used imaging flow cytometry and confocal microscopy to analyse the heterogeneity of QD uptake in human bone osteosarcoma (U-2 OS) cells after a 24-hour treatment. To quantify uptake, they determined the number and intensity of nanoparticle loaded vesicles (NLVs) and found that quantum dot uptake is best described by an over-dispersed Poisson distribution[26] and have built on this knowledge to develop a modelling technique that predicts the distribution of quantum dots in a cell population.[21] Jeynes *et al.* used ion beam analysis to determine AuNP uptake together with the mass of each cell, and found that uptake was best described by a log-normal distribution.[27]

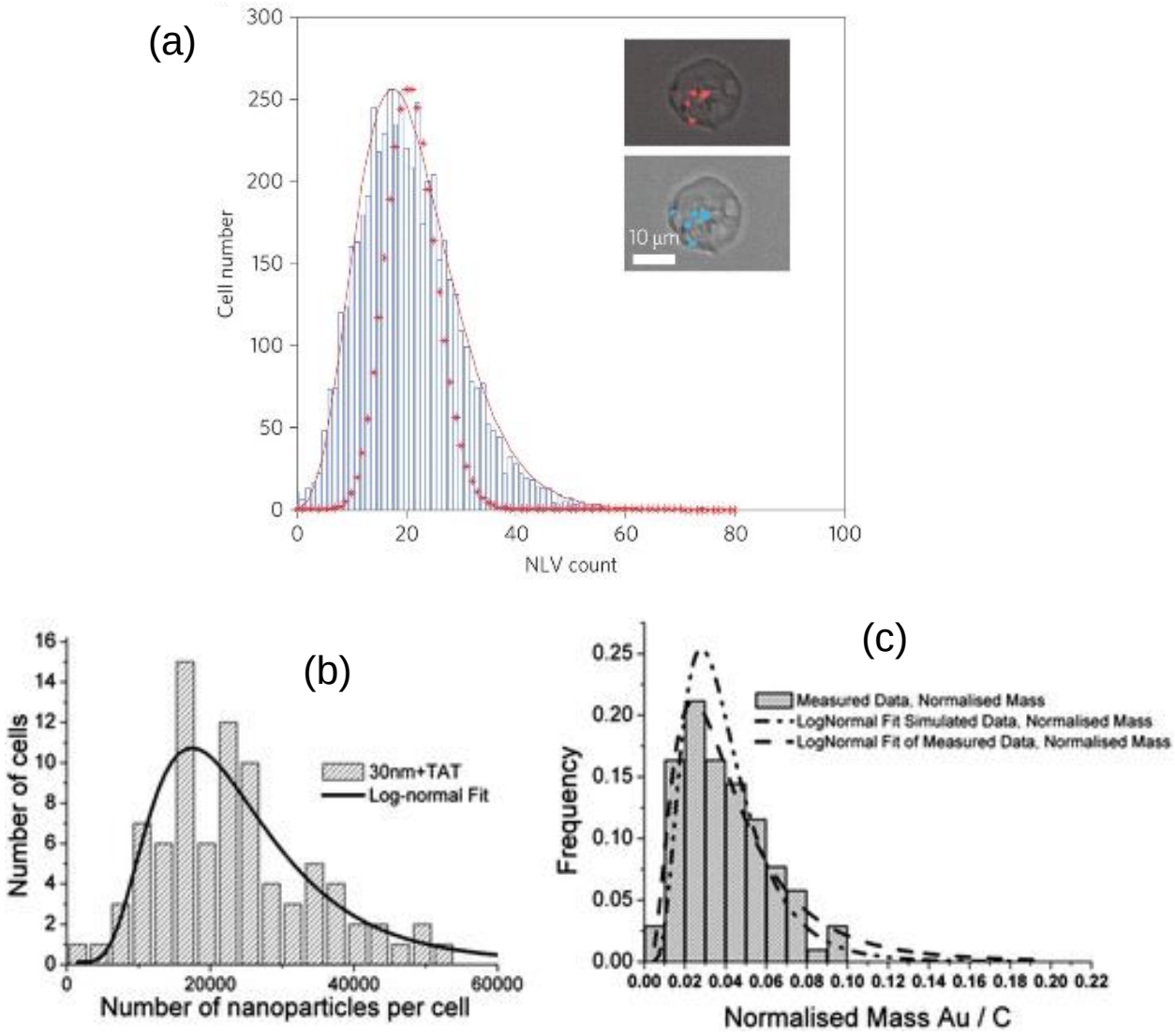


Figure 3.3 – Histograms showing uptake heterogeneity of nanoparticle uptake in previous studies. (a) Histogram of the number of nanoparticle loaded vesicles (NLV) in each cell measured by imaging cytometry, with Poisson distribution (dotted line) and over-dispersed Poisson distribution (solid line) fitted to data (reproduced from Summers *et al.*), (b) Histogram of the number of 30 nm AuNPs per cell measured by ion beam analysis with a log-normal fit and the same data normalised for the mass of each cell in (c) (reproduced from Jeynes *et al.*).

Although these detailed studies have uncovered important discoveries on uptake heterogeneity, there are some limitations owing to the techniques used. Rees, Summers and co-workers have relied on imaging flow cytometry and confocal microscopy, which have relatively high minimum limits of detection, can only detect fluorescence from clusters of quantum dots (and therefore rely on counting the number of NLVs), and suffer from low throughput that relies on computational methods to quantify the signal intensity from each

individual cell. Jeynes and co-workers used ion-beam analysis which suffers from extremely low throughput; a minimum of 55 cells were studied in each population. These studies have also studied uptake at 24- and 48-hour dose periods to counteract the effects of the cell cycle, but typically cells are treated with nanoparticles for shorter time periods and some nanoparticles have a typical half-life of a few hours in the bloodstream,[28] so an incubation length of days would not be a realistic representation of *in vivo* conditions.

As a highly sensitive, high-throughput, quantitative single cell technique, we set out to use CyTOF to study nanoparticle uptake heterogeneity. This will allow studies on uptake in cells at relevant dosing periods, with low intracellular nanoparticle content and minimal post-modification of data through computational methods, for comparative data output to previous studies with different techniques in this field, as well as furthering our own understanding of the uptake of our lanthanide gold nanoparticles.

3.1.3 Long-term Gold Nanoparticle Fate in Cell Populations

Understanding the long-term fate of internalised gold nanoparticles is important for diagnostic applications where the intention is to detect nanoparticles within cells over extended time periods, such as cell tracking.[29-34] Equally the eventual fate of gold nanoparticles, be it long-term residency in cells or elsewhere if they are expelled, is important due to potential toxicity[35] and therefore has relevance for all *in vivo* applications. Citrate-coated AuNPs have been shown to reside in mouse cells for 6 months after injection at 90% of the original administered dose[36] and recent research has discovered that injected AuNPs and other NP types can have effects as diverse as accelerating cancer metastasis,[37] highlighting the significance of their long-term fate.

It is generally accepted that AuNPs show good long-term stability in biological environments and can be detected in cells months after their original entry,[36, 38] although a recent study by Balfourier *et al.* reported almost complete degradation of 4-22 nm AuNPs in human skin

primary fibroblasts after 2 months.[39] Other than degradation, internalised nanoparticles can either be inherited by daughter cells[19, 40] or exit cells in two ways: non-vesicle related secretion if nanoparticles are no longer contained within endosomes, or exocytosis after endosomes have matured into lysosomes.[41] In this introduction, some key recent literature is discussed focussing primarily on the study of AuNPs, however some studies involving other NP types are also featured.

The release of AuNPs and other NP types by exocytosis and non-vesicle related excretion has been shown in several studies. Oh and Park used ICP-MS to show that the rate of exocytosis of AuNPs over a 48 hour period in macrophages was highly dependent on the surface chemistry.[42] Cationic AuNPs were largely retained in cells as they agglomerated within endosomes in the macrophages, but PEGylated AuNPs were found to leave endosomes and exit cells as individual particles at a higher rate. The size of the AuNPs did not have a significant effect on the exocytosis rate. Conversely, Chithrani and Chan found that the rate of exocytosis within 8 hours of incubation was higher for smaller protein-coated AuNPs and higher still for protein-coated gold nanorods compared to spheres, demonstrating that both size and shape affect AuNP exocytosis.[43] A study by Bartczak *et al*. used ICP-AES to show the exocytosis rate of 15 nm peptide-coated AuNPs in human endothelial cells (HUVECs).[44] They found that the peptide coating affected both the rate of exocytosis and the reuptake of AuNPs by cells after exocytosis. Yanes *et al.* showed that cell type also plays a major role in a study with 130 nm mesoporous silica nanoparticles.[45] The study used flow cytometry and ICP-OES to show that after a 2 h incubation with nanoparticles and subsequent cell culture for a further 24 hours, the average quantity of dose that was exocytosed ranged from 4-87% depending on the cell line, with the majority of exocytosis occurring in the first 6 hours post exposure.

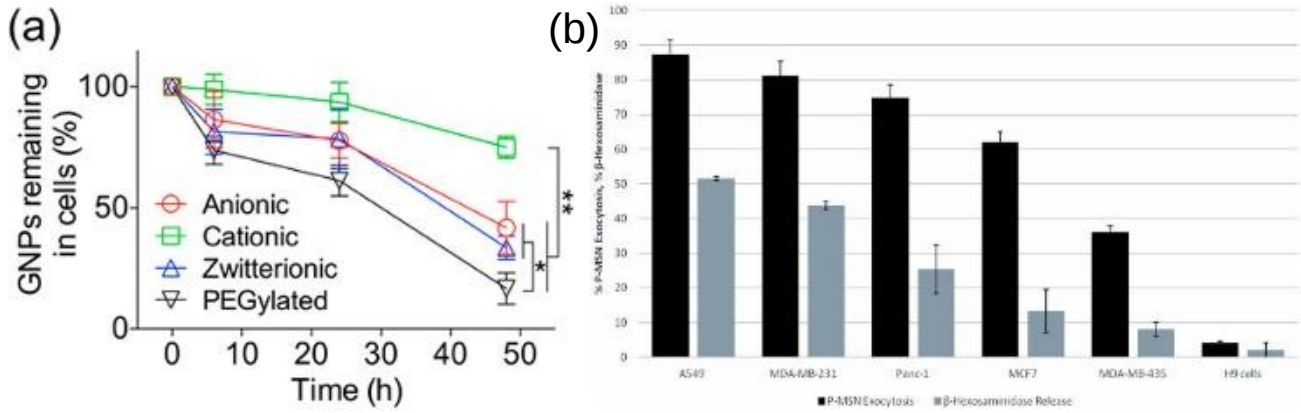


Figure 3.4 - Exocytosis of NPs is dependent on physicochemical properties and cell type. (a) Effect of surface chemistry on the exocytosis of 10 nm serum coated AuNPs up to 48 hours post exposure (reproduced from Oh *et al.*), (b) Effect of cell type on the exocytosis of 130 nm mesoporous silica nanoparticles 24 hours post exposure (reproduced from Yanes *et al.*).

Several studies have investigated the inheritance of intracellular NPs by daughter cells after cell division and in contrast to the studies discussed above, many found no evidence of nanoparticle exocytosis from cells; indicating that cell division is the key driver in NP depletion. A study published by Kim *et al.* used confocal microscopy to show that fluorescent polymeric NPs were internalised within lysosomes in A549 cells.[19] Using flow cytometry, they found that the depletion of NPs is due to cell division and that export by exocytosis or non-vesicle excretion is negligible over the studied time of 12 hours after dosing. The same research group found no evidence of SiO_2NP export over 28 hours in a similar study.[46] This is in contrast to the previously discussed study by Yanes *et al.* where A549 cells had the highest excretion rate of all cell types studied with 130 nm mesoporous silica NPs.[45] Summers, Rees and co-workers used a combination of low-throughput, high-resolution TEM and high-throughput, low-resolution optical imaging to study the inheritance of QDs in daughter cells. They found that QD inheritance between cells is highly heterogeneous, mainly due to the highly variable number of quantum dots in each vesicle.[40] Supporting this finding, Bourquin *et al.* used live cell imaging to analyse the 28 individual mitotic events of J774A.1 cells, finding that the inheritance of non-porous, 70 nm fluorescent silica NPs was highly heterogeneous between daughter cells.[47] Using ICP-OES, they also

found that 20 and 46 nm AuNPs were not significantly exocytosed by macrophages, J774A.1, or HeLa cells 48 hours post exposure. Gunduz *et al.* investigated the fate of 12 nm citrate-stabilised AuNPs over the course of 40 days and also found that cell division played a predominant role of depletion, with no evidence that exocytosis played any major role.[48]

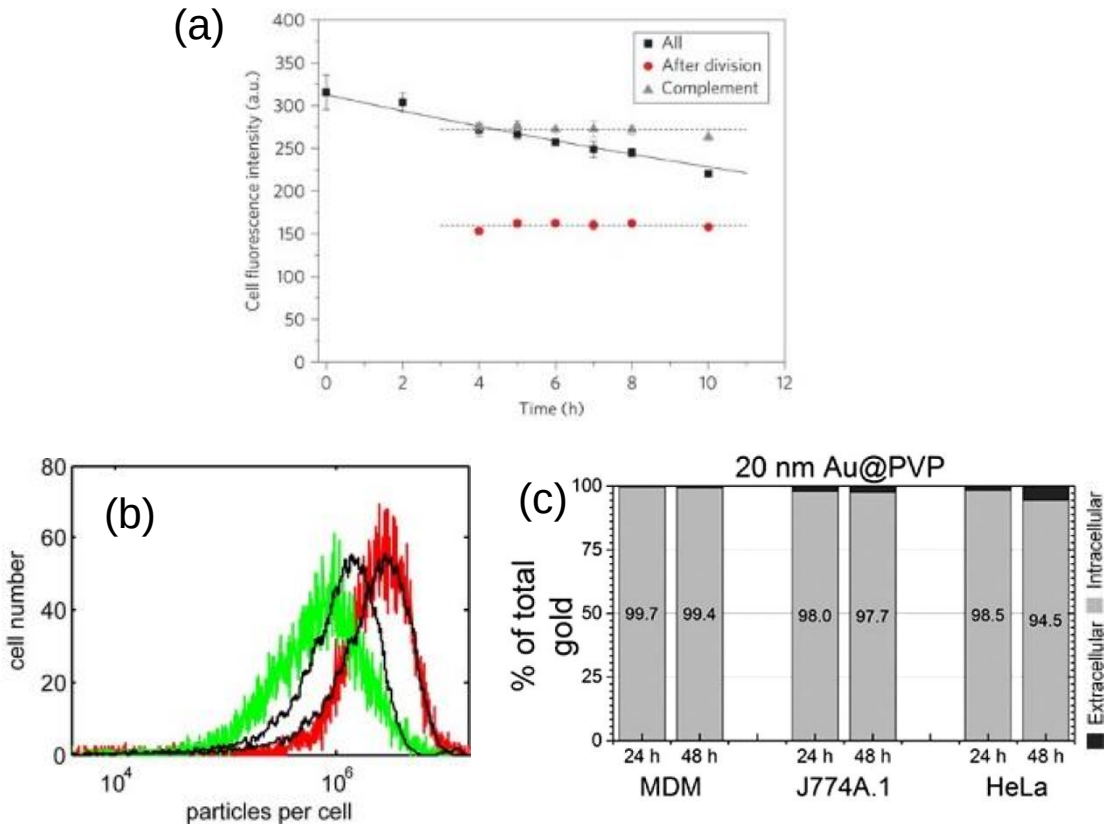


Figure 3.5 – The depletion of NP load is heavily driven by cell division. (a) After accounting for cell division, cell fluorescence intensity decreases with modelled fitting, indicating that NP export is negligible and internalised NP load decreases only as a result of cell division (reproduced from Kim *et al*.), (b) Measured (coloured lines) and predicted (black lines) frequency distributions of QD load per cell 24 and 48 hours post exposure, showing that QD inheritance is not split evenly between daughter cells (reproduced from Summers *et al*.), (c) ICP-OES analysis of the gold content from 20 nm AuNPs over a 48 hour period, with no significant reduction in load seen due to exocytosis (reproduced from Bourquin *et al.*).

To summarise, over the last decade several studies have investigated the fate of internalised NPs in cell population, but contrasting findings mean many questions remain. The export of NPs by exocytosis has been shown in many cases, particularly in the hours immediately after exposure and it is clear that this process is dependent on a number of NP physicochemical properties and cell type. Other studies have found minimal evidence

of exocytosis and find that cell division is the key source of NP depletion from cell populations over time.

In general, most of these studies have used ICP-based techniques (MS/AES/OES) to quantify the rate of exocytosis, and in some cases TEM and fluorescence techniques such as confocal microscopy and flow cytometry, all of which have some limitations. As previously mentioned, ICP-based techniques require the digestion of a very high numbers of cells to determine an average number of NPs per cell. The technique cannot discriminate between NPs within cells and NPs remaining in suspension, so relies heavily on accurate cell counting and removing all free NPs remaining in the solution, which can account for the overwhelming majority of the NP dose after incubation.[49] In our work with CyTOF, it is demonstrated that it is very difficult to remove all free NPs remaining in the solution without a much higher number of washing steps than conventionally used, and minimal errors in not doing so with ICP-based experiments could have an effect on quantifying a process such as exocytosis. TEM provides detailed information such as intracellular location of NPs and mechanistic evidence of processes, but it is not quantitative and suffers from extremely low throughput. Fluorescence based techniques can only study fluorescent NPs so are not suitable for many studies with AuNPs, often lack sensitivity for detecting low numbers or small clusters of NPs, and photobleaching of fluorophores could affect signal quantification, particularly in studies over long time periods.

Furthermore, these studies have mainly focussed on the fate of NPs in time periods of up to 24 hours post exposure to the NP dose and have not investigated fate after multiple proliferation cycles. We hypothesised that CyTOF could be a useful quantitative technique to study the long-term fate of our lanthanide coated AuNPs, with its high-throughput and sensitivity, ability to study uptake and heterogeneity in NP inheritance after cell division, and the potential for proliferative tracing over multiple proliferation cycles. This could add

to the fields understanding of the long-term fate of NPs whilst revealing the suitability of our lanthanide gold nanoparticles as long-term cellular labels.

3.2 Chapter Outline

In this chapter, the use of CyTOF as a high-throughput, single cell technique to accurately quantify our lanthanide gold nanoparticles initial uptake, composition and long-term fate in HeLa cells is explored. HeLa cells were used because of their robust nature, ease of cell culture and their extensive use in previous studies for data comparison. Several issues with acquiring CyTOF data due to saturation of the instrument detector with non-cell associated free AuNPs in solution were quickly encountered; this inadvertently led to us optimising sample preparation and investigating several methods of acquiring cell samples free of NPs in solution, discussed in the first section of this chapter alongside control experiments and gating strategy used to identify single cells. Following this, the instrument was calibrated in 'solution' mode to determine a TE for our lanthanide AuNPs for conversion to the number of LnAuNPs per cell. The mean cellular uptake of $EuQuin_2S$-AuNPs to TbS-AuNPs was then compared to investigate the effect of ligand chain length with both CyTOF and ICP-MS, to test our hypotheses that CyTOF is an accurate, quantitative technique.

Characterisation of dual-metal, europium or terbium coated AuNPs both in solution and within cells is shown to determine the average number of metal complexes on each AuNP. This dual-metal detection from single NPs within cells will be a first for the field, with the potential to reveal information on the integrity of our NPs within cellular environments.

The single cell nature of CyTOF is used to investigate the heterogeneity in uptake of $EuQuin_2S$-AuNPs at different incubation times, statistically testing whether a log-normal distribution best describes the cellular uptake over a population. Lastly, the long-term fate of $EuQuin_2S$-AuNPs within cells after their original incubation, over multiple proliferation cycles is investigated, using a metal channel in CyTOF to incorporate a proliferation dye

and monitor the proliferation of single cells and correlate this to the number of $EuQuin_2S$-AuNPs found in cells at 24-hour intervals over 96 hours. It was hypothesised that this study will contribute to our understanding of NP depletion in cells, whilst also assessing $EuQuin_2S$-AuNPs as cellular labels in CyTOF studies, setting the basis for the research in Chapter 4.

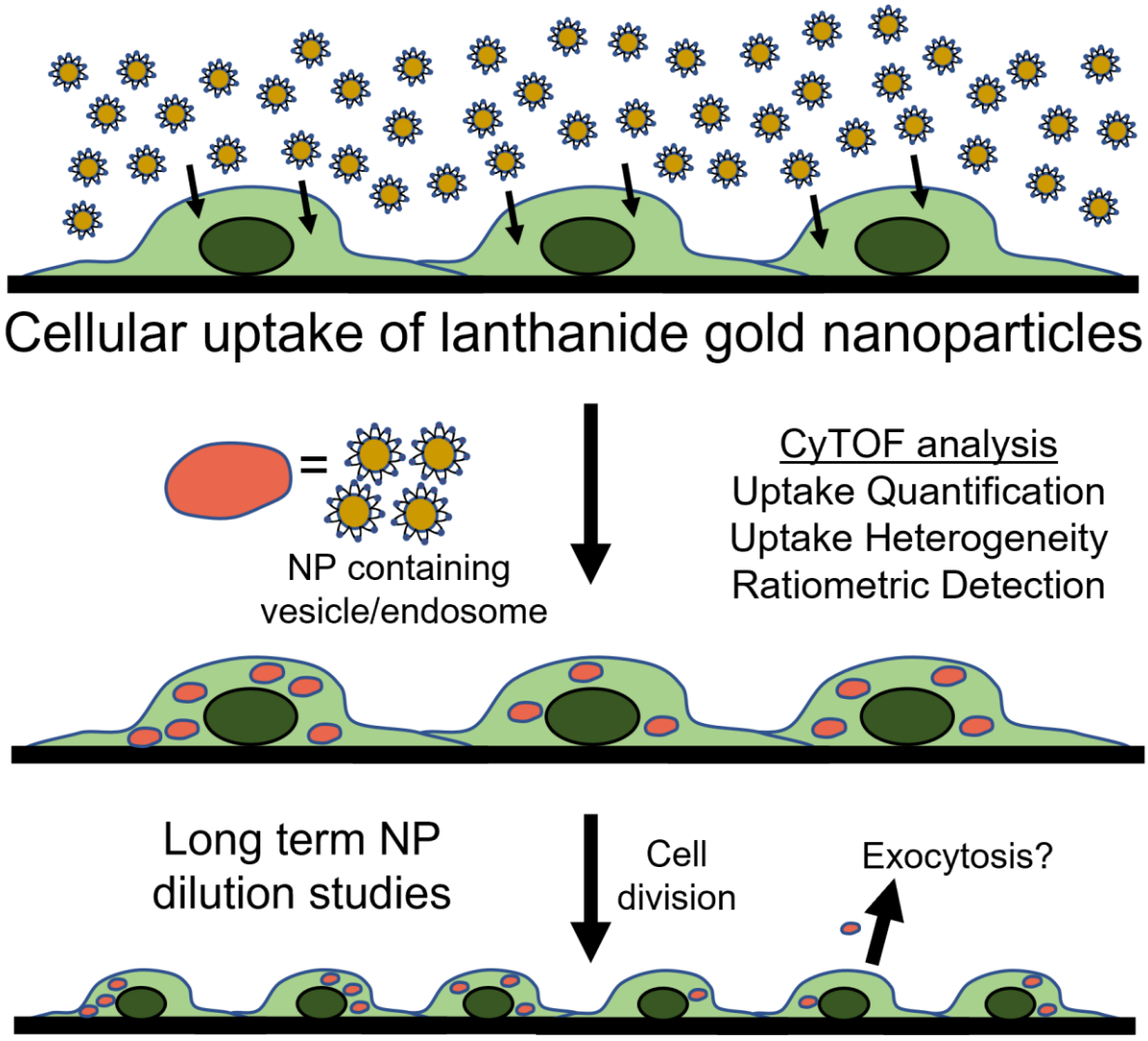


Figure 3.6 – Schematic diagram of the process to monitor cellular uptake of lanthanide gold nanoparticles with CyTOF, illustrating the incubation of HeLa cells with lanthanide gold nanoparticles and their cellular uptake in vesicles/endosomes. We seek to quantify their cellular uptake and uptake heterogeneity with CyTOF, as well as ratiometric detection of the lanthanide and gold metals, before using CyTOF to study the depletion of NPs within cells after cell division.

3.3 Optimising Sample and Data Preparation for Reliable Single Cell Data Output

3.3.1 Effect of Free Nanoparticles in Solution

As described in **Error! Reference source not found.**, when ion clouds are detected in the mass cytometer, if there are no gaps in ion signal detection between pushes the instrument cannot output data as discrete events corresponding to single cells. Any free metal contaminants such as nanoparticles in solution that may exceed the signal threshold could lead to long non-discriminate event lengths and prevent the instruments capacity to identify events containing ion-clouds corresponding to cells (Figure 3.7). Specifically, if there are lots of nanoparticles in solution, once ionised and introduced to the TOF-MS component of the CyTOF there would be a constant stream of gold ions and the instrument would not be able to discriminate between different cell events, hence one long event is measured. If this occurs the detector is completely saturated and there is no data output from the experiment, as illustrated in Figure 3.7.

Initially, this was investigated with our nanoparticle-treated cell samples. In a pilot study, HeLa cells were treated with 13 nm PEG-AuNPs NPs (0.1 nM, 16h) and washed with a protocol typical for preparing NP-treated cells for biological analysis[50-52] (see 3.10.3 for full experimental), then analysed by CyTOF. PEG-AuNPs were used in these pilot experiments due to lack of LnAuNP availability this early in this work. Details of their synthesis can be found in the Chapter 2 experimental (2.10.2.4) and their characterisation is shown in the appendix of this chapter (3.12.1). Each sample contained a constant stream of 197Au detection and therefore no FCS file could be generated from the IMD as no discrete events were produced, so the samples could not be analysed (Figure 3.7). Each 13 nm AuNP contains approximately 68,000 gold atoms and a single 13 nm AuNP will cause multiple

counts; it was clear that ionised, non-cell associated PEG-AuNPs in solution were causing the issue.

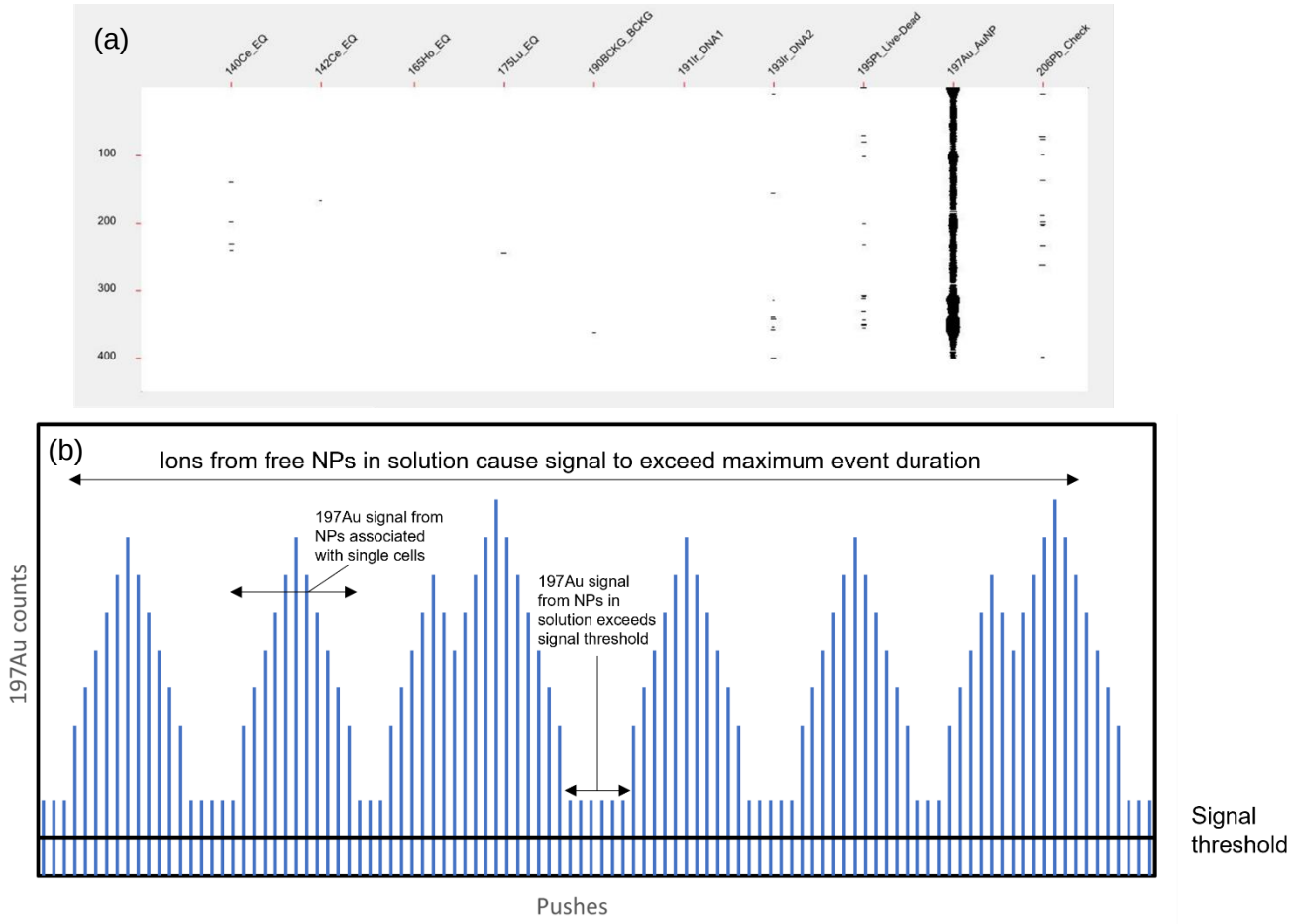


Figure 3.7 - Free nanoparticles in solution can lead to no useful data output. (a) a rain plot of metal detection from HeLa cells treated with PEG-AuNPs (0.1 nM, 16 h) and washed according to 3.10.3. Continuous detection of 197Au is measured and no discrete events were recorded. (b) A graphical representation (ie not real data) of how these data are recorded in the IMD file. No gaps between ^{197}Au ion detection are present, exceeding the maximum event duration for the data to be transferred as an FCS file.

Owing to the incredible sensitivity of CyTOF, it was quickly apparent that to study cells treated with 13 nm AuNPs at low nM concentrations, a more robust method to ensure minimal free AuNPs are in solution is necessary. For adherent (HeLa) cells, 2 methods were tested that could potentially improve cell preparation: optimising cell washing with centrifugation and fluorescence associated cell sorting (FACS), and the results from these preparation techniques are discussed from herein.

3.3.2 Optimisation of Cell Preparation Using Centrifugation Washing

Because adherent cells attach to a surface and grow as a monolayer, following incubation of cells with nanoparticle-containing media, the solution can be removed to eliminate most free nanoparticles. At this stage, further washing steps with PBS can further dilute the concentration of free nanoparticles in the sample, but some residual volume of solution is left in the culture vessel and on top of cells (that cannot be disturbed due to risk of detachment), so it is impossible to eliminate all free nanoparticles. An enzyme is then added to suspend the cells in solution and any subsequent washes require centrifugation; a common technique used in cell sample preparation to pellet cells at the bottom of the tube whilst lighter matter such as nanoparticles can be removed from the solution.[53]

It was identified that centrifugation must be optimised to remove as much solution as possible during each wash without excessive cell loss and identified the plastic tubing and the method of removing the supernatant as the most important controlling factors for thorough washing. We therefore compared the use of 15 mL Corning® Centrifuge Tubes, 5 mL Falcon™ Round-Bottom Polystyrene Test Tubes and 1.5 mL Fisherbrand™ Polypropylene Microcentrifuge Tubes and whether physically tipping the supernatant out by inversion or aspirating with a pipette would be the most suitable method. It was found that using 5 mL Falcon™ Round-Bottom Polystyrene Test Tubes and removing the supernatant by inverting the tube were the most suitable. This was most notably because the highest percentage of supernatant could be removed without disturbing the cell pellet. The data and methods used to determine this can be found in the appendix (3.12.2).

After identifying the optimal procedure for washing cells by centrifugation, cells were then treated with PEG-AuNPs NPs at a range of concentrations (0.005-0.27 nM) for 16 h, then prepared and washed using 5 mL Falcon™ Round-Bottom Polystyrene Test Tubes and inverting to remove supernatant, with additional washing steps as described in 3.10.4 before analysis by CyTOF. We chose to measure the quality of samples by determining the

number of events that had an event length ≤ 30 (an arbitrary unit) after we had previously witnessed longer event lengths in badly contaminated samples. This protocol led to excellent CyTOF data acquisition; over 97% of events were ≤ 30 in all samples (Table 3.1), implying that free nanoparticles are not considerably increasing cell event lengths and providing confidence that ^{197}Au signal from cell events comes from cell associated nanoparticles. By identifying cells using signal from the Cell-ID ^{193}Ir isotope channel, the number of events that correspond to cell events and events with no cells but ^{197}Au signal, the percentage of events corresponding to free nanoparticles in solution was determined. The number of events corresponding to free NPs in solution increased with concentration, ranging from 2 - 26%. This is expected as there will be a far greater number of nanoparticles in solution to remove at higher concentrations. This also led to a lower proportion of overall events being single cell events (Table 3.1).

Table 3.1 – Extra centrifugation washes can remove free nanoparticles from solution, leading to good data acquisition. HeLa cells were treated with PEG-AuNPs for 16 hours at a range of concentrations (0.005-0.27 nM) and prepared as described in 3.10.4. This led to good CyTOF data acquisition, with short event lengths and the majority of events recorded as single cell events.

Concentration / nM	Event length <30 / %	Free NPs in solution events / %	Single cells / %
0.005	99	2	86
0.010	99	2	91
0.018	99	3	91
0.027	99	3	91
0.045	99	4	90
0.130	99	5	81
0.160	98	15	76
0.270	97	26	70

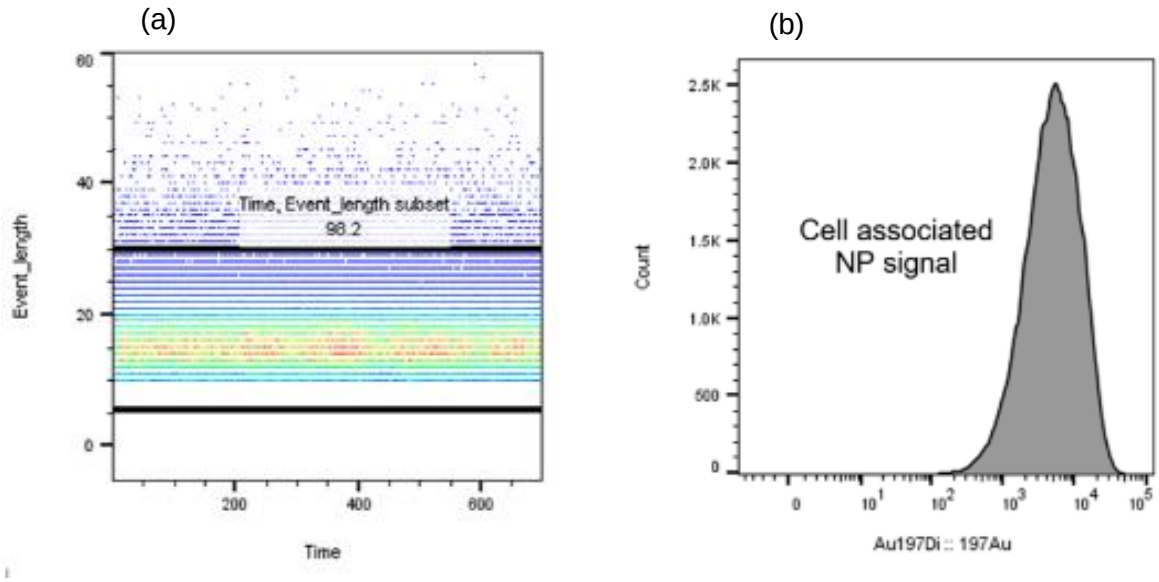


Figure 3.8 - Extra centrifugation washes can remove free nanoparticles from solution, leading to good data acquisition. (a) >97% of events were ≤30 pushes in each sample, (b) ^{197}Au mean dual counts from cell associated NP signal acquired from PEG-AuNPs.

It was found that washing steps 1-2 hours before running samples are vital to avoid free nanoparticles in solution; this probed further experiments into whether the cell permeabilisation buffer used during the DNA staining step with Cell-ID™ intercalator-Ir allows NP escape from cells (see 3.3.4).

3.3.3 Washing of Cells by Fluorescence Associated Cell Sorting

Removing free nanoparticles using fluorescence associated cell sorting (FACS) was also investigated. By measuring visible light scattering in the forward direction (forward scatter, FSC) and at 90° (side scatter, SSC), FACS can rapidly analyse the relative size and internal complexity (granularity) of single cells and particles.[54] By plotting SSC vs FSC, a population of cells can be identified and the cells of interest are directed down a separate channel into a collection vessel. This is achieved by oscillating the sample stream of liquid at a high frequency to generate drops that can then be given a positive or negative charge and separated by deflection plates on a charge basis.[54] It was hypothesised that this technique could be used to separate cells from free nanoparticles in solution (Figure 3.9).

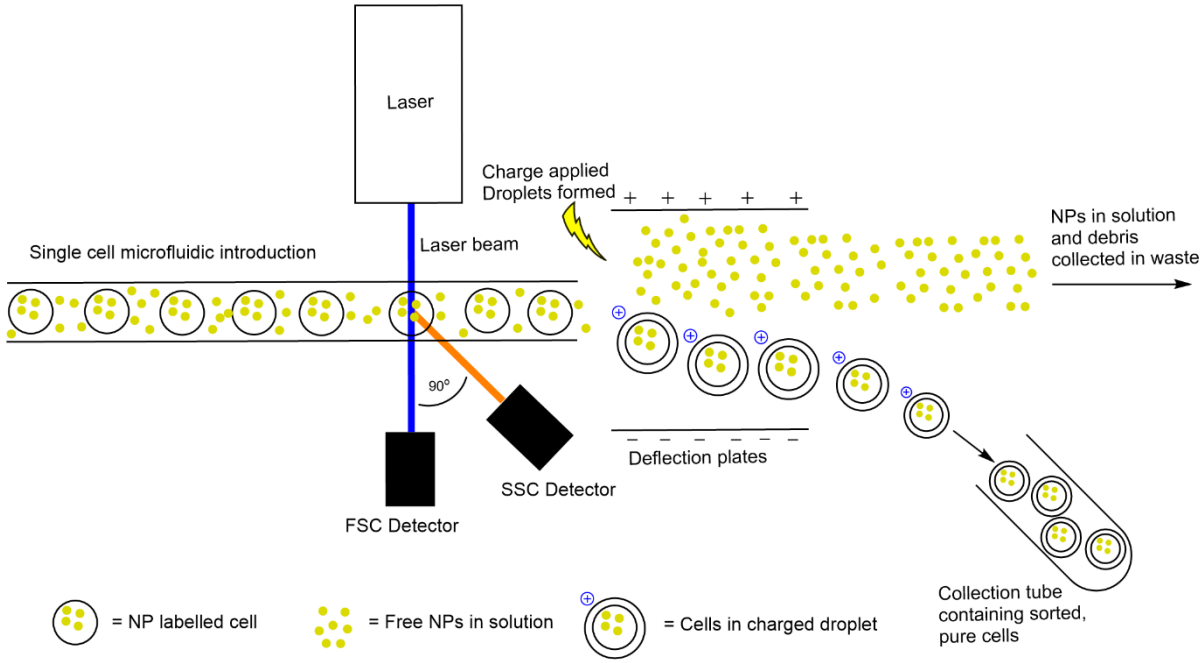


Figure 3.9 - Removing free nanoparticles in solution using flow cytometry. By measuring forward scatter and side scatter, cells and particles can be sorted based on their size and granularity by forming charged droplets. Deflection plates direct the cells of interest into a collection tube, whilst other material such as cell debris and nanoparticles are discarded.

HeLa cells were treated with PEG-AuNPs NPs (0.1 nM, 16 h), prepared as described in 3.10.3, then analysed and sorted by FACS. By plotting SSC vs FSC (Figure 3.10), a population corresponding to HeLa cells was selected for sorting and collected in PBS and stored at

4 °C until they were prepared for CyTOF later that day. 13 nm AuNPs were not observed in the SSC vs FSC plot as they are too small for detection by FACS, with limits of detection for viruses and nanoparticles reported as 50 and 140 nm respectively,[55, 56] These samples were stained with Cell-ID™ intercalator-Ir, stored overnight, washed as described in 3.10.5 and analysed by CyTOF. The cell sorting was extremely efficient in removing free nanoparticles from solution; ≥95% of events were ≤30 pushes, only 7-8% of events corresponded to free NPs, and ≥85% of events were single cell. Due to difficulties with instrument booking time and cost, it was not used for preparing HeLa cell samples in the rest of this work, however this novel washing method could be particularly useful for samples that may not be suitable for large numbers of centrifugation washing steps.

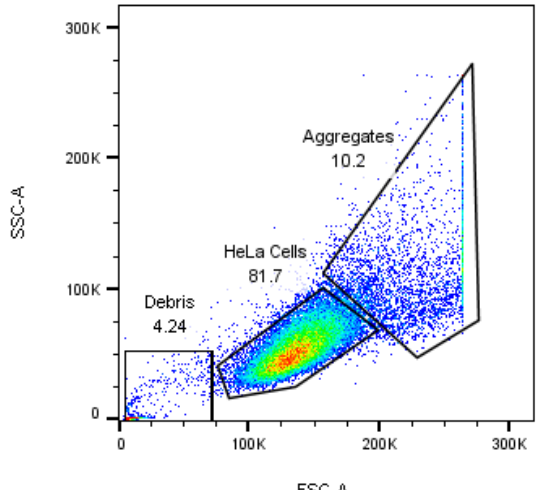


Figure 3.10 – FSC vs SSC plot of HeLa cells treated with PEG-AuNPs. HeLa cells were identifiable from debris and doublet events/cell aggregates and these cells were directed into a collection vessel and analysed by CyTOF.

Table 3.2 – The proportion of event lengths <30 (%), free NPs (%) and single cells (%) in 3 samples of HeLa cells treated with PEG-AuNPs (0.1 nM) for 16 hours, when washed by FACS and analysed by CyTOF.

Concentration / nM	Event length <30 / %	Free NPs in solution events / %	Single cells / %
0.1	98	8	86
0.1	95	7	85
0.1	98	8	91

3.3.4 Effect of Cell Permeabilisation on the Number of Nanoparticles Associated with Cells

As it was found that washing steps 1-2 hours before running samples are vital to avoid free nanoparticles in solution; this probed further experiments into whether the cell permeabilisation buffer used during the DNA staining step with Cell-ID™ intercalator-Ir allows NP escape from cells, previously shown by Oliver *et al.* with silver nanoparticles.[4]

HeLa cells were treated with PEG-AuNPs NPs for 16 hours at concentrations of 0.1-0.2 nM and prepared for analysis by CyTOF. In the control samples, no cell permeabilisation buffer or Cell-ID™ intercalator-Ir was added. Samples were analysed using the methods described in 3.5.2 to work out the number of PEG-AuNPs NPs associated with each cell. It was found that the DNA staining step had no statistically significant effect on the number of PEG-AuNPs NPs associated with each cell (Figure 3.11). This suggests that the step does not allow any significant NP escape from cells, in contrast to the findings by Oliver *et al.* One reason for different findings could be due to different cellular fates of NPs, such as whether NPs are internalised, attached to the cell membrane, inside endosomes or within

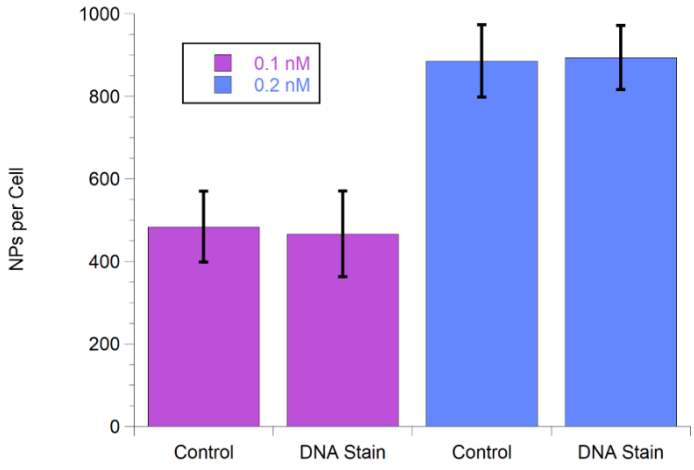


Figure 3.11 – DNA staining step during sample preparation does not cause NP escape from HeLa cells. HeLa cells were treated with PEG-Au13 NPs for 16 hours at concentrations of 0.1 and 0.2 nM. Samples were prepared as described in 3.10.4, with control samples undergoing no DNA staining step. No statistically significant difference ($p<0.05$) by independent t-test analysis between the control and DNA stain for each concentration.

cell cytoplasm. Furthermore, silver nanoparticles are known to release Ag^+ ions in cells and these ions could escape cells far more easily, lowering their Ag content.[57-59]

3.3.5 Single Cell Gating Strategy: Devising a Gating Strategy for Single Cell Analysis of Nanoparticle Treated Cells

Before cytometry data can be analysed, single cell events must first be identified. Cell-cell doublets can form in sample preparation or in the instrument fluidics prior to nebulisation, resulting in a single droplet containing two cells. Doublets can also form when two separate droplets fuse together prior to entering the TOF chamber, known as an ion-cloud fusion.[60] Additionally, some cellular debris may remain as well as free metals and nanoparticles. Failure to identify single cells could lead to over and under calculating nanoparticle uptake by analysing cell-cell doublets or debris. In flow cytometry, doublets can be excluded by their high pulse-width,[61] but this analysis is less trivial in CyTOF. Traditional single cell gating with older CyTOF instruments was simply based on DNA and event length. However, this method does not account for differences in chromatin density between cell types that can affect staining intensity,[62] or cell cycle effects such as two G_1 cells having the same amount of DNA as a G_2 or mitotic cell.[63] The newer Helios instrument used in this work reveals Gaussian parameters that allow exclusion of cell-cell doublets by discriminating between high- and low-quality pulses. This enables the specific exclusion of doublets formed by ion-cloud fusion, which is independent of cell type and less sample-dependent.[60] However as these Gaussian parameters are a property of the ion-cloud, they do not identify cell-cell doublets or aggregates formed during sample preparation, so they can be used in combination with DNA/cisplatin based gating that also excludes doublets and dead cells based on size and DNA content.

For the identification of single cell events in this work, the following gating strategy was deployed: any events longer than approximately 30 were discarded, followed by events with non-normal centre, offset or residual Gaussian parameters to remove ion-cloud fusions.

Then, by plotting ^{140}Ce vs. ^{193}Ir, events from normalisation beads and debris can be discarded. Lastly, by plotting cisplatin signal and DNA content ^{195}Pt vs. ^{193}Ir and ^{191}Ir vs ^{193}Ir, any dead cells and remaining doublets can be removed, leaving live single cells for analysis.

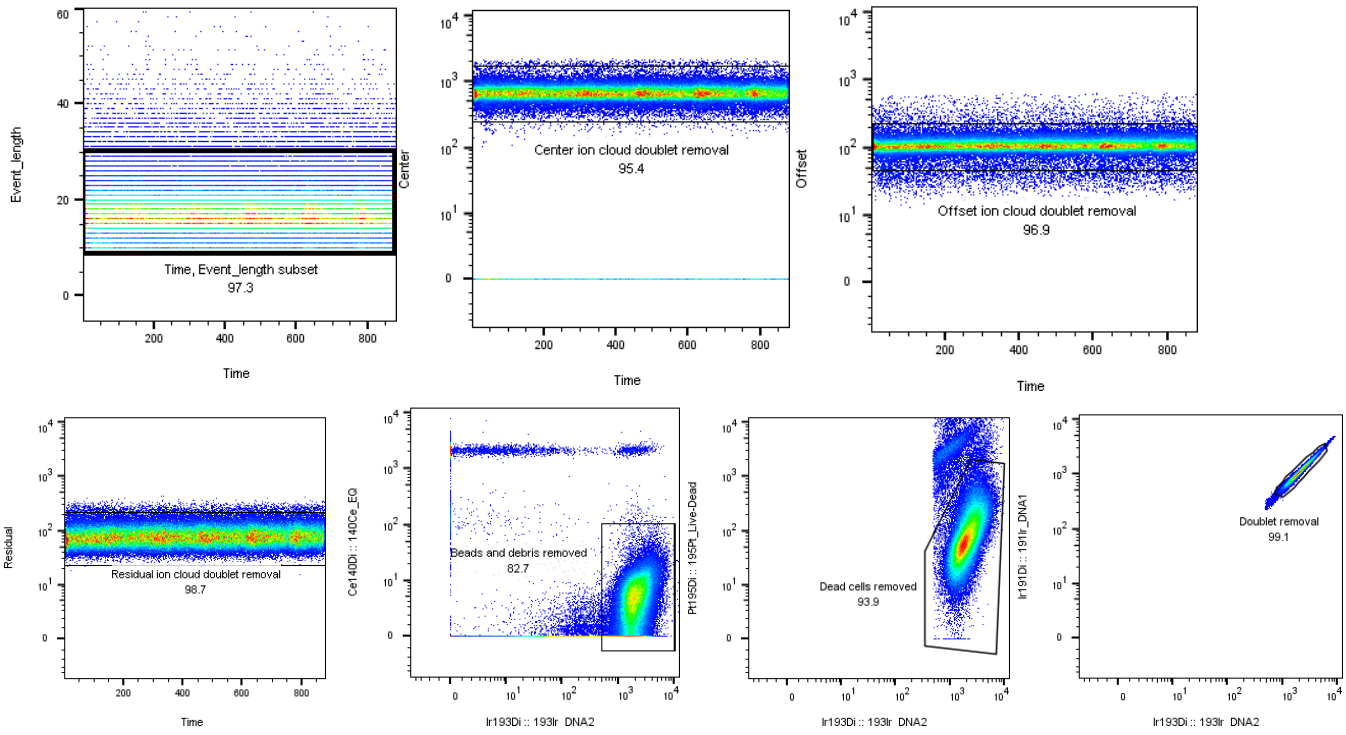


Figure 3.12 - The single cell gating strategy used during this work. The number on each graph is the percentage (%) of each events selected in each gate. An event length threshold of <30 is selected, before discarding non-normal centre, offset and residual Gaussian parameter values. Beads and debris events can then be removed by plotting ^{140}Ce vs. ^{193}Ir, then dead cells and any remaining doublets/aggregates can be removed by plotting ^{195}Pt vs. ^{193}Ir.

3.3.6 Negative Control Experiments

For every CyTOF experiment, a negative control sample was analysed, where cells were treated with MQ water from the same water source as all NP samples were synthesised from, instead of NP treatment. Cells were then stained and prepared as normal for CyTOF. These data were acquired after any 'solution mode' calibrations were acquired. In all cases, minimal ^{197}Au mean dual counts were detected. For example, a histogram of ^{197}Au mean dual counts from a representative control sample is shown in Figure 3.13. 99% of cells studied had a ^{197}Au mean dual count signal of 0 or less than 1 AuNP. In the 1% of cells that

had a positive ^{197}Au mean dual count signal, the average mean dual counts was 12 (see section 3.5 for conversion of mean dual counts to NPs), corresponding to approximately 1.5 AuNPs. This provides confidence that ^{197}Au mean dual counts from NP treated cell samples arises from cell associated NPs, rather than any contamination from other samples.

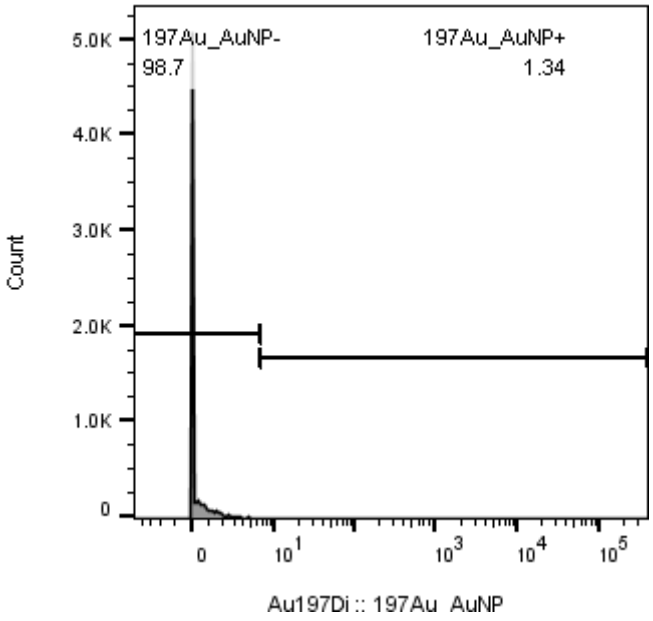


Figure 3.13 – Histogram of ^{197}Au mean dual counts detected during acquisition of a negative control sample. Cells were treated with MQ water from the same water source as all NP samples were synthesised from, instead of NP treatment. Cells were then stained and prepared as normal for CyTOF. Histogram is representative of all negative control samples which were ran every day the instrument was used.

3.4 Studying EuQuin$_2$S-AuNP Uptake by TEM

CyTOF cannot determine whether a nanoparticle is intracellularly (i.e., taken up) or extracellularly associated (i.e. externally bound to the cell membrane) with an individual cell. TEM was therefore used to investigate whether our EuQuin$_2$S-AuNPs are taken up by HeLa cells. Previous studies with gold and silver nanoparticles have shown that a significant proportion of the nanoparticles associated with a cell can be bound to the surface.[9, 64, 65] HeLa cells were treated with EuQuin$_2$S-AuNPs at a concentration of 1 nM for 16 hours and sections of cells were prepared for TEM imaging. The cells were washed the same number of times as they are subjected to in CyTOF experiments, as it was hypothesised that these washing steps could displace any nanoparticles externally attached to the cell membranes. The images show internalisation of EuQuin$_2$S-AuNPs in HeLa cells (Figure 3.14). Of the cells imaged, there was no signs of EuQuin$_2$S-AuNPs externally associated with the cell membrane, implying that the ^{197}Au signal associated with cells from CyTOF experiments is indicative of intracellular EuQuin$_2$S-AuNP uptake. Higher magnification images reveal that EuQuin$_2$S-AuNPs are located in clusters within vesicle-like structures, and no nanoparticles were found in the cytoplasm outside of vesicles in the timeframe of the incubation period. This suggests that the predominant uptake mechanism of EuQuin$_2$S-AuNPs is endocytosis.[50, 66] There was no evidence of nuclear uptake or EuQuin$_2$S-AuNPs located within mitochondria, which was shown in a previous study by the group with iridium coated gold nanoparticles.[51]

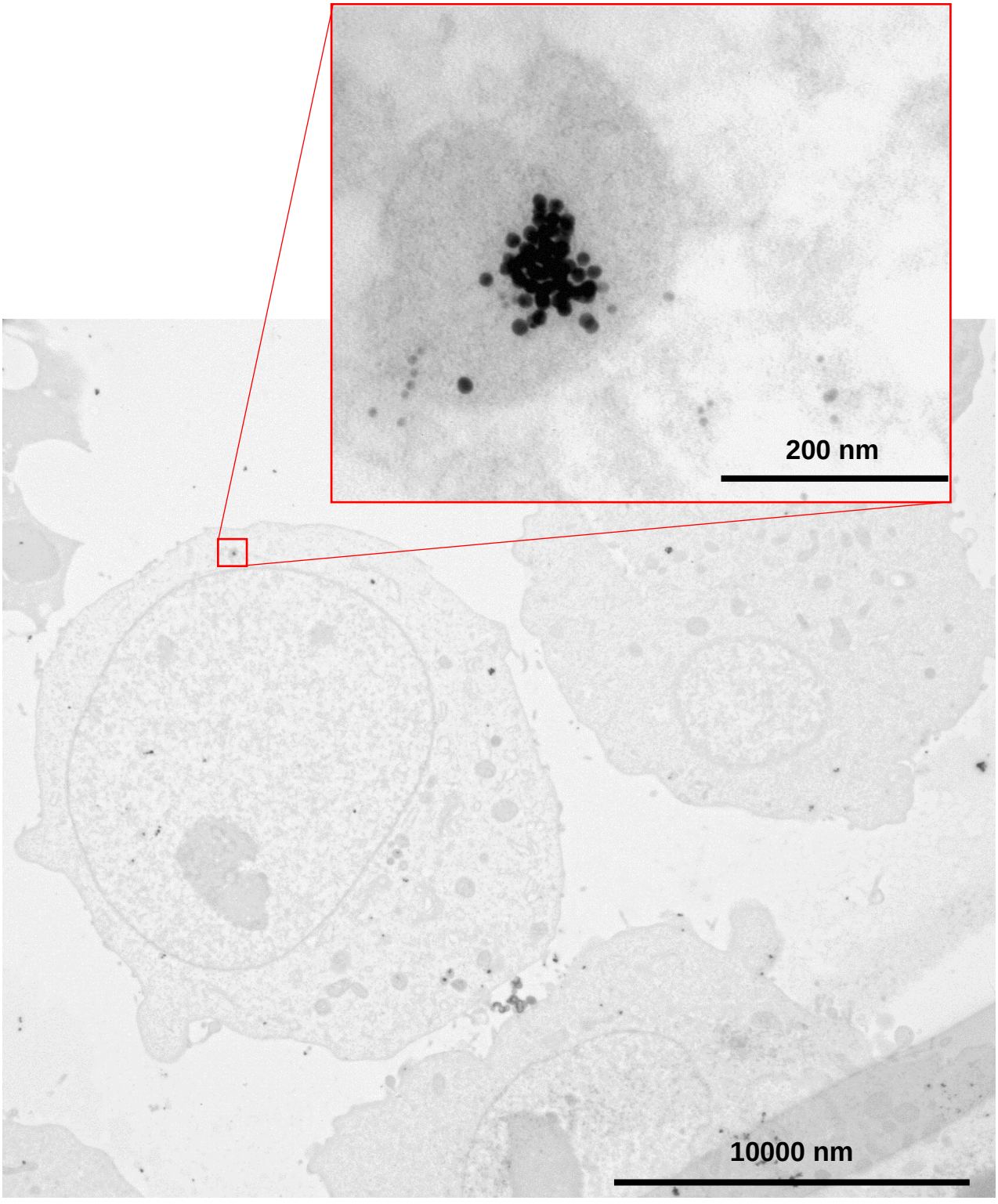
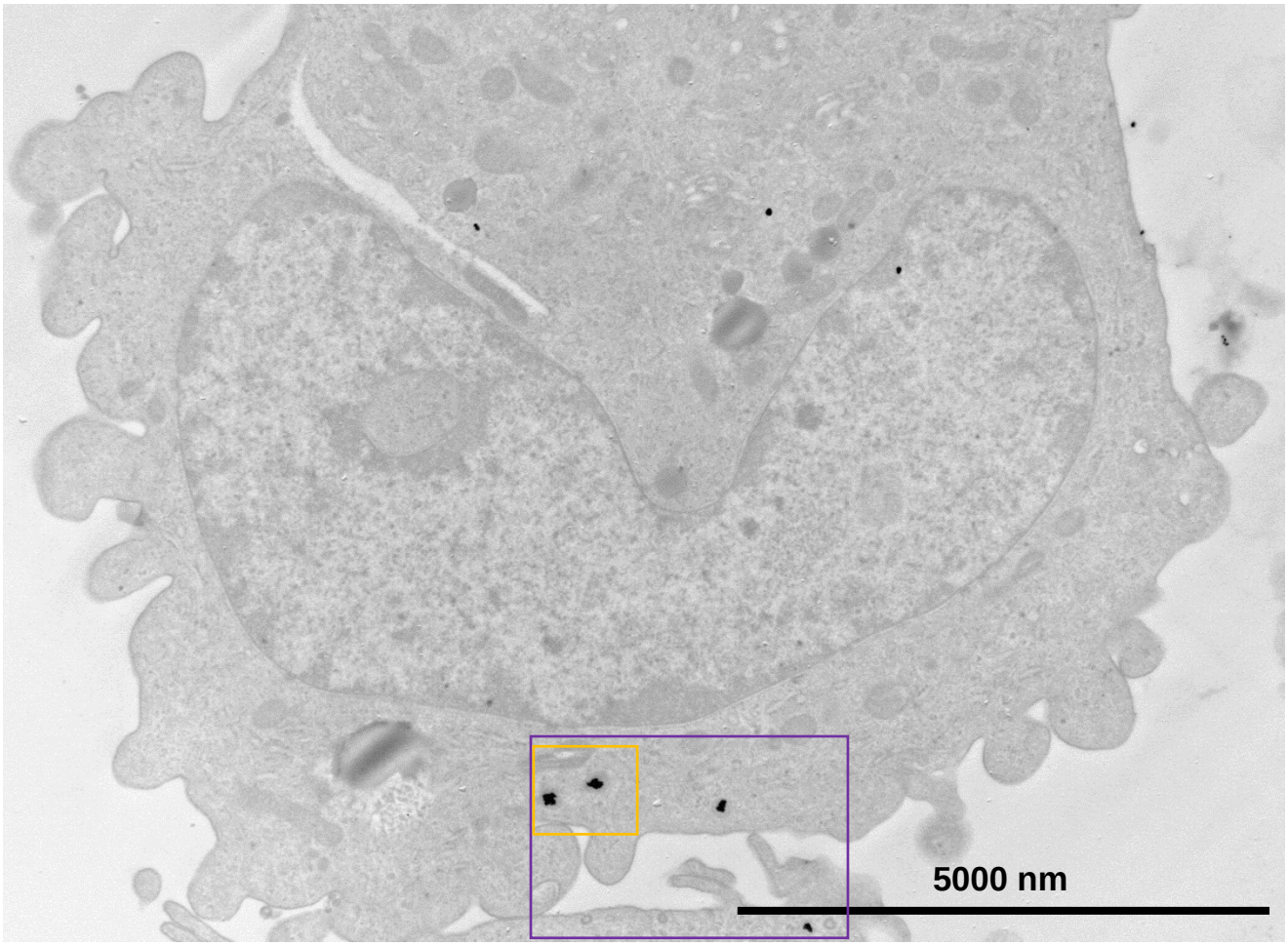
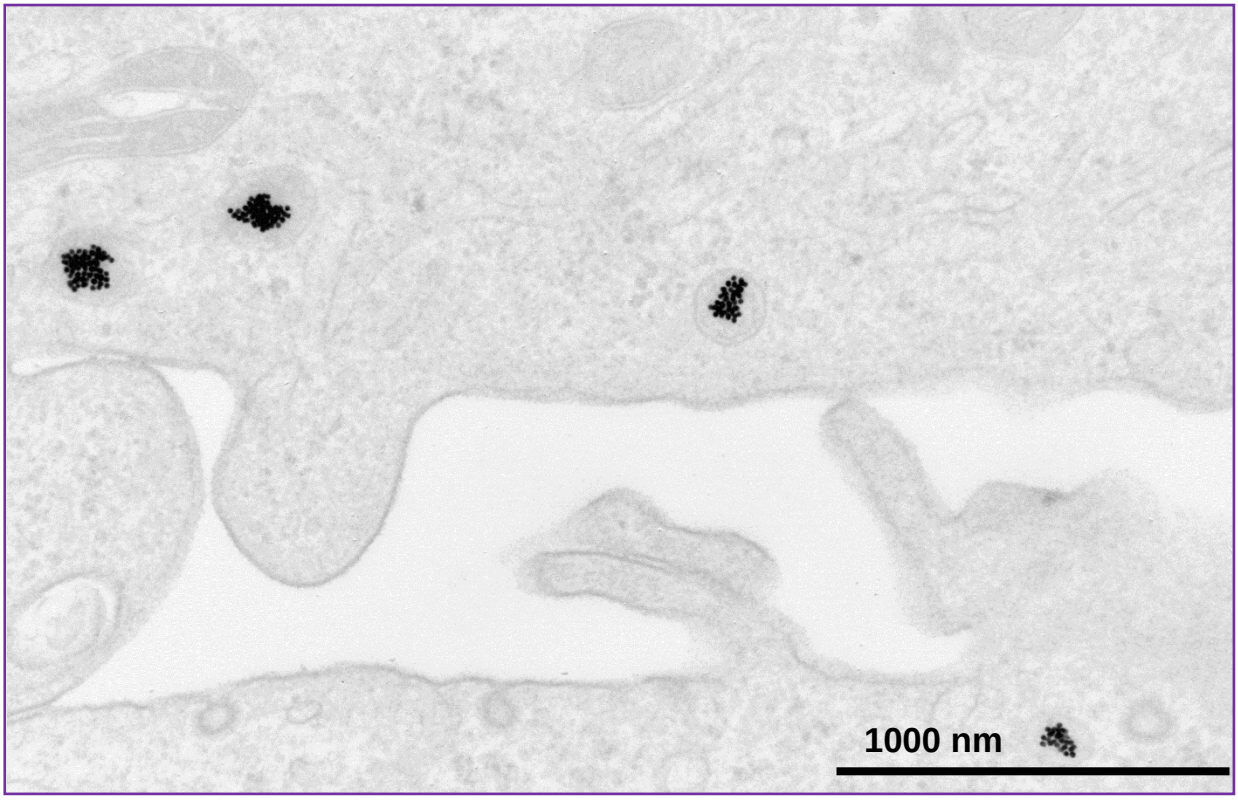
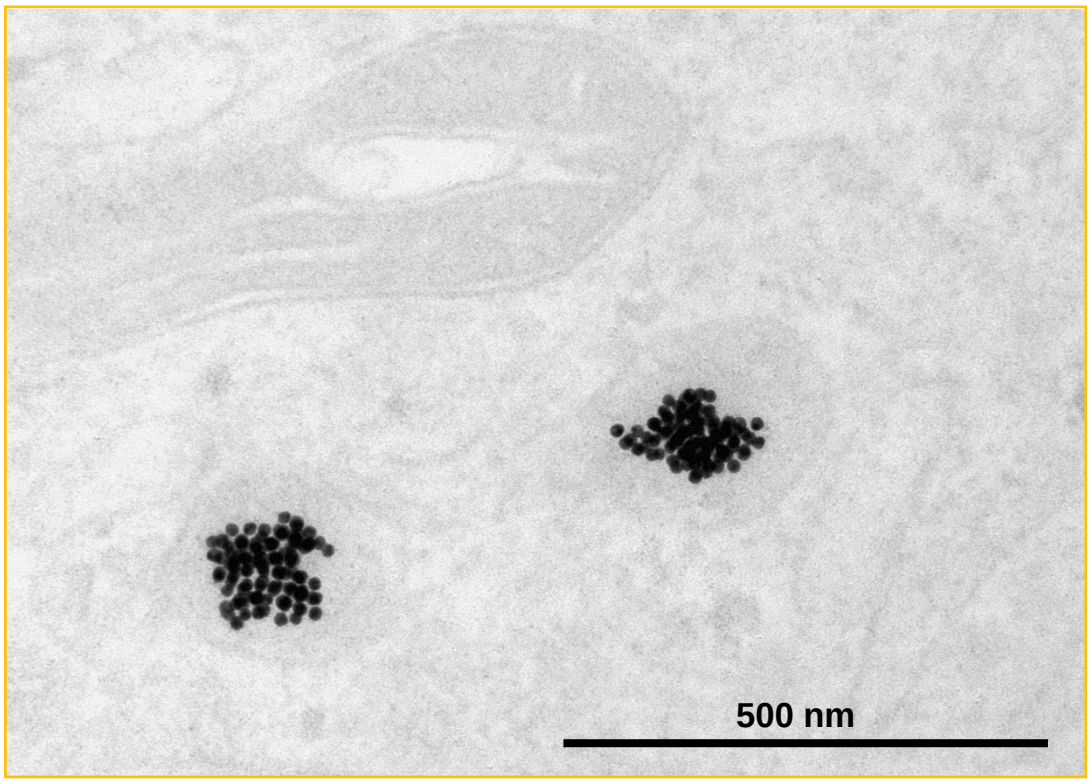
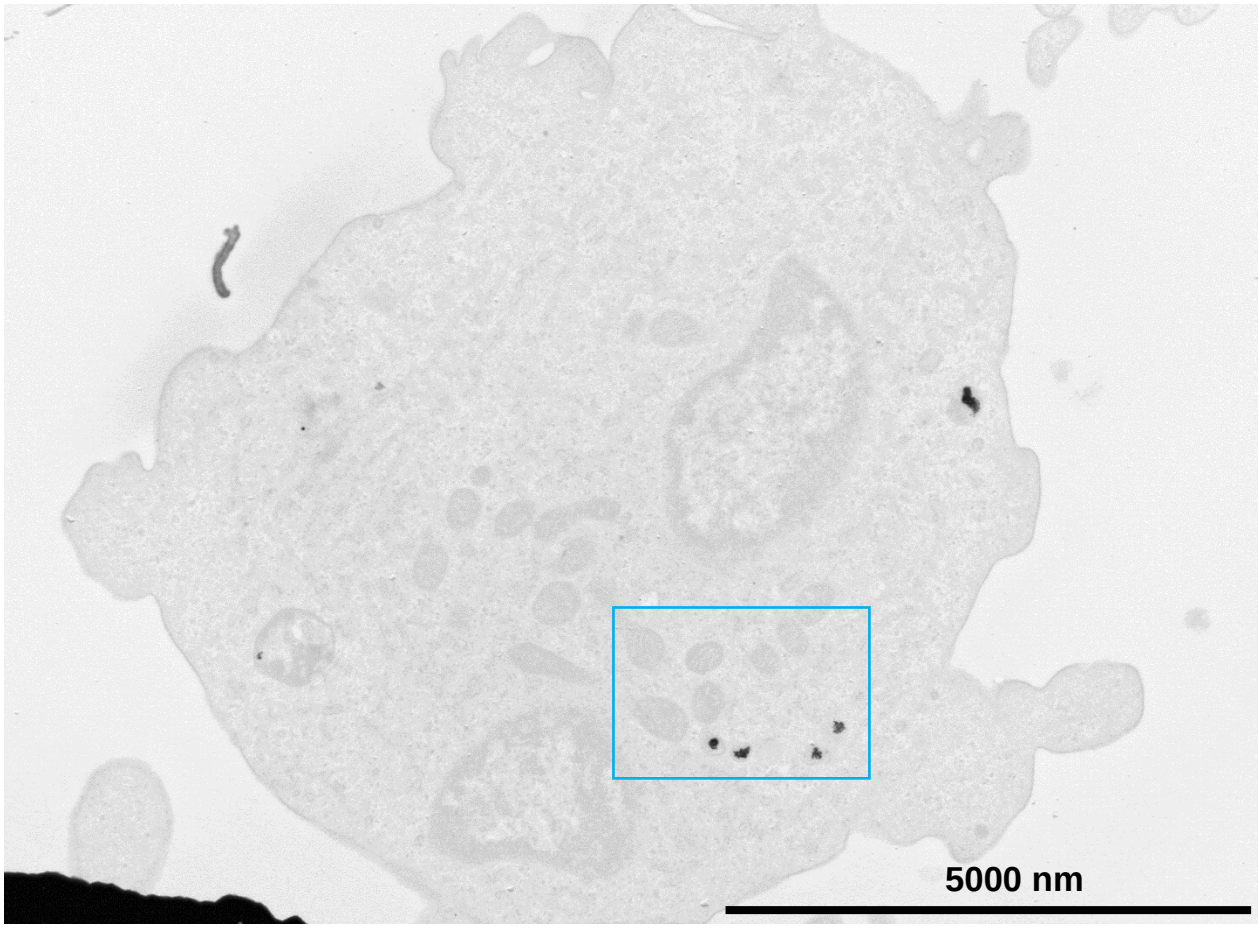


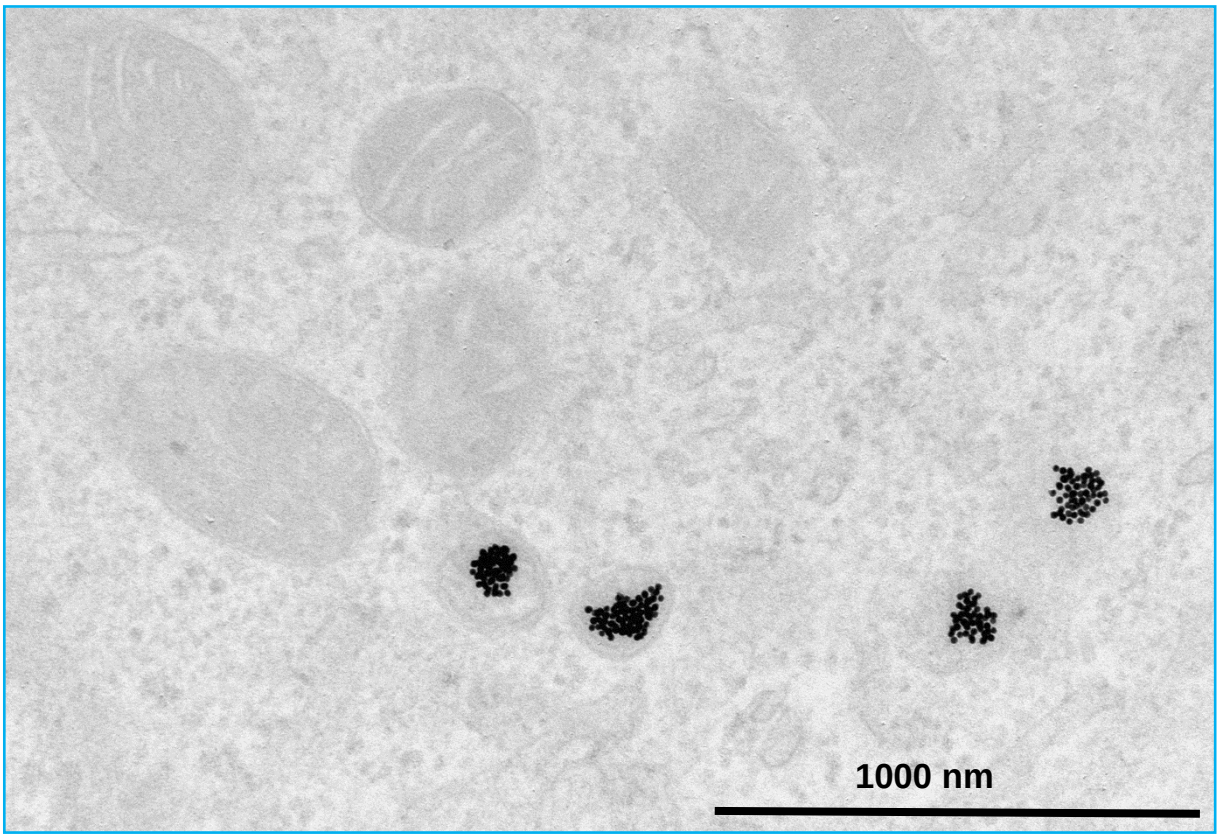
Figure 3.14 – TEM image of HeLa cells sections. HeLa cells treated with $EuQuin_2S$-AuNPs for 16 hours at a concentration of 1 nM and washed using the same protocol as used in CyTOF studies.


5000 nm


1000 nm


500 nm


5000 nm


1000 nm

3.5 Quantification of Nanoparticle Uptake by CyTOF

3.5.1 Instrument Calibration

The quantity of a metal isotope associated with each cell is given in 'mean dual counts' which can be correlated to the actual number of NPs through calibration of the instrument to determine the transmission efficiency (TE) of the metal of interest. It is possible to assess TE of metal isotopes for a Helios instrument by operating the system in 'solution mode', where the ion counts are integrated over a known amount of time. The instrument is tuned daily with a tuning solution containing isotopically pure ^{133}Cs, ^{139}La, ^{159}Tb, ^{169}Tm, ^{191}Ir and ^{193}Ir metal ions of known concentrations to determine a dual instrument (Di) count coefficient. Plotting the analog intensity counts against the digital pulse counts reveals a range at which both numbers correlate; this can be used to approximate the pulse count even at high pulse concentrations.[67] This internal calibration can be used to determine the transmission efficiency (TE) of these metals, but TE varies for each metal,[68] and we are particularly interested in accurately quantifying ^{197}Au signal from lanthanide coated AuNPs. Furthermore, Oliver *et al.* showed that the TE differs for ionic and colloidal silver nanoparticles when measured in solution mode on a CyTOFv1 instrument.[4] We therefore used the instruments solution mode to determine a TE for 13 nm lanthanide coated gold nanoparticles. To calculate TE, the theoretical expected counts must first be determined. This is the number of counts you would expect if 100% of ^{197}Au atoms were recorded as a count by the detector. In reality, when Tricot *et al.* studied the TE of isotopes ranging from 139-176 Da, most metals had a TE of ca. 0.5-1 x 10^{-4}, meaning only around 1 in 10,000-20,000 atoms make it to the detector (0.005-0.01%), although it is worth noting this study was conducted on an older CyTOF2 mass cytometer.[68] By using the concentration of the ionic solution, the natural abundance of the elemental isotope of interest, Avagadro's constant (N_A) and the injection of speed of the solution (0.5 μLs^{-1} for the Helios instrument), the theoretical expected counts (s^{-1}) can be calculated (equation x). The TE can then be

calculated from the dual counts output given per second when the instrument is in solution mode (equation x).

$$Theoretical\ expected\ counts\ (s^{-1}) = \frac{Concentration \times natural\ abundance \times N_A \times Injection\ speed}{isotope\ mass}$$

$$Transmission\ efficiency\ (TE) = \frac{dual\ counts}{theoretical\ expected\ counts}$$

TbS-AuNPs NPs were synthesised, purified, and diluted to concentrations ranging from 0.1-5 μgL^{-1} (for calculations involving the conversion of molar to mass concentrations, see appendix 3.12.4) and ion counts were recorded for 2 minutes, meaning there were 120 data points recorded for each sample. Linear regression (R^2 = 0.998) of the observed ^{197}Au counts plotted against the theoretical expected counts of TbS-AuNPs NPs of this concentration revealed a TE of 1.15 x 10^{-4} for ^{197}Au atoms (Figure 3.15). This value is within the expected magnitude and is comparable to a TE of 1.67 x 10^{-4} for AuNPs ranging from 10-100 nm in diameter in a Helios instruments 'event mode', shown in a study by Wu *et al.* at a similar time to when our work was conducted.[5] As gold is a monoisotopic element, this means that 1 in 8700 ^{197}Au atoms produces a mean dual count from the instrument and a 13 nm AuNP containing approximately 68000 ^{197}Au atoms would correspond to 7.8 mean dual counts. To assess how this calibration translated to measurements in 'event mode', a control experiment with HeLa cells with no lanthanide AuNP treatment prior to sample acquisition was run. There was however a small amount of ^{197}Au signal observed; presumably single nanoparticles remaining in the instrument fluidics from the calibration samples acquired beforehand. These ^{197}Au events centred around a peak of around 7-8 counts – in agreement with the TE calculated (Figure 3.15). Although this peak was observed during this analysis, using the mean dual counts in 'event mode' was not found as a reliable measure of determining TE, as on many occasions no peak was observed.

We therefore focussed our quantification from TE calculated in solution mode in this work. A calibration was performed on each lanthanide gold nanoparticle species before acquiring data every day the instrument was used, as different nanoparticles were studied and instrument performance can vary for reasons such as cone contamination and cleaning.[67-69] One limitation of calibrating the instrument with lanthanide gold nanoparticles in solution is that it does not account for any potential effects that the complex biological matrix may have on the ionisation of internalised nanoparticles.

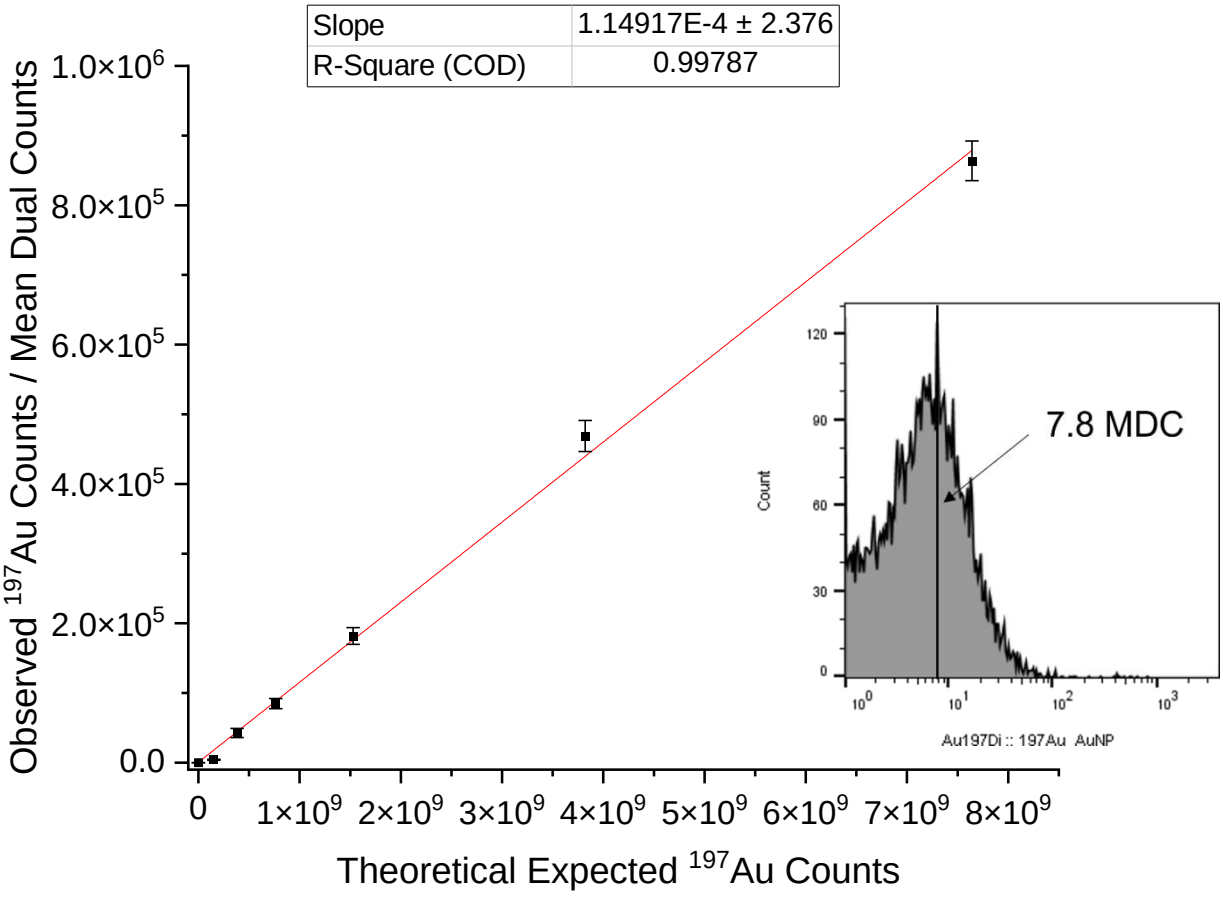


Figure 3.15 - The observed mean dual counts of 0.1-5 μgL^{-1} TbS-AuNPs in 'solution mode' plotted against the theoretical ^{197}Au counts expected for this concentration. Linear regression analysis revealed a transmission efficiency of 1.15 x 10^{-4} for ^{197}Au atoms from TbS-AuNPs. Error bars represent standard deviation from 120 measurements. Inset: ^{197}Au mean dual counts when the CyTOF was in 'cell mode' and a non-treated control of HeLa cells was analysed. The signal was attributed to single TbS-AuNPs.

3.5.2 Determination of the Number of EuQuin$_2$S-AuNPs and TbS-AuNPs per Cell with CyTOF

Having demonstrated a method to determine the TE of LnAuNPs, CyTOF was then used to quantify the number of LnAuNPs per cell within a cell population. We set out to investigate the difference in cellular uptake of EuQuin$_2$S-AuNPs and TbS-AuNPs.Through calibration of the instrument in solution mode as described in 3.4.1, the TE for TbS-AuNPs and EuQuin$_2$S-AuNPs nanoparticles were determined as 6.28×10^{-5} and 6.22×10^{-5} with both showing excellent linear fitting ($R^2 = 0.998$ and 0.999 respectively), as shown in Figure 3.16 and Figure 3.17. It is worth noting that the TE calculated for these NP species is 1.8-fold lower than the TE calculated for TbS-AuNPs in 3.5.1. This could be due a different instrument response on the day or that the NPs used in this experiment were slightly larger, meaning fewer gold atoms in each NP may have been ionised by the ICP torch, reducing the TE. It could also highlight a disadvantage of this quantification method which will be discussed in section 3.5.4.

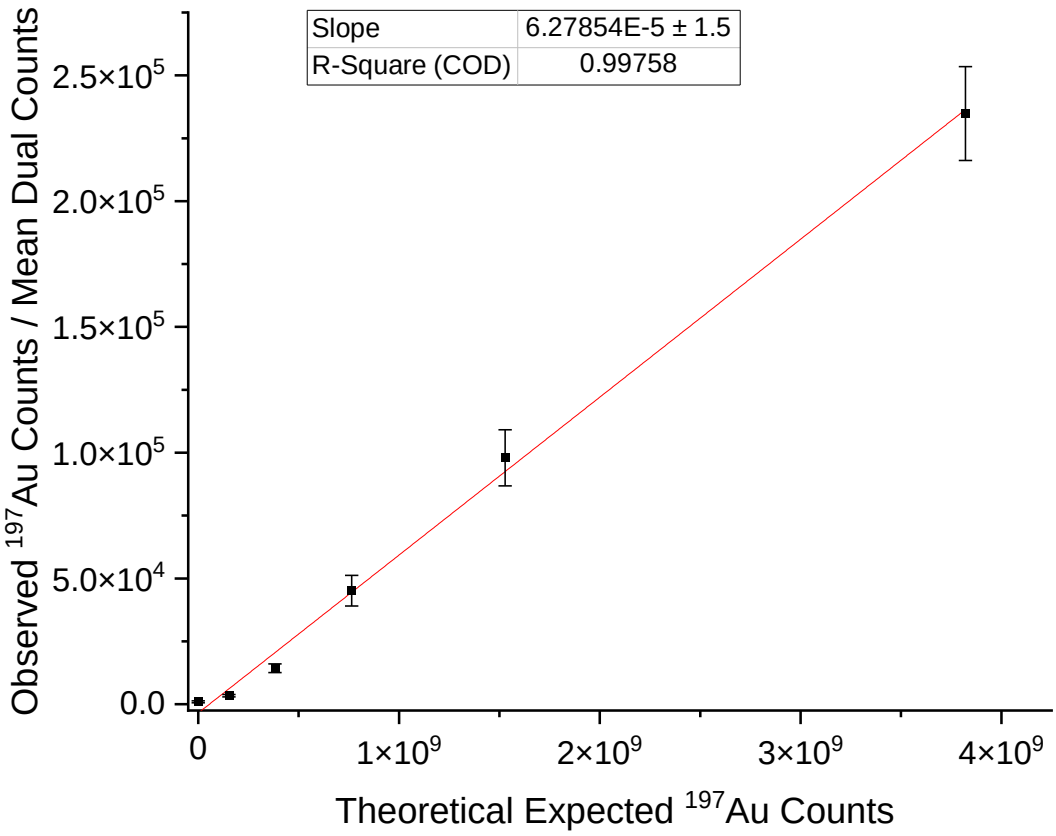


Figure 3.16 – Calibration fit of TbS-AuNPs of concentrations ranging from 0.1-1 μgL^{-1}. The 5 μgL^{-1} data point for TbS-AuNPs was discarded as an outlier. Error bars represent standard deviation from 120 measurements.

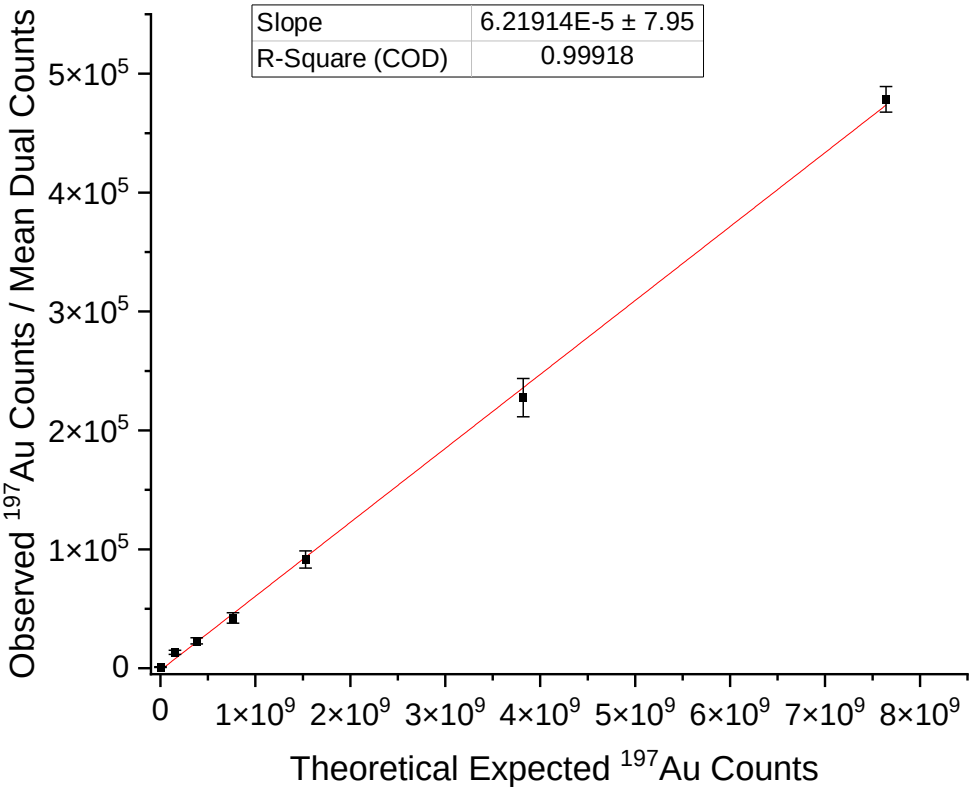


Figure 3.17 - Calibration fit $EuQuin_2S$-AuNPs of concentrations ranging from 0.1-5 μgL^{-1}. Error bars represent standard deviation from 120 measurements.

After determining a TE for ^{197}Au, the number of ^{197}Au atoms associated with each cell was calculated from the mean dual counts value provided by the instrument for every event, using the equation below:

$$Number\ of\ ^{197}Au\ atoms\ per\ cell = \frac{^{197}Au\ mean\ dual\ counts}{^{197}Au\ TE}$$

The number of ^{197}Au atoms per cell was then converted into the number of nanoparticles per cell using the equation below:

$$Number\ of\ nanoparticles\ per\ cell = \frac{^{197}Au\ atoms\ per\ cell}{Number\ of\ ^{197}Au\ atoms\ per\ nanoparticle}$$

In this work, the average number of ^{197}Au atoms per nanoparticles was determined by calculating the average diameter of the NP species from TEM images. For this batch of NPs, the average nanoparticle diameter was determined to be 14.6 ± 1.0 nm. This is a higher diameter than most NPs synthesised in this work but can be accounted for in the calculations.

HeLa cells were then treated with TbS-AuNPs and EuQuin$_2$S-AuNPs for 16 hours at a concentration of 0.3 nM and the mean number of NPs per cell was determined by CyTOF analysis. Approximately 250,000 single cell events were analysed in each sample. After identifying single cell events, the average ^{197}Au mean dual counts of for TbS-AuNP and EuQuin$_2$S-AuNP treated HeLa cells was 10865 ± 160 and 7118 ± 170 (± SD) respectively (N=3 for each type of sample). By using the equations above and the average number of ^{197}Au atoms in a 14.6 nm nanoparticle, the mean number of TbS-AuNPs and EuQuin$_2$S-AuNPs per cell was calculated as 1640 ± 10 and 1074 ± 10 respectively (± SD) (Figure 3.18). The low standard deviation of ca. 1% for TbS-AuNPs and EuQuin$_2$S-AuNPs shows excellent reproducibility between the triplicate samples. This shows that TbS-AuNPs were taken up 1.5-fold more than EuQuin$_2$S-AuNPs on average.

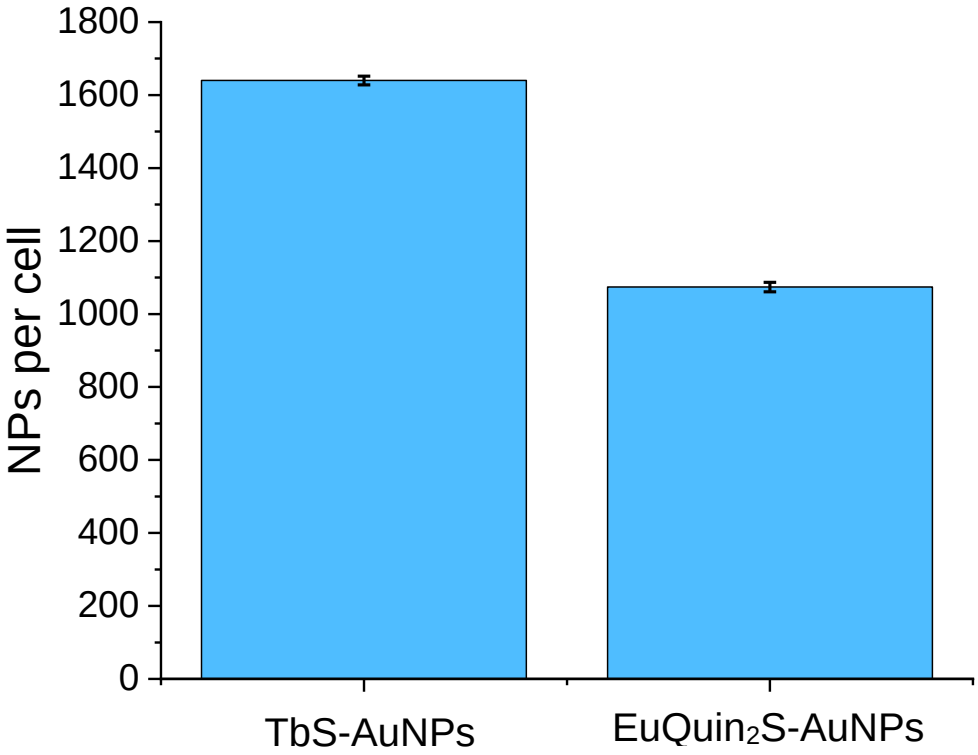


Figure 3.18 – The mean number of TbS-AuNPs and $EuQuin_2S$-AuNPs per cell determined by CyTOF analysis after HeLa cells were treated with TbS-AuNPs and $EuQuin_2S$-AuNPs for 16 h at a concentration of 0.3 nM. Error bars represent the standard deviation from triplicate repeats.

As lanthanide metal complexes are isostructural,[70] the difference of the Eu^{3+} and Tb^{3+} lanthanide centres will likely have no effect on the cellular uptake of $EuQuin_2S$-AuNPs and TbS-AuNPs. However, the difference in chain length of the metal complexes will alter the nanoparticle surface properties and this could explain the difference in uptake.

3.5.3 Validation of CyTOF as a Quantitative NP uptake technique: A Comparative Study with ICP-MS

Following from 3.5.2, the same samples were analysed by ICP-MS to compare the number of NPs per cell determined from each method. For ICP-MS analysis, the NP treated cells were digested into an ionic solution with aqua regia. A calibration plot of a solution of gold ions demonstrated good overall linear fitting of measured [Au] concentration to theoretical [Au] ppb (R^2 = 0.999) (Figure 3.19). However, as shown in the inset, at lower Au concentrations the fitting was not as optimal and at the Au concentration of samples in this

work at 20-25 ppb there is a ca. 30% difference between the linear fit and the measured values. Calibration of this instrument at these concentrations for Au could not be improved, even with different calibration standards ran in separate experiments on different days. Since it is difficult to increase the Au signal from cells in each sample as a very large number (ca. 15 million) are already prepared for each sample, this error could not be eradicated from using this technique in the timeframe of this work.

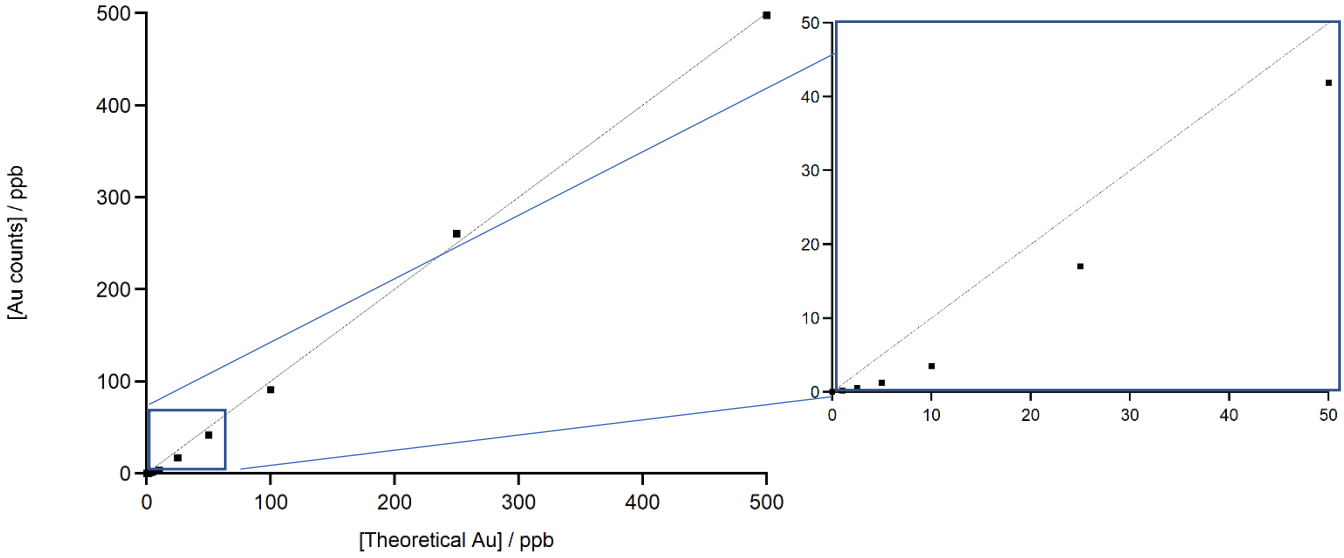


Figure 3.19 – Linear regression analysis (R^2 = 0.999) of a gold solution to calibrate an ICP-MS instrument. Inset reveals non-optimal fitting at lower Au concentrations.

From analysis of the concentration of ^{197}Au in each sample, the mean number of TbS-AuNPs and EuQuin$_2$S-AuNPs per cell from ICP-MS experiments was calculated as 1370 ± 10 and 964 ± 150 respectively (Figure 3.20). These values are very similar to the mean number of TbS-AuNPs and EuQuin$_2$S-AuNPs per cell of 1640 ± 10 and 1074 ± 10 respectively determined by CyTOF. Overall, this shows excellent agreement between ICP-MS and CyTOF for determining the number of NPs per cell, despite the differences in experimental setup and the known errors associated with the ICP-MS measurements. Yang *et al.* previously used a TE value for ^{197}Au approximated from the TE of $^{191/193}$Ir and found the number of 5 nm AuNPs per cell to be within the same order of magnitude for both CyTOF and ICP-AES, but there was a greater than 5-fold difference between the values in

some instances.[1] Our results indicate that through calibration of the lanthanide gold nanoparticle of interest, CyTOF generates NPs per cell values very similar to the gold-standard ICP-MS method at the concentration tested.

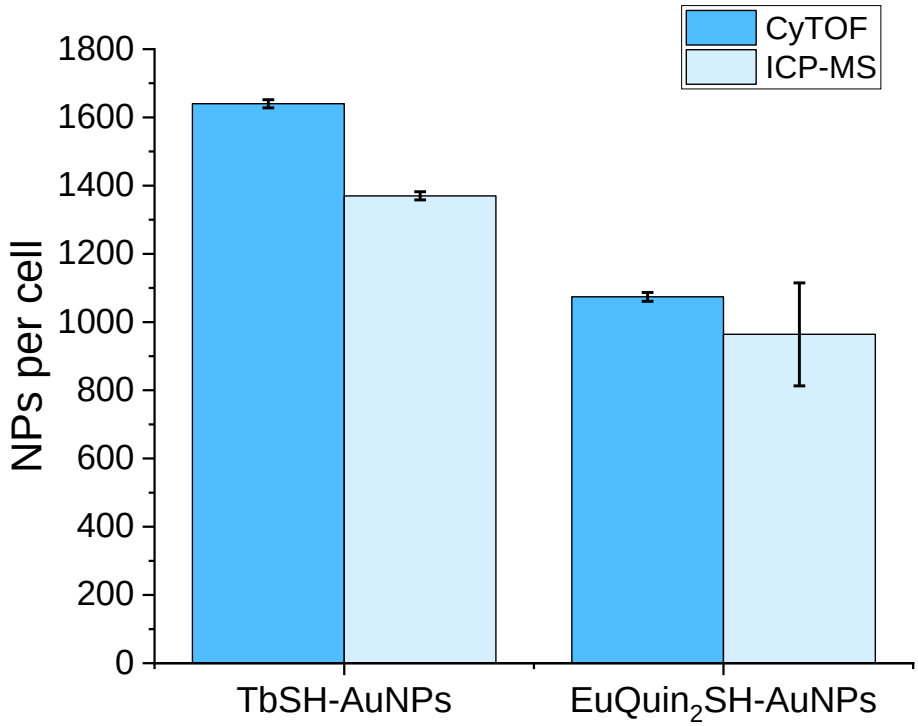


Figure 3.20 – Comparison of the mean number of TbS-AuNPs and $EuQuin_2S$-AuNPs per HeLa cell after treatment for 16 hours at a concentration of 0.3 nM, determined by CyTOF and ICP-MS. Error bars represent the standard deviation from triplicate repeats.

3.5.4 Variability of CyTOF Nanoparticle Uptake Quantification: Evaluating the Effect of Experimental Differences and Uncertainty

So far, it has been shown that lanthanide gold nanoparticle uptake quantification in HeLa cells by CyTOF analysis is highly comparable to ICPMS, with excellent agreement between replicate samples. This demonstrates both good laboratory practice and that CyTOF can reliably and agreeably quantify metal content when taking measurements on the same day. However, it does not provide insight into the reproducibility of lanthanide AuNP uptake quantification by CyTOF with independently repeated measurements. To evaluate this variability, the mean number of $EuQuin_2S$-AuNPs per cell determined by CyTOF analysis from 3 independent experiments over a time period of 8 months was compared. In each

case, HeLa cells were treated with $EuQuin_2S$-AuNPs for 4 hours at a concentration of 0.3 nM and prepared for CyTOF analysis following the same protocol. The mean number of $EuQuin_2S$-AuNPs per HeLa cells was determined as 464, 585 and 305 in each case, giving an average of 451 ± 114 (± SD).

This is a much greater variability (25%) in standard deviation of the mean number compared to triplicate repeats on the same day (1%). This is a 1.9-fold difference between the highest and lowest values, compared to a same day difference of just 0.97-fold.

There are numerous contributory effects to consider when evaluating this discrepancy. First of all, the values would not be expected to be the same. Although all cells used were from the same source, cell behaviour can also change with density, proliferation rates, growth media, the presence of contaminants and the time kept in culture, which could in turn affect the cellular uptake of NPs.[71] Furthermore, the physicochemical properties of NPs affect their uptake, so slight differences in $EuQuin_2SH$ coating and NP size may also change the uptake kinetics.

Secondly, there are many values used in order to determine the number of NPs per cell that each have their own uncertainty. NP uptake is concentration dependent[72] and it was shown in 2.5.2 that using UV-Vis spectroscopy to calculate concentration has an estimated 10% error. This could contribute to the dosing of cells with NPs as well as determining the TE of the NP species in question. Additionally, different 13 nm citrate stabilised AuNP batches were used and separately analysed from TEM images to estimate particle diameter and determine the mean number of Au atoms per NP. There are several sources of uncertainty that may contribute to uncertainty in the determination of the mean particle size, including calibration of the pixel size, digitisation and pixel noise. Temmerman *et al.* determined an uncertainty of 4% in determining average AuNP diameters from TEM images.[73] Since the number of Au atoms per NP = $30.9D^3$ (see appendix 3.12.3 for derivation), a 4% uncertainty in average diameter leads to a larger uncertainty in our

calculations. For example, a 14.6 nm AuNP has approximately 96,000 Au atoms, but a 15.2 nm AuNP has approximately 108,500 Au atoms, meaning there is an uncertainty of 12%. The uncertainty of the number of Au atoms per NP also contributes towards the determination of the TE of NP species. The variability in TE calculated from 10 independent measurements of TE of $EuQuin_2S$-AuNPs, all synthesised separately from multiple 13-nm citrate stabilised AuNP batches, an average TE of $1.02 \times 10^{-4} \pm 2.97 \times 10^{-5}$ (SD) was determined, or a standard deviation of 30%. This is in comparison to a standard deviation of 7% for $^{191/193}$Ir using the mean dual counts determined from the internal calibration ran on the instrument each day. The estimated magnitude of the uncertainty associated with each parameter used to quantify NP uptake is shown in Figure 3.21. Although TE is expected to differ on each day due to instrument performance, this higher variation in TE measurements suggests that the added complexity of calculating TE from NP solutions may add in further uncertainty. Although it is difficult to accurately quantify the level of uncertainty, from the addition of the uncertainties associated with on-the-day sample variability (1%), concentration (10%), estimation of Au atoms per NP (12%) and the additional uncertainty from TE estimates compared to the instruments internal calibration (22%), the addition of these errors leads to a crude estimate of up to 45% uncertainty of NP uptake quantification using CyTOF from independently repeated samples. More systematic studies would be required to provide more understanding of the true error associated with AuNP uptake quantification. This discrepancy should be considered when comparing the relative uptake of NPs in cells when samples have been analysed on different days and synthesised independently from different NP batches.

When the average number of NPs per HeLa cell determined from CyTOF of the three independent repeats are plotted with 45% uncertainty, there is large overlap between the error bars (Figure 3.22), although a statistical test cannot be done as there is only 1 repeat per independent sample.

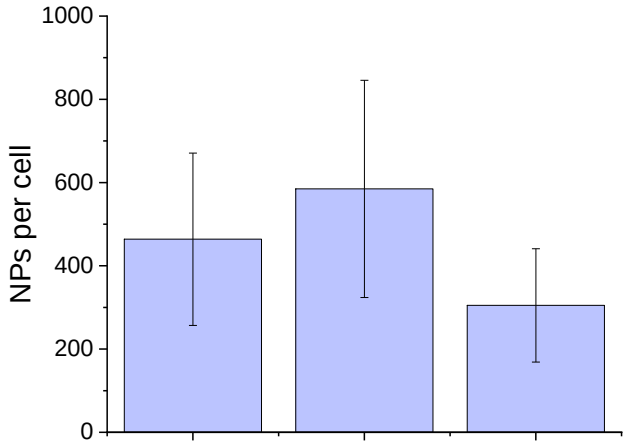


Figure 3.22 – The number of EuQuin$_2$S-AuNPs per cell determined from CyTOF analysis in 3 independent experiments with different EuQuin$_2$S-AuNP batches, with error bars to represent the crude estimate of 45% uncertainty with uptake quantification.

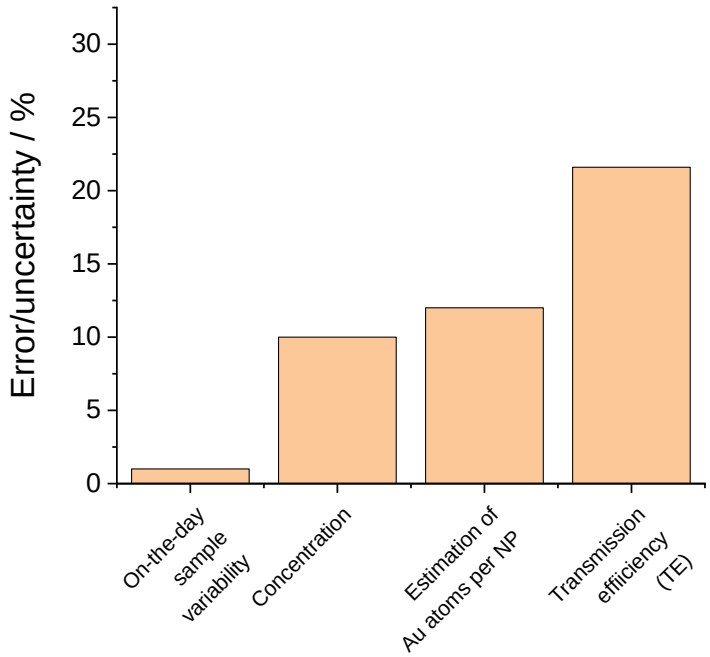


Figure 3.21 -Estimated uncertainty associated of parameters used to quantify NP uptake with CyTOF.

3.6 Ratiometric Detection of Lanthanide Gold Nanoparticles

3.6.1 Determination of the TE of ^{151}Eu, ^{153}Eu and ^{159}Tb

The europium and terbium channels in the CyTOF were used to simultaneously detect gold and europium or terbium from $EuQuin_2S$-AuNPs and TbS-AuNPs within cells. The objective for this work was to determine a gold: lanthanide ratio when the instrument is in solution and event mode to calculate the average number of lanthanide complexes per gold nanoparticle and compare these values to those determined from ICP-MS experiments.

As TE is a property of each individual metal,[68] a calibration was conducted to determine a TE for europium. An ionic solution of Eu^{3+} ions was used, and it was hypothesised that the TE would not be affected by the nanoparticle environment as the europium ions are held at the surface. ^{159}Tb is one of the four isotopes that the instrument uses for an internal calibration, meaning its TE can already be calculated and therefore no further calibration was undertaken. On the day of this experiment, the TE for ^{159}Tb was determined as 1.0×10^{-4}, similar to the TE of 1.3×10^{-4} determined for ^{197}Au from TbS-AuNPs.

The TE of ^{151}Eu and ^{153}Eu ions were determined as 9.1×10^{-5} and 1.2×10^{-4} respectively (Figure 3.23). The 1.3-fold difference between the TE of ^{151}Eu and ^{153}Eu ions is similar to the 1.2-fold difference determined in a previous study by Tricot *et al.*[68] and highlights the importance of instrument calibration as even isotopes of a similar mass of the same element can have a different TE.

Table 3.3 – The TE and its method of determination for each metal isotope used in this analysis.

Metal isotope	Transmission efficiency (TE)	Determination method
^{151}Eu	9.1×10^{-5}	Eu^{3+} ionic solution
^{153}Eu	1.2×10^{-4}	Eu^{3+} ionic solution
^{159}Tb	1.0×10^{-4}	Instrument internal calibration
^{197}Au	1.3×10^{-4}	TbS-AuNP/$EuQuin_2S$-AuNP species calibration

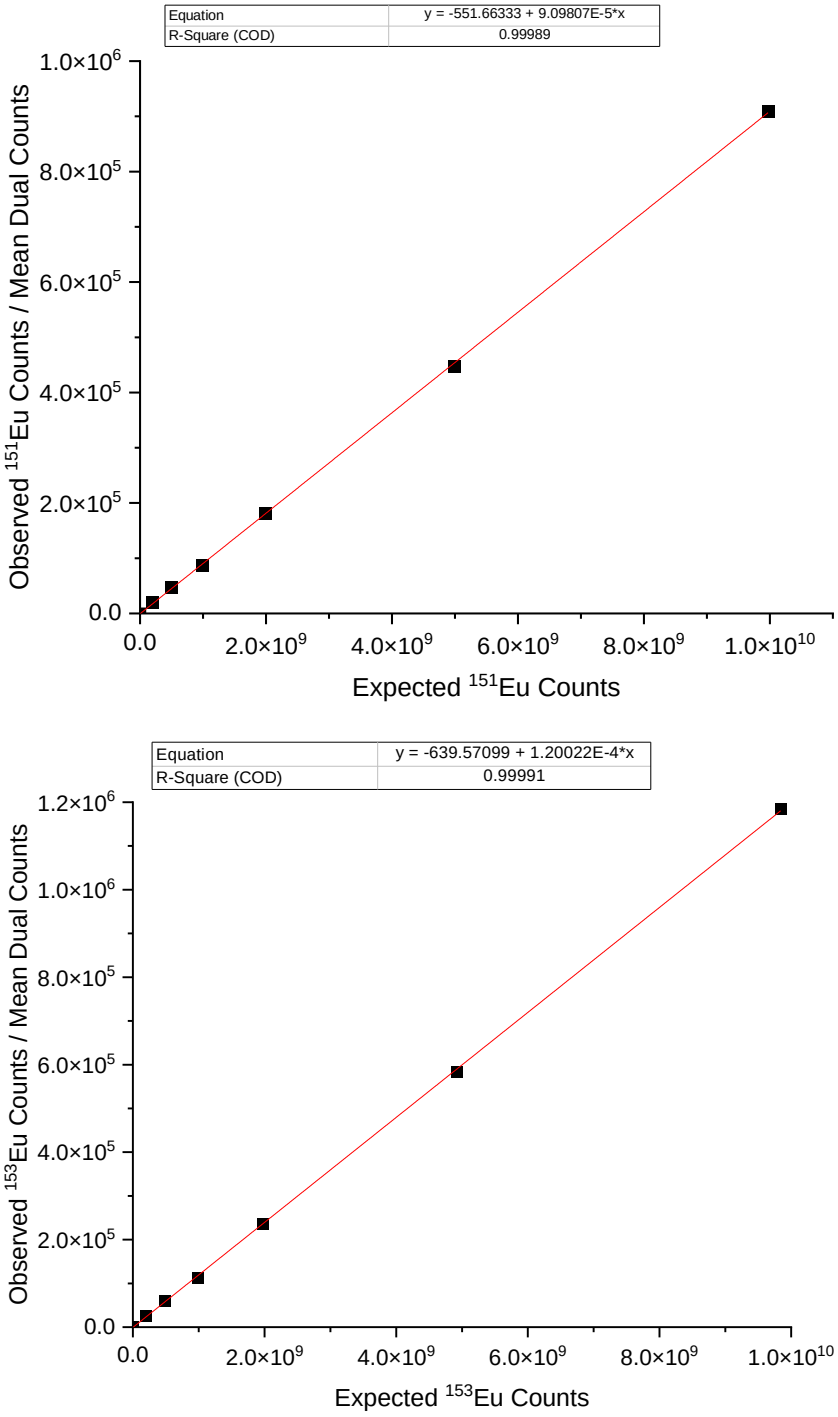
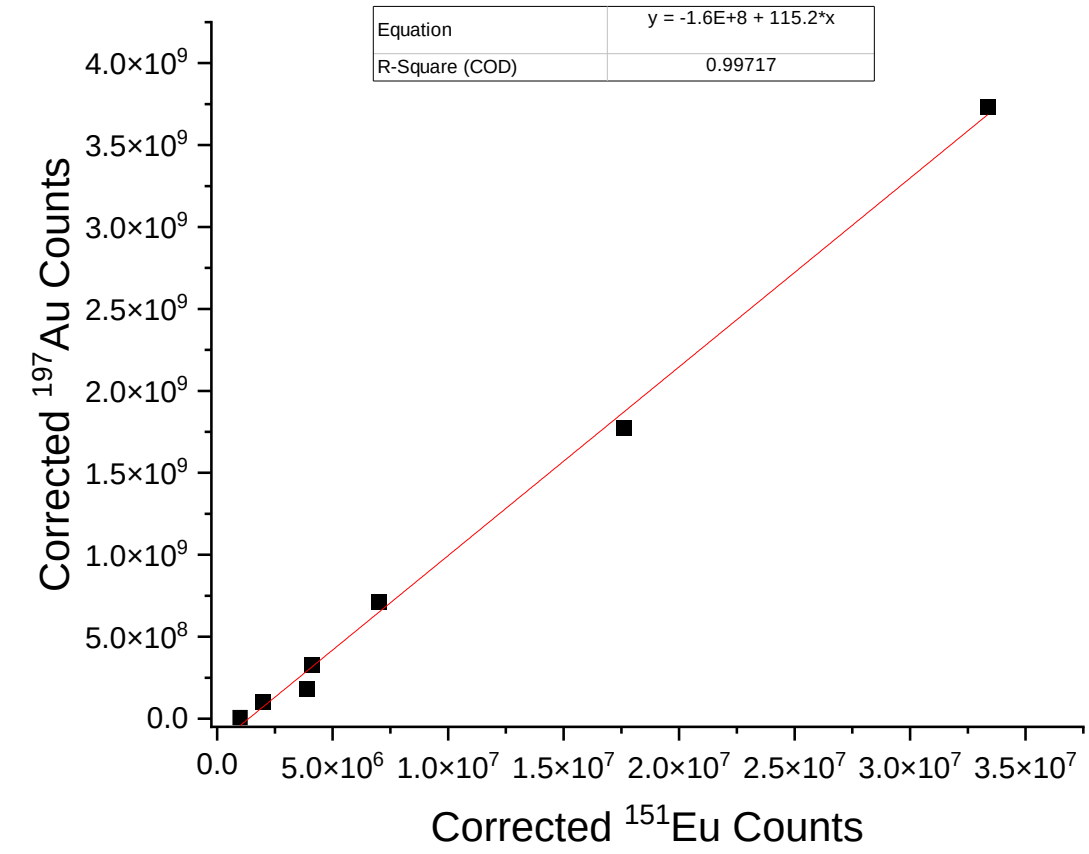
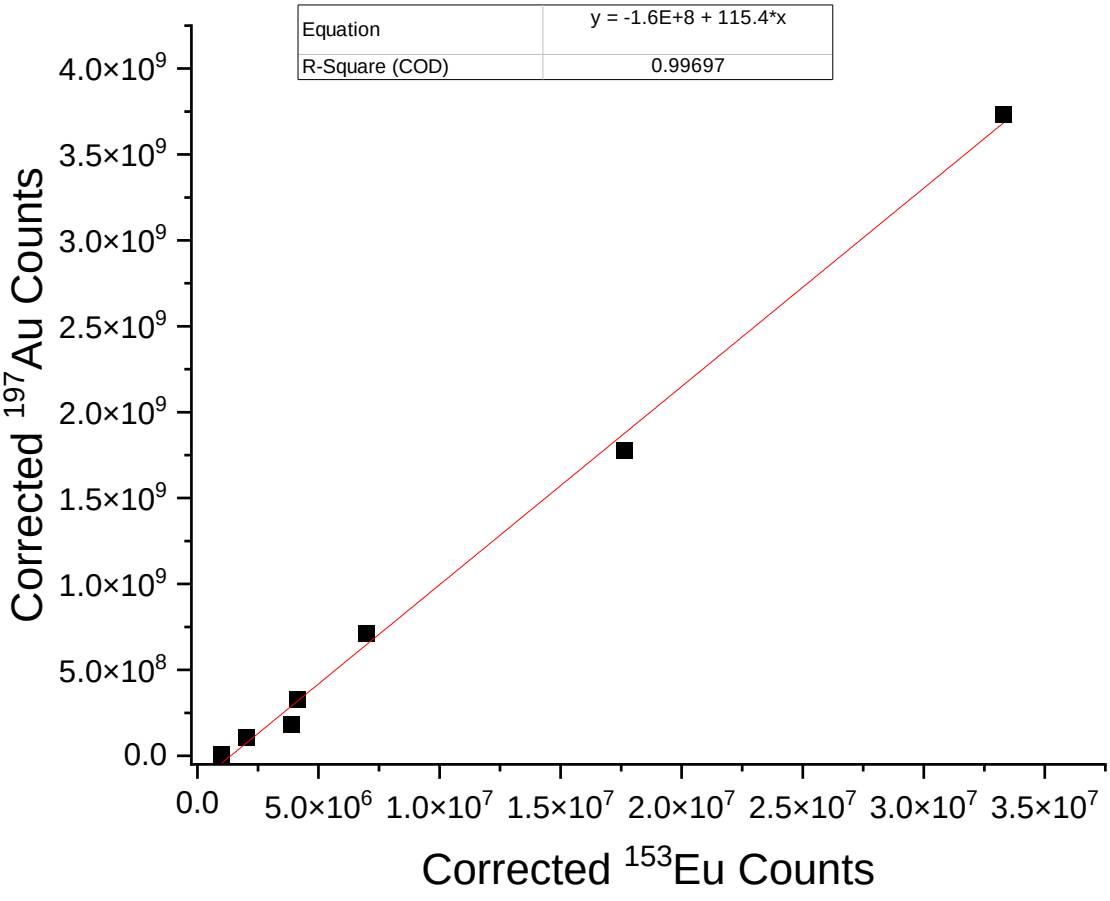


Figure 3.23 - The observed mean dual counts of ionic Eu^{3+} solutions of concentrations ranging from 0.1-5 μgL^{-1} by CyTOF analysis in 'solution mode' plotted against the theoretical Eu mean dual counts counts for ^{151}Eu and ^{153}Eu respectively. Linear regression analysis revealed TE's of 9.1 x 10^{-5} and 1.2 x 10^{-4} for ^{151}Eu and ^{153}Eu respectively, with R^2 values of ≥ 0.9999 in both cases.

3.6.2 Determination of the Average Number of Lanthanide Complexes per NP in Solution Mode

The average number of lanthanide metal complexes per nanoparticle was then calculated from the ratio of the gold: lanthanide metals detected from each NP species when the instrument was in solution mode. The mean dual counts from each metal isotope was divided by its respective TE to determine 'corrected' metal isotope counts, so that the ratio of gold: lanthanide is comparable for each NP species. The corrected metal isotope counts for each NP species were then plotted (Figure 3.24), with the gradient of a linear regression fit identifying the gold: lanthanide ratios as 115.2, 115.4 and 54.1 for ^{151}Eu, ^{153}Eu and ^{159}Tb respectively. After accounting for the natural abundance of the ^{151}Eu (48%) and ^{153}Eu (52%) isotopes, the average number of $EuQuin_2SH$ complexes per 14 nm AuNP were determined as 1540 and 1420 respectively, and the average number of TbSH complexes per NP was determined as 1570. There is an 8% divergence of the average number of $EuQuin_2SH$ complexes per NP calculated using the values for ^{151}Eu and ^{153}Eu respectively, giving an average value of 1480 complexes per AuNP. This small discrepancy could be due to errors in the calculated TE's or the error associated with the detection of the isotopes during the experiment.


Equation
y = -1.6E+8 + 115.2*x
R-Square (COD)
0.99717
Corrected 197Au Counts
Corrected 151Eu Counts
0.0
5.0×10^8
1.0×10^9
1.5×10^9
2.0×10^9
2.5×10^9
3.0×10^9
3.5×10^9
4.0×10^9
0.0
5.0×10^6
1.0×10^7
1.5×10^7
2.0×10^7
2.5×10^7
3.0×10^7
3.5×10^7


Equation
y = -1.6E+8 + 115.4*x
R-Square (COD)
0.99697
Corrected 197Au Counts
Corrected 153Eu Counts
0.0
5.0×10^8
1.0×10^9
1.5×10^9
2.0×10^9
2.5×10^9
3.0×10^9
3.5×10^9
4.0×10^9
0.0
5.0×10^6
1.0×10^7
1.5×10^7
2.0×10^7
2.5×10^7
3.0×10^7
3.5×10^7

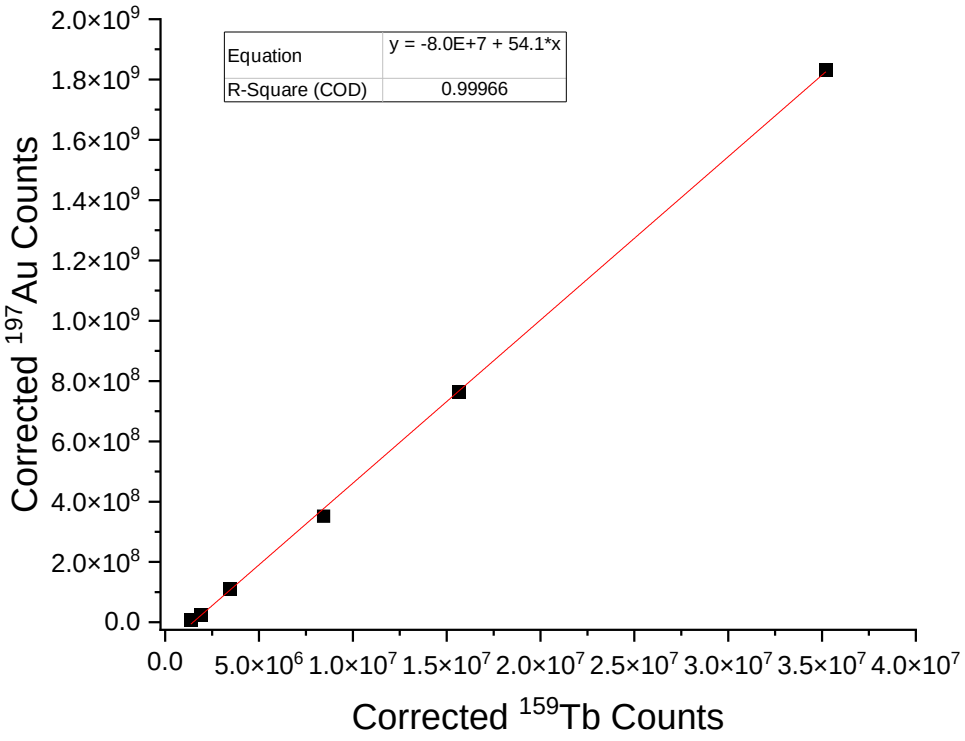


Figure 3.24 – Calculating the ratio of gold: lanthanide elements present in each NP species. Linear regression analysis of corrected ^{197}Au counts vs. corrected ^{151}Eu/^{153}Eu/^{159}Tb counts from EuQuin$_2$S-AuNP and TbS-AuNP species of concentrations ranging from 0.1-5 μgL^{-1} by CyTOF analysis in 'solution mode'. The counts were corrected using the TE for each metal isotope calculated from prior calibration experiments on the same day of the experiment.

3.6.3 Determination of the Average Number of Lanthanide Complexes per NP in Cells

Next, the average number of metal complexes per NP was calculated from the gold and lanthanide mean dual counts detected from internalised lanthanide gold nanoparticles after HeLa cells were incubated with EuQuin$_2$S-AuNPs (0.3 nM, 4 h) and TbS-AuNPs (0.3 nM, 16 h). The dot plots of the lanthanide and ^{197}Au isotope mean dual counts are shown in Figure 3.25. After accounting for each metal isotopes TE and natural abundance, the average number of EuQuin$_2$SH complexes per NP was determined as 1945 ± 250 and 1734 ± 220 for ^{151}Eu and ^{153}Eu respectively and the average number of TbSH complexes was determined as 2049 ± 62. These data suggest that the lanthanide complexes remain intact on the surface of the AuNPs, and to our knowledge is the first demonstration of dual metal detection from a single NP species within cells.

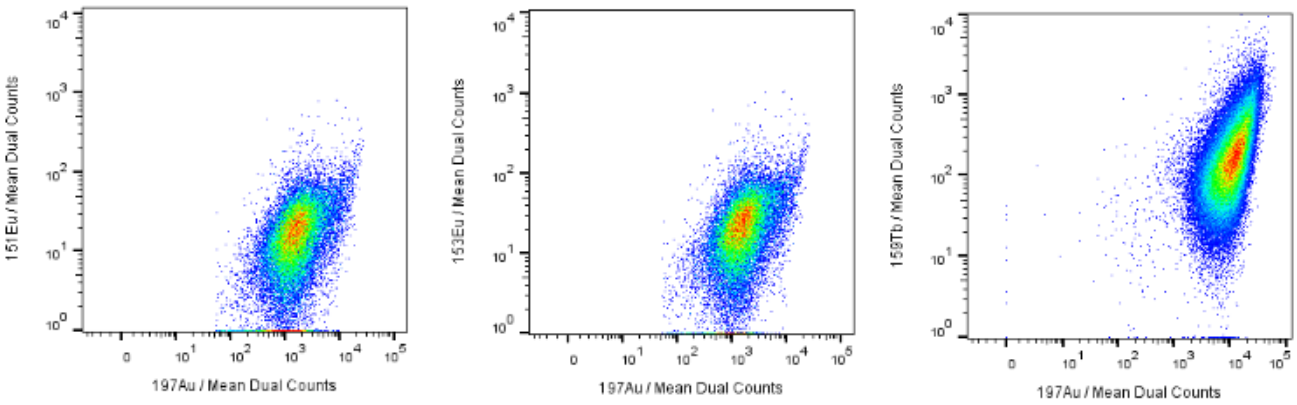


Figure 3.25 – Dot plots of the mean dual counts of $^{151/153}$Eu/^{159}Tb vs. ^{197}Au from single HeLa cells containing EuQuin$_2$S-AuNPs (4h incubation at 0.3 nM) and TbS-AuNPs (16 h incubation at 0.3 nM) after NP treatment. Each dot represents a single cell and the increasing red colour represents an increase in density of dots.

3.6.4 Comparison of the Average Number of Lanthanide Complexes per NP from Solution mode, in Cells and ICP-MS

The average number of EuQuin$_2$SH and TbSH complexes per NP determined from CyTOF in solution mode and in cells was compared to those determined by ICP-MS in solution, which was previously shown in chapter 2. For EuQuin$_2$S-AuNPs, an average from analysis of ^{151}Eu and ^{153}Eu isotopes was taken. This is shown in Figure 3.26 below.

For both complexes, the values determined from solution mode and ICP-MS are in very close agreement. When CyTOF is run in solution mode, the instrument's data output is effectively identical to the ICP-MS instrument used. The only difference is that the LnAuNPs have not been digested before analysis, like in ICP-MS. The agreeability of values gives further confidence in the accuracy of the TE's calculated for each metal isotope.

There is a slight discrepancy between the values determined in cells compared to in solution mode and ICP-MS, with a higher number of lanthanide complexes per NP determined in cells (Figure 3.26). With this determination method, the LnAuNPs are still within the complex biological cellular matrix when ionised, which could affect the TE of each

metal isotope. Further studies would be needed to investigate whether this hypothesis is true.

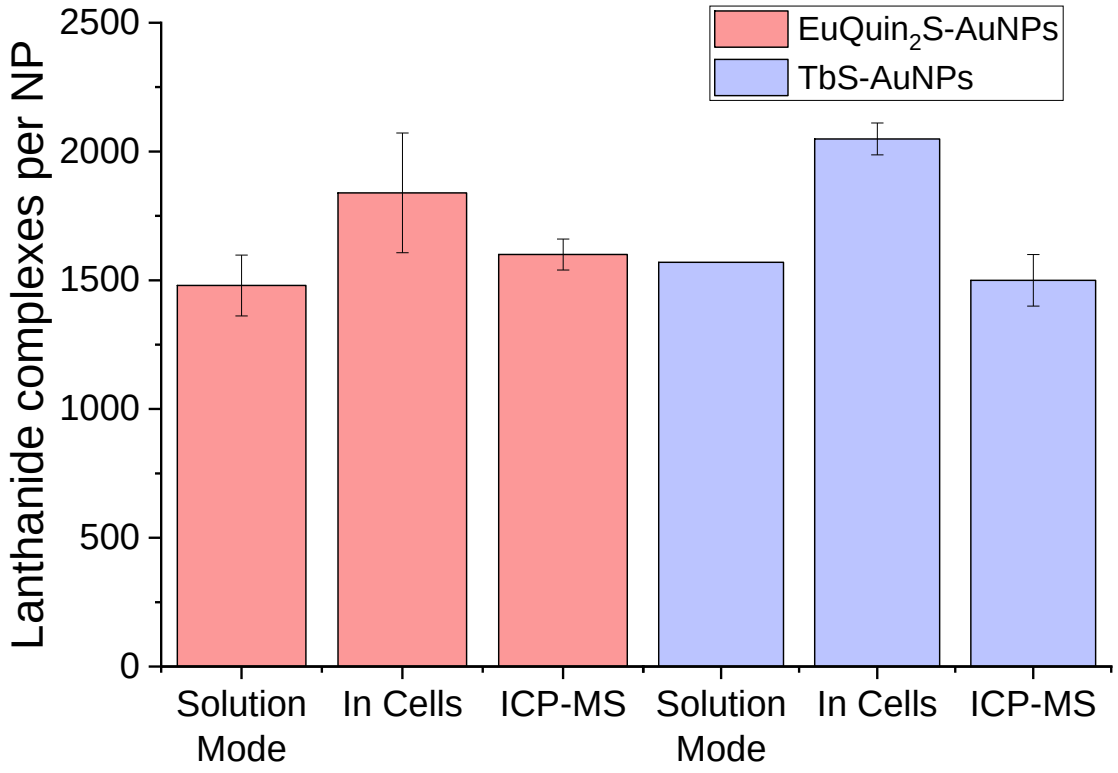


Figure 3.26 – The average number of $EuQuin_2SH$ (red) and TbSH (blue) complexes per NP determined using CyTOF in solution mode and in HeLa cells, and ICP-MS. For $EuQuin_2S$-AuNPs, an average of the ^{151}Eu and ^{153}Eu isotopes was taken. Error bars represent the SD from 3 repeat measurements for in cells and ICP-MS and the discrepancy between ^{151}Eu and ^{153}Eu isotopes for solution mode.

Here, we have used CyTOF for ratiometric detection of lanthanide and gold isotopes to characterise lanthanide gold nanoparticles and the relative number of lanthanide complexes that coat each AuNP, with comparable data output to conventional ICP-MS methods. One potential application for this detection would be to increase the limit of detection of LnAuNPs with CyTOF by up to 2 orders of magnitude. For example, with our $EuQuin_2S$-AuNPs, we have shown the Au:Eu ratio to be approximately 115. If the number of $EuQuin_2SH$ complexes per AuNP is reliably determined, when the limit of detection is reached for ^{197}Au, the concentration of $^{151/153}Eu$ isotopes would not be reached for an

intracellular NP concentration of 115-fold higher. This would allow the study of cells containing approximately 500,000 EuQuin$_2$S-AuNPs per cell.

3.7 Studying the Heterogeneity of EuQuin$_2$S-AuNP Uptake in HeLa Cells

CyTOF was used to study the heterogeneity of EuQuin$_2$S-AuNP uptake in HeLa cells at incubation times of 4 and 16 hours at a EuQuin$_2$S-AuNP concentration of 0.3 nM. After gating to remove doublet events and dead cells, the number of EuQuin$_2$S-AuNPs per cell was determined through calibration of the instrument and the number of EuQuin$_2$S-AuNPs in each cell in a given population was plotted as a histogram with a bin size of 52. At a 4-hour incubation time, a total of 38984 HeLa cells were studied and EuQuin$_2$S-AuNP uptake was highly heterogeneous with a mean and median of 680 and 587 EuQuin$_2$S-AuNPs per cell respectively and a standard deviation of 380 (Figure 3.27). A log-normal distribution appears to fit the data excellently, suggesting this is the best description of EuQuin$_2$S-AuNP uptake heterogeneity in HeLa cells at a 4-hour incubation.

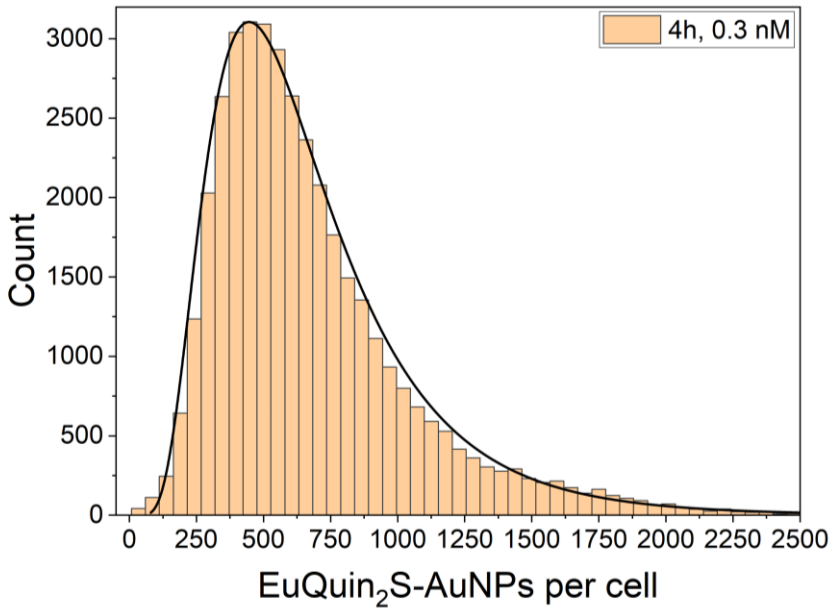


Figure 3.27 – Histogram of the number of EuQuin$_2$S-AuNPs per HeLa cell after a 4h incubation at a concentration of 0.3 nM, analysed by CyTOF. Count (y axis) refers the number of cells in each bin corresponding to its NP content. A total of 38984 live, single cells were studied. Bin size = 52. Line curve shows fit to the data using a log-normal distribution. Sample representative of 3 independent repeats.

To further analyse the distribution of nanoparticles, the data was plotted as a box plot (Figure 3.28). The 25-75% interquartile range (IQR) was 420-832 NPs per cell, meaning that 25% of cells contained less than 420 NPs per cell, and 25% of cells contained more than 832 NPs per cell.

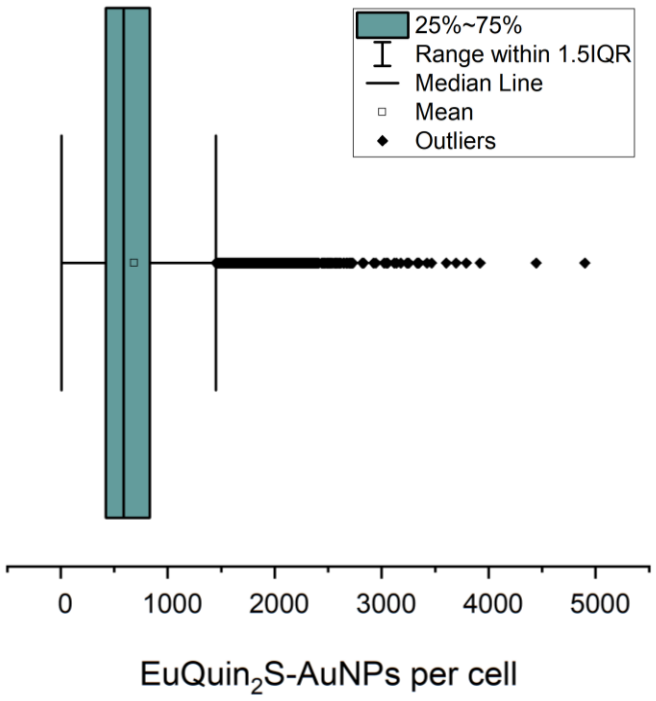


Figure 3.28 – Box plot of distribution of $EuQuin_2S$-AuNPs in a HeLa cell population after a 4h incubation at a concentration of 0.3 nM, analysed by CyTOF. A total of 38984 live, single cells were studied. Sample representative of 3 independent repeats.

At a 16-hour incubation, a total of 122156 HeLa cells were studied and the mean and median number of $EuQuin_2S$-AuNPs per cell was 1042 and 945, with a standard deviation of 522 and a log-normal distribution appearing to fit the data excellently (Figure 3.30). The distribution of nanoparticles is further shown in the box plot in Figure 3.29. The 25-75% IQR was 700-1280 NPs per cell, meaning that 25% of cells contained less than 700 NPs per cell, and 25% of cells contained more than 1280 NPs per cell.

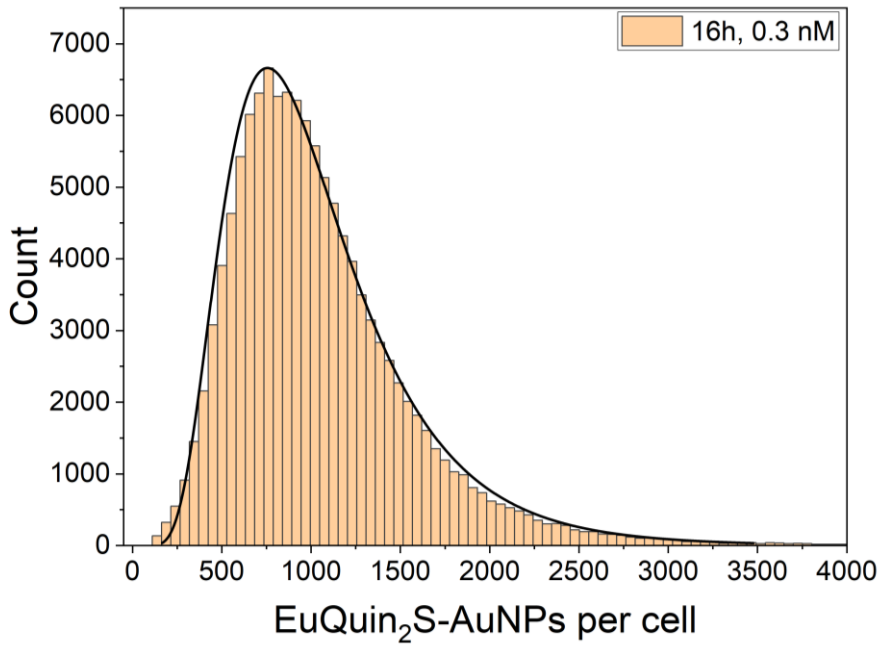


Figure 3.30 - Histogram of the number of $EuQuin_2S$-AuNPs per HeLa cell after a 16h incubation at a concentration of 0.3 nM, analysed by CyTOF. Count (y axis) refers the number of cells in each bin corresponding to its NP content. A total of 122156 live, single cells were studied. Bin size = 52. Line curve shows fit to the data using a log-normal distribution. Sample representative of 3 independent repeats.

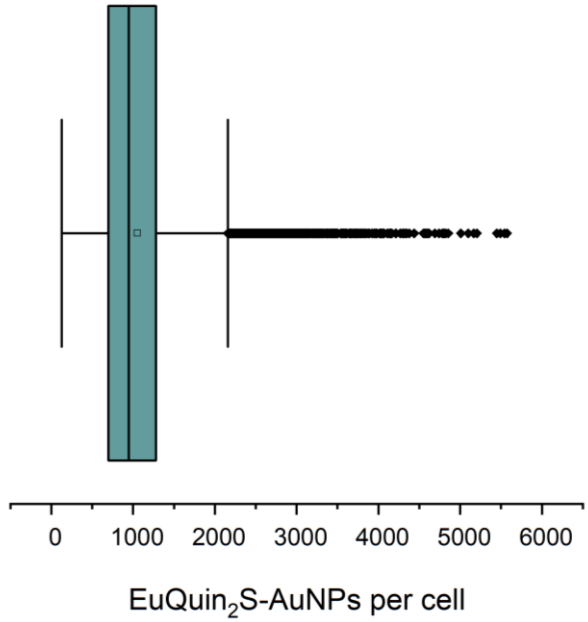


Figure 3.29 - Box plot of distribution of $EuQuin_2S$-AuNPs in a HeLa cell population after a 16h incubation at a concentration of 0.3 nM, analysed by CyTOF. A total of 122156 live, single cells were studied. Sample representative of 3 independent repeats.

Our results from statistically analysing the distribution of nanoparticles produce similar results from studies by Jeynes *et al.*[27] and Summers *et al*.[26] Jeynes had shown that the uptake of 30 nm peptide-coated gold nanoparticles followed a log-normal distribution when

normalising the mass of each individual cell after an incubation time of 48 hours, but used only a small sample size (≥ 55 cells analysed for each sample). Summers show nanoparticle uptake is best described by an over-dispersed Poisson distribution highly similar to a log-normal distribution after a 24-hour incubation. These previous studies both used long incubation times to eliminate the effects of the cell cycle on the distribution of nanoparticles and involved complicated computational methods to analyse their data. Here, the large heterogeneity in $EuQuin_2S$-AuNP uptake in HeLa cell populations is shown using CyTOF; a highly sensitive technique capable of detecting cells containing as few as 1 NP, or even 0. These data at shorter incubation times of 4h and 16h show that cell division and the cell cycle do not have a large effect on the distribution of nanoparticles in a cell population over these time periods.

3.8 Assessing the Nanoparticle Content of HeLa Cells Over Multiple Proliferation Cycles

CyTOF is next used to quantify the NP content of HeLa cells up to 96 hours after treatment with $EuQuin_2S$-AuNPs. It was hypothesised that due to cell division and potential export of our lanthanide AuNPs by processes such as exocytosis, NP content will reduce over time. In theory, CyTOF should be an excellent technique to study this due to its high-throughput, single cell nature to assess NP inheritance between daughter cells, high sensitivity to detect small changes in NP content, ability to distinguish between live and dead cells, as well as cells that do not contain any $EuQuin_2S$-AuNPs at all.

In addition, a proliferative tracing dye, Anti-FITC, is incorporated into the experiments that indicates the number of times that each cell has divided at each time point of the experiment. Proliferative tracing in cytometry experiments has been shown to be more accurate than manual cell counting as it removes counting biases due to either cell loss during harvesting or the presence of cellular debris or cell clumps.[74] It also informs whether

all cells within a population are dividing, whereas cell counting only provides an average number of divisions over the whole population. Anti-FITC proliferative tracing was first described by Good *et al.* in 2019,[75] taking inspiration from carboxyfluorescein succinimidyl ester (CFSE) fluorescence based proliferative tracing in flow cytometry. Its precursor, carboxyfluorescein diacetate succinimidyl ester (CFDA-SE) is cell-permeable and readily taken up by cells[76] where intracellular esterases cleave the acetate groups to form CFSE, which is not cell-permeable and therefore is retained within the cytoplasm of the cell.[77, 78] During cell division, partitioning of the dye is 50% between daughter cells and the quantity of CFSE, a highly fluorescent molecule, detected within cells indicates the amount of proliferation that has occurred.[79] Good *et al.* hypothesised that the structural similarity between CFSE and fluorescein isothiocyanate (FITC) would result in successful binding of an anti-FITC antibody to CFSE within cells. When metal isotopes were conjugated to anti-FITC antibodies, they were able to track changes in CFSE content within T-cells, monocytes and dendritic cells, with 50% partitioning observed and detection up to a total of 7 proliferation cycles.

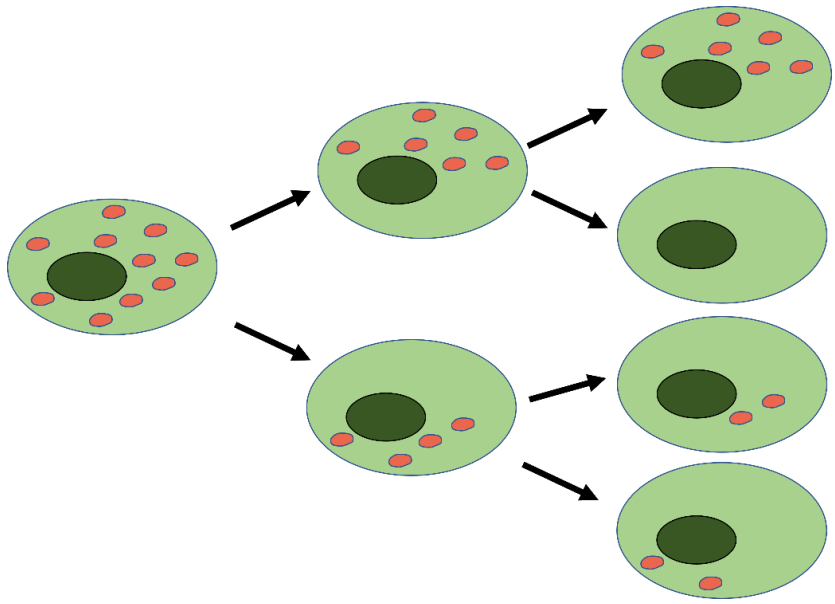


Figure 3.31 - Schematic representation of experiment scope. We set out to label HeLa cells with $EuQuin_2S$-AuNPs and leave the cells in culture and use mass cytometry to determine the NP content of single cells after multiple proliferation cycles, using an in-built proliferation assay. We hypothesise that this experiment will provide information on NP inheritance heterogeneity as well as the extent of NP export by processes such as exocytosis.

3.8.1 Optimisation of Anti-FITC Staining for Monitoring Proliferation

We first optimised the staining of HeLa cells with CFSE/Anti-FITC to determine the number of proliferation cycles during the experiments. Cells were stained with CFSE and methanol, saponin and Maxpar Fix and Perm Buffer were tested as suitable permeabilisation buffers to allow a anti-FITC antibody (Fluidigm, FIT-22), conjugated with ^{160}Gd for its detection in CyTOF, to enter cells during incubation. A schematic representation is shown below and details of the protocol used can be found in 3.10.10.1.

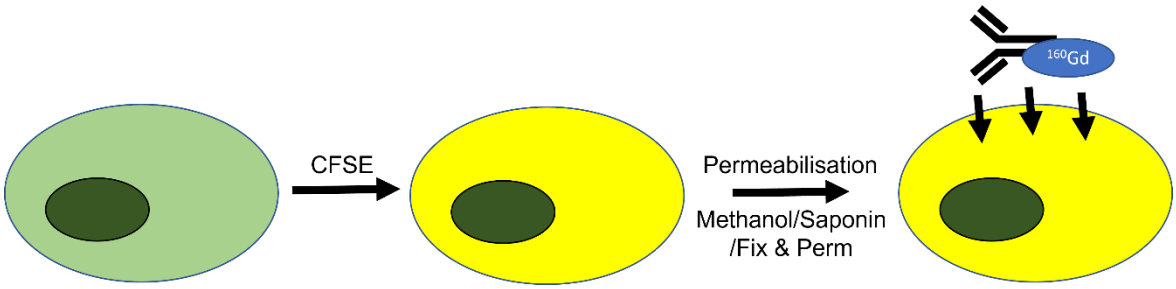


Figure 3.32 – Schematic representation of staining cells with CFSE/anti-FITC to monitor HeLa cell proliferation with mass cytometry. First HeLa cells are stained with CFSE, then the cell membrane is permeabilised to allow the entry of an anti-FITC antibody conjugated with ^{160}Gd metal isotopes that are detectable with mass cytometry.

Saponin permeabilisation led to the highest median value of mean dual counts in the ^{160}Gd channel, suggesting high anti-FITC antibody uptake (Figure 3.33) and was therefore selected as the permeabilisation buffer. An additional advantage of using saponin is that it's a mild permeabilisation technique that creates holes around 100 Å in size in the membrane so should not allow any NP escape from cells.[80] Next, a titration using anti-FITC antibody dilutions of 1:200, 1:100 and 1:50 revealed that 1:50 led to the most optimal ^{160}Gd counts (Figure 3.33).

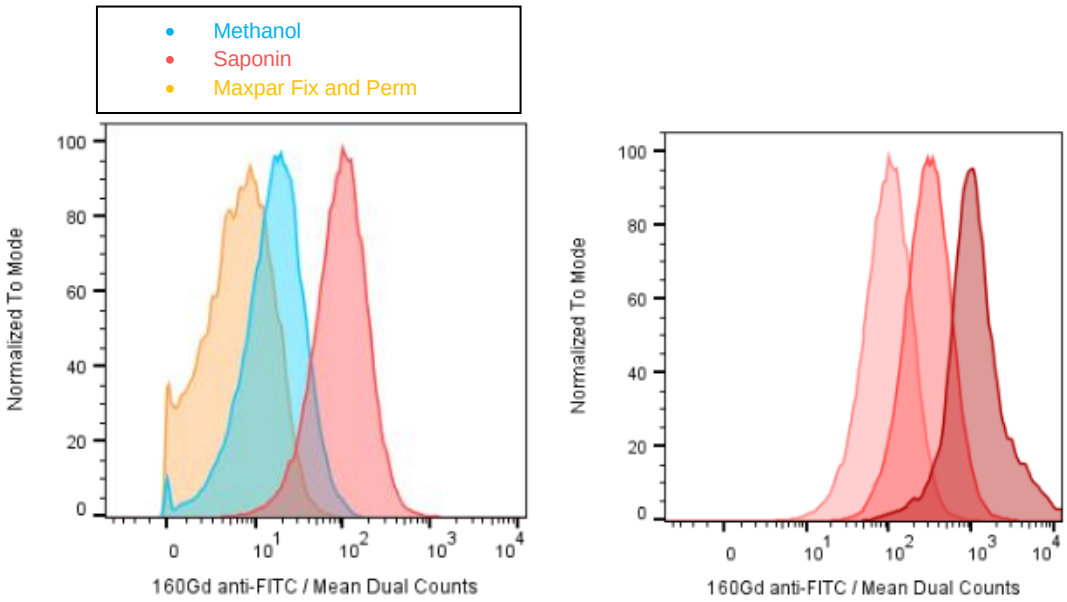


Figure 3.33 - Saponin permeabilisation at 1:50 dilution most optimal conditions for anti-FITC staining. Histogram of ^{160}Gd mean dual counts from a ^{160}Gd conjugated anti-FITC antibody using methanol, saponin and Maxpar Fix and Perm permeabilisation buffers at an antibody dilution of 1:200 (left); histogram of ^{160}Gd mean dual counts from ^{160}Gd conjugated anti-FITC antibody at 1:200, 1:100 and 1:50 dilutions using saponin permeabilisation (right).

3.8.2 Assessment of EuQuin$_2$S-AuNP Content in HeLa Cells Over Multiple Proliferation Cycles

3.8.2.1 Initial Cellular Uptake of EuQuin$_2$S-AuNPs

HeLa cells were treated with EuQuin$_2$S-AuNPs for 4 hours at a concentration of 0.3 nM and then stained with CFDA-SE and cultured for a further 24, 48, 72 and 96 hours. Culture media was replaced every 24 hours to remove any EuQuin$_2$S-AuNPs expelled from cells. At each time point, cells were then stained with ^{160}Gd conjugated anti-FITC antibody and their NP content and proliferation was analysed by CyTOF. After gating, at least 50,000 single cell events were recorded for each time point. After the 4-hour treatment, 100% of cells contained EuQuin$_2$S-AuNPs and the median uptake was 585 NPs per cell (Figure 3.34).

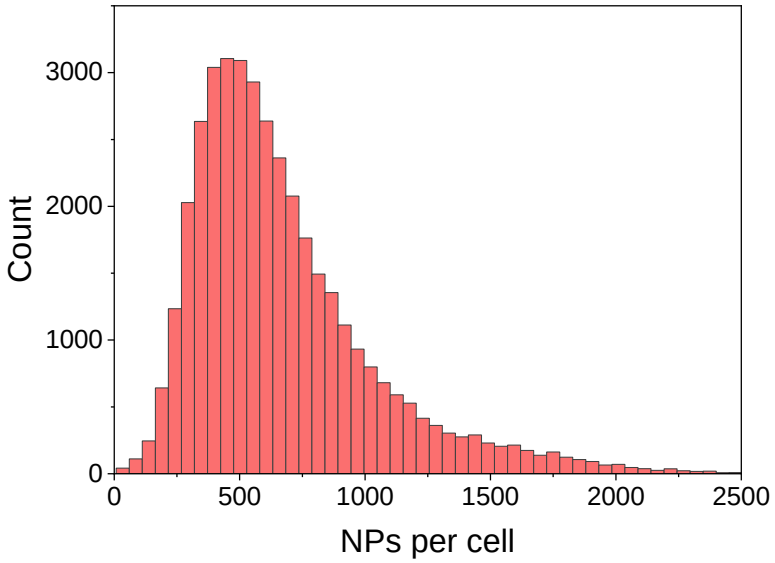


Figure 3.34 - Initial EuQuin$_2$S-AuNP uptake after 4-hour treatment at a concentration of 0.3 nM. Linear histogram of the number of EuQuin$_2$S-AuNPs per cell (right). Count (y axis) refers the number of cells in each bin corresponding to its NP content.

3.8.2.2 Effect of Proliferation Dye on EuQuin$_2$S-AuNP Content

To assess whether the proliferative tracing dye, CFSE, contained within cells or subsequent labelling with Anti-FITC in preparation for CyTOF experiments had an effect on EuQuin$_2$S-AuNP content within cells, an unstained control was also analysed under the exact same conditions. The median number of NPs per cell decreased similarly in cells treated with CFDA-SE vs. an unstained control (Figure 3.35), indicating that proliferative tracing had no effect on EuQuin$_2$S-AuNP content. Here, the median number of EuQuin$_2$S-AuNPs per cell is shown on a logarithmic scale because the increase in the number of cells is exponential during cell proliferation.

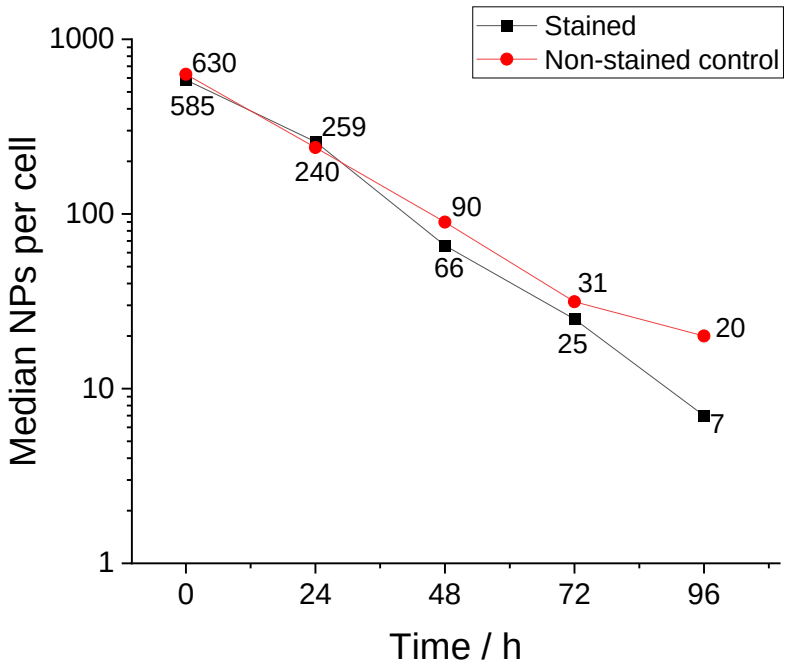


Figure 3.35 - EuQuin$_2$S-AuNP depletion unaffected by CFDA-SE staining of HeLa cells. Stained vs. non-stained control median EuQuin$_2$S-AuNP uptake in HeLa cells treated with NPs for 4 hours at a concentration of 0.3 nM, at 0, 24, 48, 72 and 96 hours after NP treatment. Shown on a logarithmic scale.

3.8.2.3 Investigating Cell Death

There was no increase in cell death over the incubation period, with 98-99% of cells studied at each timepoint found to be alive, and the NP content of dead cells was very similar to live cells at each time point (Table 3.4), suggesting that cell death is random throughout the experiment and not caused by $EuQuin_2S$-AuNP toxicity. The only large discrepancy between the number of $EuQuin_2S$-AuNPs per cell in live and dead cells was after the initial incubation period, where there was a median of 585 $EuQuin_2S$-AuNPs per cell in live cells and 242 NPs per cell in dead cells. This may be due to cell death during the incubation period that would prevent any further uptake of NPs in these cells.

Table 3.4 - The percentage of dead cells and their NP content at each time point.

Time / h	Dead cells / %	Median NPs per cell (dead)	Median NPs per cell (live)
0	1	242	585
24	2	242	259
48	1	76	66
72	1	40	25
96	2	13	7

3.8.2.4 Determination of the Number of Proliferation Cycles

The proliferation of cells was monitored by anti-FITC staining and the median ^{160}Gd intensity at each time point was studied (Figure 3.36). Anti-FITC signal decreased across the whole cell population between each time point, meaning all cells were dividing for the duration of the experiment. At 0, 24, 72 and 96 h timepoints, each population appeared log-normally distibuted (i.e. normally distributed on the logarithmic scale shown), however at 48 h there was a minor shoulder in the anti-FITC histogram. This could suggest that some cells had divided at a slightly faster rate than others between 24 and 48 hours, or it may be an artefact in the data. At least 1 cell division occurred between each time point, and the proliferation rate was highest between 24 and 48 hours. The average number of cell divisions was

calculated using the median intensity of ^{160}Gd mean dual counts for each timepoint. It was found that an average of 5.8 cell divisions occurred over 96 hours (Table 3.5), indicating the average doubling time was 16.6 hours. This is in agreement to a doubling time of 16.2 ± 1.7 h found by Kumei *et al.*,[81] though doubling times as high as 24.2 h have also been reported,[82] but many experimental factors such as cell density, pH and FBS variability can affect proliferation rates.[83] The number of cell divisions over time was plotted as a 'growth curve' (Figure 3.36) to represent the rate of growth over the experiment. Growth curves of cells in culture typically consist of a lag phase, where cells are adjusting to the culture conditions and begin to divide; exponential phase where cells divide rapidly, and saturation phase where cell division begins to slow due to high cell density and insufficient space in the culture dish to divide.[84] From this data, the lag phase is evident but appears to be short, as cell division is almost as fast between 0 to 24 hours and the exponential phase. It is worth noting that after the 72 hour timepoint, the culture dishes were reaching confluency, so cells were reseeded at a lower density to allow further cell proliferation. This may explain why no saturation phase is observed in this experiment.

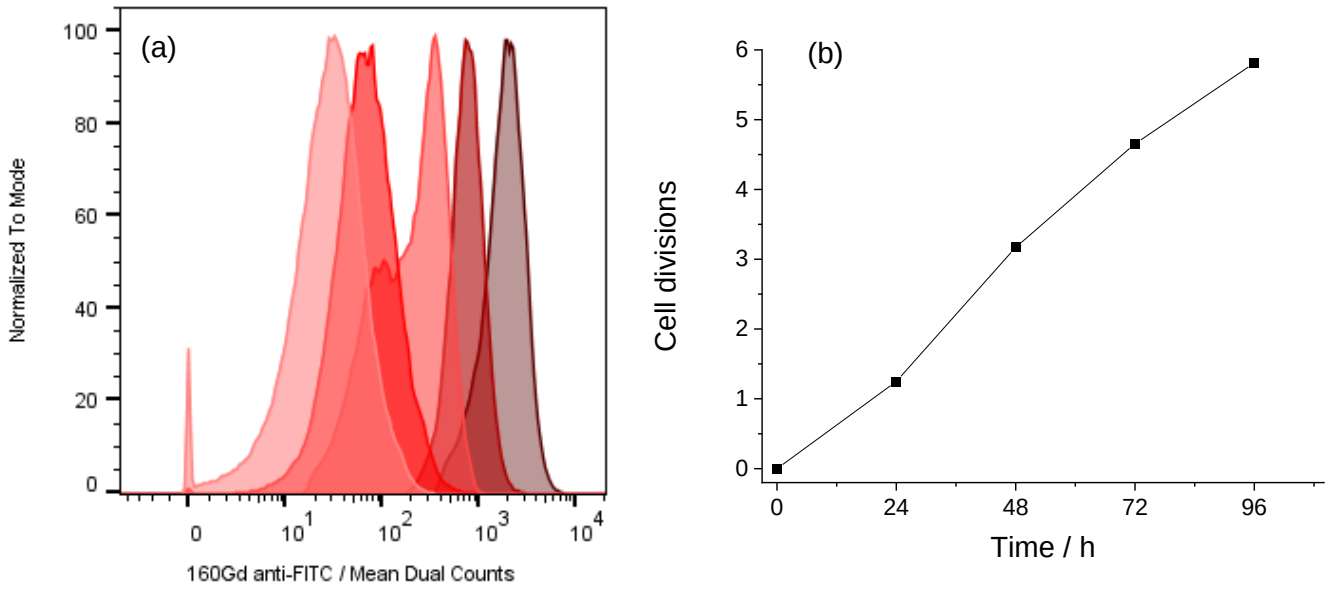


Figure 3.36 - Anti-FITC proliferative tracing reveals the number of cell divisions at 24, 48, 72 and 96 hours. (a) Histogram of ^{160}Gd mean dual counts from a ^{160}Gd conjugated anti-FITC antibody at 0, 24,48, 72 and 96 hours, (b) the number of cell divisions calculated from the median intensity of ^{160}Gd mean dual counts at each time point.

Table 3.5 - ^{160}Gd median intensity values from anti-FITC proliferation marker and the average number of cell divisions calculated at each time point.

Time / h	^{160}Gd anti-FITC Median / Intensity	^{160}Gd Median decrease from previous timepoint (T_1/T_2)	Average no. of cell divisions
0	1873	N/A	0.0
24	750	2.5	1.2
48	195	3.8	1.9
72	65.8	3.0	1.5
96	28.4	2.3	1.2
		Total	5.8

The number of cell divisions after each timepoint was also determined from manual cell counts from the stained and unstained samples. An average of 5.1 cell divisions was observed, similar to the total number average number of cell divisions determined from the proliferation dye (Figure 3.37). There was quite a large difference between the number of cell divisions calculated from the stained and unstained control, despite their similar reduction in NP signal.

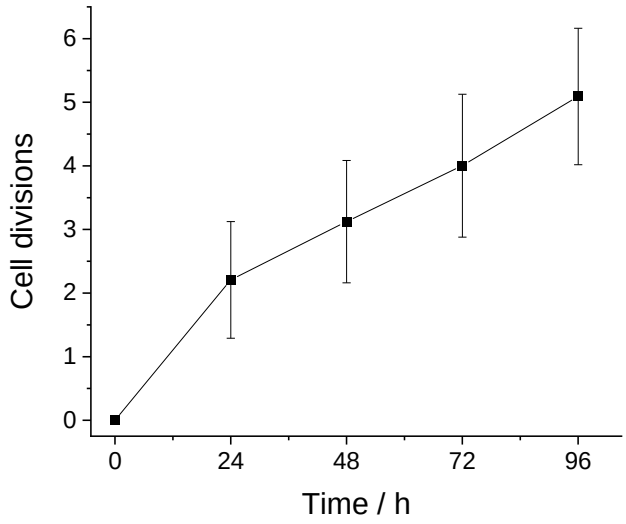


Figure 3.37 - The number of cell divisions calculated from manual cell counting at each timepoint from stained and unstained control samples. Data plotted is mean ± range from each sample.

Due to the nature of the experimental setup, there are likely additional sources of uncertainty in determining the number of cell divisions from cell counting. For each timepoint, a separate culture dish was used so that the cells collected at each timepoint did

not need to be harvested and reseeded when cells from earlier time points needed to be collected. This would mean that any small discrepancy in the original number of cells in each flask (which can only be estimated) could have a large effect on the number of cell divisions. This uncertainty does not apply to the proliferation dye method and the number of cell divisions determined from this method was used for all further analysis.

3.8.2.5 Comparing the Rate of NP Depletion with Cell Proliferation

The number of NPs per cell at each time point can be theoretically estimated based on the average number of cell divisions that occurred during the experiment. If NP depletion is a result of cell division only, then the observed median NPs per cell would be expected to be similar to the theoretical values. If NP depletion is a result of cell division and exocytosis, then the observed median NPs per cell would be lower than the theoretical values.

In this experiment with $EuQuin_2S$-AuNPs, the observed and theoretical median NPs per cell at each time point are in very close agreement (Figure 3.38). The reduction in $EuQuin_2S$-AuNPs per cell follows the rate of proliferations similarly at all time points. After 96 hours, an average of 5.8 cell divisions occurred compared to 6.2 halving's of the median NPs per cell over this time. This data suggests that $EuQuin_2S$-AuNP content is decreased predominantly by cell division and not exocytosis. Similar results were obtained when the mean number of $EuQuin_2S$-AuNPs per cell was used. This data is shown in the appendix (3.12.5).

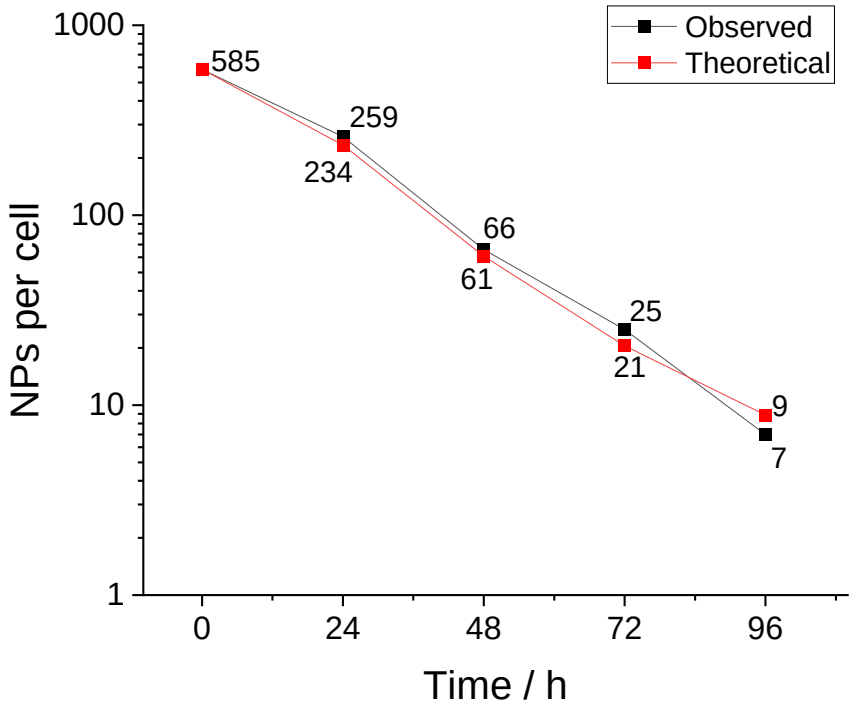


Figure 3.38 – Reduction in EuQuin$_2$S-AuNP content occurs due to cell division. Observed (black) median NPs per cell at each time point vs. theoretical (red) NPs per cell calculated from the number of cell divisions at each time point.

This experiment was carried out three times and the median number of EuQuin$_2$S-AuNPs per cell from each repeat is shown in Figure 3.39 below. Median values were normalised to an original NP content per cell of 585 so the results are comparable. Only minimal differences are observed at each time point, suggesting that the NP content shown in Figure 3.38 is representative of each experiment. It is again worth noting that factors such as seeding density effect proliferation rates, so slight discrepancies in NP content may be expected.

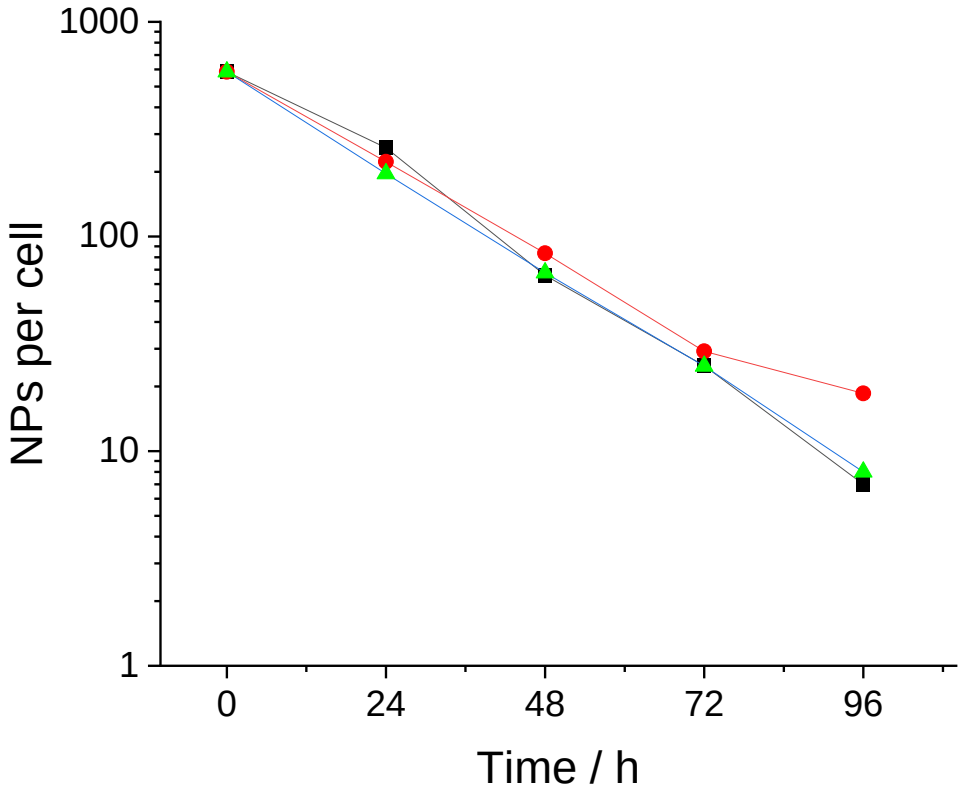


Figure 3.39 – The median number of EuQuin$_2$S-AuNPs per cell at 0, 24, 48, 72 and 96 h timepoints after a 4 h incubation at a NP concentration of 0.3 nM, in 3 different experiments. As we have shown that there is variability in absolute NP quantification by CyTOF analysis when measurements are taken on different days, the absolute number of EuQuin$_2$S-AuNPs per cell at 0 h was normalised to 585 for more comparable analysis.

This experimental data suggests that the reduction of EuQuin$_2$S-AuNPs in HeLa cells over 96 hours – a time frame in which cells divided on average 5.8 times – was predominantly due to cell division. There is little evidence for any measurable rate of exocytosis or export of NPs by cells by any other method, agreeing with previous studies by Bourquin[47] and Dawson and co-workers[19, 46] that cell division is the major driver of NP signal. Our work is the first to monitor NP depletion at the single cell level over multiple proliferation cycles with an in-built proliferation marker incorporated into the experiment. It also continues for the longest time period, except for the study Gunduz *et al.* which focussed on continuous dosing.[48] CyTOF has much higher sensitivity to flow cytometry and other techniques such

as ICP-MS used in previous studies, allowing the detection of small changes in NP signal and the detection of as little as 1 NP per cell. However, there are caveats to this experiment which must be considered. The cell media was replaced in each sample at 24-hour intervals, but reuptake of NPs that may have been expelled between each timepoint cannot be ruled out. NP reuptake is poorly understood but has been shown to be dependent on the physicochemical properties of NPs.[44] More frequent cell media exchange and analysis of former cell media for NP content, potentially using the CyTOF instrument in solution mode, may provide insight on this process. Furthermore, simultaneous analysis of cells at each time point by TEM may provide further mechanistic information on the intracellular trafficking of $EuQuin_2S$-AuNPs. For example, if escape to the cytosol has occurred, this may explain the apparent lack of exocytosis. Additionally, the uncertainty in monitoring the proliferation with the method deployed in this work is not known. The original study by Good *et al.* remains the only published work with this proliferation dye to date so there is a lack of knowledge in the associated errors. Independent repeats would reveal how accurate proliferation can be traced but were not possible due to time restraints in this work.

3.8.2.6 Heterogeneity of NP Inheritance Between Daughter Cells

CyTOF was then used to study the heterogeneity of NP load inheritance in daughter cells after cell division over multiple proliferation cycles at high throughput. It was first found that even after 24 hours, 6% ± 4% of cells did not contain any NPs at all. The number of cells containing $EuQuin_2S$-AuNPs steadily dropped to 94% ± 3.6% after 24 hours, 83% ± 4% after 48 hours, 74% ± 10% after 72 hours and 66% ± 7% after 96 hours. After 24 hours, the median intensity of ^{160}Gd was 654 in cells containing no NPs compared to 750 in the whole population, which suggests that cell division is not significantly different. It was unexpected to observe some cells already containing no NPs at this point. However, as shown in Figure 3.34, the initial uptake of NPs is highly heterogeneous, with some cells taking up far less than the median average of 585 NPs per cell. For example, the median number of

$EuQuin_2S$-AuNPs per cell was 150 in the 5th percentile of cells. As NP inheritance has been shown to be highly heterogeneous in previous studies,[47, 85] it is likely that this result demonstrates that some daughter cells do not inherit any vesicle-containing NPs. A study by Xiong *et al.* found that the endocytic uptake of QDs led to only 80% of cells containing detectable levels QDs.[86] This reduced to 40% after approximately 3 cell divisions, and less than 10% after 5 cell divisions, although it is worth noting that flow cytometry was used to detect fluorescence, which as previously discussed is far less sensitive than CyTOF, so it is possible that cells still contain QDs, but at an undetectable level.

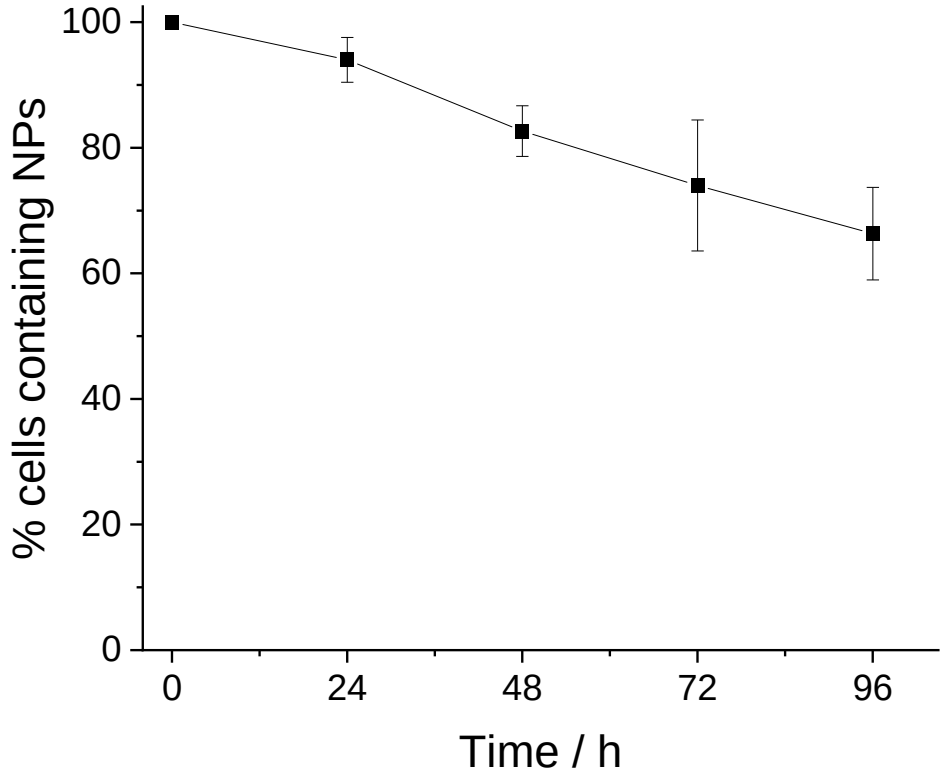


Figure 3.40 – The percentage of cells containing $EuQuin_2S$-AuNPs at each time point. Shown is the mean average ± SD from 3 repeat experiments.

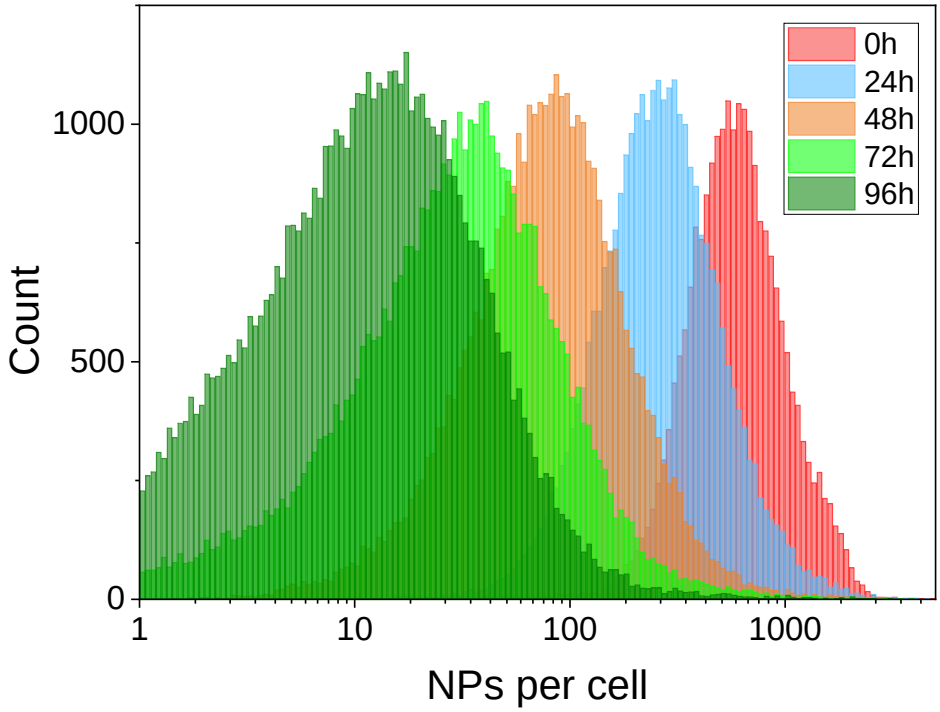


Figure 3.41 – Histogram overlay of the number of EuQuin$_2$S-AuNPs per cell in each cell population at each time point. Shown on a logarithmic scale for clearer visualisation of the wide dynamic range of EuQuin$_2$S-AuNP content.. Count (y axis) refers the number of cells in each bin corresponding to its NP content.

Next, we studied the heterogeneity in NP inheritance in cells containing NPs. The histograms of the number of EuQuin$_2$S-AuNPs in each cell population are shown in Figure 3.41. A reduction in the number of NPs per cell is observed across the whole population, as to be expected. The coefficient of variation (CV) has previously been shown by Lijster *et al.* to be an accurate means of measuring the asymmetry of nanoparticle inheritance in daughter cells.[87] The CV of a population can be calculated using the equation below:

$$CV = \frac{Standard\ Deviation}{Mean}$$

As equal partitioning of the proliferation marker used has been previously shown,[75] there should not be a large increase in CV over the time course of the experiment, as shown with CFSE proliferation dyes.[74] We therefore compared the CV of EuQuin$_2$S-AuNPs and the ^{160}Gd channel to assess NP inheritance heterogeneity (Figure 3.42). CV increased from

95% ± 32% at 0 h to 344% ± 78% at 96 h, compared to increase from 83% to 160% over the same time period for the proliferation marker.

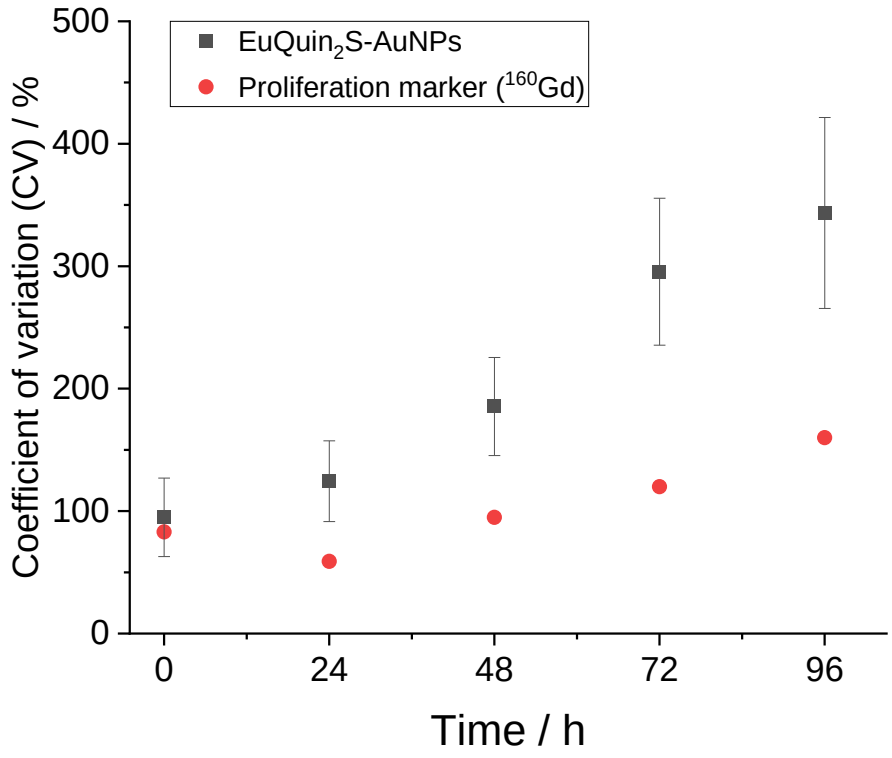


Figure 3.42 – Increase in coefficient of variation (CV) of $EuQuin_2S$-AuNPs and proliferation marker at 0, 24, 48, 72 and 96 h timepoints. Error bars represent SD from 3 repeat experiments.

The 3.6-fold increase in CV for $EuQuin_2S$-AuNPs compared to a 1.9-fold increase in CV for the proliferation marker suggests that NP inheritance is highly heterogeneous and is in agreement with increases in CV shown in with asymmetric theoretical modelling shown by. Lijster *et al.*[87] Due to the large standard deviation in CV, it is difficult to determine whether inheritance heterogeneity increases at a higher rate after a certain number of cell divisions.

3.9 Conclusion and Future Work

In this chapter, it was shown the that the high sensitivity of CyTOF can cause challenges with the acquisition of single cell data when analysing AuNP treated cells. This is due to free NPs in solution not fully removed by conventional washing procedures that would usually be undetected by less sensitive instrumentation. Two protocols have been established in this work for sample preparation that overcome these issues by removing

free NPs sufficiently: extra centrifugation steps in 5 mL Falcon™ Round-Bottom Polystyrene Test Tubes and removing the supernatant by inverting the tube, or the use of FACS cell sorting.

It was shown that the use of a cell permeabilisation buffer to stain cells with Cell-ID^{TM} intercalator-Ir does not affect the number of NPs associated with each cell. TEM was used to show that cell associated EuQuin$_2$S-AuNPs are located inside cells, within endosomes, suggesting that EuQuin$_2$S-AuNPs are taken up by endocytosis mechanisms. Further studies with CyTOF could reveal the specific endocytosis pathways and could be combined with TEM to reveal information on the intracellular locations of EuQuin$_2$S-AuNPs.

I have developed a solution-based calibration method that can be run on the day of each experiment with the NP batch to be analysed, for determining the TE of lanthanide coated gold nanoparticles in order to determine the average number of NPs per cell from CyTOF analysis. This TE agreed with the mean dual counts observed from 1 NP detected in event mode. I then showed that the number of EuQuin$_2$S-AuNPs and TbS-AuNPs per cell determined by CyTOF was in close agreement to simultaneous analysis by ICP-MS, validating our use of CyTOF as an accurate NP uptake quantification method. This also revealed that TbS-AuNPs were taken up by cells more readily than EuQuin$_2$S-AuNPs, attributed to the shorter chain length of the lanthanide complex.

Excellent reproducibility of NP uptake quantification was shown with replicated samples ran on the same day, but then revealed a much larger disparity of EuQuin$_2$S-AuNP uptake quantification by CyTOF when analysing EuQuin$_2$S-AuNPs synthesised from different citrate AuNP batches, on different days over a time period of 8 months. Although this could be due to biological and experimental factors, several sources of uncertainty with our method of determining NP uptake were discussed that could be attributed to the difference in uptake quantification, such as uncertainty with calculating the concentration of NPs and the number of Au atoms per NP from TEM image analysis. These factors could contribute

to uncertainty of the TE of the NP species, which was found to have a much greater variance than the TE calculated from the tuning solution the instrument uses for internal calibration. This uncertainty should be considered when comparing uptake quantification of NP species separately synthesised and analysed on different days. A more systematic approach in studies to determine the true uncertainty associated with CyTOF uptake quantification is needed, alongside similar studies with other techniques. Additionally, more precise synthesis of AuNP to reduce batch-to-batch variability would significantly reduce the uncertainty in measurements. Microfluidic approaches to AuNP synthesis are in development.[88]

Ratiometric detection of gold:europium/terbium was demonstrated to characterise the number of lanthanide complexes attached to each AuNP and we showed dual-metal detection from a single NP species for the first time in cells. These values were in rough agreement with ICP-MS measurements and this ratiometric detection could be used to increase the limit of detecting lanthanide gold nanoparticles by 2 orders of magnitude. We were also able to show that the distribution of $EuQuin_2S$-AuNPs follows a log-normal distribution, regardless of the incubation time period, although a Kolmogorov-Smirnoff goodness of fit test was rejected when a high number of cells were studied.

Lastly, we used CyTOF to show the depletion of $EuQuin_2S$-AuNPs in HeLa cells over multiple proliferation cycles. We used an in-built proliferation assay to determine the number of times a cell has divided and correlated this with the reduction in the median number of $EuQuin_2S$-AuNPs per cell, indicating that NP depletion was due to cell division and not exocytosis of NPs. Even after an average of 5.8 cell division, we were able to detect $EuQuin_2S$-AuNPs in two thirds of cells with CyTOF, which shows good potential for their use as cellular labels in cytometry experiments, which we investigate further in chapter 4. Although there are limitations to our findings, this experimental framework has the potential to further our understanding of NP depletion and could answer important questions on

exocytosis rates. Future work could involve determining the level of uncertainty associated with the proliferation dye, as well as increasing the frequency of cell media renewal to eliminate the potential for reuptake of exocytosed NPs.

This work demonstrates CyTOF as a single cell, high throughput, quantitative technique to explore NP-cell interactions and is built on in chapter 4 as we investigate the uptake and fate of our $EuQuin_2S$-AuNP in immune cells and assess their suitability as cellular labels.

3.10 Experimental

3.10.1 HeLa Cell Culture Conditions

Human cervical cancer cell line HeLa (Catalogue no. 93021013) were grown as monolayer cultures in vented cap T75 flasks using Dulbecco's Modified Eagle Medium (DMEM, Gibco® Thermo Fisher Scientific), which was supplemented with 10% Fetal Bovine Serum (FBS), penicillin (100 U/mL) and streptomycin (0.2 µg/mL). The cells were kept at 37 °C in a humidified atmosphere with 5% CO_2 concentration.

3.10.2 Nanoparticle Treatment Conditions

Cells were seeded in a suitable culture flask, dish, or plate depending on the number of cells needed for the experiment and cultured under the conditions previously described overnight. The following day, the cell media was removed, washed twice with PBS, and a pre-mixed, pre-warmed, cell media/NP mixture (9:1) was carefully added to the culture vessel. The cells were kept under standard culture conditions for the required treatment duration before washing and preparation steps outlined in each experimental.

3.10.3 Preparation of Cells for CyTOF with Conventional Number of Washes

HeLa cells were treated with PEG-AuNPs at a concentration of 0.1 nM for 16 hours. After treatment, the cell media was removed and each well was washed three times with PBS and TrypLE Express Enzyme was added to detach the adherent cells. The cells were

transferred to 1.5 mL Eppendorf tubes, suspended in PBS and centrifuged. The supernatant was removed by aspiration and the cells were suspended in 300 µL of pre-warmed, serum-free DMEM. Cisplatin (300 µL, 10 µM) was added to each sample, mixed thoroughly and incubated at room temperature. After 5 min, pre-warmed serum containing DMEM was added. The cells were centrifuged once, the supernatant was removed by aspiration and 1 mL of BD CellFix was added and the cells were resuspended and incubated for 30 minutes at 4 °C. The cells were centrifuged and washed once with PBS by centrifugation. The supernatant was removed by aspiration and 1 mL of Iridium DNA intercalator (0.125 µM, Fluidigm inc.) in Maxpar Fix and Perm buffer (1 mL, Fluidigm inc.) and stored at 4 °C. overnight. The following morning, the cells were centrifuged, the supernatant was removed by aspiration and washed once with Maxpar Cell staining buffer and once more with water, before being resuspended in water to achieve a concentration of 500,000 cells/mL, before acquisition on the Helios CyTOF instrument.

3.10.4 Preparation of Cells for CyTOF with Washing by Centrifugation

HeLa cells were treated with PEG-AuNPs at a concentration of 0.1 nM for 16 hours. After treatment, the cell media was removed and each well was washed three times with PBS and TrypLE Express Enzyme was added to detach the adherent cells. The cells were transferred to 5 mL Falcon™ Round-Bottom Polystyrene Test Tubes, suspended in PBS and centrifuged twice. From herein, the supernatant was removed by inversion. To remove by inversion, a sheet of paper towel was first laid in the cell culture hood and the 5 mL Falcon™ Round-Bottom Polystyrene Test Tubes containing pelleted cells was tipped and pressed onto the paper towel, to ensure as much of the supernatant as possible was removed. After supernatant removal, cells were suspended in 300 µL of pre-warmed, serum-free DMEM. Cisplatin (300 µL, 10 µM) was added to each sample, mixed thoroughly and incubated at room temperature. After 5 min, pre-warmed serum containing DMEM was added. The cells were centrifuged once, the supernatant was removed and then washed

twice in cell staining buffer. The supernatant was removed and 1 mL of BD CellFix was added and the cells were resuspended and incubated for 30 minutes at 4 °C. The cells were centrifuged and washed once with PBS by centrifugation, followed by one wash with cell staining buffer. The supernatant was removed and 1 mL of Iridium DNA intercalator (0.125 µM, Fluidigm inc.) in Maxpar Fix and Perm buffer (1 mL, Fluidigm inc.) and stored at 4 °C overnight. The following morning, the cells were centrifuged, the supernatant was removed and washed twice with Maxpar Cell staining buffer and once more with water just before acquisition. The cells were then resuspended in water to achieve a concentration of 500,000 cells/mL before acquisition on the Helios CyTOF instrument.

3.10.5 Preparation of Cells for CyTOF with Washing by Fluorescence Associated Cell Sorting

HeLa cells were treated with PEG-AuNPs at a concentration of 0.1 nM for 16 hours. After treatment, the cell media was removed and each well was washed three times with PBS and TrypLE Express Enzyme was added to detach the adherent cells. The cells were transferred to 5 mL Falcon™ Round-Bottom Polystyrene Test Tubes, suspended in PBS and centrifuged. The supernatant was removed and the cells were suspended in 300 µL of pre-warmed, serum-free DMEM. Cisplatin (300 µL, 10 µM) was added to each sample, mixed thoroughly and incubated at room temperature. After 5 min, pre-warmed serum containing DMEM was added. The cells were centrifuged once, the supernatant was removed and 1 mL of BD CellFix was added and the cells were resuspended and incubated for 30 minutes at 4 °C. The cells were centrifuged, washed once with PBS and resuspended in 500 µL of FACS buffer. Cells were then sorted on a BD FACSAria™ Fusion, collecting cells in 5 mL Falcon™ Round-Bottom Polystyrene Test Tubes. The cells were then centrifuged, the supernatant removed and 1 mL of Iridium DNA intercalator (0.125 µM, Fluidigm inc.) in Maxpar Fix and Perm buffer (1 mL, Fluidigm inc.) was added and stored at 4 °C overnight. The following morning, the cells were centrifuged, the supernatant was

removed and washed once with Maxpar Cell staining buffer and once more with water. The cells were then resuspended in water to achieve a concentration of 500,000 cells/mL before acquisition on the Helios CyTOF instrument.

3.10.6 CyTOF Instrument Calibration Using Solutions of Lanthanide Gold Nanoparticles

The molar concentration of the lanthanide AuNP species of interest (TbS-AuNPs or $EuQuin_2S$-AuNPs) was determined from UV-Vis spectroscopy. The concentration was then converted to ugL^{-1} (see appendix 3.12.4) and the NPs were diluted with ultrapure water to a concentration of 100 ugL^{-1}, which was used as a stock solution to make up each calibration standard. From the stock solution, calibration standards of 0, 0.1, 0.25, 0.5, 1.0, 2.5 and 5.0 ugL^{-1} were made and mixed thoroughly. These solutions were made no more than 24 hours before instrument calibration on the CyTOF and were stored at 4 °C until their use. With the CyTOF instrument in solution mode, the mean dual counts were recorded for 2 min per calibration standard from the lowest to the highest concentration, with 2 min washing with ultrapure water in between each standard. Linear regression analysis of the linear calibration plots was used to determine the TE of each NP species every day an experiment was performed.

3.10.7 CyTOF Instrument Calibration Using Solutions of Eu^{3+}

An ionic Eu^{3+} PlasmaCal calibration standard (QMX laboratories) was used to prepare a 100 ugL^{-1} stock solution, diluted with ultrapure water. From the stock solution, calibration standards of 0, 0.1, 0.25, 0.5, 1.0, 2.5 and 5.0 ugL^{-1} were made and mixed thoroughly. Preparation and acquisition was the same as described above.

3.10.8 Preparation of Cells for ICP-MS Experiments

HeLa cells were treated with TbS-AuNPs and $EuQuin_2S$-AuNPs at a concentration of 0.3 nM for 16 hours and prepared for CyTOF analysis as described in 3.10.1. Half of the

cells from each sample were analysed by CyTOF and the other half were prepared for ICP-MS analysis. Cells were redispersed in PBS (200 µL) and transferred to glass vials. Ultrapure aqua regia (500 µL) was added and the vials were left in a fume cupboard for three days. After three days all solid material had visibly dissolved and the samples were made up to a total volume of 5 mL, transferred to polypropylene tubes (Agilent) for ICP-MS and taken for analysis at the University of Warwick.

3.10.9 Preparation of Cells for TEM

HeLa cells were treated with RPMI containing $EuQuin_2S$-AuNPs (1 nM) for 16 hours. After differentiation from THP-1 monocytes, M1 macrophages were treated with RPMI containing $EuQuin_2S$-AuNPs (1 nM) for 16 hours. Each type of cell was then washed 3 times by centrifugation to remove any nanoparticles remaining in solution, then fixed in 2.5 % glutaraldehyde solution for 90 min at 4 ^oC, then taken for processing at the Centre for Electron Microscopy at the University of Birmingham. Ultrathin sections of approximately 100 µm were mounted onto Formvar-coated 200 mesh copper grids. Samples were analysed on a JEOL 1200 EX transmission electron microscope operated at 80kV in imaging mode, acquiring images using Digital Micrograph Version 1.83.842.

3.10.10 Assessment of $EuQuin_2S$-AuNP Content in HeLa Cells Over Multiple Proliferation Cycles

3.10.10.1 CFSE/Anti-FITC Staining

The experimental was adapted from previously published protocols for CFSE and Anti-FITC staining by Quah *et al.* (Quah 2010) and Good *et al.* (Good 2019). HeLa cells were cultured as normal in DMEM (10% FBS, 1% P/S)). Cells were detached using TrypLE express, washed once with PBS, and thoroughly resuspended in 1 mL of warm DMEM at a concentration of 4 x 10^6 cells/mL in a 15 mL Corning® Centrifuge Tube. The tube was then laid horizontally and 110 µL of PBS was added to the non-wetted part of the top of the tube,

ensuring no contact was made with the cell solution. 17.6 µL of CFDA-SE (5 mM, DMSO, Stratech Scientific Ltd.) was added to the 110 µL drop of PBS and mixed by pipetting. The tube was then capped, inverted and immediately vortexed to achieve quick uniform mixing of the solution. The cells were incubated for 5 min at room temperature, then 10 mL of PBS was added and the cells were centrifuged (5 min x 300 g). The cells were then washed once more in PBS (10 mL), once in serum-free DMEM (10 mL) and resuspended in 300 µL of serum-free DMEM. 300 µL of serum-free DMEM containing cisplatin (10 µM) was then added, mixed well and incubated at room temperature for 5 minutes, DMEM (2.4 mL) was then added, the cells were then centrifuged (5 min x 300 g), then washed with Cell Staining Buffer (Fluidigm). Cells were then fixed 1 mL of BD CellFix™ (BD Biosciences), incubated for 20 min at 4 °C, and washed once with Cell Staining buffer. Cells were then transferred to 3 x 5 mL Falcon™ Round-Bottom Polystyrene Tubes and permeabilised by one of three methods: 4 °C methanol (1 mL) for 10 min on ice, in 0.2% saponin (1 mL) for 20 min at room temperature, or Maxpar Fix and Perm Buffer (1 mL) for 20 min at room temperature. Cells were then centrifuged and washed with Cell Staining Buffer. Cells were then resuspended in 50 µL of Cell staining buffer. 50 µL of Cell Staining Buffer containing ^{160}Gd-Anti-FITC (Clone: FIT 22, Fluidigm) was then added to each tube to obtain a final ^{160}Gd-Anti-FITC concentration of 1:100. Each tube was gently vortexed and incubated at room temperature for 30 min, then washed twice with cell staining buffer. Cells were then incubated with a Iridium DNA intercalator (0.125 µM, Fluidigm) in Maxpar Fix and Perm Buffer overnight at 4 °C. Cells were then washed once with cell staining buffer and resuspended in 300 µL water ready for sample acquisition.

3.10.10.2 Assessment of EuQuin$_2$S-AuNP Content in HeLa Cells Over Multiple Proliferation Cycles

5 x 10^6 cells were seeded in a T175 flask and left to adhere overnight. The following day, the cell media was removed, cells were washed twice with PBS and treated with EuQuin$_2$S-

AuNP containing DMEM (0.3 nM) for 4 hours. After 4 hours, the media was removed, cells were washed three times with PBS and TrypLE Express Enzyme was added to detach the adherent cells. After centrifugation, the cells were washed a further two times with PBS, the supernatant was removed and cells were suspended in pre-warmed DMEM and transferred to a 15 mL Corning® Centrifuge Tube. Cells were then stained with CFSE as described above in 3.10.10.1. After cells were stained with CFSE, 2 x 10^6 cells were collected in a 5 mL Falcon™ Round-Bottom Polystyrene Test Tube for the analysis of the initial uptake of $EuQuin_2S$-AuNPs. These cells were resuspended in in 300 µL of serum-free DMEM. 300 µL of serum-free DMEM containing cisplatin (10 µM) was then added, mixed well and incubated at room temperature for 5 minutes, DMEM (2.4 mL) was then added, the cells were then centrifuged (5 min x 300 g), then washed with Cell Staining Buffer (Fluidigm). Cells were then fixed 1 mL of BD CellFix™ (BD Biosciences), incubated for 20 min at 4 °C, and washed once with Cell Staining buffer. After the supernatant was removed, 0.2% saponin (1 mL) was added and the cells were incubated for 20 min at room temperature. Cells were then centrifuged and washed with Cell Staining Buffer. Cells were then resuspended in 50 µL of Cell staining buffer. 50 µL of Cell Staining Buffer containing ^{160}Gd-Anti-FITC (Clone: FIT 22, Fluidigm) was then added to each tube to obtain a final ^{160}Gd-Anti-FITC concentration of 1:100. Each tube was gently vortexed and incubated at room temperature for 30 min, then washed twice with cell staining buffer. Cells were then incubated with a Iridium DNA intercalator (0.125 µM, Fluidigm) in Maxpar Fix and Perm Buffer for 30 min and then then frozen in cryovials until the day of the experiment, which has been shown to have no effect on CyTOF data acquisition in previous studies.[89] The remaining cells were seeded in four 100 mm dishes and remained in culture under standard culture conditions for 24, 48, 72 and 96 hours. The cell media was replaced with fresh media once every 24 hours. Once the duration of the timepoint had passed, the cells were harvested and 2 x 10^6 cells from each sample were prepared as previously described and frozen in cryovials until the day of the experiment. On the day of the experiment, the cells

were thawed by the addition of cell staining buffer and transferred to 5 mL Falcon™ Round-Bottom Polystyrene Tubes. The cells were then centrifuged, the supernatant was removed and washed twice with Maxpar Cell staining buffer and once more with water just before acquisition. The cells were then resuspended in water to achieve a concentration of 500,000 cells/mL before acquisition on the Helios CyTOF instrument. For control samples, the preparation of cells was identical except no CFDA-SE staining step or Anti-FITC staining was performed.

3.11 References

1. Y. S. Yang, P. U. Atukorale, K. D. Moynihan, A. Bekdemir, K. Rakhra, L. Tang, F. Stellacci and D. J. Irvine, *Nature Communications*, 2017, **8**, 14069.
2. Y. S. Yang, K. D. Moynihan, A. Bekdemir, T. M. Dichwalkar, M. M. Noh, N. Watson, M. Melo, J. Ingram, H. Suh, H. Ploegh, F. R. Stellacci and D. J. Irvine, *Biomaterials Science*, 2018, **7**, 113-124.
3. A. Ivask, A. J. Mitchell, C. M. Hope, S. C. Barry, E. Lombi and N. H. Voelcker, *Analytical Chemistry*, 2017, **89**, 8228-8232.
4. A. Lopez-Serrano Oliver, A. Haase, A. Peddinghaus, D. Wittke, N. Jakubowski, A. Luch, A. Grutzkau and S. Baumgart, *Analytical Chemistry*, 2019, **91**, 11514-11519.
5. Q. Wu, J. Shi, X. Ji, T. Xia, L. Zeng, G. Li, Y. Wang, J. Gao, L. Yao, J. Ma, X. Liu, N. Liu, L. Hu, B. He, Y. Liang, G. Qu and G. Jiang, *ACS Nano*, 2020, **14**, 12828-12839.
6. M. K. Ha, J.-S. Choi, S. J. Kwon, J. Song, Y. Lee, Y.-E. Kim and T. H. Yoon, *Environmental Science: Nano*, 2020, **7**, 1102-1114.
7. M. K. Ha, S. J. Kwon, J. S. Choi, N. T. Nguyen, J. Song, Y. Lee, Y. E. Kim, I. Shin, J. W. Nam and T. H. Yoon, *Small*, 2020, DOI: 10.1002/smll.201907674, e1907674.
8. J. Bae, M. Ha, H. Perumalsamy, Y. Lee, J. Song and T.-H. Yoon, *Journal*, 2022, **14**.
9. A. Malysheva, A. Ivask, C. L. Doolette, N. H. Voelcker and E. Lombi, *Nature Nanotechnology*, 2021, **16**, 926-932.
10. B. Ouyang, W. Poon, Y.-N. Zhang, Z. P. Lin, B. R. Kingston, A. J. Tavares, Y. Zhang, J. Chen, M. S. Valic, A. M. Syed, P. MacMillan, J. Couture-Senécal, G. Zheng and W. C. W. Chan, *Nature Materials*, 2020, **19**, 1362-1371.
11. X. Huang, P. K. Jain, I. H. El-Sayed and M. A. El-Sayed, *Photochemistry and Photobiology*, 2006, **82**, 412-417.
12. N. S. b. Rosli, A. A. Rahman, A. A. Aziz and S. Shamsuddin, *AIP Conference Proceedings*, 2015, **1657**, 060001.
13. Q. Xia, J. Huang, Q. Feng, X. Chen, X. Liu, X. Li, T. Zhang, S. Xiao, H. Li, Z. Zhong and K. Xiao, *International Journal of Nanomedicine*, 2019, **14**, 6957-6970.
14. Z. Lin, N. A. Monteiro-Riviere, R. Kannan and J. E. Riviere, *Nanomedicine*, 2015, **11**, 107-119.
15. V. Fortino, P. A. S. Kinaret, M. Fratello, A. Serra, L. A. Saarimäki, A. Gallud, G. Gupta, G. Vales, M. Correia, O. Rasool, J. Ytterberg, M. Monopoli, T. Skoog, P. Ritchie, S. Moya, S. Vázquez-Campos, R. Handy, R. Grafström, L. Tran, R. Zubarev, R. Lahesmaa, K. Dawson, K. Loeschner, E. H. Larsen, F. Krombach, H.

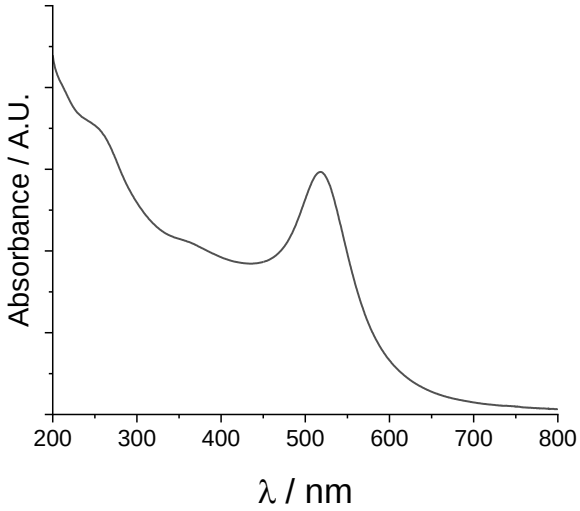
Norppa, J. Kere, K. Savolainen, H. Alenius, B. Fadeel and D. Greco, *Nature Communications*, 2022, **13**, 3798.
16. B. Youden, R. Jiang, A. J. Carrier, M. R. Servos and X. Zhang, *ACS Nano*, 2022, **16**, 17497-17551.
17. B. Snijder and L. Pelkmans, *Nature Reviews Molecular Cell Biology*, 2011, **12**, 119-125.
18. P. Cossart and A. Helenius, *Cold Spring Harb Perspect Biol*, 2014, **6**.
19. J. A. Kim, C. Aberg, A. Salvati and K. A. Dawson, *Nature Nanotechnology*, 2011, **7**, 62-68.
20. E. Panet, T. Mashriki, R. Lahmi, A. Jacob, E. Ozer, M. Vecsler, I. Lazar and A. Tzur, *Nature Nanotechnology*, 2017, **12**, 598-600.
21. P. Rees, J. W. Wills, M. R. Brown, C. M. Barnes and H. D. Summers, *Nature Communications*, 2019, **10**, 2341.
22. S. Tenzer, D. Docter, J. Kuharev, A. Musyanovych, V. Fetz, R. Hecht, F. Schlenk, D. Fischer, K. Kiouptsi, C. Reinhardt, K. Landfester, H. Schild, M. Maskos, S. K. Knauer and R. H. Stauber, *Nature Nanotechnology*, 2013, **8**, 772-781.
23. M. P. Monopoli, C. Åberg, A. Salvati and K. A. Dawson, *Nature Nanotechnology*, 2012, **7**, 779-786.
24. S. Zhang, J. Li, G. Lykotrafitis, G. Bao and S. Suresh, *Advanced Materials*, 2009, **21**, 419-424.
25. M. Ehrlich, W. Boll, A. van Oijen, R. Hariharan, K. Chandran, M. L. Nibert and T. Kirchhausen, *Cell*, 2004, **118**, 591-605.
26. H. D. Summers, P. Rees, M. D. Holton, M. R. Brown, S. C. Chappell, P. J. Smith and R. J. Errington, *Nature Nanotechnology*, 2011, **6**, 170-174.
27. J. C. G. Jeynes, C. Jeynes, M. J. Merchant and K. J. Kirkby, *Analyst*, 2013, **138**, 7070-7074.
28. F. Alexis, E. Pridgen, L. K. Molnar and O. C. Farokhzad, *Molecular Pharmaceutics*, 2008, **5**, 505-515.
29. D. Tsvirkun, Y. Ben-Nun, E. Merquiol, I. Zlotver, K. Meir, T. Weiss-Sadan, I. Matok, R. Popovtzer and G. Blum, *Journal of the American Chemical Society*, 2018, **140**, 12010-12020.
30. R. Meir, K. Shamalov, T. Sadan, M. Motiei, G. Yaari, C. J. Cohen and R. Popovtzer, *ACS Nano*, 2017, **11**, 11127-11134.
31. O. Betzer, R. Meir, T. Dreifuss, K. Shamalov, M. Motiei, A. Shwartz, K. Baranes, C. J. Cohen, N. Shraga-Heled, R. Ofir, G. Yadid and R. Popovtzer, *Scientific Reports*, 2015, **5**, 15400.
32. R. Meir, K. Shamalov, O. Betzer, M. Motiei, M. Horovitz-Fried, R. Yehuda, A. Popovtzer, R. Popovtzer and C. J. Cohen, *ACS Nano*, 2015, **9**, 6363-6372.
33. F. Chen, K. Ma, B. Madajewski, L. Zhuang, L. Zhang, K. Rickert, M. Marelli, B. Yoo, M. Z. Turker, M. Overholtzer, T. P. Quinn, M. Gonen, P. Zanzonico, A. Tuesca, M. A. Bowen, L. Norton, J. A. Subramony, U. Wiesner and M. S. Bradbury, *Nature Communications*, 2018, **9**, 4141.
34. R. J. Errington, M. R. Brown, O. Silvestre, K. L. Njoh, S. C. Chappell, I. Khan, P. Rees, S. P. Wilks, P. J. Smith and H. D. Summers, *Cell Cycle*, 2010, **9**, 121-130.
35. W. S. Cho, M. Cho, J. Jeong, M. Choi, H. Y. Cho, B. S. Han, S. H. Kim, H. O. Kim, Y. T. Lim, B. H. Chung and J. Jeong, *Toxicology and Applied Pharmacology*, 2009, **236**, 16-24.
36. E. Sadauskas, G. Danscher, M. Stoltenberg, U. Vogel, A. Larsen and H. Wallin, *Nanomedicine*, 2009, **5**, 162-169.
37. F. Peng, M. I. Setyawati, J. K. Tee, X. Ding, J. Wang, M. E. Nga, H. K. Ho and D. T. Leong, *Nature Nanotechnology*, 2019, **14**, 279-286.
38. A. V. Epanchintseva, J. E. Poletaeva, D. V. Pyshnyi, E. I. Ryabchikova and I. A. Pyshnaya, *Beilstein Journal of Nanotechnology*, 2019, **10**, 2568-2578.

39. A. Balfourier, N. Luciani, G. Wang, G. Lelong, O. Ersen, A. Khelfa, D. Alloyeau, F. Gazeau and F. Carn, *Proceedings of the National Academy of Sciences*, 2020, **117**, 103-113.
40. H. D. Summers, M. R. Brown, M. D. Holton, J. A. Tonkin, N. Hondow, A. P. Brown, R. Brydson and P. Rees, *ACS Nano*, 2013, **7**, 6129-6137.
41. N. Oh and J. H. Park, *International Journal of Nanomedicine*, 2014, **9 Suppl 1**, 51-63.
42. N. Oh and J.-H. Park, *ACS Nano*, 2014, **8**, 6232-6241.
43. B. D. Chithrani and W. C. W. Chan, *Nano Letters*, 2007, **7**, 1542-1550.
44. D. Bartczak, S. Nitti, T. M. Millar and A. G. Kanaras, *Nanoscale*, 2012, **4**, 4470-4472.
45. R. E. Yanes, D. Tarn, A. A. Hwang, D. P. Ferris, S. P. Sherman, C. R. Thomas, J. Lu, A. D. Pyle, J. I. Zink and F. Tamanoi, *Small*, 2013, **9**, 697-704.
46. K. Shapero, F. Fenaroli, I. Lynch, D. C. Cottell, A. Salvati and K. A. Dawson, *Molecular Biosystems*, 2011, **7**, 371-378.
47. J. Bourquin, D. Septiadi, D. Vanhecke, S. Balog, L. Steinmetz, M. Spuch-Calvar, P. Taladriz-Blanco, A. Petri-Fink and B. Rothen-Rutishauser, *ACS Nano*, 2019, **13**, 7759-7770.
48. N. Gunduz, H. Ceylan, M. O. Guler and A. B. Tekinay, *Scientific Reports*, 2017, **7**, 40493.
49. N. Feliu, X. Sun, R. A. Alvarez Puebla and W. J. Parak, *Langmuir*, 2017, **33**, 6639-6646.
50. A. N. Dosumu, S. Claire, L. S. Watson, P. M. Girio, S. A. M. Osborne, Z. Pikramenou and N. J. Hodges, *JACS Au*, 2021, **1**, 174-186.
51. S. M. King, S. Claire, R. I. Teixeira, A. N. Dosumu, A. J. Carrod, H. Dehghani, M. J. Hannon, A. D. Ward, R. Bicknell, S. W. Botchway, N. J. Hodges and Z. Pikramenou, *Journal of the American Chemical Society*, 2018, **140**, 10242-10249.
52. H. Shin, M. Kwak, T. G. Lee and J. Y. Lee, *Nanoscale*, 2020, **12**, 15743-15751.
53. M. C. Phelan, *Current Protocols in Cell Biology*, 2007, **Chapter 1**, Unit 1 1.
54. A. Fernandez-Castane, H. Li, O. R. T. Thomas and T. W. Overton, *Scientific Reports*, 2017, **7**, 13118.
55. H. B. Steen, *Cytometry A*, 2004, **57**, 94-99.
56. R. M. Zucker, J. N. Ortenzio and W. K. Boyes, *Cytometry A*, 2016, **89**, 169-183.
57. C. Levard, E. M. Hotze, G. V. Lowry and G. E. Brown, Jr., *Environmental Science and Technology*, 2012, **46**, 6900-6914.
58. J. Liu, D. A. Sonshine, S. Shervani and R. H. Hurt, *ACS Nano*, 2010, **4**, 6903-6913.
59. B. Reidy, A. Haase, A. Luch, K. A. Dawson and I. Lynch, *Materials*, 2013, **6**, 2295-2350.
60. B. H. Lee and A. H. Rahman, *Methods in Molecular Biology*, 2019, **1989**, 13-31.
61. R. P. Wersto, F. J. Chrest, J. F. Leary, C. Morris, M. A. Stetler-Stevenson and E. Gabrielson, *Cytometry*, 2001, **46**, 296-306.
62. I. M. Jensen, J. Ellegaard and P. Hokland, *Cytometry*, 1993, **14**, 936-942.
63. C. B. Bagwell, M. Inokuma, B. Hunsberger, D. Herbert, C. Bray, B. Hill, G. Stelzer, S. Li, A. Kollipara, O. Ornatsky and V. Baranov, *Cytometry A*, 2020, **97**, 184-198.
64. S. Hou, K. N. Sikora, R. Tang, Y. Liu, Y. W. Lee, S. T. Kim, Z. Jiang, R. W. Vachet and V. M. Rotello, *ACS Nano*, 2016, **10**, 6731-6736.
65. A. Ivask, M. Visnapuu, P. Vallotton, E. R. Marzouk, E. Lombi and N. H. Voelcker, *NanoImpact*, 2016, **1**, 29-38.
66. P. Foroozandeh and A. A. Aziz, *Nanoscale Research Letters*, 2018, **13**, 339.
67. L. R. Olsen, M. D. Leipold, C. B. Pedersen and H. T. Maecker, *Cytometry A*, 2019, **95**, 156-172.

68. S. Tricot, M. Meyrand, C. Sammicheli, J. Elhmouzi-Younes, A. Corneau, S. Bertholet, M. Malissen, R. Le Grand, S. Nuti, H. Luche and A. Cosma, *Cytometry A*, 2015, **87**, 357-368.
69. R. Finck, E. F. Simonds, A. Jager, S. Krishnaswamy, K. Sachs, W. Fantl, D. Pe'er, G. P. Nolan and S. C. Bendall, *Cytometry A*, 2013, **83**, 483-494.
70. J. V. Caspar and T. J. Meyer, *Journal of the American Chemical Society*, 1983, **105**, 5583-5590.
71. P. Hughes, D. Marshall, Y. Reid, H. Parkes and C. Gelber, *BioTechniques*, 2007, **43**, 575-586.
72. B. D. Chithrani, A. A. Ghazani and W. C. W. Chan, *Nano Letters*, 2006, **6**, 662-668.
73. P.-J. De Temmerman, E. Verleysen, J. Lammertyn and J. Mast, *Journal of Nanoparticle Research*, 2014, **16**, 2628.
74. T. F. Pereira, G. Levin, C. DeOcesano-Pereira, A. S. Caodaglio, A. Fujita, A. Tonso and M. C. Sogayar, *BMC Res Notes*, 2020, **13**, 57.
75. Z. Good, L. Borges, N. Vivanco Gonzalez, B. Sahaf, N. Samusik, R. Tibshirani, G. P. Nolan and S. C. Bendall, *Nature Biotechnology*, 2019, **37**, 259-266.
76. C. R. Parish, M. H. Glidden, B. J. Quah and H. S. Warren, *Current Protocols in Immunology*, 2009, **Chapter 4**, Unit4.9.
77. I. E. Dumitriu, W. Mohr, W. Kolowos, P. Kern, J. R. Kalden and M. Herrmann, *Analytical and Bioanalytical Chemistry*, 2001, **299**, 247-252.
78. B. J. Quah, H. S. Warren and C. R. Parish, *Nature Nanotechnology*, 2007, **2**, 2049-2056.
79. S. Bernard, L. Pujo-Menjouet and M. C. Mackey, *Biophysical Journal*, 2003, **84**, 3414-3424.
80. M. C. Jamur and C. Oliver, *Methods in Molecular Biology*, 2010, **588**, 63-66.
81. Y. Kumei, T. Nakajima, A. Sato, N. Kamata and S. Enomoto, *Journal of Cell Science*, 1989, **93**, 221-226.
82. T. Kihara, K. Kashitani and J. Miyake, *BMC Research Notes*, 2017, **10**, 283.
83. M. Wright Muelas, F. Ortega, R. Breitling, C. Bendtsen and H. V. Westerhoff, *Scientific Reports*, 2018, **8**, 3029.
84. B. G. Hall, H. Acar, A. Nandipati and M. Barlow, *Molecular Biology and Evolution*, 2014, **31**, 232-238.
85. Y. Yan, Z. W. Lai, R. J. Goode, J. Cui, T. Bacic, M. M. Kamphuis, E. C. Nice and F. Caruso, *ACS Nano*, 2013, **7**, 5558-5567.
86. R. Xiong, F. Joris, S. Liang, R. De Rycke, S. Lippens, J. Demeester, A. Skirtach, K. Raemdonck, U. Himmelreich, S. C. De Smedt and K. Braeckmans, *Nano Letters*, 2016, **16**, 5975-5986.
87. T. Lijster and C. Åberg, *PLoS One*, 2020, **15**, e0242547.
88. Q. Cai, V. Castagnola, L. Boselli, A. Moura, H. Lopez, W. Zhang, J. M. de Araújo and K. A. Dawson, *Nanoscale Horizons*, 2022, **7**, 288-298.
89. D. Geanon, B. Lee, E. Gonzalez-Kozlova, G. Kelly, D. Handler, B. Upadhyaya, J. Leech, R. M. De Real, M. Herbinet, A. Magen, D. Del Valle, A. Charney, S. Kim-Schulze, S. Gnjatic, M. Merad and A. H. Rahman, *Cytometry A*, 2021, **99**, 446-461.
90. R. P. Carney, J. Y. Kim, H. Qian, R. Jin, H. Mehenni, F. Stellacci and O. M. Bakr, *Nature Communications*, 2011, **2**, 335.

3.12 Appendix

3.12.1 PEG-AuNP Characterisation



Appendix Figure 3.1 UV-Vis spectrum of 13-nm PEG-AuNPs after purification by centrifugation.

Appendix Table 3.1 Average hydrodynamic diameter of PEG-AuNPs measured by DLS, ζ-potential measurements and the λ_{SPR} measured by UV-Vis Spectroscopy.

Number / nm	Intensity / nm	PDI	ζ-potential / mV	λ_{SPR}
16	27	0.13	-50	518

3.12.2 Determining the Optimal Tube Type For Washing Nanoparticle Treated HeLa Cells

PBS containing 1 x 10^5 cells/mL was added to each type of tube (10 mL, 3 mL and 1.5 mL total volume for each 15, 5 and 1.5 mL tube respectively) and the cells were centrifuged at 300 g for 5 min. The volume of supernatant removed was calculated by determining the difference in mass before and after inversion or aspiration. It was found that using 5 mL Falcon™ Round-Bottom Polystyrene Test Tubes and removing the supernatant by inverting the tube were the most suitable, with 97 ± 1% of the supernatant removed (Appendix table 3.2). The 15 mL Corning® Centrifuge Tubes and 1.5 mL Fisherbrand™ Polypropylene Microcentrifuge Tubes both led to 92 ± 2% of supernatant removed by tipping, and

aspiration led to less supernatant removed with a higher range for each type of tube. We hypothesise the suitability of 5 mL Falcon™ Round-Bottom Polystyrene Test Tubes is due to the round-bottomed shape of the tube withholding less supernatant during inversion. Although the difference between the percentage of supernatant removed by each type of tube is small, it may have a significant impact when considering the total number of washes during cell preparation, particularly for the preparation of suspension cells where it is not possible to remove any solution NPs before centrifugation steps.

Appendix Table 3.2 The % (± range from 3 independent repeat measurements) of supernatant removed with each type of tube and supernatant removal method. Total supernatant volumes were 10 mL, 3 mL and 1.5 mL for 15 mL Corning® Centrifuge Tubes, 5 mL Falcon™ Round-Bottom Polystyrene Test Tubes and 1.5 mL Fisherbrand™ Polypropylene Microcentrifuge Tubes respectively.

	Supernatant removed by inverting / %	Supernatant removed by pipette aspiration / %
15 mL Corning® Centrifuge Tubes	92 ± 2	91 ± 3
5 mL Falcon™ Round-Bottom Polystyrene Test Tubes	97 ± 1	95 ± 3
1.5 mL Fisherbrand™ Polypropylene Microcentrifuge Tubes	92 ± 2	92 ± 3

3.12.3 Calculation the Number of Au Atoms per NP

This calculation assumes that each AuNPs are perfectly spherical and contain gold atoms arranged in an FCC lattice with a density of 19.32 gcm^{-3}. A full derivation of the equation can be found in an article by Carney *et al.*[90]

$$N = \frac{\rho \times \pi D^3}{6 \times Mr} \times N_A = \frac{19.32 \times 10^{-21} g\ nm^{-3} \times \pi D^3}{6 \times 196.97\ g\ mol^{-1}} \times 6.022 \times 10^{23} mol^{-1}$$

$$\therefore N = 30.9\ D^3$$

3.12.4 Conversion of Molar Nanoparticle concentration to Mass Concentration

Example: converting a 13 nm AuNP species with a molar concentration of 1.6 nM into a mass concentration

$$Using\ the\ equation\ above, there\ are\ approximately\ 67{,}900\ Au\ atoms\ per\ 13\ nm\ AuNP.$$

$$The\ mass\ of\ a\ single\ Au\ atom\ =\ 3.27\ \times 10^{-27} g$$

$$Mass\ of\ 1\ 13\ nm\ AuNP = 3.27\ \times 10^{-27} g \times 67{,}900 = 2.22\ \times 10^{-27} g$$

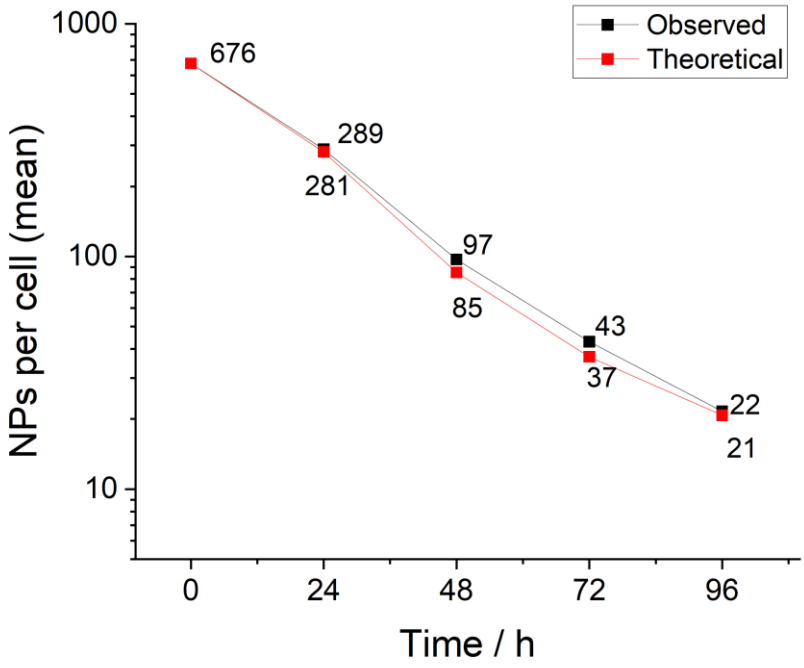
$$Molar\ concentration\ of\ 13\ nm\ AuNP\ species = 1.6\ nM = 1.6 \times 10^{-9} mol$$

$$NPs\ per\ litre = 1.6 \times 10^{-9} mol \times 6.022 \times 10^{23} mol^{-1} = 9.64 \times 10^{14} NP\ L^{-1}$$

$$Concentration\ in\ \ gL^{-1} = 9.64 \times 10^{14} NP\ L^{-1} \times 2.22\ \times 10^{-27} g$$

$$= 0.0214\ gL^{-1} = 0.021\ \ gL^{-1}\ (2\ s.f.)$$

3.12.5 The Mean Number of EuQuin$_2$S-AuNPs per Cell At Each Time Point



Appendix Figure 3.2 Observed (black) mean EuQuin$_2$S-AuNPs per cell at each time point vs. theoretical (red) NPs per cell calculated from the number of cell divisions at each time point

Chapter 4: Investigative Studies into the Use of $EuQuin_2S$-AuNPs as Multimodal Cellular Labels

4.1 Introduction

This chapter contains our work concerning the use of $EuQuin_2S$-AuNPs as multimodal cellular labels; detecting $EuQuin_2S$-AuNPs in monocytes and monocytes that have differentiated into macrophages and dendritic cells with CyTOF, TEM and luminescence microscopy. In the introduction, monocytes – the cell type we are primarily interested in – are briefly discussed, followed by the concept and purpose of cellular labelling, including a brief summary of currently available cellular labels. The topic of multimodal cellular labels and how functionalised AuNPs are ideal candidates is then introduced, setting the basis for our work.

4.1.1 Monocytes: Multi-functional, Yet Not Fully Understood Cells

Monocytes are the largest type of leukocyte (white blood cell) and are part of the innate (or non-specific) immune system.[1] Monocytes are produced in the bone marrow and then enter blood circulation before they are recruited into tissues throughout the body, where they play distinct roles. Monocytes can differentiate into tissue macrophages, which for half a century was thought their only role,[2] but it is now known that monocytes also have the ability to function as effector cells and differentiate into both macrophages and dendritic cells, forming the mononuclear phagocyte system.[3] Alongside their diverse role in protective immunity and homeostasis, monocytes also contribute to many pathological processes. For example, monocytes infiltrate almost all solid tumours and their differentiation into tumour-associated macrophages results in poor prognosis.[4] There is also much interest in their use for therapeutic benefits;[5] however our incomplete understanding of monocyte function, migration and differentiation has limited their potential in clinical settings.

Fate mapping can be used to track the developmental lineage of monocytes in an organism and over recent years, these techniques have provided important insight into the roles of

monocytes in the immune response and the development of various diseases.[6] Once cells have been labelled with markers, techniques such as flow cytometry can be used to determine where monocytes migrate to, how they differentiate and what their specific functions are in different tissues.[7] For example, tracking of monocytes circulating in the blood has revealed their migration into tissues such as lymph nodes,[8] the arteries,[9] lungs[10] and liver.[11] The cellular labelling of monocytes also allows the tracking of their effectiveness in treating diseases, which has also led to recent advances in the use of monocytes for cell based therapies.[12] Herein, this introduction discusses the concept of cellular labelling for understanding the function of cells such as monocytes and the importance of recently emerging multimodal cellular labels.

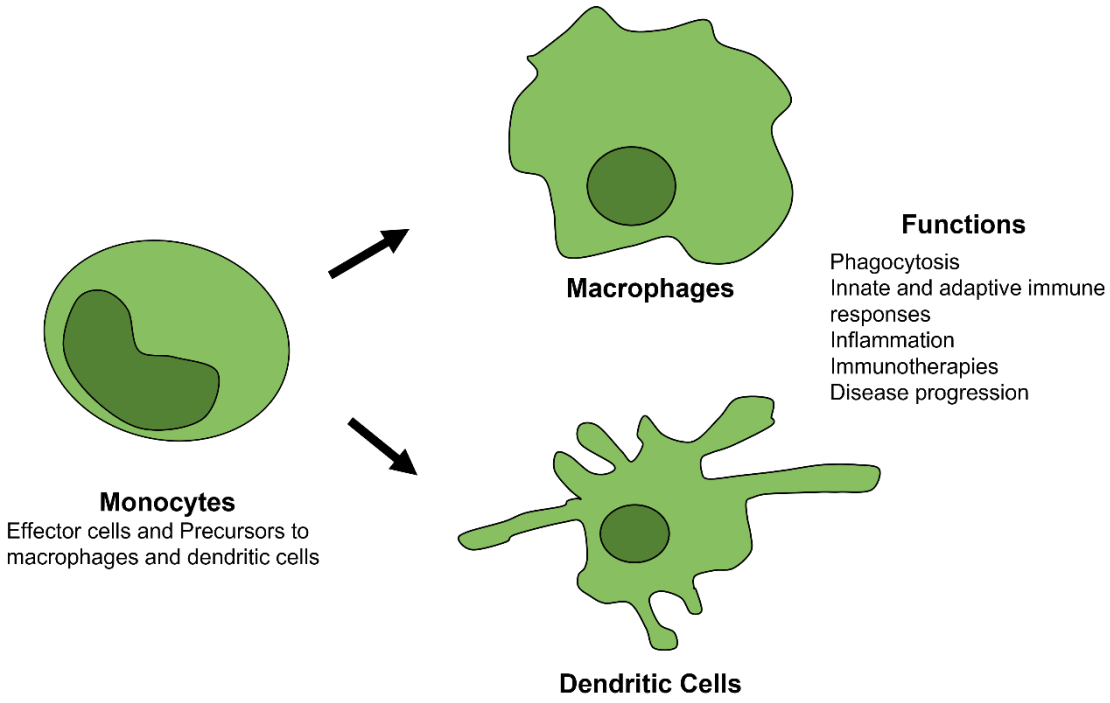


Figure 4.1 - The mononuclear phagocyte system. Monocytes are a type of leukocyte that both act as effector cells and differentiate into macrophages and dendritic cells. Together, the three cell types make up the mononuclear phagocyte system. These cells have diverse roles in immunity, homeostasis and contribute to many pathological diseases.

4.1.2 Cellular Labelling and Detection of Cells to Understand Their Function

In order to track and identify cells in a body or tissue/animal model, they require labelling with a marker that allows for their detection. There are many existing tools for labelling cells such as proteins, small molecules, metal complexes and nanoparticles that have intrinsic properties such as fluorescence. These cellular labels allow the study of cells like monocytes with many techniques including genomic/epigenomic approaches that can map the fate of monocyte-derived cells;[13-15] phenotyping assays of collected cells analysed by flow cytometry;[16, 17] microscopy-based approaches for *in vivo* and *in vitro* live cell visualisation such as intravital microscopy,[18] multiphoton and confocal laser scanning microscopy;[19, 20] magnetic resonance (MRI)[21] and computed tomography (CT).[22] Cellular labelling is widely used in various fields of research such as cell biology,[14] immunology[23] and regenerative medicine.[24]

Cellular labelling can be done directly, by isolating the cell type of interest and labelling with the agent *ex vivo*, or indirectly where specific antigens from the cell of interest are targeted *in vivo*. Indirect labelling may simply involve labelling with fluorescent monoclonal antibodies, but expression of a target antigen on other cell types and uptake by other major organs are a major limitation of this method.[25] Genetic engineering of cells to express fluorescent proteins such as green fluorescent protein (GFP) is the most commonly used indirect labelling technique. These reporter genes are transfected into the cells of interest under the control of a given promoter and for *in vivo* imaging with techniques such as bioluminescence imaging, which is particularly useful in pre-clinical animal studies.[26, 27] As daughter cells inherit and express the reporter gene, there is no depletion from proliferation and thus it allows long-term tracking. However transfection efficiency can be low, GFP expression can vary considerably,[28] there is conflicting views on toxicity[29, 30] and it is difficult to translate into human studies due to safety and regulatory issues surrounding the

involvement of genetic manipulation.[25] Increased risk of random insertional mutagenesis from reporter genes has been observed in previous clinical trials.[31, 32]

Direct labelling of cells is an alternative approach commonly used in pre-clinical and clinical studies as there is no requirement to genetically modify cells. It is particularly useful for tracking cell-based immunotherapies, where the patients cells are isolated and expanded *ex vivo* to increase the cell population, then reintroduced into the patient for their required action.[33]

Optical imaging techniques are useful for detection of cells in both *in vitro* and *in vivo* studies. In theory, any protein, molecule or nanoparticle with intrinsic fluorescence or luminescence could be suitable for labelling cells for detection by optical imaging. For *in vivo* imaging, techniques such as confocal laser scanning microscopy are limited to a few tens of micrometres owing to scattering.[34] Two photon laser scanning microscopy allows greater imaging depth, owing to the reduced scattering of long wavelength light. Two photon excitation involves the absorption of two photons by a fluorophore, each of which contributes half of the total energy required for excitation. For example, Miller *et al.* demonstrated the use of two-photon microscopy to image T cells labelled with CFSE to allow for live *in vivo* cell tracking in mice.[35]

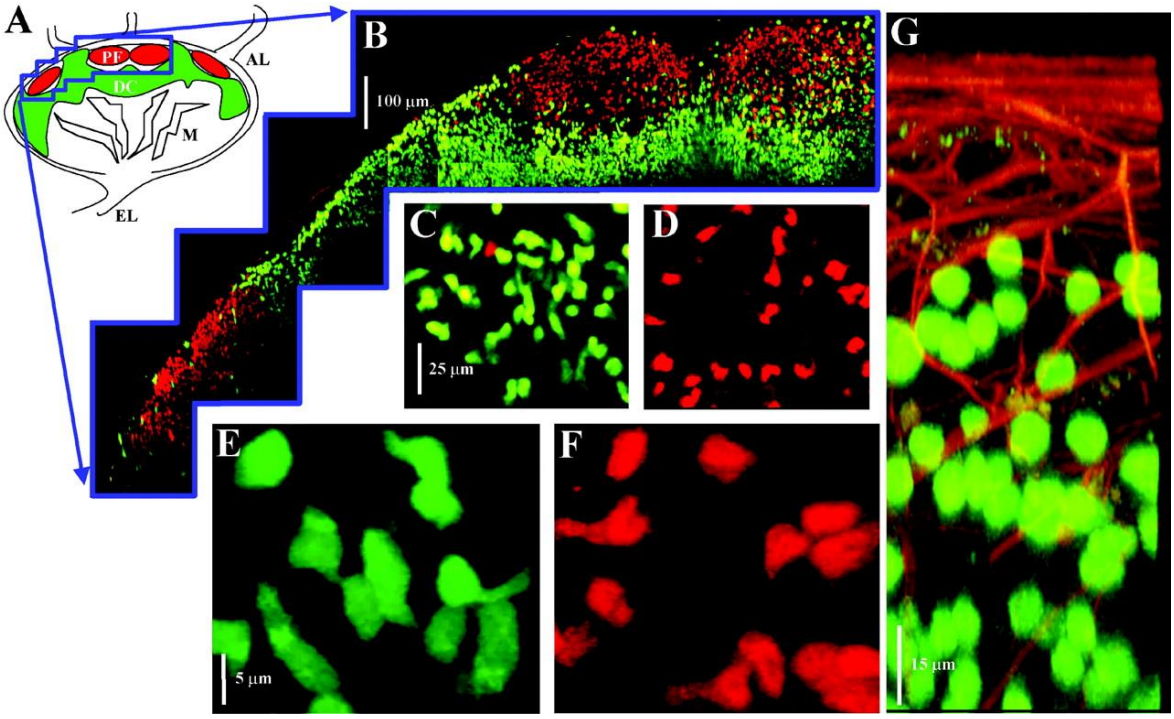


Figure 4.2 - Two-photon imaging of living T and B lymphocytes within an intact lymph node in mice. Green shows CFSE-labelled T cells.

Cytometric methods such as flow cytometry and CyTOF are useful quantitative techniques for detecting labelled cells at specific stages of development and identifying their descendants as the organism develops.[36] They can be used to determine the proportion of descendant cells that derived from the originally labelled cells as well as allowing simultaneous phenotypical analysis to identify the type of cell it has become (e.g. differentiation of a labelled monocyte to a macrophage or dendritic cell). Cytometric techniques allow *in vivo* studies of the development and fate of specific cell populations, which can provide valuable information about how different cell types form and contribute to the formation of different tissues and organs, as well as disease pathology.[37] Flow cytometry has been a central technique for furthering our understanding of monocyte migration and function. Saban and co-workers used fate mapping to reveal that monocyte-derived macrophages are definitively distinguishable to microglia in the retina. In mice, they labelled both microglia and monocytes with different fluorescent reporters (GFP and red fluorescent protein respectively) and isolated the retina for analysis. Alongside a flow

cytometry panel with 12 phenotypical markers, they were able to distinguish different cellular phenotypes for microglia and monocytes that had differentiated into macrophages.[38] In mice, Yona *et al.* used a reporter gene for fate mapping to reveal the origins and dynamics of monocytes and tissue macrophages under homeostasis. After isolating cells from the bone marrow and blood of mice, they found that monocytes are essential steady-state precursors of a monocyte subset that initiate alternatively activated (M2) macrophages.[14]

There are several types of direct cellular labels available for flow cytometry, including fluorescent dyes such as CFSE which can also track proliferative state,[39] and fluorescent nanomaterials such as quantum dots.[40, 41] There are however cellular labels that have been specifically designed and tested for their use in CyTOF. CyTOF can measure more cellular parameters simultaneously than flow cytometry, allowing for deeper phenotypical studies that could provide more insight into cell differentiation and function. We hypothesise that our $EuQuin_2S$-AuNPs may be suitable candidates to address this shortfall, which is discussed later.

Non-invasive clinical imaging techniques such as MRI, CT, positron emission tomography (PET) and single photon emission CT (SPECT) are also useful for detecting labelled cells *in vivo* owing to their great penetration depth through tissue to allow imaging of whole animals. Gadolinium complexes, superparamagnetic iron oxide nanoparticles (SPIONS) and molecules containing ^{19}F are all useful contrast agents for MRI. Geng *et al.* located mesenchymal stem cells within the brains of rats after their labelling with a Gd-DTPA complex.[42] ^{19}F-based MRI contrast agents have been used to label and detect natural killer cells 8 days after injection,[43] and macrophages in murine tumours.[44] SPIONS have been studied intensively in recent years, including for stem cell[45] and immune cell[46] tracking, but questions remain about their toxicity.[47]

Indium-111 is a radioactive isotope of Indium with a short half-life of 2.8 days and complexes containing In-111 are used as imaging contrast agents in single photon emission CT (SPECT).[48] For example, Potts *et al.* labelled neutrophils with In-111 to show neutrophil migration in severe alcoholic hepatitis.[49] However, the short half-life and significant efflux of In-111 complexes means that they are not suitable to longer term labelling.[50]

PET is a commonly used technique for cell tracking as it is superior in image quality, sensitivity, spatial resolution, and quantification to SPECT.[51] Labelled cells can be tracked using PET when labelled with appropriate radioisotopes, such as ^{89}Zr, a positron (β)-emitting radioisotope that has a relatively long half-life of 3.3 days.[52] Man *et al.* recently demonstrated that [^{89}Zr]Zr-oxine is a highly suitable labelling agent for tracking white blood cells for 1 week in an *in vitro* study.[53]

In summary, there are many techniques that can be used to track labelled cells in order to further understand their fate and function. However, each of these modalities has its limitations: bioluminescence imaging and confocal microscopy are highly informative techniques for *in vitro* studies, but even with two-photon excitation they suffer from limited penetration depth in tissue. Cytometric techniques like flow cytometry allow immunological phenotyping to reveal characteristics on proliferation, function and population heterogeneity, but biopsy or blood samples from the region of interest are required for analysis. Clinical techniques such as MRI and CT allow the imaging of whole organs and animals, but their relatively lower resolution means only large clusters of cells can be imaged.[54, 55] Furthermore, these techniques are generally only effective for days due to signal depletion from proliferation, or short half-life of radioactive labels. Although there are many labelling agents available for detection of cells by each of these techniques, there is lack of labelling agents detectable by more than one of these techniques, i.e., multimodal labels, which will be discussed in the next section.

4.1.3 Multimodal Probes for Cell Labelling and Tracking

Multimodal probes are detectable by multiple modalities and are therefore more versatile cellular labels. This allows for the combination of techniques in studies in order to maximise their strengths and provide complimentary information. For example, a multimodal probe could be detectable by confocal microscopy, flow cytometry and CT. Confocal microscopy would allow single cell resolution for *in vitro* studies and may also be useful for high resolution pre-clinical studies. CT would allow for whole organ/body imaging in the subsequent clinical studies where confocal microscopy struggles with deep tissue penetration. Flow cytometry may allow for deep immunophenotyping to reveal functional characteristics throughout all studies.

Inorganic nanoparticles are particularly attractive agents for multimodal detection. Their dense metal centres are often detectable by clinical imaging techniques (e.g. AuNPs for CT, SPIONS for MRI) and their surface or core can be functionalised with moieties that offer a secondary method of recognition. Furthermore, this concentrates any moiety around/within the NP for dense contrast, compared to molecular probes that may be evenly spread within a single cell. Several studies have used SPIONS as multimodal cellular labels.[56, 57] For example, Misri *et al.* conjugated ^{111}In complexes and targeting antibodies to

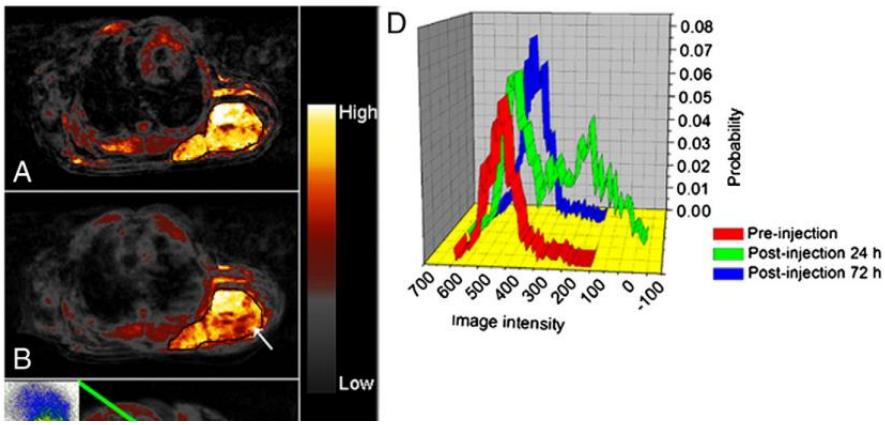


Figure 4.3 - MRI for tumours of mice injected with SPIONS conjugated with ^{111}In complexes and targeting antibodies pre injection (A), 24 (B) and 72 hours (C) post-injection. (D) shows the intensity at the region of interest, with suppression of signal intensity most apparent at 24 hours indicating the presence of SPIONS in tumours. Image reproduced from Misri *et al.*

SPIONS and were able to show localisation of the probes in mesothelin-expressing tumours in mice using MRI and SPECT.[58] Silica nanoparticles have also attracted attention;[59] Huang *et al.* embedded a near-infrared dye, Gd-DTTA complex and ^{64}Cu into mesoporous silica nanoparticles for long-term imaging of tumour draining lymph nodes for up to 3 weeks, using MRI, positron emission tomography (PET) and near-infrared fluorescence imaging.[60] AuNPs are also attractive candidates and will be discussed in the next section.

Multimodal imaging has also been achieved by using more than one cellular label, with most research combining the use of reporter genes with a second clinical imaging modality. For example, Niers *et al*. demonstrated that brain tumours expressing a biotinylated, membrane-bound form of *Gaussia* luciferase allowed binding of SPIONS and ^{111}In-DTPA complexes, allowing imaging in mice by fluorescence tomographic imaging, MRI and SPECT.[61] Comenge *et al.* used bioluminescence and multispectral optoacoustic tomography to detect reporter gene expression and silica-coated gold nanorods, allowing imaging from systemic administration to tumour growth in mice.[62] Jackson *et al.* labelled stem cells with iron oxide and a radioligand [^{11}C]raclopride PET tracer to image stem cell transplantation in rats by MRI and PET.[63] Vocht *et al.* used bioluminescence imaging and MRI to image stem cells labelled with GFP and iron oxide, revealing different stem cell/environment-associated characteristics following grafting in the central nervous system of mice.[64] Kelly *et al.* developed a reporter gene that was capable of multimodal imaging by engineering cells to express a td-tomato gene for fluorescence, a firefly luciferase gene for bioluminescence, and a clinically used MRI reporter, Oatp1a1, that enabled the binding of a clinically approved Gd-EOB-DTPA complex.[65] This allowed the localisation and tracking of cells in tumours.

4.1.4 Gold Nanoparticles as Multimodal Labels

Gold nanoparticles are promising candidates for multimodal imaging. As described above, their dense gold core makes them detectable by CT. Furthermore, their surfaces can be

functionalised with metal complexes for detection by luminescence. As previously described, our group has established the attachment of lanthanide and transition metal complexes to spherical 13 and 25 nm AuNPs and applied these probes to imaging cells *in vitro*.[66-69]

A recent study by Gunnlaugsson and co-workers demonstrated the use of europium-coated AuNPs to image bone with two-photon excitation.[70] The authors designed a tetra-substituted macrocycle; three arms of the macrocycle were functionalised with diethyl iminodiacetate pendant arms in order to yield a heptadentate coordination environment and one arm was functionalised with a C_{11} thiol-terminated alkyl chain for attachment to 4 nm AuNPs and to minimise quenching from the gold surface. Base hydrolysis of the ligand would also afford the corresponding disodium iminodiacetate which is able to bind Ca (II) ions found in high concentrations in microdamaged regions of bone. The authors were able to image microdamaged bovine bone with 3D two-photon excitation (λ_{exc} = 750 nm) microscopy, demonstrating for the first time two-photon excitation of lanthanide functionalised AuNPs.

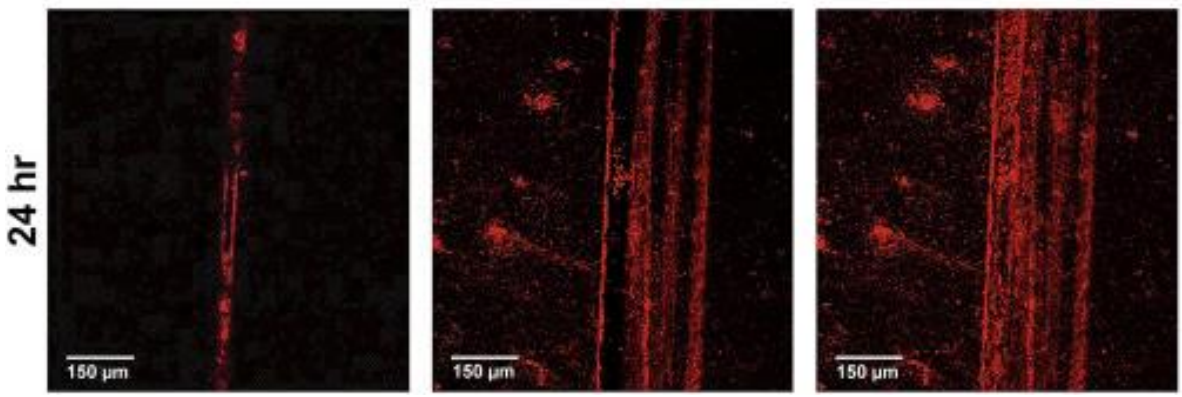


Figure 4.4 - Two photon excitation fluorescence microscopy of microdamaged bovine structure after immersion with an aqueous solution of 4 nm europium-coated AuNPs for 24 hours. Image reproduced from Gunnlaugsson *et al.*

As shown in Chapter 3, AuNPs are also detectable by CyTOF, which can not only allow quantification of AuNP uptake at the single cell level, but also reveal cellular characteristics from high parameter immunophenotyping.[71, 72]

The dense gold core of AuNPs attenuate x-rays strongly and they have been utilised as contrast agents for CT. Chhour *et al.* labelled monocytes with 15 nm, 11-

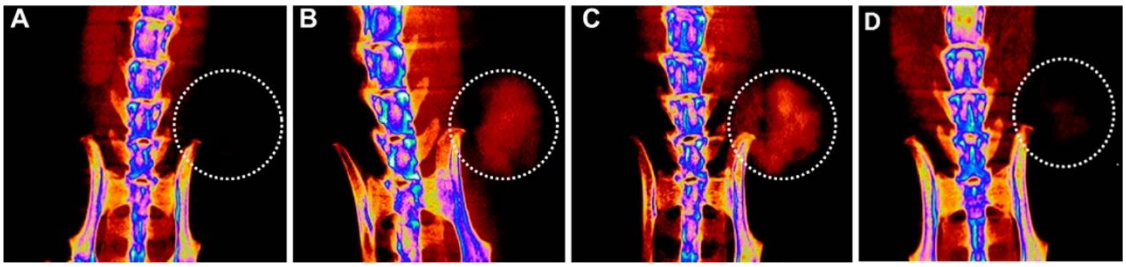


Figure 4.5 -CT images of a mouse A) Pre-injection, B) 24 hours post injection, C) 48 hours post injection, and D) 72 hours post injection. Melanoma-specific T cells loaded with AuNPs accumulate at the tumour site. Image reproduced from Popovtzer *et al*.

mercaptoundecanoic acid coated AuNPs to track their recruitment in atherosclerosis in mice, with monocytes found within plaques up to 5 days after treatment.[22] Popovtzer and co-workers used 20 nm, glucose coated AuNPs to label and track cancer-specific T cells used for immunotherapy, using CT to show localisation within the tumour of mice for up to 3 days post injection.[73]

4.2 Chapter Outline

Herein, I present our work concerning $EuQuin_2S$-AuNPs as labels for mononuclear phagocytes and we will explore their detection by CyTOF and two-photon confocal microscopy. Unlike flow cytometry, there are currently no agents specifically designed as intracellular labels for CyTOF experiments. It was hypothesised that the high sensitivity of CyTOF will allow the detection of $EuQuin_2S$-AuNPs in monocytes despite depletion of NP content from multiple proliferation cycles, allowing the identification of labelled cells days to weeks after their original labelling. We will also investigate the detection of $EuQuin_2S$-AuNPs in macrophages with TEM and two-photon confocal microscopy; the latter would hypothetically allow for deeper tissue penetration depth in subsequent pre-clinical studies.

First I show the differentiation of THP-1 monocytes into macrophages and dendritic cells and investigate whether pre-treatment with $EuQuin_2S$-AuNPs has any effect on differentiation. With THP-1 monocytes, we use ratiometric detection to validate

quantification at high intracellular content. I then show internalisation of $EuQuin_2S$-AuNPs in macrophages by TEM. I then explore the cellular uptake of $EuQuin_2S$-AuNPs in THP-1 monocytes, macrophages and dendritic cells with CyTOF at a range of concentrations. This will not only reveal an optimal concentration dose for subsequent CyTOF experiments, but also allow novel studies of NP uptake in these three cell types at the single cell level. We then investigate the suitability of $EuQuin_2S$-AuNPs as cellular labels for detecting THP-1 monocytes, some of which have been differentiated to macrophages and dendritic cells, in CyTOF experiments. Lastly, I show the detection of $EuQuin_2S$-AuNPs in macrophages and HeLa cells using two-photon confocal microscopy in preliminary studies.

4.3 Results and Discussion

4.3.1 The Effect of $EuQuin_2S$-AuNP Treatment on THP-1 Monocyte Differentiation into Macrophages and Dendritic Cells

We have chosen to study monocytes and their differentiation into macrophages and dendritic cells due to their interesting characteristics and because of our incomplete understanding of their function in certain disease progression, which has led to a subsequent lack of their use in cellular-based therapies. Furthermore, their ability to differentiate into non-dividing macrophages and dendritic cells meant that we could study $EuQuin_2S$-AuNP content in more detail. Originally, we had intended to use monocytes from patient samples but this was not possible due to a lack of availability during the COVID-19 pandemic. Instead, we have used a THP-1 monocyte cell line that has been shown as a valuable cell line for investigating monocyte structure and function in both health and disease.[74] In this section, we show the differentiation of THP-1 monocytes into macrophages and dendritic cells as well as the effect of $EuQuin_2S$-AuNPs on differentiation.

4.3.1.1 Differentiation of THP-1 Monocytes into Macrophages and Dendritic Cells

THP-1 monocytes were differentiated into macrophages and dendritic cells following protocols outlined by Chanput *et al.*[75] and Deng *et al.*[76] respectively. The reagents used for differentiation were phorbol myristate acetate (PMA), interleukin-4 (IL-4) and lipopolysaccharide (LPS), all of which play important roles in regulating numerous physiological functions.[77] Differentiation involved 2 days of treatment with 100 $ngmL^{-1}$ of PMA and 2 days resting to form resting stage (M0) macrophages, followed by 2 days stimulation with LPS to form classically activated M1 macrophages. To form mature dendritic cells (mDC), THP-1 monocytes were treated with 20 $ngmL^{-1}$ PMA and IL-4 (Figure 4.6).

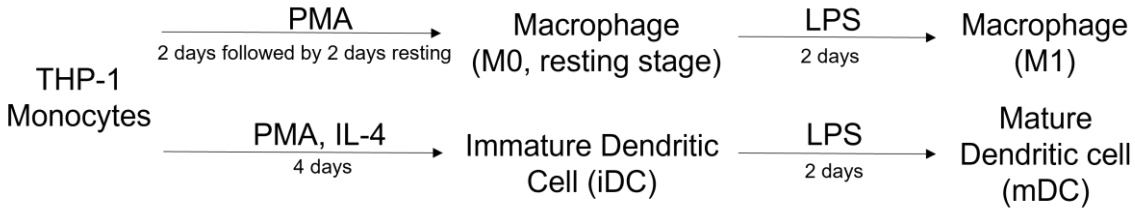


Figure 4.6 - Schematic to show the differentiation of THP-1 monocytes into classically activated M1 macrophages and mature dendritic cells (mDC).

In this section, we show morphological changes as evidence for THP-1 monocyte differentiation to macrophages and dendritic cells, followed by phenotypical evidence and the effects of $EuQuin_2S$-AuNP on phenotype and cell death.

4.3.1.2 Morphological Changes Observed from Light Microscopy Images

Phase gradient contrast images were acquired of THP-1 monocytes before differentiation, resting stage M0 and classically activated M1 macrophages, immature (iDC) and mature dendritic cells (mDC) to assess any changes to their morphology from stimulation by PMA/ PMA and IL-4, followed by LPS treatment. As shown in Figure 4.7, THP-1 monocytes are suspension cells that do not adhere to the surface of the culture vessel, therefore they appear rounded and smaller than their relatively large size.

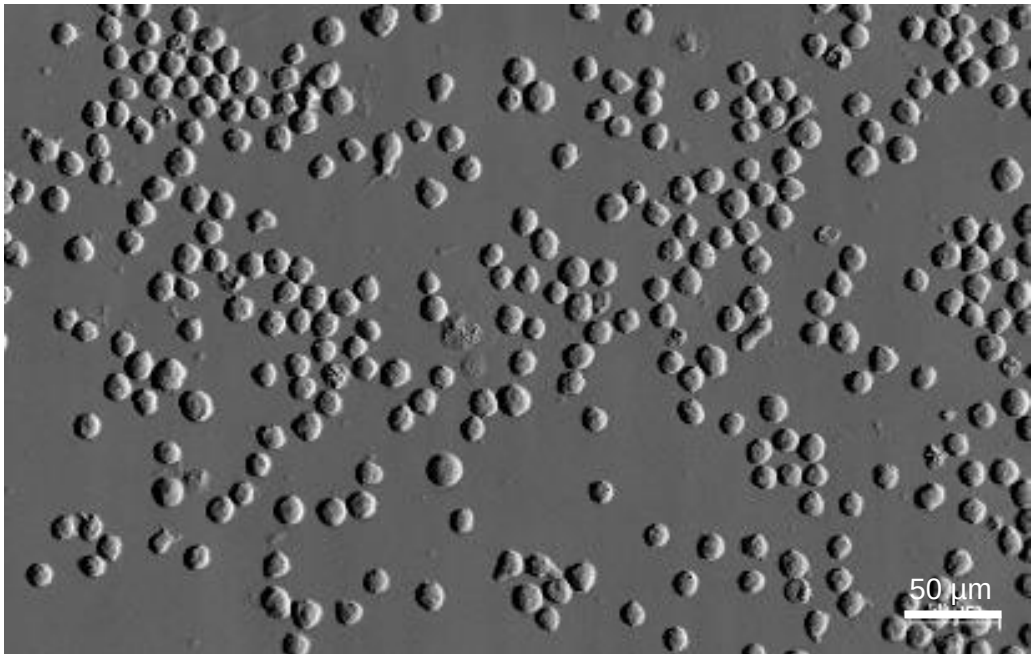
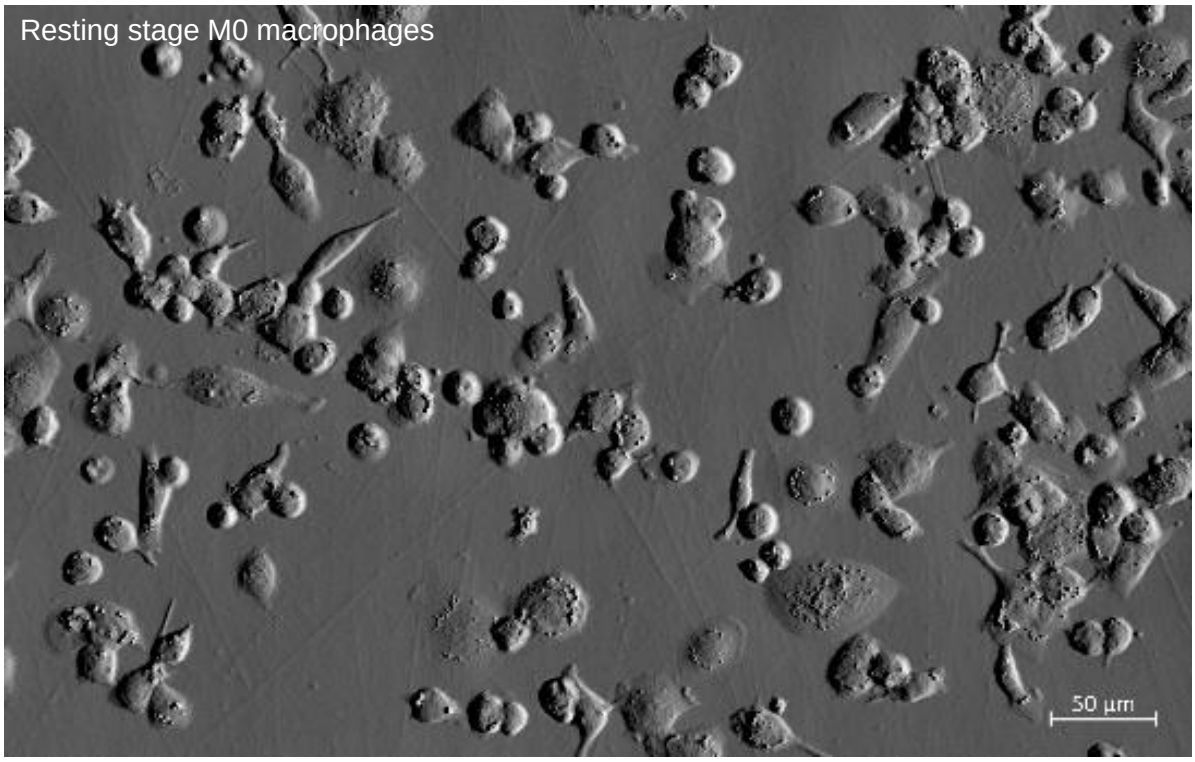
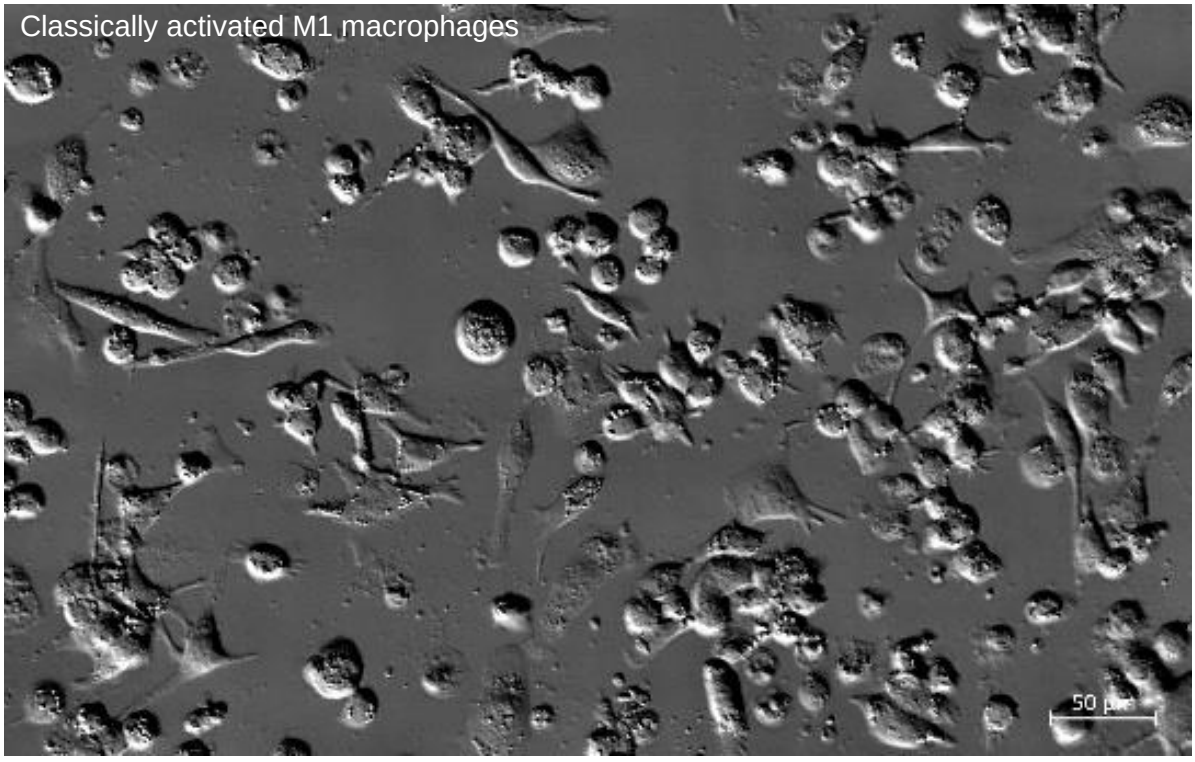


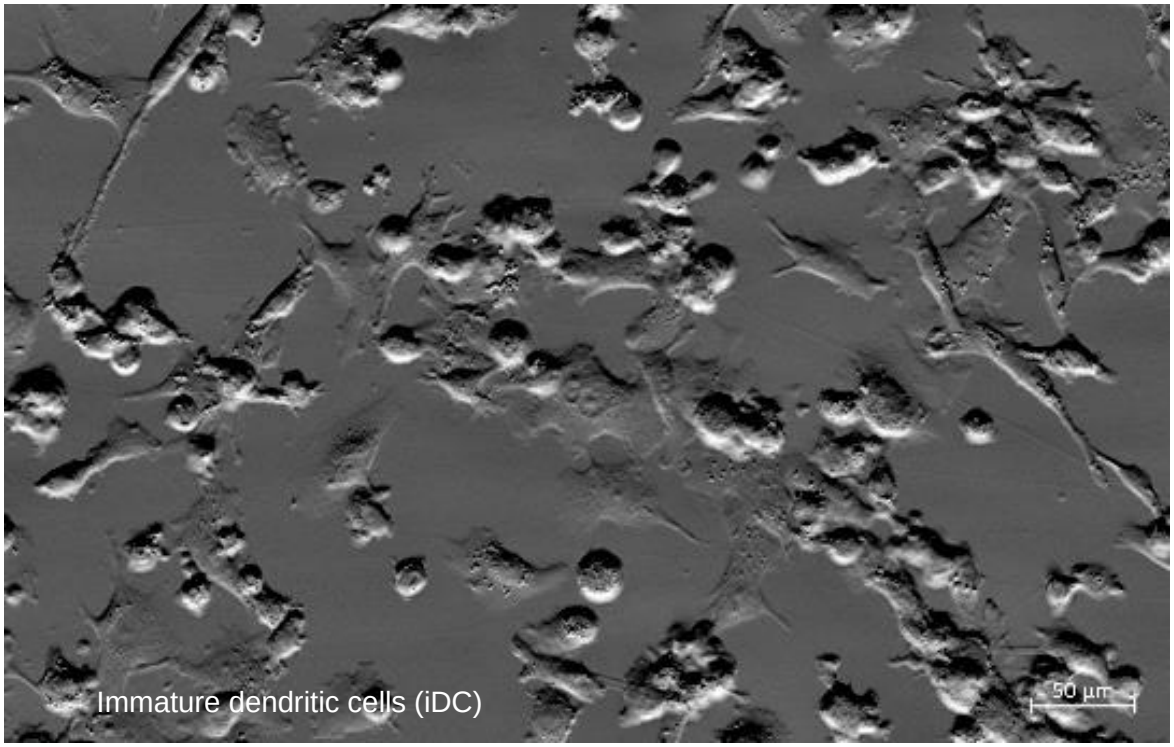
Figure 4.7 - Reflectance Microscopy Images of THP-1 monocytes. THP-1 monocytes that were not subject to any stimulation for differentiation. Images were acquired on a Zeiss Celldiscoverer 7 with a magnification of 20x and a numerical aperture of 0.9 with phase gradient contrast. Scale bar = 50 µm.

After either 2 days of treatment with 100 ng/mL of PMA and 2 days resting or 4 days treatment with 20 ng/mL of PMA and 20 ng/mL of IL-4, THP-1 monocytes had differentiated into resting stage macrophages (M0, Figure 4.8) and immature dendritic-like cells (iDC, Figure 4.8) respectively. Phase gradient contrast images revealed both cell types had adhered to the culture plate surface, unlike their THP-1 precursors. The macrophage-like cells had generally retained their globosity but appear larger in size due to their adherence to the culture plate. The dendritic-like cells had elongated, displaying multiple cytoplasmic projections, and had generally lost their globosity. After 2 days stimulation with LPS, maturation to classical M1 macrophages (Figure 4.8) and mature dendritic-like cells (Figure 4.8) was observed. The M1 macrophages appeared similar in morphology to their M0 precursors, and the mature dendritic-like cells displayed an increased number of cytoplasmic projections. Although these images were acquired with cells that were not subject to $EuQuin_2S$-AuNP treatment, $EuQuin_2S$-AuNP treated THP-1 monocytes (2 nM, 4

hours) were identical to the morphologies described when viewed under the microscope during their culture.







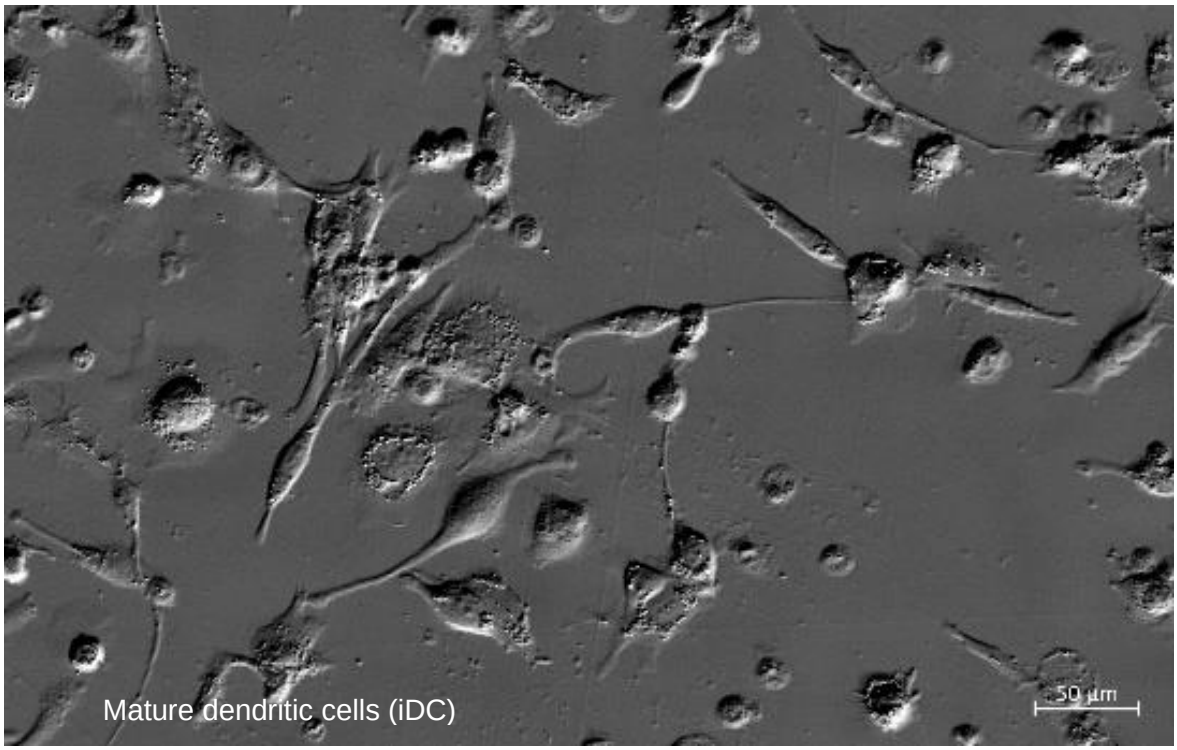


Figure 4.8 - Reflectance microscopy reveals morphological changes of THP-1 to macrophage and dendritic-like cells. THP-1 cells were subjected to differentiation conditions and reflectance images were taken at each stage of the process. Images were acquired on a Zeiss Celldiscoverer 7 with a magnification of 20x and a numerical aperture of 0.9 with phase gradient contrast. Scale bars = 50 µm.

4.3.1.3 The Effect of EuQuin$_2$S-AuNP Treatment on Phenotypical Changes During THP-1 Monocyte Differentiation

To further characterise the cells differentiated from THP-1 monocytes, cells treated with RPMI media containing EuQuin$_2$S-AuNPs (2 nM) for 4 hours prior to cell stimulation and compared to a non-treated control to assess the impact of nanoparticle uptake on cell differentiation and phenotype. Cells were then stained with fluorescent antibodies and their cell surface marker expression was measured by flow cytometry. Flow cytometry was used for this experiment rather than CyTOF due to the availability of antibodies for studying cell surface marker expression.

Live, single cells were identified by a conventional gating strategy (see appendix 4.7.1). The size and granularity of M1 macrophages and mDCs appeared to decrease with respect to monocytes which was expected as monocytes are the largest type of leukocyte.[1] Low cell death was observed in the undifferentiated THP-1 monocytes but differentiation of THP-1 monocytes to M1 and mDCs caused cell death in 40% and 50% of each cell type respectively. There was however no clear change in cell survival induced by EuQuin$_2$S-AuNP treatment.

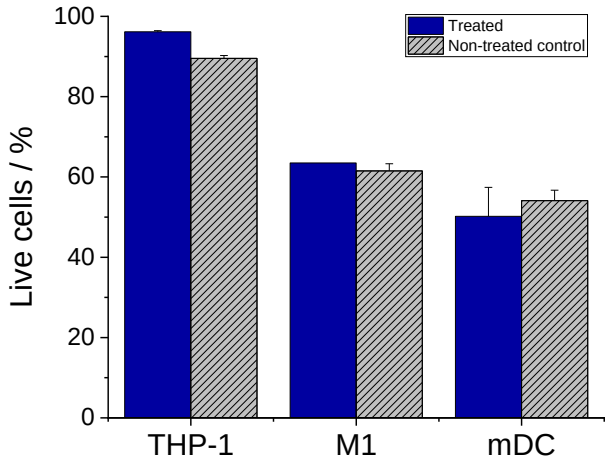


Figure 4.9 - EuQuin$_2$S-AuNP treatment of THP-1 cells prior to differentiation does not increase cell death. Cell survival assay of EuQuin$_2$S-AuNP treated and non-treated control THP-1 monocytes, M1 macrophages and mature dendritic cells (mDC) measured by flow cytometry. Each bar represents the mean number of live cells, error bars = range (N=2).

In both $EuQuin_2S$-AuNP treated and negative control samples, an increase in expression of CD14 associated with macrophages and dendritic cells was observed for M1 and mDC cells (Figure 4.10), as shown in previous studies.[78] The expression of CD11c, a marker commonly used to define dendritic cells,[79] increased in both mDCs and M1 cells (Figure 4.10). CD68 expression increased greatly in M1 – in agreement with a study by Ramprasad *et al.* – and an even further increase in mDC was observed (Figure 4.10).[80] CD80, a cell surface marker present specifically on macrophages, DCs, T-cells and B-cells,[81] increased in expression greatly in both M1 and mDC (Figure 4.10). CD11c, CD14 and CD80 expression agree with Wichers study on THP-1 maturation to M1 and mDCs.[76] Lastly, the expression of HLA-DR, a major histocompatibility complex (MHC) class II receptor found on antigen presenting cells (APCs) increased by around two-fold in both M1 and mDC (Figure 4.10). Histogram plots of each cell surface marker for each population reveal a distinct increase in expression of each marker studied for both M1 and mDCs in the majority of the cell population (Figure 4.10), with the exception of HLA-DR, where expression is increased to a lesser extent.

In general, treatment with $EuQuin_2S$-AuNPs led to comparable increases in cell surface marker expression but some minor discrepancies were observed. CD11c and CD14 expression appears to be suppressed in $EuQuin_2S$-AuNP treated THP-1 monocytes, highlighted further in the contour plot (Figure 4.11). $EuQuin_2S$-AuNPs appeared to elevate CD14, CD68 and CD80 expression in M1 macrophages, as well as CD68 and CD80 in mDCs. However, as this experiment was only carried out with 2 independent tests for each sample type, it is not possible to carry out statistical analysis to evaluate whether these differences are significant.

In summary, there is clear morphological and phenotypical evidence that stimulation of THP-1 monocytes to M1 macrophages and mature dendritic cells has been successfully achieved through stimulation with PMA, IL-4 and LPS under the conditions noted.

Treatment of THP-1 monocytes with 2 nM EuQuin$_2$S-AuNPs prior to the differentiation process does not appear to have a significant impact, and causes no increase in cell death, though more independent repeat experiments would be needed to confirm whether any small effects on cell surface marker expression are statistically significant.

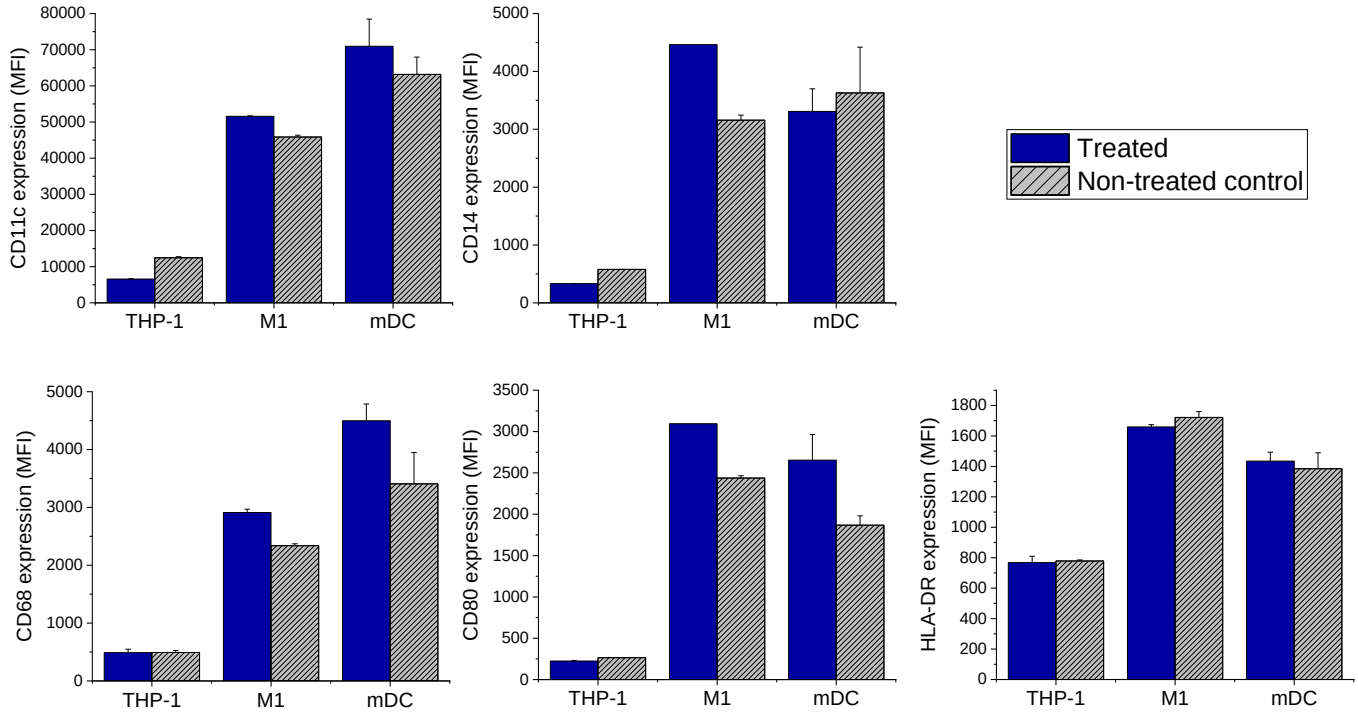


Figure 4.10 - Flow cytometry reveals macrophage and dendritic-like phenotypical changes in NP treated and non-treated THP-1 cells. Cell surface marker expression of EuQuin$_2$S-AuNP treated and non-treated control THP-1, M1 macrophages and mature dendritic cells (mDC). Samples were stained with fluorescent antibodies and the median fluorescence intensity (MFI) was measured by flow cytometry. The results represent the mean MFI ± range from 2 independent experiments. Blue = treated with 2 nM EuQuin$_2$S-AuNPs for 4 hours prior to treatment, grey-dashed = no EuQuin$_2$S-AuNP treatment (non-treated control).

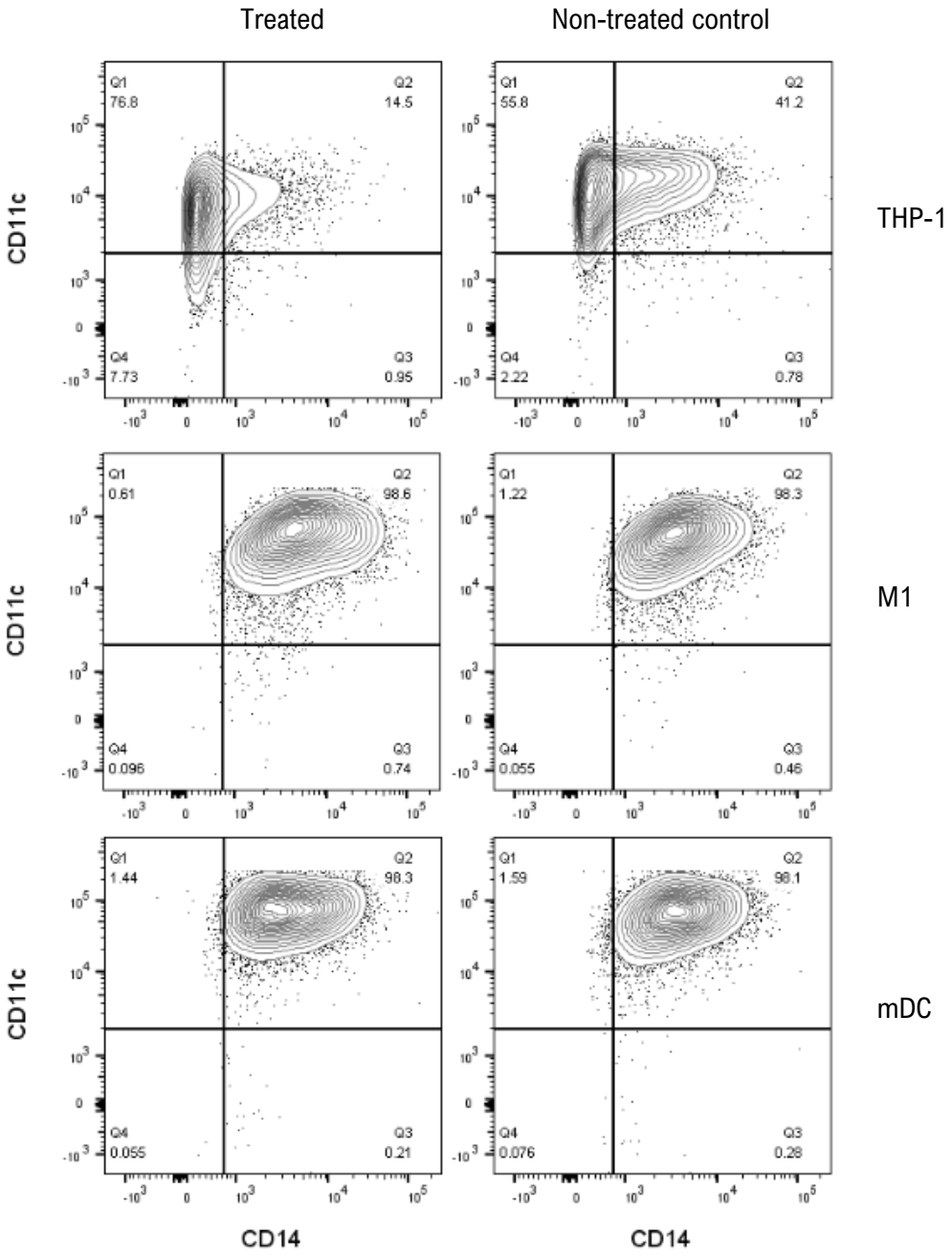
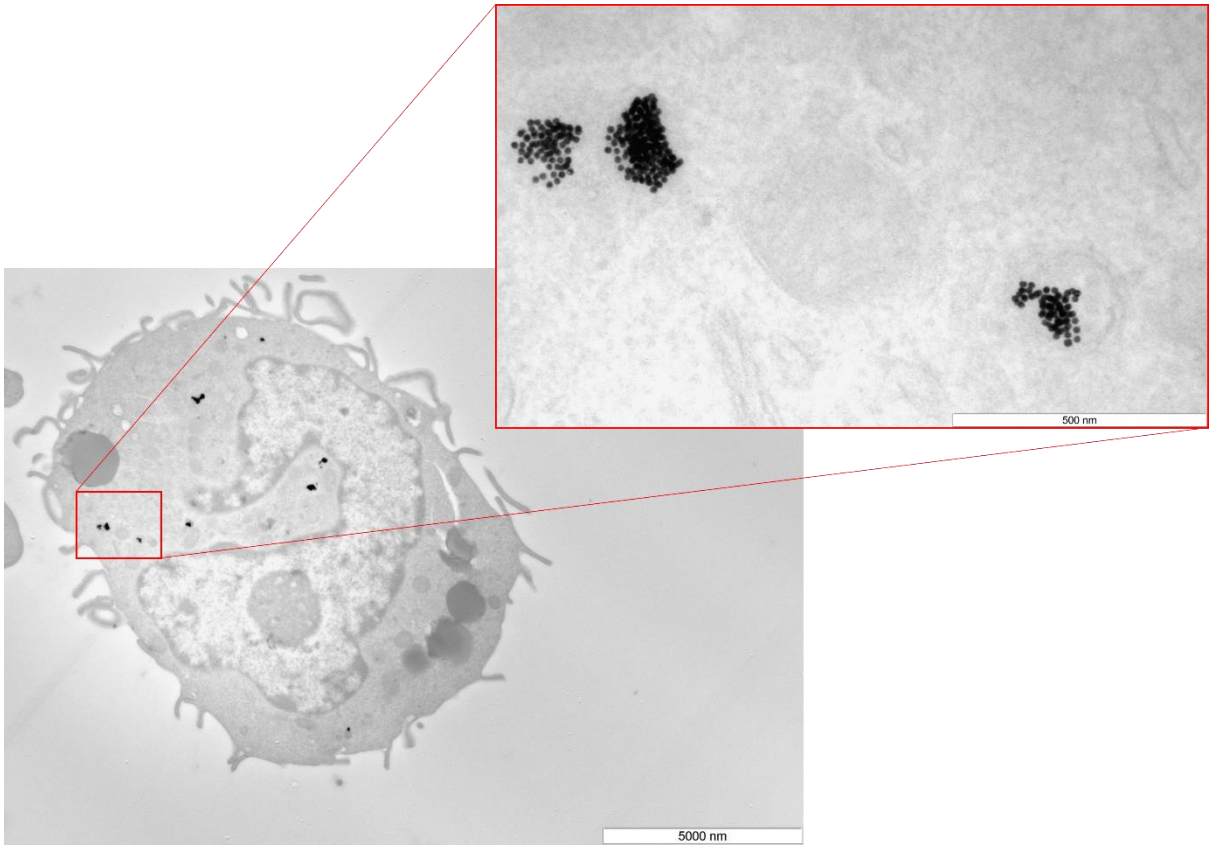
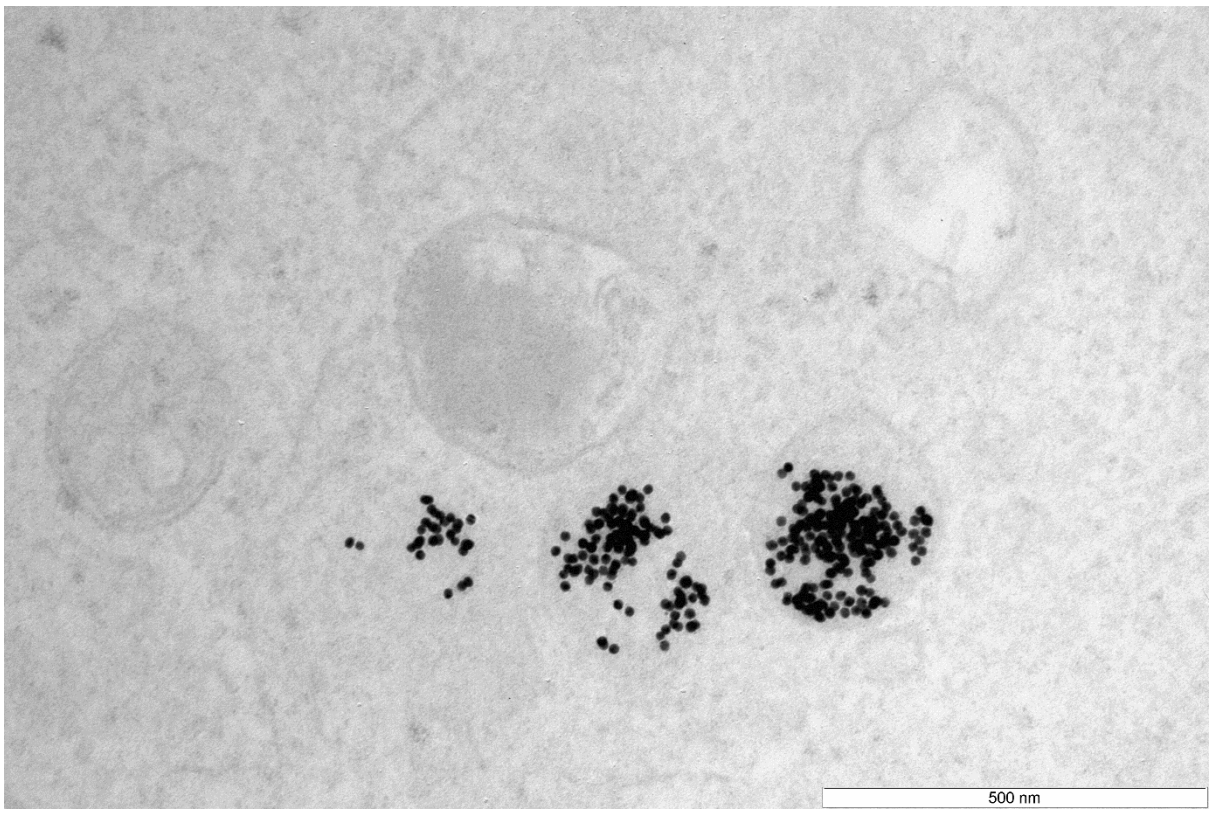


Figure 4.11 - Contour plots of CD11c vs CD14 cell surface marker expression of THP-1 monocytes, M1 macrophages and mature denritic cells (mDC) treated with $EuQuin_2S$-AuNPs for 4 h [2 nM] vs. untreated control. Samples were stained with fluorescent antibodies and the fluorescence intensity was measured by flow cytometry. One representative contour plot from each sample type shown. Treated = treated with 2 nM $EuQuin_2S$-AuNPs for 4 hours prior to treatment, non-treated control = no $EuQuin_2S$-AuNP treatment.

4.3.2 Studying EuQuin$_2$S-AuNP uptake by TEM in M1 Macrophages

To confirm that NPs were internalised by cells, transmission electron microscopy images of M1 macrophages were acquired after EuQuin$_2$S-AuNP treatment. After differentiation of THP-1 monocytes to classically activated M1 macrophages, cells were treated with EuQuin$_2$S-AuNPs at a final concentration of 1 nM for 16 hours. It is worth noting that this is a longer incubation time than used in CyTOF experiments. Cells were then washed and prepared for TEM analysis as described in 3.10.9. Small clusters of EuQuin$_2$S-AuNPs were found within ultra-thin sections of multiple M1 macrophages. Higher magnification images suggest that these agglomerates of NPs are within vesicle-like structures in the cytoplasm. Previous studies by the group have shown that metal-complex coated nanoparticles are taken up by endocytosis pathways.[66] The discovery of these NPs exclusively in vesicle like structures suggests that EuQuin$_2$S-AuNPs are taken up by endosomal mechanisms. From the images taken, there was no evidence of any NPs inside the nucleus, cytoplasm, or any other organelles such as mitochondria at a timepoint of 16 hours. No EuQuin$_2$S-AuNPs were found externally bound to the surfaces of any cells imaged. An average diameter of 13.8 nm was determined from size analysis; consistent with measurements determined from TEM images of EuQuin$_2$S-AuNPs in solution. More images of EuQuin$_2$S-AuNPs contained within M1 macrophages can be found in the appendix (4.7.2).


500 nm
5000 nm


500 nm

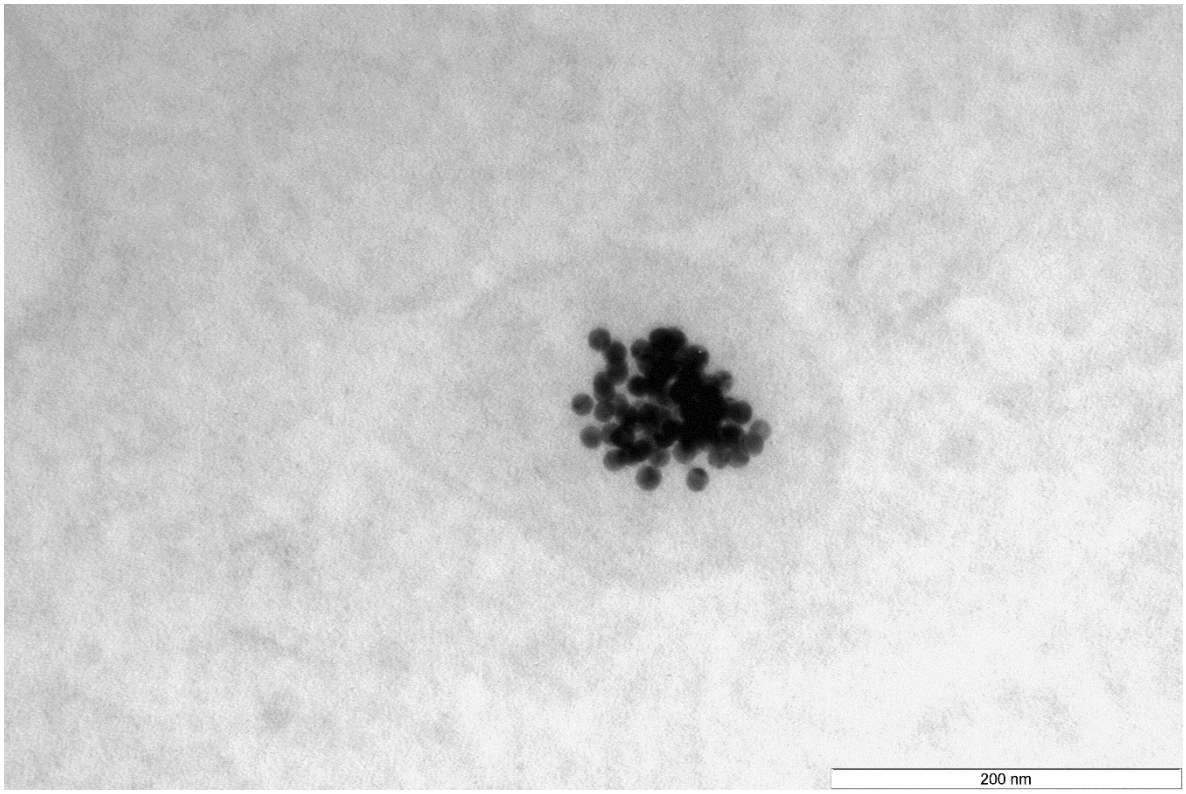


Figure 4.12 - Transmission electron microscopy images reveal endocytotic uptake pathway and intracellular localisation of $EuQuin_2S$-AuNPs in vesicles. TEM images of sections of M1 macrophages treated with $EuQuin_2S$-AuNPs for 16 hours at a concentration of 1 nM.

4.3.3 Uptake of EuQuin$_2$S-AuNPs in Mononuclear Phagocytes

In this section, data concerning the cellular uptake of EuQuin$_2$S-AuNPs in THP-1 Monocytes, M1 Macrophages and Mature Dendritic Cells measured with CyTOF is reported. We treated each cell type with EuQuin$_2$S-AuNPs for 4 hours at different concentrations in order to study uptake and also determine an optimal concentration for CyTOF cell labelling experiments later in this chapter. Different treatment concentrations were used for each cell type because pilot experiments revealed different uptake kinetics in each case. However, after the data from each cell type is shown, EuQuin$_2$S-AuNP uptake is compared at 0.3 nM in each cell type. Like in chapter 3, we generally use median averages due to the non-normally distributed nature of the data.

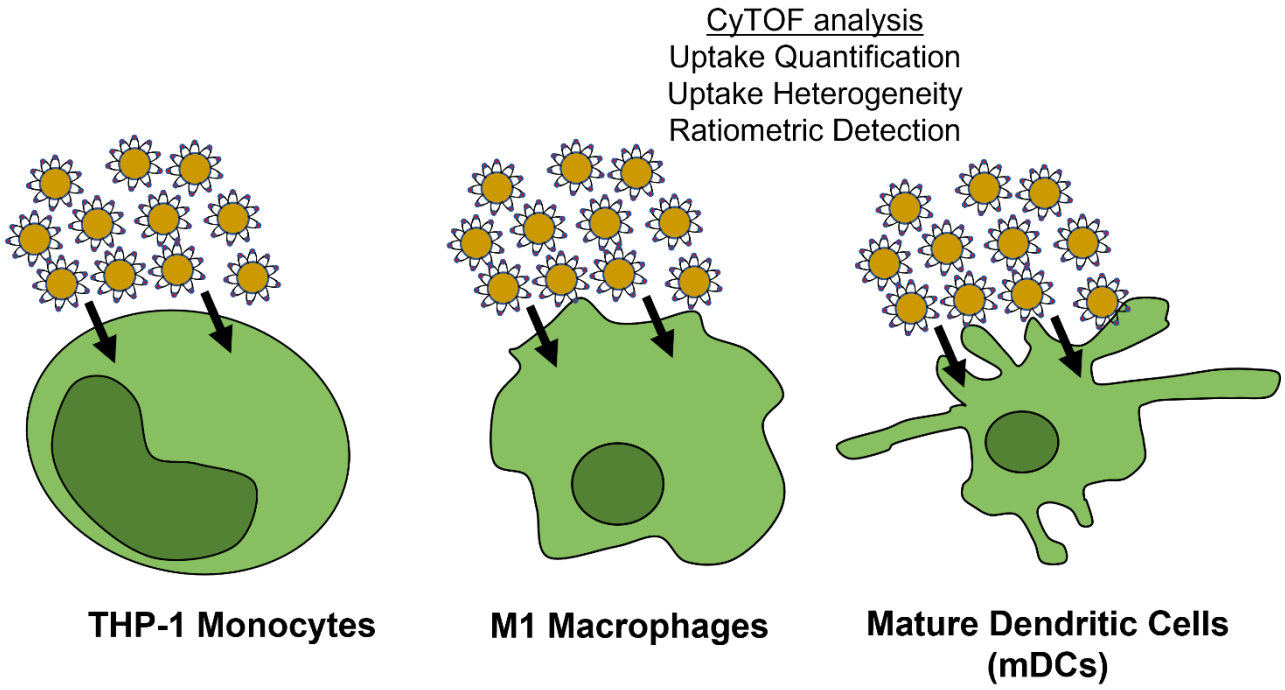


Figure 4.13 - Schematic representation of analysing the cellular uptake of EuQuin$_2$S-AuNPs with CyTOF, the results of which are discussed in this section.

4.3.3.1 THP-1 Monocytes

THP-1 monocytes were treated with $EuQuin_2S$-AuNPs for 4 hours at NP concentrations ranging from 0.2-2 nM. Cells were then prepared for CyTOF analysis to study their cellular uptake. A cisplatin viability assay was used to discriminate between live and dead cells; 92% of cells were live in a non-treated control sample and between 88-93% of cells were live in $EuQuin_2S$-AuNP treated samples (Figure 4.14). We concluded from this data that NP treatment had no effect on cell death during the experiment.

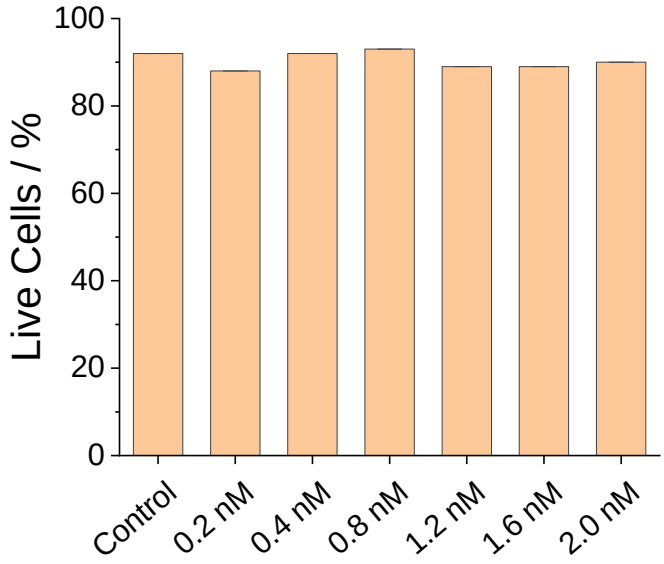


Figure 4.14 - The number of live THP-1 Monocytes at each $EuQuin_2S$-AuNP treatment concentration.

After single cell gating and determining the number of $EuQuin_2S$-AuNPs per cell by conversion of the mean dual counts with data from instrument calibration, the median number of NPs per cell was used to analyse the average uptake at each treatment concentration. It was found the median number of NPs per cell increased proportionally (R^2 = 0.999) with increasing concentration from 22 $EuQuin_2S$-AuNPs per cell at 0.2 nM to 241 at 2 nM (Figure 4.15). This low uptake may be explained by a study by Chhour *et al.*, where they studied the uptake of PEG coated AuNPs with a terminal carboxylic acid group in a RAW 264.7 monocyte cell line.[82] They found that the cellular uptake of smaller, 15 and 25

nm PEG-COOH AuNPs in monocytes was very low compared to larger 50 and 75 nm AuNPs.

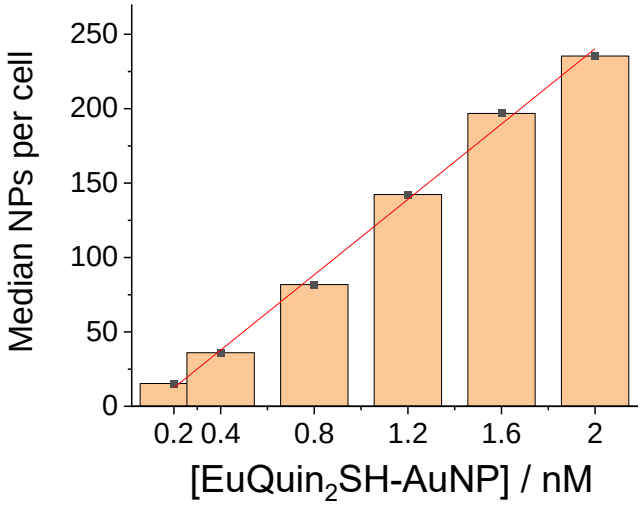


Figure 4.15 - Median uptake of $EuQuin_2S$-AuNPs in THP-1 Monocytes after incubation for 4 hours at concentrations ranging from 0.2-2 nM.

To show the heterogeneity in uptake across THP-1 monocytes at each incubation concentration, first the ^{197}Au mean dual counts determined from CyTOF analysis of $EuQuin_2S$-AuNP uptake were plotted as an overlayed logarithmic histogram on FlowJo (Figure 4.16). Unlike the analysis shown in Chapter 3 regarding $EuQuin_2S$-AuNP uptake in HeLa cells where uptake across the cell population was log-normally distributed, a small subset of THP-1 Monocytes, ranging from 7-10% of the overall population in each sample, had a much higher uptake than the larger population. The data was then transformed to the number of $EuQuin_2S$-AuNPs per cell and the main larger population and the small subset population were plotted as linear histograms (Figure 4.16). The large population of cells did not closely match a log-normal distribution fitted to the data like HeLa cells (data shown in the appendix (4.7.3).

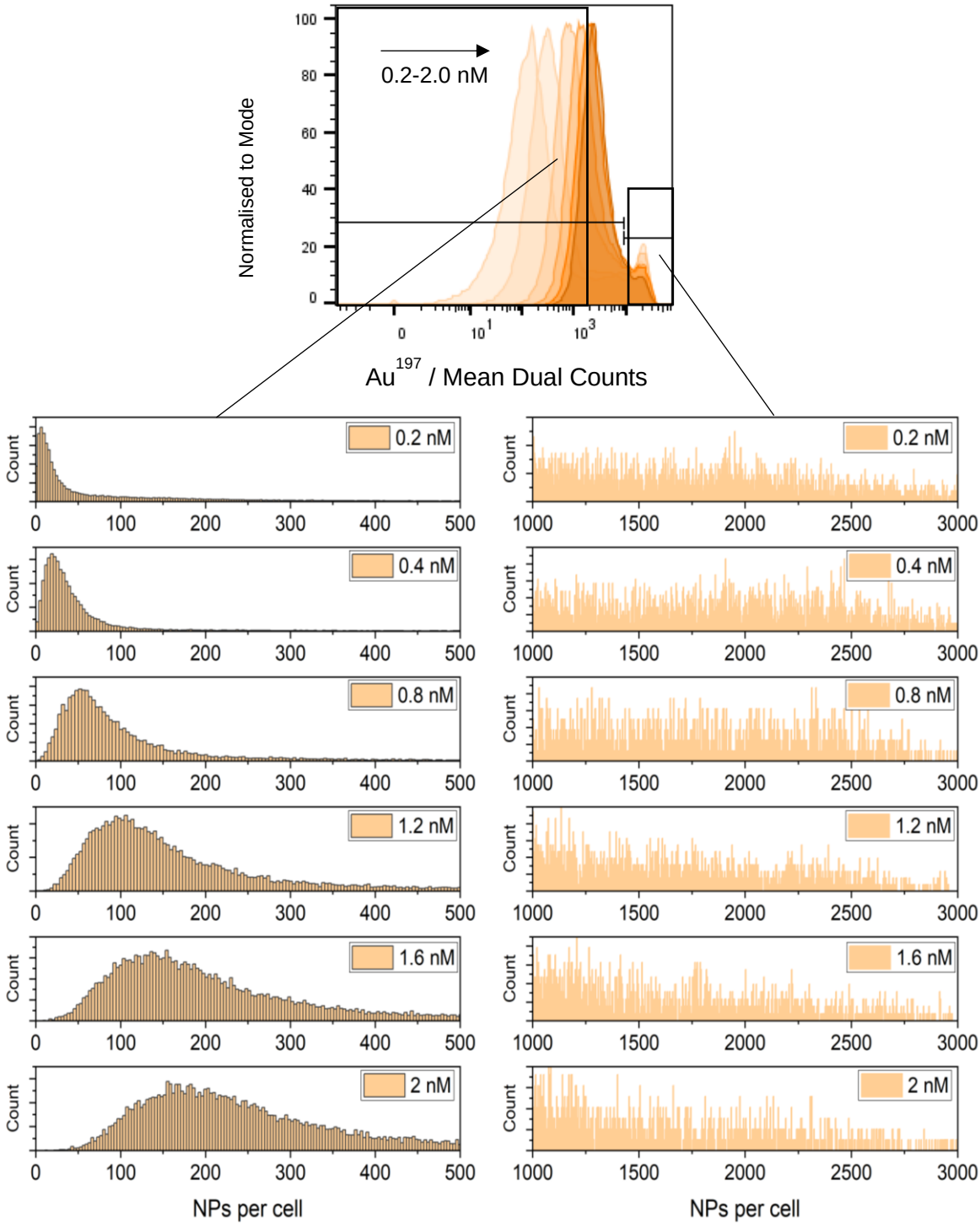


Figure 4.16 - Logarithmic histogram overlay of the ^{197}Au mean dual counts associated with THP-1 Monocyte populations treated with EuQuin$_2$S-AuNPs at concentrations ranging from 0.2-2 nM for 4 hours. Darker colour represents increase in incubation concentration. Horizontal gate lines represent minor (7-10% of overall population) and major population with lower and higher uptake respectively (top). After converting the mean dual counts signal to number of EuQuin$_2$S-AuNPs, the number of NPs per cell was plotted in histograms on a linear scale at each incubation concentration, bottom left panel shows the main cell population uptake and bottom right panel shows the small subset with higher NP uptake. Count (y axis) refers the number of cells in each bin corresponding to its NP content.

The median number of EuQuin$_2$S-AuNPs per cell in the main population increased linearly (R^2 0.995) from 16 to 247 with increasing concentration from 0.2-2 nM. Interestingly, in the small subset population, the median number of EuQuin$_2$S-AuNPs per THP-1 monocyte ranged from 1501 to 1724 and did not increase as concentration increased (Figure 4.17).

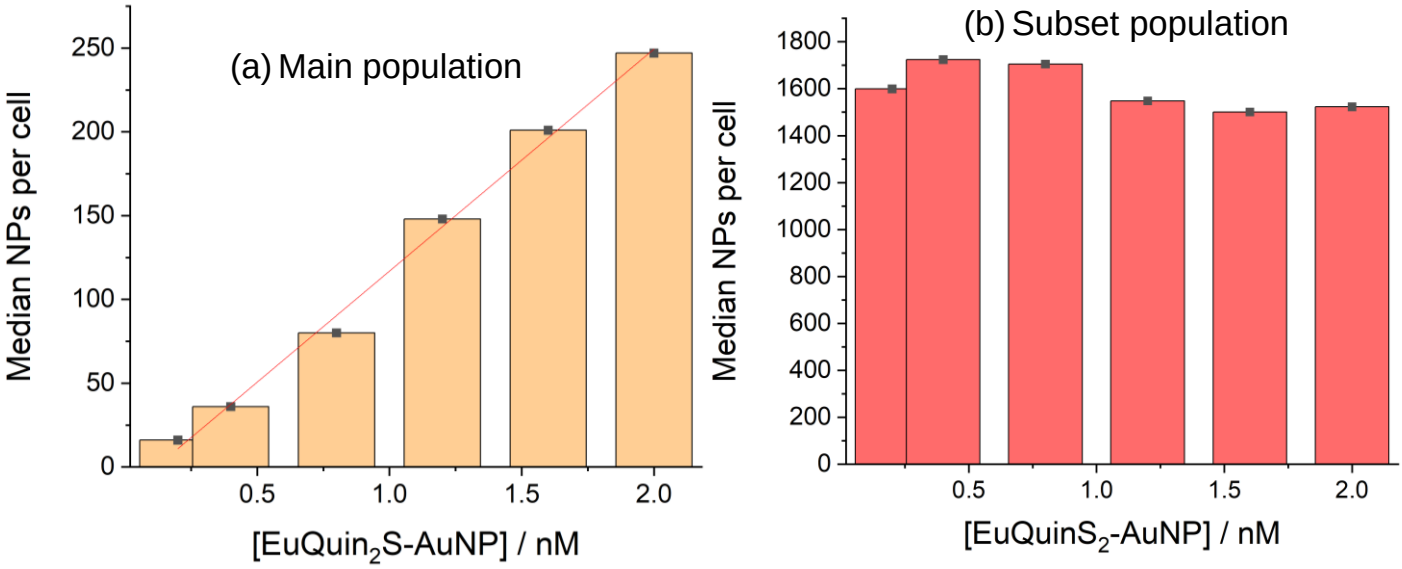


Figure 4.17 - The median number of EuQuin$_2$S-AuNPs per THP-1 monocyte after treatment for 4 hours at 0.2-2 nM in (a) the main population and (b) the subset population outlined in Figure 4.16.

Although the signal in the ^{197}Au channel is within the limits of detection of the CyTOF instrument, the ^{153}Eu signal from EuQuin$_2$S-AuNPs was also analysed for comparison. From analysis of the number of EuQuin$_2$SH complexes per AuNP calculated from the calibration, a ^{197}Au:^{153}Eu of 89:1 was calculated. After accounting for the ^{197}Au:^{153}Eu ratio, the number of EuQuin$_2$S-AuNPs per cell determined from the ^{153}Eu channel ranged from 1072 to 1634, but also did not increase linearly with concentration, although the population with a 2 nM treatment had the highest uptake (Figure 4.18). Although there is a greater variation between each concentration, these values are in broad agreement with the magnitude calculated from the ^{197}Au signal. Further studies are required to understand why EuQuin$_2$S-AuNP uptake does not increase in this small subset population.

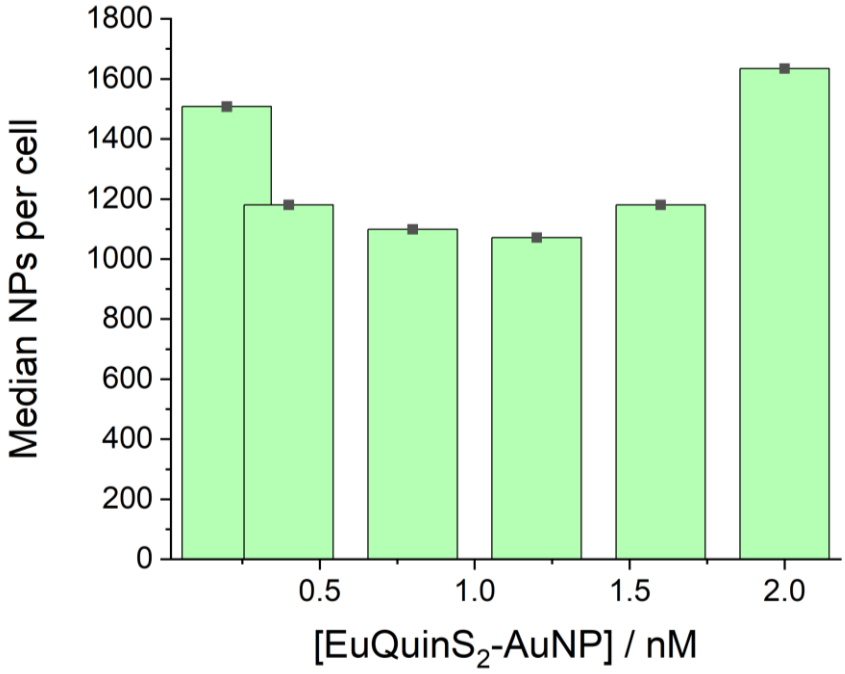


Figure 4.18 - The median number of $EuQuin_2S$-AuNPs per THP-1 monocyte calculated using signal from the ^{153}Eu channel after treatment for 4 hours at 0.2-2 nM] the subset population outlined in Figure 4.16.

In order to gain some understanding into the heterogeneity of $EuQuin_2S$-AuNP uptake, the phenotype of $EuQuin_2S$-AuNP treated THP-1 monocytes was analysed by flow cytometry. Analysis revealed that 5% of THP-1 cells were CD80+ and 9% were CD68+, as well as 13% HLA-DR+ (Figure 4.19).

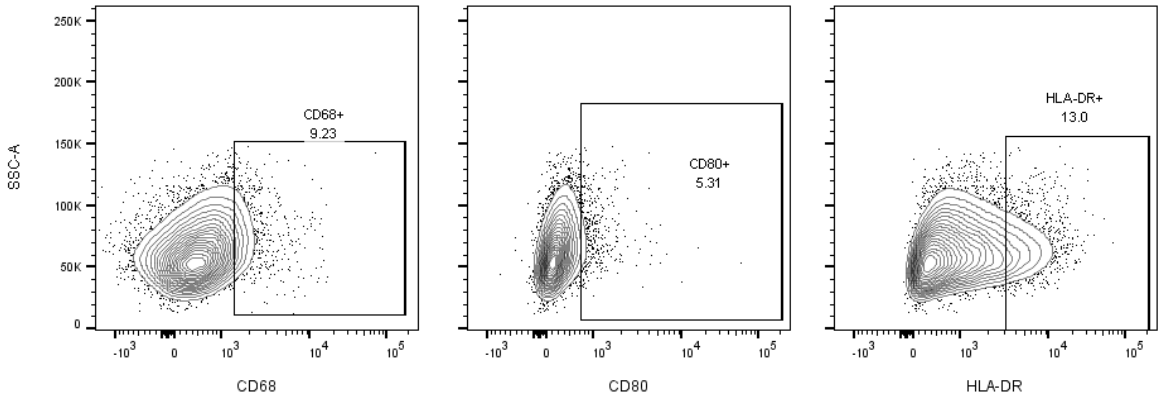


Figure 4.19 - Expression of macrophage cell surface markers in subset THP-1 monocyte population may explain high NP uptake in small subset of population. SSC-A vs. CD68, CD80 and HLA-DR contour plots of a THP-1 monocyte population. Cells were stained with fluorescent antibodies and analysed by flow cytometry.

These cell surface markers are characteristic of macrophages that are known to have a higher phagocytic rate than monocytes,[83, 84] suggesting that more nanoparticles may be taken up by endocytosis in this population subset during $EuQuin_2S$-AuNP treatment. The prevalence of high expression of CD80 (5%), CD68 (9%) and HLA-DR (13%) are similar to the size of the subset of population with high uptake (7-10%). This could suggest that this subset of cells are more macrophage-like, which may explain their higher uptake. Future studies could incorporate cell surface markers for CD80, CD68 and HLA-DR into the same CyTOF experiment to directly study their phenotype, however the development of a larger CyTOF panel was not possible within the timeframe of this work.

4.3.3.2 M1 Macrophages

After treatment of M1 macrophages with $EuQuin_2S$-AuNPs for 4 hours at NP concentrations ranging from 0.05-0.6 nM, nanoparticle uptake was analysed by CyTOF. 78-84% of cells studied were live, a higher relative percentage with respect to viability studies in 4.3.1.3. No correlation between cell death and NP treatment concentration were observed (Figure 4.20).

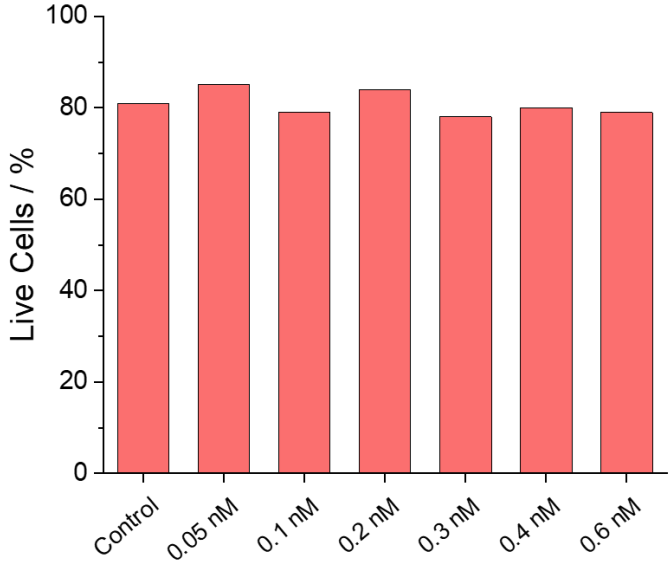


Figure 4.20 - The number of live M1 macrophages at each $EuQuin_2S$-AuNP treatment concentration.

The median number of NPs per cell increased proportionally with NP treatment concentration from 176 to 1670 (R^2 = 0.990), much higher than observed with THP-1 monocytes. This agrees with a previous uptake study with macrophage and monocyte precursors with AuNPs.[85] At 0.05 and 0.1 nM treatments, 3% and 1.7% of cells contained no $EuQuin_2S$-AuNPs (Figure 4.21).

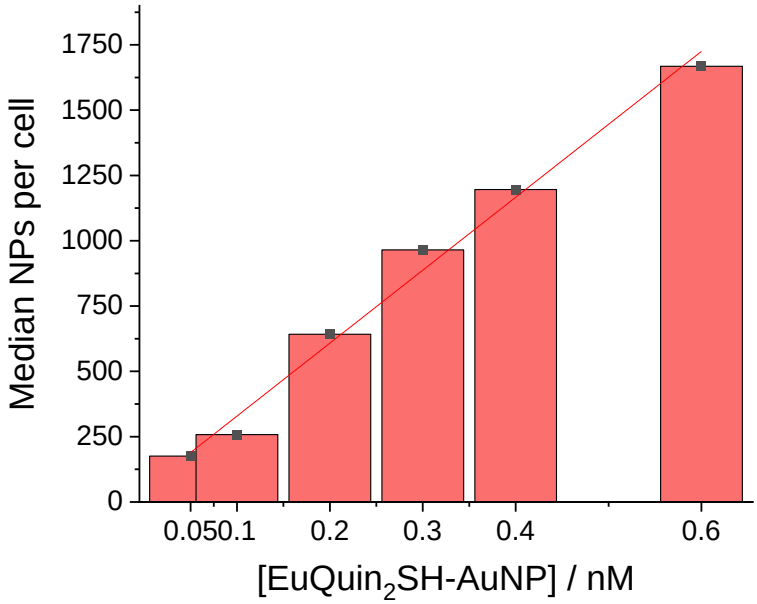


Figure 4.21 - Median uptake of $EuQuin_2S$-AuNPs in M1 macrophages after incubation for 4 hours at concentrations ranging from 0.2-2 nM.

The number of $EuQuin_2S$-AuNPs per cell was then plotted as a linear histogram, revealing that there were two distinct populations – a population with high NP content that represented 54-66% of the total number of cells, and a population with lower NP content making up 34-46% of cells (Figure 4.22). The median number of $EuQuin_2S$-AuNPs per cell increase linearly from 24 to 189 (R^2 = 0.995) and from 771 to 2442 (R^2 = 0.961) in each respective high and low uptake population at each concentration (Figure 4.23). This is unlike the observation in the THP-1 monocyte high uptake subset, where uptake did not increase with concentration. Phenotyping by FACS indicated that around 70% of the population was CD68+, which could suggest that not the whole cell population is behaving like macrophages, explaining their lower uptake. This is discussed further in section 4.3.3.4.

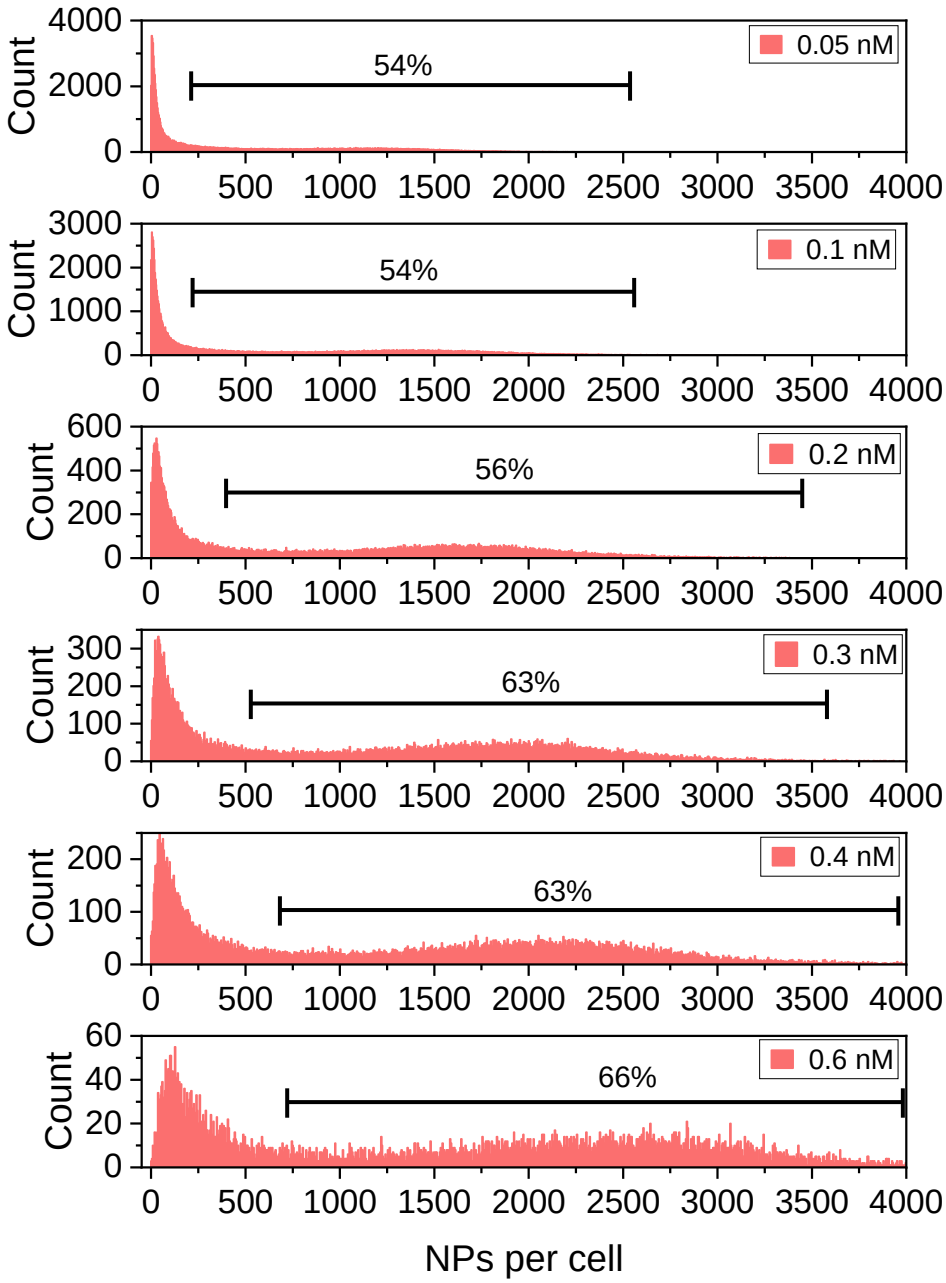


Figure 4.22 - Linear histograms of the number of EuQuin$_2$S-AuNPs per M1 macrophage after treatment for 4 hours at concentrations ranging from 0.05-0.6 nM. Percentage indicates the number of cells that had a much higher uptake at each concentration. Count (y axis) refers the number of cells in each bin corresponding to its NP content.

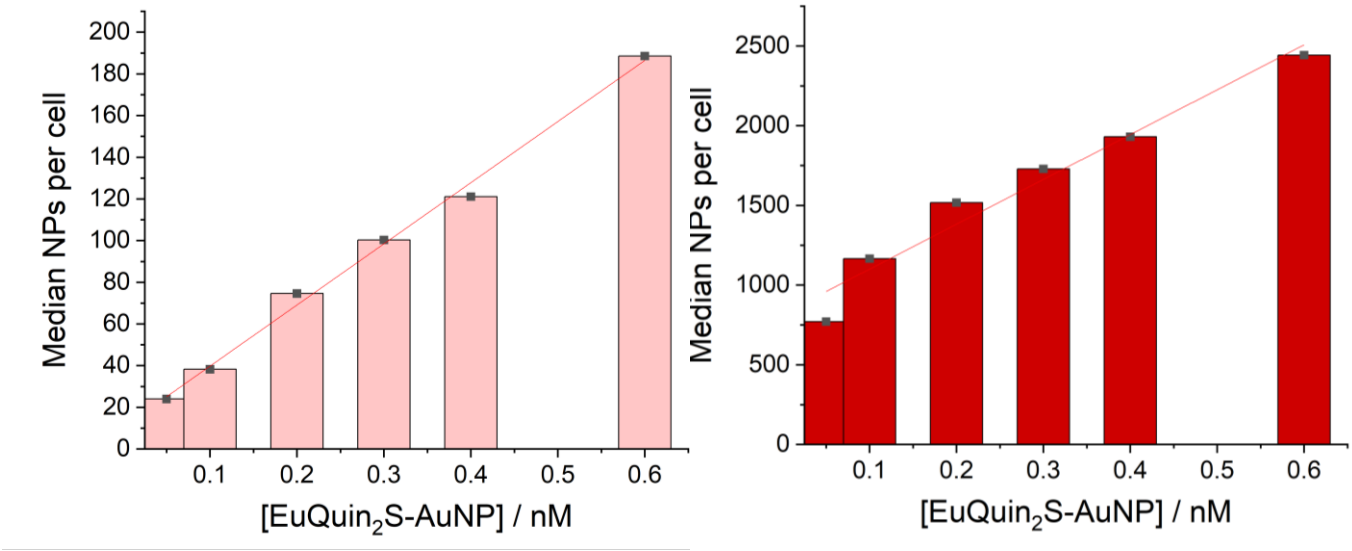


Figure 4.23 - The median number of $EuQuin_2S$-AuNPs per M1 macrophage in the population with low (left) and high (right) uptake at each treatment concentration.

4.3.3.3 Mature Dendritic Cells (mDCs)

After treatment of mDCs with $EuQuin_2S$-AuNPs for 4 hours at NP concentrations ranging from 0.017-0.4 nM, nanoparticle uptake was analysed by CyTOF. Only 52-63% of cells were alive (Figure 4.24), but no increase in cell death was observed from $EuQuin_2S$-AuNP treatment at any of the concentrations tested. The high amount of cell death is likely due to the stress of the differentiation process during cell culture and is similar to the observed fraction of dead cells found from FACS experiments in 4.3.1.2.

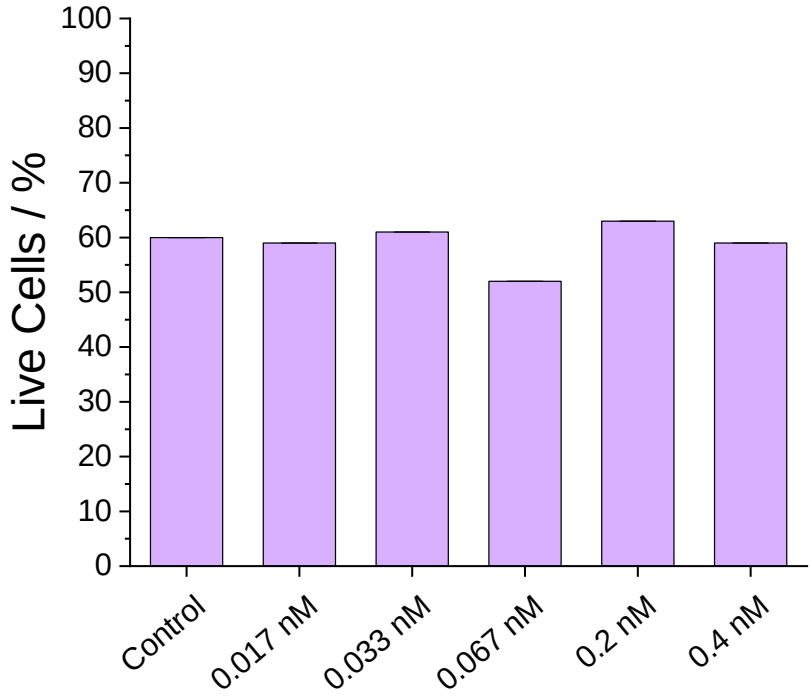


Figure 4.24 - The number of live mDCs at each $EuQuin_2S$-AuNP after 4 hours treatment at concentrations ranging from 0.017-0.4 nM.

In live, single cells, $EuQuin_2S$-AuNP uptake increased proportionally with increasing concentration (R^2 = 0.995) from 7 at 0.017 nM to 265 at 0.4 nM (R^2 = 0.995, Figure 4.25). At 0.017 and 0.033 nM treatments, 56% and 34% of mDCs contained no $EuQuin_2S$-AuNPs (Figure 4.25). At 0.067 nM treatment concentration, 95% of mDCs contained $EuQuin_2S$-AuNPs and 100% of mDCs contained $EuQuin_2S$-AuNPs at 0.2 and 0.4 nM.

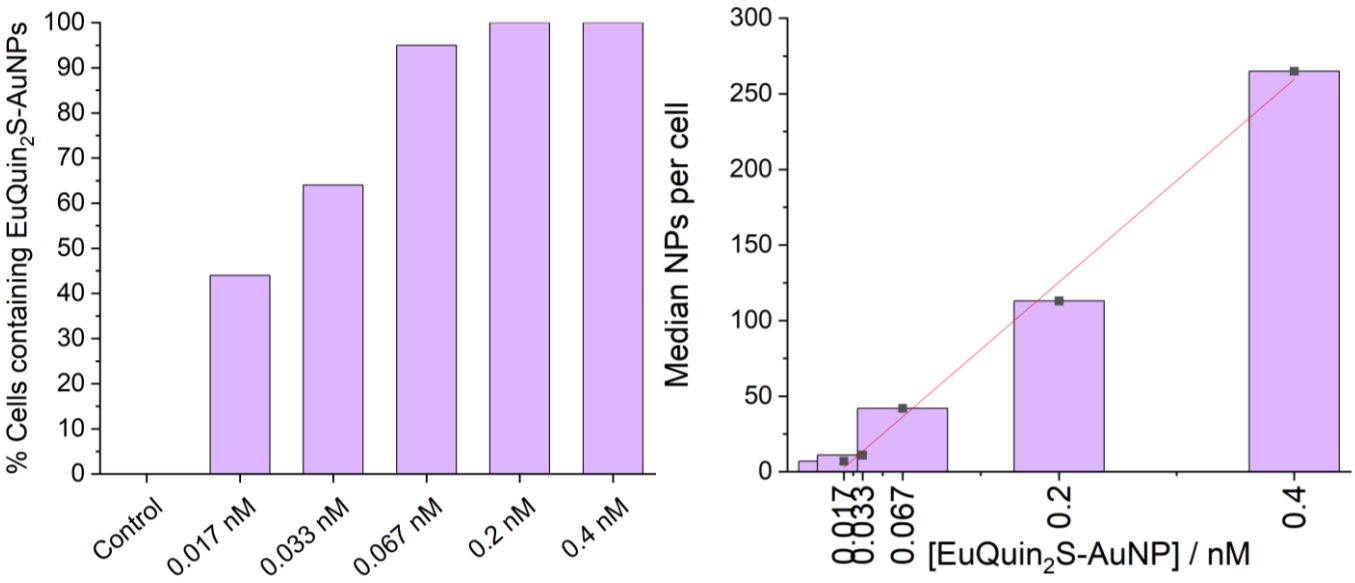


Figure 4.25 - The percentage of mDCs containing EuQuin$_2$S-AuNPs (left) and the median number of EuQuin$_2$S-AuNPs per mDC after 4 hours treatment at concentrations ranging from 0.017-0.4 nM.

Linear histograms of the number of EuQuin$_2$S-AuNPs per mDC were then plotted to show the distribution of NPs within the population (Figure 4.26). Although there was a large variation in NP uptake, there was no apparent 2nd population of cells with a much larger uptake as was observed in THP-1 monocytes and M1 macrophages. As one distinct population was observed, a log-normal distribution was fitted to the histograms. This distribution fitted well, demonstrating that EuQuin$_2$S-AuNP uptake in an mDC population differentiated from THP-1 monocytes is best described by a log-normal distribution, similar to HeLa cells.

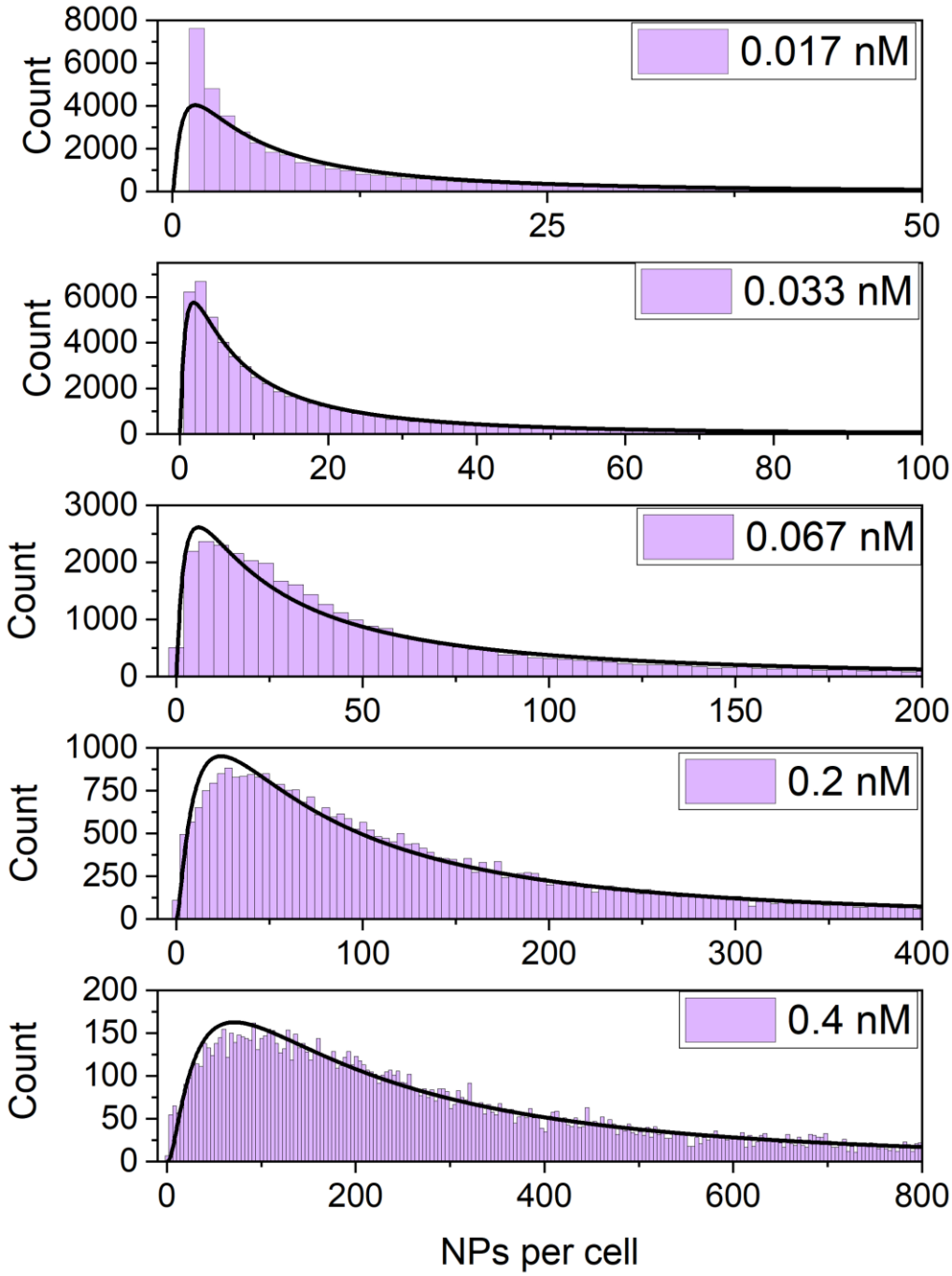


Figure 4.26 - Linear histograms of the number of EuQuin$_2$S-AuNPs per mDC at each treatment concentration. NOTE: varying x-axis scale to highlight uptake at low concentration. Count (y axis) refers the number of cells in each bin corresponding to its NP content.

4.3.3.4 Comparing $EuQuin_2S$-AuNP uptake in THP-1 Monocytes, M1 Macrophages and Mature Dendritic Cells

So far in this section, we have shown the distribution of $EuQuin_2S$-AuNPs in three types of mononuclear phagocytic cells at the single cell level. After a 4-hour treatment with $EuQuin_2S$-AuNPs at a range of concentrations, THP-1 monocytes, M1 macrophages and mDCs each showed distinctly different uptake dynamics. Here, we compare the cellular uptake of $EuQuin_2S$-AuNPs in each cell type at a $EuQuin_2S$-AuNP concentration of 0.4 nM.

CyTOF analysis revealed, over the whole population for each cell type, there was a stark difference in cellular uptake between each type of mononuclear phagocyte. THP-1 monocytes had the lowest average uptake with a median of 36 $EuQuin_2S$-AuNPs per cell. mDCs had a median uptake 265 and M1s had a much higher median uptake of 1200 $EuQuin_2S$-AuNPs per cell (Figure 4.27).

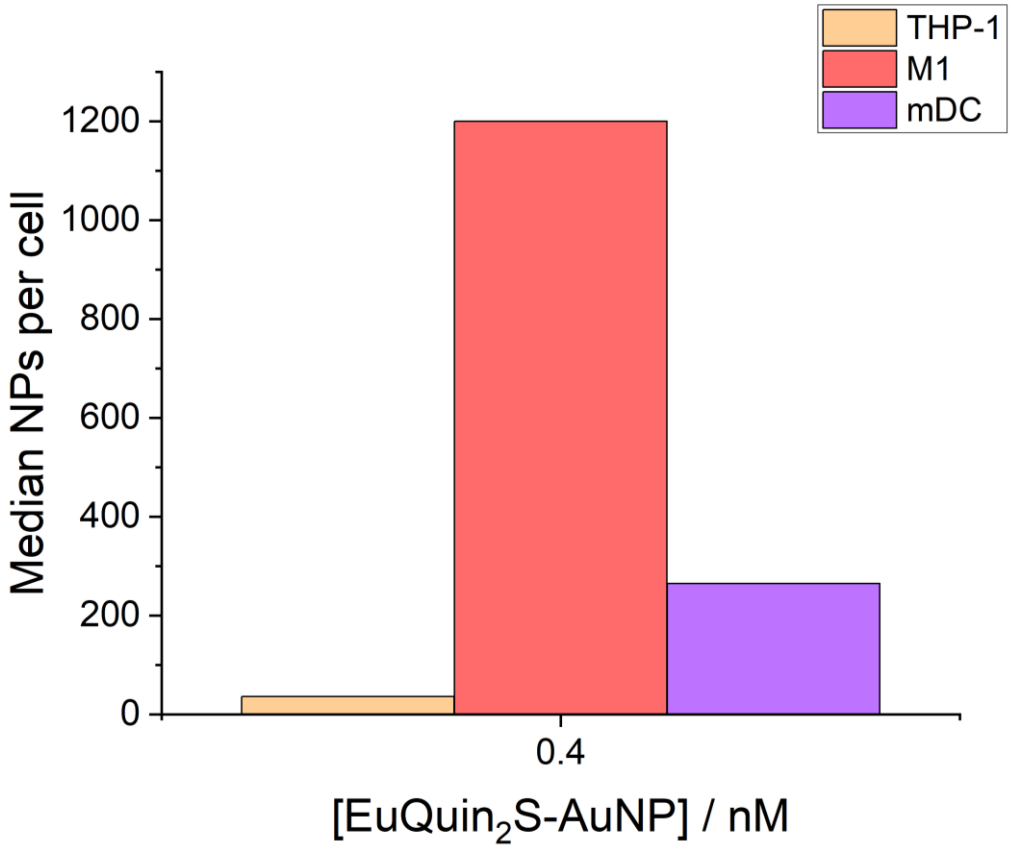


Figure 4.27 - Comparison of the median number of $EuQuin_2S$-AuNPs per cell in THP-1 monocytes, M1 macrophages and mature dendritic cells (mDCs) after NP treatment at a concentration of 0.4 nM for 4 hours.

Next, the histogram outline of each cell type was overlayed (Figure 4.28). Note that this histogram is plotted on a logarithmic scale with logarithmic binning in order to more easily visualise the wide dynamic range in uptake, so the size of each population appears different to those presented earlier in this section due to the logarithmic binning used.[86] As NP uptake within each cell population was highly heterogeneous, there is a large overlap in their respective NPs per cell histograms. In particular, the small subset of THP-1 monocytes with high uptake has a similar uptake to the M1 macrophage population with high uptake, which is mirrored in their subset median values of 1724 and 1931 $EuQuin_2S$-AuNPs per cell respectively (Figure 4.29). This supports the hypothesis that this subset of THP-1 monocytes has macrophage like behaviour and phenotype, as discussed in 4.3.3.1.

Additionally, the subset of M1 macrophages with lower uptake had a similar median uptake (235) of $EuQuin_2S$-AuNPs to mDCs (265). This may suggest that this population of M1 macrophages behave more like mDCs, which may also be supported by the microscopy images of M1 macrophages in 4.3.1.2 that revealed dendritic cell-like elongation and cytoplasmic projections in some M1 macrophages. This is further supported by some high level of CD11c expression shown in 4.3.1.3, a marker commonly used to define dendritic cells.[79]

We have already discussed in 4.3.3.1 that the low uptake in THP-1 monocytes may be due to the small size of our $EuQuin_2S$-AuNPs, given Chhour *et al.*'s size dependent study.[82] A study by Oh *et al.* also showed higher uptake of 10, 20 and 40 AuNPs in U937 cells differentiated into macrophages than in their undifferentiated monocyte counterparts, in agreement with our work.[85] Studies by Lutsiak *et al.* and Yang *et al.* have both previously shown similar levels of NP uptake in both macrophages and dendritic cells with 500 nm polymeric NPs and 3 nm amphiphilic NPs respectively.[71, 87] However, other studies have shown that uptake in macrophages is highly dependent on protein corona and NP surface charge, so these studied may not be useful for comparison.[88, 89] Furthermore, both of these

studies used leukocytes directly isolated from mice rather than human cell lines used in our work.

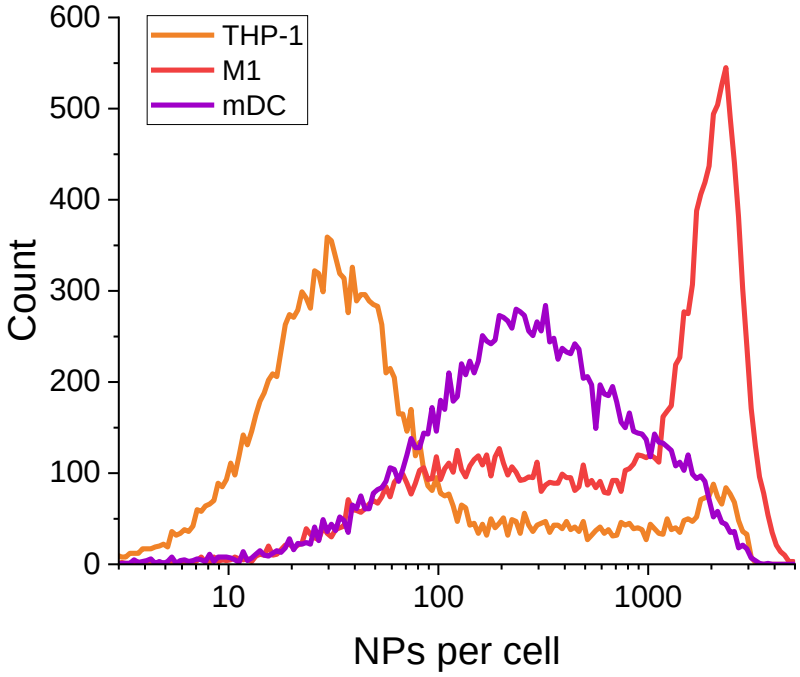


Figure 4.28 - Logarithmic histogram overlay of the number of $EuQuin_2S$-AuNPs per cell in THP-1 monocyte, M1 macrophage and mDC populations after NP treatment for 4 hours at a concentration of 0.4 nM. Count (y axis) refers the number of cells in each bin corresponding to its NP content.

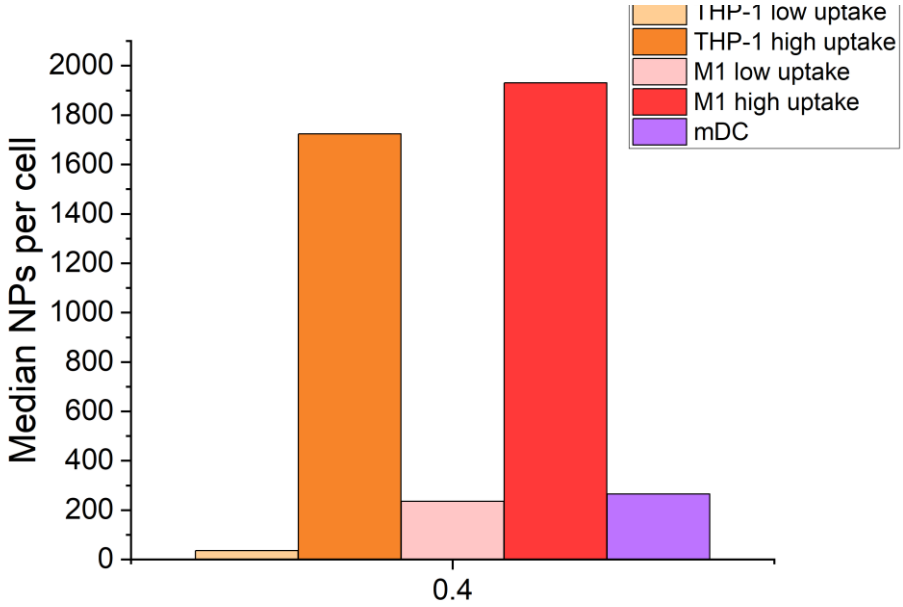


Figure 4.29 - Median number of $EuQuin_2S$-AuNPs per cell in the high and low uptake populations of THP-1 monocyte, M1 macrophage and mDCs after NP treatment for 4 hours at a concentration of 0.4 nM.

In summary, we have here shown the uptake of EuQuin$_2$S-AuNPs in THP-1 monocytes and M1 macrophages and mDCs. Cellular uptake followed the trend: M1 macrophages > mDCs > THP-1 monocytes. This is the first study of its kind where a human monocytic cell line has been used to produce differentiated macrophages and dendritic cells. Furthermore, single cell analysis revealed the high heterogeneity in uptake and similarities in uptake between subsets of each cell population. This was attributed to morphological and phenotypical heterogeneity in each population. However, a full CyTOF phenotyping panel is needed within these experiments to confirm correlations between phenotype and uptake.

4.3.4 EuQuin$_2$S-AuNPs as Cellular Labels for Detecting THP-1 Monocytes and their Differentiation into M1 Macrophages and Dendritic Cells with CyTOF

There is a requirement for multimodal, long-term cell tracking agents to understand monocyte migration and their differentiation into cells such as macrophages and dendritic cells. We hypothesise that our luminescent EuQuin$_2$S-AuNPs, detectable by CyTOF – a highly sensitive technique – will be detectable within cells after multiple proliferation cycles. In this section, we assess the use of EuQuin$_2$S-AuNPs as cellular labels for detecting THP-1 monocytes over extended time periods. We first treat THP-1 monocytes with EuQuin$_2$S-AuNPs and assess their initial uptake. We then investigate the depletion of EuQuin$_2$S-AuNP content in THP-1 monocytes that were allowed to proliferate for 276 hours after initial EuQuin$_2$S-AuNP treatment. We also differentiate some EuQuin$_2$S-AuNP treated THP-1 monocytes into M1 macrophages and mDCs and assess their EuQuin$_2$S-AuNP content over time. This is because we are interested in the ability of EuQuin$_2$S-AuNPs to label monocytes and detect them in sites of interest, were they to be used as multimodal labels in pre-clinical studies to help understanding of monocyte migration, fate and function.

The results from these experiments are shown before a general discussion of their implications.

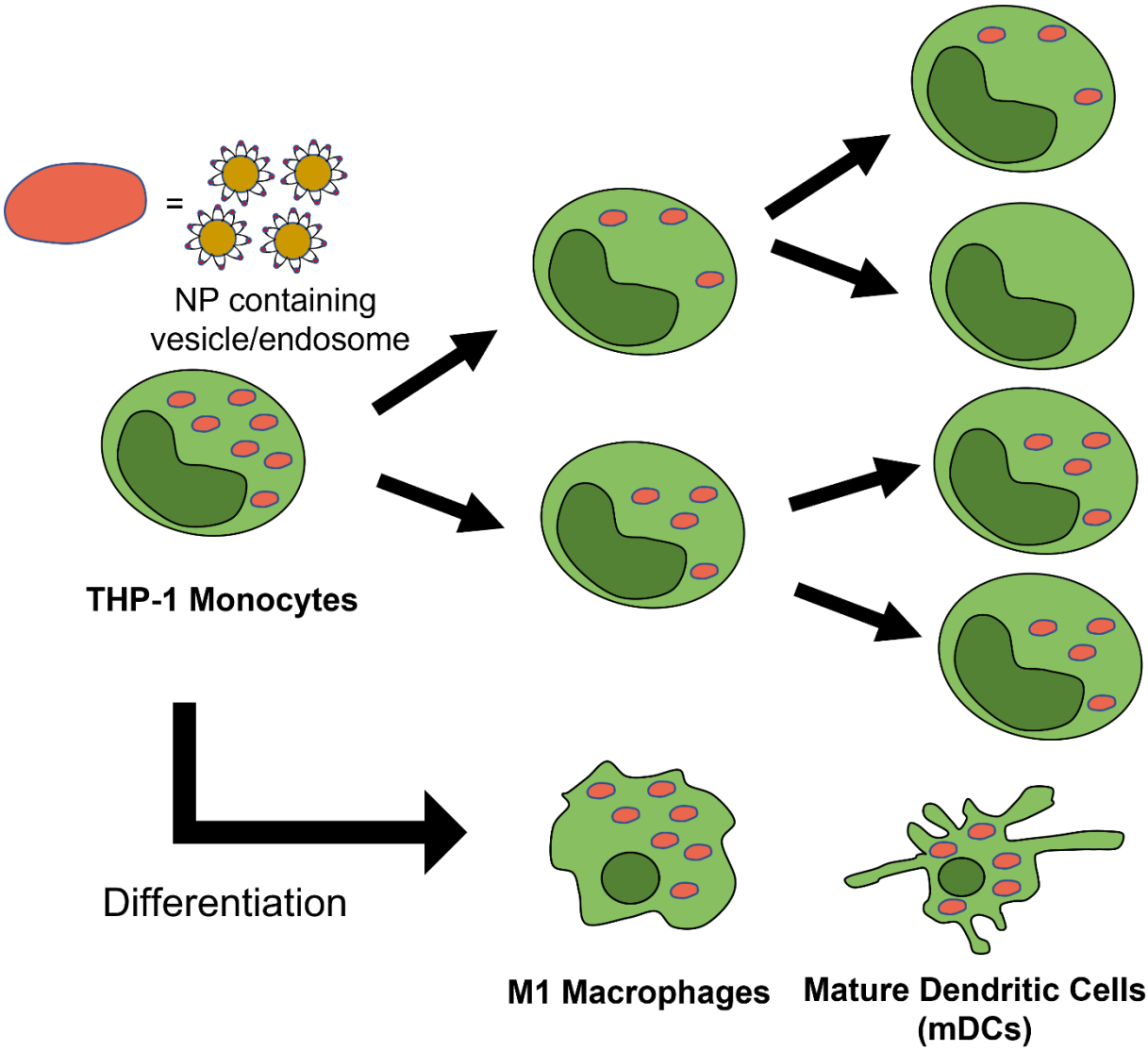


Figure 4.30 - Here, we use CyTOF to assess the content of $EuQuin_2S$-AuNP treated THP-1 monocytes under two conditions: as proliferative THP-1 monocytes not subject to differentiation, or THP-1 monocytes that have been differentiated into M1 macrophages and dendritic cells. This will test our hypotheses regarding the suitability of $EuQuin_2S$-AuNPs as cellular labels in CyTOF experiments for applications such as cell tracking.

4.3.4.1 Initial uptake of EuQuin$_2$S-AuNPs

THP-1 monocytes were treated with EuQuin$_2$S-AuNPs for 4 hours and their NP content was analysed by CyTOF. Due to the relatively low uptake observed in THP-1 monocytes in 4.3.3.1, the highest treatment concentration of 2 nM was chosen for this work. From CyTOF analysis, the median number of EuQuin$_2$S-AuNPs per cell was 226, in very close agreement with 241 NPs per cell determined from our previous study. 12% of the overall population had significantly higher uptake (median NPs per cell = 2986) than the major population (median NPs per cell = 193). As discussed previously, an independent flow cytometry experiment revealed that this could be due to a small subset of the THP-1 population expressing macrophage phenotype.

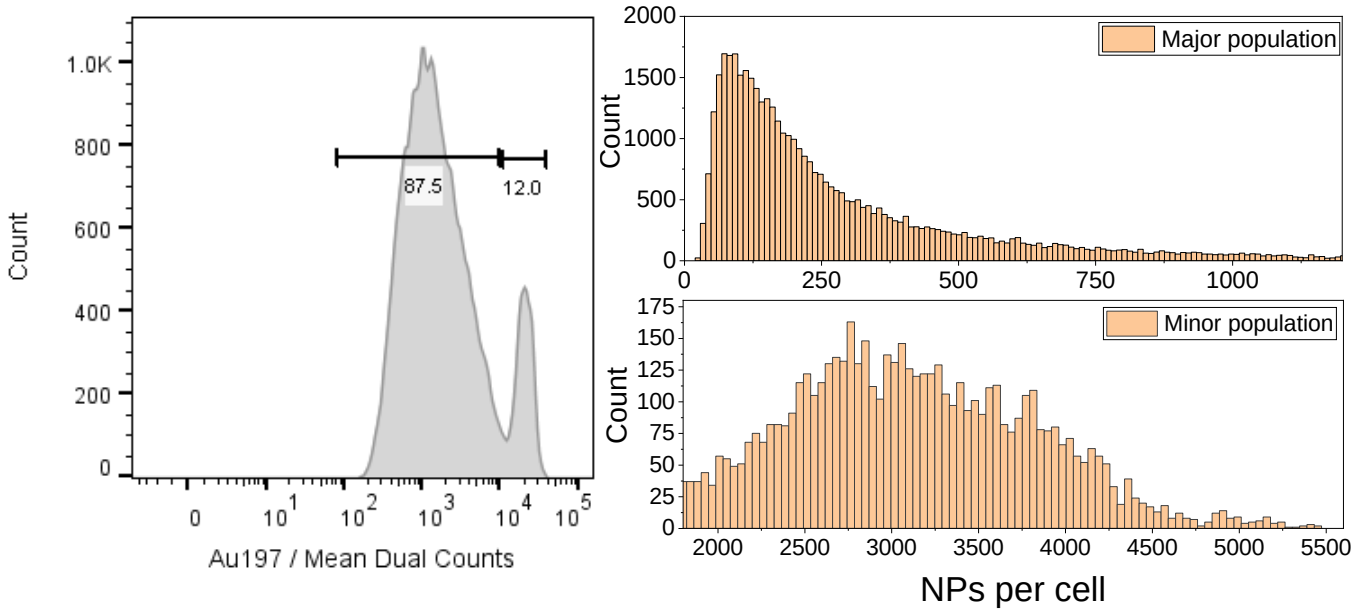


Figure 4.31 - EuQuin$_2$S-AuNP distribution in a THP-1 cell population. Logarithmic histogram of ^{197}Au counts from EuQuin$_2$S-AuNPs treated THP-1 cells (4h incubation, 2 nM) analysed by CyTOF, with gates denoting minor and major populations (left), the number of nanoparticles per cell of major (top right) and minor (bottom right) populations. Count (y axis) refers the number of cells in each bin corresponding to its NP content.

After this initial incubation, cells were cultured under standard cell culture conditions described in 4.5.1 for a further 276 hours and analysed for their EuQuin$_2$S-AuNP content every 48 to 72 hours.

4.3.4.2 The Detection of EuQuin$_2$S-AuNPs in Non-Differentiated THP-1 Monocytes Over Multiple Proliferation Cycles

After the original 4-hour incubation, THP-1 cells were cultured for a further 276 hours under standard cell culture conditions. At 48, 120, 168, 216 and 276 h timepoints their NP content was analysed. Cell death did not increase during the experiment – the number of live cells was 91-96% at each time point compared to 96% in a non-treated control sample. This is further evidence that labelling THP-1 monocytes with EuQuin$_2$S-AuNPs does not cause cell death, as also shown previously in 4.3.1.3. Plotting an overlayed histogram revealed that the number of EuQuin$_2$S-AuNPs per THP-1 monocyte population decreased over time in the major population (Figure 4.32). A logarithmic scale was chosen for this for clearer visualisation of the wide dynamic range of EuQuin$_2$S-AuNP content; however, the minor population retained a high NP content over all time points tested. We studied the number of EuQuin$_2$S-AuNPs per THP-1 monocyte in this minor population, calculated from ^{197}Au and ^{153}Eu signal from the NPs. From the ^{197}Au signal, the number of EuQuin$_2$S-AuNPs per cell decreased from 2987 ± 674 to 2669 ± 754 NPs per cell at 0 and 276 hours respectively (± SD). From the ^{153}Eu signal, the number of EuQuin$_2$S-AuNPs per cell decreased from 3415 ± 1274 to 2658 ± 1290 at 0 and 276 hours respectively (± SD), but there is no obvious correlation between time and decrease of EuQuin$_2$S-AuNP content in this minor population over the time points. ^{197}Au and ^{153}Eu CV did not increase over time in the minor population (Figure 4.32), indicating that this subset of the population is not proliferative.[90] This theory is further supported by the decreasing proportion of total cells this subset represents as the overall cell count increased from the main monocyte-like THP-1 cells divide over this time (Figure 4.32). Additionally, macrophages derived from THP-1 cells have been shown to have minimal proliferative activity,[91] which may explain why this subset population (that likely has macrophage phenotype) does not appear to proliferate. Due to the evidence that this population of cells with high uptake is not proliferative and our interest in assessing

$EuQuin_2S$-AuNP detection in proliferating THP-1 monocytes, the population was discarded from the rest of analysis in this experiment.

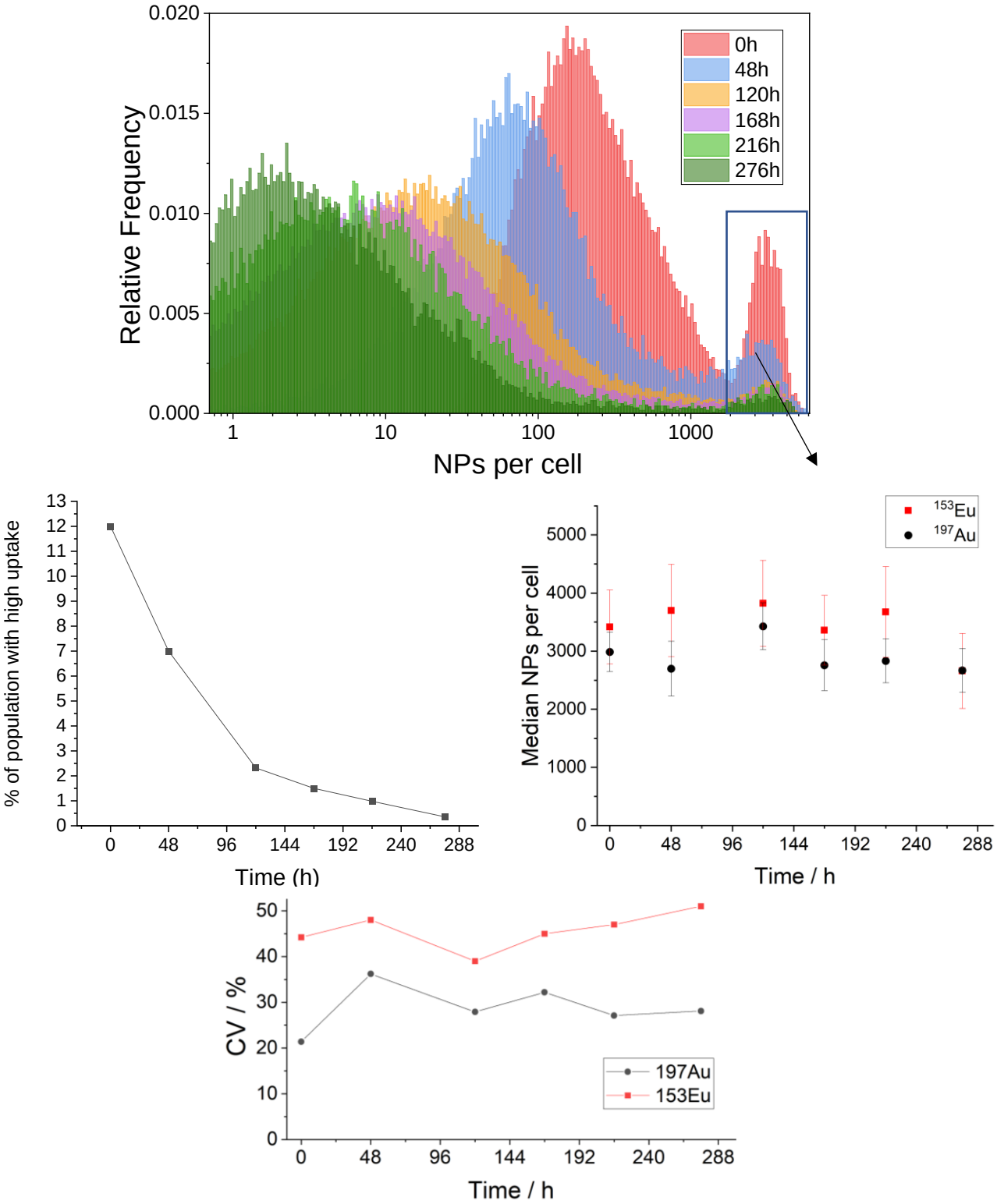


Figure 4.32 - Logarithmic histogram overlay of the number of NPs in THP-1 cell populations analysed by CyTOF at 0, 48, 120, 168, 216 and 276h timepoints (top); the percentage of the overall number of THP-1 cells in each sample that had high uptake (minor population) (middle left); median number of $EuQuin_2S$-AuNPs per cell of the minor population at each time point tested determined from analysis of ^{153}Eu (red squares) and ^{197}Au (black dots) signal (middle right). Error bars represent SD; ^{197}Au and ^{153}Eu CV values at each timepoint of the experiment (bottom).

The number of EuQuin$_2$S-AuNPs per cell in the main THP-1 monocyte population decreased across the whole population at each time point as shown in the logarithmic histogram (Figure 4.33). After 276 hours, the median number of EuQuin$_2$S-AuNPs was 2.5 in cells that still contained NPs and 0 across the whole THP-1 monocyte population, demonstrating the high amount of NP depletion. The CV increased significantly during the experiment from 91% at 0 hours to 481% at 276 hours (Figure 4.33), suggesting that EuQuin$_2$S-AuNP inheritance between daughter cells is highly asymmetric.[90]

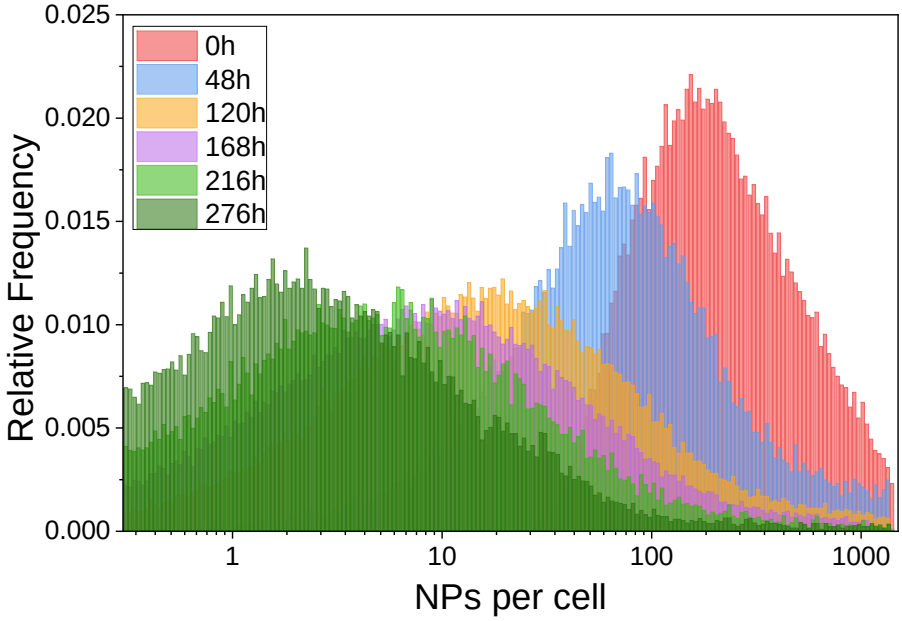


Figure 4.33 - Histogram overlay of the number of EuQuin$_2$S-AuNPs per THP-1 monocytes in the dividing population analysed by CyTOF at 0, 48, 120, 168, 216 and 276h timepoints. Data plotted as a logarithmic histogram.

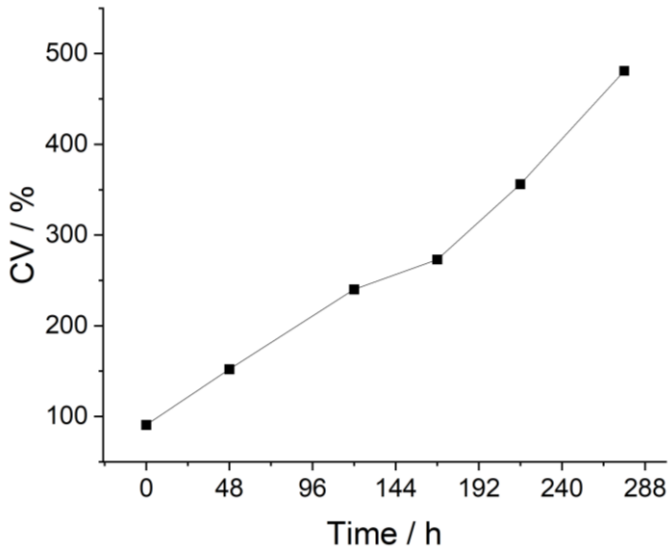


Figure 4.34 - The coefficient of variation (CV, %) of EuQuin$_2$S-AuNPs per THP-1 monocyte at each timepoint in the experiment. Increase in CV suggests asymmetric inheritance of NPs between daughter cells after cell division.

Next, the number of THP-1 monocytes containing EuQuin$_2$S-AuNPs was studied. The number of THP-1 monocytes containing EuQuin$_2$S-AuNPs dropped from 100% at 0 hours to just 29% after 276 hours (Figure 4.35).

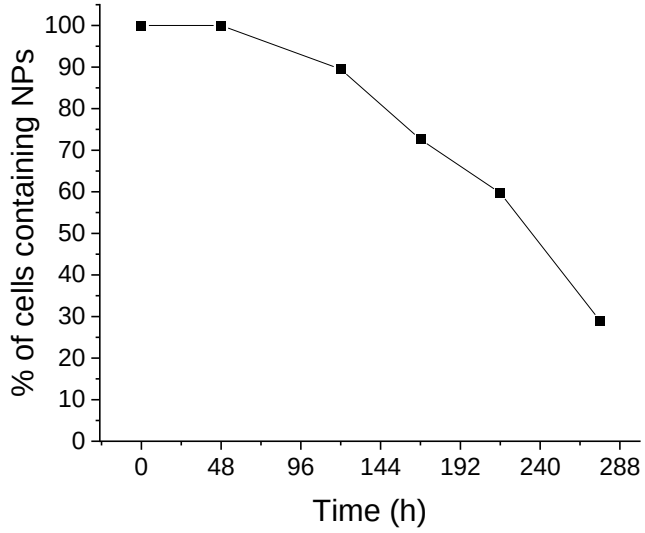


Figure 4.35 - The number of cells containing EuQuin$_2$S-AuNPs at each timepoint in the experiment.

We then analysed the median number of EuQuin$_2$S-AuNPs per THP-1 monocyte at each time point, finding that the median decreased over time from 193 at 0h to 0 at 276h (Figure

4.37). To determine whether the reduction in NP content was due to predominantly cell division or exocytosis, we compared $EuQuin_2S$-AuNP content to the number of cell divisions that occurred during the experiment, as shown in 3.8.2.4. Due to time restraints, the CFSE/Anti-FITC proliferation dye used in chapter 3 could not be incorporated into the experiment. Instead, we manually counted cells at each timepoint of the experiment. It is worth noting that although in Chapter 3 we suggested that manual cell counting with have a high amount of associated error, we hypothesise that in this experiment will be a much lower associated error. This is because all cells were cultured in a single flask so there is no discrepancy between the original number of cells in each sample like in 3.8. Figure 4.36 shows the average number of cell divisions that had occurred at each time point of the experiment. A total number of 4.6 cell divisions occurred over the 276-time period and there is no apparent change in the rate of cell division. This is likely because the cells were maintained at the optimal concentrations for cell division for the duration of the experiment, preventing a saturation phase commonly observed in growth curves of cells in culture.

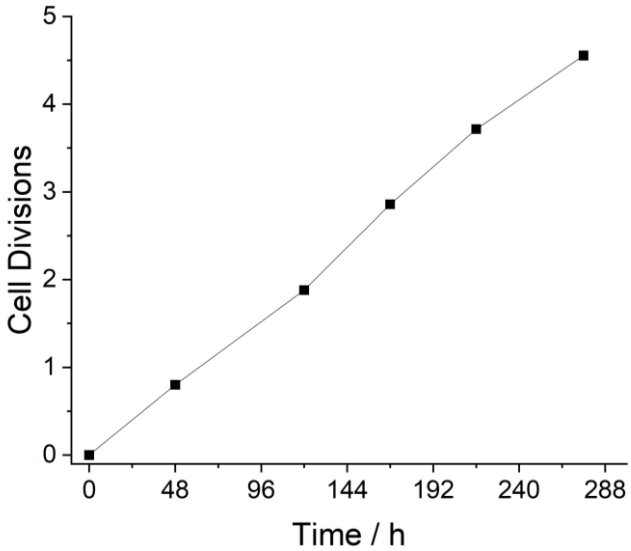


Figure 4.36 - The average number of cell divisions determined from manual cell counting during culture of $EuQuin_2S$-AuNP treated THP-1 monocytes for 276 hours.

An overlay of the number of $EuQuin_2S$-AuNPs per cell observed in CyTOF experiments compared to the number of $EuQuin_2S$-AuNPs that would theoretically be expected if depletion was solely due to cell division is shown in Figure 4.37. After 48 hours, 104

$EuQuin_2S$-AuNPs per cell were found by CyTOF, 86% of the theoretical value of 121. At 120 hours, 26 $EuQuin_2S$-AuNPs per cell were found, just 46% of the theoretical value. By 168 and 216 hours, 14% and 12% of the theoretical value remained, respectively. At 276 hours, 71% of THP-1 monocytes contained no $EuQuin_2S$-AuNPs, so the median was 0 and can't be plotted on a logarithmic axis. This suggests that exocytosis is also playing a major role in depletion of $EuQuin_2S$-AuNPs from THP-1 monocytes.

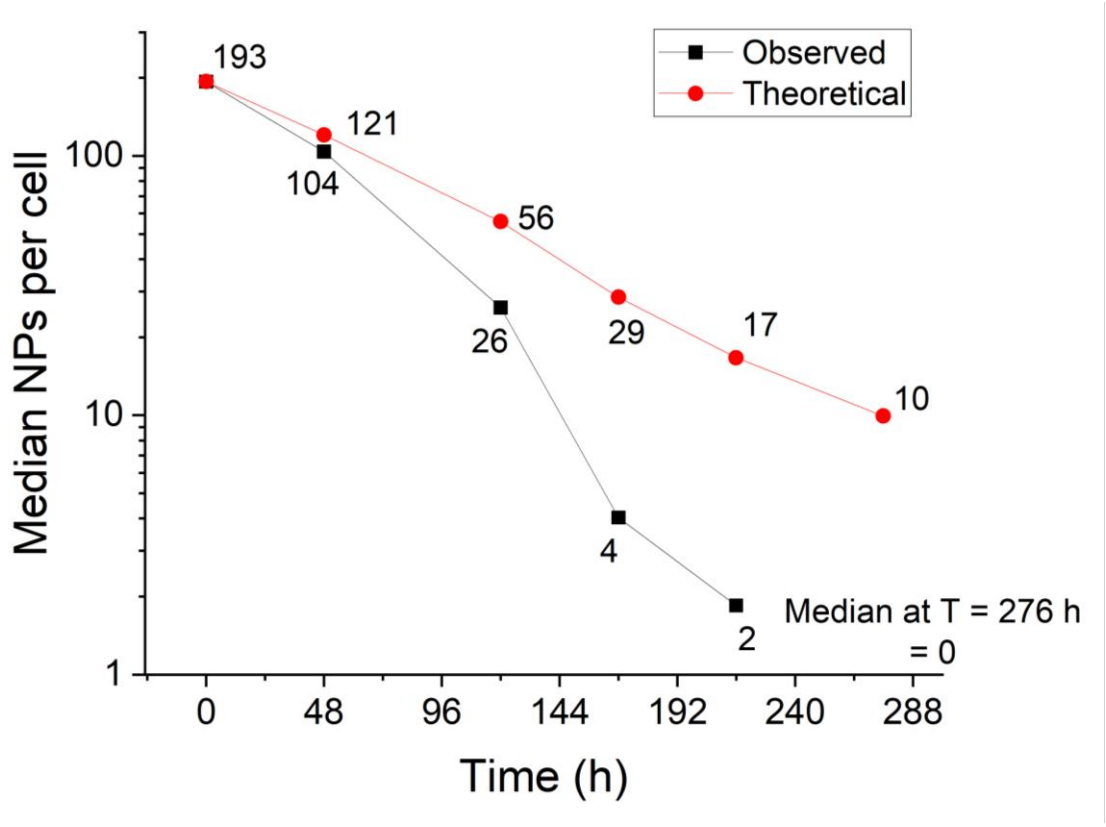


Figure 4.37 - The observed (black squares) median number of $EuQuin_2S$-AuNPs per THP-1 monocyte compared to the theoretical (red dots) values calculated from determination of the number of cell divisions, assuming that NP depletion is exclusively due to cell division. Plotted on a logarithmic scale due to the exponential nature of cell division.

So far we have primarily chosen to use median averages as they are less skewed by outliers (or in our case cells that contain high numbers of NPs) so better represent the non-normal distribution of NPs within cell populations.[92] However, due to the high number of cells containing no $EuQuin_2S$-AuNPs at late timepoints in this experiment, the mean number of $EuQuin_2S$-AuNPs is also examined. The mean number of $EuQuin_2S$-AuNPs per THP-1 monocyte after initial treatment was 288. This dropped to 153 after 48 hours (85%

of theoretical value), 45 at 120 hours (54% of theoretical value), 19 at 168 hours (44% of theoretical value), 11 at 216 hours (44% of theoretical value) and 6 after 276 hours (40% of theoretical value) (Figure 4.38).

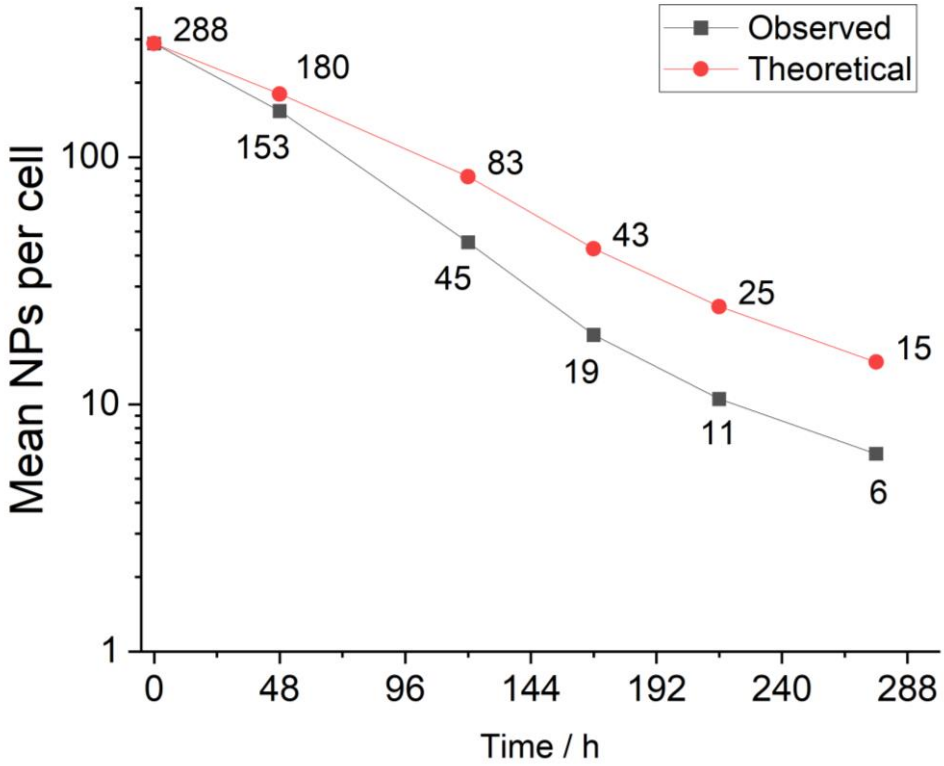


Figure 4.38 - The observed (black squares) mean number of EuQuin$_2$S-AuNPs per THP-1 monocyte compared to the theoretical (red dots) values calculated from determination of the number of cell divisions, assuming that NP depletion is exclusively due to cell division. Plotted on a logarithmic scale due to the exponential nature of cell division.

Figure 4.39 shows the proportion of EuQuin2S-AuNP depletion from cell division and exocytosis from the median and mean averages. Cell division is responsible for 86% and 85% of NP depletion after 48 hours and 46% and 54% at 120 hours, according to median and mean values respectively. At 168 and 216 hours, the median and mean values deviate slightly; median values suggest exocytosis is responsible for 86% and 88% of NP depletion, but the mean values suggest that exocytosis is responsible for 56-60% of NP depletion. The median value for 276 hours was discarded as the value was 0 when in fact 29% of cells still contained EuQuin$_2$S-AuNPs. This data suggests that in THP-1 monocytes over

this time period, exocytosis is playing a significant role in the depletion of EuQuin$_2$S-AuNPs, unlike the experimental data for HeLa cells seen in 3.8.

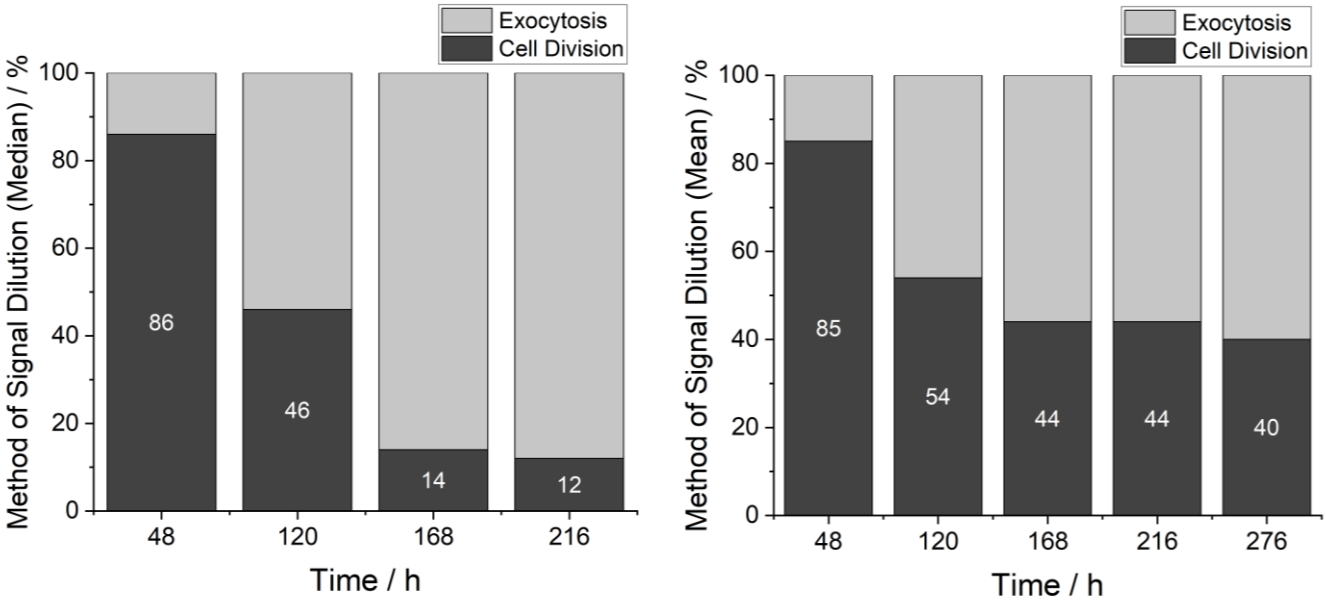


Figure 4.39 - Method of EuQuin$_2$S-AuNP depletion (exocytosis or cell division) at each time point using median (left) and mean (right) averages. The median value for 276 hours was discarded as the value was 0 when in fact 29% of cells still contained EuQuin$_2$S-AuNPs.

4.3.4.3 The Detection of EuQuin$_2$S-AuNPs in THP-1 Monocytes Differentiated into M1 Macrophages and Mature Dendritic Cells

We next assessed the capability of detecting THP-1 monocytes labelled with EuQuin$_2$S-AuNPs after their differentiation to M1 macrophages and mDCs. After initial treatment with EuQuin$_2$S-AuNPs (4h, 2 nM) as described above, THP-1 cells were cultured for a further 30 hours before undergoing differentiation to M1s (N=2) and mDCs (N=2) under conditions previously described (4.5.2). After the 6-day process, the NP content and viability of the cell populations were analysed by CyTOF, 168 hours (or 7 days) after their initial NP treatment. After 168 hours, an average of 84% and 71% of M1 macrophages and mDCs were found to be alive, higher than previously observed from previous analyses in 4.3.1.3 and 4.3.3, again supporting the theory that EuQuin$_2$S-AuNPs are not increasing cell death

in this time period. The distribution of EuQuin$_2$S-AuNPs after initial treatment and in M1 macrophages and mDCs after 168 hours is shown in linear histograms below (Figure 4.40).

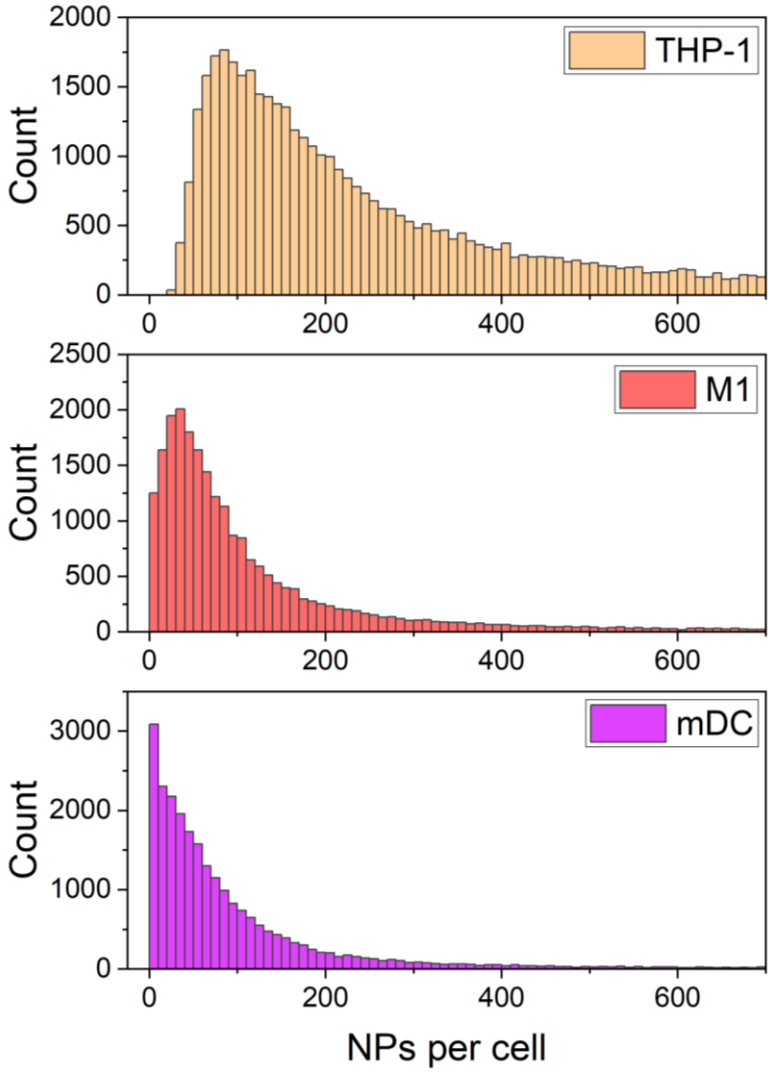


Figure 4.40 - Linear histograms representing the number of EuQuin$_2$S-AuNPs per THP-1 monocyte (orange) after initial treatment and after their differentiation to M1 macrophages (red) and mDCs (purple). Count (y axis) refers the number of cells in each bin corresponding to its NP content.

EuQuin$_2$S-AuNPs could still be detected in 99% of M1 macrophages and 98% of mDCs, and the median number of NPs per cell decreased from 193 after the initial incubation period to 89 ± 25 in M1 macrophages and 63 ± 2 (± range of 2 measurements) in mDCs, representing 46% and 35% of the initial median uptake respectively. This compares to a median value of 4 EuQuin$_2$S-AuNPs per cell in non-differentiated THP-1 monocytes when 73% of cells contained NPs (Figure 4.41).

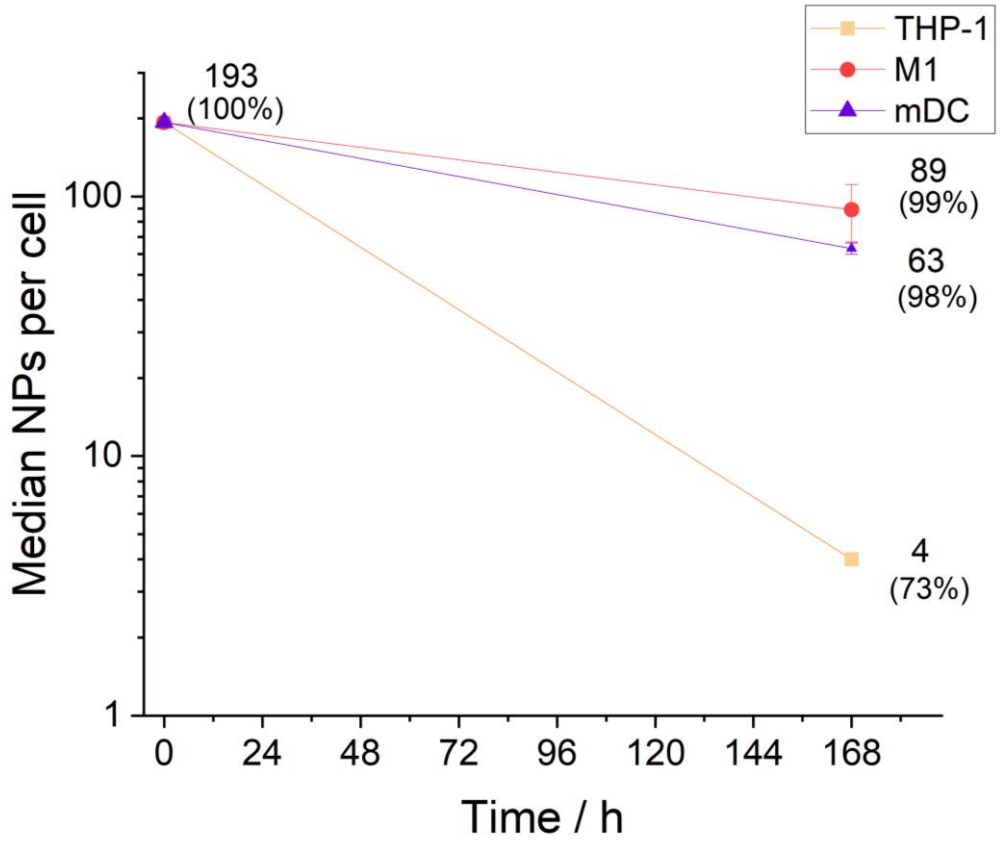


Figure 4.41 - The median number of EuQuin$_2$S-AuNPs per THP-1 monocyte (non-differentiated) and those differentiated to M1 macrophages and mDCs, 168 hours after initial treatment. Brackets denote the percentage of cells that contained EuQuin$_2$S-AuNPs in each cell population. Error bars represent the range in values determined from 2 repeat measurements for M1 macrophages and mDCs.

In M1 macrophages and mDCs, the median number of EuQuin$_2$S-AuNPs per cell was 54% and 65% lower than it was initially in THP-1 monocytes, after 168 hours. However, this reduction is much smaller than the 98% of the signal lost in non-differentiated THP-1 monocytes over this time period. This smaller reduction was expected because once the cell differentiation process has started, M1 macrophages and mDCs are not proliferative.[91] The cells were cultured for 30 hours after NP treatment before the differentiation process was initiated, which will have allowed for some cell division, so it is likely a combination of cell division and exocytosis that led to the decrease in EuQuin$_2$S-AuNP content. From this data, it is not possible to accurately quantify the proportion of signal loss that was from cell division and exocytosis. However, if the rate of cell division was equivalent to previous

experiments in 4.3.4.2, an average of 0.5 cell divisions can be predicted. From this prediction, it can be estimated that 45% of $EuQuin_2S$-AuNP content was lost from cell division (and 55% from exocytosis) for M1 macrophages and 35% from cell division (and 65% from exocytosis) for mDCs.

4.3.4.4 Discussion

We have shown detection of $EuQuin_2S$-AuNP labelled non-differentiated THP-1 monocytes with CyTOF up to 276 hours after their initial treatment, as well as those differentiated into M1 macrophages and mDCs 168 hours after initial treatment. After 276 hours, only 29% of $EuQuin_2S$-AuNP labelled, non-differentiated THP-1 monocytes could be detected with CyTOF. This is likely explained by asymmetric inheritance between daughter cells revealed by the CV values from our single cell analysis. Our results show that depletion of $EuQuin_2S$-AuNPs in cells was likely a result of both cell division and exocytosis. An average of 4.6 cell divisions took place during the experimental timeframe and by interpreting the NP content from mean values, it was estimated that cell division accounted for 40% of $EuQuin_2S$-AuNP depletion and 60% due to exocytosis. This is in contrast to our results from Chapter 3 that indicated $EuQuin_2S$-AuNP depletion was predominantly due to cell division. However, cell type has been shown to significantly effect exocytosis rates[93] and we studied THP-1 monocytes for 276 hours compared to 96 hours for HeLa cells. Independent repeat measurements of this experiment are required to validate our findings. Furthermore, the uncertainty of the number of cell divisions determined during the experiment is not known, therefore the accuracy of quantifying the method of $EuQuin_2S$-AuNP depletion is also unknown.

99% and 98% of THP-1 monocytes differentiated into M1 macrophages and mDCs still contained $EuQuin_2S$-AuNPs after 168 hours, with a median of 89 ± 25 and 63 ± 2 $EuQuin_2S$-AuNPs in each respective cell type, demonstrating excellent detectability with CyTOF. Cell division was responsible for 45% and 35% of $EuQuin_2S$-AuNP depletion in M1

macrophages and mDCs respectively, although this is only considered a rough estimation as the number of cell divisions during the experiment was not confirmed. The much lower depletion of EuQuin$_2$S-AuNPs is likely due to the lack of proliferation once the differentiation process was initiated.

Our main hypothesis was to investigate the suitability of EuQuin$_2$S-AuNPs as cellular labels for detecting differentiated monocytes with CyTOF. We have demonstrated excellent detectability in ≥98% of differentiated cells when THP-1 monocytes were allowed to rest for 30 hours, similar to the half-life time of circulating monocytes in humans.[94] Current cellular labels such as CFSE for comparable flow cytometry experiments require high intracellular concentrations for detection, and CFSE has been shown to kill dividing cells and modulate expression of activation markers.[95] More parameters can be simultaneously studied with CyTOF when compared to flow cytometry[96] but no cellular label currently exists, with the exception of CFSE staining that also required subsequent Anti-FITC staining. We show that EuQuin$_2$S-AuNPs are detectable in differentiated cells with CyTOF without subsequent labelling with the added advantage that an extremely low initial internalised dose is required. However, some of our findings question the suitability of EuQuin$_2$S-AuNPs as suitable labels for CyTOF experiments. Some EuQuin$_2$S-AuNP depletion appears to be a result of exocytosis. Mononuclear phagocytes, particularly macrophages, can ingest circulating NPs[97] and in 4.3.3.2 we showed that they have high uptake rates of EuQuin$_2$S-AuNPs. In theory, macrophage containing EuQuin$_2$S-AuNPs that have not originated from originally labelled cells could be mistakenly identified as false positives. Furthermore, asymmetric inheritance of NPs between daughter cells leads to some THP-1 monocytes no longer containing EuQuin$_2$S-AuNPs, which in turn means that it is difficult to estimate the number of proliferation cycles from their content. CFSE labelling techniques can allow detection after 8 to 10 proliferation cycles,[98] but we were only able to detect 29% of cells with EuQuin$_2$S-AuNPs after 4.6 proliferation cycles. However, as we are interested

in detecting differentiated monocytes, with their 1 to 3-day half-life before differentiation, it is not anticipated that they would divide as many times as this. Furthermore, a higher initial dose of $EuQuin_2S$-AuNPs could however increase the length of detection.

4.3.5 Two-photon Excitation Confocal Microscopy Images of $EuQuin_2S$-AuNP Treated Macrophages and HeLa Cells

Next, we sought to image cells treated with $EuQuin_2S$-AuNPs using two-photon confocal microscopy. In this work, an Olympus FVMPE-RS multiphoton laser scanning microscope was used. We first attempted two-photon excitation of $EuQuin_2S$-AuNPs suspended in MQ water in a 12-well plate at a concentration of 1 nM . When subject to light of wavelength 940 nm, signal was observed in the 575-645 nm wavelength channel (Figure 4.42). As no signal was observed in a MQ water control sample, we attributed this signal to emission from the Eu(III) $^5D_0 \rightarrow {}^7F_{0\text{-}2}$ transition bands of $EuQuin_2S$-AuNPs at 580, 595 and 615 nm, as illustrated in the emission spectrum of $EuQuin_2S$-AuNPs recorded on an Edinburgh Instruments photospectrometer using a Xe excitation lamp in Figure 4.46.

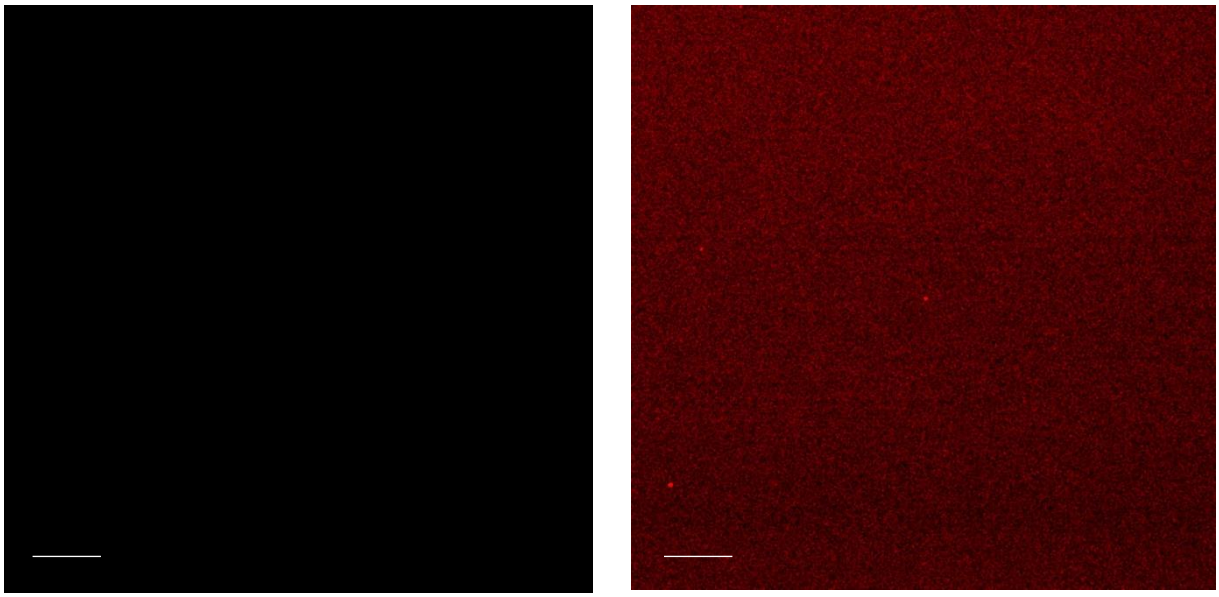


Figure 4.42 - Imaging $EuQuin_2S$-AuNPs in solution with an Olympus FVMPE-RS multiphoton laser scanning microscope. MQ water control (left) and $EuQuin_2S$-AuNPs suspended in MQ water at a concentration of 1 nM (right) (λ_{exc} = 940 nm, λ_{exc} = 575-645 nm). Scale bars = 50 µm.

M1 Macrophages were treated with HeLa cells for 20 hours at a concentration of 5 nM. Cells were then washed, suspended in RPMI media and live cell imaging was acquired on a $EuQuin_2S$-AuNPs were on an Olympus FVMPE-RS multiphoton laser scanning microscope. When subject to light of 940 nm wavelength, emission was observed in the 575-645 nm channel (Figure 4.43), appearing as bright spots clustered closely together in the image. We attributed this emission to the Eu(III) $^5D_0 \rightarrow {}^7F_{0\text{-}2}$ transition bands of $EuQuin_2S$-AuNPs. Emission was also observed in the 400-470 nm which we attributed to emission directly from the quinoline, as shown in the $EuQuin_2S$-AuNP emission spectrum (Figure 4.44).

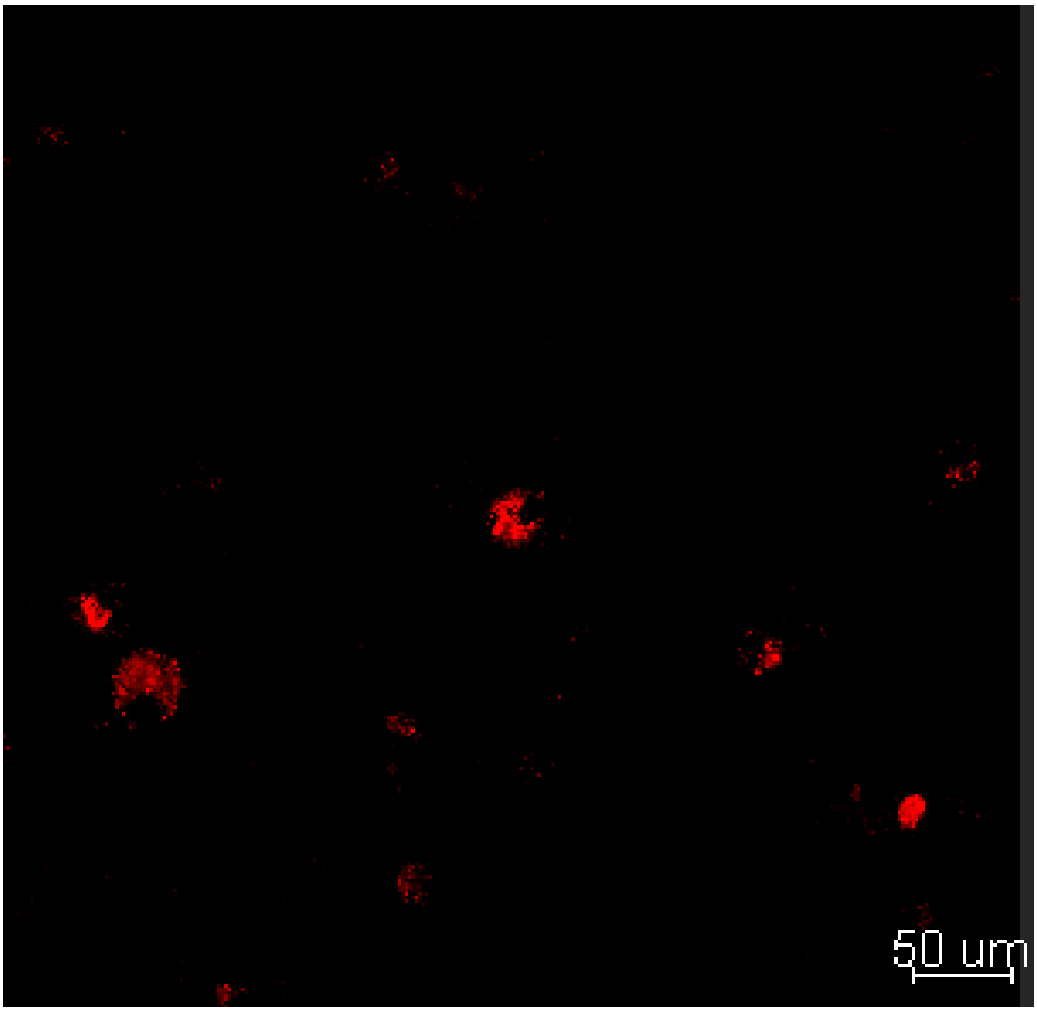


Figure 4.43 - Live cell imaging of $EuQuin_2SH$-AuNP uptake in M1 macrophages, treated with a concentration of 5 nM for 20 hours. λ_{exc}= 940 nm, λ_{em} = 575-645 nm.

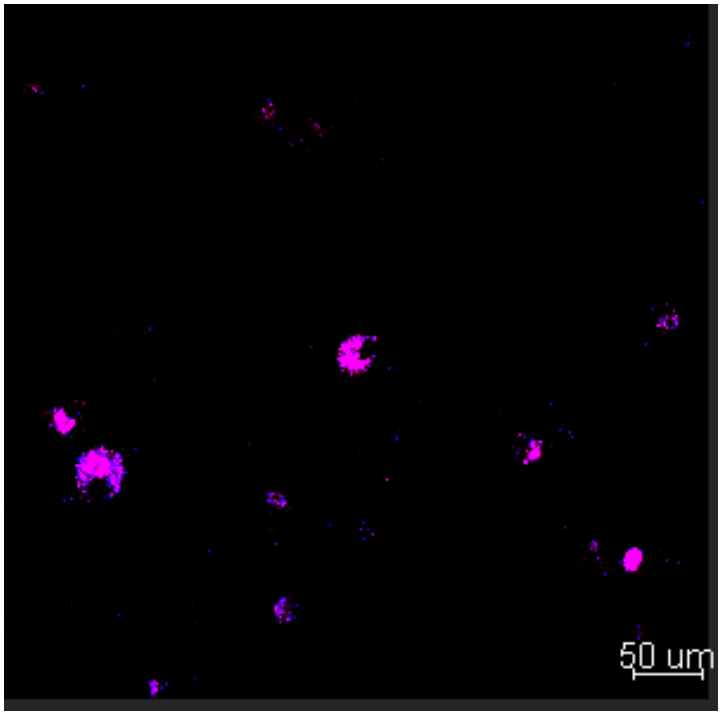


Figure 4.44 - Live cell imaging of $EuQuin_2SH$-AuNP uptake in M1 macrophages, treated with a concentration of 5 nM for 20 hours. Overlay of emission from the blue and red (shown in purple in this image) channels, suggesting that emission is seen directly from the quinoline and also Eu(III). λ_{exc}= 940 nm, λ_{em} = 400-470, 575-645 nm.

Next, we treated cells with Hoechst 33258, a fluorescent molecule that stains the nuclei of cells.[99] Colocalisation of emission from the 400-470 nm channel (containing Hoechst 33258 and quinoline emission) and the 575-645 nm channel, suggesting that $EuQuin_2S$-AuNP signal is coming from within M1 macrophages (Figure 4.45). We also observed emission from HeLa cells under the same conditions and these images can be found in the appendix (4.7.4).

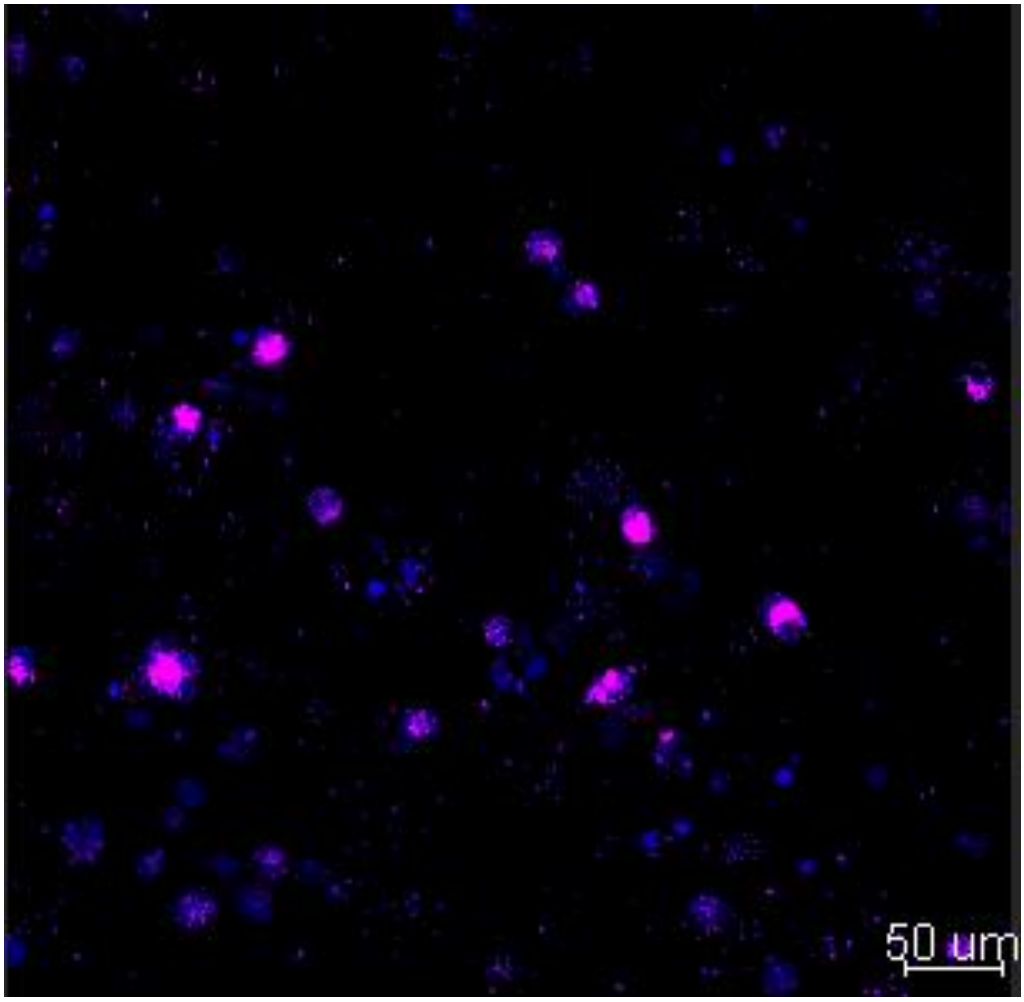


Figure 4.45 - Live cell imaging of EuQuinSH-Au13 NP uptake in M1 macrophages, treated with a concentration of 5 nM for 20 hours and then incubated with a Hoechst 33258 nuclear staining dye for 10 min. Overlay of emission from the blue (Hoechst 33258 and quinoline) and red (Eu(III)) channels. λ_{exc}= 940 nm, λ_{em} = 400-470, 575-645 nm.

When considering the single-photon excitation spectrum of $EuQuin_2S$-AuNPs (Figure 4.46), no intensity is observed after approximately 390 nm, suggesting that two-photon excitation of the quinoline sensitiser directly is not possible when using 940 nm wavelength light (corresponding to a single photon wavelength of 470 nm.). The one-photon excitation spectrum of Hoechst 33258 also tails off by around 405 nm, but has been reported to have two-photon excitation up to 880 nm.[100] Two-photon excitation spectra are often broader and different in profile to one-photon excitation spectra due to different quantum mechanical backgrounds[101] and powerful excitation lasers relative to the xenon excitation source used

in the single-photon excitation spectra were used for the imaging. Furthermore, plasmonic enhancement of two-photon excited luminescence from quantum dots and fluorophores such as Hoechst 33258 by gold nanorods and nanospheres has been previously observed.[102, 103] We are pursuing collaborations for power-dependent studies to provide further evidence of two-photon excitation in these preliminary findings.

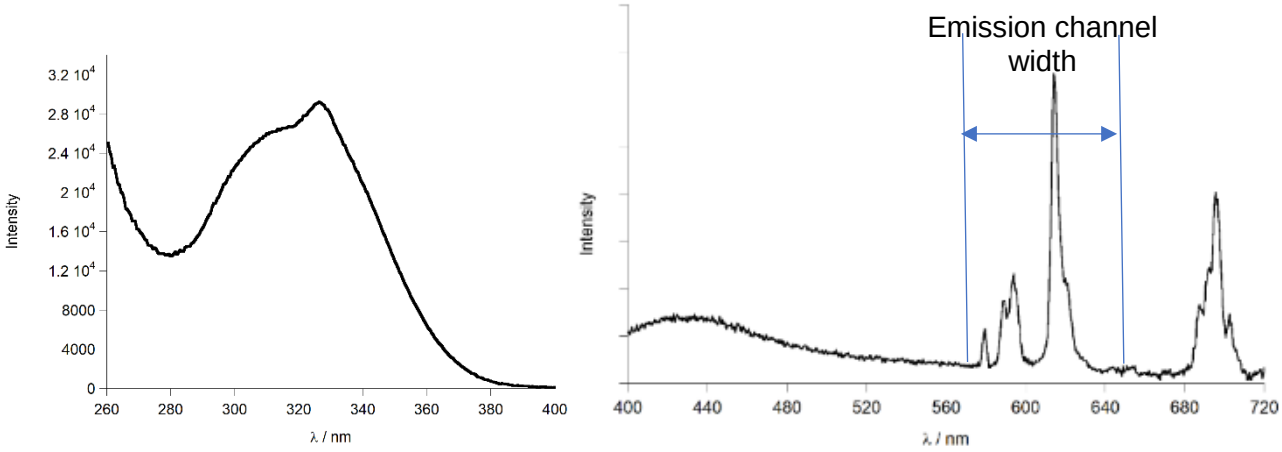


Figure 4.46 - Single-photon excitation (left) and emission spectra of $EuQuin_2S$-AuNPs in MQ water at a concentration of 2.5 nM. (λ_{exc} = 350 nm for emission spectrum, λ_{em} = 615 nm for the excitation spectrum).

4.4 Concluding Remarks

In this chapter, $EuQuin_2S$-AuNPs were assessed as multimodal cellular labels for the detection of THP-1 monocytes and their differentiation into M1 macrophages and mature dendritic cells. First, the differentiation of THP-1 monocytes into M1 macrophages and mature dendritic cells after 6 days was demonstrated, evidenced by morphological changes observed with light microscopy and the presence of macrophage- and dendritic cell-like cell surface markers shown with flow cytometry. Treatment of THP-1 monocytes prior to differentiation appeared to have no effect on the differentiation process or cell death, shown with both flow cytometry and CyTOF. Internalisation of $EuQuin_2S$-AuNPs was confirmed in M1 macrophages by TEM analysis where all NPs were confined within endosomes, suggesting that uptake occurred via endocytosis pathways. CyTOF was used to quantify

the cellular uptake of EuQuin$_2$S-AuNPs in THP-1 monocytes, M1 macrophages and mDCs, observing much higher uptake in M1 macrophages, followed by mDCs and THP-1 monocytes had low uptake. This agrees with pervious literature and it was hypothesised that this could be due to the higher phagocytic activity of M1 macrophages. Single cell analysis revealed differences in uptake heterogeneity in each cell type. The majority of THP-1 monocytes had low uptake and a log-normal distribution did not fit this population well, but a small subset of cells had a much higher uptake that did not increase with concentration. Phenotypical analysis indicated that this small subset of cells may have had a similar phenotype to M1 macrophages, which their EuQuin$_2$S-AuNP also suggested. Most M1 macrophages had high uptake but 34-46% of cells had a lower uptake more similar to that observed in mDCs. The uptake in mDCs was log-normally distributed across the population.

Next, the detection of EuQuin$_2$S-AuNPs with CyTOF in THP-1 monocytes, M1 macrophages and mDCs was demonstrated. EuQuin$_2$S-AuNPs were detectable in 29% of THP-1 monocytes after 268 hours; after this time the mean NP content per cell was only 6 due to multiple proliferation cycles alongside suspected exocytosis depleting the signal. However, in THP-1 monocytes that had differentiated to M1 macrophages and mDCs, EuQuin$_2$S-AuNPs were still detectable in 98-99% of cells and their median content was higher due to less cell division occurring. This demonstrates suitability of EuQuin$_2$S-AuNPs as cellular labels for identifying and monitoring monocyte differentiation, migration and function in CyTOF studies. However, the expulsion of EuQuin$_2$S-AuNPs by suspected exocytosis could be an issue if these NPs were to be taken up by other cells and mistaken for the originally labelled cell lineage of interest. Finally, preliminary results show the detection and localisation of EuQuin$_2$S-AuNPs in M1 macrophages with multiphoton laser scanning confocal microscopy, though further studies are needed to confirm two-photon excitation.

Future work should incorporate a large cell surface maker panel into CyTOF experiments to simultaneously measure the phenotype of single cells to correlate this to their $EuQuin_2S$-AuNP content; this would allow more solid conclusions into the relationship between mononuclear phagocyte phenotype and NP uptake. The suitability of CyTOF to measure the depletion of NPs over extended time periods has been demonstrated and further experiments into the extent of $EuQuin_2S$-AuNP exocytosis would further assess their suitability as labels for CyTOF. TEM images throughout these long-term experiments to show the intracellular localisation of $EuQuin_2S$-AuNPs, providing more insight into the nature of NP depletion over time. Furthermore, TEM images of THP-1 monocytes and mDCs directly after $EuQuin_2S$-AuNP treatment would also confirm our claims of intracellular uptake in these cell types. Finally, given the promise of $EuQuin_2S$-AuNPs as multimodal cellular labels with CyTOF detection and luminescence imaging already shown, their detectability in cells with CT could also be explored, providing a third modality of detection.

4.5 Experimental

4.5.1 Cell Culture of THP-1 Monocytes, M1 Macrophages and Mature Dendritic Cells

Cells from the human monocytic leukemia cell line THP-1 in T75 flasks using Roswell Park Memorial Institute 1640 (RPMI-1640, Sigma-Merck; R0883) media supplemented with heat-inactivated sterile-filtered FBS (10% by volume), L-glutamine (50 μM), penicillin (100 U/mL), streptomycin (0.2 μg/mL). The cells were kept at 37 °C in a humidified atmosphere with 5% CO_2 concentration. Cells were kept at a concentration of 0.5-1 x 10^6 cells/mL for a maximum of 12 weeks before a new passage was started. M1 macrophages or matured dendritic cells were cultured under the same conditions after their differentiation from THP-1 monocytes.

4.5.2 Differentiation of THP-1 Monocytes to M1 Macrophages and Mature Dendritic Cells

THP-1 monocytes were differentiated into resting macrophages (M0) as described by Chanput *et al.* (Chanput 2013). THP-1 monocytes were added to a well/flask in RPMI media containing 100 ng/mL PMA at a concentration of 0.5 x 10^6 cells/mL. After 2 days, the media was removed, cells were washed twice with PBS, and cultured with RPMI media for a further 2 days. To stimulate M0 cells to classical M1 macrophages, the media was removed and cells were cultured for a further 2 days in RPMI media containing 500 ng/mL LPS. THP-1 monocytes were differentiated into immature dendritic cells (iDC) as described by Deng *et al.* (Deng 2020/2021). THP-1 monocytes (0.25 x 10^6 cells/mL) were cultured in RPMI media containing IL-4 and PMA at a concentration of 20 ng/mL. After 4 days, cells were washed twice with PBS and cultured for a further 2 days in RPMI media containing LPS (1 µg/mL) to stimulate iDCs to mature dendritic cells (mDC).

4.5.3 Studying Changes to Cell Morphology During Cell Differentiation with Light Microscopy

THP-1 monocytes were added to a 24-well plate and left untreated or differentiated to M0, M1, iDC and mDCs under the conditions described in 4.5.2. Phase gradient contrast images of live cells were then acquired automatically in 9 randomly selected positions in each well by a Zeiss CellDiscover 7 using a 40 x objective lens.

4.5.4 Studying the Effect of $EuQuin_2S$-AuNP Treatment on Phenotypical Changes During THP-1 Monocyte Differentiation by Flow Cytometry

All reagents were diluted in FACS buffer unless specified otherwise. THP-1 monocytes were treated with RPMI cell media containing $EuQuin_2S$-AuNPs (2 nM) in T75 flasks at a concentration of 0.8 x 10^6 cells/mL and incubated at 37 ^oC (5% CO_2) for 4 hours. The cells were washed 4 times by centrifugation (300 x g, 5 min) to remove free $EuQuin_2S$-AuNPs.

Cells were then stimulated to differentiate THP-1 monoctyes to M1 macrophages and mDCs. After the differentiation process, adherent cells were detached by incubation with TrypLE™ Express Enzyme for 20 min, filtered (100 µm pore size), washed 2 times by centrifugation and resuspended in 100 µL of Fc block (BioLegend, 422302) at 1:100 dilution and incubated on ice for 20 min. Samples were washed once and incubated for 30 min at room temperature in 100 µL of FACS buffer containing surface marker antibody cocktail and Fixable Viability dye ef780. Samples were washed twice in FACS buffer and then fixed in 4% PFA for 20 min at 4 ^{o}C. Finally, samples were washed twice, resuspended in 300 µL FACS buffer and stored at 4 ^{o}C for 24 hours before acquisition.

Target	Fluorophore	Clone	Dilution	Manufacturer
CD11c	PeCy7	3.9	1:200	BioLegend
CD14	BV421	HCD14	1:200	BioLegend
CD68	BV785	Y1/82A	1:200	BioLegend
CD80	BV711	2D10	1:200	BioLegend
HLA-DR	PerCP	L243	1:200	BioLegend
Nuclear stain (Live/Dead assay)	APCCy7	N/A	1:1000	ThermoFisher

4.5.5 Transmission Electron Microscopy Images of EuQuin$_2$S-AuNP treated M1 Macrophages

After differentiation from THP-1 monocytes, M1 macrophages were treated with RPMI containing EuQuin$_2$S-AuNPs (0.6 nM) for 4 hours. Cells were then washed 3 times by centrifugation to remove any nanoparticles remaining in solution, then fixed in 2.5 %

glutaraldehyde solution for 90 min at 4 °C, then taken for processing at the Centre for Electron Microscopy (University of Birmingham). Ultrathin sections of approximately 100 µm were mounted onto Formvar-coated 200 mesh copper grids. Samples were analysed on a JEOL 1200 EX transmission electron microscope operated at 80kV in imaging mode, acquiring images using Digital Micrograph Version 1.83.842.

4.5.6 Uptake of EuQuin$_2$S-AuNPs in Mononuclear Phagocytes

4.5.6.1 THP-1 Monocytes

THP-1 monocytes were suspended in pre-warmed, supplemented RPMI media at a concentration of 0.8 x 10^6 cells/mL. EuQuin$_2$S-AuNPs were added and mixed thoroughly to produce a 9:1 RPMI:EuQuin$_2$S-AuNP mixture at final NP concentrations ranging from 0.2 – 2 nM. The media:NP mixture was added to a 100 mm dish, ensuring that cells were spread out as a monolayer within the dish. After 4 hours incubation, the cells were harvested and washed four times with PBS. The cells were then prepared for CyTOF experiments as previously described.

4.5.6.2 M1 Macrophages and Mature Dendritic Cells

After differentiation from THP-1 monocytes, M1 macrophages and Mature Dendritic cells were treated with pre-mixed, pre-warmed supplemented RPMI containing EuQuin$_2$S-AuNPs (9:1) at concentrations ranging from 0.05 – 0.6 nM and 0.017 – 0.4 nM for M1 macrophages and Mature Dendritic Cells respectively. After 4 hours, cells were washed three times with PBS and TrypLE Express Enzyme was added to detach the adherent cells. The cells were transferred to 5 mL Falcon™ Round-Bottom Polystyrene Test Tubes and prepared for CyTOF experiments as previously described.

4.5.7 EuQuin$_2$S-AuNPs as Cellular Labels for Detecting THP-1 Monocytes and their Differentiation into M1 Macrophages and Mature Dendritic Cells

4.5.7.1 The Detection of EuQuin$_2$S-AuNPs in Non-Differentiated THP-1 Monocytes Over Multiple Proliferation Cycles

5 x 10^6 THP-1 monocytes were suspended in pre-warmed, supplemented RPMI media at a concentration of 0.8 x 10^6 cells/mL. EuQuin$_2$S-AuNPs were added and mixed thoroughly to produce a 9:1 RPMI:EuQuin$_2$S-AuNP mixture at a final NP concentration of 2 nM and cells were seeded in a T75 flask and cells were kept under standard cell culture conditions. After 4 hours, cells were washed four times with PBS and 2 x 10^6 cells were transferred to a 5 mL Falcon™ Round-Bottom Polystyrene Test Tube and prepared for CyTOF analysis as previously described. After 30 min incubation with Iridium DNA intercalator (0.125 µM, Fluidigm) in Maxpar Fix and Perm Buffer at 4 °C, the sample was frozen in a cryovial until the day of the experiment. The remaining cells were cultured under standard cell culture conditions, with replacement of the cell media with fresh media every 24 hours. At 48 to 72 hour intervals, 1.5 x 10^6 cells were removed from the culture flask, prepared for CyTOF experiments and frozen until the day of the experiment. On the day of the experiment, the cells were thawed by the addition of cell staining buffer and transferred to 5 mL Falcon™ Round-Bottom Polystyrene Tubes. The cells were then centrifuged, the supernatant was removed and washed twice with Maxpar Cell staining buffer and once more with water just before acquisition. The cells were then resuspended in water to achieve a concentration of 500,000 cells/mL before acquisition on the Helios CyTOF instrument.

4.5.7.2 The Detection of EuQuin$_2$S-AuNPs in THP-1 Monocytes Differentiated into M1 Macrophages and Mature Dendritic Cells

1.2 x 10^7 THP-1 Monocytes were suspended in pre-warmed, supplemented RPMI media at a concentration of 0.8 x 10^6 cells/mL. EuQuin$_2$S-AuNPs were added and mixed thoroughly to produce a 9:1 RPMI:EuQuin$_2$S-AuNP mixture at a final NP concentration of 2 nM and cells were seeded in a 100 mm dish and cells were kept under standard cell culture conditions for 4 hours. Cells were then washed four times with PBS and allowed to culture for a further 30 hours. Cells were then differentiated into M1 Macrophages and Mature Dendritic cells under the conditions previously described. After the differentiation process, cells were then washed three times with PBS and TrypLE Express Enzyme was added to detach the adherent cells. The cells were transferred to 5 mL Falcon™ Round-Bottom Polystyrene Test Tubes and prepared for CyTOF experiments as previously descrived

4.5.8 Two-Photon Confocal Micrscopy Imaging of EuQuin$_2$S-AuNP treated M1 Macrophages and HeLa Cells

HeLa cells were seeded in 6-well plates at a density of 6 x 10^5 cells per well and allowed to adhere overnight. M1 macrophages were differentiated from THP-1 monocytes. Following treatment with EuQuin$_2$S-AuNPs for 20 hours at a concentration of 5 nM, cells in half of the well plates of each cell type were washed three times with PBS then incubated with Hoechst 33258 (2.5 µg/mL) for 10 min. After a further 3 washes with PBS, cells were imaged live in RPMI media and images were acquired using an Olympus FVMPE-RS multiphoton laser scanning microscope. Fluorescence from Hoechst 33258 and EuQuin$_2$S-AuNPs were acquired with an excitation wavelength of 940 nm in the blue (400-470 nm) and red (575-645 nm) channels respectively.

4.6 References

1. B. A. Nichols, D. F. Bainton and M. G. Farquhar, *Journal of Cell Biology*, 1971, **50**, 498-515.
2. C. Varol, A. Mildner and S. Jung, *Annual Review of Immunology*, 2015, **33**, 643-675.
3. Y. C. Teh, J. L. Ding, L. G. Ng and S. Z. Chong, *Frontiers in Immunology*, 2019, **10**, 834.
4. C. E. Lewis and J. W. Pollard, *Cancer Research*, 2006, **66**, 605-612.
5. F. Ginhoux and S. Jung, *Nature Reviews Immunology*, 2014, **14**, 392-404.
6. S. VanHorn and S. A. Morris, *Developmental Cell*, 2021, **56**, 7-21.
7. C. Chen, Y. Liao and G. Peng, *Protein & Cell*, 2022, **13**, 790-807.
8. G. J. Randolph, *Current Opinions in Lipidology*, 2008, **19**, 462-468.
9. K. Ley, Y. I. Miller and C. C. Hedrick, *Arterioscler Thromb Vasc Biol*, 2011, **31**, 1506-1516.
10. X. C. Li, M. Miyasaka and T. B. Issekutz, *Journal of Immunology*, 1998, **161**, 6258-6264.
11. M. S. Longhi, R. R. Mitry, M. Samyn, A. Scalori, M. J. Hussain, A. Quaglia, G. Mieli-Vergani, Y. Ma and D. Vergani, *Hepatology*, 2009, **50**, 130-142.
12. M. W. Y. Chan and S. Viswanathan, *Cytotherapy*, 2019, **21**, 393-415.
13. Z. Liu, Y. Gu, S. Chakarov, C. Bleriot, I. Kwok, X. Chen, A. Shin, W. Huang, R. J. Dress, C. A. Dutertre, A. Schlitzer, J. Chen, L. G. Ng, H. Wang, Z. Liu, B. Su and F. Ginhoux, *Cell*, 2019, **178**, 1509-1525.e1519.
14. S. Yona, K. W. Kim, Y. Wolf, A. Mildner, D. Varol, M. Breker, D. Strauss-Ayali, S. Viukov, M. Guilliams, A. Misharin, D. A. Hume, H. Perlman, B. Malissen, E. Zelzer and S. Jung, *Immunity*, 2013, **38**, 79-91.
15. H.-R. Chen, Y.-Y. Sun, C.-W. Chen, Y.-M. Kuo, I. S. Kuan, Z.-R. Tiger Li, J. C. Short-Miller, M. R. Smucker and C.-Y. Kuan, *Science Advances*, **6**, eabb2119.
16. S. Nowotschin and A. K. Hadjantonakis, *BMC Dev Biol*, 2009, **9**, 49.
17. A. N. Desch, S. L. Gibbings, R. Goyal, R. Kolde, J. Bednarek, T. Bruno, J. E. Slansky, J. Jacobelli, R. Mason, Y. Ito, E. Messier, G. J. Randolph, M. Prabagar, S. M. Atif, E. Segura, R. J. Xavier, D. L. Bratton, W. J. Janssen, P. M. Henson and C. V. Jakubzick, *American Journal of Respiratory and Critical Care Medicine*, 2016, **193**, 614-626.
18. A. Zarbock and K. Ley, *Current Topics in Microbiology and Immunology*, 2009, **334**, 129-152.
19. K. Hashimoto, N. Kataoka, E. Nakamura, K. Hagihara, T. Okamoto, H. Kanouchi, S. Mohri, K. Tsujioka and F. Kajiya, *Journal of Physiological Science*, 2012, **62**, 63-69.
20. P. Bousso and H. D. Moreau, *Nature Reviews Immunology*, 2012, **12**, 858-864.
21. R. D. Engberink, S. M. van der Pol, P. Walczak, A. van der Toorn, M. A. Viergever, C. D. Dijkstra, J. W. Bulte, H. E. de Vries and E. L. Blezer, *Molecular Imaging*, 2010, **9**, 268-277.
22. P. Chhour, P. C. Naha, S. M. O'Neill, H. I. Litt, M. P. Reilly, V. A. Ferrari and D. P. Cormode, *Biomaterials*, 2016, **87**, 93-103.
23. G. Pasqual, A. Chudnovskiy, J. M. J. Tas, M. Agudelo, L. D. Schweitzer, A. Cui, N. Hacohen and G. D. Victora, *Nature*, 2018, **553**, 496-500.
24. E. Buzhor, L. Leshansky, J. Blumenthal, H. Barash, D. Warshawsky, Y. Mazor and R. Shtrichman, *Regenerative Medicine*, 2014, **9**, 649-672.
25. F. Galli, M. Varani, C. Lauri, G. G. Silveri, L. Onofrio and A. Signore, *EJNMMI Radiopharmacy and Chemistry*, 2021, **6**, 7.

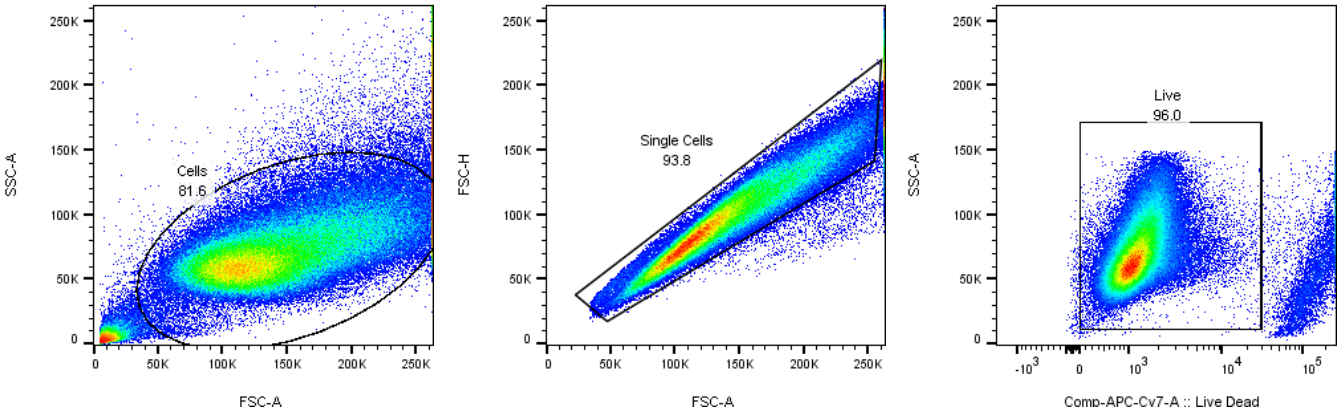
26. J. Eun Kim, B. C. Ahn, H. Won Lee, M. H. Hwang, S. Hyun Shin, S. Woo Lee, Y. Kwan Sung and J. Lee, *Molecular Imaging*, 2013, **12**, 310-317.
27. J. E. Kim, S. Kalimuthu and B. C. Ahn, *Nuclear Medicine and Molecular Imaging*, 2015, **49**, 3-10.
28. E. C. Jensen, *The Anatomical Record*, 2012, **295**, 2031-2036.
29. T. R. Brazelton and H. M. Blau, *Stem Cells*, 2005, **23**, 1251-1265.
30. H. S. Liu, M. S. Jan, C. K. Chou, P. H. Chen and N. J. Ke, *Biochemical and Biophysics Research Communications*, 1999, **260**, 712-717.
31. M. C. Milone and U. O'Doherty, *Leukemia*, 2018, **32**, 1529-1541.
32. S. J. Howe, M. R. Mansour, K. Schwarzwaelder, C. Bartholomae, M. Hubank, H. Kempski, M. H. Brugman, K. Pike-Overzet, S. J. Chatters, D. de Ridder, K. C. Gilmour, S. Adams, S. I. Thornhill, K. L. Parsley, F. J. Staal, R. E. Gale, D. C. Linch, J. Bayford, L. Brown, M. Quaye, C. Kinnon, P. Ancliff, D. K. Webb, M. Schmidt, C. von Kalle, H. B. Gaspar and A. J. Thrasher, *Journal of Clinical Investment*, 2008, **118**, 3143-3150.
33. M. Rodriguez-Porcel, M. W. Kronenberg, T. D. Henry, J. H. Traverse, C. J. Pepine, S. G. Ellis, J. T. Willerson, L. A. Moyé and R. D. Simari, *JACC: Cardiovascular Imaging*, 2012, **5**, 559-565.
34. M. D. Cahalan, I. Parker, S. H. Wei and M. J. Miller, *Nature Reviews Immunology*, 2002, **2**, 872-880.
35. M. J. Miller, S. H. Wei, I. Parker and M. D. Cahalan, *Science*, 2002, **296**, 1869-1873.
36. E. Porpiglia, N. Samusik, A. T. V. Ho, B. D. Cosgrove, T. Mai, K. L. Davis, A. Jager, G. P. Nolan, S. C. Bendall, W. J. Fantl and H. M. Blau, *Nature Cell Biology*, 2017, **19**, 558-567.
37. H. Pan, C. Xue, B. J. Auerbach, J. Fan, A. C. Bashore, J. Cui, D. Y. Yang, S. B. Trignano, W. Liu, J. Shi, C. O. Ihuegbu, E. C. Bush, J. Worley, L. Vlahos, P. Laise, R. A. Solomon, E. S. Connolly, A. Califano, P. A. Sims, H. Zhang, M. Li and M. P. Reilly, *Circulation*, 2020, **142**, 2060-2075.
38. E. G. O'Koren, R. Mathew and D. R. Saban, *Scientific Reports*, 2016, **6**, 20636.
39. A. B. Lyons, S. J. Blake and K. V. Doherty, *Current Protocols in Cytometry*, 2013, **Chapter 9**, 9.11.11-19.11.12.
40. R. J. Errington, M. R. Brown, O. Silvestre, K. L. Njoh, S. C. Chappell, I. Khan, P. Rees, S. P. Wilks, P. J. Smith and H. D. Summers, *Cell Cycle*, 2010, **9**, 121-130.
41. M. R. Brown, H. D. Summers, P. Rees, S. C. Chappell, O. F. Silvestre, I. A. Khan, P. J. Smith and R. J. Errington, *Cytometry A*, 2010, **77**, 925-932.
42. K. Geng, Z. X. Yang, D. Huang, M. Yi, Y. Jia, G. Yan, X. Cheng and R. Wu, *Molecular Medicine Reports*, 2015, **11**, 954-960.
43. M. N. Bouchlaka, K. D. Ludwig, J. W. Gordon, M. P. Kutz, B. P. Bednarz, S. B. Fain and C. M. Capitini, *Oncoimmunology*, 2016, **5**, e1143996.
44. A. V. Makela and P. J. Foster, *Magma*, 2019, **32**, 123-132.
45. E. Bull, S. Y. Madani, R. Sheth, A. Seifalian, M. Green and A. M. Seifalian, *International Journal of Nanomedicine*, 2014, **9**, 1641-1653.
46. S. Chung, R. A. Revia and M. Zhang, *Nanoscale Horizons*, 2021, **6**, 696-717.
47. N. Malhotra, J. S. Lee, R. A. D. Liman, J. M. S. Ruallo, O. B. Villaflores, T. R. Ger and C. D. Hsiao, *Molecules*, 2020, **25**.
48. E. Salmanoglu, S. Kim and M. L. Thakur, *Seminars in Nuclear Medicine*, 2018, **48**, 86-99.
49. J. R. Potts, N. Farahi, M. R. Howard, M. R. Taylor, S. Heard, A. N. Shankar, G. J. Alexander, E. R. Chilvers, S. Verma and A. M. Peters, *Bioscience Reports*, 2018, **38**.
50. J. Perrin, M. Capitao, M. Mougin-Degraef, F. Guérard, A. Faivre-Chauvet, L. Rbah-Vidal, J. Gaschet, Y. Guilloux, F. Kraeber-Bodéré, M. Chérel and J. Barbet, *Frontiers in Medicine*, 2020, **7**, 34.

51. A. Rahmim and H. Zaidi, *Nuclear Medicine Communications*, 2008, **29**, 193-207.
52. Y. Kurebayashi, P. L. Choyke and N. Sato, *Nanotheranostics*, 2021, **5**, 27-35.
53. F. Man, A. A. Khan, A. Carrascal-Miniц╠o, P. J. Blower and R. T.M. de Rosales, *Nuclear Medicine and Biology*, 2020, **90**, 31-40.
54. Y. Torrente, M. Gavina, M. Belicchi, F. Fiori, V. Komlev, N. Bresolin and F. Rustichelli, *FEBS Lett*, 2006, **580**, 5759-5764.
55. R. H. Menk, E. Schültke, C. Hall, F. Arfelli, A. Astolfo, L. Rigon, A. Round, K. Ataelmannan, S. R. MacDonald and B. H. Juurlink, *Nanomedicine*, 2011, **7**, 647-654.
56. N. Lee, D. Yoo, D. Ling, M. H. Cho, T. Hyeon and J. Cheon, *Chemical Reviews*, 2015, **115**, 10637-10689.
57. E. Alphandéry, *RSC Advances*, 2019, **9**, 40577-40587.
58. R. Misri, D. Meier, A. C. Yung, P. Kozlowski and U. O. Häfeli, *Nanomedicine*, 2012, **8**, 1007-1016.
59. X. Zheng, S. Zeng, J. Hu, L. Wu and X. Hou, *Applied Spectroscopy Reviews*, 2018, **53**, 377-394.
60. X. Huang, F. Zhang, S. Lee, M. Swierczewska, D. O. Kiesewetter, L. Lang, G. Zhang, L. Zhu, H. Gao, H. S. Choi, G. Niu and X. Chen, *Biomaterials*, 2012, **33**, 4370-4378.
61. J. M. Niers, J. W. Chen, G. Lewandrowski, M. Kerami, E. Garanger, G. Wojtkiewicz, P. Waterman, E. Keliher, R. Weissleder and B. A. Tannous, *Journal of the American Chemical Society*, 2012, **134**, 5149-5156.
62. J. Comenge, J. Sharkey, O. Fragueiro, B. Wilm, M. Brust, P. Murray, R. Levy and A. Plagge, *eLife*, 2018, **7**, e33140.
63. J. Jackson, C. Chapon, W. Jones, E. Hirani, A. Qassim and K. Bhakoo, *Journal of Neuroscience Methods*, 2009, **183**, 141-148.
64. N. De Vocht, K. Reekmans, I. Bergwerf, J. Praet, C. Hoornaert, D. Le Blon, J. Daans, Z. Berneman, A. Van der Linden and P. Ponsaerts, *Journal of Visual Experiments*, 2012, DOI: 10.3791/3906, e3906.
65. J. J. Kelly, M. Saee-Marand, N. N. Nyström, M. M. Evans, Y. Chen, F. M. Martinez, A. M. Hamilton and J. A. Ronald, *Science Advances*, 2021, **7**.
66. A. N. Dosumu, S. Claire, L. S. Watson, P. M. Girio, S. A. M. Osborne, Z. Pikramenou and N. J. Hodges, *JACS Au*, 2021, **1**, 174-186.
67. S. M. King, S. Claire, R. I. Teixeira, A. N. Dosumu, A. J. Carrod, H. Dehghani, M. J. Hannon, A. D. Ward, R. Bicknell, S. W. Botchway, N. J. Hodges and Z. Pikramenou, *Journal of the American Chemical Society*, 2018, **140**, 10242-10249.
68. N. J. Rogers, H. C. Jeffery, S. Claire, D. J. Lewis, G. Zikeli, N. J. Hodges, S. Egginton, G. B. Nash and Z. Pikramenou, *Nanomedicine*, 2017, **12**, 2725-2740.
69. N. J. Rogers, S. Claire, R. M. Harris, S. Farabi, G. Zikeli, I. B. Styles, N. J. Hodges and Z. Pikramenou, *Chemical Communications*, 2014, **50**, 617-619.
70. Esther M. Surender, S. Comby, B. L. Cavanagh, O. Brennan, T. C. Lee and T. Gunnlaugsson, *Chem*, 2016, **1**, 438-455.
71. Y. S. Yang, K. D. Moynihan, A. Bekdemir, T. M. Dichwalkar, M. M. Noh, N. Watson, M. Melo, J. Ingram, H. Suh, H. Ploegh, F. R. Stellacci and D. J. Irvine, *Biomaterials Science*, 2018, **7**, 113-124.
72. Y. S. Yang, P. U. Atukorale, K. D. Moynihan, A. Bekdemir, K. Rakhra, L. Tang, F. Stellacci and D. J. Irvine, *Nature Communications*, 2017, **8**, 14069.
73. R. Meir, K. Shamalov, O. Betzer, M. Motiei, M. Horovitz-Fried, R. Yehuda, A. Popovtzer, R. Popovtzer and C. J. Cohen, *ACS Nano*, 2015, **9**, 6363-6372.
74. H. Bosshart and M. Heinzelmann, *Annals of Translational Medicine*, 2016, **4**, 438.
75. W. Chanput, J. J. Mes, H. F. Savelkoul and H. J. Wichers, *Food and Function*, 2013, **4**, 266-276.

76. Y. Deng, C. Govers, E. Ter Beest, A. J. van Dijk, K. Hettinga and H. J. Wichers, *Frontiers in Nutrition*, 2020, **7**, 612397.
77. C. E. Hellweg, A. Arenz, S. Bogner, C. Schmitz and C. Baumstark-Khan, *Annals of the New York Academy of Sciences*, 2006, **1091**, 191-204.
78. G. Jimenez-Duran, R. Luque-Martin, M. Patel, E. Koppe, S. Bernard, C. Sharp, N. Buchan, C. Rea, M. P. J. de Winther, N. Turan, D. Angell, C. A. Wells, R. Cousins, P. K. Mander and S. L. Masters, *EBioMedicine*, 2020, **61**, 103039.
79. J. Qualai, L. X. Li, J. Cantero, A. Tarrats, M. A. Fernandez, L. Sumoy, A. Rodolosse, S. J. McSorley and M. Genesca, *PLoS One*, 2016, **11**, e0154253.
80. M. P. Ramprasad, V. Terpstra, N. Kondratenko, O. Quehenberger and D. Steinberg, *Proceedings of the National Academy of Sciences*, 1996, **93**, 14833-14838.
81. R. J. Peach, J. Bajorath, J. Naemura, G. Leytze, J. Greene, A. Aruffo and P. S. Linsley, *Journal of Biological Chemistry*, 1995, **270**, 21181-21187.
82. P. Chhour, J. Kim, B. Benardo, A. Tovar, S. Mian, H. I. Litt, V. A. Ferrari and D. P. Cormode, *Bioconjugate Chemistry*, 2016, **28**, 260-269.
83. M. Rabinovitch, *Trends in Cellular Biology*, 1995, **5**, 85-87.
84. E. Uribe-Querol and C. Rosales, *Frontiers in Immunology*, 2020, **11**, 1066.
85. N. Oh and J.-H. Park, *ACS Nano*, 2014, **8**, 6232-6241.
86. D. Novo and J. Wood, *Cytometry A*, 2008, **73**, 685-692.
87. M. E. C. Lutsiak, D. R. Robinson, C. Coester, G. S. Kwon and J. Samuel, *Pharmaceutical Research*, 2002, **19**, 1480-1487.
88. Y. Yan, K. T. Gause, M. M. J. Kamphuis, C.-S. Ang, N. M. O'Brien-Simpson, J. C. Lenzo, E. C. Reynolds, E. C. Nice and F. Caruso, *ACS Nano*, 2013, **7**, 10960-10970.
89. L. Thiele, B. Rothen-Rutishauser, S. Jilek, H. Wunderli-Allenspach, H. P. Merkle and E. Walter, *Journal of Controlled Release*, 2001, **76**, 59-71.
90. T. Lijster and C. Åberg, *PLoS One*, 2020, **15**, e0242547.
91. S. Tedesco, F. De Majo, J. Kim, A. Trenti, L. Trevisi, G. P. Fadini, C. Bolego, P. W. Zandstra, A. Cignarella and L. Vitiello, *Frontiers in Pharmacology*, 2018, **9**, 71.
92. S. Manikandan, *Journal of Pharmacology and Pharmacotherapeutics*, 2011, **2**, 214-215.
93. R. E. Yanes, D. Tarn, A. A. Hwang, D. P. Ferris, S. P. Sherman, C. R. Thomas, J. Lu, A. D. Pyle, J. I. Zink and F. Tamanoi, *Small*, 2013, **9**, 697-704.
94. J. Yang, L. Zhang, C. Yu, X.-F. Yang and H. Wang, *Biomarker Research*, 2014, **2**, 1.
95. J. Last'ovicka, V. Budinský, R. Spísek and J. Bartůnková, *Cell Immunology*, 2009, **256**, 79-85.
96. R. Gadalla, B. Noamani, B. L. MacLeod, R. J. Dickson, M. Guo, W. Xu, S. Lukhele, H. J. Elsaesser, A. R. A. Razak, N. Hirano, T. L. McGaha, B. Wang, M. Butler, C. J. Guidos, P. S. Ohashi, L. L. Siu and D. G. Brooks, *Frontiers in Oncology*, 2019, **9**, 415.
97. H. H. Gustafson, D. Holt-Casper, D. W. Grainger and H. Ghandehari, *Nano Today*, 2015, **10**, 487-510.
98. A. B. Lyons, *Journal of Immunology Methods*, 2000, **243**, 147-154.
99. B. I. Tarnowski, F. G. Spinale and J. H. Nicholson, *Biotech Histochem*, 1991, **66**, 297-302.
100. J. Olesiak-Banska, K. Matczyszyn, R. Zaleśny, N. A. Murugan, J. Kongsted, H. Ågren, W. Bartkowiak and M. Samoc, *The Journal of Physical Chemistry B*, 2013, **117**, 12013-12019.
101. P. R. Callis, *Annual Review of Physical Chemistry*, 1997, **48**, 271-297.
102. W. Zhang, M. Caldarola, X. Lu and M. Orrit, *ACS Photonics*, 2018, **5**, 2960-2968.
103. Y. Zhang, D. J. S. Birch and Y. Chen, *Applied Physics Letters*, 2011, **99**, 103701.

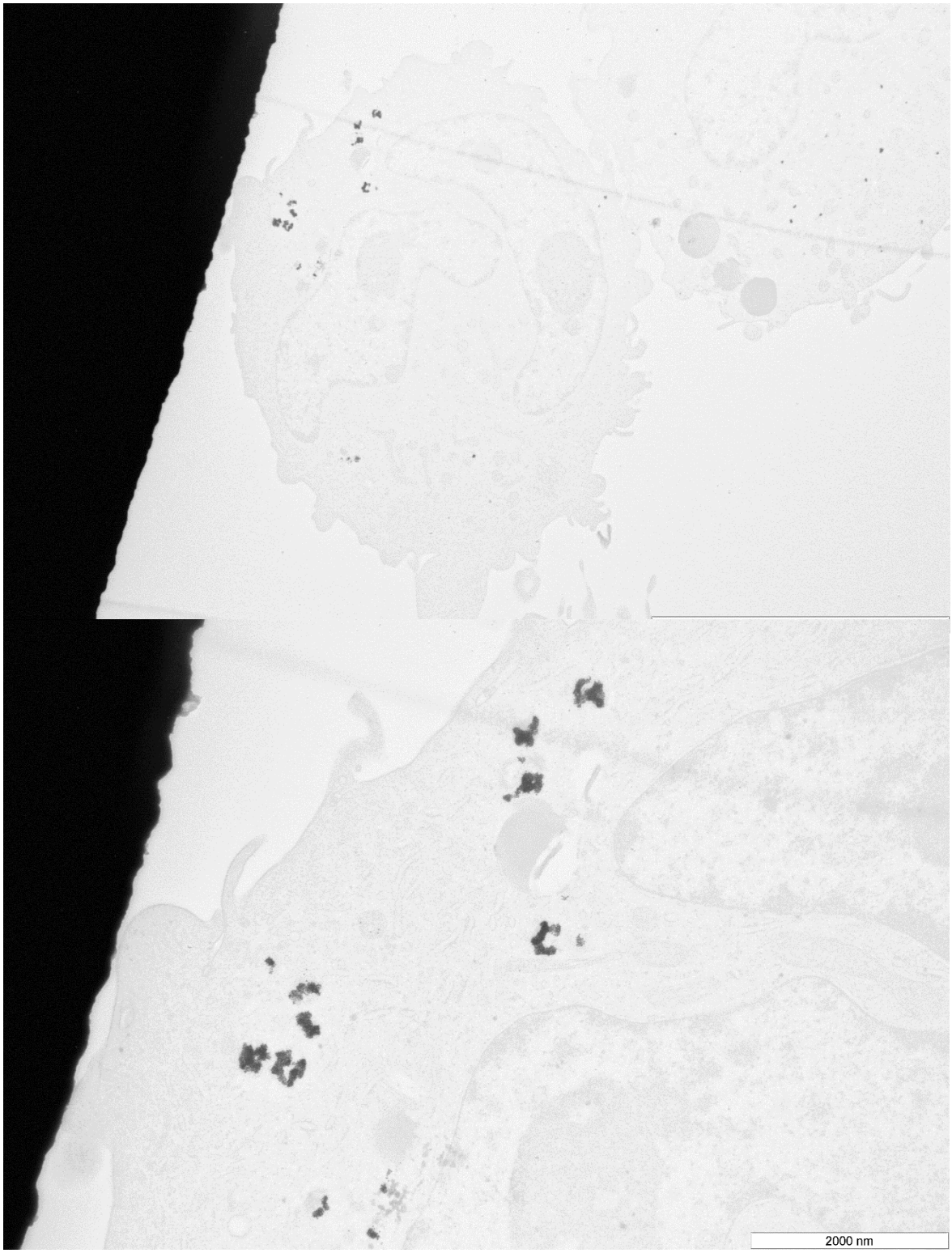
4.7 Appendix

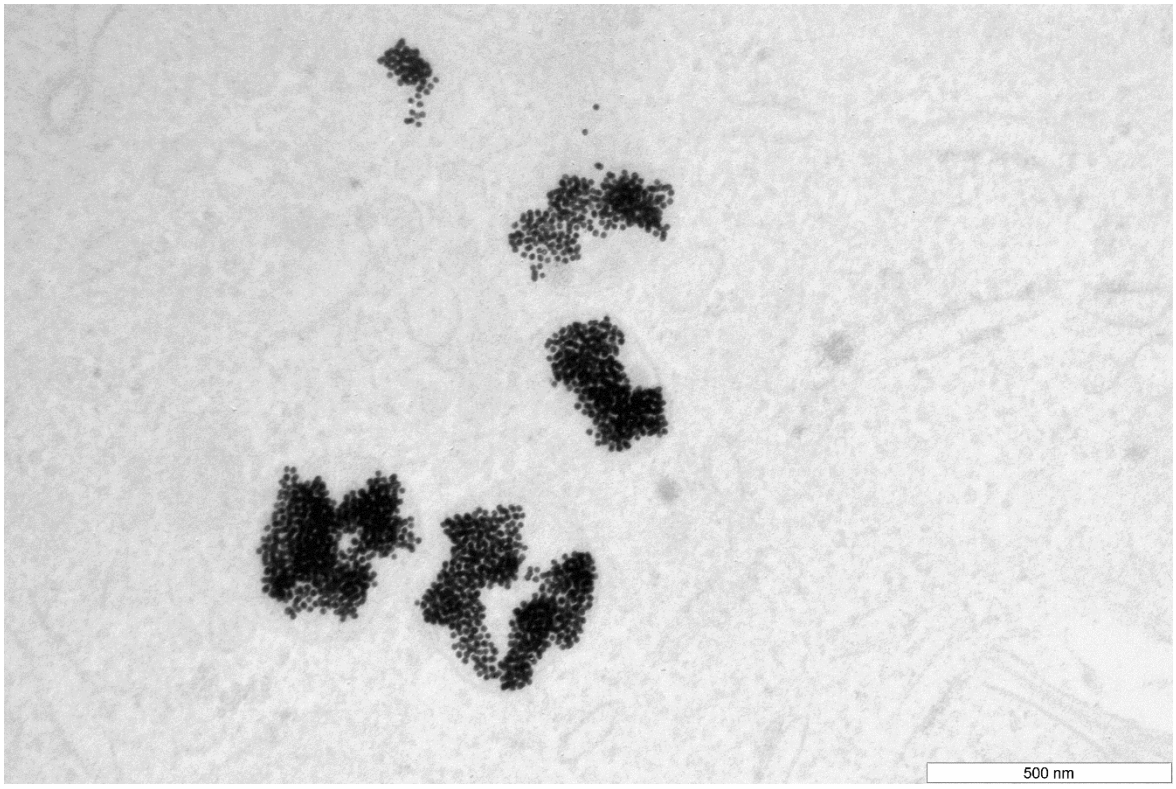
4.7.1 Gating Strategy for Live Single Cell Analysis with Flow Cytometry



Appendix Figure 4.1 – Gating strategy to identify live single cells during flow cytometry experiments. Firstly cells are identified and debris removed from analysis on a side scatter area vs forward scatter area plot (left), before identifying single cells from doublets on a forward scatter height vs forward scatter area plot (middle). Finally, dead cells are excluded from analysis on a side scatter area vs. APC-Cy7 plot, where dead cells are identifiable from nuclear staining with a viability dye (right).

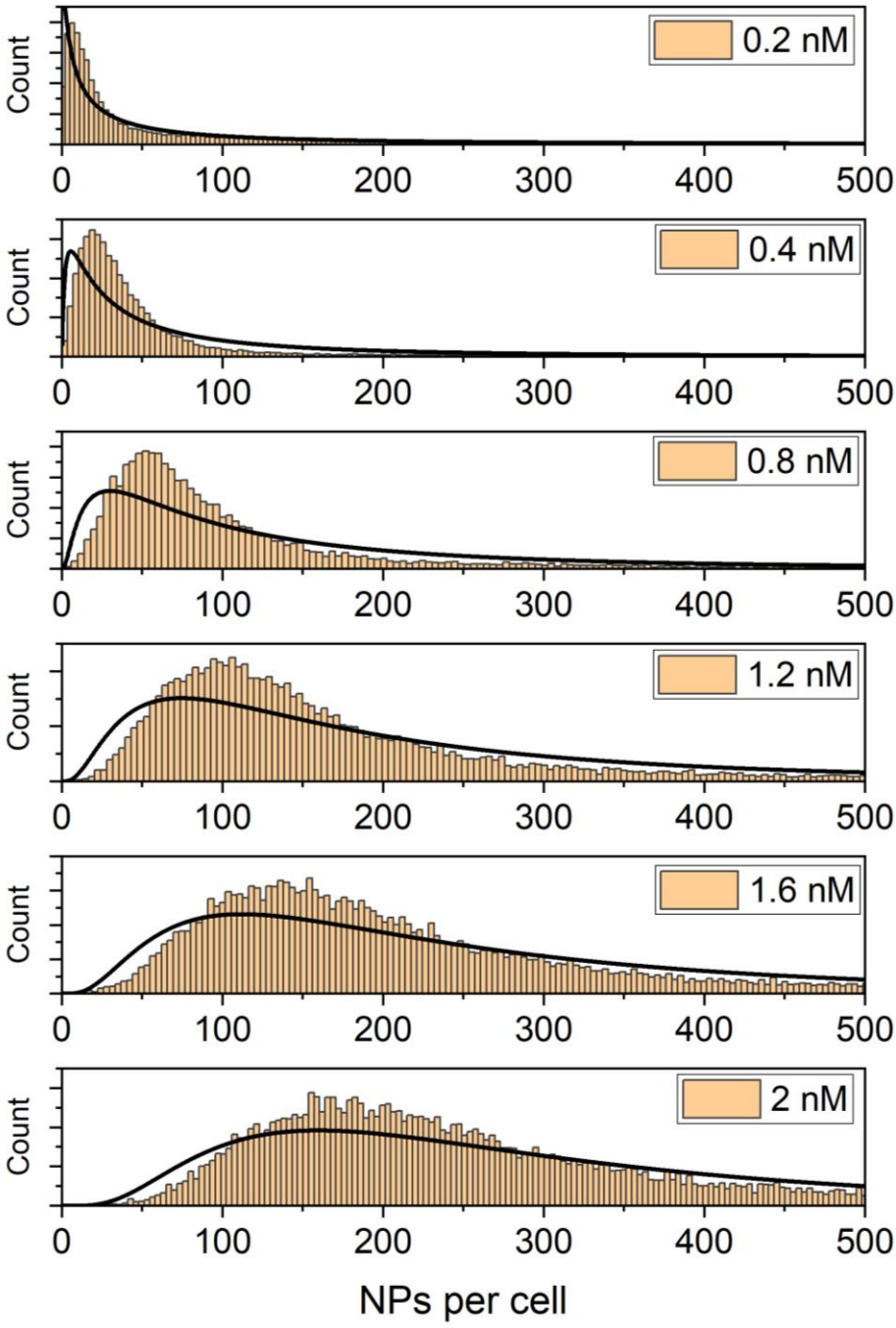
4.7.2 Studying $EuQuin_2S$-AuNP uptake by TEM in M1 Macrophages – Additional Images





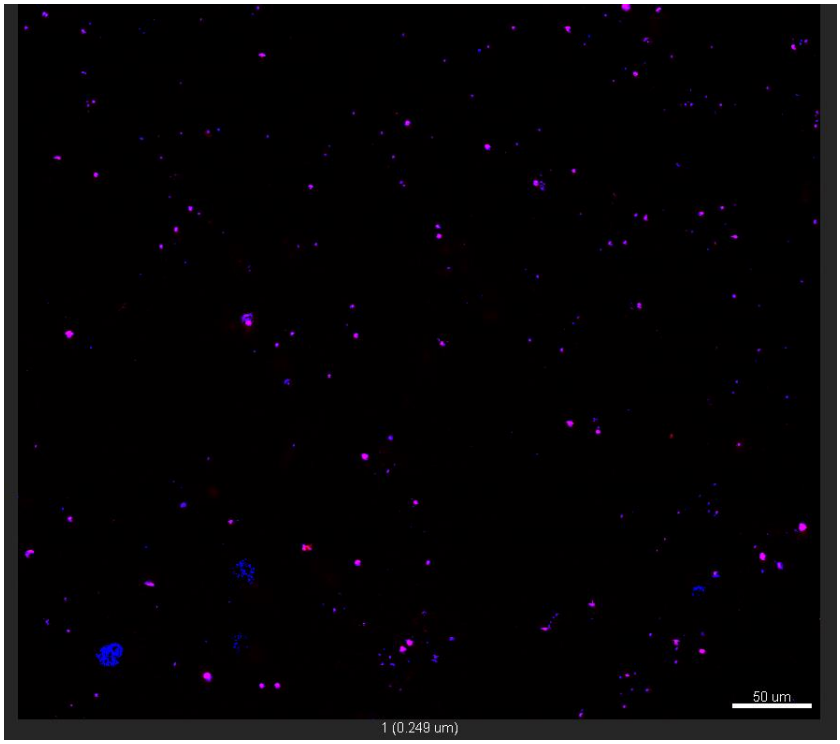
Appendix Figure 4.2 Additional images of $EuQuin_2S$-AuNPs located within endosomes of M1 macrophages after their treatment for 20 hours at a concentration of 1 nM.

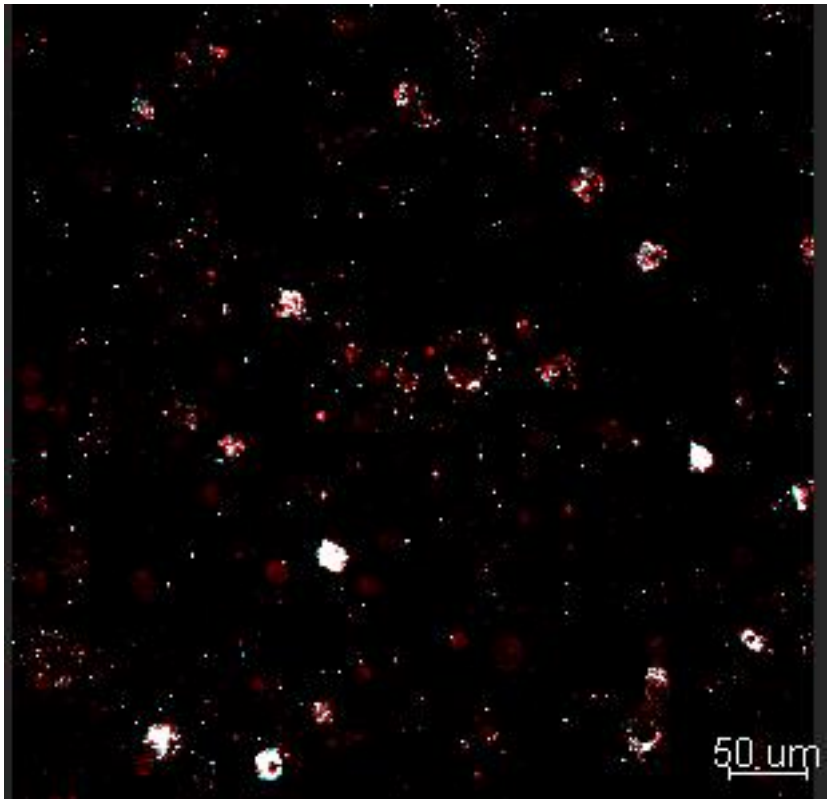
4.7.3 Log-normal Distribution Fitting of THP-1 Monocytes



Appendix figure 4.3 Log-normal distribution fitted to the number of EuQuin$_2$S-AuNPs per THP-1 monocyte at each treatment concentration after 4 hours.

4.7.4 Two-Photon Confocal Micrscopy Imaging of EuQuin$_2$S-AuNP treated HeLa Cells





Appendix Figure 4.4 Live cell imaging of EuQuinSH-Au13 NP uptake in HeLa cells, treated with a concentration of 5 nM for 20 hours. Overlay of emission from the blue (Quinoline) and red Europium) channels. λ_{exc}= 940 nm, λ_{em} = 420-470, 600-670 nm.

Chapter 5: General Conclusions

5.1 General Conclusion and Future Work

In this work, the synthesis and characterisation of lanthanide coated gold nanoparticles has been shown, as well as their cellular uptake and long-term fate in cells with CyTOF, and their suitability as multimodal cellular labels for monitoring monocyte differentiation into macrophages and dendritic cells was assessed. With the use of STEM and EELS, we have provided further evidence that europium complexes, $EuQuin_2SH$ and EuSH, are attached to AuNP surfaces and held away from the surface by the distance of their organic ligands. The organic ligand of lanthanide complexes also affects their cellular uptake, with shorter chain TbS-AuNPs taken up in higher quantities than $EuQuin_2S$-AuNPs. Further evidence of a binding event at the AuNP surface has been demonstrated through ITC analysis and determined association constants of $EuQuin_2SH$ and TbSH binding to AuNPs. The effect of fluorinated surfactants Zonyl FSA and TFD, as well as a PEG polymer on the photophysical properties of $EuQuin_2S$-AuNPs was studied. These surfactants/polymers only had minor effects on the loading and photophysical properties, however Zonyl FSA and TFD both enhanced the cellular uptake in HeLa cells.

Using CyTOF, the detection of both europium/terbium and gold from $EuQuin_2S$-AuNPs and TbS-AuNPs was shown respectively. This ratiometric detection allowed the quantification of the number of lanthanide complexes per NP, yielding similar results to ICP-MS analysis. $EuQuin_2S$-AuNP uptake was also quanitified by analysing the signal from both europium and gold channels in THP-1 monocytes, which supported the findings that NP uptake did not increase with concentration in the population with high uptake.

The heterogeneity of $EuQuin_2S$-AuNP uptake in HeLa cells and mononuclear phagocytes (monocytes, macrophages and dendritic cells) was studied. The uptake in HeLa cells and

dendritic cells was best described by a log-normal distribution. Uptake in monocytes and macrophages was bimodally distributed, likely due to phenotypical heterogeneity within the cell populations. Using CyTOF's high sensitivity, the depletion of $EuQuin_2S$-AuNPs in proliferating HeLa cells and monocytes was studied over multiple cell divisions. Inheritance of $EuQuin_2S$-AuNPs was asymmetric in both HeLa and monocytes but the extent of exocytosis was cell-type dependent; $EuQuin_2S$-AuNPs were exocytosed from monocytes significantly, but not in HeLa cells. $EuQuin_2S$-AuNPs were detected in macrophages and dendritic cells that had differentiated from monocytes by CyTOF, demonstrating their capabilities as cellular labels for fate mapping immune cells in cytometry experiments. $EuQuin_2S$-AuNPs were also detected in macrophages by TEM and confocal microscopy, where we preliminarily showed two-photon excitation of $EuQuin_2S$-AuNPs.

Future work should further study the capabilities of $EuQuin_2S$-AuNPs as multimodal cellular labels. As $EuQuin_2S$-Zonyl-AuNPs had a 5-fold higher uptake in HeLa cells than $EuQuin_2S$-AuNPs, their interactions and uptake with monocytes should be explored. Higher cellular uptake may increase the length of time they can be detected for in cells or allow shorter incubation treatments or lower initial dosing. The ability of detection of $EuQuin_2S$-AuNPs in mononuclear phagocytes by CT should be explored to give more applicability to whole animal imaging studies. We are actively engaged in collaborations to further study two-photon excitation of $EuQuin_2S$-AuNPs and hope to confirm their suitability for deeper penetration luminescence imaging agents. We are also pursuing further studies of $EuQuin_2S$-AuNPs and EuS-AuNPs by STEM and EELS. Future work should focus on attempting to quantify the number of europium atoms held at the surface of single AuNPs to compare with data determined from ICP-MS and CyTOF experiments.

More generally, we hope that our demonstration of using CyTOF as a highly sensitive, quantifiable technique for measuring cellular uptake helps to increase its use in studying AuNP-cell interactions. Our longer-term studies into NP content within cells after initial

treatment outline a framework, that with minor improvements, may aid the field with longstanding questions regarding the fate of NPs in cells over time and the extent to which exocytosis occurs under the selected conditions. These investigations may be particularly useful in the study of cytotoxic AuNPs, where cell death, phenotype and cytokine profiling alongside AuNP quantification over time could provide further understanding of NP-cell interactions in terms of toxicity.

Chapter 6: General Experimental

6.1 Materials

All chemicals and solvents were purchased from Sigma Aldrich or Fischer Scientific and reactions were completed under inert atmosphere using a Schlenk line, with solvents dried using 3Å molecular sieves.

6.2 Techniques and Instrumentation

6.2.1 NMR and Mass Spectrometry

^{1}H and ^{13}C spectra were recorded on Bruker AVIII300 and AVIII400 instruments and spectra were processed using MestreNova. A Waters Micromass LCT-TOF mass spectrometer was used for all electrospray mass spectrometry, using a nitrogen laser in positive electrospray mode.

6.2.2 UV-Vis spectroscopy

A Varian Cary 60 was used to conduct UV-Vis absorption spectroscopy with a rate of 300 nm min^{-1} for a range of 200-800 nm at room temperature. The baseline was corrected using a solvent that matched the sample being analysed. The samples were placed in quartz cuvettes with a path length of 1 cm and extinction coefficients were determined using the Beer-Lambert law.

6.2.3 Dynamic Light Scattering and Zeta potential

A Malvern Zetasizer nano ZSP was used to acquire all Dynamic Light Scattering (DLS) and Zeta Potential Measurements. DTS0012 1 cm disposable cuvettes were used for size analysis and folded capillary cells were used for Zeta Potential measurements. The samples were analysed according to a standard operating procedure with the following settings: Refractive index: 1.33, absorption: 1.00, dispersant: water, temperature: 25 °C. The instrument was allowed to equilibrate at 25 °C for 180 seconds prior to the

measurements. For DLS samples, 5 runs were recorded, each with 15 measurements and the average was taken. For Zeta potential samples, 10 runs were recorded with between 10-100 measurements. Data was recorded and processed using the Malvern Zetasizer software. Polydispersity index was calculated by dividing the standard deviation (σ) of the particle diameter by twice the mean particle diameter (a):

$$PDI = (\frac{\sigma}{2a})^2$$

6.2.4 Transmission Electron Microscopy

Samples were acquired at the centre for electron microscopy at the University of Birmingham using a JEOL 1200 EX TEM fitted with a Gatan camera. Samples were prepared on 200-mesh formvar-coated copper grids. Images were captured using Gatan software before analysis using Image J.

6.2.5 Isotherm Titration Calorimetry

ITC was performed using a MicroCal PEAQ-ITC Malvern Panalytical instrument. The instrument cell was equilibrated for 30 min at 25 °C and this temperature was maintained throughout the experiment. The heat changes were recorded as the differential power required to maintain a zero-temperature difference between the sample and reference cells. The titration began with an initial injection of 0.4 µL followed by 19 consecutive 2 µL injections at 150 second intervals at a rate of 0.5 μLs^{-1} with a stirring speed of 750 rpm maintained throughout the experiment.

6.2.6 SuperSTEM

Samples were prepared at the University of Birmingham and posted to the SuperSTEM laboratory at the EPSRC National Research Facility for Advanced Electron Microscopy (Daresbury, UK). Samples were dropcasted onto ultra-thin carbon/gold supports. STEM imaging (HDAAF/BF) and EELS was acquired with a Nion UltraSTEM 100 instrument

equipped with a Gatan Enfina Spectrometer and Metlin DED Quantum Detectors for EELS. Images were acquired at 100 kV acceleration voltage, equipped with a probe aberration corrector. The probe size was <0.9 Å. The convergence semi-angle was 27 mrad for HDAAF/BF and 36 mrad for EELS. During data processing, EELS was denoised with principle component analysis.

6.2.7 Steady-State and Time-resolved Spectroscopy

Emission and excitation spectra were recorded on Edinburgh Instruments FLS920 fluorescence spectrometer with a 450 W xenon arc lamp illumination source and a R928 visible Hamamatsu photomultiplier tube. Appropriate cut-off filters and a cuvette with a 1 cm path length were used for all experiments. Data was recorded on Edinburgh F900 software. Luminescence lifetime experiments were carried out using an Edinburgh Instruments microsecond flashlamp as the excitation source. A time-correlated single-photon counting module was used to record data using a R928 visible Hamamatsu photomultiplier tube. Lifetimes were fitted using Edinburgh Instruments FAST software and fitted to single components unless stated otherwise with an error of ± 10%. Chi-squared (χ^2) values of 1-1.4 were achieved for all luminescence lifetime fittings. When deuterated solvents were used, samples were freshly prepared straight before analysis.

An integrated sphere attachment on an Edinburgh Instruments FLS920 fluorescence spectrometer was used to perform quantum yield (φ) experiments. This method involved comparing a reference standard to the sample, as outlined in the equation below. The reference standard used was the same solvent the samples was dissolved in.

$$\varphi = \frac{E_s - E_r}{S_r - S_s}$$

Where E_s is emission from the sample, E_r is emission from the reference, S_r is scattering from the sample and S_r is scattering from the reference.

6.2.8 ICP-MS

ICP-MS was carried out at the University of Warwick using an Agilent 7900 ICPMS instrument equipped with an integrated auto-sampler. Calibration standards with concentrations of 0, 1, 2.5, 5, 10, 25, 50, 100, 250, 500 and 1000 ppb were made up the day before each experiment and acquired on the day of the experiment. Metal concentrations were determined using PlasmaCal calibration standards (QMX laboratories) with R^2 values > 0.999 from linear regression analysis of linear calibration plots. Samples were run through the instrument in 4% HNO_3 solution.

6.2.9 Mass Cytometry (CyTOF)

All samples were acquired on a Helios™ Mass Cytometer – CyTOF ® (Fluidigm). On each day an experiment was ran, the instrument was calibrated with the internal calibration solution followed by a nanoparticle calibration described in 3.10.6. Each sample was mixed with EQ Four Element Calibration Beads (PN 201078) then acquired with an injection speed of 0.5 μLs^{-1}. Data was analysed using FlowJo version 10.7 and Origin Pro.

6.2.10 Flow Cytometry

Flow cytometry analysis was conducted on a BD LSR Fortessa X-20 Cell analyser BD FACSDiva v.9 software for data acquisition. Cells were labelled with the antibody panel outlined in 4.5.4. Compensation controls were performed for each fluorophore. Data was analysed using FlowJo version 10.7 and Origin Pro.

6.2.11 Centrifugation of Cells

During cell culture and before cell fixation, all cells were centrifuged at 300 g for 5 min. After cell fixation, cells were centrifuged at 800 g for 5 min.